The Halogen Bond: X-Ray Crystallography and Multinuclear Magnetic Resonance Investigation

Patrick Szell

A thesis submitted in partial fulfillment of the requirements for the
Doctorate in Philosophy degree in Chemistry

Department of Chemistry and Biomolecular Sciences
Faculty of Science
University of Ottawa

Graphical Abstract.

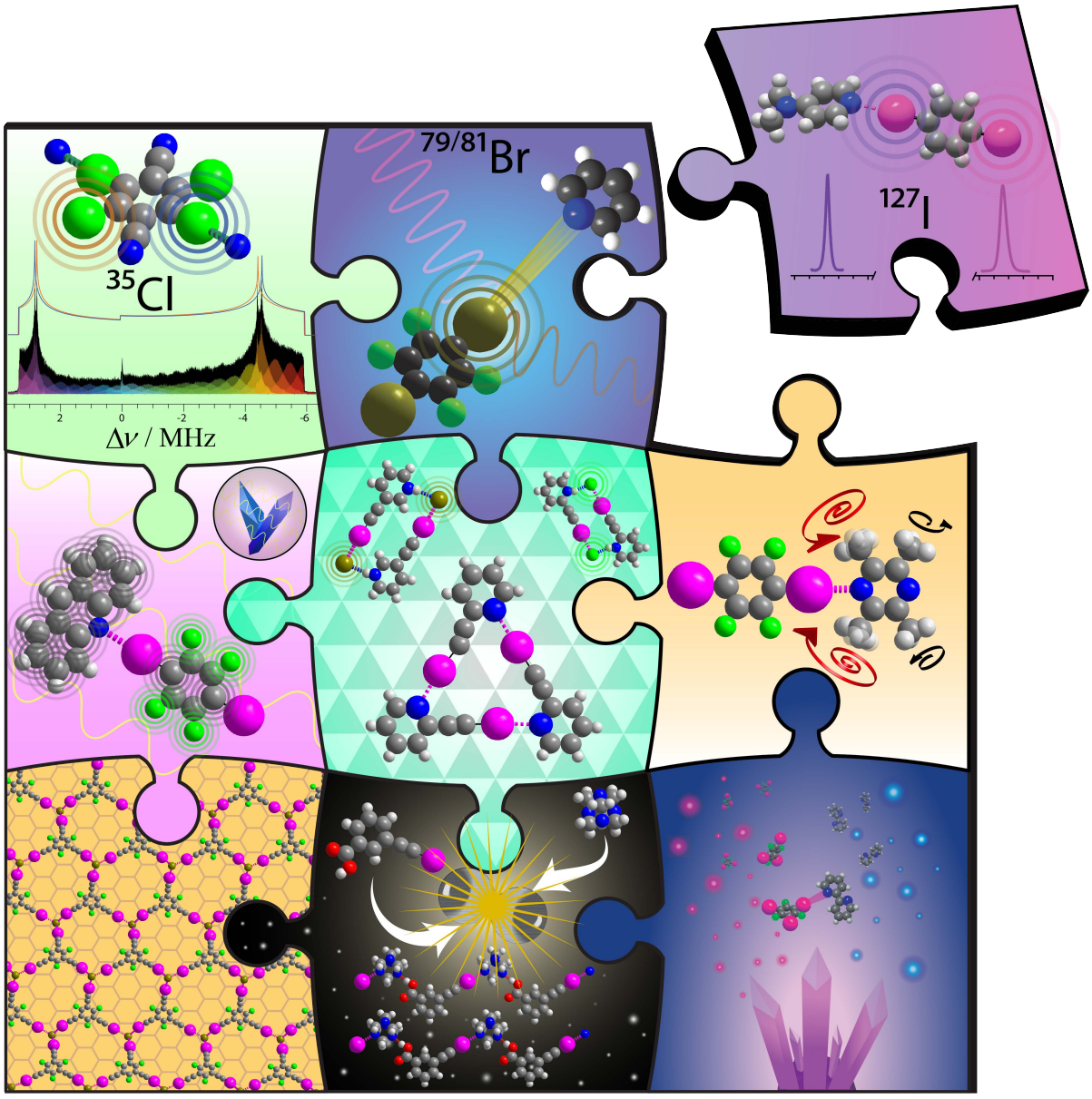

Abstract.

The halogen bond has recently risen in prominence as a non-covalent interaction for use in supramolecular chemistry, allowing for the rational design of materials, pharmaceuticals, and functional molecules. The occurrence of the σ-hole opposite to the C-X covalent bond (X = F, Cl, Br, I) renders the halogen bond a highly directional and tuneable interaction, offering desirable features to crystal engineers. The halogen bond can be divided into its two components: the halogen bond donor bearing the halogen atom, and the electron-rich halogen bond acceptor. In this thesis, we investigate the nature of the halogen bond, its role in supramolecular assembly and impact on the local dynamics, along with developing synthetic methods to prepare this class of materials. We begin by fully characterizing the halogen bond donor by using ^{35}Cl ultra-wideline solid-state nuclear magnetic resonance (NMR) spectroscopy on a series of single-component chloronitriles exhibiting the C-Cl···N halogen bond. We then perform the first modern nuclear quadrupole resonance (NQR) investigations of the halogen bond, observing the $^{79/81}$Br and ^{127}I nuclei in a series of cocrystals exhibiting the C-Br···N and C-I···N halogen bond, respectively. Computational results attribute the observed increases in the quadrupolar coupling constants (C_Q) to a reduction in the carbon-halogen σ-bonding contribution to V_{33} and an increase in the lone-pair and core orbital contributions, providing the first model of the electronic changes occurring on the halogen bond donor upon the formation of the halogen bond. Attention is then turned on characterizing the halogen bond acceptor and its surrounding environment, beginning by investigating a solid-state NMR approach relying on the ^{19}F nucleus to characterize perfluorinated cocrystals. This strategy has reduced analysis times from hours to minutes while providing higher sensitivity and resolution, with the resulting chemical shifts permitting the unambiguous identification of the halogen bond and allowing for the refinement of X-ray crystal structures. The halogen bond acceptor is then investigated in a series of

isomorphous dimers exhibiting both the halogen bond and hydrogen bond in the C≡C-I···X-···H-N^+ motif, revealing the halogen bond's relative contribution to the electric field gradient increasing in the order of Cl^- > Br^- > I^-, contrasting the contributions of the hydrogen bond. We then explore the impact of the halogen bond on the surrounding environment, using the rotating methyl groups of 2,3,5,6-tetramethylpyrazine as a model. Upon the introduction of a halogen bond, we observe a reduction in the rotational energy barrier of 56% on average, overshadowing the 36% reduction observed in the hydrogen bonded cocrystals. This is the first instance of the halogen bond directly catalyzing the local dynamics, coining the term "dynamics catalyst". These results provide an effective strategy of enhancing the dynamics in molecular systems, such as molecular machines, supramolecular catalyst, as well as correcting the faulty dynamics encountered in diseased proteins. The role of halogen bonding in crystal engineering is then explored, reporting the first supramolecular triangle, a series of discrete charged dimers, and supramolecular architectures built from 1,3,5-tri(iodoethynyl)-2,4,6-trifluorobenzene, with the potential of creating fully organic porous structures for gas absorption. Mechanochemistry is then investigated as a synthetic method, allowing for the preparation of cocrystals featuring 3-iodoethynylbenzoic acid as the donor, with the resulting structures exhibiting concurrent halogen and hydrogen bonding. Mechanochemical ball milling is shown to reduce preparation times of powdered cocrystals from days to a single hour, while using a fraction of the organic solvent. Lastly, we pioneer cosublimation as a solvent-free synthetic technique for rapidly preparing halogen bonded cocrystals, yielding quality single crystals within a few hours, and a microcrystalline product within 15 minutes. Among its advantages, cosublimation offers a significant acceleration of discovery, while eliminating the environmental footprint associated with conventional synthetic methods.

Acknowledgements.

The University of Ottawa has been my home for many years and is thanked for providing a quality environment for higher learning, as well as hosting a world class research facility. I remain grateful to all the resources that were made available to me, including workshops, an abundance of services, and friendly supporting staff. The Graduate and Postdoctoral Studies is also thanked for awarding me with several scholarships that have helped me throughout my graduate studies. In particular, the student mobility bursary had a contributing role in allowing me to study in France, and I remain thankful to its availability. I also thank the Natural Sciences and Engineering Research Council of Canada for their support through scholarships.

An enormous thank you is given to my supervisor Dr. David Bryce, who has provided me with the environment and opportunities that have allowed me to flourish to the scientist I am today. I am grateful for your endless support in all my endeavors, no matter how crazy they may be. What comes to mind is your support for my idea of pulling a tube filled with silver cyanide through the NMR spectrometer in order to acquire the ^{109}Ag spectrum. Further, I am also thankful for all the conferences that you have sent me to, in addition to allowing me to bring my research abilities to the international scene, in both Italy and France. My graduate studies have been an extremely pleasant experience stemming from your friendship and leadership.

The NMR facility at the University of Ottawa has been key to the success of these projects. The facility manager Dr. Glenn Facey is thanked for being remarkably knowledgeable in NMR spectroscopy, which has helped me throughout my graduate studies. Your expertise in deuterium NMR was integral to the success of Chapter 9, and I thank you for all the time you have given me. Dr. Eric Ye and Dr. Peter Pallister are thanked for their helpful discussions which has furthered my understanding of the experimental and technical aspects of NMR spectroscopy, in addition to their assistance in performing the experiments. To Dr. Victor

Terskikh, you have made my experience at the 900 MHz NMR facility rewarding and educational. For all the times you have assisted me with using the equipment, I thank you.

To the X-ray facility staff, Dr. Jeffrey Ovens, Dr. Bulat Gabidullin, Dr. Ilia Korobkov, and Dr. Tara Kell, I thank you all for your time, knowledge, and showing me the basics of X-ray crystallography. All your trainings and assistance has allowed me to learn how to perform my own single crystal X-ray and powder X-ray diffractions, which has greatly accelerated the rate of discovery during my graduate studies. Further, I give a special thanks to Dr. Bulat Gabidullin, which has solved and refined a large portion of the crystal structures reported in this thesis.

I wish to thank Dr. Pierangelo Metrangolo for allowing me to perform research in his laboratory over the summer of 2015. The time spent in Milan has been a privilege and allowed me to further my abilities in synthetic chemistry. The excellent researchers in the group, Dr. Giuseppe Resnati, Dr. Gabriella Cavallo, Dr. Giancarlo Terraneo, Dr. Luisa Lascialfari and the others, are also thanked for their various contributions that has made my time in Milan both educational and enjoyable.

I also wish to express my gratitude and thank Dr. Marc Fourmigué who has allowed me to develop cosublimation in his laboratory during the fall of 2017 to winter 2018. My time in Rennes was an incredible experience, and your knowledge in crystal engineering is inspiring. To Dr. Olivier Jeannin, you are an exceptionally hard worker, and I thank you for all of your help. To Fabien Lucas, Lambert Sicard, Giseok Oh, and Asia-Marie Riel, thank you for your many contributions and friendships.

I am thankful to all my past and current colleagues for their friendship and helpful discussions. To Fred, Kevin, and Jasmine, you have presented me with the foundations of NMR spectroscopy as well as general research techniques, to which I remain thankful. Collette, you

have an enormous amount of patience, which has been proven ten-fold over the collection of your single crystal NMR data. Scott, I remain impressed as to how you manage to balance graduate studies, military life, and still show up for work at 7 am. César, your skills in NMR spectroscopy are inspiring, and will surely bring you great success. Vijith, who I first met in Milan, your talents in crystal engineering are remarkable, and I thank you for our many discussions. Estelle, Vincent, Carl, and Ryan, it was a pleasure to work alongside you and I hope you have enjoyed listening to the top 1500 best techno songs of 2007.

The work featured in this thesis would not have been possible without the help of many brave students, which performed research under my guidance. To all these students, namely Shaina Gabriel, Scott Zablotny, Stephen Harrigan, Shirley Wan, Russell Gill, Vincent Nguyen, Ludovic Brunet, Cedric Farthouat, Tanya Yeuchyk, Mathilde Papillon, Julien Dragon, Justine Zavattero, Estelle Caron-Poulin, Vincent Morin, and Lorraine Grebert, I thank you all for your hard work, the time you have spent in the lab, and your patience. It has been a privilege to work with you all.

I wish to thank Dr. Tom Woo and his group for maintaining the Wookie cluster. In addition, Dr. Hartmut Schmidt from Compute Canada is also thanked for his assistance with the HPCVL. I also thank my thesis committee members for taking the time in reviewing my thesis and offering their guidance.

Lastly, I thank my family and friends for their love, continued support, and patience.

Statement of Originality.

I certify that the research presented in this thesis is of my own work, and all referenced work performed by others is made explicit using standard methods. As this thesis contains ten scientific articles, the acknowledgements to other authors and the copyright permissions are presented before each article. My supervisor, Dr. David L. Bryce, is acknowledged for having contributed to the revisions and editing of the manuscripts presented here, along with scientific guidance and support.

Table of Contents

List of Figures in the Introductions, Theory, and Conclusions

Part 1 – Introduction & Theory

Part 2 – Investigating the Halogen Bond Donor

List of Recurring Symbols and Abbreviations.

a, b, c	Crystallographic unit cell lengths
α, β, γ	Crystallographic unit cell angles
$\alpha_E, \beta_E, \gamma_E$	Euler angles relating the orientation of the EFG tensor to the CSA tensor
γ_L	Gyromagnetic ratio
δ_{iso}	Isotropic chemical shift
δ^+, δ^-	Partial positive and negative charge, respectively.
η	Quadrupolar asymmetry parameter
$\theta_{R\text{-}X\cdots Y}$	Halogen bond angle relative to the R-X···Y axis
κ	Chemical shift tensor skew
λ	Wavelength
ν_L	Larmor frequency
ν_{MAS}	Magic angle spinning frequency
ν_Q	Quadrupolar coupling frequency
ν_R	Resonant frequency
σ_{CS}	Nuclear shielding
σ-hole	Area of positive electrostatic potential associated with the halogen bond donor
τ	Spin echo delay
Ω	Chemical shift tensor span
ADF	Amsterdam Density Functional
DFT	Density functional theory
CPMAS	Cross-polarization magic angle spinning
CPMG	Carr-Purcell-Meiboom-Gill
CSA	Chemical shift anisotropy
C_Q	Quadrupolar coupling constant
d_{vdW}	van der Waals radius
$d_{x\cdots y}$	Halogen bond length
EFG	Electric field gradient
h	Planck constant
IR	Infrared

k	Boltzmann constant
MAS	Magic angle spinning
NLMO	Natural localized molecular orbital
NMR	Nuclear magnetic resonance
NQR	Nuclear quadrupole resonance
*p*DITFB	1,4-diiodotetrafluorobenzene
QCPMG	Quadrupolar Carr-Purcell-Meiboom-Gill
PXRD	Powder X-ray diffraction
RF	Radiofrequency
R_{XB}	Normalized distance parameter
SCXRD	Single crystal X-ray diffraction
SSNMR	Solid-state nuclear magnetic resonance
*sym*TFTIB	1,3,5-trifluoro-2,4,6-triiodobenzene
*sym*TIETFB	1,3,5-tri(iodoethynyl)-2,4,6-trifluorobenzene
μ_o	Vacuum permeability constant
V	Unit cell volume
VOCS	Variable offset cumulative spectral acquisition
Z	Crystallographic formula unit
ZORA	Zeroth order regular approximation

Part 1 – Introduction & Theory
Chapter 1 – Introduction

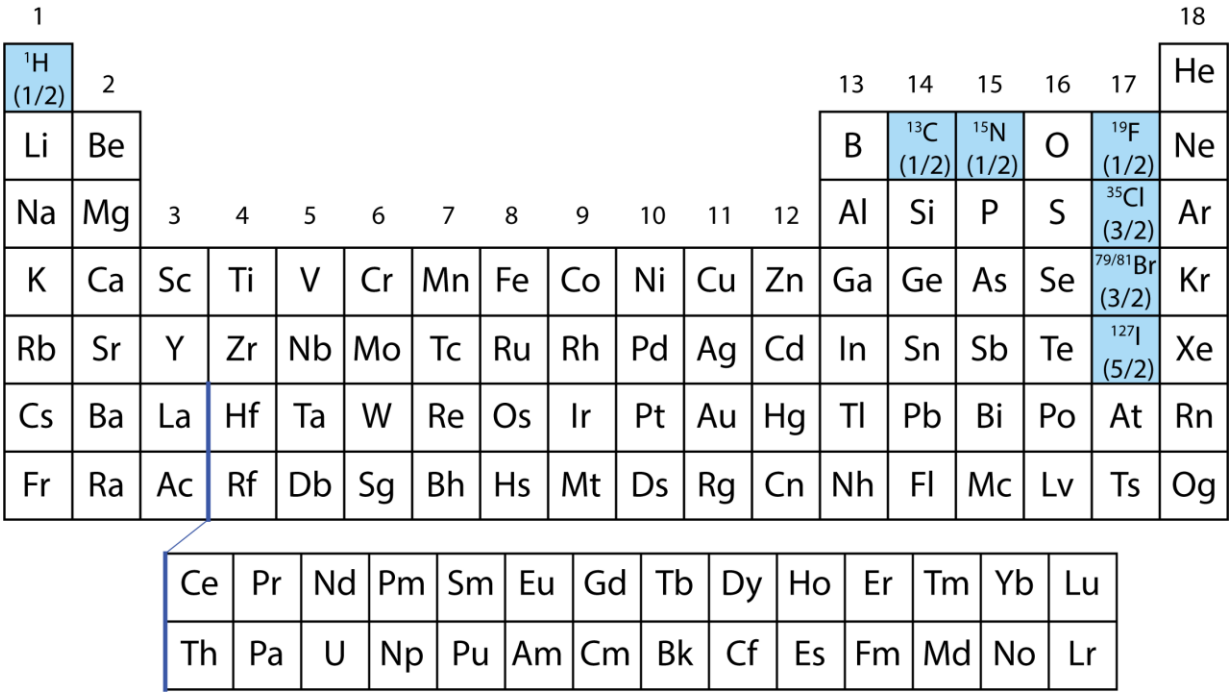

Figure 1.1.1. Periodic table of elements. The group numbers are given above each column, and the light blue denote the isotopes of interest in this thesis, with their nuclear spin given in parenthesis.

1.1 - The chemical bond.

The periodic table shown in Figure 1.1.1 is a beautiful result of centuries of human ambition and dedication towards chemistry. The elements on the periodic table can participate in chemical bonds, thereby forming molecules. The most commonly recognized chemical bond is named the *covalent bond*, which involves the sharing of electrons between two atoms.[1] The covalent bond can be described using a simple Lewis dot structure, which involves the contribution of at least one electron from each atom. When more than one electron is shared between both atoms, a higher order bonding is achieved, forming: double bonds (e.g., alkenes),

triple bonds (e.g., alkynes), and even the quadruple bonds observed in transition metal complexes.[2,3] The sharing of electrons can be described quantum mechanically through the overlap of atomic orbitals, creating molecular orbitals. When two atomic orbitals overlap in a linear fashion, they form σ bonds, whereas the overlap of atomic orbitals in a side-to-side fashion form π bonds. For instance, when an acetylene molecule (H-C≡C-H) is described in context of the Lewis dot structure, the first sharing of the electrons between the carbon atoms forms the σ-bond, with the remaining two overlapping *p*-orbitals forming the two π-bonds. If the overlapping atomic orbitals were out of phase, they would generate σ* and π* antibonding orbitals, which occupy a higher energy level than the more stable σ-bond and π-bond. The strength of the covalent bond therefore increases with the degree of unsaturation, with a C-C bond having a dissociation energy of 276 kJ/mol and a length of 1.53 Å, the C=C bond having a strength of 472 kJ/mol and a length of 1.34 Å, and the C≡C bond having a strength of 628 kJ/mol and a length of 1.20 Å.[1,4]

Chemical bonding is not limited to the sharing of electrons, however. An ionic bond is an example where one atom (electron donor) transfers the electrons to another atom (electron acceptor). Following the transfer of electrons, both atoms are charged, causing the attraction between both species through Coulombic forces. The dative bond is another example of an unequal sharing of the electrons, which is where one atom provides both electrons in the bond.[5] While this remains the tip of the iceberg in terms of the types of covalent bonding, the rudimentary concept of atoms and bonding largely defines molecules. With an array of elements on the periodic table, with each carrying unique properties, it is no surprise that the world of chemistry holds many opportunities.

1.2 - The non-covalent bond.

Chemistry is, admiringly, much more than just bonds connecting a variety of elements. Not only do atoms interact *via* covalent bonding, but they can also interact without sharing or losing their electrons, which are known as *non-covalent interactions*.[6] These non-covalent interactions vary in strength and nature, but can generally be explained using Coulomb's law of electrostatics: positive (+) and negative (-) attract, while same signs repel.[7] These electrostatic interactions can arise between charged atoms, such as Na^+ and Cl^-, but can also occur between partially charged atoms, labelled δ^+ and δ^-. A covalent bond between atoms of sufficiently different electronegativities can lead to the formation of a permanent dipole moment in the molecule. These dipole moments can then interact repulsively or attractively, forming the dipole···dipole interaction. These dipole···dipole interactions are significantly weaker than a covalent bond, with interaction energies on the order of several kJ/mol depending on the geometry and size of the dipole. An instantaneous dipole can be formed by dispersion which changes the electric field of an atom and induces the formation of a partial charge. The instantaneous formation of a dipole consists of the London dispersion forces. Further, a dipole can induce the formation of a partial charge through the polarization of an adjacent atom, named the Debye force. While weak in nature, these dipole···dipole interactions make up the van der Waals interactions, and have been known to steer the formation of molecular assemblies. Charge-transfer complexes are another type of non-covalent interaction, which has been attributed to a partial transfer of the electrons occurring between an electron donor and an electron acceptor.[8,9] The resulting interaction yields a strong attractive force that can be used in molecular assembly.[10,11]

The hydrogen bond has been featured in supramolecular chemistry, which occurs between an electrophilic hydrogen atom and a nucleophile.[12] Given its ubiquity in organic molecules, it has been widely involved in natural processes, such as in the structures of DNA and proteins,[13] and has been exploited in synthetic chemistry,[14] including pharmaceutical and material sciences.[15] While simple in appearance, the nature of the hydrogen bond has received a significant amount of attention. Amongst the theoretical description of the hydrogen bond includes contributions from electrostatics, dispersion, polarization, and molecular orbitals.[16,17] However, a "specialized" non-covalent interaction is not unique to the hydrogen atom, with most elements on the periodic table having a subset of non-covalent interactions. Interesting examples including argentophilic[18] and aurophilic interactions,[19] which involves silver and gold atoms, respectively.

The importance of these interactions has created the field named *supramolecular chemistry*, which is focused on how molecules interact amongst themselves. Non-covalent interactions are responsible for many microscopic and macroscopic properties, such as how pharmaceuticals bind to their targets and why water remains liquid at room temperature. Consequently, the study of emerging non-covalent interactions may lead to functional materials, pharmaceuticals with higher specificities, and perhaps even solutions to other emerging problems.

1.3 - The halogens.

Amongst the elements on the periodic table are the *halogens*. In the order of decreasing electronegativity, the halogens are fluorine (F), chlorine (Cl), bromine (Br), iodine (I), astatine

(At), and most recently, Tennessine (Ts), making up group 17 of the periodic table (see Figure 1.1.1). The name "halogen" is Greek in origin, meaning "to form salts".[20] This name has been given due to their occurrence in a variety of salts, including alkali salts (e.g., sodium chloride), metal salts (e.g., copper iodide), and organic salts (e.g., tetraphenylphosphonium bromide). From the time of their individual discovery, each halogen has found an array of applications. For instance, fluorine was found to be particularly useful in non-stick coatings (Teflon) and as an active ingredient in tooth paste (sodium fluoride). Chlorine is found in both table salt and sodium hypochlorite (Bleach) and has had sinister applications in chemical warfare. Bromine has sparse biological applications but has been used in sanitizers and flame retardants.[21] Iodine is an essential mineral that has a role in thyroid hormones and is thus added to table salt in the form of sodium iodide, preventing diseases such as goiters. In addition, iodophors are an excellent class of sanitizers, with povidone-iodine[22] being featured on the World Health Organization's list of essential medicine.[23] In contrast, astatine and tennessine are unstable elements with very short half-life and currently have no application.

To chemists, the halogens have many applications in synthesis, behaving as good leaving groups, playing a role in strong acids (e.g., hydrochloric acid) and even in oxidizing or reducing agents. Additionally, halogens are relevant to creating carbon–carbon covalent bonds, with a role in the *Sonogashira coupling* reaction.[24] While halogens typically participate in one covalent bond, they can also have multiple covalent bonds,[25,26] with this configuration being named *hypervalent*. Hypervalent iodine has been featured as an organic catalyst and has been proposed for use in *green chemistry*.[27] Unfortunately, the halogens are commonly considered to be merely electronegative atoms with a desire to fill their electron octet or to act as heavy elements. While

this adequately describes the stability of the halides, it fails to completely describe the chemistry of the halogens, dismissing its role in molecular assembly.

Indeed, there is more to the halogen atoms than their reactivities, as they can form non-covalent interactions that can allow for the construction of supramolecular architectures. Specifically, the halogen···halogen interaction has already been recognized for its potential in molecular assembly, with the resulting R_1-X···X-R_2 (X = F, Cl, Br, I; R_1, R_2 = substituents) motif being classified into two categories: type I and type II interactions.[28] In type I interactions, the two halogens approach head-on, with the R_1-X···X bond angle being roughly equal to the X···X-R_2 bond angle and occurs primarily due to crystal packing effects.[29] In contrast, type II interactions involves the halogen atoms interacting at right angles (e.g., $\theta_{R1\text{-}X\cdots X}$ = 180°; $\theta_{X\cdots X\text{-}R2}$ = 90°).[30,31] The type II halogen···halogen interaction can be explained by considering the presence of a positive electrostatic potential on the front of the halogen and surrounded by a belt of negative electrostatic potential, favoring a perpendicular halogen···halogen interaction geometry.[32]

1.4 - The σ-hole.

When covalently bonded to an electronegative atom such as carbon and nitrogen, the halogens experience an anisotropic distribution in their electrons, yielding an oblate spheroid rather than a sphere.[33,34,35] This polar flattening[36] results in a region of lower electron density formed opposite to the covalent bond,[37] as shown in Figure 1.1.2. Consequently, this area is associated with a positive electrostatic potential named the σ-hole,[38,39,40] allowing the halogens to

form attractive interactions with sites of negative electrostatic potential. The resulting non-covalent interaction has been named *the halogen bond*.[41]

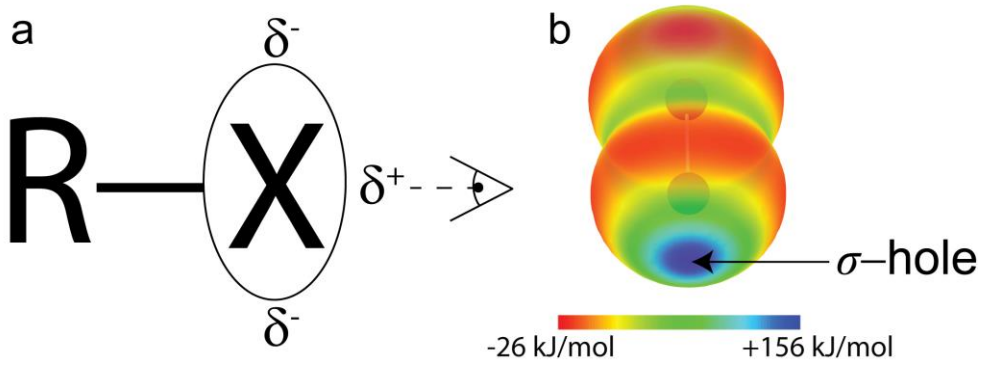

Figure 1.1.2. (**a**) Diagram showing the polar flattening occurring on a halogen (X) covalently bonded to a substituent (R). The δ^+ and δ^- denote the positive and negative electrostatic potentials, respectively. (**b**) Electrostatic potential of I_2 with a perspective along the I-I covalent bond axis, showing the positive σ-hole (in blue, 156 kJ/mol) and the negative potential (in red, -26 kJ/mol). The contour radius is of 0.002 a.u. with enhanced coloring for clarity.

The electrostatic potential of the σ-hole can be calculated by considering the charge contributions of both the electrons and the nucleus, and integrating over the electron density, given in Eq. 1.1.1.[42]

$$V(r) = \sum_A \frac{Z_A}{|R_A - r|} - \int \frac{p(r')dr'}{|r' - r|} \quad \text{Eq. 1.1.1}$$

Here, V(r) is the electrostatic potential at point r, Z_A is the nuclear charge, $|R_A - r|$ is the distance between the nucleus and point r, $p(r')dr'$ is the electronic charge, and $|r' - r|$ is the distance between the electron and point r. The electrostatic potentials in this thesis are expressed in units of kJ/mol using a contour radius of 0.002 a.u., following the literature.[43,44]

The polarizability of the electrons on the halogen is a critical attribute that has a contributing factor to the magnitude of the σ-hole. The larger halogens have more polarizable electrons and thus the magnitude of the σ-hole is greatest in the order of: At > I > Br > Cl >> F.[40]

As a result, fluorine rarely participates in halogen bonding,[45] while chlorine generally offers weak σ-holes. In contrast, bromine and iodine have sizeable σ-holes, while astatine, given its short half-life, has only recently been shown to participate in halogen bonding.[46]

The attractive features of the σ-hole lie in its manipulability. Firstly, the addition of nearby electron-withdrawing groups can increase the magnitude of the σ-hole, favoring the occurrence of stronger interactions. Consequently, σ-hole based interactions can be tuned by varying the nearby substituents.[47] The addition of fluorine atoms to the halogen bond donor is a commonly encountered strategy, with the resulting fluorinated molecule offering a strong halogen bond.[48] Secondly, due to the σ-hole being localized opposite to the covalent bond, it favors highly linear interactions relative to the R-X bond axis.[49] This manipulability of the σ-hole is illustrated in Figure 1.1.3.

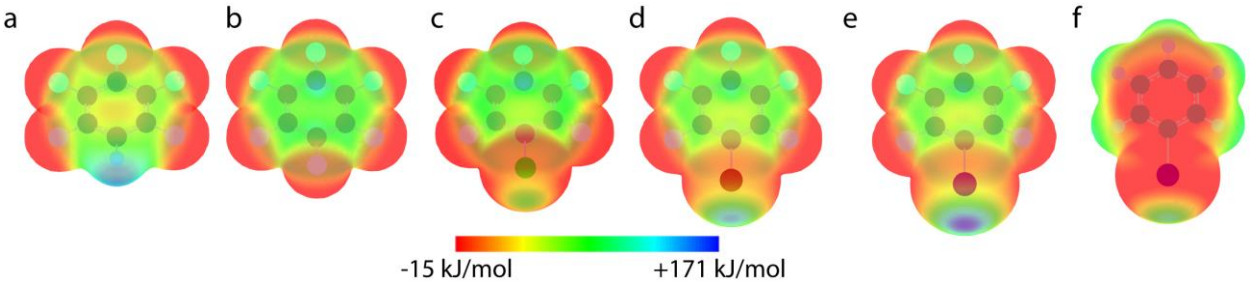

Figure 1.1.3. The electrostatic potential surface of pentafluorobenzene (**a**, 157.5 kJ/mol), hexafluorobenzene (**b**, -30 kJ/mol), chloropentafluorobenzene (**c**, 70.7 kJ/mol), bromopentafluorobenzene (**d**, 137.8 kJ/mol), iodopentafluorobenzene (**e**, 171.3 kJ/mol), and iodobenzene (**f**, 101.3 kJ/mol). The region of positive electrostatic potential is represented in blue, and the negative electrostatic potentials are represented in red, shown in the color legend. The calculations were performed using the B3LYP functional with the 3-21G basis set.

From Figure 1.1.3, the magnitude of the σ-hole increases with the size of the halogen, being largest for iodine (1.1.3e), smallest for chlorine (1.1.3c), while fluorine is associated with a negative potential (1.1.3b). The impact of fluorination can be clearly seen by comparing

iodoperfluorobenzene (1.1.3e) to iodobenzene (1.1.3f), with the magnitude of the σ-hole on iodobenzene being comparable to that of bromoperfluorobenzene (1.1.3d). When comparing iodoperfluorobenzene (1.1.3e) to the hydrogenated analogue (1.1.3a), not only is the potential of iodoperfluorobenzene greater, but the σ-hole on the iodine atom is also significantly more localized than the positive potential on the hydrogen atom. As a result, the halogen bond is comparable to the hydrogen bond, while offering a unique supramolecular tool due to its tuneability and linearity.[50,51,52,53,54,55]

As the σ-hole forms opposite to the covalent bond, hypervalent halogen compounds can have more than one σ-hole.[56,57] Consequently, hypervalent halogens can simultaneously participate in numerous instances of halogen bonding, such as the example of diphenyliodonium iodide shown in Figure 1.1.4. [58] In this case, an iodine atom is participating in two carbon-iodine covalent bonds, with the σ-holes forming opposite to each covalent bond. This allows for the formation of a charged dimer mediated by four I···I halogen bonds.

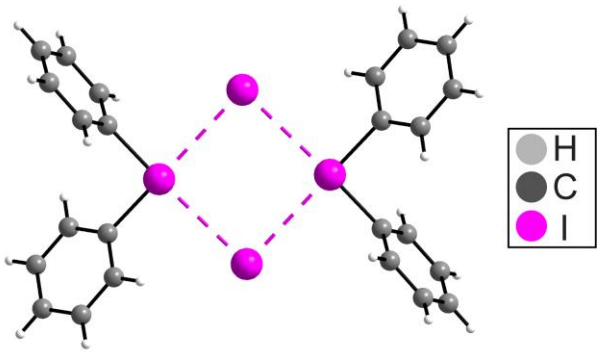

Figure 1.1.4. Crystal structure of diphenyliodonium iodide taken from Alcock and Countryman.[58] The dashed magenta line denotes the halogen bonds occurring in a hypervalent iodine compound.

This σ-hole interpretation occurring on the extension of several covalent bonds, with an example shown in Figure 1.1.4, has led to the understanding of non-covalent interactions that

occur for other groups on the periodic table which may exhibit more than one covalent bond. Much like the halogen bond, these other σ-hole based interactions were named from their electrophilic site,[59] including the chalcogen bond (involving: oxygen, sulfur, selenium, tellurium, …),[60,61,62,63] the pnictogen bond (involving: nitrogen, phosphorus, arsenic, …),[64,65] the tetrel bond (involving: carbon, silicon, germanium, …)[66,67,68] and even the aerogen bond (involving: helium, neon, argon, …).[69] While there are notable examples of their use in crystal engineering,[70,71] these interactions are typically weaker than the halogen bond. Further, these interactions typically require the use of toxic heavy metals, whereas the halogens are associated with a degree of biocompatibility.

1.5 - The Halogen Bond.

Halogen bonding was initially observed in 1813 but remained unrecognized until relatively recently. The first experiments took place in the laboratory of J.L. Gay-Lussac, a researcher in France who had first proposed the name *iode* due to its violet color. The combination of dry iodine with ammonia by M. Colin yielded a red-brown liquid that emitted ammonia, but in the presence of water, gave an explosive powder which was attributed to the formation of ammonium hydroiodide.[72,73] For some time, halogen bonding held the name *charge transfer complex*, and it wouldn't be before the late 1990's that it would be called *halogen bonding*.[74,75] In fact, nature was the first to exploit the halogen bond, with the iodine atoms in our thyroid hormones interacting with their receptors *via* halogen bonding.[76] Given its favorable attributes, the halogen bond has risen in prominence[73] and has been featured in a multitude of applications, which are discussed later.

The halogen bond is defined as the attractive interaction between the σ-hole occurring on a covalently bonded halogen (F, Cl, Br, I, At) and a nucleophilic center (Y).[41] The halogen bond length ($d_{X\cdots Y}$) is typically shorter than the sum of the van der Waals radii of both X and Y, and the halogen bond angle ($\theta_{R\text{-}X\cdots Y}$) favors linearity, typically between 150° and 180°. These geometric parameters render the halogen bond unique from other interactions and a brief overview of its applications is discussed below. The strength of the halogen bond varies from 10 to 150 kJ/mol, making it a strong non-covalent interaction.[73] The *halogen bond donor* is the electrophilic (δ^+) halogen which accepts electron density, and the *halogen bond acceptor* is the nucleophile (δ^-) that donates electron density. A summary of the general halogen bonding template is given in Figure 1.1.5.

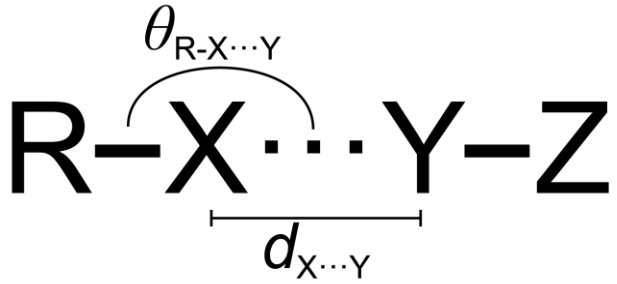

Figure 1.1.5. The general halogen bonding motif: X is the halogen bond donor, Y is the halogen bond acceptor, while R and Z are substituents. The halogen bond angle $\theta_{R\text{-}X\cdots Y}$ is typically between 150 and 180 degrees, while the bond distance $d_{X\cdots Y}$ is shorter than the sum of their van der Waal radii.

The halogen bond acceptor can be, in theory, any area associated with a negative electrostatic potential. In parallel to the σ-hole, the halogen bond acceptor can be tuned through the addition of nearby electron donating groups, with the goal of maximizing its negative electrostatic potential in order to increase the strength of the halogen bond. In practice, the halogen bond acceptor tends to be an electron rich atom or functional group, with nitrogen being

amongst the most versatile atoms as it can be featured in several unique arrangements (i.e., heterocycles, amines, and nitrile groups).[77] In addition, the halides (F^-, Cl^-, Br^-, I^-) have been widely exploited as halogen bond acceptors, typically combined with an ammonium or phosphonium cation (i.e., tetrabutylammonium chloride, tetraphenylphosphonium chloride).[78,79] It can be advantageous for the crystal engineer to use neutral compounds, as they generally offer a higher degree of predictability. As the cation of the halide salt does not directly participate in halogen bonding, it is thus difficult to predict the resulting framework. For the reasons above, and as nitrogen is extensively included in organic chemicals and biologically relevant molecules, the studies presented in this thesis has a focus on the C-X···N halogen bonding motif.

Alternate halogen bond acceptor atoms include oxygen,[80] sulfur,[81] selenium,[82] carbenes,[83] and recently, even phosphorus,[84] arsenic, and antimony.[85] These atoms are typically featured in arrangements that strongly activates the acceptor site through the addition of electron donating groups. Moreover, the halogen bond acceptor is not limited to an atom with a negative electrostatic potential, and there have even been reports of alkynes[86,87] and aromatic rings[88] participating in halogen bonds. In contrast, halogen bonding to transition metals rarely occur, with platinum acting as a halogen bond acceptor being only recently reported.[89]

While covalent bonds typically range from 0.9 to 2 Å,[90] the length of the halogen bond is on the order of 2.5 – 3.5 Å, which varies with the size of the atoms participating in the interaction. Due to the significant differences in the van der Waals radii (d_{vdW}) of the halogens,[91] of 1.47 Å for fluorine and 1.98 Å for iodine, it is difficult to directly compare the halogen bond length ($d_{X\cdots Y}$) across several motifs (i.e. comparing C-I···N to C-Cl···N). Moreover, the atomic radius of the halogen bond acceptor also has an effect, with nitrogen (R_{vdW} = 1.55 Å)[91] being quite smaller than tellurium (R_{vdW} = 2.06 Å).[91] Consequently, in order to obtain a qualitative

measurement of the halogen bond, we take the ratio between the halogen bond length and the sum of the van der Waals radius of both atoms ($\sum d_{vdW}$), yielding the reduced distance parameter (R_{XB}). In this case, both the halogen bond donor and acceptor atoms can be thought of as spherical, and the stronger the interaction, the more the spheres overlap. The R_{XB}, given in Eq. 1.1.2., takes into consideration the different sizes of atoms, allowing for the comparison of the halogen bond length across different motifs.

$$R_{XB} = \frac{d_{X\cdots Y}}{\sum d_{vdW}} \qquad \text{Eq. 1.1.2}$$

The R_{XB} of halogen bonded complexes are typically between 0.70 and 0.90, with stronger halogen bonds favoring shorter interactions. As the R_{XB} only considers interatomic distances, it remains a qualitative measurement. A lower R_{XB} does not necessarily indicate a strong halogen bond, as there can be secondary effects in the compound. Moreover, an R_{XB} above 1 does not necessarily indicate the absence of an interaction, but these longer halogen bonds do remain less significant.

1.6 - The Halogen Bond in Crystal Structures.

The *Cambridge Structural Database* (CSD)[92] is a repository containing over 900,000 crystal structures of small organic molecules and metal complexes. As many of these structures include halogen atoms but does not focus on the halogen bond, the CSD has been useful to investigate the geometrical properties of all contacts involving halogen atoms. A database search for the C-Br···N and C-I···N contacts within an R_{XB} of ~1 is shown in Figure 1.1.6, plotting the $\theta_{C\text{-}X\cdots N}$ angle as a function of the $d_{X\cdots N}$ distance.

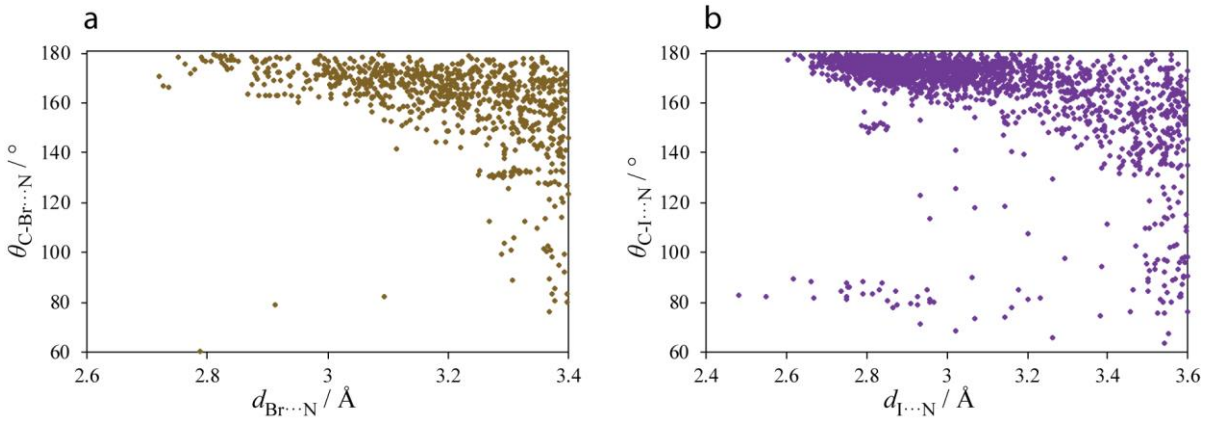

Figure 1.1.6. Halogen bond length ($d_{X\cdots N}$) of the C-X···N motif as a function of the bond angle ($\theta_{C\text{-}X\cdots N}$) for (**a**) X = Br and (**b**) X = I. Each data point represents a unique motif found on the Cambridge Structural Database.[92]

Shown in Figure 1.1.6, there is a clear preference for linearity ($\theta_{C\text{-}X\cdots N}$ = ~150 – 180°) at short $d_{X\cdots N}$ bond lengths, for both the C-Br···N and the C-I···N motifs. This preference can be ascribed to the localization of the σ-hole, which favors interactions in line with the C-X covalent bond. A pronounced agglomeration of data points can be seen in Figure 1.1.6b at bond lengths between 2.8 – 3 Å, with the resulting R_{XB} being of approximately 0.80. This preference in the geometry highlights the advantage of implementing the C-I···N motif in crystal engineering, due to its predictable outcome. In comparison, while the weaker C-Br···N motif does favor the same trend, it is less pronounced, with a clear loss of linearity at $d_{Br\cdots N}$ above 3.2 Å. The greater number of data points in Figure 1.1.6b versus 1.1.6a can be attributed to the higher number of crystal structures reported featuring the C-I···N motif. The data points on Figure 1.1.6b with bond lengths between 2.6 to 3.2 Å and an angle of approximately 90° are associated with hypervalent iodine compounds (i.e. perpendicular to the C-I bond axis, such as in the example shown in Figure 1.1.4).

A similar database search was performed for all halogens in a halobenzene group and interpreted graphically using the software *Isostar*,[93] with the results shown in Figure 1.1.7.

Rather than being shown on a 2-dimensional scatterplot, each C-X···N motif is shown in 3-dimensional space relative to the halogen bond donor for each of the halogens (F, Cl, Br, I), with the data point representing the actual nitrogen atom. The coloring denotes the relative concentration of the data points, with red being the most concentrated, blue being the least concentrated, and green being in the middle. As there are significantly more crystal structures reported of molecules bearing fluorine and chlorine, the coloring accounts for the relative populations, allowing for the direct comparison of the spread for each halogen. For purposes of clarity, the search was restricted to angles of $\theta_{C\text{-}X\cdots N}$ between 120 and 180º.

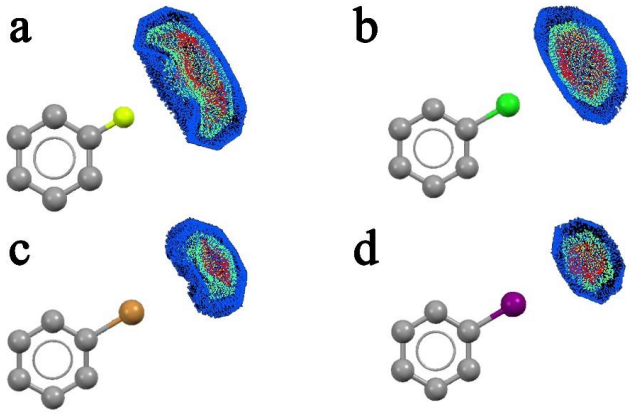

Figure 1.1.7. Distribution of X···N contacts involving the halogen atom in halobenzenes (a: fluoro, b: chloro, c: bromo, d: iodo). The red indicates the areas with the highest density of data points, and regions with the lowest data point density are indicated in blue. These plots are based on empirical data obtained from the Cambridge Structural Database[92] created using the software *IsoStar*.[93]

In Figure 1.1.7, we clearly see that the spread of the C-X···N motif is smallest in the case of iodine (Figure 1.1.7d), and greatest in the case of fluorine (Figure 1.1.7a). This localization is due to the C-I···N halogen bond strongly favoring linearity and an R_{XB} of approximately 0.80. The spread increases as the halogen bond donor atom weakens, with chlorine only offering some directionality. While the case of fluorine suggests a degree of potential as a halogen bond donor,

the spread is quite large and may have resulted from the sampling parameters. Clearly, the directionality of the halogen bond is of relevance to supramolecular chemistry, and the predictability of the halogen bond can be exploited for the rational design of crystalline architectures.

1.7 - The Halogen Bond in Crystal Engineering.

Cocrystals, which consist of two or more molecular components in a crystal,[94,95,96,97,98] are an excellent strategy to study the nature of the halogen bond. This approach requires modifying either the halogen bond donor or the halogen bond acceptor and studying the resulting effects on the crystal structure or in their spectroscopic response. Consequently, this reduces the number of variables in the experiment which may arise from synthesizing new single-component molecules. An example of such an approach is shown in Figure 1.1.8, with the crystal structure of 1,4-diiodotetrafluorobenzene (*p*DITFB) cocrystallized with 4,4'-bipyridyl.

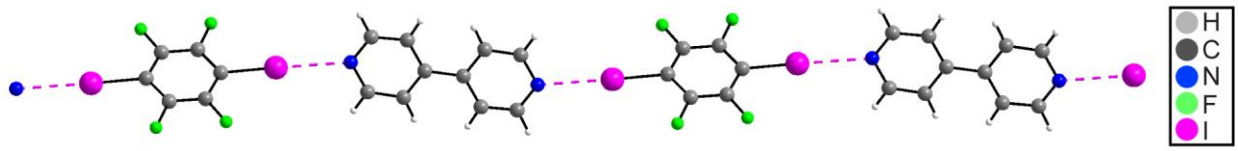

Figure 1.1.8. Depiction of the crystal structure of (1,4-diiodotetrafluorobenzene)(4,4'-bipyridyl) taken from Pennington and coworkers.[99] The dashed magenta line denotes the halogen bond. A legend of the atomic colors is shown on the right.

The linear architecture observed in Figure 1.1.8 is typical for the combination of a *para* substituted halogen bond donor and halogen bond acceptor. Modifying the substitution pattern of either the donor or the acceptor molecule may result in a new supramolecular motif, which can be exploited to obtain a desirable framework. Cocrystals have been featured throughout this

thesis, studying the spectroscopic response of a halogen bond donor after modifying the halogen bond acceptor. For instance, in Chapter 5, the halogen bond donor 1,4-dibromotetrafluorobenzene is studied in its pure form and subsequently in a series of cocrystals. Consequently, the spectroscopic changes observed experimentally can be associated to the formation of C-Br···N halogen bonds, allowing us to make conclusions on the nature of the halogen bond.

The halogen bond has been featured in several crystal engineering endeavors,[100,101] with the purpose of rationally designing new supramolecular architectures.[102] As shown in Figure 1.1.8, the combination of a linear donor and acceptor will form a linear framework mediated by C-I···N halogen bonds. [103] The use of halide salts can yield unique motifs due to the possibility of multiple simultaneous instances of halogen bonding, in contrast to an amine group which can typically only accommodates a single halogen bond. An example of 1,3,5-trifluoro-2,4,6-triiodobenzene (*sym*TITFB) cocrystallized with tetraphenylphosphonium bromide is shown in Figure 1.1.9, highlighting the coordination sphere surrounding the halide.[104]

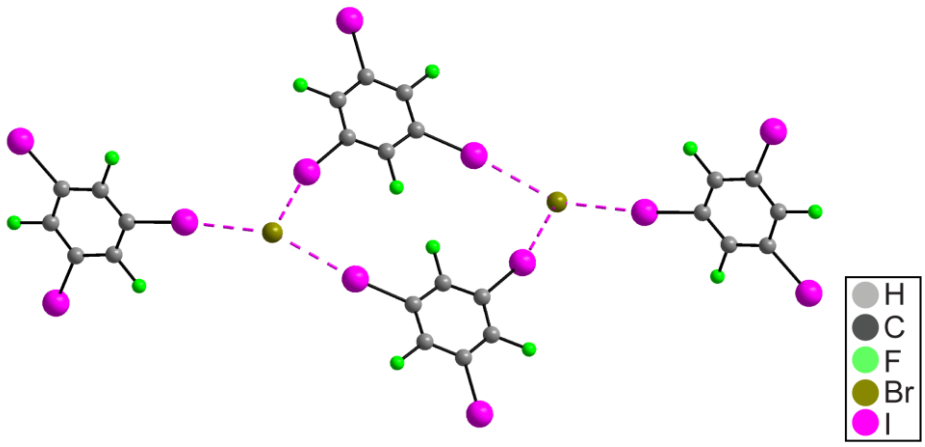

Figure 1.1.9. Depiction of the crystal structure of (1,3,5-trifluoro-2,4,6-triiodobenzene)(tetraphenylphosphonium bromide), taken from Fourmigué and coworkers.[104] The dashed magenta line denotes the C-I···Br^- halogen bond. The cation is hidden for clarity.

In the case of Figure 1.1.9, the halide participates in three C-I···Br^- halogen bonds, forming a framework through the crystal. The number of halogen bonds coordinating the halide anion ranges from one to eight,[105,106,107,108] which varies according to the size of the cation and the number of halogen bond donor groups. However, it can be difficult to control which framework is obtained due to the degrees of freedom for the cation of the halide salt.

The fluorinated halogen bond donors have been extensively explored in the field of crystal engineering, with notable examples being *p*DITFB along with its *o*DITFB and *m*DITFB analogues, *sym*TITFB, and diiodoperfluoroalkylcarbons,[109] with numerous articles published.[110,111,112,113,114] These donors have been featured in either charged or neutral frameworks exhibiting the C-I···X^-,[115,116,117,118,119] C-I···N,[120,121,122,123,124,125] C-I···O,[22,126,127,128,129,130,131] or C-I···S/Se/Te[132,133,134,135,136,137] halogen bonding motifs. An interesting example of crystal engineering was reported through the combination of a linear halogen bond donor (*p*DITFB) with a pseudo-octahedral halogen bond acceptor, forming a supramolecular cage through the formation of eight simultaneous C-I···N halogen bonds.[138] In addition, the combination of a large macrocycle (pillar[5,6]arene) with a halogen bond donor and acceptor system yielded an halogen bonded framework penetrating the large rings.[139] Another example is the combination of a basket-shaped molecule (calix[4]arene ring) and a halogen bond donor and acceptor system, yielding a supramolecular capsule for host-guest interactions.[140] With these being selected examples, it is expected that the fluorinated halogen bond donors experience a continued growth in their popularity. Consequently, the development of synthetic methods to prepare these materials and analytical techniques to characterize them will be important in accelerating the discovery of new supramolecular architectures.

The haloethynyl functional group, which is further discussed in Part 4 of this thesis, has been a strategy for strongly activating the halogen bond donor without resorting to fluorination. The triple bond forms a compact electron withdrawing group located directly adjacent to the halogen atom, creating a potent inducting effect on the halogen bond donor. There are several examples of this strategy, with the (iodoethynyl)nitrobenzene molecules being amongst the strongest carbon-based halogen bond donors.[141] An effective example of this strategy was the functionalization of the boarder of a basket-shaped molecule with haloethynyl groups, forming a molecular cavity capable of accommodating a guest. The addition of a halogen bond acceptor effectively "closes" the basket, sealing the guest molecule within the cavity.[142] Another notable example is the cocrystallization of a tetrahedral halogen bond donor, tetrakis(4-(iodoethynyl)phenyl)methane, with a series of halide salts to yield a unique diamandoid architectures.[143] Unfortunately, despite their relevance to crystal engineering, reports on the iodoethynyl group remain few, and further investigations are clearly required if they are to be featured in advanced materials.

1.8 - The Applications of Halogen Bonding.

Halogen bonding is currently being explored for numerous applications, with full reviews available in the literature.[73,144,145,146,147,148] Anion recognition[149] is a fascinating application, with the goal of capturing and identifying the anion in the solution. This ability has been achieved by designing molecules with halogen bond donor groups capable of binding anions selectively, causing a change to the physicochemical property of the solution. Given the linearity and tuneability associated with the halogen bond, these receptors can be designed to accommodate a specific anion by placing several halogen bond donor groups in the geometry that optimally

binds the desired anion. A recent approach consists of a macrocycle penetrated by a dumbbell shaped molecules, called a rotaxanes, which experiences a change in its dynamics upon the introduction of anions in the solution, mediated by I···Y$^-$ halogen bonds.[150,151,152,153,154] Other examples include molecules that fluoresce upon the introduction of their target anion,[155] in addition to molecules that can bind exotic anionic species.[156,157]

The halogen bond has been featured in several types of functional materials, acting as a directional interaction for molecular assembly. For instance, halogen bonding in optical materials has been experiencing a surge of interest given the potential of altering functional materials to have a particular purpose, such as fluorescence.[158,159] For example, the cocrystallization of *p*DITFB with heavily conjugated organic molecules has allowed for the optimal arrangement of molecules for use as waveguides in photonics, with the cocrystals outperforming the individual starting materials.[160] Another application in material science has been in piezochromic and piezoelectric compounds. The role of halogen bonding in these cases has been primarily in the assembly and stability of these materials, allowing for the creation of haptic sensors with higher sensitivity,[161] and compounds with exceptional piezoelectric coefficients.[162]

The inclusion of guest molecules within halogen bonded frameworks is a topic with growing interest as an alternative to the current materials under investigations, such as metal-organic frameworks and zeolites. The use of halogen bonding would allow the preparation of fully organic complexes devoid of metals, but would instead require the incorporation of the halogens, especially bromine and iodine. Obtaining porous organic compounds is quite challenging, especially when considering the weak nature of these non-covalent interactions. The use of strong halogen bonds has been shown to be a way of obtaining porosity,[163,164,165,166]

and few studies go so far as to even shown the possibility of incorporating guest molecules within these frameworks.[167,168,169,170] In one report, the halogen bond has allowed a porous framework to stretch upon the addition of gasses, such as carbon dioxide, allowing for the creation of a system with dynamic behavior.[171] As these articles are relatively recent, with many published in the previous year, it can be anticipated that interest in halogen bonded frameworks capable of hosting guest molecules will continue to grow.

Other applications exploiting the specificity of the halogen bond has been in the field of catalysis,[172,173] allowing for the preparation of highly selective and potent catalysts.[174,175,176] Moreover, halogen bonding has also been featured in liquid crystals,[177] ionic liquids, and polymers.[178] The resulting ionic liquids have shown some interest for the absorption of CO_2,[179,180] and polymers bearing halogen bond acceptor groups have been combined with halogen bond donors to yield copolymers.[181]

The halogen bond is not limited solely to applications in synthetic chemistry but has been shown to be of relevance to biochemical processes, drug design, as well as medicinal chemistry. While many pharmaceutical products contain halogen atoms, their role in drug design were not entirely understood at the time. In the early stages of developments, a study of the crystal structure of a halogenated inhibitor bound to an aldose reductase enzyme revealed that Br···O contacts between the drug and the target were crucial to its selectivity.[182] Another example shows the stabilization of Holliday junctions through Br···O halogen bonding by introducing 5-bromouracil to the DNA sequence.[183] The halogen bond has since been used as a directional interaction in biomolecules,[184] allowing for a control on their conformation.[185,186] Further, it has been shown that halogen bonding can serve a role in drug development, increasing the selectivity and binding affinity between a drug candidate and its target.[187,188,189] With its favorable

attributes, halogen bonding is projected to play an increasing role in the field of pharmaceuticals.[190,191]

1.9 - Investigating the Halogen Bond.

Several analytical tools are available to investigate the halogen bond. Single crystal X-ray diffraction (SCXRD) is perhaps the most powerful of these analytical methods, yielding the precise atomic coordinates in the form of a *crystal structure*, with examples previously shown in Figures 1.1.4, 1.1.8 and 1.1.9. From the crystal structure, the halogen bond can be recognized by measuring the contacts involving the halogen atom of interest and will also give information on the overall supramolecular motif. Powder X-ray diffraction (PXRD) is a tool analogous to SCXRD, which can be used to ensure sample quality and to verify that the structure of powdered crystals agrees with the structure acquired from SCXRD. In some cases, PXRD can even lead to the crystal structure[192] and can be used *in situ* to follow mechanochemical synthesis.[193]

Microscopy has been a useful tool to characterize the halogen bond on surfaces,[194] with a notable example being 1,3,5-tris(3,5-dibromophenyl)benzene formed on a gold surface.[195] In addition, electrical stimulation through scanning tunneling microscopy was shown to be of use in arranging halogen bonded frameworks on surfaces.[196] Microscopy has also revealed the possibility of forming cocrystals on a halogen bond acceptor surface, with the tip of the microscope directing the deposition of the halogen bond donor.[197] While microscopy is a convenient method, it is restricted to the study of surfaces.

There exist several spectroscopic methods to analyze the halogen bond donor and acceptor, which are reviewed more closely in the introduction of Part 2. Infrared (IR)

spectroscopy is amongst the most routinely applied spectroscopic techniques, observing the vibrations of chemical bonds. Upon the formation of an R-X···Y halogen bond, the IR absorbance band assigned to the R-X covalent bond is subject to a frequency shift,[198,199] which has served as a tool to survey whether a compound has successfully formed a halogen bonded cocrystal. The advantages of IR are the short analysis times and low sample volumes, being overall a convenient analytical tool. However, the information offered by IR spectroscopy is limited and serves best as a preliminary step in the investigation of halogen bonding.

Nuclear magnetic resonance (NMR) spectroscopy observes the response of a nucleus subjected to radiofrequency pulses in the presence of an external magnetic field. The chemical environment surrounding the nucleus produces a change to its response frequency, which is known as the *chemical shift*. Moreover, nuclei can interact through chemical bonds, named *J-coupling*, which yields characteristic multiplets. In solution NMR, the interpretation of the chemical shift and *J*-coupling can lead to the molecule structure, with several 2-dimensional methods supporting the interpretation. While the majority of the elements on the periodic table have an NMR-active isotope, solution NMR is routinely performed on the ^{1}H, ^{13}C, ^{15}N, ^{19}F, and ^{31}P isotopes of organic molecules, with NMR now being a staple amongst chemistry departments. Consequently, the halogen bond has been subjected to numerous solution NMR studies,[200,201] with titration experiments being key to determining the association constant between a halogen bond donor and acceptor.[202,203,204]

Throughout our discussion on halogen bonding, we have surveyed several applications of halogen bonding in solids, including crystalline supramolecular architectures. Fortunately, NMR spectroscopy is applicable to analyzing solids, offering information that is otherwise averaged in solution. This includes the *chemical shift anisotropy* and the *dipolar coupling*, which are the

dependence of the chemical shift on the orientation of the spin relative to the external magnetic field and the magnetic interaction between NMR-active spins, respectively. Moreover, solid-state NMR (SSNMR) can be applied to analyze quadrupolar nuclei (spin $I > ½$), which constitute nearly three-quarters of the periodic table, yielding information on the electric field gradient (EFG) through the quadrupolar coupling. As a result, SSNMR boasts the ability to offer insights into both the electronic and chemical environment of the nuclei participating in the halogen bond, as well as the surrounding environment.

SSNMR is a unique tool to probe the structure of halogen bonded compounds,[205,206,207] which has been a subject of ongoing investigations in our laboratory. The information accessible by SSNMR of relevance to halogen bonding includes changes in the chemical shifts, notably the ^{13}C covalently bonded to the halogen bond donor (i.e. ^{13}C-I),[208,209] the quadrupolar coupling of the nuclei acting as halogen bond acceptors,[210,211,212] the *J*-coupling in the acceptor molecule,[213,214] and the molecular dynamics.[215,216,217] Additionally, the dipolar coupling can be used to measure interatomic distances, which has been applied to extract the I···N halogen bond length.[218] Unfortunately, the most important atom, the halogen bond donor, has remained elusive to SSNMR investigations due to the large quadrupolar coupling encountered for the $^{35/37}$Cl, $^{79/81}$Br, and ^{127}I nuclei when covalently bonded to carbon. The analysis of these isotopes requires either the use of ultra-wideline techniques or nuclear quadrupole resonance (NQR) spectroscopy, which is further discussed and compared to NMR in Chapter 3. NQR spectroscopy is a tool analogous to NMR but performed in the absence of an external magnetic field, with a history of characterizing charge-transfer complexes. Despite the availability of NQR and NMR, there lacks a modern analysis of the EFG tensor at the halogen bond donor.

Although SSNMR has the potential of offering site-specific information, the sensitivity of the ^{19}F nucleus has been underexploited as a tool to characterize halogen bonded cocrystals featuring a perfluorinated halogen bond donor. Furthermore, the routine method of analyzing the ^{13}C nucleus by transferring the polarization from the ^{1}H spins to the ^{13}C spins has significant limitations in characterizing the fluorinated halogen bond donor molecule. As a result of the large distances between the ^{1}H nuclei of the halogen bond acceptor and the ^{13}C nuclei of the halogen bond donor, cross-polarization is rendered inefficient, and plagued by secondary broadening caused by the ^{19}F nuclei. While $^{19}F \rightarrow {}^{13}C$ cross-polarization would yield a significant increase in the sensitivity and resolution when characterizing the halogen bond donor, it has yet to be fully investigated.

While the ^{13}C chemical shift of the ^{13}C-I···Y has been shown to correlate with the halogen bond geometry,[208,209] the effect of the identity of the halogen bond acceptor (Y) on the chemical shift has yet to be fully investigated. As a result, a comparison between several C-I···Y motifs in isomorphous compounds, where Y can be N, Cl^-, Br^- or I^-, is required to fully interpret the effect of the halogen bond.

1.10 – The Preparation of Halogen Bonded Cocrystals.

There are several techniques for growing high quality cocrystals for analysis, with the majority of these techniques being solvent-based.[219,220] An effective approach is to dissolve both the halogen bond donor and acceptor in an organic solvent, combine the solutions and allow the solvent to evaporate slowly over the course of several days. As the solvent evaporates, the solution becomes supersaturated, and upon nucleation, the cocrystals will grow. There are

several alternative techniques following this principle, including solvent layering and solvent diffusion. However, this method has major drawbacks, such as requiring screening the solvents, lengthy experimental times, and the inevitable need for trial and error. The choice of the organic solvent is crucial, as both compounds must have approximately the same solubility, otherwise each compound may crystallize separately. In other instances, the solvent may be present in the cocrystal, creating a solvatomorph. Consequently, solvent-based preparation methods limit the accessibility of many halogen bonded frameworks, with a clear need of new approaches.

Further discussed in Part 4, mechanochemistry has been an effective approach to prepare halogen bonded cocrystals. This method consists of grinding the halogen bond donor and acceptor using a mortar & pestle or using more sophisticated equipment such as a ball mill. While liquid assisted grinding has shown to be of some use, mechanochemistry can be performed in the absence of organic solvents, removing the need of solvent screening. In addition, mechanochemistry can be performed in a brief amount of time, allowing for the high throughput screening of halogen bonded cocrystals.

While sublimation is a solvent-free method of growing crystals,[221] it typically yields crystals with insufficient quality, leading to difficulties in the data collection. However, when performed carefully, sublimation can yield the crystals at a much faster rate than solvent evaporation, while avoiding the need to screen solvents. Unfortunately, there is very little information available in the literature for preparing cocrystals using *cosublimation*, with a clear need for developing this synthetic method.

SSNMR is well-poised to analyze the products obtained from these alternative synthetic methods, with the resulting spectrum offering characteristic changes in the chemical shifts upon

the formation of a cocrystals. By comparing the SSNMR spectrum of the starting material to the cocrystal, the changes in the chemical shifts may indicate the occurrence of a halogen bond. Further, the development of ^{19}F SSNMR methods will allow for a rapid analysis of halogen bonded cocrystals featuring a fluorinated halogen bond donor, reducing analysis times from hours to approximately 5 minutes.

1.11 - Thesis Objectives.

In this thesis, we explore the nature of the halogen bond, its use in crystal engineering, and synthetic methods for preparing halogen bonded cocrystals. In order to enhance clarity, these investigations are divided into three parts: characterizing the halogen bond donor (Part 2), characterizing the halogen bond acceptor & its surrounding environment (Part 3), along with the crystal engineering, and exploring alternative methods of preparing halogen bonded cocrystals (Part 4). In order to meet these objectives, we will use a combination of X-ray crystallography, multinuclear solid-state magnetic resonance spectroscopy, and computational chemistry. Moreover, our solid-state NMR approach will provide nucleus-specific information at the sites of halogen bonding, offering unique information on the changes in the chemical and electronic environment upon the formation of the halogen bond.

Part 1 of this thesis has the goal of introducing the halogen bond. The purpose of Chapter 1 is to summarize the current state of the field, contextualizing the investigations discussed herein. Chapter 2 aims to review the theory behind the experimental techniques applied in this thesis, covering the fundamental principles necessary to understand the experimental approaches and results. Chapter 3 has the goal of comparing solid-state NMR to NQR, which will be

important to fully understanding the experimental difficulties which are surmounted in our investigations of the halogen bond donor.

The goal of Part 2 is to perform the first direct investigations of the chlorine, bromine, and iodine halogen bond donors in the C-X···N motif, offering direct information on the changes in the quadrupolar coupling upon the occurrence of the halogen bond. Chapter 4 will focus on the characterization of the chlorine halogen bond donor in single-component chloronitrile compounds by ^{35}Cl ultra-wideline solid-state NMR spectroscopy. In order to circumvent the difficulties in preparing C-Cl···N halogen bonded cocrystals, we exploit crystallographic symmetry in order to measure the influence of the halogen bond on the quadrupolar coupling. In Chapter 5, we resort to NQR spectroscopy to measure the $^{79/81}$Br quadrupolar coupling in cocrystals featuring 1,4-dibromotetrafluorobenzene as the halogen bond donor, and a series of nitrogen-containing heterocycles as the halogen bond acceptor. This is the first modern NQR approach to study the halogen bond, with the resulting changes in the quadrupolar coupling offering a rapid and reliable crystallographic tool for detecting the occurrence of a halogen bond. Chapter 6 is the final chapter of Part 2 which aims to characterize the iodine-based halogen bond donor - the strongest and most popular donor atom. The extreme quadrupolar couplings encountered for the iodine atom will be characterized by ^{127}I NQR spectroscopy on a series of cocrystals consisting of 1,4-diiodobenzene and nitrogen-containing heterocycles. Moreover, Chapter 6 aims to combine the ^{127}I results with the ^{35}Cl data from Chapters 4 and $^{79/81}$Br data from Chapter 5, in order to create a global model on the changes in the quadrupolar coupling for all halogens, contributing the first inter-halogen investigation on the electronic changes encountered at the halogen bond donor.

The objective of Part 3 is to characterize the halogen bond acceptor & its surrounding environment, using solid-state NMR spectroscopy to observe unique changes in the chemical shift, quadrupolar coupling, and changes to the dynamics occurring on the halogen bond acceptor. In Chapter 7, we develop a ^{19}F and ^{13}C solid-state NMR approach to characterize a series of halogen bonded cocrystals exhibiting the C-I···N moiety, with the ^{19}F experiment offering a significant enhancement in detecting impurities and side phases that were key to the success of the later chapters. Moreover, the ^{19}F and ^{13}C experimental chemical shifts are combined with DFT calculations in order to refine crystal structures derived from X-ray data. Chapter 8 aims to exploit self-complimentary halogen bonded compounds consisted of 2- & 3-iodoethynylpyridine, forming the first supramolecular triangle and a zig-zag pattern. These compounds will be derived to their salt forms (hydrochloride, hydrobromide, and hydroiodide), offering the rare opportunity of comparing the C-I···X^-···H-N^+ motif across all halogens in terms of the ^{1}H and ^{13}C chemical shifts, and the ^{35}Cl, $^{79/81}Br$, and ^{127}I quadrupolar coupling. Chapter 9 has the objective of investigating the direct effects of halogen bonding on the nearby environment, using the rotation of the methyl groups on the halogen bond acceptor 2,3,5,6-tetramethylpyrazine as a model. Amongst the effects, we aim to show the first instance of halogen bonding reducing the rotational energy barrier of the nearby methyl group, coining the term "dynamics catalysis". The halogen bond will be shown to be amongst the best dynamics catalyst, with potential applications in rendering molecular machines more efficient along with developing the next generation of pharmaceuticals.

The objective of Part 4 is to exploit the halogen bond in crystal engineering and to explore alternative methods of preparing halogen bonded cocrystal. Chapter 10 aims to explore a series of halogen bonded cocrystals featuring the 1,3,5-tri(iodoethynyl)-2,4,6-trifluorobenzene

as the halogen bond donor and a series of halide salts as a halogen bond acceptor. A series of halide salts with increasing size are chosen in order to investigate the impact of the cation on the resulting frameworks. Solvent evaporation has been applied to prepare these samples, with the products exhibiting unique halogen bonded architectures. Chapter 11 has the objective of preparing halogen bonded cocrystals between 3-iodoethynylbenzoic acid (3-IEBA) and a series of nitrogen-containing heterocycles using mechanochemistry. This halogen bond donor, bearing hydrogen bonding capabilities, offers a unique advantage of being able to form both hydrogen and halogen bonds to the acceptor molecule, offering a higher degree of predictability in the products. A second objective to this study is to explore mechanochemistry as an alternative method to prepare these cocrystals, with the intent of decreasing preparation times and solvent requirements. Chapter 12 has the objective of establishing cosublimation as a solvent-free method for rapidly preparing halogen bonded cocrystals, directly yielding crystals suitable for single-crystal X-ray diffraction that may be otherwise unobtainable through other methods. This technique aims to remove all solvent requirements while greatly accelerating the rate of discovery, in what would be the first thorough investigation on cosublimation.

Finally, the goal of Part 5 is to recapitulate the studies in this thesis, and to provide a global synthesis of the experimental results. In addition, Part 5 aims to present the key conclusion, as well as a perspective on the future developments in the field.

Rather than providing the articles in manuscript form, which would have been prohibitive in length while requiring cutting important results, the articles are presented in their published form. The exceptions are Chapter 6 and Chapter 9, which are preprints provided in manuscript form, with the supplementary information available in the Appendix. Each article has been

written individually much like if it was included in manuscript form. All coauthor permissions and journal permissions are provided immediately before each article is presented.

References for Chapter 1.

[1] Haynes, W.M.; Lide, D.R.; Bruno, T.J. *CRC Handbook of Chemistry and Physics.* CRC Press, Boca Raton, **2016**.

[2] Radius, U.; Breher, F. *Angew. Chem. Int. Ed.* **2006**, *45*, 3006-3010.

[3] Shaik, S.; Danovich, D.; Wu, W.; Su, P.; Rzepa, H.S.; Hiberty, P.C. *Nat. Chem.* **2012**, *4*, 195-200.

[4] Cottrell, T.L. *The Strengths of Chemical Bonds.* Butterworths Publication Ltd., London, **1954**.

[5] Miessler, G.L.; Fischer, P.J.; Tarr, D.A. *Inorganic Chemistry 5th,* Pearson Education, Inc., Boston, **2013**.

[6] de la Roza, A.O.; Dilabio, G.A. *Non-Covalent Interactions in Quantum Chemistry and Physics. Theory and Applications.* Elsevier, Cambridge, **2017**.

[7] Feynman, R.P. *Phys. Rev.* **1939**, *56*, 340-343.

[8] Bender, C.J. *Chem. Soc. Rev.* **1986**, *15*, 475-502.

[9] Mulliken, R.S. *J. Am. Chem. Soc.* **1950**, *72*, 600-608.

[10] Jiang, H.; Hu, P.; Ye, J.; Zhang, K.K.; Long, Y.; Hu, W.; Kloc, C. *J. Mater. Chem. C* **2018**, *6*, 1884-1902.

[11] Linderman, S.V.; Hecht, J.; Kochi, J.K. *J. Am. Chem. Soc.* **2003**, *125*, 11597-11606.

[12] Arunan, E.; Desiraju, G.R.; Klein, R.A.; Sadlej, J.; Scheiner, S.; Alkorta, I.; Clary, D.C.; Crabtree, R.H.; Dannenberg, J.J.; Hobza, P.; Kjaergaard, H.G.; Legon, A.C.; Mennucci, B.; Nesbitt, D.J. *Pure Appl. Chem.* **2011**, *8*, 1637-1641.

[13] Watson, J.D.; Crick, F.H.C. *Nature.* **1953**, *171*, 737-738.

[14] Clark, J.H.; Miller, J.M. *J. Am. Chem. Soc.* **1977**, *99*, 498-504.

[15] Moulton, B.; Zaworotko, M.J. *Chem. Rev.* **2001**, *101*, 1629-1658.

[16] Paoloni, L. *J. Chem. Phys.* **1959**, *30*, 1045-1058.

[17] Gilli, G.; Gilli, G. *The Nature of the Hydrogen Bond: Outline of a Comprehensive Hydrogen Bond Theory.* Oxford University Press, New York, **2009**.

[18] Schmidbaur, H.; Schier, A. *Angew. Chem. Int. Ed.* **2015**, *54*, 746-784.

[19] Schmidbaur, H.; Schier, A. *Chem. Soc. Rev.* **2012**, *41*, 370-412.

[20] Berzelius, J.J.; Bache, A.D. *Am. J. Sci.* **1832**, *22*, 248-276.

[21] Alaee, M.; Arias, P.; Sjödin, A.; Bergman, A. *Environ. Int.* **2003**, *29*, 683-689.

[22] Goodwin, M.J.; Steed, B.W.; Yufit, D.S.; Musa, O.M.; Berry, D.J.; Steed, J.W. *Cryst. Growth Des.* **2017**, *17*, 5552-5558.

[23] World Health Organization (WHO), *WHO Organization Model List of Essential Medicines,* 19th edition. **2015.** Accessed January 5th 2019.

[24] Sonogashira, K. *J. Org. Chem.* **2002**, *653*, 46-49.

[25] Farooq, U.; Shah, A.-u.-H.; Wirth, T. *Angew. Chem. Int. Ed.* **2009**, *48*, 1018-1020.

[26] Wirth, T. *Hypervalent Iodine Chemistry.* Springer, Cham, **2016**.

[27] Tundo, P.; Anastas, P.; Black, D.S.; Breen, J.; Collins, T.; Memoli, S.; Miyamoto, J.; Polyakoff, M.; Tumas, W. *Pure Appl. Chem.* **2000**, *72*, 1207-1228.

[28] Desiraju, G.R.; Parthasarathy, R. *J. Am. Chem. Soc.* **1989**, *111*, 8725-8726.

[29] Ramasubbu, N.; Parthasarathy, R.; Murray-Rust, P. *J. Am. Chem. Soc.* **1986**, *108*, 4308-4314.

[30] Sakurai, T.; Sundaralingam, M.; Jeffrey, G.A. *Acta Cryst.* **1963**, *16*, 354-363.

[31] Mukherjee, A.; Desiraju, G.R. *IUCrJ.* **2014**, *1*, 49-60.

[32] Metrangolo, P.; Resnati, G. *IUCrJ.* **2014**, *1*, 5-7.

[33] Nyburg, S.C.; Faerman, C.H. *Acta Cryst.* **1985**, *B41*, 274-279.

[34] Metrangolo, P.; Murray, J.S.; Pilati, T.; Politzer, P.; Resnati, G.; Terraneo, G. *Cryst. Growth Des.* **2011**, *11*, 4238-4246.

[35] Sedlak, R.; Kolár, M.H.; Hobza, P. *J. Chem. Theory Comput.* **2015**, *11*, 4727-4732.

[36] Nyburg, S.C. *Acta Cryst.* **1979**, *A35*, 641-645.

[37] Politzer, P.; Murray, J.S. *Crystals.* **2017**, *7*, 212.

[38] Politzer, P.; Murray, J.S. *ChemPhysChem.* **2013**, *14*, 278-294.

[39] Politzer, P.; Murray, J.S.; Clark, T.; Resnati, G. *Phys. Chem. Chem. Phys.* **2017**, *19*, 32166-32178.

[40] Clark, T.; Hennemann, M.; Murray, J.S.; Politzer, P. *J. Mol. Model.* **2007**, *13*, 291-296.

[41] Desiraju, G.R.; Shing Ho, P.; Kloo, L.; Legon, A.C.; Marquardt, R.; Metrangolo, P.; Politzer, P.; Resnati, G.; Rissanen, K. *Pure Appl. Chem.* **2013**, *85*, 1711-1713.

[42] Politzer, P.; Murray, J.S.; Clark, T.; Resnati, G. *Phys. Chem. Chem. Phys.* **2017**, *19*, 32166-32178.

[43] Aakeröy, C.B.; Wijethunga, T.K.; Desper, J.; Đaković, M. *Cryst. Growth Des.* **2016**, *16*, 2662-2670.

[44] Perera, M.D.; Desper, J.; Sinha, A.S.; Aakeröy, C.B. *CrystEngComm.* **2016**, *18*, 8631-8636.

[45] Eskandari, K.; Lesani, M. *Chem. Eur. J.* **2015**, *21*, 4739-4746.

[46] Guo, N.; Maurice, R.; Teze, D.; Graton, J.; Champion, J.; Montavon, G.; Galland, N. *Nat. Chem.* **2018**, *10*, 428-434.

[47] Riley, K.E.; Murray, J.S.; Fanfrlík, J.; Řezáč, J.; Solá, R.J.; Concha, M.C.; Ramos, F.M.; Politzer, P. *J. Mol. Model.* **2013**, *19*, 4651-4659.

[48] Riley, K.E.; Murray, J.S.; Fanfrlík, J.; Řezáč, J.; Solá, R.J.; Concha, M.C.; Ramos, F.M.; Politzer, P. *J. Mol. Model.* **2011**, *17*, 3309-3318.

[49] Huber, S.M.; Scanlon, J.D.; Jimenez-Izal, E.; Ugalde, J.M.; Infante, I. *Phys. Chem. Chem. Phys.* **2013**, *15*, 10350-10357.

[50] Metrangolo, P.; Neukirch, H.; Pilati, T.; Resnati, G. *Acc. Chem. Res.* **2005**, *38*, 386-395.

[51] Scheiner, S. *J. Phys. Chem. A* **2017**, *121*, 3606-3615.

[52] Zhao, C.; Lu, Y.; Zhu, Z.; Liu, H. *J. Phys. Chem. A* **2018**, *122*, 5058-5068.

[53] Nepal, B.; Scheiner, S. *Phys. Chem. Chem. Phys.* **2016**, *18*, 18015-18023.

[54] Shirman, T.; Boterashvili, M.; Orbach, M.; Freeman, D.; Shimon, L.J.W.; Lahav, M.; van der Boom, M.E. *Cryst. Growth Des.* **2015**, *15*, 4756-4759.

[55] Corradi, E.; Meille, S.V.; Messina, M.T.; Metrangolo, P.; Resnati, G. *Angew. Chem. Int. Ed.* **2000**, *39*, 1782-1786.

[56] Kirshenboim, O.; Kozuch, S. *J. Phys. Chem. A* **2016**, *120*, 9431-9445.

[57] Catalano, L.; Cavallo, G.; Metrangolo, P.; Resnati, G.; Terraneo, G. *Top. Curr. Chem.* **2016**, *373*, 289-310.

[58] Alcock, N.W.; Countryman, R.M. *J. Chem. Soc., Dalton Trans.* **1977**, *0*, 217-219.

[59] Cavallo, G.; Metrangolo, P.; Pilati, T.; Resnati, G.; Terraneo, G. *Cryst. Growth Des.* **2014**, *14*, 2697-2702.

[60] Pascoe, D.J.; Ling, K.B.; Cockroft, S.L. *J. Am. Chem. Soc.* **2017**, *139*, 15160-15167.

[61] Lim, J.Y.C.; Marques, I.; Thompson, A.L.; Christensen, K.E.; Félix, V.; Beer, P.D. *J. Am. Chem. Soc.* **2017**, *139*, 3122-3133.

[62] Geboes, Y.; De Vleeschauwer, F.; De Proft, F.; Herrebout, W.A. *Chem. Eur. J.* **2017**, *23*, 17384-17392.

[63] Benz, S.; López-Andarias, J.; Mareda, J.; Sakai, N.; Matile, S. *Angew. Chem. Int. Ed.* **2017**, *56*, 812-815.

[64] Yang, M.; Tofan, D.; Chen, C.-H.; Jack, J.M.; Gabaï, F.P. *Angew. Chem. Int. Ed.* **2018**, *57*, 13868-13872.

[65] Zahn, S.; Frank, R.; Hey-Hawkins, E.; Kirchner, B. *Chem. Eur. J.* **2011**, *17*, 6034-6038.

[66] Bauzá, A.; Mooibroek, T.J.; Frontera, A. *Angew. Chem. Int. Ed.* **2013**, *52*, 12317-12321.

[67] Mani, D.; Arunan, E. *Phys. Chem. Chem. Phys.* **2013**, *15*, 14377-14383.

[68] Mundlapati, V.R.; Sahoo, D.K.; Bhaumik, S.; Jena, S.; Chandrakar, A.; Biswal, H.S. *Angew. Chem. Int. Ed.* **2018**, *57*, 16496-16500.

[69] Bauzá, A.; Frontera, A. *Angew. Chem. Int. Ed.* **2015**, *54*, 7340-7343.

[70] Jeannin, O.; Huynh, H.-T.; Riel, A.M.S.; Fourmigué, M. *New J. Chem.* **2018**, *42*, 10502-10509.

[71] Kumar, V.; Leroy, C.; Bryce, D.L. *CrystEngComm*. **2018**, *20*, 6406-6411.

[72] Gay-Lussac, J.L. *Annales de chimie, ou recueil de mémoires concernant la chimie et les arts qui en dépendent.* **1814**, *91*, 5-272.

[73] Cavallo, G.; Metrangolo, P.; Milani, R.; Pilati, T.; Priimagi, A.; Resnati, G.; Terraneo, G. *Chem. Rev.* **2016**, *116*, 2478-2601.

[74] Metrangolo, P.; Resnati, G. *Chem. Eur. J.* **2001**, *7*, 2511-2519.

[75] Legon, A.C. *Angew. Chem. Int. Ed.* **1999**, *38*, 2686-2714.

[76] Valadares, N.F.; Salum, L.B.; Polikarpov, I.; Andricopulo, A.D.; Garratt, R.C. *J. Chem. Inf. Model.* **2009***, 49*, 2606-2616.

[77] Han, N.; Zeng, Y.; Sun, C.; Li, X.; Sun, Z.; Meng, L. *J. Phys. Chem. A* **2014**, *118*, 7058-7065.

[78] Cavallo, G.; Metrangolo, P.; Pilati, T.; Resnati, G.; Sansotera, M.; Terraneo, G. *Chem. Soc. Rev.* **2010**, *39*, 3772-3783.

[79] Fourmigué, M. *Acta Cryst.* **2017**, *B73*, 138-139.

[80] Kratzer, P.; Ramming, B.; Römisch, S.; Maas, G. *CrystEngComm.* **2015**, *17*, 4486-4494.

[81] Le Gal, Y.; Lorcy, D.; Jeannin, O.; Barrière, F.; Dorcet, V.; Lieffrig, J.; Fourmigué, M. *CrystEngComm*. **2016**, *18*, 5474-5481.

[82] Torubaev, Y.V.; Skabitskiy, I.V.; Pavlova, A.V.; Pasynskii, A.A. *New J. Chem.* **2017**, *41*, 3606-3611.

[83] Lv, H.; Zhuo, H.-Y.; Li, Q.-Z.; Yang, X.; Li, W.-Z.; Cheng, J.-B. *Mol. Phys.* **2014**, *112*, 3024-3032.

[84] Xu, Y.; Huang, J.; Gabidullin, B.; Bryce, D.L. *Chem. Commun.* **2018**, *54*, 11041-11043.

[85] Lisac, K.; Topić, F.; Arhangelskis, M.; Cepić, S.; Julien, P.A.; Nickels, C.W.; Morris, A.J.; Friščić, T.; Cinčić, D. *Nat. Comm.* **2019**, *10*, 61.

[86] Dumele, O.; Wu, D.; Trapp, N.; Goroff, N.; Diederich, F. *Org. Lett.* **2014**, *16*, 4722-4725.

[87] Aakeröy, C.B.; Welideniya, D.; Desper, J. *CrystEngComm.* **2017**, *19*, 11-13.

[88] Gao, H.Y.; Shen, Q.J.; Zhao, X.R.; Yan, X.Q.; Pang, X.; Jin, W.J. *J. Mater. Chem.* **2012**, *22*, 5336-5343.

[89] Ivanov, D.M.; Nokikov, A.S.; Ananyev, I.V.; Kirina, Y.V.; Kukushkin, V.Y. *Chem. Commun.* **2016**, *52*, 5565-5568.

[90] Allen, F.H.; Kennard, O.; Watson, D.G.; Brammer, L.; Orpen, A.G.; Taylor, R. *J. Chem. Soc., Perkin Trans.* **1987**, *0*, S1-S19.

[91] Bondi, A. *J. Phys. Chem.* **1964**, *68*, 441-451.

[92] Groom, C.R.; Bruno, I.J.; Lightfoot, M.P.; Ward, S.C. *Acta Cryst.* **2016**, *B72*, 171-179.

[93] Bruno, I.J.; Cole, J.C.; Lommerse, J.P.M.; Rowland, R.S.; Taylor, R.; Verdonk, M.L. *J. Comput. -Aided Mol. Des.* **1997**, *11*, 525-537.

[94] Aitipamula, S. et al. *Cryst. Growth Des.* **2012**, *12*, 2147-2152.

[95] Aakeröy, C.B.; Salmon, D.J. *CrystEngComm.* **2015**, *7*, 439-448.

[96] Bond, A.D. *CrystEngComm.* **2007**, *9*, 833-834.

[97] Childs, S.L.; Stahly, G.P.; Park, A. *Mol. Pharmaceutics.* **2007**, *4*, 323-338.

[98] Grothe, E.; Meekes, H.; Vlieg, E.; ter Horst, J.H.; de Gelder, R. *Cryst. Growth Des.* **2016**, *16*, 3237-3243.

[99] Walsh, R.B.; Padgett, C.W.; Metrangolo, P.; Resnati, G.; Hanks, T.W.; Pennington, W.T. *Cryst. Growth Des.* **2001**, *1*, 165-175.

[100] Mukherjee, A.; Teyssandier, J.; Hennrich, G.; De Feyter, S.; Mali, K.S. *Chem. Sci.* **2017**, *8*, 3759-3769.

[101] Ateş, Ö.D.; Zorlu, Y.; Zanmazalp, S.D.; Chumakov, Y.; Gürek, A.G.; Ayhan, M.M. *CrystEngComm.* **2018**, *20*, 3858-3867.

[102] Mukherjee, A.; Tothadi, S.; Desiraju, G.R. *Acc. Chem. Res.* **2014**, *47*, 2514-2524.

[103] Walsh, R.B.; Padgett, C.W.; Metrangolo, P.; Resnati, G.; Hanks, T.W.; Pennington, W.T. *Cryst. Growth Des.* **2001**, *1*, 165-175.

[104] Triguero, S.; Llusar, R.; Polo, V.; Fourmigué, M. *Cryst. Growth Des.* **2008**, *8*, 2241-2247.

[105] Lieffrig, J.; Jeannin, O.; Fourmigué, M. *J. Am. Chem. Soc.* **2013**, *135*, 6200-6210.

[106] Yamamoto, H.M.; Yamaura, J.-I.; Kato, R. *J. Am. Chem. Soc.* **1998**, *120*, 5905-5913.

[107] Yamamoto, H.M.; Kosaka, Y.; Maeda, R.; Yamaura, J.-I.; Nakao, A.; Nakamura, T.; Kato, R. *ACS Nano.,* **2008**, *2*, 143-155.

[108] Müller, U.; Krug, V. *Acta Cryst.* **1990**, *C46*, 523-525.

[109] Cardillo, P.; Corradi, E.; Lunghi, A.; Meille, S.V.; Messina, M.T.; Metrangolo, P.; Resnati, G. *Tetrahedron,* **2000**, *56*, 5535-5550.

[110] Ding, X.-H.; Ou, C.-J.; Xie, L.-H.; Lin, J.-Y.; Wang, J.-P.; Huang, W. *CrystEngComm*. **2017**, *19*, 5504-5521

[111] Nemec, V.; Fotović, L.; Friščić, T.; Cinčić, D. *Cryst. Growth Des.* **2017**, *17*, 6169-6173.

[112] Zbačnik, M.; Vitković, M.; Vulić, V.; Nogalo, I.; Cinčić, D. *Cryst. Growth Des.* **2016**, *16*, 6381-6389.

[113] Zbačnik, M.; Pajski, M.; Stilinović, V.; Vitković, M.; Cinčič, D. *CrystEngComm*. **2017**, *19*, 5576-5582.

[114] Cinčič, D.; Friščić, T.; Jones, W. *J. Am. Chem. Soc.* **2008**, *130*, 7524-7525.

[115] Metrangolo, P.; Meyer, F.; Pilati, T.; Resnati, G.; Terraneo, G. *Chem. Commun.* **2008**, 1635-1637.

[116] Grebe, J.; Geiseler, G.; Harms, K.; Dehnicke, K. *Z. Naturforsch.* **1999**, *54b*, 77-86.

[117] Grebe, J.; Geiseler, G.; Harms, K.; Neumüller, B.; Dehnicke, K. *Angew. Chem. Int. Ed.* **1999**, *38*, 222-225.

[118] Pfrunder, M.C.; Micallef, A.S.; Rintoul, L.; Arnold, D.P.; Davy, K.J.P.; McMurtrie, J. *Cryst. Growth Des.* **2012**, *12*, 714-724.

[119] Cavallo, G.; Biella, S.; Lü, J.; Metrangolo, P.; Pilati, T.; Resnati, G.; Terraneo, G. *J. Fluorine Chem.* **2010**, *131*, 1165-1172.

[120] Capuccci, D.; Balestri, D.; Mazzeo, P.P.; Pelagatti, P.; Rubini, K.; Bacchi, A. *Cryst. Growth Des.* **2017**, *17*, 4958-4964.

[121] Dziuk, B.; Ośmiałowski, B.; Zarychta, B.; Ejsmont, K. *IUCrData*, **1**, x161466.

[122] Perera, M.D.; Desper, J.; Sinha, A.S.; Aakeröy, C.B. *CrystEngComm.* **2016**, *18*, 8631-8636.

[123] Pigge, F.C.; Kapadia, P.P.; Swenson, D.C. *CrystEngComm*. **2013**, *15*, 4386-4391.

[124] Ravat, P.; Seethalekshmi, S.; Biswas, S.N.; Nandy, P.; Varughese, S. *Cryst. Growth Des.* **2015**, *15*, 2389-2401.

[125] Vartanian, M.; Lucassen, A.C.B.; Shimon, L.J.W.; van der Boom, M.E. *Cryst. Growth Des.* **2008**, *8*, 786-790.

[126] Xu, Y.; Champion, L.; Gabidullin, B.; Bryce, D.L. *Chem. Commun.* **2017**, *53*, 9930-9933.

[127] Cinčič, D.; Friščić, T.; Jones, W. *CrystEngComm*. **2011**, *13*, 3224-3231.

[128] Liu, R.; Wang, H.; Jin, W.J. *Cryst. Growth Des.* **2017**, *17*, 3331-3337.

[129] Cinčič, D.; Friščić, T.; Jones, W. *Chem. Eur. J.* **2008***, 14*, 747-753.

[130] Pang, X.; Zhao, X.R.; Wang, H.; Sun, H.-L.; Jin, W.J. *Cryst. Growth Des.* **2013**, *13*, 3739-3745.

[131] Xu, Y.; Viger-Gravel, J.; Korobkov, I.; Bryce, D.L. *J. Phys. Chem. C* **2015**, *119*, 27104-27117.

[132] Cauliez, P.; Polo, V.; Roisnel, T.; Llusar, R.; Fourmigué, M. *CrystEngComm.* **2010**, *12*, 558-566.

[133] Jay, J.I.; Padget, C.W.; Walsh, R.D.B.; Hanks, T.W.; Pennington, W.T. *Cryst. Growth Des.* **2001**, *1*, 501-507.

[134] Viger-Gravel, J.; Meyer, J.E.; Korobkov, I.; Bryce, D.L. *CrystEngComm.* **2014**, *16*, 7285-7297.

[135] Viger-Gravel, J.; Korobkov, I.; Bryce, D.L. *Cryst. Growth Des.* **2011**, *11*, 4984-4995.

[136] Eccles, K.S.; Morrison, R.E.; Sinha, A.S.; Maguire, A.R.; Lawrence, S.E. *Cryst. Growth Des.* **2015**, *15*, 3442-3451.

[137] Torubaev, Y.V.; Skabitskiy, I.V.; Rusina, P.; Pasynskii, A.A.; Rai, D.K.; Singh, A. *CrystEngComm*. **2018**, *20*, 2258-2266.

[138] Pfrunder, M.C.; Brock, A.J.; Brown, J.J.; Grosjean, A.; Ward, J.; McMurtrie, J.C.; Clegg, J.K. *Chem. Commun.* **2018**, *54*, 3974-3976.

[139] Han, C.; Zhao, D.; Dong, S. *Chem. Commun.* **2018**, *54*, 13099-13102.

[140] Aakeröy, C.B.; Rajbanshi, A.; Metrangolo, P.; Resnati, G.; Parisi, M.F.; Desper, J.; Pilati, T. *CrystEngComm*. **2012**, *14*, 6366-6368.

[141] Aakeröy, C.; Wijethunga, T.K.; Desper, J.; Đaković, M. *Cryst. Growth Des.* **2015**, *15*, 3853-3861.

[142] Turunen, L.; Pan, F.; Beyeh, N.K.; Trant, J.F.; Ras, R.H.A.; Rissanen, K. *Cryst. Growth Des.* **2018**, *18*, 513-520.

[143] Gunawardana, C.A.; Đaković, M.; Aakeröy, C.B. *Chem. Comm.* **2018**, *54*, 607-610.

[144] Erdélyi, M. *Chem. Soc. Rev.* **2012**, *41*, 3547-3557.

[145] Gilday, L.C.; Robinson, S.W.; Barendt, T.A.; Langton, M.J.; Mullaney, B.R.; Beer, P.D. *Chem. Rev.* **2015**, *115*, 7118-7195.

[146] Berger, G.; Soubhye, J.; Meyer, F. *Polym. Chem.* **2015**, *6*, 3559-3580.

[147] Priimagi, A.; Cavallo, G.; Metrangolo, P.; Resnati, G. *Acc. Chem. Res.* **2013**, *46*, 2686-2695.

[148] Tepper, R.; Schubert, U.S. *Angew. Chem. Int. Ed.* **2018**, *57*, 6004-6016.

[149] Molina, P.; Zapata, F.; Caballero, A. *Chem. Rev.* **2017**, *117*, 9907-9972.

[150] Mullaney, B.R.; Thompson, A.L.; Beer, P.D. *Angew. Chem. Int. Ed.* **2014**, *53*, 11458-11462.

[151] Langton, M.J.; Robinson, S.W.; Marques, I.; Félix, V.; Beer, P.D. *Nat. Chem.* **2014**, *6*, 1039-1043.

[152] Lim, J.Y.C.; Marques, I.; Félix, V.; Beer, P.D. *Angew. Chem. Int. Ed.* **2018**, *8*, 584-588.

[153] Lim, J.Y.C.; Marques, I.; Félix, V.; Beer, P.D. *J. Am. Chem. Soc.* **2017**, *139*, 12228-12239.

[154] Barendt, T.A.; Robinson, S.W.; Beer, P.D. *Chem. Sci.* **2016**, *7*, 5171-5180.

[155] Sabater, P.; Zapata, F.; Caballero, A.; de la Visitación, N.; Alkorta, I.; Elguero, J.; Molina, P. *J. Org. Chem.* **2016**, *81*, 7448-7458.

[156] Ravi, A.; Oshchepkov, A.S.; German, K.E.; Kirakosyan, G.A.; Safonov, A.V.; Khrustalev, V.N.; Kataev, E.A. *Chem. Commun.* **2018**, *54*, 4826-4829.

[157] Lim, J.Y.C.; Marques, I.; Félix, V.; Beer, P.D. *Chem. Commun.* **2018**, *54*, 10851-10854.

[158] Yan, D.; Delori, A.; Lloyd, G.O.; Friščić, T.; Day, G.M.; Jones, W.; Lu, J.; Wei, M.; Evans, D.G.; Duan, X. *Angew. Chem. Int. Ed.* **2011**, *50*, 12483-12486.

[159] Christopherson, J.-C.; Topić, F.; Barrett, C.J.; Friščić, T. *Cryst. Growth Des.* **2018**, *18*, 1245-1259.

[160] Zhuo, M.-P.; Tao, Y.-C.; Wang, X.-D.; Wu, Y.; Chen, S.; Liao, L.-S.; Jiang, L. *Angew. Chem. Int. Ed.* **2018**, *57*, 11300-11304.

[161] Bai, L.; Bose, P.; Gao, Q.; Li, Y.; Ganguly, R.; Zhao, Y. *J. Am. Chem. Soc.* **2017**, *139*, 436-441.

[162] Liao, W.-Q.; Tang, Y.-Y.; Li, P.-F.; You, Y.-M.; Xiong, R.-G. *J. Am. Chem. Soc.* **2018**, *140*, 3975-3980.

[163] Silly, F.; Viala, C.; Bonvoisin, J. *J. Phys. Chem. C* **2018**, *122*, 17143-17148.

[164] Saha, B.K.; Jetti, R.K.R.; Reddy, L.S.; Antipamula, S.; Nangia, A. *Cryst. Growth Des.* **2005**, *5*, 887-899.

[165] González, L.; Graus, S.; Tejedor, R.M.; López, P.; Elguero, J.; Serrano, J.L.; Uriel, S. *CrystEngComm*. **2018**, *20*, 3167-3170.

[166] Shankar, S.; Chovnik, O.; Shimon, L.J.W.; Lahav, M.; van der Boom, M.E. *Cryst. Growth Des.* **2018**, *18*, 1967-1977.

[167] Wu, W.X.; Wang, H.; Jin, W.J. *Cryst. Growth Des.* **2018**, *18*, 6742-6747.

[168] Wu, J.; Li, J.; Dong, M.; Miao, K.; Miao, X.; Wu, Y.; Deng, W. *J. Phys. Chem. C* **2018**, *122*, 22597-22604.

[169] Pigge, F.C.; Vangala, V.R.; Kapadia, P.P.; Swenson, D.C.; Rath, N.P. *Chem. Commun.* **2008**, 4726-4728.

[170] Ahmed, F.; Roy, S.; Naskar, K.; Sinha, C.; Alam, S.M.; Kundu, S.; Vittal, J.J.; Mir, M.H. *Cryst. Growth Des.* **2016**, *16*, 5514-5519.

[171] Nikalayenko, V.I.; Castell, D.C.; van Heerden, D.P.; Barbour, L.J. *Angew. Chem. Int. Ed.* **2018**, *130*, 12262-12267.

[172] Heinen, F.; Engelage, E.; Dreger, A.; Weiss, R.; Huber, S.M. *Angew. Chem. Int. Ed.* **2018**, *57*, 3830-3833.

[173] Kobayashi, Y.; Nakatsuji, Y.; Li, S.; Tsuzuki, S.; Takemoto, Y. *Angew. Chem. Int. Ed.* **2018**, *57*, 3646-3650.

[174] Chan, Y.-C.; Yeung, Y.-Y. *Angew. Chem. Int. Ed.* **2018**, *57*, 3483-3487.

[175] Haraguchi, R.; Hoshino, S.; Sakai, M.; Tanazawa, S.-g.; Morita, Y.; Komatsu, T.; Fukuzawa, S.-i. *Chem. Commun.* **2018**, *54*, 10320-10323.

[176] Gliese, J.-P.; Jungbauer, S.H.; Huber, S.M. *Chem. Commun.* **2017**, *53*, 12052-12055.

[177] Cavallo, G.; Terraneo, G.; Monfredini, A.; Saccone, M.; Priimagi, A.; Pilati, T.; Resnati, G.; Metrangolo, P.; Bruce, D.W. *Angew. Chem. Int. Ed.* **2016**, *55*, 6300-6304.

[178] Milani, R.; Houbenov, N.; Fernandez-Palacio, F.; Cavallo, G.; Luzio, A.; Haataja, J.; Giancane, G.; Saccone, M.; Priimagi, A.; Metrangolo, P.; Ikkala, O. *Chem.* **2017**, *2*, 417-426.

[179] Rao, S.S.; Gejji, S.P. *J. Phys. Chem. A* **2016**, *120*, 1243-1260.

[180] Lodeiro, L.; Contreras, R.; Ormazábal-Toledo, R. *J. Phys. Chem. B* **2018**, *122*, 7907-7914.

[181] Saccone, M.; Dichiarante, V.; Forni, A.; Goulet-Hanssens, A.; Cavallo, G.; Vapaavuori, J.; Terraneo, G.; Barrett, C.J.; Resnati, G.; Metrangolo, P.; Priimagi, A. *J. Mater. Chem. C* **2015**, *3*, 759-768.

[182] Howard, E.I.; Sanishvili, R.; Cachau, R.E.; Mitschler, A.; Chevrier, B.; Barth, P.; Lamour, V.; Van Zandt, M.; Sibley, E.; Bon, C.; Moras, D.; Schneider, T.R.; Joachimiak, A.; Podjarny, A. *Proteins.* **2004**, *55*, 792-804.

[183] Hays, F.A.; Vargason, J.M.; Shing Ho, P. *Biochemistry.* **2003**, *42*, 9586-9597.

[184] Auffinger, P.; Hays, F.A.; Westhof, E.; Shing Ho, P. *Proc. Natl. Acad. Sci. U.S.A.* **2004**, *101*, 16789-16794.

[185] Voth, A.R.; Hays, F.A.; Shing Ho, P. *Proc. Natl. Acad. Sci. U.S.A*. **2007**, *104*, 6188-6193.

[186] Carter, M.; Voth, A.R.; Scholfield, M.R.; Rummel, B.; Sowers, L.C.; Shing Ho, P. *Biochemistry.* **2013**, *52*, 4891-4903.

[187] Xu, Z.; Liu, Z.; Chen. T.; Chen, T.; Wang, Z.; Tian, G.; Shi, J.; Wang, X.; Lu, Y.; Yan, X.; Wang, G.; Jiang, H.; Chen, K.; Wang, S.; Xu, Y.; Shen, J.; Zhu, W. *J. Med. Chem.* **2011**, *54*, 5607-5611.

[188] Xu, Z.; Yang, Z.; Liu, Y.; Lu, Y.; Chen, K.; Zhu, W. *J. Chem. Inf. Model.* **2014**, *54*, 69-78.

[189] Hardegger, L.A.; Kuhn, B.; Spinnler, B.; Anselm, L.; Ecabert, R.; Stihle, M.; Gsell, B.; Thoma, R.; Diez, J.; Benz, J.; Plancher, J.-M.; Hartmann, G.; Banner, D.W.; Haap, W.; Diederich, F. *Angew. Chem. Int. Ed.* **2011**, *50*, 314-318.

[190] Shing Ho, P. *Future Med. Chem.* **2017**, 637-640.

[191] Wilcken, R.; Zimmermann, M.O.; Lange, A.; Joerger, A.C.; Boeckler, F.M. *J. Med. Chem.* **2013**, *56*, 1363-1388.

[192] Rietveld, H.M. *J. Appl. Cryst.* **1969**, *2*, 65-71.

[193] Katsenis, A.D. et al. *Nat. Comm.* **2015**, *6*, 6662.

[194] Zha, B.; Dong, M.; Miao, X.; Miao, K.; Hu, Y.; Wu, Y.; Xu, L.; Deng, W. *J. Phys. Chem. Lett.* **2016**, *7*, 3164-3170.

[195] Peyvot, D.; Silly, M.G.; Silly, F. *Phys. Chem. Chem. Phys.* **2018**, *20*, 3918-3924.

[196] Zheng, Q.-N.; Liu, X.-H.; Chen, T.; Yan, H.-J.; Cook, T.; Wang, D.; Stang, P.J.; Wan, L.-J. *J. Am. Chem. Soc.* **2015**, *137*, 6128-6131.

[197] Boterashvili, M.; Lahav, M.; Shankar, S.; Facchetti, A.; van der Boom, M.E. *J. Am. Chem. Soc.* **2014**, *136*, 11926-11929.

[198] Wang, C.; Danovich, D.; Shaik, S.; Mo, Y. *J. Chem. Theory Comput.* **2017**, *13*, 1626-1637.

[199] Wang, W.; Hobza, P. *J. Phys. Chem. A* **2008**, *112*, 4114-4119.

[200] Lindblad, S.; Mehmeti, K.; Veiga, A.X.; Nekoueishahraki, B.; Gräfensetin, J.; Erdélyi, M. *J. Am. Chem. Soc.* **2018**, *140*, 13503-13513.

[201] Ciancaleoni, G.; Macchioni, A.; Rocchigiani, L.; Zuccaccia, C. *RSC Adv.* **2016**, *6*, 80604-80612.

[202] Sarwar, M.G.; Dragisic, B.; Sagoo, S.; Taylor, M.S. *Angew. Chem. Int. Ed.* **2010**, *49*, 1674-1677.

[203] Beale, T.M.; Chudzinskim, M.G.; Sarwar, M.G.; Taylor, M.S. *Chem. Soc. Rev.* **2013**, *42*, 1667-1680.

[204] Vanderkooy, A.; Pfefferkorn, P.; Taylor, M.S. *Macromolecules.* **2017**, *50*, 3807-3817.

[205] Bryce, D.L.; Viger-Gravel, J. *Top. Curr. Chem.* **2015**, *358*, 183-204.

[206] Szell, P.M.J.; Bryce, D.L. *Modern Magn. Reson.* **2016**, pp. 1-18.

[207] Cerreia Vioglio, P.; Chierotti, M.R.; Gobetto, R. *CrystEngComm.* **2016**, *18*, 9173-9184.

[208] Viger-Gravel, J.; Leclerc, S.; Korobkov, I.; Bryce, D.L. *CrystEngComm.* **2013**, *15*, 3168-3177.

[209] Cerreia Vioglio, P.; Catalano, L.; Vasylyeva, V.; Nervi, C.; Chierotti, M.R.; Resnati, G.; Robetto, R.; Metrangolo, P. *Chem. Eur. J.* **2016**, *22*, 16819-16828.

[210] Widdifield, C.M.; Cavallo, G.; Facey, G.A.; Pilati, T.; Lin, J.; Metrangolo, P.; Resnati, G.; Bryce, D.L. *Chem. Eur. J.* **2013**, *19*, 11949-11962.

[211] Attrell, R.J.; Widdifield, C.M.; Korobkov, I.; Bryce, D.L. *Cryst. Growth Des.* **2012**, *12*, 1641-1653.

[212] Viger-Gravel, J.; Leclerc, S.; Korobkov, I.; Bryce, D.L. *J. Am. Chem. Soc.* **2014**, *136*, 6929-6942.

[213] Viger-Gravel, J.; Meyer, J.; Korobkov, I.; Bryce, D.L. *CrystEngComm.* **2014**, *16*, 7285-7297.

[214] Xu, Y.; Viger-Gravel, J.; Korobkov, I.; Bryce, D.L. *J. Phys. Chem. C* **2015**, *119*, 27104-27117.

[215] Catalano, L.; Pérez-Estrada, S.; Terraneo, G.; Pilati, T.; Resnati, G.; Metrangolo, P.; Garcia-Garibay, M.A. *J. Am. Chem. Soc.* **2015**, *137*, 15386-15389.

[216] Lemouchi, C.; Vogelsberg, C.S.; Zorina, L.; Simonov, S.; Batail, P.; Brown, S.; Garcia-Garibay, M.A. *J. Am. Chem. Soc.* **2011**, *133*, 6371-6379.

[217] Catalano, L.; Perez-Estrada, S.; Wang, H.-H.; Ayitou, A.J.-L.; Khan, S.I.; Terraneo, G.; Metrangolo, P.; Brown, S.; Garcia-Garibay, M.A. *J. Am. Chem. Soc.* **2017**, *139*, 843-848.

[218] Weingarth, M.; Raouafi, N.; Jouvelet, B.; Duma, L.; Bodenhausen, G.; Boujlel, K.; Schöllhorn, B.; Tekely, P. *Chem. Commun.* **2008**, 5981-5983.

[219] Nishinaga, T. *Jpn. J. Appl. Phys.* **2015,** *54*, 050101.

[220] Gilman, J.J. *The Art and Science of Growing Crystals*. John Wiley & Sons Inc., New York, **1963**.

[221] Mullin, J.W. *Crystallization*. Butterworth-Heinemann, Burlington, **2001**.

Chapter 2 – Theory

The goal of this chapter is to present readers from a variety of backgrounds the fundamental concepts required to understand the experimental approaches and results shown in this thesis. This discussion will therefore focus on the theory of NMR spectroscopy, computational chemistry, and X-ray crystallography, providing a general overview rather than a comprehensive discussion of these topics.

2.1. Nuclear Magnetic Resonance Spectroscopy.

With most elements on the periodic table having a spin-active isotope, nuclear magnetic resonance (NMR) spectroscopy has become a popular technique for probing the chemical and electronic environment of a nucleus in a sample.[1,2,3] The nuclear intrinsic angular momentum (spin) is associated with a magnetic moment (μ) which can interact with an external magnetic field.[4] The spin quantum number has $2I+1$ states (m) and can have several values with the most common spins being: 0, 1/2, 1, 3/2, 5/2, 7/2, and 9/2. Our discussion will begin with a spin-1/2 nucleus, which has two energy levels: +1/2 (denoted here as α), and -1/2 (denoted here as β). In the absence of an external magnetic field, these two spin states share the same energy level, and are therefore *degenerate*. However, the addition of an external magnetic field breaks this degeneracy, with the resulting *Zeeman splitting* perturbing the energy levels, quantified by Eq. 1.2.1.[5]

$$\Delta E = \frac{h}{2\pi}\gamma_L B_0 \qquad \text{Eq. 1.2.1}$$

In Eq. 1.2.1, ΔE is the difference in energy between the β and α state, h is Planck's constant (J·s), γ_L is the gyromagnetic ratio of the nucleus (rad s^{-1} T^{-1}), and B_0 is the strength of the external magnetic field (T). Consequently, a stronger applied magnetic field will result in a larger Zeeman splitting, with this dependency of the energy levels on B_0 shown in Figure 1.2.1. NMR is now routinely performed at fields of over 9.4 T, which is orders of magnitude stronger than a refrigerator magnet (~5 mT). These fields can be achieved using superconducting magnets operating at liquid helium temperatures (~4 K), reducing the energy requirements associated with resistive magnets, which otherwise lose their energy as heat.

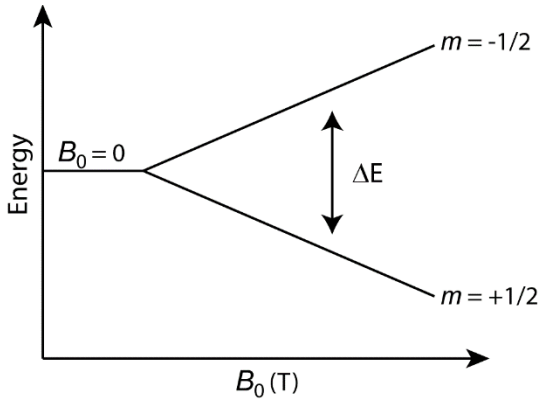

Figure 1.2.1. The Zeeman splitting of a spin-1/2 nucleus as a function of the external magnetic field strength (B_0).

The application of electromagnetic radiation can stimulate the transition from the lower energy state to the upper energy state, which can be calculated from Eq. 1.2.1 using Planck's formula ($E = h\nu$) and solving for ν. The resulting equation gives the frequency satisfying the transition energy, called the *Larmor frequency* (ν_L), given in Eq. 1.2.2.[6]

$$\nu_L = \frac{\gamma_L B_0}{2\pi} \qquad \text{Eq. 1.2.2}$$

For a nuclear spin, such as the proton ($\gamma_L(^1H)$ = 267.5x10^6 rad s^{-1} T^{-1}),[7] the required electromagnetic radiation is in the radiofrequency region, with the resulting Larmor frequency in a 21.1 T magnetic field being 900 MHz.

Unfortunately, the energy difference between the α and β state is not substantial, which allows only a limited difference in their population. The ratio of the populations in the α and β state can be calculated using the Boltzmann distribution in Eq. 1.2.3:

$$\frac{N_\alpha}{N_\beta} = e^{\frac{\Delta E}{kT}} \qquad \text{Eq. 1.2.3}$$

Here, N_α represents the population in the α state, N_β represents the population in the β state, k is Boltzmann's constant (m² kg s^{-2} K^{-1}), and T is the temperature (K). This relatively small population difference between the α and β states render NMR spectroscopy as inherently insensitive, with higher magnetic fields strengths providing an increase in the sensitivity.

Prior to entering the magnetic field, the spins in the sample are randomly oriented. As the lower energy state is favored by the Boltzmann distribution given in Eq. 1.2.3, the spin population in the α state is slightly higher than that of the β state. Consequently, a small net magnetic moment is created in the sample, corresponding to the excess spins in the α state, which aligns with the external magnetic field.[8] The rate at which the spins relax to this lower energy state is the *spin-lattice relaxation time*, abbreviated as T_1 and given in Eq. 1.2.4.[9] As a convention, the external magnetic field is in line with the Z axis.

$$M_t = M_0(1 - e^{-\frac{t}{T_1}}) \qquad \text{Eq. 1.2.4}$$

In Eq. 1.2.4, the M_t denotes the sample magnetization at time t, t denotes the time spent in the magnetic field, and M_0 denotes the magnetization at $t \rightarrow \infty$. Using a vector model, the process of

building the magnetization along an external magnetic field in the Z-axis is shown in Figure 1.2.2.

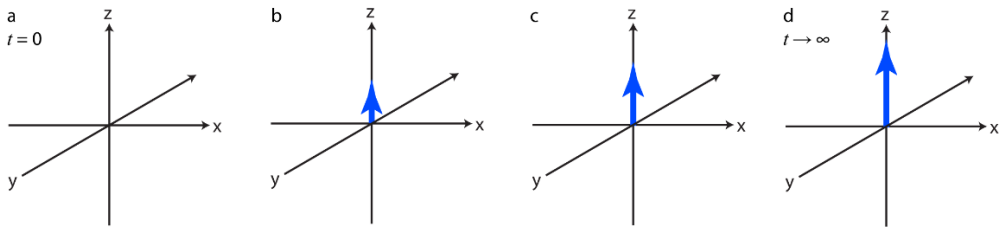

Figure 1.2.2. The sample magnetization (represented as a blue arrow) upon the introduction of an external magnetic field aligned with the Z axis at $t = 0$ (**a**), after an infinite amount of time (**d**, $t \rightarrow \infty$), and the intermediate cases (**b**, **c**).

The net magnetic moment of the sample can be manipulated using an oscillating magnetic field, which is achieved through the application of radiofrequencies (RF).[10] In Fourier transform NMR, short RF pulses are applied in order to reorient the magnetization vector into the XY plane, with pulse lengths on the order of μs (10^{-6} s). An RF pulse that reorients the magnetization from the Z axis to the X or Y axis is named a 90° pulse, or "π/2" radians. Following this RF pulse, the magnetization will return to its thermodynamic equilibrium by precessing about the magnetic field at the Larmor frequency.[11] As it precesses, the oscillating magnetic field of the spins induces a current in the RF coil, which is placed perpendicular to the external magnetic field (in the XY plane).[12,13] This characteristic signal, named the *free induction decay* (FID),[8] is then received and analyzed by the NMR spectrometer, converting the signal from the time domain to the frequency domain using a Fourier transformation. In order to facilitate the data interpretation, a frame of reference rotating with the carrier frequency is employed and thus any deviations from the carrier frequency can easily be measured. An example of this process is shown in Figure 1.2.3.

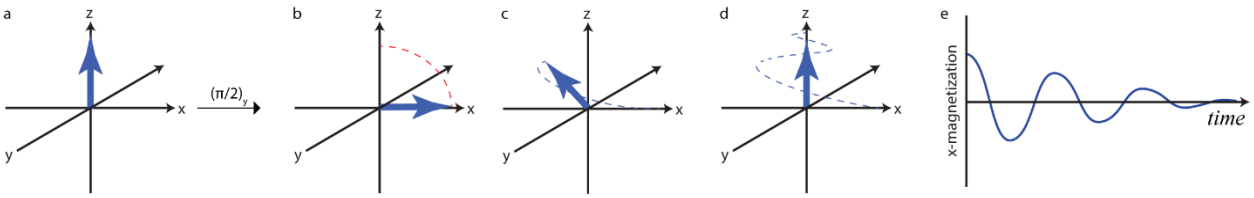

Figure 1.2.3. The bulk magnetization at equilibrium (**a**) rotates to the X-axis upon the application of a $(\pi/2)_y$ RF pulse (**b**) and precesses back to thermodynamic equilibrium (**c**, **d**), showing the resulting free induction decay in **e**.

The rate at which the spins lose their magnetization along the XY plane (M_{XY}) is named the *spin-spin relaxation time*, abbreviated as T_2, and given in Eq. 1.2.5.[3] Following the uncertainty principle, longer T_2 relaxation times provide sharper NMR linewidths, while shorter T_2 relaxation times yield broader linewidths.

$$M_{xy}(t) = M_{xy,0}e^{-t/T_2} \qquad \text{Eq. 1.2.5}$$

In Eq. 1.2.5, $M_{xy}(t)$ denotes the magnetization in the XY plane at time t, and $M_{XY,0}$ denotes the magnetization in the XY plane immediately after the pulse. Several experimental conditions can lead to shorter observed T_2 relaxation times (T_2*), such as magnetic field inhomogeneity or *RF* inhomogeneity. The magnetic field is thus made homogeneous by modifying the current in a set of electromagnetic coils placed in the bore of the magnet, which are called the *shims*. In solution NMR, deuterium locks are used to stabilize any field drifts associated with the magnet, allowing for the collection of higher quality NMR data.

The Fourier transformation converts the FID into a frequency domain, named the NMR spectrum. Deviations in the frequencies leads to the chemical shift, which offers information on the environment surrounding the nucleus.[14] Rather than using the absolute resonance frequency,

which varies from field to field, the chemical shift is expressed in units of ppm relative to a reference frequency, given in Eq. 1.2.6.

$$\delta_{iso} = \frac{\nu_R - \nu_{ref}}{\nu_{ref}} x10^6 \qquad \text{Eq. 1.2.6}$$

Here, δ_{iso} represents the isotropic chemical shift, ν_R is the resonance frequency, and ν_{ref} is the resonance frequency of the reference. The chemical shift arises due to the shielding of the nucleus by its surrounding electronic environment, including both diamagnetic and paramagnetic contributions, yielding a nucleus that experiences a magnetic field differing from B_0.[14] The diamagnetic contribution, which is the most important contribution for the ^{1}H nucleus, is due to the movement of electrons in their ground state, with the electronic density playing an important role.[14] Moreover, the paramagnetic contribution is due to the electrons moving from the ground state to the excited state, creating a local magnetic field.[14] Neighboring atoms lead to a change in the chemical shift, and consequently, the chemical shift is a diagnostic tool leading to the molecular structure.[15] While the nuclear shielding (σ_{CS}) can be difficult to measure experimentally, the chemical shift can easily be measured using NMR experiments, with Eq. 1.2.7 relating nuclear shielding to the chemical shift.

$$\delta = (1 - \sigma_{CS}) \frac{\gamma B_0}{2\pi} \qquad \text{Eq. 1.2.7}$$

The chemical shift is anisotropic, which means that the chemical shift has a dependence on the spin's orientation relative to the external magnetic field. In solution, this dependence is averaged by Brownian motion,[16] giving an isotropic chemical shift. In contrast, nuclei in solids are not averaged, with the resulting chemical shift anisotropy (CSA) causing a broadening of the resonances.[13] The chemical shift can be expressed as a tensor with three components: $\delta_{11} \geq \delta_{22} \geq$

δ_{33}. Following the Herzfeld-Berger convention, the characteristic lineshapes from the CSA can be described by the isotropic chemical shift (δ_{iso}), the span (Ω), and the skew (κ), given in Eqs. 1.2.8 to 1.2.10.[17]

$$\delta_{iso} = \frac{\delta_{11} + \delta_{22} + \delta_{33}}{3} \qquad \text{Eq. 1.2.8}$$

$$\Omega = \delta_{11} - \delta_{33} \qquad \text{Eq. 1.2.9}$$

$$\kappa = \frac{3(\delta_{22} + \delta_{iso})}{\Omega} \qquad \text{Eq. 1.2.10}$$

While acquiring the full CSA line shape can give useful crystallographic information, the signal is spread out, leading to difficulties in experimentally acquiring the entire spectrum. Furthermore, the overlap from multiple resonances can cause difficulties in the interpretation, leading to the requirement of high resolution solid-state NMR techniques.[18] To this end, magic angle spinning (MAS) has been developed as a method to average the CSA observed in powdered samples, reducing the large linewidth to a solution-like isotropic chemical shift.[19,20,21] Magic angle spinning consists of rotating the sample at the magic angle (θ_{MAS} = 54.74°) at high speeds (ν_{MAS} > 1000 Hz), averaging the second-order Legendre polynomial.[19] In Figure 1.2.4, we compare the simulated ^{13}C solid-state NMR spectrum under stationary condition to that of the MAS conditions.

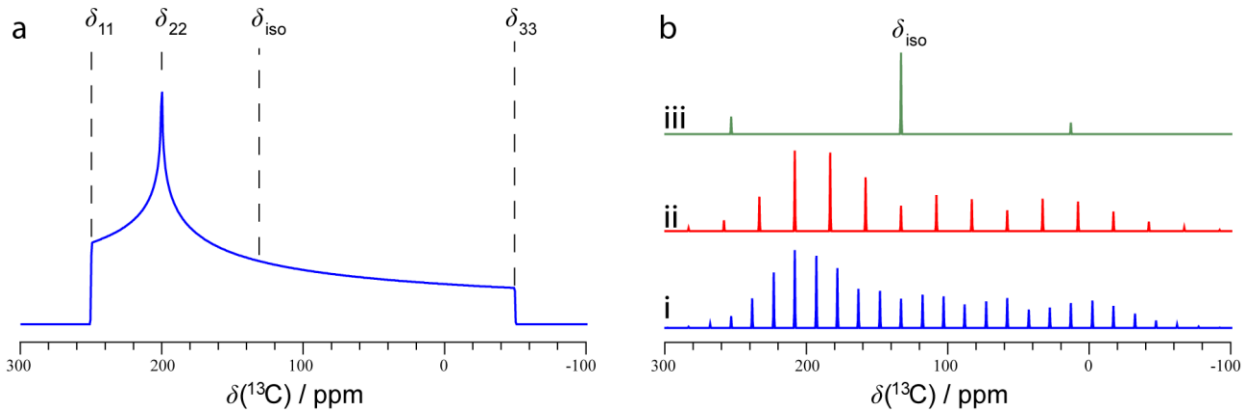

Figure 1.2.4. Simulated ^{13}C solid-state NMR spectrum at 9.4 T containing one site with δ_{11} = 250 ppm, δ_{22} = 200 ppm, δ_{33} = -50 ppm under (a) stationary conditions and (b) under magic angle spinning at frequencies of 1.5 kHz (i), 2.5 kHz (ii), and 12 kHz (iii).

While the fictional ^{13}C lineshape spans 300 ppm under stationary conditions (Figure 1.2.4a), the ^{13}C NMR spectrum under MAS conditions consist of a series of narrow peaks at intervals of the MAS frequency. In the case of Figure 1.2.4b, the sample's spinning frequency is shown to have an important role, with the manifestation of spinning sidebands at integers of the spinning speed.[22] These spinning sidebands can overlap with other resonances and hamper interpretation, with faster spinning speeds typically yielding the simplest spectrum due to the lower quantity of spinning sidebands. For instance, at a spinning speed of 12 kHz (Figure 1.2.4b,iii), the isotropic chemical shift can easily be measured, with only two spinning sidebands. In contrast, the spectrum simulated with a spinning speed of 1.5 kHz has several sidebands (Figure 1.2.4b,i). Fitting the MAS spinning sidebands can lead to the CSA tensor and the use of multiple spinning speeds allows for the identification of the isotropic chemical shift.[17] In this thesis, one of the applications of measuring the isotropic chemical shift was to detect the occurrence of the halogen bond. For instance, in Chapters 7 and 12, the ^{19}F isotropic chemical shifts were used to quickly determine whether the compounds had successfully cocrystallized, in addition to identifying the presence of side phases and remaining material.

If the NMR spectrum under stationary conditions is desired, a single pulse experiment may not be suitable to acquire the full lineshape. As the spectrum is very wide, the T_2 relaxation times are very short, with the signal fading before the detector is even recording. Pulse sequences using echoes[23,24] have been developed to acquire these signals despite the short relaxation times, with a notable example of the Hahn echo pulse sequence shown in Figure 1.2.5.[23]

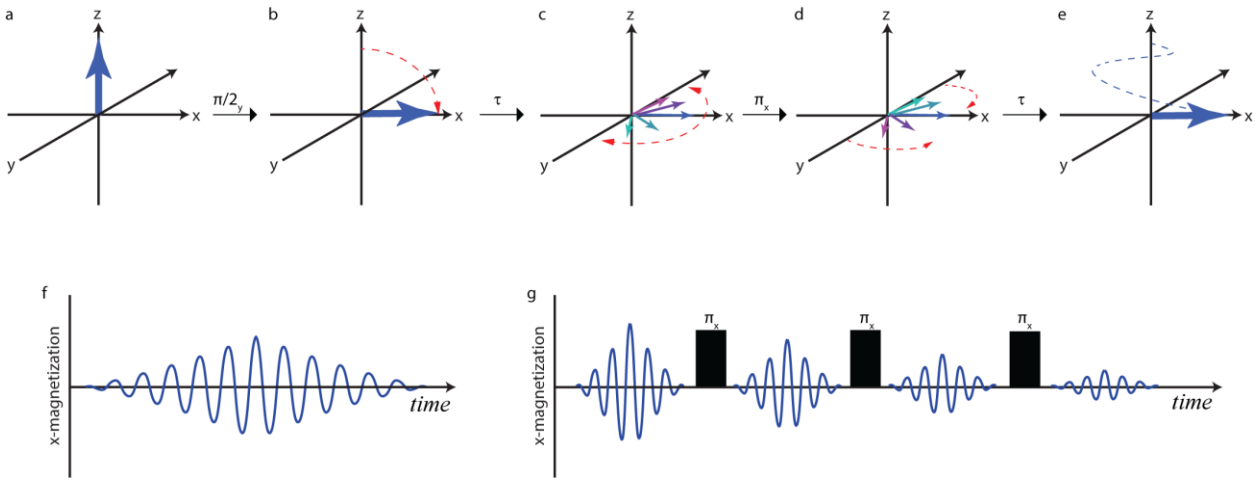

Figure 1.2.5. Vector model showing a spin echo pulse sequence (**a** – **e**), the resulting FID (**f**), and (**g**) the FID obtained if the π pulse is repeated. The red dotted arrows denote the relative movement of the dephasing and refocusing.

Following a π/2 pulse, the spins dephase during a set period of time (τ). The spins are then refocused using a π pulse after the period of time τ, creating an "echo" in the NMR signal. The receiver can then begin recording after a ring-down period, allowing the signal to be detected with a small compromise on its intensity. If the π pulse is repeated, the echo can potentially be recorded several times as a way of enhancing the signal intensity. The latter pulse sequence is called the Carr-Purcell-Meiboom-Gill (CPMG),[25] with a variant of this sequence applied for the analysis of quadrupolar nuclei.

The occurrence of indirect spin-spin interactions mediated by the electrons has rendered NMR spectroscopy unique from other spectroscopic methods, offering information on interatomic connectivity.[26] The resulting interaction, named *J*-coupling, is manifested by the splitting of resonances into characteristic multiplets (e.g. doublet, triplet, …) which can be used with the chemical shift to decipher the molecular structure of an analyte.[15] The contributions to the *J*-coupling include the Fermi contact, the spin-dipole interaction, and the paramagnetic & diamagnetic spin-orbital mechanisms.[27] The observed multiplet resulting from *J*-coupling has a dependence on the strength of the magnetic field, with strong *J*-couplings relative to ν_L causing second order effects. In such a case, fitting the multiplet at several fields using software can allow for the extraction of many variables from complex coupling systems,[28] such as the ^{13}C-^{19}F couplings observed in 1,3,5-tri(iodoethynyl)-2,4,6-trifluorobenzene and discussed in Chapter 10.

In addition to the CSA and *J*-coupling, dipolar coupling (DC) is an important magnetic···magnetic interaction that occurs between nuclei in the solid state.[3] This interaction is directly dependent on the gyromagnetic ratios of the coupled nuclei (γ_S, γ_I) and their internuclear distances (r_{SI}). The dipolar coupling constant can be calculated using Eq. 1.2.11.[29]

$$D = \frac{\mu_0}{4\pi}\frac{\gamma_S\gamma_I\hbar}{r_{SI}^3}\cdot\frac{1}{2\pi} \qquad \text{Eq. 1.2.11}$$

Where μ_0 is the vacuum permeability constant (4π x 10^{-7} N / A²), ħ is the reduced Planck constant, and the resulting units are in Hz. As dipolar coupling has an orientation dependence, MAS can average the dipolar coupling, leading to a further enhancement on the signal resolution.[30] While the measurement of dipolar coupling has not been exploited in this thesis, it has allowed for the increase in signal sensitivity through the use of *cross polarization*.[18,31,32]

As the energy splitting increases with the gyromagnetic ratio, low-γ_L nuclei suffer from low sensitivity. The solution is to transfer the polarization from an abundant spin with a high gyromagnetic ratio to a spin with a lower gyromagnetic ratio through the simultaneous irradiation of both spin pairs. The cross-polarization pulse sequence is shown in Figure 1.2.6.

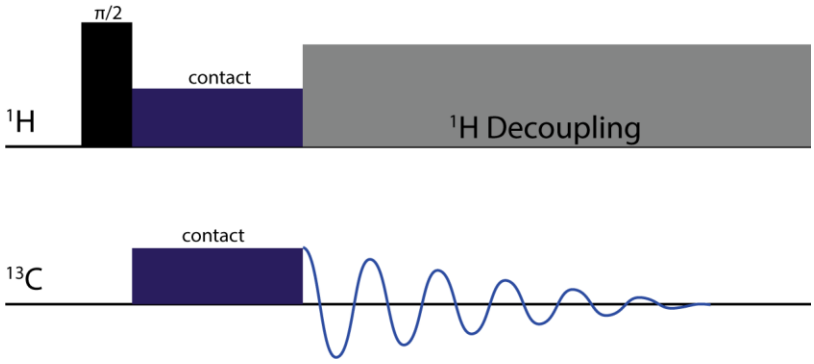

Figure 1.2.6. Cross-polarization pulse sequence for the ^{1}H→^{13}C spin pairs.

Cross-polarization is now routinely combined with magic angle spinning, yielding a signal enhancement on the ratio of $\gamma_L(^1H)/\ \gamma_L(^{13}C)$ for the case of ^{1}H→^{13}C.[31] Further, as the relaxation times of the ^{1}H are typically much shorter than ^{13}C, more transients can be taken rather than through the direct excitation of the ^{13}C nuclei. The pulse sequence, shown in Figure 1.2.6, begins with a π/2-pulse on the proton channel. The simultaneous irradiation of both the ^{1}H and ^{13}C nuclei, named the spin lock, allows for the transfer of magnetization when the Hartmann-Hahn condition is met. Proton decoupling, which is the irradiation of the protons during the acquisition,[33,34] allows for a further enhancement of signal quality by reducing secondary broadening effects. In this thesis, cross-polarization magic angle spinning (CPMAS) has been applied for the analysis of the ^{13}C & ^{15}N nuclides, and we compare the signal enhancement between ^{19}F→^{13}C and ^{1}H→^{13}C for characterizing the fluorinated donor molecule in Chapter 7.

Thus far, we have considered only spin ½ nuclei. However, approximately three quarters of the periodic table consists of quadrupolar nuclei, which have a spin greater than ½. These nuclei have an asymmetric charge distribution at the nucleus and consequently have a quadrupole moment associated to them.[35] The quadrupole moment (Q) can be either positive (prolate nucleus), or negative (oblate nucleus), with the magnitude of Q influencing the quadrupolar coupling.[36] When a nucleus has an asymmetric distribution of its electrons, it generates an electric field gradient (EFG), which is defined by Eq. 1.2.12.

$$V_{\alpha,\beta} = \frac{\partial^2 \Phi}{\partial r_\alpha \, \partial r_\beta} \qquad \text{Eq. 1.2.12}$$

Here, Φ is the electric potential, r_α and r_β are distances in polar spherical coordinates. The quadrupole moment associated with the nucleus couples to the EFG, leading to the *quadrupolar coupling*.[36,37] While Q is a constant, the EFG changes with the local symmetry and environment. For example, an EFG of zero is expected for a cubic structure, while a large EFG is expected for atoms exhibiting a single covalent bond.[38] As a result, the measurement of the quadrupolar coupling allows for the measurement of the EFG at the nucleus, which then provides insights into its electronic structure and crystallographic environment.[39] The EFG can be described by a second rank symmetrical tensor with three components, following the convention: $|V_{33}| \geq |V_{22}| \geq |V_{11}|$. The EFG tensor is traceless, and therefore the sum of all 3 components gives 0, shown in Eq. 1.2.13.

$$V_{33} + V_{22} + V_{11} = 0 \qquad \text{Eq. 1.2.13}$$

As the quadrupole moment is a constant, the quadrupolar coupling can be described by two variables: the quadrupolar coupling constant, C_Q (in MHz, Eq. 1.2.14) – which describes the

magnitude of the interaction, and η (no units, Eq. 1.2.15) – the asymmetry parameter which describes the shape of the tensor.

$$C_Q = \frac{eQV_{33}}{h} \qquad \text{Eq. 1.2.14}$$

$$\eta = \frac{V_{11} - V_{22}}{V_{33}} \qquad \text{Eq. 1.2.15}$$

Here, e is the elementary charge (1.6021×10^{-19} C), Q is the quadrupole moment (in mb or 10^{-28} m^2), h is Planck's constant, and V_{33}, V_{22}, V_{11} are the EFG tensor components. From perturbation theory, we can obtain our first order quadrupolar coupling frequency (ν_Q), resulting in equation 1.2.16.[37]

$$\nu_Q = \frac{3}{4}\left(\frac{C_Q}{2I(2I-1)}\right)(3\cos^2\beta_Q - 1 + \eta\sin^2\beta_Q\cos 2\alpha_Q) \qquad \text{Eq. 1.2.16}$$

Where I is the nuclear spin quantum number, α_Q and β_Q are Euler angles. Following perturbation theory, the effect of quadrupolar coupling on the energy levels can be well estimated using the 1st order and 2nd order quadrupolar coupling terms for nuclei where $\nu_Q/\nu_L < 0.1$, shown in Figure 1.2.7. In cases where $\nu_Q/\nu_L > 0.1$, treatment with exact theory yields better results.[40,41]

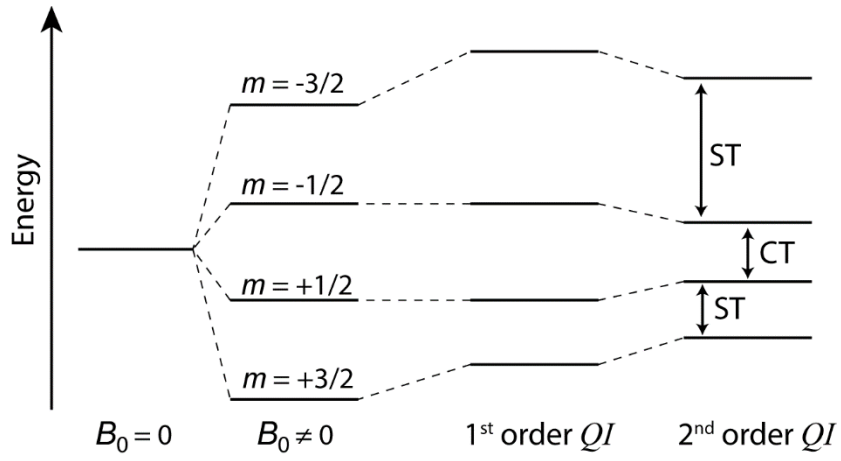

Figure 1.2.7. Zeeman splitting for a spin 3/2 nucleus showing the effects of the 1st and 2nd order quadrupolar interaction. ST and CT denote the satellite transitions and central transitions.

While the satellite transitions (ST) can be observed in nuclei subject to small quadrupolar couplings, the central transition (CT) is typically the most amenable by solid-state NMR spectroscopy. Further, the spectral width of the CT for quadrupolar nuclei is inversely proportional to ν_L, and consequently, stronger magnetic fields are favorable for the analysis of quadrupolar nuclei by narrowing the spectrum while increasing the signal sensitivity.[42] However, even with the use of very high magnetic fields, the CT can be excessively broad, requiring specialized acquisition techniques in order to acquire the full spectrum. While the quadrupolar echo is certainly useful, the quadrupolar CPMG sequence[43,44] in combination with wideline excitation pulses has been shown to be a powerful approach to characterize quadrupolar nuclei. The introduction of WURST pulses have been shown to have a large excitation bandwidth, achieved through a phase modulated frequency sweep.[45] In addition, a spectrum can be acquired in a series of subspectra by offsetting the RF transmitter, which are then coadded in the frequency domain to yield the full spectrum. The technique is named variable offset cumulative spectral acquisition (VOCS) and has allowed for the acquisition of broad spectra.[46]

The WURST-QCPMG pulse sequence,[47,48] shown in Figure 1.2.8, can be combined with VOCS in order to acquire ultra-wideline spectra,[49] which would otherwise be very difficult to acquire using an echo.

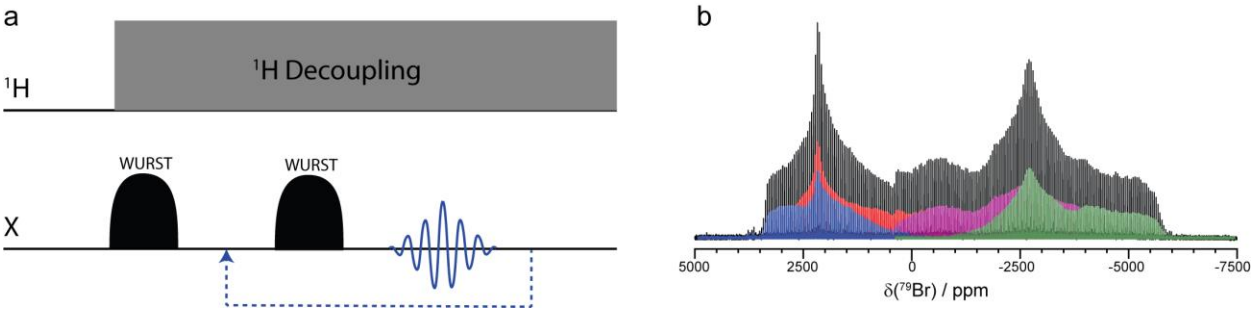

Figure 1.2.8. (a) The WURST-QCPMG pulse sequence, where the blue arrow denotes a repetition. (b) The experimental ^{79}Br spectrum of 2-iodoethynylpyridinium hydrobromide taken from Chapter 8, obtained using WURST-QCPMG and VOCS. Each subspectrum is shown in color and coadded to give the full spectrum in black.

In the case of very large quadrupolar interactions, nuclear quadrupole resonance (NQR) spectroscopy can be advantageous, yielding relatively sharp linewidths while being performed in the complete absence of a magnetic field.[50,51] In Chapter 3, we discuss NQR further and compare it to NMR in terms of fundamental theory and acquisition techniques, with the quadrupolar halogens serving as examples. In part 2 of this thesis, we combine NMR and NQR to investigate the halogen bond donor due to the large quadrupolar coupling observed in the covalently bonded halogens (Cl, Br, I).

The general solid-state NMR Hamiltonian is given in Eq. 1.2.17, which combines the Hamiltonians of the Zeeman interaction (H_Z), the RF interaction (H_{RF}), the chemical shift anisotropy (H_{CSA}), the *J*-coupling (H_{JC}), the dipolar coupling (H_{DC}), and the quadrupolar coupling (H_{QC}).

$$H_{SSNMR} = H_Z + H_{RF} + H_{CSA} + H_{JC} + H_{DC} + H_{QC} \qquad \text{Eq. 1.2.17}$$

Consequently, a solid-state NMR spectrum is rich with structural information as it offers insights into the chemical and electronic environment, interatomic distances and connectivity. The NMR spectrum can be described by the chemical shift anisotropy tensor (δ_{iso}, Ω, κ), the quadrupolar coupling tensor (C_Q, η), the Euler angles (α_E, β_E, γ_E) which relate the CSA tensor orientation to the EFG tensor,[52] as well as any dipolar coupling and *J*-coupling. The combination of these interactions is manifested as spectral features such as shoulders, breaks, and peaks. In order to fully interpret the spectrum, simulations are required to extract the NMR parameters. With the availability of high-performance processors and NMR simulation software, spectral interpretation can be accomplished through iterative fitting. That is, each NMR parameter is altered until the simulated spectrum matches the experimental spectrum at multiple magnetic field strengths.[53] Several programs exist to extract the information from NMR spectra, each with different advantages. This list includes and is not limited to: DMFIT,[54] wSolids,[55] QUEST,[41] EasyGoing,[56] and QuadFit.[57] Of these, QUEST[41] has been developed in our laboratory to allow exact spectral fitting of nuclei subject to large quadrupolar coupling and has therefore been an important tool throughout this thesis.

The information offered by NMR spectroscopy is not limited to the analysis of spectra, but measuring the relaxation times (T_1 and T_2) can provide information on the dynamics occurring in the sample. The correlation time, τ_c, defines the time required for the motion to complete 1 radian, and is the inverse of the rate of motion.[58] At temperatures where quantum tunneling contributions become negligible, this rate of motion follows the Arrhenius equation. In the fast motion limit, the T_1 relaxation time is proportional to τ_c, and it has been shown that the T_1 relaxation times varies with certain dynamics processes,[59] such as a methyl group rotation.

Consequently, measuring the T_1 relaxation times at temperatures where quantum tunneling is insignificant gives direct access to the Arrhenius parameters, given in Eq. 1.2.18.[60,61]

$$T_1 \propto \frac{1}{\tau_c} = A \exp\left(\frac{-E_a}{RT}\right) \qquad \text{Eq. 1.2.18}$$

In this equation, A is the preexponential constant, E_a is the Arrhenius activation energy, R is the gas constant, and T is the sample temperature. The T_1 relaxation time of a sample can be measured using techniques such as the inversion recovery, and when performed at several temperature increments, can yield the Arrhenius activation energy by plotting $\ln(T_1)$ as a function of 1/T. The temperature can be varied by cooling dry nitrogen gas through a heat exchanger, with the gas then heated to the desired temperature and passed onto the sample. Moreover, given the low natural abundance of 0.01% associated with deuterium (^{2}H), the isotopic labelling of a molecule allows for site-specific investigations of the dynamics. Being a quadrupolar nucleus (I = 1), the ^{2}H line shape has been shown to be sensitive to the occurrence of dynamics, and can be fit using software such as EXPRESS in order to extract information on the motion.[62] In Chapter 9, we exploit T_1 relaxation measurements to observe the influence of the halogen bond on the rotational energy barrier associated with a nearby methyl group. Further, the ^{2}H line shape has been a diagnostic tool supporting the absence of major secondary dynamics processes that may have affected the results.

Solid-state NMR has served a central role in this thesis, providing direct insights into the changes in the EFG on the halogen bond donor atom upon the introduction of a halogen bond. Due to the extreme quadrupolar couplings observed for covalently bonded chlorine, bromine, and iodine, NMR is combined with NQR in order to effectively characterize the halogen bond donor atom. The EFG was also used to characterize the halogen bond acceptor in a series of isomorphous compounds featuring the C-I$\cdots$X$^-\cdots$H-N$^+$ moiety (X = Cl, Br, I), allowing for the

direct comparison of the halogen bond involving several different acceptor atoms. Moreover, changes in chemical shifts were paramount to discriminate side phases and starting materials from the halogen bonded cocrystal, which was key to the success of Chapters 11 and 12. Lastly, we have employed variable-temperature ^{2}D solid-state NMR to measure the influence of the halogen bond on the nearby dynamics, using the rotating methyl groups of 2,3,5,6-tetramethylpyrazine as a model. These topics are discussed further during the introduction for each part of the thesis, putting them in context of the current literature.

2.2. Computational Chemistry

In order to support the interpretation of the experimental results, computational chemistry has provided a powerful tool offering theoretical insights into the fundamental interactions at hand. Models can be created either by using the atomic coordinates directly from the experimental crystal structures or by creating new models using software such as GaussView.[63] The atomic positions and bond lengths of these models are generally optimized in order to correct any flaws, such as correcting the carbon-proton bond length which may be underestimated by X-ray diffraction.[64,65] Most NMR observables can be calculated from these models, such as the chemical shift, *J*-coupling constants, and quadrupolar coupling. Further, these calculations can permit the contributions of each NMR observable to be decomposed into a set of molecular orbitals which can assist the data interpretation. In this thesis, cluster models are built by including both the halogen bond donor and acceptor molecules in order to investigate the influence of the halogen bond on the NMR observables. In most instances, the models have been generated using the experimental atomic coordinates from the crystal structure, followed by a geometry optimization while constraining the $d_{X\cdots Y}$ and $\theta_{C\text{-}X\cdots Y}$ of the halogen bond to prevent

any significant deviations from the experimental structure. In Chapters 4 and 6, we have created models using simple halogen bond donors interacting with an acceptor molecule, varying the distance ($d_{X\cdots Y}$) or interaction angle ($\theta_{C\text{-}X\cdots Y}$) at incremental steps. In these cases, we calculate the C_Q and η, along with a decomposition of the EFG tensor in terms of natural localized molecular orbitals.

These calculations were performed using density functional theory (DFT), which has become a widespread method due to the higher computational efficiency.[66,67] Rather than solving complex Schrödinger equations for a many-body problem, DFT uses the ground state electron density functional to determine the wave function and the Hamiltonian, leading to the energy.[68,69] The electrons are considered as individual particles, calculating their kinetic energy, nuclear-electron interaction energy, electron-electron repulsion energy, and an exchange-correlation energy.[67] The exchange-correlation energy is then approximated using approaches such as the local density approximation (LDA)[70] and generalized gradient approximation (GGA).[71] With these results, sufficient information is available to then calculate the desired NMR properties.

A large portion of the DFT calculations presented in this thesis were performed using the Amsterdam Density Functional (ADF) software,[72,73,74] which implements a variety of features important to obtaining accurate results. With heavy atoms, such as bromine and iodine, comes relativistic effects arising from the rapid motion of the electrons, especially in the outer orbitals. However, the incorporation of relativistic effects in the calculation involves using the Dirac equation which increases the computational demand. The zeroth order regular approximation (ZORA) is an efficient approach to incorporate scalar and spin orbit relativistic

corrections to the calculations,[75,76,77,78] resulting in a boost in accuracy when investigating heavy atoms.

An additional feature available in ADF is the ability to decompose the NMR observable in terms of individual contributions from natural localized molecular orbitals (NLMO).[79] In contrast to atomic orbitals, molecular orbitals describe the wavefunction of an electron in a molecule. NLMOs are a computationally efficient variant of the natural bonding orbital which are an intermediate between both the atomic orbital and molecular orbital, allowing the results to be interpreted using molecular orbitals familiar to chemists. For the analysis of the EFG tensor performed in Chapters 4, 6, and 8, an analysis of the contributions from each NLMO is given for the EFG tensor components, reporting both their Lewis and non-Lewis contributions.[80] The NLMOs are divided into several categories: core orbitals, lone pair orbitals, bonding orbitals, antibonding orbitals, and few additional others. The calculated changes in the NLMO contributions to the EFG tensor offers direct insights into the electronic changes that occur when introducing the halogen bond.

While a model consisted of a few molecules can be an effective approach, long range effects arising from the lattice periodicity does have a noticeable impact on the NMR observables.[81] The purpose of the gauge-including projector augmented-wave (GIPAW) method is to include periodic boundary conditions using supercells.[82,83] Several approximations are made to lower the computational cost, such as the use of pseudopotentials to describe the inner-electrons and a frozen core approximation.[84] These features are included in the CASTEP software,[85] as part of Materials Studio. The use of CASTEP has served an important role in calculating the ^{13}C and ^{19}F chemical shifts in Chapter 7. In addition, we show that an initial optimization of the crystal structures using CASTEP leads to a better agreement between the

experimental chemical shifts and the calculated results, allowing for the refinement of crystal structures supported by solid-state NMR spectroscopy.

2.3. X-ray Crystallography

In the last century, there have been significant advancements in the field of X-ray crystallography. Crystal structures are now routinely solved based on the diffraction of X-ray beams from single crystals.[86] Early diffractometry required a significant amount of bench time to determine even the simplest crystal structures, as all the calculations and measurements had to be done manually.[86] With the introduction of computers and technological advancements in X-ray crystallography, a crystal structure can now be determined in as little as one hour. The early advancements in X-ray diffraction[87] awarded the 1915 Nobel prize in physics to William H. Bragg and William L. Bragg.[88]

X-rays can be generated using a cathode tube, which accelerate electrons in a strong electric field onto a metallic surface, such as copper or molybdenum. Upon hitting the metallic surface, the deceleration of the electron by an electrostatic interaction with the nucleus causes the emission of Bremsstrahlung X-rays, which is a broad distribution in the wavelengths. However, if the X-rays instead cause the ejection of an electron from the metallic atom, typically from the inner shells, the subsequent electronic rearrangement occurring in the atom causes the emission of an X-ray with a characteristic wavelength, such as the $K\alpha$ and $K\beta$ radiation.[89] The $K\alpha$ radiation is selected as a result of its higher intensity and narrow distribution in the wavelength, which is later made monochromatic by filtering out all other wavelengths.

The analysis of crystals by diffraction requires a photon with a wavelength comparable to that of a chemical bond length (approximately 1 to 2 Å). These are the wavelengths associated

with X-rays, and the constructive interference associated with diffraction can be characterized using Bragg's law (Eq. 1.2.19).[90]

$$n\lambda = 2d \sin\theta \qquad \text{Eq. 1.2.19}$$

Here, n is an integer denoting the number of scattering planes, λ is the wavelength associated with the X-ray, d is the distance between the planes, and θ is the angle between the scattering plane and the diffracted X-ray beam. A representation of the X-ray diffraction occurring on two crystallographic planes is given in Figure 1.2.9, showing the geometrical parameters of Bragg's law.

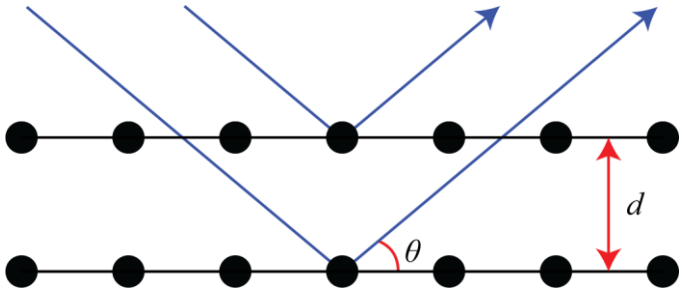

Figure 1.2.9. X-rays (blue arrows) diffracting at an angle of θ from a plane separated by a distance, d.

Crystals are associated with a degree of order and can be described as a periodic repetition of a subunit called the unit cell. The unit cell describes the shape of the repeating unit in the crystalline lattice and reflects the crystallographic symmetry of the crystal. There are several lattice systems, such as the triclinic and cubic systems, shown in Figure 1.2.10, in addition to monoclinic, orthorhombic, tetragonal, hexagonal, and rhombohedral.[86]

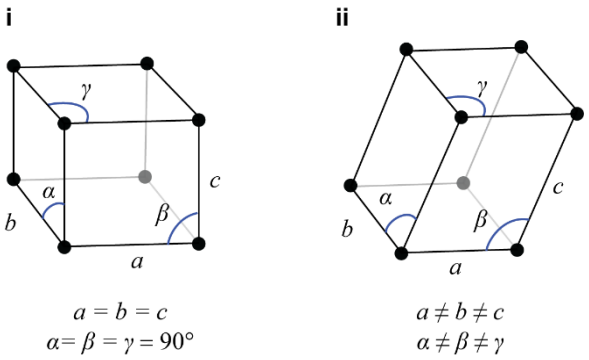

Figure 1.2.10. (i) The cubic and (ii) triclinic unit cells. The geometric criteria for each unit cell are also given.

The unit cell can be described from its lengths (in Å), *a*, *b*, and *c*, following the convention $a < b < c$. The angles describe the relative shape of the unit cell (in °), with γ being between the angle between the *a* and *b* axis, β being between the *a* and *c* axis, and α being between the *b* and *c* axis. The volume (*V*) of the unit cell is the geometrical relation between the axis lengths and the angles and describes the overall size of the unit cell (in Å^3). Further, *Z* is the formula unit, relating the number of molecules in the unit cell to the molecular formula. The unit cell can be further described using one of 230 space groups, which characterizes the symmetry elements occurring in the unit cell.[91] As the X-rays are diffracting from the electron densities, the intensity of the diffracted X-rays can be used to assign elements in the crystal structure using the structure factor. Consequently, X-ray crystallography has become the tool of choice for determining the precise atomic positioning in solids.

2.3.1 – Single Crystal X-Ray Diffraction

In single crystal X-ray diffraction (SCXRD), a crystal is mounted on a goniometer and positioned between an X-ray source and a detector, shown in Figure 1.2.11. Upon the exposing of the crystal to the X-ray beam, diffraction occurs, with both the intensity and diffraction angles

measured by the detector. In order to obtain the full diffractogram, the crystal is rotated on several axes and the detector is positioned accordingly to observe these.

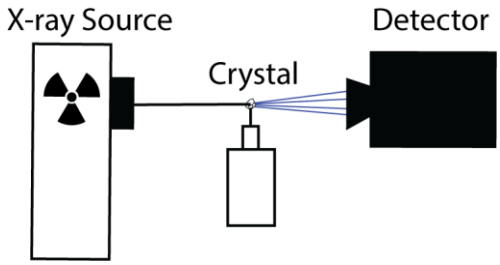

Figure 1.2.11. Simplified single crystal X-ray diffractometer. The X-ray source (left) emits a beam of X-rays into the crystal (middle), with the diffractions (blue) collected by the detector (right).

Both the intensity and angles are used in solving the crystal structures, which can be interpreted using one of several methods, such as the Patterson method[92] and direct methods.[93] Disorder can occur in the sample, especially when the data is collected at high temperatures, which is manifested as either an overlap of atoms or the atom occupying several positions. In the case where the crystal is twinned, the data must be refined by considering both crystal domains.[94] At times, the crystal can absorb incident X-rays, which must be considered by using absorption correction.[95,96] Solving and refining the X-ray structure can be performed with a variety of programs,[97,98,99,100] with the final crystal structure being packaged in the CIF format. The CIF file then contains all experimental and crystallographic parameters required to describe the structure of the compound under investigation.[101] The thermal ellipsoid plot, one of the final products of the crystallography process, gives information on the positioning and vibrations occurring on the atoms from the crystal structure. An example of the thermal ellipsoid plot of the crystal structure of (1,4-diiodobenzene)(1,4-bis(4-pyridyl)ethane)[102] is shown in Figure 1.2.12.

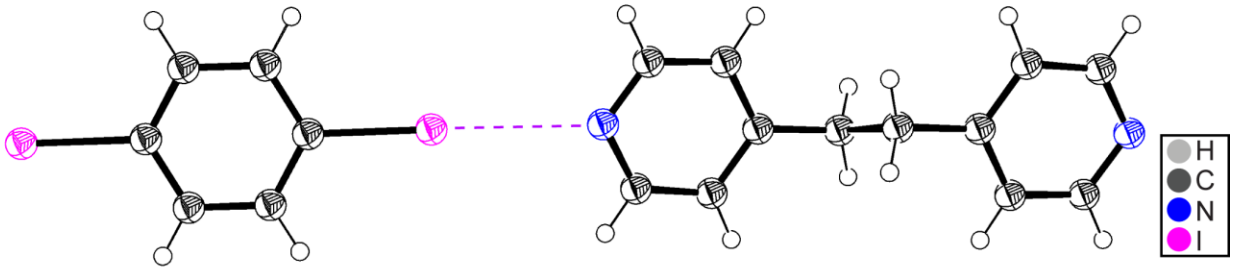

Figure 1.2.12. Thermal ellipsoid plot of (1,4-diiodobenzene)(1,4-bis(4-pyridyl)ethane). The crystal structure has been taken from P. Cerreia Vioglio et al.[102] The plot has been generated using Ortep.[99]

In order to perform SCXRD, one must first grow crystals of sufficient quality to permit the experiment. While certain imperfections exist, such as twinning, they can be considered during the refinement process. However, the growth of quality crystals allows for the collection of better data, leading to better results. While cocrystals are traditionally obtained from solvent evaporation methods, we develop cosublimation as a method of rapidly obtaining halogen bonded cocrystals of suitable quality.

2.3.2 – Powder X-Ray Diffraction

Powder X-ray diffraction (PXRD) is an analytical tool that has been used for the purpose of identifying the structure of powdered samples as well as verifying its phase purity. In contrast to SCXRD which observes X-ray diffractions from a single crystal in select orientations, a powdered sample of sufficient quantity theoretically contains all crystallite orientations, and therefore the resulting diffraction pattern yields a fingerprint of the crystal structure. The powder X-ray diffractogram can give the unit cell parameters, while developments have allowed for the refinement of the entire crystal structure.[103]

The Bragg-Brentano geometry is a popular approach to PXRD, which consists of moving both the X-ray source and detector at relative angles in unison, shown in Figure 1.2.13. The X-rays are emitted from the source, filtered through a monochromator to ensure a single wavelength is present, then collimated. The sample is exposed to the X-rays and upon satisfying Bragg's law, diffract and reach the detector which measures the counts per second (CPS). A powder X-ray diffractogram is rich in information, with the diffraction positions offering unit cell parameters, the width offering information on the crystallinity, and the relative intensities at times allowing for a quantitative analysis. In addition, PXRD is well suited to identify the occurrence of polymorphism, which is when a solid can adopt more than one crystalline structure.[104]

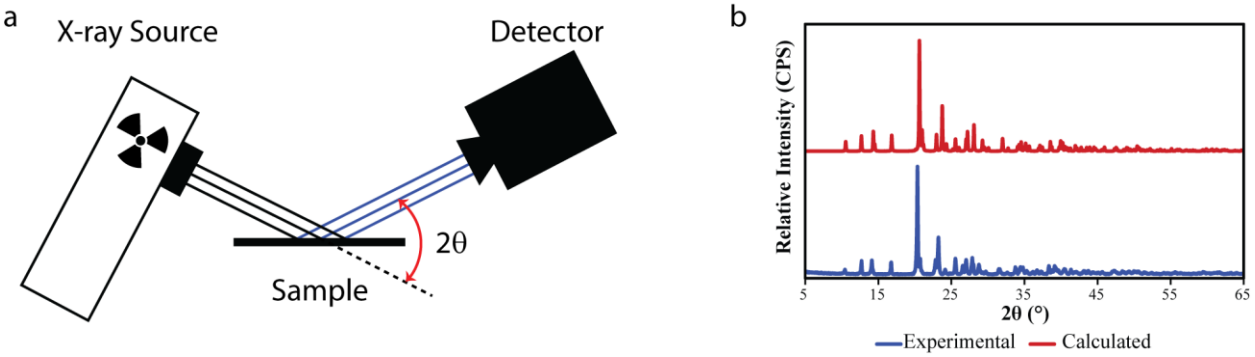

Figure 1.2.13. (**a**) Simplified diagram of a powder X-ray diffractometer operating in the Bragg-Brentano geometry, showing the X-ray source, detector, sample, and X-rays (black lines). (**b**) Experimental (blue, lower) and calculated (red, upper) powder X-ray diffractogram of (1,4-diiodobenzene)(1,4-bis(4-pyridyl)ethane).

Powdered samples are prepared by crushing crystals with a mortar and pestle, then placed on the sample holder. Once placed on the sample holder, it must be flat to ensure that no unwanted diffractions occur. The experimental diffractogram can then be compared to a theoretical diffractogram calculated from the crystal structure. Deviations between the

experimental and calculated intensities can at times be attributed to preferred orientations in the crystallites, while the presence of new reflections may indicate the presence of a side phase or impurity. In this thesis, PXRD has been primarily used to ensure that the crystal structure obtained from SCXRD is representative of the powdered sample under investigation. All samples in this this thesis have been analyzed by PXRD prior to the solid-state NMR analysis.

References for Chapter 2.

[1] Duer, M.J. *Solid-state NMR spectroscopy: principles and applications.* Wiley-Blackwell, Oxford, **2001**.

[2] Apperley, D.C.; Harris, R.K.; Hodgkinson, P. *Solid-state NMR: Basic Principles & Practice.* Momentum Press, **2012**.

[3] Abragam, A. *Principles of Nuclear Magnetism.* Clarendon Press, Oxford, **1983.**

[4] Breit, G.; Rabi, I.I. *Phys. Rev.* **1931**, *38*, 2082-2083.

[5] Zeeman, P. *Philos. Mag.* **1897***, 43*, 226-239.

[6] Larmor, J. *Philos. Mag.* **1897**, *44*, 503-512.

[7] Haynes, W.M.; Lide, D.R.; Bruno, T.J. *CRC Handbook of Chemistry and Physics.* CRC Press, Boca Raton, 2016.

[8] Keeler, J. *Understanding NMR Spectroscopy.* John Wiley & Sons, Chinchester, **2010**.

[9] Torchia, D.A.; Szabo, A. *J. Magn. Reson.* **1982**, *49*, 107-121.

[10] Rabi, I.I.; Zacharias, J.R.; Millman, S.; Kusch, P. *Phys. Rev.* **1938**, *53*, 318.

[11] Bloch, F.; Hansen, W.W.; Packard, M. *Phys. Rev.* **1946**, *69*, 127.

[12] Bloch, F.; Hansen, W.W.; Packard, M. *Phys. Rev.* **1946**, *70*, 474-485.

[13] Purcell, E.M.; Torrey, H.C.; Pound, R.V. *Phys. Rev.* **1946**, *69*, 37-38.

[14] Ramsey, N.F. *Phys. Rev.* **1950**, *78*, 699-703.

[15] Macomber, R.S. *A Complete Introduction to Modern NMR Spectroscopy.* Wiley-Interscience, New York, **1998**.

[16] Woessner, D.E. *Concepts Magn. Reson.* **1996**, *8*, 397-421.

[17] Herzfeld, J.; Berger, A.E. *J. Chem. Phys.* **1980**, *73*, 6021-6030.

[18] Stejskal, E.O.; Memory, J.D. *High Resolution NMR in the Solid State: Fundamentals of CP/MAS.* Oxford University Press, Oxford, **1995.**

[19] Lowe, I.J. *Phys. Rev. Lett.* **1959**, *2*, 285-287.

[20] Hennel, J.W.; Klinowski, J. *Top. Curr. Chem.* **2004**, *246*, 1-14.

[21] Polenova, T.; Gupta, R.; Goldbourt, A. *Anal. Chem.* **2015**, *87*, 5458-5469.

[22] Thomas Dixon, W. *J. Chem. Phys.* **1982**, *77*, 1800-1809.

[23] Hahn, E.L. *Phys. Rev.* **1950**, *80*, 580-594.

[24] Carr, H.Y.; Purcell, E.M. *Phys. Rev.* **1954**, *94*, 630-638.

[25] Meiboom, S.; Gill, D. *Rev. Sci. Inst.* **1958**, *29*, 688-691.

[26] Silverstein, R.M.; Webster, F.X.; Kiemle, D.J.; Bryce, D.L. *Spectrometric Identification of Organic Compounds.* John Wiley & Sons, Chinchester, **2014**.

[27] Ramsey, N.F. *Phys. Rev.* **1953**, *91*, 303-307.

[28] *DAISY. Version 2.0.0*. Bruker Biospin GmbH, Rheinstetten, Germany.

[29] Wasylishen, R.E. *Dipolar and Indirect Coupling: Basics.* in *eMagRes.* John Wiley & Sons, Chinchester, **2009**.

[30] Polenova, T.; Gupta, R.; Goldbourt, A. *Anal. Chem.* **2015**, *87*, 5458-5469.

[31] Pines, A.; Gibby, M.G.; Waugh, J.S. *J. Chem. Phys.* **1972**, *56*, 1776-1777.

[32] Pines, A.; Gibby, M.G.; Waugh, J.S. *J. Chem. Phys.* **1973**, *59*, 569-590.

[33] Vanderhart, D.L.; Earl, W.L.; Garroway, A.N. *J. Magn. Reson.* **1981**, *44*, 361-401.

[34] Sarles, L.R.; Cotts, R.M. *Phys. Rev.* **1958**, *111*, 853-859.

[35] Pyykkö, P. *Mol. Phys.* **2018**, *116*, 1328-1338.

[36] Pound, R.V. *Phys. Rev.* **1950**, *79*, 685-702.

[37] Man, P.P. *Quadrupole Couplings in Nuclear Magnetic Resonance, General.* Chapter in *Encyclopedia of Analytical Chemistry*. John Wiley & Sons, Chinchester, **2000**.

[38] Lucken, E.A.C. *Nuclear Quadrupole Coupling Constants.* Academic Press Inc., New York, **1969**.

[39] Perras, F.A.; Korovkob, I.; Bryce, D.L. *CrystEngComm*. **2013**, *15*, 8727-8738.

[40] Widdifield, C.M.; Bain, A.D.; Bryce, D.L. *Phys. Chem. Chem. Phys.* **2011**, *13*, 12413-12420.

[41] Perras, F.A.; Widdifield, C.M.; Bryce, D.L. *Solid State Nucl. Magn. Reson.* **2012**, *45-46*, 36-44.

[42] Amoureux, J.P.; Fernandez, C.; Granger, P. *Interpretation of quadrupolar powder spectra : static and MAS experiments.* Chapter in: *Multinuclear Magnetic resonance in Liquids and Solids: Chemical Applications*, NATO ASI Series C, volume 332. Kluwer Academic Publishers, Dordrecht, **1990**.

[43] Bloom, M.; Sternin, E. *Biochemistry*. **1987**, *26*, 2101-2105.

[44] Larsen, F.H.; Jakobsen, H.J.; Ellis, P.D.; Nielsen, N.C. *J. Magn. Reson.* **1998**, *131*, 144-147.

[45] O'Dell, L.A. *Solid State Nucl. Magn. Reson.* **2013**, *55-56*, 28-41.

[46] Massiot, D.M.; Farnan, I.; Gautier, N.; Trumeau, D.; Trokiner, J.; Coutures, J.P. *Solid State Nucl. Magn. Reson.* **1995**, *4*, 241-248.

[47] O'Dell, L.A.; Schurko, R.W. *Chem. Phys. Lett.* **2008**, *464*, 97-102.

[48] Hung, I.; Gan, Z. *J. Magn. Reson.* **2010**, *204*, 256-265.

[49] Schurko, R.W. *Acc. Chem. Res.* **2013**, *46*, 1985-1995.

[50] Drago, R.S. *Rep. Anal. Chem.* **1966**, *38*, 31-38.

[51] Smith, J.A.S. *J. Chem. Edu.* **1971**, *48*, 39-48.

[52] Cheng, J.T.; Edwards, J.C.; Ellis, P.D. *J. Phys. Chem.* **1990**, *94*, 553-561.

[53] Power, W.P.; Wasylishen, R.E.; Mooibroek, S.; Pettitt, B.A.; Danchura, W. *J. Phys. Chem.* **1990**, *94*, 591-598.

[54] Massiot, D.; Fayon, F.; Capron, M.; King, I.; Le Calvé, S.; Alonso, B.; Durand, J.-O.; Bujoli, B.; Gan, Z.; Hoatson, G. *Magn. Reson. Chem.* **2002**, *40*, 70-76.

[55] Eichele, K. *WSolids1 ver. 1.21.3*, Universität Tübingen, **2015**.

[56] Grimminck, D.L.A.G.; Polman, B.J.W.; Kentgens, A.P.M.; Meerts, W.L. *J. Magn. Reson.* **2011**, *211*, 114-120.

[57] Kemp, T.F.; Smith, M.E. *Solid State Nucl. Magn. Reson.* **2009**, *35*, 243-252.

[58] Latanowicz, L. *Concepts. Magn. Reson.* **2012**, *40A*, 66-79.

[59] Farrar, T. *Pulse and Fourier Transform NMR. Introduction to Theory and methods.* Academic Press Inc., New York, **1971**.

[60] Kowalewski, J.; Liljefors, T. *Chem. Phys. Lett.* **1979**, *64*, 170-174.

[61] Spěváček, J.; Schneider, B. *Czech. J. Phys.* **1974**, *B24*, 593-604.

[62] Vold, R.L.; Hoatson, G.L. *J. Magn. Reson.* **2009**, *198*, 57-72.

[63] Frisch, M.J. *et al*. *Gaussian*. Gaussian, Inc., Wallingford CT, **2016**.

[64] Stewart, R.F.; Davidson, E.R.; Simpson, W.T. *J. Chem. Phys.* **1965**, *42*, 3175-3187.

[65] Cooper, R.I.; Thompson, A.L.; Watkin, D.J. *J. Appl. Cryst.* **2010**, *43*, 1100-1107.

[66] Becke, A.D. *Phys. Rev. A* **1988**, *38*, 3098-3100.

[67] Cramer, C.J. *Essentials of Computational Chemistry. Theory and Models.* John Wiley & Sons, Chinchester, **2004**.

[68] Kohn, W.; Sham, L.J. *Phys. Rev.* **1965**, *140*, 1133-1138.

[69] Hohenberg, P.; Kohn, W. *Phys. Rev.* **1964**, *136*, 864-871.

[70] Vosko, S.H.; Wilk, L.; Nusair, M. *Can. J. Phys.* **1980**, *58*, 1200-1211.

[71] Perdew, J.P.; Burke, K.; Ernzerhof, M. *Phys. Rev. Lett.* **1996**, *77*, 3865-3868.

[72] ADF2017, SCM, Theoretical Chemistry, Vrije Universiteit, Amsterdam, The Netherlands.

[73] Fonseca Guerra, C.; Snijders, J.G.; te Velde, G.; Baerends E.J. *Theo. Chem. Acc.* **1998**, *99*, 391-403.

[74] Te Velde, G. et al. *J. Comp. Chem.* **2001**, *22*, 931-967.

[75] van Lenthe, E.; Baerends, E.J.; Snijders, J.G. *J. Chem. Phys.* **1993**, *99*, 4597-4610.

[76] van Lenthe, E.; Snijders, J.G.; Baerends, E.J. *J. Chem. Phys.* **1996**, *105*, 6505-6516.

[77] van Lenthe, E.; Baerends, E.J.; Snijders, J.G. *J. Chem. Phys.* **1994**, *101*, 9783-9792.

[78] van Lenthe, E.; Ehlers, A.; Baerends, E.-J. *J. Chem. Phys.* **1999**, *110*, 8943-8953.

[79] Reed, A.E.; Weinhold, F. *J. Chem. Phys.* **1985**, *83*, 1736-1740.

[80] Autschbach, J.; Zheng, S.; Schurko, R.W. *Concepts Magn. Reson.* **2010**, *36A*, 84-126.

[81] Mauri, F.; Pfrommer, B.G.; Louie, S.G. *Phys. Rev. Lett.* **1996**, *77*, 5300-5303.

[82] Blöchl, P.E. *Phys. Rev.* **1994**, *B50*, 17953-17979.

[83] Pickard, C.J.; Mauri, F. *Phys. Rev.* **2001**, *63B*, 245101.

[84] von Barth, U.; Gelatt, C.D. *Phys. Rev.* **1980**, *21B*, 2222-2228.

[85] Clark, S.J.; Segall, M.D.; Pickard, C.J.; Hasnip, P.J.; Probert, M.J.; Refson, K.; Payne, M.C. *Z. Kristallogr. Cryst. Mater.* **2005**, *220*, 567-570.

[86] Gregory S. Girolami. *X-ray Crystallography,* University Science Books, Mill Valley, **2016**.

[87] Bragg, W.H. *Nature.* **1912**, *90*, 219.

[88] "The Nobel Prize in Physics 1915". Accessed January 20th, 2019. From: http://www.nobelprize.org/nobel_prizes/physics/laureates/1915/

[89] Barkla, C.G. *Philos. Mag.* **1911**, *22*, 396-412.

[90] Bragg, W.H.; Bragg, W.L. *Proc. Royal Soc. A* **1913**, 428-438.

[91] Hahn, T. *International Tables for Crystallography, Volulme A: Space-Group Symmetry. 5th Edition.* Springer, Dordrecht, **2005**.

[92] Patterson, A.L. *Z. Kristallogr. Cryst. Mater.* **1935**, *90*, 517-542.

[93] Hauptman, H. *Science.* **1986**, *233*, 178-183.

[94] Sheldrick, G. M. *TWINABS. Version 2012/1*. **2012**, Georg-August-Universität Göttingen, Göttingen, Germany.

[95] North, A.C.T.; Phillips, D.C. *Acta Cryst.* **1968**, *A24*, 351-359.

[96] Blessing, R.H. *Acta Cryst.* **1995**, *A51*, 33-38.

[97] Hübschle, C.B.; Sheldrick, G.M.; Dittrich, B. *J. Appl. Cryst.* **2011**, *44*, 1281-1284

[98] Farrugia, L.J. *J. Appl. Cryst.* **1999**, *32*, 837-838.

[99] Farrugia, L.J. *J. Appl. Cryst.* **2012**, *45*, 849-854.

[100] Dolomanov, O.V.; Blake, A.J.; Champness, N.R.; Schröder, M. *J. Appl. Cryst.* **2003**, *36*, 1283-1284.

[101] Hall, S.R.; Allen, F.H.; Brown, I.D. *Acta Cryst.* **1991**, *A47*, 655-685.

[102] Cerreia Vioglio, P.; Catalano, L.; Vasylyeva, V.; Nervi, C.; Chierotti, M.R.; Resnati, G.; Gobetto, R.; Metrangolo, P. *Chem. Eur. J.* **2016**, *22*, 16819-16828.

[103] Reitveld, H.M. *J. Appl. Cryst.* **1969**, *2*, 65-71.

[104] Cruz-Cabeza, A.J.; Bernstein, J. *Chem. Rev.* **2014**, *114*, 2170-2191.

Chapter 3 – Solid-state nuclear magnetic resonance and nuclear quadrupole resonance as complementary tools to study quadrupolar nuclei in solids

Statement of Authenticity. I certify that I have prepared the following article featuring my own work, with guidance, support, and contributions from my supervisor Dr. David Bryce.

Permissions. I declare that I have obtained permission from the coauthor to include this article in my thesis. Chapter 3 was reproduced from *Concepts Magn. Reson. Part A.* 2016, 45A, e21412, with permission from John Wiley & Sons, Inc. (DOI: 10.1002/cmr.a.21412)

Received: 22 September 2017 | Revised: 24 November 2017 | Accepted: 28 November 2017

DOI: 10.1002/cmr.a.21412

RESEARCH ARTICLE

WILEY

Solid-state nuclear magnetic resonance and nuclear quadrupole resonance as complementary tools to study quadrupolar nuclei in solids

Patrick M.J. Szell | **David L. Bryce**

Department of Chemistry and Biomolecular Sciences & Centre for Catalysis Research and Innovation, University of Ottawa, Ottawa, ON, Canada

Correspondence
D.L. Bryce, Department of Chemistry and Biomolecular Sciences & Centre for Catalysis Research and Innovation, University of Ottawa, Ottawa, ON, Canada.
Email: dbryce@uottawa.ca

This article is a contribution to the special issue in honor of Alex Bain.

Funding information
Natural Sciences and Engineering Research Council of Canada; consortium of Canadian Universities; National Research Council Canada; Bruker BioSpin; University of Ottawa; National Science Foundation, Grant/Award Number: DMR-1157490; State of Florida

Abstract

Solid-state nuclear magnetic resonance (SSNMR) spectroscopy has largely overtaken nuclear quadrupole resonance (NQR) spectroscopy for the study of quadrupolar nuclei. In addition to information on the electric field gradient, SSNMR spectra may offer additional information concerning other NMR interactions such as magnetic shielding. With continued technological advances contributing to developments such as higher magnetic fields, SSNMR boasts several practical advantages over NQR. However, NQR is still a relevant technique, as it may often be the most practical approach in cases of extremely large quadrupolar coupling constants. Here, we discuss the advantages and disadvantages of SSNMR and NQR spectroscopies, with the quadrupolar halogens serving as examples. The purpose of this article is to serve as a guide on using SSNMR and NQR as complementary tools, covering some of their practicalities, limitations, and experimental challenges.

KEYWORDS
nuclear quadrupole resonance, quadrupolar halogens, quadrupolar nuclei, solid-state nuclear magnetic resonance

1 | INTRODUCTION

Solid-state NMR (SSNMR) spectroscopy has become a widely implemented analytical tool, offering information on chemical, crystallographic, and electronic environments, as well as dynamical information. Due to the nature of SSNMR, it boasts some advantages over diffraction-based techniques, such as the ability to study glasses and other amorphous and heterogeneous systems, host-guest systems, and molecular dynamics and disorder. Although NMR experiments are most routinely applied to spin $I = ½$ nuclei, such as ^{1}H and ^{13}C, approximately 75% of the periodic table is composed of quadrupolar nuclei ($I > ½$). Of course, SSNMR is not limited to spin-½ nuclei, and there is an extensive history and literature on the analysis of quadrupolar nuclei by SSNMR.[1] A technique analogous to SSNMR, but performed in the absence of a magnetic field, is nuclear quadrupole resonance (NQR) spectroscopy, which is applicable strictly in the cases of quadrupolar nuclei ($I > ½$).[2-4] NQR does not require the application of an external magnetic field due to the fact that the quadrupolar interaction perturbs the energy levels of the nuclear spin states, allowing transitions to occur between the resulting nondegenerate energy levels.

Over the course of its evolution, SSNMR has largely overtaken NQR spectroscopy for the investigation of solids. As shown in Figure 1, mentions of SSNMR in the scientific literature have greatly surpassed NQR. In part, this can be attributed to the former's higher sensitivity and the accessibility of spin ½ nuclei, in addition to the higher abundance of information obtained from spin manipulation

In honor of the significant contributions and impact of Alex Bain in the field of nuclear magnetic resonance.

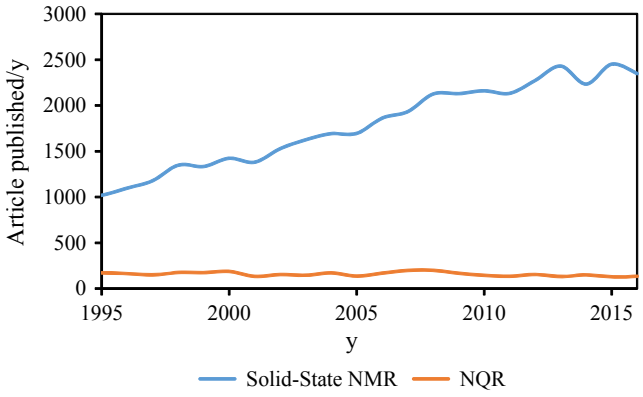

FIGURE 1 Number of Web of Science[70] literature results per year for the queries "Solid-State NMR" and "Nuclear Quadrupole Resonance" in the last 20 years (1995 to 2016)

via advanced multipulse and multidimensional experiments. A key practical advantage to SSNMR experiments is that the spectrum is always predictably roughly centered on the Larmor frequency. Contrarily, in NQR experiments, one may be forced to search over extremely wide spectral windows (tens of MHz or more) to find the resonances in the absence of a priori information on the magnitude of the quadrupolar interaction in a given sample. Additionally, with technological developments, such as high magnetic fields and so-called ultra-fast magic angle spinning rates,[5] SSNMR can be used routinely to obtain information on the chemical shift tensor, quadrupolar coupling tensor, the dipolar coupling tensor, and *J*-coupling.[6] However, NQR is not obsolete, as it can be used to study quadrupolar nuclei with large quadrupole moments, offering comparatively sharp resonances without the need for a stable external magnetic field. This advantage allows NQR to be applied in instances where SSNMR experiments would be difficult to perform, notably in cases when nuclei are subject to very large quadrupolar interactions. At a minimum, NQR can often be used as a complementary tool to SSNMR, allowing for a rapid verification of the quadrupolar coupling parameters. This verification can be particularly advantageous if the SSNMR spectrum results from a subtle interplay between a dominant quadrupolar coupling interaction and a relatively small anisotropic magnetic shielding interaction.

The quadrupolar interaction is the result of coupling between the electric field gradient (EFG) at a nucleus and its quadrupole moment (Q). The quadrupolar interaction offers structural information through the distortion of the electronic environment surrounding the nucleus. Several recent papers in the literature have focused on nuclei featuring large quadrupolar interactions and concomitantly broad SSNMR spectral breadths, which are time-consuming to fully acquire. NQR can play a role in these studies, and one might ask, "under which circumstances should I perform NMR experiments and when should I perform NQR experiments?" Here, we offer a discussion on the use of SSNMR and NQR to study quadrupolar nuclei, first by covering some basic theory, and then by discussing some of the practical aspects of both techniques with emphasis on their advantages and limitations. The focus is solely on powdered samples. As several articles have already offered a complete theoretical treatment of the quadrupolar interaction,[7,8] the theory offered here covers only the fundamentals required to understand the practical differences between NQR and SSNMR spectroscopies. This *Concepts* article will serve as a complement to the comparisons between SSNMR and NQR available in the literature,[9] including elegant and insightful work by Alex Bain.[10,11]

2 | REVIEW OF BASIC THEORY

The quadrupolar interaction arises as a result of the coupling between the nuclear quadrupole moment (Q) and the electric field gradient (EFG) tensor. The quadrupole moment arises due to an asymmetrical charge distribution within the nucleus itself, whereas the EFG is the second derivative of the electrostatic potential at the nucleus. The EFG is represented by a traceless second-rank tensor, and in its principal axis system, its magnitude can be expressed by three principal components: V_{11}, V_{22}, and V_{33}. By convention, the largest component of the tensor is V_{33}, such that $|V_{33}| \geq |V_{22}| \geq |V_{11}|$. These magnitudes can also be conveniently described by the quadrupolar coupling constant, C_Q (Equation 1), and the asymmetry parameter, η (Equation 2).

$$C_Q = \frac{eV_{33}Q}{h} \tag{1}$$

$$\eta = \frac{V_{11} - V_{22}}{V_{33}} \tag{2}$$

Here, e is the fundamental charge (expressed in C), V_{33} is expressed in atomic units, Q is the quadrupole moment (expressed in fm²), and h is Planck's constant (expressed in J s). The full details of dealing with the units of Equation 1 have been discussed previously.[12] The value of C_Q indicates the magnitude of the quadrupolar interaction, whereas η describes the axial symmetry of the tensor. In cases of high symmetry, such as the cubic structures of alkali salts (eg, NaCl), the EFG at these nuclei would be very small, owing to the fact that all principal components are identical ($V_{11} = V_{22} = V_{33} = 0$).[13] In contrast, for compounds with asymmetric charge distribution about a nucleus, such as a nucleus with one covalent bond, the resulting EFG would be much larger. Consequently, the quadrupolar interaction

is expected to be large, which varies as a function of the value of Q for a given nuclide. The interpretation of the quadrupolar coupling tensor can become quite detailed, and the reader is referred to an excellent *Concepts* article by Autschbach et al.[14]

In SSNMR, the influence of the quadrupolar interaction on the spectrum (in particular its breadth) will depend on the size of the quadrupolar interaction. In the cases where the quadrupolar interaction is small, the total NMR Hamiltonian (H_{NMR}) can be approximated as a perturbation on the Zeeman Hamiltonian (H_{Zeeman}), given in Equation 3:

$$H_{NMR} = H_{Zeeman} + H_{RF} + H_J + H_{DC} + H_Q \quad (3)$$

Here, we refer to the Hamiltonians of the radiofrequency interactions (H_{RF}), the J-coupling interaction (H_J), the dipolar coupling interaction (H_{DC}), and the quadrupolar coupling interaction (H_Q). Second-order perturbation theory has proven to be quite successful in the interpretation of the SSNMR spectra of quadrupolar nuclei.[8,10] However, there are limits to its applicability, namely in the cases where the quadrupolar interaction becomes dominant.[15,16] It has been proposed that for perturbation theory to be applied reliably, the ratio of the Larmor frequency, ν_L (Equation 4), and the quadrupolar frequency, ν_Q (Equation 5), should be above 10.[15]

$$\nu_L = \frac{\gamma B_0}{2\pi} \quad (4)$$

$$\nu_Q = \frac{3C_Q\sqrt{1+\frac{\eta^2}{3}}}{2I(2I-1)} \quad (5)$$

In Equation 4, γ refers to the gyromagnetic ratio of the nucleus and B_0 refers to the external magnetic field strength, whereas in Equation 5, I refers to the spin quantum number of the nucleus. Note that the third-order correction has been shown to be zero by Alex Bain.[17] When performing SSNMR experiments on half-integer spin quadrupolar nuclei, it is generally suggested to go to higher applied magnetic fields, as the width of the central-transition (CT) NMR spectrum is inversely proportional to ν_L, shown in Equation 6.[18,19]

$$\Delta\nu_{CT} = \left(\frac{25+22\eta+\eta^2}{144}\right)\left[\frac{(3C_Q)^2}{((2I)(2I-1))^2}\right]\left[\frac{I(I+1)-\frac{3}{4}}{\nu_L}\right] \quad (6)$$

However, sufficiently strong magnetic fields may either not be available or not be practical, in which case the absence of a magnetic field can be beneficial for the analysis of nuclei subject to large quadrupolar interactions.

As pure NQR is performed in the absence of a magnetic field, the Zeeman interaction term can be dropped from Equation 3, giving the basic Hamiltonian for NQR in Equation 7:

$$H_{NQR} = H_{RF} + H_J + H_{DC} + H_Q \quad (7)$$

Here, the terms are the same as for Equation 3; however, the quadrupolar interaction is generally the dominant term. As the H_J and H_{DC} terms are not dropped, however, they do contribute to the NQR line shape, usually in the form of line broadening.[20] As a consequence of Equation 1 and Equation 5, when nuclei with small quadrupole moments are analyzed with NQR, such as ^{2}H (Q = 2.860(15) mb)[21] and ^{6}Li (Q = −0.808 mb),[21] the expected NQR frequencies are very low (kHz range).[22]

The energy level diagram pertaining to the analysis of an arbitrary spin-3/2 nucleus by SSNMR and NQR is presented in Figure 2. In cases where ν_Q approaches zero, the energy levels are dictated by the Zeeman interaction and the corresponding NMR spectrum would simply reflect the Zeeman splitting (Figure 2A). Upon the introduction of a weak quadrupolar interaction ($\nu_L/\nu_Q > 10$), first-order (Figure 2B) and second-order (Figure 2C) perturbations are applied to the energy levels. In the case of a spin-3/2 nucleus exhibiting a large quadrupolar interaction relative to the Zeeman interaction ($\nu_L/\nu_Q < 10$), the energy levels shift substantially from the high-field regime (Figure 2D) and perturbation theory is no longer reliable. In the absence of a magnetic field, these energy levels collapse to two degenerate states, the ±1/2 state and the ±3/2 state (Figure 2E). In the pure NQR spectrum of a spin-3/2 nucleus, the ±1/2 → ±3/2 transition is observed, with the energy levels and resulting frequency dictated by the quadrupolar interaction. Although only one NQR transition is observed for I = 3/2 nuclei, more generally the number of NQR transitions varies as a function of the spin quantum number. For instance, for a spin 5/2 nucleus, the observed transitions are typically ±1/2 → ±3/2 and ±3/2 →±5/2. It is to be noted that the overtone transition, ±1/2 → ±5/2, can sometimes be observed.[23,24] As the Boltzmann spin population is proportional to the difference in the energy levels, the sensitivity of NQR experiments generally increases with the magnitude of the QI. However, in SSNMR experiments, spectral widths increase with the magnitude of the QI, leading to a spread of the inherent signal over a broader frequency range and therefore an effectively lower signal-to-noise ratio. A higher magnetic field results in a narrower NMR spectrum and a gain in sensitivity, overall being favorable for the analysis of quadrupolar nuclei by SSNMR.

Although perturbation theory certainly has its uses, it does not hold in the cases of large quadrupolar interactions ($\nu_L/\nu_Q < 10$), and an exact theory must be applied in order to accurately simulate the resulting spectra.[15,24] The QUadrupole Exact SofTware (QUEST)[24] has been developed in

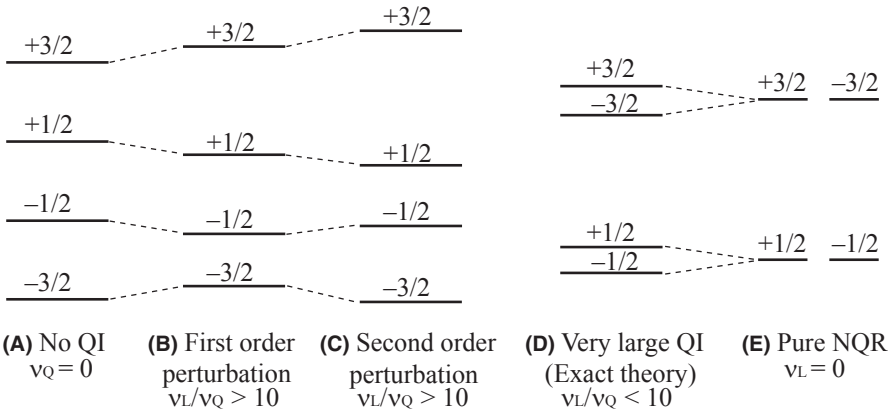

FIGURE 2 Energy level diagram (not to scale) for a spin $I = 3/2$ nucleus subjected to the Zeeman interaction A, with a first-order perturbation from the quadrupolar interaction B, with first- and second-order perturbations from the quadrupolar interaction C, with a large quadrupolar interaction relative to the Zeeman interaction D, and a quadrupolar interaction without Zeeman splitting E. ν_Q refers to the quadrupolar frequency and ν_L refers to the Larmor frequency. The ordering of the spin states on the left depends on the sign of the gyromagnetic ratio

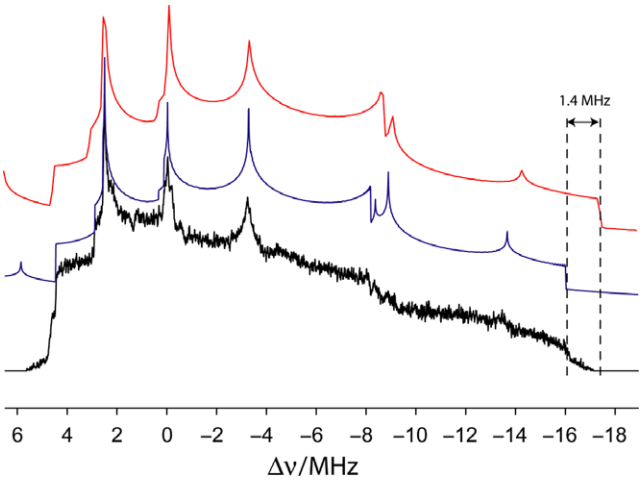

FIGURE 3 $^{79/81}$Br NMR spectrum of $CaBr_2$ acquired at 4.7 T, showing the difference between simulations using an exact Hamiltonian diagonalization (blue) and second-order perturbation theory (red). (Figure taken from *Solid State Nucl. Magn. Reson.* **2012**, *45-46*, 36-44.[24] Used with permission.)

our laboratory to treat the quadrupolar interaction exactly, allowing one to extract spectral parameters from NMR and NQR spectra accurately over the full range shown in Figure 2. Shown in Figure 3 is an example of the importance of using exact theory when dealing with large quadrupolar interactions relative to the Zeeman interaction.[24] Ultra-wideline $^{79/81}$Br SSNMR spectroscopy was performed on solid powdered $CaBr_2$ in an applied magnetic field of 4.7 T, with a final CT spectral width of approximately 20 MHz. A 1.4 MHz discrepancy is seen between second-order perturbation theory and exact theory on the right edge of the spectrum.

3 | USING A SSNMR SPECTROMETER FOR NQR SPECTROSCOPY

Although a proper NQR spectrometer is evidently the most appropriate for NQR experiments, a modern SSNMR spectrometer can double as a NQR spectrometer in many cases. Due to the resemblances in the experiments and hardware requirements, one can operate an NMR probe in the absence of a magnetic field and obtain the NQR transitions. The general limiting factors are first in generating the desired radiofrequencies and secondly in acquiring the signal through the NMR hardware. Most modern SSNMR spectrometers, for instance, the Bruker Avance III console in our laboratory, will have a wide operational frequency range for the X nucleus and a relatively limited range for the ^{1}H/^{19}F channel. The frequency ranges for the signal generating unit and the amplifier typically span hundreds of MHz, with the ranges varying to suit the strength of the applied magnetic field. However, NMR spectrometers may be limited to generating frequencies above 5 MHz, and a low-frequency NQR spectrometer[25] would be advantageous to perform experiments at lower frequencies. When using your SSNMR spectrometer for NQR, considerations should be made to use the appropriate preamplifier and filters, to ensure that output or input frequencies are not being attenuated.

Perhaps the most restrictive criterion for performing NQR on a SSNMR spectrometer is the tuning range of the NMR probe. A commercial NMR probe is typically manufactured to tune to the Larmor frequency for a range of nuclei, such as ^{15}N through ^{31}P, with a specific applied magnetic field in mind. Consequently, the tuning range of

such a probe is customized according to the magnetic field strength in which it was meant to operate. However, one is not restricted to use the NMR probe intended for a specific magnetic field, as the only essential aspect is being able to tune in the range of the anticipated NQR frequency. Where a wide tuning range is needed, such as for ^{127}I NQR experiments, building a dedicated single-channel solenoid NQR probe can offer the required flexibility. This can be accomplished without most of the space restraints associated with building an NMR probe, and there are various designs available in the literature.[26,27] Additionally, with access to an automatic tuning and matching probe,[28] NQR experiments can be performed without the agony associated with staring at noise while continuously retuning the probe to search for NQR transitions.

Once the appropriate hardware setup has been prepared, the desired frequency must be generated from the amplifiers. From there, the frequency offset is varied, step by step, in order to find the NQR transition(s). Although the experiment can be performed using direct one-pulse excitation, a spin-echo pulse sequence can also be used to minimize the probe ringing, which is especially useful at low frequencies ($\nu_Q < 20$ MHz). Prior to commencing the experiment, the pulse lengths should be optimized on a sample with a known NQR frequency, with the goal of maximizing the signal intensity. The size of the frequency steps should also be chosen appropriately, as taking large steps can result in "missing" the signal, whereas taking small steps can become overly time-consuming. The size of the frequency steps can be optimized using the same sample by changing the offset until the signal can barely be observed. A typical step size used in our laboratory is 250 kHz. In cases where the nucleus of interest is dilute and/or the amount of sample available is small, smaller frequency steps can be advantageous to maximize the chances of observing the NQR signal(s). Shaped pulses have been shown to be useful in NQR spectroscopy, maximizing the excitation bandwidths of the pulses and thereby reducing the number of steps required.[16]

One of the inherent disadvantages of performing NQR using a SSNMR spectrometer is the possible presence of a stray magnetic field from the nearby superconducting magnet. Although modern shielded magnets greatly reduce the size and strength of the stray magnetic field, stray fields are nevertheless an important consideration as the presence of a magnetic field will induce an undesirable Zeeman splitting or spectral broadening. Therefore, the NQR experiment should be performed as far away from the NMR magnet as possible, to avoid any interactions with the stray magnetic field. Otherwise, the result is generally a broadening in the NQR line shape due in part from the magnetic field inhomogeneity, rendering it more difficult to observe. To demonstrate this effect, we have performed ^{35}Cl NQR experiments on tetrachloroterephthalonitrile ($\nu_Q \sim 38$ MHz), using a Bruker Avance III console operating near an unshielded Oxford Instruments 200 MHz NMR magnet. We have varied the distance between the probe head and the center of the bore of the superconducting magnet in several steps: 3 m, 2 m, 1 m, and 0.5 m away, and inside the magnet. Shown in Figure 4 is the result of each experiment, with a clear reduction in the signal-to-noise ratio and a 10 kHz frequency shift of the resonance between spectra (A) and (D).

4 | FURTHER PRACTICALITIES, LIMITATIONS, AND EXPERIMENTAL CHALLENGES

As mentioned above, both SSNMR and NQR have their particular advantages. SSNMR offers insights into both the chemical shift tensor and the quadrupolar coupling tensor.

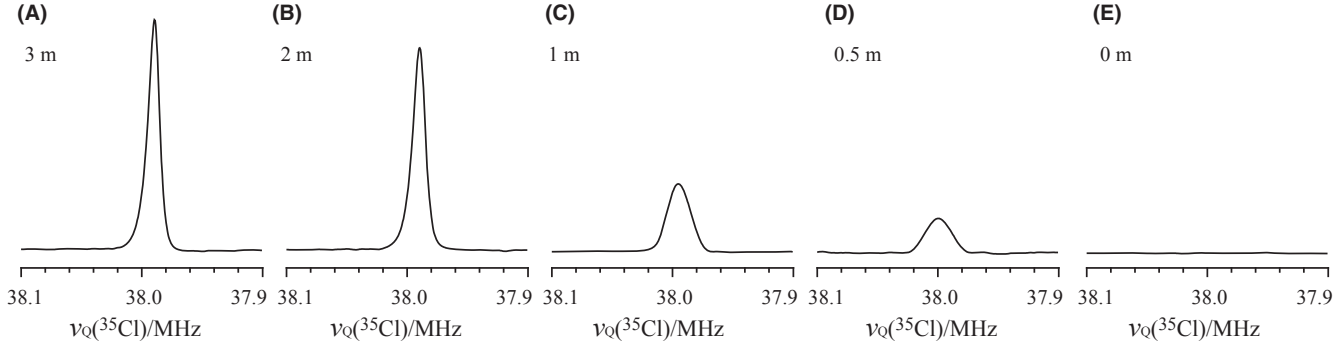

FIGURE 4 ^{35}Cl NQR spectra of tetrachloroterephthalonitrile acquired at room temperature on a Bruker Avance III console near a 200 MHz (4.7 T) unshielded Oxford Instruments magnet. The NQR experiment was performed at a distance of A, 3 meters (~0.3 mT), B, 2 meters (~0.7 mT), C, 1 meter (~4.0 mT), D, 0.5 meters (>5.0 mT), and E, 0 meters (inside the magnet), in order to demonstrate the effect of stray magnetic field on the NQR line shape. Each spectrum was acquired with a Hahn echo, 512 transients, and a 1 s recycle delay. Stray magnetic field strengths and distances are approximate

A set of NMR parameters can be extracted by iteratively fitting the experimental NMR spectrum using software such as QUEST[24] for exact simulations or WSolids[29] for second-order perturbation simulations. However, the acquisition of SSNMR spectra of quadrupolar nuclei is dictated by the receptivity of the nucleus, the line widths, and availability of high magnetic fields, to name a few considerations.[19] In comparison, pure NQR is relatively straightforward to perform using an NMR console, but as it is measured through the magnetic induction from the nuclear magnetic moments,[30] the sensitivity is also dependent on the receptivity of the nucleus. In the case of a spin-3/2 nucleus, the pure NQR spectrum would yield the product of the C_Q and η, ν_Q (Equation 5). In the cases of $I > 3/2$ and $I = 1$, obtaining more than one NQR transition would offer the values of both C_Q and η. However, pure NQR offers no information on magnetic field dependent (in frequency units) observables, such as the chemical shift tensor, and thus, SSNMR is inherently richer in information.

As mentioned earlier, in SSNMR, the second-order quadrupolar interaction scales inversely with the strength of the applied magnetic field. Consequently, higher magnetic fields are desirable for the analysis of quadrupolar nuclei, as they not only increase the sensitivity of the experiment, but also yield narrower quadrupolar line shapes. SSNMR analysis can be performed either under spinning conditions or under static conditions. In the case of analyzing a quadrupolar nucleus under spinning conditions, the most popular technique is magic angle spinning (MAS), where the sample is spun about the magic angle (54.74°)[31] with respect to the magnetic field, at a rate that would exceed the CT spectral width. Additionally, several MAS pulse sequences allow for the measurement of dipolar coupling and CSA under spinning conditions.[32] Alternative spinning methods include double rotation NMR (DOR),[33,34] where the first- and second-order quadrupolar interactions can be averaged by spinning both about the magic angle and an angle of 30.56° with respect to the magic angle. Other spinning methods exist, such as variable-angle spinning[35] and dynamic angle spinning,[36] offering alternative methods of analyzing quadrupolar nuclei. However, a nucleus exhibiting large quadrupolar interactions would either require impractically fast spinning speeds (perhaps on the order of MHz) or the deconvolution of unresolved spinning sidebands from the isotropic peaks. Multiple quantum magic angle spinning (MQMAS) is another alternative, which combines MAS with a multipulse sequence in order to obtain high-resolution spectra.[37] Additionally, new pulse sequences with the combination of fast MAS and indirect detection offer several advantages compared to the aforementioned techniques.[38] It is also possible to gain information on the C_Q indirectly through the SSNMR observation of neighboring nuclei. Fitting the resulting MAS line shapes can yield not only the value of C_Q, but has also been useful in determining the absolute sign of C_Q.[39]

Despite the applicability of MAS, SSNMR analysis of quadrupolar nuclei under static conditions is technologically more straightforward, while still offering an abundance of information. Signal enhancement techniques and advances in pulse sequences have allowed for the acquisition of very broad static NMR spectra. There is a wealth of information concerning signal enhancement of quadrupolar nuclei, perhaps with the most important being the Carr-Purcell-Meiboom-Gill (CPMG) pulse sequence applied to quadrupolar nuclei.[40] The combination of signal enhancement techniques, shaped pulses (ie, WURST pulses[41]), and variable offset cumulative spectral acquisition (VOCS)[42] enable "ultra wideline" SSNMR.[43,44] These techniques have made it possible to acquire spectra spanning hundreds of kHz and even several MHz.

In Figure 5A, the ultra-wideline ^{35}Cl solid-state NMR spectra of tetrachloroterephthalonitrile, acquired at field strengths of 35.2 T and 21.1 T using WURST-QCPMG are presented.[45] The central-transition ^{35}Cl NMR spectrum spans roughly 5.5 MHz at 35.2 T and 9 MHz at 21.1 T, requiring the acquisition of 14 subspectra near 35.2 T by sweeping the magnetic field, and 20 subspectra at 21.1 T using multiple transmitter offsets. The resulting spectrum at 21.1 T was fitted with QUEST,[24] yielding the values of C_Q, η, and δ_{iso} from a single 1D spectrum for two crystallographically distinct chlorine sites. The pure ^{35}Cl NQR spectrum of the same compound is presented in Figure 5C, with line widths of approximately 10 kHz. Only the quadrupolar product frequencies, ν_Q, are available from this spectrum. In this example, NQR was used as a complementary tool to SSNMR, allowing for the verification of the quadrupolar coupling parameters obtained from SSNMR.[45] Whereas the SSNMR spectrum took roughly 8 hours to acquire at 21.1 T, the NQR experiments took just 20 minutes to perform, but only with the knowledge of where to search for the resonances gained first from the SSNMR experiment.

Although it may be theoretically possible to acquire the SSNMR spectra of compounds exhibiting arbitrarily large quadrupolar interactions, in practice, there are limitations. A large quadrupolar interaction may result in CT broadening over many MHz or even over hundreds of MHz, precluding the acquisition of any signal. In Figure 6, we present a comparison between simulated SSNMR and NQR spectra of 1,4-dichlorobenzene (p-$Cl_2C_6H_4$), 1,4-dibromobenzene (p-$Br_2C_6H_4$), and 1,4-diiodobenzene (p-$I_2C_6H_4$). In each case, the spectra were simulated using an applied magnetic field strength of 21.1 T using QUEST[24] and literature quadrupolar frequency values, which are summarized in Table 1. The satellite transitions were included in the

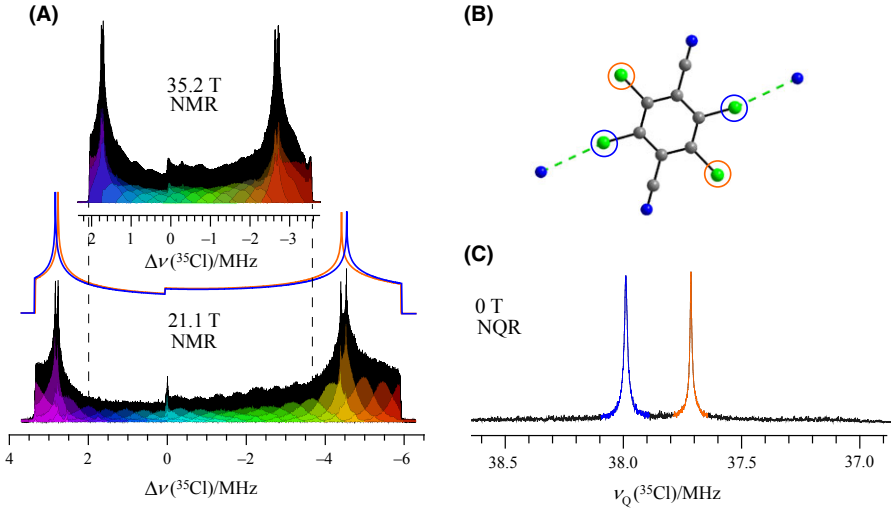

FIGURE 5 A, ^{35}Cl solid-state NMR spectrum of tetrachloroterephthalonitrile acquired at 35.2 T (upper) and 21.1 T (lower). At 35.2 T, a total of 14 subspectra were acquired, whereas at 21.1 T, a total of 20 subspectra were acquired (shown in color) and co-added in the frequency domain to yield the full spectrum (black). The QUEST simulated spectra for each of the two crystallographically distinct sites at 21.1 T are shown in blue and orange. B, The crystal structure of tetrachloroterephthalonitrile, showing the distinct chlorine sites in blue and orange. C, The ^{35}Cl NQR spectrum of tetrachloroterephthalonitrile. The blue and orange peaks correspond to the respective colored sites shown in the structure above. Experimental parameters for the 21.1 T and NQR acquisitions can be found in the original article[45]

simulations, with the area corresponding to the central transitions filled in with color. Much like the case in Figure 5A, the line widths of the central transition of $^{35/37}$Cl (Q(^{35}Cl) = −81.65(80) mb, Q(^{37}Cl) = −64.35(64) mb)[21] covalently bonded to carbon are manageable by SSNMR[45,46] and also provide information on the chemical shift. As is immediately apparent however, the line widths of the central transitions of $^{79/81}$Br (Q(^{79}Br) = 313(3) mb, Q(^{81}Br) = 262(3) mb)[21], and ^{127}I (Q(^{127}I) = −696(12) mb)[21] covalently bonded to carbon become prohibitively large, spanning hundreds of MHz. In contrast, the NQR signals are orders of magnitude sharper.

In the case of ^{127}I, which is a spin-5/2 nucleus, the acquisition of both pure NQR transition frequencies (±1/2 ↔ ±3/2, ν_1; ±3/2 ↔ ±5/2, ν_2) yields the same information on the quadrupolar coupling parameters as would SSNMR, that is, independent values of C_Q and η. In order to perform the SSNMR experiment, an impractically high magnetic field strength would be required. For instance, using the data presented in Table 1 on p-$I_2C_6H_4$, the ^{127}I CT spectral width can be reduced from approximately ~164 MHz at 21.1 T to ~42 MHz at 300 T. In contrast, NQR would require searching for transitions over tens of MHz. Therefore, in this case, performing the pure NQR experiment is the only practical form of RF spectroscopy.

Where sample size and receptivity are not an issue, a principal drawback of NQR lies in finding the NQR transitions over a potentially large frequency range. Knowing the

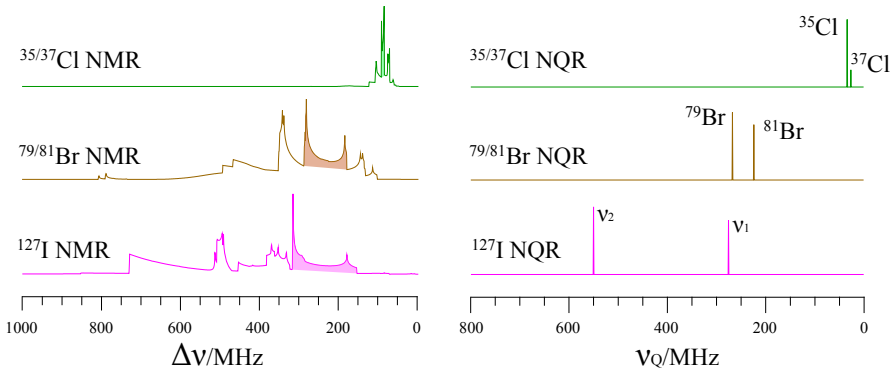

FIGURE 6 Simulated $^{35/37}$Cl, $^{79/81}$Br, and ^{127}I SSNMR spectra (left; B_0 = 21.1 T) and corresponding NQR spectra (right) of powdered p-$Cl_2C_6H_4$, p-$Br_2C_6H_4$, and p-$I_2C_6H_4$. Experimental quadrupolar coupling data are summarized in Table 1. The highlighted regions of the SSNMR spectra denote the central transitions. For the ^{127}I spectra, only one site was used in the simulation (C_Q = 1834.7 MHz, η = 0.0477), with ν_1 corresponding to the ±1/2 ↔ ±3/2 transition and ν_2 corresponding to the ±3/2 ↔ ±5/2 transition. All spectra were simulated using an exact Hamiltonian diagonalization in QUEST

TABLE 1 Experimental quadrupolar coupling constants (C_Q), asymmetry parameters (η), and NQR frequencies (ν_Q) for the $^{35/37}$Cl, $^{79/81}$Br, and ^{127}I nuclei in *p*-$Cl_2C_6H_4$, *p*-$Br_2C_6H_4$, and *p*-$I_2C_6H_4$, respectively, obtained from the literature

Compound	C_Q/MHz	η	ν_Q/MHz	References
p-$Cl_2C_6H_4$	*53.9 ± 0.2* (^{37}Cl) *68.5 ± 0.2* (^{35}Cl)	0.075 ± 0.002[a]	*26.98* (^{37}Cl) 34.25 (^{35}Cl)	V. Rehn[71]
p-$Br_2C_6H_4$	*448.2 ± 0.5* (^{81}Br) *535.5 ± 0.5* (^{79}Br)	0.045 ± 0.002[b,i]	223.8 (^{81}Br) 267.9[ii] (^{79}Br)	i P. Bucci et al.[72] ii G.W. Ludwig[65]
p-$I_2C_6H_4$	1834.7 ± 1.0[c] 1839.4 ± 1.0[c]	0.0477 ± 0.0040[c] 0.0365 ± 0.0050[c]	275.89 ± 0.15 (ν_1) 550.16 ± 0.30 (ν_2) 276.31 ± 0.15 (ν_1) 551.68 ± 0.30 (ν_2)	G.W. Ludwig[65]

The italicized numbers have been derived from the experimental data.

[a]Measured using the NQR field frequency method.

[b]Measured using Zeeman-perturbed NQR.

[c]The multiplicity of the C_Q & η values has been attributed to the presence of two crystal phases by Schawlow,[73] as there is only one iodine site in the asymmetric unit.[74]

coordination sphere surrounding the nuclide of interest, in addition to knowledge of literature results for analogous compounds, can dramatically reduce the frequency range to be searched. However, in the cases where possible C_Q values can span a wide range, such as covalently bonded bromine (300 to 600 MHz, ^{81}Br) and iodine (1600 to 2100 MHz, ^{127}I),[2,45,47,48] finding the NQR transitions without an autotuning probe can become a herculean task. For instance, scanning a frequency range of just 10 MHz using 250 kHz steps every 5 minutes would require 3 hours and 20 minutes of continuous effort. Several techniques have been implemented to help get around these issues, such as ultra-broadband electronics[49] and frequency swept pulses,[16] which allow for larger frequency steps.

NQR is commonly performed on nitrogen-14 ($I = 1$) and has been shown to be a potentially effective technique for routine analysis in the fields of explosives[50,51] and pharmaceuticals.[52] As a result of its moderate quadrupole moment ($Q(^{14}N) = 20.44(3)$ mb),[21] and lack of a central transition, ^{14}N SSNMR can be experimentally challenging to perform due to the first-order quadrupolar broadening. Nevertheless, ^{14}N has been the subject of many SSNMR investigations, with advances reported in overtone spectroscopy[53-55] and ultra-wideline ^{14}N SSNMR.[56-58] Although SSNMR is inherently richer in information and more sensitive, the instrumental simplicity gives ^{14}N NQR the practical advantage of being portable and applicable at the site of sample collection. However, as the ^{14}N NQR frequencies are typically in the hundreds of kHz to MHz regime, sensitivity can be problematic.

We have discussed NQR in terms of acquiring a single one-dimensional spectrum for a powdered sample in the absence of a magnetic field. As mentioned previously, one of the limitations of pure one-dimensional NQR of spin-3/2 nuclei is the inability to provide independent values of η and C_Q. However, several NQR techniques allow for the extraction of both η and C_Q from a single NQR transition. Nutation NQR is perhaps the most straightforward to perform, as it can be done using a standard NMR probe without any additional modifications.[59,60] Nutation NQR is implemented as a two-dimensional experiment, where a series of one-dimensional spectra are acquired with incremented pulse lengths. This experiment relies on the dependence of the nutation frequency on the angle between the quadrupolar tensor and the radiofrequency coil axis, allowing for an estimation of η from the line shape of the sheared 2D spectrum. Due to the long pulse lengths and the requirement for high power, one of the drawbacks of nutation NQR is the RF heating, which can result in a loss of resolution.[59] This issue can be mitigated either by having a longer recycle delay, or a device that maintains the sample temperature. Alternatively, Zeeman-perturbed NQR is one of the earlier methods of extracting η and C_Q from NQR transitions using weak magnetic fields.[61] Although many additional experiments exist, a full review of experimental techniques is beyond the scope of this article.

The temperature dependence of the quadrupolar interaction, and therefore the NQR frequency, has long been a subject of interest.[62,63] It is important to consider the temperature when reproducing literature results, as oftentimes NQR frequencies are reported at liquid nitrogen temperature (77 K). The origin of this effect can greatly vary according to the nature of the sample; however, it is most often attributed to molecular vibrations, librations, other forms of dynamics, or even changes in volume.[63]

While we have limited the discussion to crystalline samples, it is worth mentioning that both SSNMR and NQR are known to be powerful tools for the analysis of samples with disorder or low crystallinity,[64] which can be otherwise troublesome to analyze by diffraction-based techniques. The signal afforded from these techniques can be used to extract parameters related to the structure, such as

internuclear dipolar coupling in the case of SSNMR. The line shapes can be fit to model the disorder present in the sample,[65] which is typically manifested through broadening of line shapes. For quadrupolar nuclei, the combination of both SSNMR and NQR can be used to probe the distribution in the QI. In certain cases, NQR resonances can be broadened to span hundreds of kHz, and even several MHz,[66] in which case frequency swept pulses can be beneficial to decrease experimental time.[16]

When performing ultra wideline SSNMR or even NQR, it is important to consider overlap arising from crystallographically distinct sites,[67] overlap from other nuclides, and possible interference from nearby radio transmissions.[68] For instance, while acquiring ultra wideline ^{35}Cl SSNMR spectra at 21.1 T (ν_L = 88.2 MHz), samples that were packed in zirconium rotors produced large ^{91}Zr signals (ν_L = 83.7 MHz), inconveniently overlapping with singularities at -4.5 MHz on the ^{35}Cl spectrum. This problem can easily be circumvented by instead packing the samples in glass tubes. Although it is not noticeable in Figure 5 as a result of the large signal intensity from the sample of interest, radio interference is observed in the +2 MHz region, which corresponds to the local radio stations (~90 MHz). Another issue that has been observed experimentally is the lack of power linearity of the amplifiers. Over a large frequency range, the power output of the amplifier may change subtly. These subtle changes in power output can lead to distortions in the final spectrum. Anisotropy in the spin-lattice and spin-spin relaxation times may also contribute to the distortion of an ultra wideline SSNMR spectrum. Additionally, the Boltzmann population of the spin states may vary across broad spectra, which may further contribute to spectral distortions and lead to a stronger signal intensity at higher frequencies.

Although several methods are available to extract the quadrupolar coupling parameters mathematically from NQR spectra,[69] iteratively fitting the spectra using software is also straightforward. QUEST is available for simulating NQR spectra based on the spin quantum number and the values of η and C_Q.[24]

5 | CONCLUDING REMARKS

Both SSNMR and NQR are valuable tools for the analysis of compounds containing quadrupolar nuclei. Here, we have discussed some of the advantages and disadvantages of both techniques, with the quadrupolar halogens serving as examples. Although the advent of higher magnetic fields and new pulse techniques makes SSNMR a more versatile technique, the presence of very large quadrupolar interactions can hinder its application, with NQR being in some cases the RF spectroscopy of choice. We have discussed some of the practical aspects related to how a SSNMR console can double as a NQR spectrometer, along with some of the associated experimental challenges. Although SSNMR is inherently richer in information, it is clear that a combination of both techniques is the best approach, particularly for nuclei subject to strong quadrupolar interactions, as one technique can help to compensate for the shortcomings of the other.

ACKNOWLEDGMENTS

PMJS and DLB thank the Natural Sciences and Engineering Research Council of Canada for research funding. Access to the 21.1 T NMR spectrometer was provided by the National Ultrahigh-Field NMR Facility for Solids (Ottawa, Canada), a national research facility funded by a consortium of Canadian Universities, supported by the National Research Council Canada and Bruker BioSpin, and managed by the University of Ottawa (http://nmr900.ca). We are grateful to Ivan Hung and Zhehong Gan for acquiring the ^{35}Cl NMR spectrum using a series-connected hybrid magnet operating at 35.2 T. This portion of the work was performed at the National High Magnetic Field Laboratory, which is supported by National Science Foundation Cooperative Agreement No. DMR-1157490 and the State of Florida.

ORCID

Patrick M.J. Szell https://orcid.org/0000-0002-3185-9892
David L. Bryce http://orcid.org/0000-0001-9989-796X

REFERENCES

1. Ashbrook SE, Duer MJ. Structural Information from Quadrupolar Nuclei in Solid State NMR. *Concepts Magn Reson Part A*. 2006;28A:183-248.
2. Lucken EAC. *Nuclear Quadrupole Coupling Constants*. London: Academic Press Inc.; 1969.
3. Grechishkin VS. Nuclear quadrupole resonance. *Usp Fiz Nauk*. 1959;69:189-216.
4. Smith JAS. Nuclear quadrupole resonance spectroscopy. *J Chem Educ*. 1971;48:39-48.
5. Pandey MK, Hashi K, Ohki S, Nishijima G, Matsumoto S, Noguchi T, et al. 24 T high-resolution and sensitivity solid-state NMR measurements of low-gamma half-integer quadrupolar nuclei ^{35}Cl and ^{37}Cl. *Anal Sci*. 2016;32:1339-1345.
6. Jakobsen HJ, Bildsøe H, Brorson M, Wu G, Gor'kov PL, Gan Z, et al. High-Field ^{17}O MAS NMR Reveals ^{1}J(^{17}O-^{127}I) with its Sign and the NMR Crystallography of the Scheelite Structures for $NaIO_4$ and KIO_4. *J Phys Chem C*. 2015;119:14434-14442.
7. Bain AD. NMR quadrupole Liouvillians for arbitrary spin: exact symbolic expressions and perturbation solutions. *Concepts Magn Reson*. 2013;42A:45-58.

8. Bain AD. The NMR of quadrupolar nuclei. Relationship between exact and perturbation solutions for spin 3/2. *Chem Phys Lett*. 2012;531:267-271.
9. Lee YK. Spin-1 nuclear quadrupole resonance theory with comparisons to nuclear magnetic resonance. *Concepts Magn Reson Part A*. 2002;14:155-171.
10. Bain AD. Quadrupole interactions: NMR, NQR, and in between from a single viewpoint. *Magn Reson Chem*. 2017;55: 198-205.
11. Bain AD, Khasawneh M. From NQR to NMR: the complete range of quadrupole interactions. *Concepts Magn Reson*. 2004;22A:69-78.
12. Adiga S, Aebi D, Bryce DL. EFGShield – A program for parsing and summarizing the results of electric field gradient and nuclear magnetic shielding tensor calculations. *Can J Chem*. 2007;85:496-505.
13. Mestechkin MM. Electric field gradient in cubic and other ionic crystals. *J Phys Condens Matter*. 1995;7:611-623.
14. Autschbach J, Zheng S, Schurko RW. Analysis of electric field gradient tensors at quadrupolar nuclei in common structural motifs. *Concepts Magn Reson*. 2010;36A:84-126.
15. Widdifield CM, Bain AD, Bryce DL. Definitive solid-state $^{185/187}$Re NMR spectral evidence for and analysis of the origin of high-order quadrupole-induced effects for $I = 5/2$. *Phys Chem Chem Phys*. 2011;13:12413-12420.
16. Rossini AJ, Hamaed H, Schurko RW. The application of frequency swept pulses for the acquisition of nuclear quadrupole resonance spectra. *J Magn Reson*. 2010;206:32-40.
17. Bain AD. A simple proof that third-order quadrupole perturbations of the NMR central transition of half-integral spin nuclei are zero. *J Magn Reson*. 2006;179:308-310.
18. Amoureux JP, Fernandez C, Granger P. Interpretation of quadrupolar powder spectra: static and MAS experiments. (Tutorial Session). In: Granger P, Harris RK, eds. *Multinuclear Magnetic Resonance in Liquids and Solids: Chemical Applications*. NATO ASI Series C – Vol. 322. Dordrecht, Netherlands: Kluwer Academic Publishers; 1990:409-424.
19. Bryce DL, Bernard GM, Gee M, Lumsden MD, Eichele K, Wasylishen RE. Practical aspects of modern routine solid-state multinuclear magnetic resonance spectroscopy: one-dimensional experiments. *Can J Anal Sci Spect*. 2001;46:46-82.
20. Van Vleck JH. The dipolar broadening of magnetic resonance lines in crystals. *Phys Rev*. 1948;74:1168-1183.
21. Pyykkö P. Year-2008 nuclear quadrupole moments. *Mol Phys*. 2008;106:1965-1974.
22. Zax DB, Bielecki A, Zilm KW, Pines A, Weitekamp DP. Zero field NMR and NQR. *J Chem Phys*. 1985;83:4877-4905.
23. Widdifield CM, Perras FA, Bryce DL. Solid-state $^{185/187}$Re NMR and GIPAW DFT study of perrhenates and $Re_2(CO)_{10}$: chemical shift anisotropy, NMR crystallography, and a metal-metal bond. *Phys Chem Chem Phys*. 2015;17:10118-10134.
24. Perras FA, Widdifield CM, Bryce DL. QUEST – QUadrupolar Exact SofTware: A fast graphical program for the exact simulation of NMR and NQR spectra for quadrupolar nuclei. *Solid State Nucl Magn Reson*. 2012;45–46:36-44.
25. Beguš S, Jazbinšek V, Pirnat J, Trontelj Z. A miniaturized NQR spectrometer for a multi-channel NQR-based detection device. *J Magn Reson*. 2014;247:22-30.
26. Scharfetter H. An electronically tuned wideband probehead for NQR spectroscopy in the VHF range. *J Magn Reson*. 2016; 271:90-98.
27. Sato-Akaba H. Design and testing of a low impedance transceiver circuit for nitrogen-14 nuclear quadrupole resonance. *Solid State Nucl Magn Reson*. 2014;63–64:30-36.
28. Pecher O, Halat DM, Lee J, Liu Z, Griffith KJ, Braun M, et al. Enhanced efficiency of solid-state NMR investigations of energy materials using an external automatic tuning/matching (eATM) robot. *J Magn Reson*. 2017;275:127-136.
29. Eichele K. *WSolids1 ver. 1.21.3*. Germany: Universität Tübingen; 2015.
30. Abragam A. *The Principles of Nuclear Magnetism*. London: Oxford University Press; 1961.
31. Lowe IJ. Free induction decays of rotating solids. *Phys Rev Lett*. 1959;2:285-287.
32. Gullion T. Introduction to rotational-echo, double-resonance NMR. *Concepts Magn Reson Part A*. 1998;10:277-289.
33. Samason A, Lippmaa E, Pines A. High resolution solid-state N.M.R. Averaging of second-order effects by means of a double-rotor. *Mol Phys*. 1988;65:1013-1018.
34. Samoson A, Pines A. Double rotor for solid-state NMR. *Rev Sci Instrum*. 1989;60:3239-3241.
35. Frydman L, Chingas GC, Lee YK, Grandinetti PJ, Eastman MA, Barrall GA, et al. Variable-angle correlation spectroscopy in solid-state nuclear magnetic resonance. *J Chem Phys*. 1992;97:4800-4808.
36. Wang SH, Xu Z, Baltisberger JH, Bull LM, Stebbins JF, Pines A. Multiple-quantum magic-angle spinning and dynamic-angle spinning NMR spectroscopy of quadrupolar nuclei. *Solid State Nucl Magn Reson*. 1997;8:1-16.
37. Frydman L, Harwood JS. Isotropic Spectra of Half-Integer Quadrupolar Spins from Bidimensional Magic-Angle Spinning NMR. *J, Am, Chem, Soc*. 1995;117:5367-5368.
38. Rossini AJ, Hanrahan MP, Thuo M. Rapid acquisition of wideline MAS solid-state NMR spectra with fast MAS, proton detection, and dipolar HMQC pulse sequences. *Phys Chem Chem Phys*. 2016;18:25284-25295.
39. Eichele K, Wasylishen RE, Grossert JS, Olivieri AC. The Influence of Chlorine-Carbon Dipolar and Indirect Spin-Spin Interactions on High-Resolution Carbon-13 NMR Spectra of Chloroketosulfones in the Solid State. *J Phys Chem*. 1995;99:10110-10113.
40. Siegel R, Nakashima TT, Wasylishen RE. Signal-to-Noise Enhancement of NMR Spectra of Solids Using Multiple-Pulse Spin-Echo Experiments. *Concepts Magn Reson*. 2005;26A:62-77.
41. O'Dell LA, Schurko RW. QCPMG Using Adiabatic Pulses for Faster Acquisition of Ultra-Wideline NMR Spectra. *Chem Phys Lett*. 2008;464:97-102.
42. Massiot D, Farnan I, Gautier N, Trumeau D, Trokiner A, Coutures JP. ^{71}Ga and ^{69}Ga nuclear magnetic resonance study of β-Ga_2O_3: resolution of four- and six-fold coordinated Ga sites in static conditions. *Solid State Nucl Magn Reson*. 1995;4:241-248.
43. O'Dell LA, Rossini AJ, Schurko RW. Acquisition of ultra-wideline NMR spectra from quadrupolar nuclei by frequency stepped WURST-QCPMG. *Chem Phys Lett*. 2009;468:330-335.
44. Schurko RW. Ultra-Wideline Solid-State NMR Spectroscopy. *Acc Chem Res*. 2013;46:1985-1995.

45. Szell PMJ, Bryce DL. ^{35}Cl solid-state NMR and computational study of chlorine halogen bond donors in single-component crystalline chloronitriles. *J Phys Chem C*. 2016;120:11121-11130.
46. Perras FA, Bryce DL. Direct investigation of covalently bound chlorine in organic compounds by solid-state ^{35}Cl NMR spectroscopy and exact spectral line-shape simulations. *Angew Chem Int Ed*. 2012;51:4227-4230.
47. Szell PMJ, Bryce DL. Recent advances in Chlorine, Bromine, and Iodine solid-state NMR spectroscopy. *Annu Rep NMR Spectrosc*. 2015;84:115-165.
48. Widdifield CM, Chapman RP, Bryce DL. Chlorine, Bromine, and Iodine Solid-State NMR Spectroscopy. *Annu Rep NMR Spectrosc*. 2009;66:195-326.
49. Mandal S, Song Y-Q. Two-dimensional NQR using ultra-broadband electronics. *J Magn Reson*. 2014;240:16-23.
50. Osán TM, Cerioni LMC, Forguez J, Ollé JM, Pusiol DJ. NQR: From imaging to explosives and drugs detection. *Physica B*. 2007;389:45-50.
51. Smith JAS, Rowe MD, Althoefer K, Peirson NF, Barras J. ^{14}N NQR, relaxation and molecular dynamics of the explosive TNT. *Solid State Nucl Magn Reson*. 2015;71:61-66.
52. Barras J, Murnane D, Althoefer K, Assi S, Rowe MD, Poplett IJF, et al. Nitrogen-14 nuclear quadrupole resonance spectroscopy: a promising analytical methodology for medicines authentication and counterfeit antimalarial analysis. *Anal Chem*. 2013;85:2746-2753.
53. Tycko R, Opella SJ. High-resolution ^{14}N overtone spectroscopy: an approach to natural abundance nitrogen NMR of oriented and polycrystalline systems. *J Am Chem Soc*. 1986;108:3531-3532.
54. O'Dell LA, Ratcliffe CI. ^{14}N magic angle spinning overtone NMR spectra. *Chem Phys Lett*. 2011;514:168-173.
55. O'Dell LA, Brinkmann A. ^{14}N Overtone NMR spectra under magic angle spinning: experiments and numerically exact simulations. *J Chem Phys*. 2013;138:064201.
56. Veinberg SL, Lindquist AW, Jaroszewicz MJ, Schurko RW. Practical considerations for the acquisition of ultra-wideline ^{14}N NMR spectra. *Solid State Nucl Magn Reson*. 2017;84:45-58.
57. O'Dell LA, Ratcliffe CI. Ultra-wideline ^{14}N NMR spectroscopy as a probe of molecular dynamics. *Chem Commun*. 2010;46:6774-6776.
58. O'Dell LA, Schurko RW, Harris KJ, Autschbach J, Ratcliffe CI. Interaction tensors and local dynamics in common structural motifs of nitrogen: a solid-state ^{14}N NMR and DFT study. *J Am Chem Soc*. 2011;133:527-546.
59. Harbison GS, Slokenbergs A, Barbara TM. Two-dimensional zero-field nutation nuclear quadrupole resonance spectroscopy. *J Chem Phys*. 1989;90:5292-5298.
60. Sinjavsky N, Ostafin M, Maćkowiak M. Determination of the asymmetry parameter of EFG tensor from moments and NQR nutation spectra in powders. *Appl Magn Reson*. 1998;15:215-225.
61. Bai NS, Reddy N, Ramachandran R. Zeeman-Perturbed Spin-Echo FT NQR Spectroscopy. *J Magn Reson*. 1993;102:137-143.
62. Ramesh KP, Suresh KS, Raghavendra Rao C, Ramakrishna J. Pressure and temperature dependence of the chlorine NQR in caesium and sodium chlorates. *Magn Reson Chem*. 2008;46:525-533.
63. Kushida T, Benedek GB, Bloembergen N. Dependence of the pure quadrupole resonance frequency on pressure and temperature. *Phys Rev*. 1956;104:1364-1377.
64. Bryce DL. NMR crystallography: structure and properties of materials from solid-state nuclear magnetic resonance observables. *IUCrJ*. 2017;4:350-359.
65. Kroeker S, Wasylishen RE, Hanna JV. The structure of solid Copper(I) Cyanide: a multinuclear magnetic and quadrupole resonance study. *J Am Chem Soc*. 1999;121:1582-1590.
66. Rubinstein M, Taylor PC. Nuclear quadrupole resonance in amorphous and crystalline As_2S_3. *Phys Rev B*. 1974;9:4258-4276.
67. Jaroszewicz MJ, Frydman L, Schurko RW. Relaxation-assisted separation of overlapping patterns in ultra-wideline NMR spectra. *J Phys Chem A*. 2017;121:51-65.
68. See http://u-of-o-nmr-facility.blogspot.ca/2008/05/interference-from-fm-radio-stations.html
69. Ludwig GW. Some Bromine, Iodine, and Indium nuclear quadrupole interaction frequencies. *J Chem Phys*. 1956;25:159-171.
70. Web of Science Version 5.25.1. [database online]. Philadelphia, PA: Clarivate Analytics; 2017. www.webofknowledge.com. Accessed August 28th 2017.
71. Rehn V. Covalent-Bond Asymmetries from Zeeman-Split NQR. *J Chem Phys*. 1963;38:749-759.
72. Bucci P, Cecchi P, Colligiani A. The Zeeman Effect of Nuclear Quadrupole Resonance in Single Crystals of Sodium Bromate and p-Dibromobenzene. *J Am Chem Soc*. 1964;86:2513-2514.
73. Schawlow AL. Nuclear Quadrupole Resonances in Solid Bromine in Iodine Compounds. *J Chem Phys*. 1954;22:1211-1214.
74. Hinchliffe A, Munn RW, Pritchard RG, Spicer CJ. The Structure of a Solution-Grown Crystal of 1,4-Diiodobenzene. *J Mol Struct*. 1985;130:93-96.

How to cite this article: Szell PMJ, Bryce DL. Solid-state nuclear magnetic resonance and nuclear quadrupole resonance as complementary tools to study quadrupolar nuclei in solids. *Concepts Magn Reson Part A*. 2016;45A:e21412. https://doi.org/10.1002/cmr.a.21412

Part 2 – Investigating the Halogen Bond Donor

This part of the thesis details a systematic characterization of the halogen bond donor using a combination of solid-state NMR and NQR spectroscopy observing the ^{35}Cl, $^{79/81}$Br and ^{127}I nuclei. As mentioned in the previous chapter, aside from fluorine which has a spin of ½, the halogens are quadrupolar: chlorine-35/37 and bromine-79/81 each have a spin of 3/2, whereas iodine-127 has a spin of 5/2. The quadrupole moments of each nucleus increase significantly with the size of the halogen (Q[^{35}Cl] = -81.12 mb; Q[^{81}Br] = 257.9(2) mb; Q[^{79}Br] = 308.7(2) mb; Q[^{127}I] = -617 mb)[1], with the resulting quadrupolar interaction being substantial for covalently bonded bromine and iodine (see Figure 6 of Chapter 3). Measuring the quadrupolar coupling parameters C_Q and η yields the full EFG tensor, which provides information on the electronic configuration. The following studies performed on ^{35}Cl, $^{79/81}$Br, and ^{127}I seek to observe changes in the quadrupolar coupling at the halogen bond donor following the introduction of a C-X···N halogen bond (X = Cl, Br, I), thus allowing for direct insights on how the halogen bond has affected the electronic configuration of the halogen bond donor atom. Furthermore, changes in the NQR frequencies are shown to be sensitive to the occurrence of the halogen bond, with shifts on the order of MHz for $^{79/81}$Br and ^{127}I, and kHz for ^{35}Cl, offering a reliable indicator of cocrystallization.

Previous studies that have aimed to characterize the halogen bond donor by spectroscopy have employed a colorful range of techniques. Vibrational spectroscopy is a convenient investigational tool, requiring only a few milligrams of sample and a few minutes, with the C-I absorption band being sensitive to the halogen bond.[2] The red-shift in the C-I band has been

attributed to the lengthening of the C-I covalent bond upon the introduction of a halogen bond.[3,4] As this wavenumber is quite low (~150-270 cm^{-1})[5] a specialized infrared (IR) spectrometer is typically required to reach it. The absorption bands associated with the halogen bond acceptor are also sensitive to the occurrence of halogen bonding, and the IR spectrum is a useful preliminary analytical tool prior to implementing further analysis. As IR spectroscopy relies on the vibrations of chemical bonds, it does not directly offer information on the EFG. While other vibrational spectroscopies have been applied to characterize the halogen bond donor, such as Raman spectroscopy,[6,7] they also do not offer information on the EFG.

Rotational spectroscopy has a history in the investigation of non-covalent interactions occurring in the gas phase,[8,9,10] including interactions involving halogen atoms.[11,12] Unlike vibrational spectroscopy, the quadrupolar coupling can be measured by rotational spectroscopy, and is not limited to very large coupling magnitudes, such as those encountered for covalently bonded ^{127}I.[13] Although applied to analyze molecules in the gas phase, several reports have characterized halogen bonded complexes, such as the $FCl\cdots H_2O$[14] and $CF_3Cl\cdots CO$ complexes.[15] As microwave spectroscopy is applied to the gas phase,[16] many halogen bonded systems are rendered inaccessible by this method.

X-ray absorption spectroscopy has recently been introduced to the field, which offers information on the electronic structure in halogen bonded compounds.[17] While the technique requires specialized X-ray equipment in addition to expertise in interpreting the data, it has been successfully applied to characterize the halogen bond involving dyes.[18] The use of K-edge X-ray absorption spectroscopy has also been applied to the $I\cdots Cl^-$ / $I\cdots Br^-$ motif, supporting the role of charge transfer in the halogen bond with a degree of covalency comparable to that of a dative bond.[19]

Mössbauer spectroscopy is a very powerful tool which requires irradiating a solid sample with γ-rays.[20,21] Much like NMR spectroscopy, there is an isomer shift akin to the chemical shift, and it does offer information on the quadrupolar coupling.[22,23] However, the technique suffers from the need of specific γ-radiation sources, and consequently not all quadrupolar nuclei are experimentally accessible by Mössbauer spectroscopy. Iodine-129 is a suitable nucleus,[24] and there have been a few reports investigating compounds matching the halogen bond descriptor. In a series of complexes formed between IBr or ICl and pyridine derivatives, the ^{129}I C_Q increases in magnitude by 13 MHz to 209 MHz relative to the pure starting material.[25] These increases were attributed to the formation of the N-I-X motif. Investigations of the I_2 halogen bond donor yielded similar trends upon the formation of molecular complexes,[26,27] and the formation of I···N interactions in poly(vinylpyridines) further support those observations.[28] With the gain in popularity of the iodine···nitrogen complex, which have become known as strong charge-transfer complexes, other motifs have been explored, such as the I_2···benzene motif.[29] Mössbauer spectroscopy has also been applied to characterize nuclei not directly participating in the halogen bond, such as the ^{57}Fe nucleus.[30,31]

Requiring a magnetic field and RF equipment, solid-state NMR can be routinely performed on halogen bonded samples without the need of ionizing radiation. Further, as most of the elements on the periodic table have an NMR-active nucleus, solid-state NMR can offer isotope and site-specific information. Previous studies on characterizing the halogen bond donor by solid-state NMR have observed changes in the ^{13}C chemical shift of the carbon atom covalently bonded to iodine.[32,33] As a result of the residual dipolar coupling to ^{127}I, along with its large quadrupolar coupling, the ^{13}C-I resonance is broadened and rendered difficult to observe.[34] In the initial investigations, the authors have measured an increase in the ^{13}C-I

chemical shift upon halogen bonding, correlating with the length of the carbon-iodine covalent bond.[33,35] An article investigating compounds featuring the C-I···N bond by ^{13}C and ^{15}N SSNMR find similar trends between the C-I bond length and the ^{13}C-I chemical shift.[32] While ^{13}C SSNMR does offer an indicator for the occurrence of a halogen bond, experimental times required to observe the ^{13}C-I resonance can be quite lengthy, and consists of an indirect probe. Furthermore, the broadened features of the ^{13}C-X resonance,[36] along with its low signal-to-noise ratio, makes it difficult to extract information on the quadrupolar coupling by fitting the ^{13}C line shape,[37] while it has been possible for the ^{13}C-Cl motif.[38] Consequently, the most suitable approach to study the halogen bond donor is through the direct observation of the ^{35}Cl, $^{79/81}Br$ and ^{127}I nuclei using a combination of SSNMR and NQR, as discussed in Chapter 3, with the support of X-ray crystallography.

At the time of conceiving the experimental design for Chapter 4, our laboratory had recently established a $^{35/37}Cl$ solid-state NMR method to probe covalently bonded chlorine at 21.1 T,[39] using exact simulations[40] and ultra-wideline acquisition techniques.[41,42] As halogen bond donors are primarily carbon-based (i.e. C-Cl, C-Br & C-I), these developments were key to the success of the project, allowing us to perform the first direct investigation of the chlorine halogen bond donor. Unfortunately, the chlorine halogen bond donor is also very weak, and the occurrence of halogen bonding based on the C-Cl moiety is rare. Further, attempts at cocrystallizing the fluorinated chlorine-based donor 1,3,5-trichloro-2,4,6-trifluorobenzene with a series of halogen bond acceptors proved unsuccessful. The project was plagued by the difficulty in first obtaining suitable samples for analysis.

Rather than cocrystallizing the sample, in Chapter 4 we conceived an approach relying on crystallographic symmetry. We would compare the EFG parameters for chemically equivalent

and crystallographically inequivalent chlorine sites, where one site participates in a halogen bond and the other site does not exhibit any contacts. After searching the CSD,[43] there were a few chlorinated compounds matching our criteria: one chlorine must participate in a C-Cl···N halogen bond, and an otherwise chemically equivalent chlorine must have no contacts, acting as the control. By chemical equivalence, this indicates that aside from its crystallographic environment, the chlorine atoms are related by molecular symmetry. As a result, the chlorines share the same chemical environment, with any changes in the quadrupolar interaction and chemical shift being attributed to changes in their crystallographic environment. An example is shown in Figure 2.1.

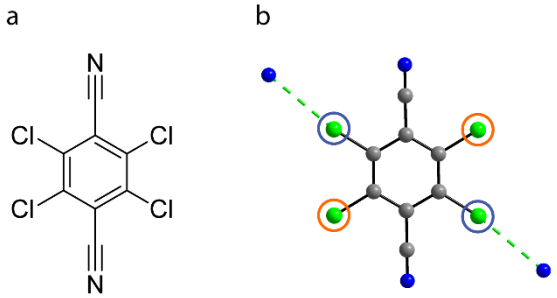

Figure 2.1. The molecular structure (a) and a depiction of the crystal structure (b) of tetrachloroterephthalonitrile,[44] showing the Cl···N halogen bond by a dashed green line. The two crystallographically independent chlorine sites are circled in blue and orange.

While the molecular structure of tetrachloroterephthalonitrile (Figure 2.1a) exhibits several elements of symmetry, the crystal structure (Figure 2.1b) does not display the same symmetry elements.[44] Rather, there are two crystallographically independent chlorine atoms, with one chlorine atom participating in a C-Cl···N halogen bond and the other chlorine atom not participating in any contacts within its van der Waals radius. Therefore, there are two independent chlorine sites, which are expected to have different NMR parameters, notably in

their quadrupolar coupling. These changes are directly attributed to the halogen bond, which offers information on how the halogen bond modifies the EFG at the chlorine donor.

Due to the fact that there are limited crystal structures meeting these criteria, the compounds were selected with further characteristics, such as C-Cl···H contacts, and comparing the C-Cl···O halogen bond to the C-Cl···N halogen bond in DDQ.[45] The ^{35}Cl solid-state NMR experiments span ~10 MHz, and were therefore quite challenging both in their acquisition and in their interpretation. As it is favorable to acquire the same spectrum at multiple fields to verify the fitting parameters, NQR experiments were performed, with the resulting ^{35}Cl NQR frequency aiding in the data refinement.

Chapter 5, performed in collaboration with Dr. Roberto Gobetto's group from the University of Turin, offers the first modern ^{79}Br and ^{81}Br NQR analysis of a series of halogen bonded cocrystals featuring 1,4-dibromotetrafluorobenzene donor and a series of nitrogen-containing heterocycles. Unfortunately, the strong quadrupolar coupling that occurs on a bromine atom covalently bonded to carbon prohibits its analysis by SSNMR, with the resulting spectra expected to span hundreds of MHz (see Chapter 3). The challenge in this experiment is then finding the NQR resonances, which requires scanning the large frequency windows at steps of ~0.2 MHz. As the ^{81}Br NQR frequencies typically span between 200 and 300 MHz, "finding" the transitions requires a significant time investment. Furthermore, when the expected signal has not been observed, the origin of the problem may not be clear. For instance, it could be related to the signal being broadened with a resulting low signal-to-noise ratio, instrument limitations, or even taking steps too large and missing the signal. As spin-3/2 nuclei, only a single transition is observed in the pure NQR spectra of both the ^{79}Br and ^{81}Br nuclides. Consequently, nutation NQR was employed in order to gain information on the asymmetry parameter (η). As the

$\nu(^{79}Br)/\nu(^{81}Br)$ ratio is related by a factor of approximately 1.20, finding the NQR resonances for both nuclei increases the confidence of the results. This project focuses on the potential of $^{79/81}Br$ NQR as a crystallographic tool to probe the occurrence of halogen bonding, rather than an interpretation on the changes in the EFG.

Chapter 6 features a modern ^{127}I NQR investigation on a series of cocrystals featuring the C-I···N halogen bonding motif, thus completing the analysis of each quadrupolar halogen bond donor. The project first began using 1,4-diiodotetrafluorobenzene but was later substituted with 1,4-diiodobenzene due to equipment limitations. As a result, 1,4-diiodobenzene is investigated in its pure form, and subsequently in a series of cocrystals with nitrogen-containing heterocycles. As the C_Q of the pure starting material is on the order of 1900 MHz,[46] ^{127}I SSNMR would again not be feasible, thus requiring NQR. The project presented an enormous challenge of observing two NQR transitions, even requiring modifications to the equipment in order to observe the upper transition at frequencies over 550 MHz. The experimental results are then complemented with a series of DFT calculations performed on models of haloperfluorobenzenes (chloro/bromo/iodo) interacting with pyridine, varying the $d_{X\cdots N}$ incrementally. Using the experimental and calculated results of Chapter 4, 5, and 6, we propose a model to explain the increases in the C_Q occurring on the halogen bond donor upon the formation of a halogen bond.

References.

[1] Pyykkö, P. *Mol. Phys.* **2018**, *116*, 1328-1338.

[2] Oliveira, V.; Kraka, E.; Cremer, D. *Inorg. Chem.* **2017**, *56*, 488-502.

[3] Wang, C.; Danovich, D.; Shaik, S.; Mo, Y. *J. Chem. Theory Comput.* **2017**, *13*, 1626-1637.

[4] Wang, W.; Hobza, P. *J. Phys. Chem. A* **2008**, *112*, 4114-4119.

[5] Fugaeva, O.M.; Korobeinicheva, I.K.; Bardin, V.V. *J. Mol. Struc.* **1993**, *293*, 209-212.

[6] Nagels, N.; Hauchecorne, D.; Herrebout, W.A. *Molecules.* **2013**, *18*, 6829-6851.

[7] Wang, H.; Jin, W.J. *Acta Cryst.* **2017**, *B73*, 210-216.

[8] Legon, A.C.; Thorn, J.C. *Chem. Phys. Lett.* **1994**, *227*, 472-479.

[9] Legon, A.C.; Millen, D.J. *Chem. Rev.* **1986**, *86*, 635-657.

[10] Legon, A.C. *Faraday Discuss.* **1994**, *97*, 19-33.

[11] Cotti, G.; Cooke, S.A.; Evans, C.M.; Holloway, J.H.; Legon, A.C. *Chem. Phys. Lett.* **1996**, *260*, 388-394.

[12] Bloemink, H.I.; Hinds, K.; Holloway, J.H.; Legon, A.C. *Chem. Phys. Lett.* **1995**, *245*, 598-604.

[13] Cooper, G.A.; Anderson, C.J.; Medcraft, C.; Walker, N.R. *J. Mol. Spec.* **2018**, *354*, 15-23.

[14] Cooke, S.A.; Gotti, G.; Evans, C.M.; Holloway, J.H.; Kisiel, Z.; Legon, A.C.; Thumwood, J.M.A. *Chem. Eur. J.* **2001**, *7*, 2295-2305.

[15] Caminati, W.; Evangelisti, L.; Feng, G.; Giuliano, B.M.; Gou, Q.; Melandri, S.; Grabow, J.-U. *Phys. Chem. Chem. Phys.* **2016**, *18*, 17851-17855.

[16] Bryce, D.L.; Wasylishen, R.E. *Acc. Chem. Res.* **2003**, *36*, 327-334.

[17] Robinson, S.W.; Mustoe, C.L.; White, N.G.; Brown, A.; Thompson, A.L.; Kennephl, P.; Beer, P.D. *J. Am. Chem. Soc.* **2015**, *137*, 499-507.

[18] Parlane, F.G.L.; Mustoe, C.; Kellett, C.W.; Simon, S.J.; Swords, W.B.; Meyer, G.J.; Kennephl, P.; Berlinguette, C.P. *Nat. Comm.* **2017**, *8*, 1761.

[19] Mustoe, C.L.; Gunabalasingam, M.; Yu, D.; Patrick B.O.; Kennepohl, P. *Faraday Discuss.* **2017**, *203*, 79-91.

[20] Hogarth, C.A. *Mössbauer Effect: Principles and Applications.* Academic Press, Inc., New York, **1964**.

[21] Mössbauer, R.L. *Z. Physik.* **1958**, *151*, 124-143.

[22] Devoe, J.R.; Spikerman, J.J. *Anal. Chem.* **1970**, *42*, 366-388.

[23] Hafemeister, D.W. *Advan. Chem. Ser.* **1967**, *68*, 126-146.

[24] Ehrlich, B.S.; Kaplan, M. *J. Chem. Phys.* **1971**, *54*, 612-620.

[25] Wynter, C.I.; Hill, J.; Bledsoe, W. *J. Chem. Phys.* **1969**, *50*, 3872-3874.

[26] Bukshpan, S.; Golstein, C.; Sonnino, T. May, L.; Pasternak, M. *J. Chem. Phys.* **1975**, *62*, 2606-2609.

[27] Bukshpan, S.; Pasternak, M.; Sonnino, T. *J. Chem. Phys.* **1975**, *62*, 2916-2917.

[28] Sakai, H.; Matsuyama, T.; Maeda, Y.; Yamaoka, H. *J. Chem. Phys.* **1981**, *75*, 5155-5159.

[29] Sakai, H.; Maeda, Y.; Ichiba, S.; Negita, H. *J. Chem. Phys.* **1980**, *72*, 6192-6198.

[30] Syssa-Magalé, J.-L., Boubekeur, K.; Palvadeau, P.; Meerschaut, A.; Schöllhorn, B. *J. Mol. Struc.* **2004**, *691*, 79-84.

[31] de Sousa, D.P.; Wegeberg, C.; Vad, M.S.; Mørup, S.; Frandsen, C.; Donald, W.A.; McKenzie, C.J. *Chem. Eur. J.* **2016**, *22*, 3810-3820.

[32] Cerreia Vioglio, P.; Catalano, L.; Vasylyeva, V.; Nervi, C.; Chierotti, M.R.; Resnati, G.; Gobetto, R.; Metrangolo, P. *Chem. Eur. J.* **2016**, *22*, 16819-16828.

[33] Viger-Gravel, J.; Leclerc, S.; Korobkov, I.; Bryce, D.L. *CrystEngComm.* **2013**, *15*, 3168-3177.

[34] Terskikh, V.V.; Lang, S.J.; Gordon, P.G.; Enright, G.D.; Ripmeester, J. *Magn. Reson. Chem.* **2009**, *47*, 394-406.

[35] Widdifield, C.M.; Cavallo, G.; Facey, G.A.; Pilati, T.; Lin, J.; Metrangolo, P.; Resnati, G.; Bryce, D.L. *Chem. Eur. J.* **2013**, *19*, 11949-11962.

[36] Terskikh, V.V.; Lang, S.J.; Gordon, P.G.; Enright, G.D.; Ripmeester, J.A. *Magn. Reson. Chem.* **2009**, *47*, 398-406.

[37] Bryce, D.L.; Sward, G.D. *Magn. Reson. Chem.* **2006**, *44*, 409-450.

[38] Eichele, K.; Wasylishen, R.E.; Grossert, J.S.; Olivieri, A.C. *J. Phys. Chem.* **1995**, *99*, 10110-10113.

[39] Perras, F.A.; Bryce, D.L. *Angew. Chem. Int. Ed.* **2012**, *51*, 4227-4230.

[40] Perras, F.A.; Widdifield, C.M.; Bryce, D.L. *Solid State Nucl. Magn. Reson.* **2012**, *45-46*, 36-44.

[41] Massiot, D.M.; Farnan, I.; Gautier, N.; Trumeau, D.; Trokiner, J.; Coutures, J.P. *Solid State Nucl. Magn. Reson.* **1995**, *4*, 241-248.

[42] O'Dell, L.A.; Schurko, R.W. *Chem. Phys. Lett.* **2008**, *464*, 97-102.

[43] Groom, C.R.; Bruno, I.J.; Lightfoot, M.P.; Ward, S.C. *Acta Cryst.* **2016**, *B72*, 171-179.

[44] Britton, D. *Cryst. Struct. Commun.* **1981**, *10*, 1501-1508.

[45] Zanotti, G.; Bardi, R.; Del Pra, A. *Acta Crystallogr., Sect. B: Struct. Crystallogr. Cryst. Chem.* **1980**, *36*, 136-171.

[46] Ludwig, G.W. *J. Chem. Phys.* **1956**, *25*, 159-171.

Chapter 4 – ^{35}Cl Solid-State NMR and Computational Study of Chlorine Halogen Bond Donors in Single-Component Crystalline Chloronitriles

Statement of Authenticity. I certify that I have prepared the following article featuring my own work, with guidance from my supervisor Dr. David Bryce. Dr. Victor Terskikh is acknowledged for reacquiring the ^{35}Cl spectra with a different probe, and assisted me during my time at the 900 MHz NMR facility. Dr. David Bryce is acknowledged for support and contributions to the manuscript. Dr. Ilia Korobkov is acknowledged for acquiring and solving the crystal structures presented in the article. Dr. Frederic Perras is acknowledged for helpful discussions.

Permissions. I declare that I have obtained permission from the coauthor to include this article in my thesis. Chapter 4 has been reprinted with permission from *J. Phys. Chem. C* **2016**, *120*, 11121-11130. Copyright 2019 American Chemical Society. (DOI: 10.1021/acs.jpcc.6b02806)

Supporting Information. All supporting information for this article can be retrieved on the ACS website: https://pubs.acs.org/doi/10.1021/acs.jpcc.6b02806

THE JOURNAL OF PHYSICAL CHEMISTRY C

Article

pubs.acs.org/JPCC

^{35}Cl Solid-State NMR and Computational Study of Chlorine Halogen Bond Donors in Single-Component Crystalline Chloronitriles

Patrick M. J. Szell and David L. Bryce*

Department of Chemistry and Biomolecular Sciences & Centre for Catalysis Research and Innovation, University of Ottawa, 10 Marie Curie Private, Ottawa, Ontario K1N 6N5 Canada

Supporting Information

ABSTRACT: Halogen bonding is a noncovalent interaction between the electrophilic region of a halogen (σ-hole) and an electron donor, which has gained popularity in the field of crystal engineering due to its strength and linearity. Here, we present a ^{35}Cl solid-state NMR study of chlorine atoms as halogen bond donors, with interpretation aided by crystallographic symmetry and computational chemistry. In a series of chlorinated benzonitrile compounds, the magnitude of the ^{35}Cl quadrupolar coupling constant (C_Q) was found to increase, and the quadrupolar asymmetry parameter (η) was found to decrease upon halogen bonding. A natural localized molecular orbital (NLMO) analysis attributes these changes to an increase in the contribution from the lone pair NLMOs to $|C_Q|$. This is distinguished from a short proton-chlorine contact, which causes an increase in the magnitude of the σ-bond contribution and a decrease in the lone pair contribution, resulting in an overall decrease in $|C_Q|$. This first direct ^{35}Cl solid-state NMR study of chlorine as a halogen bond donor provides new physical insight into the relationship between NMR observables and the halogen bond.

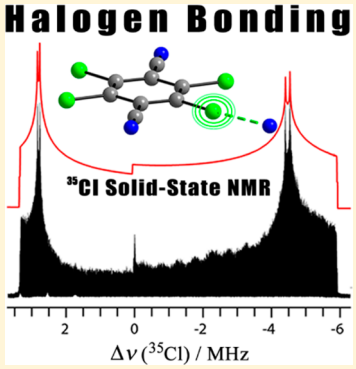

INTRODUCTION

Halogen bonding is a noncovalent interaction between the electrophilic region of a halogen, named the σ-hole, and an electron donor such as a Lewis base.[1−3] The halogen participating in the halogen bond (X) is referred to as the halogen bond donor, and the Lewis base (Y) is referred to as the halogen bond acceptor.[1] The RX···YZ halogen bond is typically linear in nature, with a bond angle between 150° and 180°,[4] and the bond length ($d_{X\cdots Y}$) is less than the sum of the van der Waals radii (d_{vdW})[5] of the participating atoms, as expressed by the normalized distance parameter, R_{XB} (eq 1):

$$R_{XB} = \frac{d_{X\cdots Y}}{\sum d_{vdW}} \quad (1)$$

Due to its strength and linearity,[6] halogen bonding has found its place in the fields of supramolecular chemistry[7] and materials chemistry as a complement to hydrogen bonding.[8]

Much effort has been expended to better understand the nature of the halogen bond.[9] Solid-state NMR has proven to be a powerful tool in characterizing the halogen bond,[10] allowing for direct observation of the halogen bond acceptor,[11−13] the effects of halogen bonding on the ^{13}C chemical shifts of the halogen bond donor groups,[14] and J-coupling between nuclei in the halogen bond acceptor.[15] Despite these advances, the halogen bond donor atom remains uncharacterized by NMR due to the difficulties associated with chlorine, bromine, and iodine solid-state NMR of covalently bonded halogens.[16,17] This impediment arises as a consequence of the coupling between their nuclear quadrupole moments and the electric field gradient (EFG) at the nucleus, resulting in NMR spectra that are often impractically broad to acquire. The magnitude of the quadrupolar interaction may be described using the quadrupolar coupling constant (C_Q) and the asymmetry parameter (η) (see eqs 2 and 3):

$$C_Q = eV_{33}Q/h \quad (2)$$

$$\eta = (V_{11} - V_{22})/V_{33} \quad (3)$$

where $|V_{11}| \leq |V_{22}| \leq |V_{33}|$ are the principal components of the EFG tensor. With the availability of increasingly high magnetic field strengths, and the development of ultrawideline techniques,[18] solid-state NMR of $^{35/37}$Cl (spin I = 3/2) has recently been demonstrated on chlorine covalently bonded to carbon in a series of small organic compounds.[19] However, solid-state NMR of $^{79/81}$Br (I = 3/2) and ^{127}I (I = 5/2) covalently bonded to carbon remains spectroscopically impractical due to their significantly larger spectral widths. Typical values of $|C_Q|$ for halogens covalently bonded to carbon are 65 to 75 MHz (^{35}Cl), 300 to 600 MHz (^{81}Br), and 1600 to 2100 MHz (^{127}I). Typical values of $|C_Q|$ for halide ions are 0 to 10 MHz (^{35}Cl), 0 to 60 MHz (^{81}Br), and 0 to 500 MHz (^{127}I).[16,20,21]

There is a long history of nuclear quadrupole resonance (NQR) spectroscopic studies of the quadrupolar halogens.[21−24] However, in the case of $^{35/37}$Cl and $^{79/81}$Br, standard pure NQR experiments provide information only on the quadrupolar

Received: March 17, 2016
Revised: April 29, 2016
Published: April 29, 2016

DOI: 10.1021/acs.jpcc.6b02806
J. Phys. Chem. C 2016, 120, 11121−11130

frequency, ν_Q (eq 4).[25] It is possible to obtain the values of the C_Q and η with the addition of a weak magnetic field or via nutation experiments. The relationship between C_Q, η, and ν_Q for a spin-3/2 nuclide such as ^{35}Cl is given by

$$\nu_Q = \frac{C_Q}{2}\cdot\sqrt{1+\frac{\eta^2}{3}} \quad (4)$$

NQR studies have been performed on halogen bonded compounds.[26−31] Solid-state NMR of ^{35}Cl boasts some advantages over pure ^{35}Cl NQR, such as being able to simultaneously measure both C_Q and η in a single one-dimensional spectrum on a powdered sample. Although the NMR spectra are broad (several MHz), one does not have to search for the resonance frequency. Furthermore, solid-state NMR may provide information on the magnetic shielding of the nucleus, yielding insight into the chemical environment in question. It is to be noted that the results obtained from ^{35}Cl solid-state NMR can be further verified using ^{35}Cl NQR spectroscopy, and vice versa. One can employ the experimentally measured NQR frequencies in a complementary manner to further improve the accuracy and precision of the fits of the ^{35}Cl solid-state NMR spectra.

Chlorine is the second weakest halogen bond donor after fluorine, and observations of compounds exhibiting a chlorine halogen bond are somewhat rare in comparison to bromine and iodine due to the small relative magnitude of chlorine's σ-hole.[2] A search of the Cambridge Structural Database (CSD)[32] reveals a number of structures that feature chlorine halogen bonds to nitrile groups. This may be, in part, due to the electron density surrounding the nitrile group, which could help to compensate for chlorine's small σ-hole. The halogen bonds in these compounds are indeed weak (*vide infra*), but were determined to be present by measuring the bond length ($d_{Cl\cdots N}$) and the bond angle ($\theta_{C-Cl\cdots N}$) as shown in Figure 1. The bond angle helps to discriminate between the chlorine halogen bond and other types of short contacts.

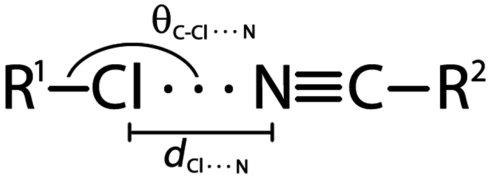

Figure 1. Chlorine···nitrile halogen bonded moiety, where Cl is the halogen bond donor, N is the halogen bond acceptor, and R^1 and R^2 are the remaining parts of the molecules.

In order to observe the effect of halogen bonding on the NMR parameters of chlorine halogen bond donors, our strategy is to take advantage of molecular and crystallographic symmetry in small organic molecules exhibiting a chlorine halogen bond. The crystal structure must have one chlorine site exhibiting a halogen bond, and one molecularly symmetrical site with no halogen bond. As both chlorine sites are chemically equivalent, any differences in the NMR parameters between both sites may be attributed to their crystallographic differences, the most dominant of which is the presence or absence of a halogen bond.[33] For instance, in compound **1** (tetrachloroterephthalonitrile), the presence of an inversion center at the center of the aromatic ring gives rise to two unique chlorine sites, as shown in Figure 2. One of these chlorine sites exhibits a halogen bond to an adjacent molecule (R_{XB} = 0.941, $\theta_{C-Cl\cdots N}$ = 168.78°), whereas the other chlorine site is without any contacts.[34] These two sites can then simply be compared to determine the effect of the halogen bond on the ^{35}Cl NMR parameters.

In this study, a series of chlorinated benzonitrile compounds exhibiting a degree of molecular symmetry with at least two chemically equivalent chlorines are analyzed by ^{35}Cl solid-state NMR and NQR. The ^{35}Cl quadrupolar coupling parameters from the chlorine exhibiting a halogen bond are compared to those for its crystallographic counterpart that has no halogen bond. This will allow the direct measurement of the changes in the EFG at chlorine as a result of halogen bonding. In addition, 4-chloro-DL-*p*-phenylalanine (**7**) is revisited[19] in order to attribute particular spectral features to its crystal structure. To further verify our experimental observations, density functional theory (DFT) calculations were performed to offer additional insights by modeling the noncovalent interaction. Moreover, natural localized molecular orbital (NLMO) analyses were performed on each compound to visualize the effect of the halogen bond on the molecular orbitals of the halogen bond donor. Such calculations have previously proven useful in understanding the orbitals' contributions to various NMR parameters of the halogen bond acceptor.[11]

EXPERIMENTAL SECTION

Compounds **1**, **2**, **3**, **4**, and **7** were purchased from Sigma-Aldrich and analyzed without further purification. Compounds **5** and **6** were purchased from Alfa Aesar and used without further purification. Single crystals of **6** were prepared by dissolving it in acetonitrile and allowing the solvent to evaporate over the course of a few days, affording crystals suitable for diffraction. Single crystals of **7** were prepared by adding an excess to boiling water for 30 min and filtering the solution. The filtrate was allowed to slowly cool to 4 °C to afford crystals suitable for diffraction. The crystal structure for each powdered sample was verified by powder X-ray diffraction on a Rigaku Ultima IV instrument with 2θ ranging from 5° to 65° in increments of 0.02° at a rate of 1° per minute using CuKα radiation to ensure phase purity (see Supporting Information).

^{35}Cl Solid-State NMR and NQR. All ^{35}Cl NMR spectra were acquired at the National Ultrahigh-Field NMR Facility for Solids using a 21.1 T Bruker Avance II spectrometer equipped with a home-built dual coil probe. All ^{35}Cl chemical shifts are referenced to NaCl(s) at −41.11 ppm.[17] The WURST-QCPMG pulse sequence was used with 25 μs pulses swept over a 2 MHz frequency range, and 10000 Hz spike separation.[18] The variable-offset cumulative spectral (VOCS) acquisition method was used with offsets changed at increments of 250 kHz with 2048 transients acquired.[39] A series of spectra was obtained for each sample, processed, and then coadded in the frequency domain to yield the full spectrum. Proton decoupling (15 kHz) was used for the samples containing hydrogen. In all cases, the ^{35}Cl NMR spectra were fit using QUEST for exact simulation.[40] When using a regular zirconia rotor, ^{91}Zr signals were acquired from the rotor which hampered the acquisition of the lower frequency pieces. However, this problem was easily avoided by packing samples in glass tubes instead. Furthermore, due to the large ^{35}Cl line widths, power linearity became an issue in our preliminary experiments as the amplifiers exhibit slightly variable power outputs over this large spectral range. This issue was mitigated by choosing a probe with a larger bandwidth, which reduced the number of steps required per spectrum. Otherwise, this

DOI: 10.1021/acs.jpcc.6b02806
J. Phys. Chem. C 2016, 120, 11121−11130

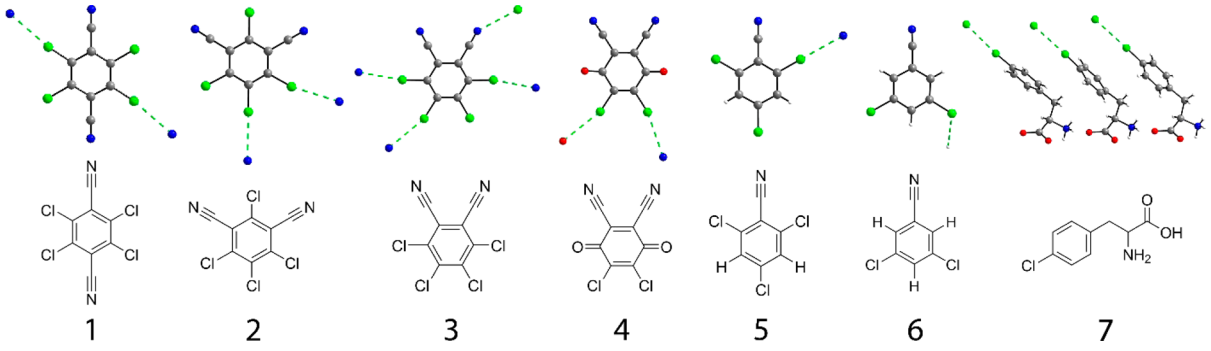

Figure 2. Compounds used in this work: tetrachloroterephthalonitrile[34] (**1**), tetrachloroisophthalonitrile (chlorothalonil)[35] (**2**), tetrachlorophthalonitrile[34] (**3**), 2,3-dichloro-5,6-dicyano-1,4-benzoquinone (DDQ)[36] (**4**), 2,4,6-trichlorobenzonitrile[37,38] (**5**), 3,5-dichlorobenzonitrile (**6**), and 4-chloro-DL-phenylalanine (**7**). The top row shows excerpts from the X-ray crystal structures, where relevant close contacts to atoms on adjacent molecules are indicated by dashed lines.

issue can cause unequal signal intensity in each slice, which can appear to distort the spectrum. As was previously reported,[19] radio interference also manifests itself in the ^{35}Cl NMR spectra, as the frequency region of interest is in the range of local radio stations. This interference did not cause any problems in the interpretation of the spectra.

^{35}Cl NQR spectroscopy was performed using an NMR probe and console in the absence of a magnetic field, at room temperature, and scanning the frequency regions of interest at 100 kHz intervals using a Hahn-echo sequence with a 3 μs rf pulse.

^{13}C Solid-State NMR. All ^{13}C NMR experiments were performed at 9.4 T on a Bruker Avance III spectrometer, using a Bruker 7 mm HX magic angle spinning (MAS) probe with a spinning frequency of 5 kHz. For samples **1**, **2**, **3**, **4**, and **6**, Bloch decay ^{13}C MAS NMR spectra were recorded using a $\pi/6$ pulse of 11 μs with a 60 s recycle delay. A total of 1024 transients were collected for each sample. For samples **5** and **6**, ^{13}C cross-polarization magic angle spinning (CP/MAS) was used with a 2 ms contact time, a proton $\pi/2$ pulse of 4.60 μs, a 3 s recycle delay, and a total of 20 480 transients were collected.

Computational details. All gauge-including projector augmented-wave (GIPAW) density functional theory (DFT) calculations were accomplished using the Cambridge Serial Total Energy Package (CASTEP)[41] using Accelrys Materials Studio 4.4. The PBE generalized gradient approximation (GGA) functional was used in all cases. Further information on energy cut-offs and k-points is given in the Supporting Information. The crystal structures for **1**,[34] **2**,[35] **3**,[34] and **4**,[36] were used without geometry optimization. The proton positions were optimized for **5**,[37,38] **6**, and **7**. The output files were interpreted using EFGShield (version 4.1).[42] The calculated magnetic shielding values were converted to chemical shifts using $\delta_{calc} = \frac{\sigma_{ref} - \sigma_{calc}}{1 - \sigma_{ref}}$ where σ_{ref} for ^{35}Cl is 974 ppm.[43] The values of C_Q were obtained using eq 2, where $Q = -81.65$ mb.[44−46]

Additional DFT calculations were performed using the Amsterdam Density Functional software (ADF, 2009.01)[47−49] with the revised GGA exchange-correlation functional (revPBE) of Zhang and Yang[50] and the TZP basis set. The diffuse function-augmented version of this basis set was used on chlorine. Scalar and spin−orbit relativistic effects were accounted for using ZORA[51] (zeroth-order regular approximation). Analogous test calculations carried out without such a relativistic treatment resulted in changes in $|C_Q(^{35}Cl)|$ on the order of −1 to −2%. NLMO calculations were also performed using ADF. Models for each compound were generated using GaussView,[52] with atomic positions taken from their respective crystal structures. Each model consisted of the molecule of interest plus any additional molecules in close contact (e.g., halogen bonded). For compound **7**, the amino acid side chains were replaced by methyl groups to reduce the computational time.

X-ray Crystallography. Data collection results for compounds **6** and **7** represent the best data sets obtained in several trials for each sample. The crystals were mounted on thin glass fibers using paraffin oil. Prior to data collection, crystals were cooled to 200.15 K. Data were collected on a Bruker AXS SMART single crystal diffractometer equipped with a sealed Mo tube source (wavelength 0.71073 Å) APEX II CCD detector. Raw data collection and processing were performed with the APEX II software package from BRUKER AXS.[53] Diffraction data for sample **6** were collected with a sequence of 0.3° ω scans at 0, 120, and 240° in φ. Due to the lower unit cell symmetry, in order to ensure adequate data redundancy, diffraction data for **7** were collected with a sequence of 0.3° ω scans at 0, 90, 180, and 270° in φ. Initial unit cell parameters were determined from 60 data frames with 0.3° ω scan each, collected at the different sections of the Ewald sphere. Semiempirical absorption corrections based on equivalent reflections were applied.[54] Systematic absences in the diffraction data set and unit cell parameters were consistent with triclinic $P\bar{1}$ (No. 2) for compound **7** and monoclinic $P2_1/c$ (No. 14) for compound **6**. Solutions in the centrosymmetric space groups for both data sets yielded chemically reasonable and computationally stable results of refinement. The structures were solved by direct methods, completed with difference Fourier synthesis, and refined with full-matrix least-squares procedures based on F^2.

Refinement of the structural model for **7** revealed that the asymmetric unit contains three symmetry unrelated molecules located in general positions. Initial structure refinement results suggested the presence of two nonmerohedrally twinned domains. Careful examination of the original data frames and reciprocal space diffraction pictures confirmed the initial twinning assumption. In order to find the independent orientation matrices, 1327 reflections were collected from 4 sets of 40 frames each in the different sections of the Ewald sphere. Collected reflection data were treated with CELL_NOW software[55] and yielded two independent orientation matrices. The data set was reintegrated with two

DOI: 10.1021/acs.jpcc.6b02806
J. Phys. Chem. C 2016, 120, 11121−11130

obtained matrices, treated for twinning absorption corrections, and consecutive model refinement was performed using the HKLF5 reflection data file. The twinning domain ratio coefficient (BASF) was refined to 0.20076.

The structural model of **6** includes one molecule located on a general position. For both compounds, all non-hydrogen atoms were refined with the full set of anisotropic thermal displacement coefficients. All hydrogen atomic positions for both structural models were calculated based on the geometry of related non-hydrogen atoms. All hydrogen atoms were treated as idealized contributions during the refinement. All scattering factors are contained in several versions of the SHELXTL program library, with the latest version used being 6.12.[56]

RESULTS AND DISCUSSION

I. X-ray Crystallography. The crystal structures for both **6** and **7** were solved, and the structures reveal a short chlorine contact with hydrogen and chlorine, respectively (Table 1 and Supporting Information). In the case of **6**, although the chemical structure has a C_2 axis of symmetry, the crystal structure revealed two inequivalent chlorine sites, denoted as 6a and 6b in Figure 3. An interaction between a chlorine atom of one molecule and a nitrogen atom of an adjacent molecule was anticipated, but the crystal structure revealed a nonlinear contact between chlorine 6a and a hydrogen atom at a distance of 2.9062 Å (98.5% of the sum of the van der Waals radii) and an angle $\theta_{C-Cl\cdots H}$ of 109.47°. This does not fall within the definition of a halogen bond, and is defined as a van der Waals contact.[57] This provides an opportunity to gain some insight into the differences between a chlorine atom acting as a halogen bond donor and a chlorine van der Waals contact. By comparing the quadrupolar coupling parameters from the chlorine carrying the proton contact (6a) with the chlorine that has no contact (6b), this may also offer insights into the effect of the bond distance and angle on the chlorine NMR parameters for nonhalogen bonded compounds.

Compound **7** was revisited from Perras et al.[19] in order to attribute the reported quadrupolar coupling parameters for each site to the differences in their crystallographic environments. The X-ray crystal structure revealed nonequivalent chlorine sites denoted as 7a, 7b, and 7c in Figure 4. For each chlorine site, a chlorine−chlorine contact was observed with unique contact angles and distances. The first two chlorine sites, 7a and 7b, are almost equivalent, and interact with each other at a distance of 3.436 Å and contact angles ($\theta_{C-Cl\cdots Cl}$) of 155.61° and 138.64°, respectively. The third chlorine site, 7c, is distinctly different and interacts with itself in the adjacent cell with a contact length of 3.367 Å and a contact angle, $\theta_{C-Cl\cdots Cl}$, of 147.48°. In this case, ^{35}Cl solid-state NMR parameters will be reflective of the contact angle and contact distance of each chlorine in the case of chlorine−chlorine contacts. These contacts do not qualify as halogen bonds.[58]

Selected distances and angles, obtained from X-ray crystallography for compounds **1** to **7**, are given in Table 2.

ii. ^{35}Cl Solid-State NMR. The ^{35}Cl WURST-QCPMG NMR spectra of compounds **1** to **6** are presented in Figure 5, along with spectral simulations using an exact Zeeman-quadrupolar Hamiltonian diagonalization method.[40] The central-transition spectra are approximately 9 MHz across. Nevertheless, good signal-to-noise is achieved in all cases except for **3**, where only the edges of the spectrum were acquired due to the significant amount of time required. Proton decoupling was highly valuable for compounds **5** and **6**, resulting in spectra

Table 1. Selected Single-Crystal X-ray Crystallographic Data for Compounds 6 and 7

compound	6	7
empirical formula	$C_{28}H_{12}Cl_8N_4$	$C_{27}H_{30}Cl_3N_3O_6$
FW (g/mol)	688.02	598.89
crystal color	colorless	colorless
crystal size (mm)	0.230 × 0.180 × 0.140	0.220 × 0.160 × 0.100
crystal system	monoclinic	triclinic
crystal space group	$P2_1/c$	$P\text{-}1$
T (K)	200(2)	200(2)
a (Å)	3.8642(2)	6.0602(4)
b (Å)	13.7861(7)	13.2376(7)
c (Å)	13.8809(7)	17.2213(10)
α (deg)	90(0)	88.871(2)
β (deg)	91.073(4)	85.214(2)
γ (deg)	90(0)	79.282(2)
V (Å^3)	739.34(7)	1352.69(14)
Z	1	2
R_1 (final)	0.0367	0.0454
wR_2 (final)	0.1018	0.1276

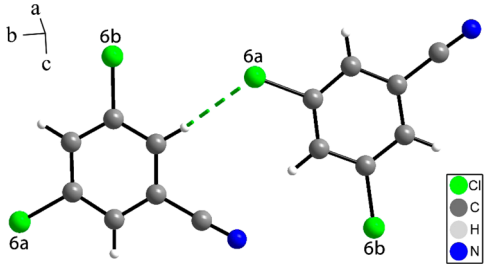

Figure 3. Crystal packing of 3,5-dichlorobenzonitrile (**6**) showing a short chlorine−hydrogen contact. The proton−chlorine distance is 2.9062 Å, and the C−Cl···H angle is 109.47°.

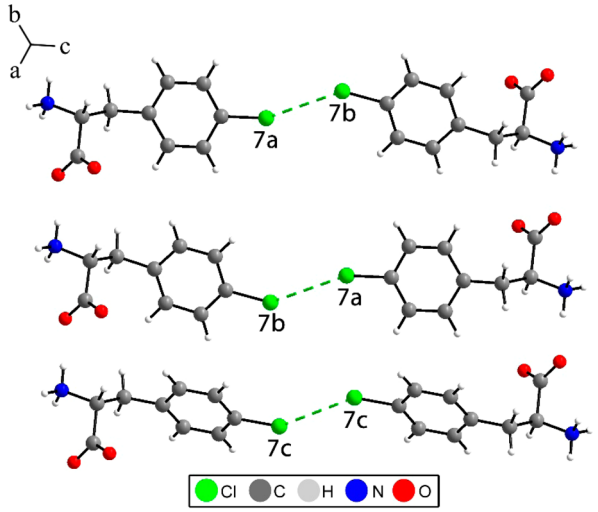

Figure 4. Crystal packing of **7** showing all chlorine−chlorine contacts. The distance between chlorine sites 7a and 7b is 3.436 Å, and the distance between chlorine site 7c and 7c is 3.367 Å. The C−Cl(7a)···Cl(7b) angle is 155.61°, the C−Cl(7b)···Cl(7a) angle is 138.64°, and the C−Cl(7c)···Cl(7c) angle is 147.48°.

DOI: 10.1021/acs.jpcc.6b02806
J. Phys. Chem. C 2016, 120, 11121−11130

Table 2. Selected Information on the Geometry of the Close Contacts in the Compounds Studied[a]

	1	2	4[b]	5	6 (X = H)	7[c] (X = Cl)
$d_{Cl\cdots X}$ (Å)	3.106	3.137	3.207 (N) 3.223 (O)	3.222	2.906	3.436 Cl(1/2) 3.367 Cl(3/3)
$\theta_{C-Cl\cdots X}$ (deg)	168.78	167.14	166.04 (N) 160.06 (O)	177.50	109.47	155.61 Cl(1) 138.64 Cl(2) 147.48 Cl(3)
R^c	0.941	0.951	0.972 (N) 0.986 (O)	0.976	0.985	0.982 Cl(1/2) 0.962 Cl(3)

[a]For comparison, the distances from the chlorines *without* close contacts to the nearest atoms are 3.656 (to Cl), 3.849 (to Cl), 3.415 (N), 3.081(to H), and 3.508 (to Cl) Å for compounds **1**–**6**, respectively. [b]One site has a short contact with nitrogen (N), the other site has a short contact with oxygen (O). [c]This row contains R_{XB} values (see eq 1) for halogen-bonded compounds **1** to **5**; for compounds **6** and **7**, analogous values are listed, which describe a short proton–chlorine contact (**6**) and chlorine–chlorine contact (7).

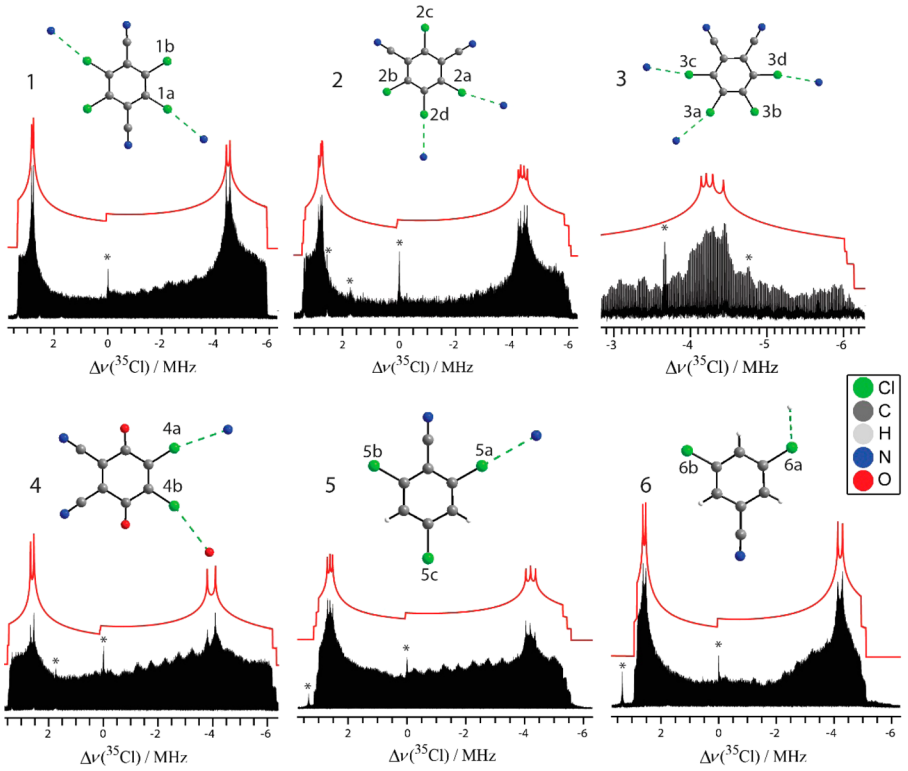

Figure 5. ^{35}Cl WURST-QCPMG solid-state NMR spectra (lower traces) of compounds **1**–**6** and their QUEST spectral simulations (upper traces, red). The asterisks denote radio interference and trace NaCl(s). Note that only the right and left edges of the spectrum of compound **3** were acquired. Deconvolutions are shown in the Supporting Information.

with a higher signal-to-noise ratio. The spectra are dominated by the ^{35}Cl quadrupolar interaction. Despite the breadth of the spectra, discontinuities due to multiple crystallographically distinct sites are resolved in all cases. The experimentally determined ^{35}Cl quadrupolar coupling constants, asymmetry parameters, and isotropic chemical shifts are reported in Table 3. Where possible, the quadrupolar coupling data were corroborated by independent ^{35}Cl NQR experiments. NQR spectra are shown in the Supporting Information, and the resulting parameters are given in Table 3.

For compounds exhibiting at least one axis of molecular symmetry, it can be challenging to assign the ^{35}Cl NMR parameters to the correct crystallographic site. One strategy in solid-state NMR for assigning each site in a crystal structure is to use correlation experiments. However, in these compounds, correlation experiments involving ^{35}Cl are impractical. Only small differences in the chemical shift are expected upon halogen bonding, and thus any large differences in the chemical shift can be attributed to chemical nonequivalence from being in a different position on the aromatic ring relative to the nitrile groups. Assignments were also aided by GIPAW DFT calculations of asymmetry parameters, quadrupolar coupling constants, and shielding constants, where the first have been shown to be the most reliable.[19] Signal intensity can also be used to assign the chlorine sites, as will be discussed for the assignments of compound **7**.

The molecular structure of **1** shows four chlorines (Figure 2). However, the crystal structure indicates an inversion center at the center of the aromatic ring, meaning that there are only two nonequivalent chlorine sites in the asymmetric unit, denoted as 1a and 1b. Chlorine site 1a exhibits a halogen bond to the nitrile group (R_{XB} = 0.941, $\theta_{C-Cl\cdots N}$ = 168.78°), and chlorine site 1b has no halogen bond. Chlorine site 1a has a C_Q of −75.78 ± 0.03 MHz and a η of 0.136 ± 0.002, whereas chlorine site 1b has a C_Q of −75.21 ± 0.03 MHz, and a η of 0.149 ± 0.003. Comparison of these sites reveals an increase in

DOI: 10.1021/acs.jpcc.6b02806
J. Phys. Chem. C 2016, 120, 11121–11130

Table 3. Experimental ^{35}Cl NMR Parameters, GIPAW DFT Calculated ^{35}Cl NMR Parameters (*in Parentheses*), and Experimental ^{35}Cl NQR Frequencies (ν_Q)

compound and site	δ_{iso}/ppm[a]	C_Q/MHz	η	ν_Q/MHz	notes[b]
1a	400 ± 50 *(395)*	−75.78 ± 0.03 *(−73.53)*	0.136 ± 0.002 *(0.161)*	37.99 ± 0.01	halogen bonded
1b	400 ± 50 *(395)*	−75.21 ± 0.03 *(−72.99)*	0.149 ± 0.003 *(0.177)*	37.71 ± 0.01	nonhalogen bonded counterpart
2a	500 ± 50 *(433)*	−74.88 ± 0.08 *(−72.68)*	0.178 ± 0.007 *(0.205)*	37.70 ± 0.01	halogen bonded
2b	500 ± 50 *(434)*	−74.58 ± 0.04 *(−72.92)*	0.155 ± 0.002 *(0.228)*	37.59 ± 0.01	nonhalogen bonded counterpart
2c	325 ± 50 *(403)*	−76.19 ± 0.02 *(−72.58)*	0.148 ± 0.001 *(0.175)*	38.23 ± 0.01	nonequivalent
2d	250 ± 50 *(392)*	−75.48 ± 0.08 *(−74.01)*	0.156 ± 0.002 *(0.177)*	37.82 ± 0.01	nonequivalent
4a	400 ± 50 *(404)*	−75.15 ± 0.06 *(−71.89)*	0.207 ± 0.002 *(0.276)*	37.82 ± 0.01	halogen bonded to N
4b	400 ± 50 *(425)*	−74.57 ± 0.05 *(−71.31)*	0.255 ± 0.003 *(0.326)*	37.70 ± 0.01	halogen bonded to O
5a	350 ± 50 *(555)*	−73.75 ± 0.05 *(−74.98)*	0.125 ± 0.004 *(0.144)*	36.95 ± 0.01	halogen bonded
5b	350 ± 50 *(495)*	−72.58 ± 0.05 *(−73.41)*	0.131 ± 0.002 *(0.143)*	36.39 ± 0.01	nonhalogen bonded counterpart
5c	400 ± 50 *(599)*	−71.49 ± 0.04 *(−64.33)*	0.136 ± 0.002 *(0.216)*	35.85 ± 0.01	nonequivalent
6a	400 ± 50 *(354)*	−70.45 ± 0.05 *(−68.94)*	0.091 ± 0.002 *(0.113)*	35.22 ± 0.01	Cl···H contact
6b	400 ± 50 *(365)*	−71.74 ± 0.04 *(−70.39)*	0.088 ± 0.003 *(0.121)*	35.90 ± 0.01	Cl···H contact counterpart
7a	350 ± 100 *(329)*	−69.0 ± 0.2 *(−67.8)*	0.093 ± 0.003 *(0.106)*	34.73 ± 0.01	from Perras et al.[19]
7b	350 ± 100 *(330)*	−69.0 ± 0.2 *(−67.3)*	0.093 ± 0.003 *(0.130)*	34.73 ± 0.01	from Perras et al.[19]
7c	300 ± 150 *(327)*	−69.5 ± 0.2 *(−67.8)*	0.073 ± 0.003 *(0.125)*	34.67 ± 0.01	from Perras et al.[19]

[a]All ^{35}Cl chemical shifts are referenced to NaCl(s) at −41.11 ppm. [b]Sites are indicated in Figure 5, where the molecularly equivalent chlorine sites with no halogen bond are labeled "counterpart", and "nonequivalent" indicates sites with no molecularly equivalent counterpart.

magnitude of C_Q by 0.57 ± 0.04 MHz, and a decrease in η by 0.013 ± 0.004 upon halogen bonding.

Spectral fitting for **2** proved to be difficult due to the presence of four crystallographically unique chlorine sites, denoted as 2a, 2b, 2c, and 2d. Chlorine sites 2a (R_{XB} = 0.951, $\theta_{C-Cl\cdots N}$ = 167.14°) and 2d (R_{XB} = 0.930, $\theta_{C-Cl\cdots N}$ = 176.68°) exhibit a halogen bond, whereas chlorine sites 2b and 2c have no halogen bond. The two chemically equivalent sites (2a and 2b) can be assigned by their identical chemical shifts of 500 ppm. These two sites could then be differentiated on the basis of their quadrupolar coupling constants. Chlorine site 2a has a C_Q of −74.88 ± 0.08 MHz, and a η of 0.178 ± 0.007, whereas chlorine site 2b has a C_Q of −74.58 ± 0.04 MHz and a η of 0.155 ± 0.002. The other chlorine sites (2c and 2d) each exhibit different chemical shifts of 325 ± 50 ppm and 250 ± 50 ppm. The comparison between sites 2a and 2b marks an increase in magnitude of the C_Q by 0.30 ± 0.09 MHz, and an increase in η by 0.023 ± 0.007 upon halogen bonding.

Compound **4** only has two chlorine sites, which proved straightforward to assign by GIPAW DFT calculations. The chlorine site bearing the halogen bond to nitrogen, 4a (R_{XB} = 0.972, $\theta_{C-Cl\cdots N}$ = 166.04°), has a C_Q of −75.15 ± 0.06 MHz, and a η of 0.207 ± 0.002. The chlorine site bearing the halogen bond to oxygen, 4b (R_{XB} = 0.986, $\theta_{C-Cl\cdots N}$ = 160.06°), has a C_Q of −74.57 ± 0.05 MHz, and a η of 0.255 ± 0.003. The comparison between both sites shows an increase in magnitude of C_Q by 0.58 ± 0.08 MHz and a decrease in η by 0.048 ± 0.004 from the chlorine carrying the halogen bond to nitrogen and the chlorine carrying the halogen bond to oxygen.

The assignments of compound **5** were made using GIPAW DFT calculations, and verified using experimental δ_{iso}(^{35}Cl) values. Chlorine site 5a (R_{XB} = 0.976, $\theta_{C-Cl\cdots N}$ = 177.50°) has a C_Q of −73.75 ± 0.05 MHz and a η of 0.125 ± 0.004, whereas chlorine site 5b has a C_Q of −72.58 ± 0.05 MHz and a η of 0.131 ± 0.002. The comparison between both sites marks an increase in magnitude of C_Q by 1.17 ± 0.07 MHz, and a decrease in η by 0.006 ± 0.004 upon halogen bonding. The assignments and quadrupolar coupling parameters proved to be in agreement with the NQR results obtained by Negita et al., who had assigned the sites using the ^{35}Cl NQR zero-splitting pattern.[59]

The assignments for compound **6** were much easier due to the presence of only two chlorine sites, which were also assigned by GIPAW DFT calculations. Chlorine site 6a (R = 0.985, $\theta_{C-Cl\cdots H}$ = 109.47°) has a C_Q of −70.45 ± 0.05 MHz, and a η of 0.091 ± 0.002, whereas chlorine site 6b has a C_Q of −71.74 ± 0.04 MHz and a η of 0.088 ± 0.003. In contrast to the above cases of halogen bonding, the comparison between both sites marks a decrease in magnitude of the C_Q by 1.29 ± 0.06 MHz, and a negligible change in η as a result of the chlorine-hydrogen van der Waals contact.

For compound **7**, the sites were assigned to their reported NMR parameters from Perras et al.[19] according to their relative intensity, both in the ^{35}Cl solid-state NMR spectrum and the ^{35}Cl NQR spectrum. Due to the similar contact angles and contact distances for sites 7a and 7b, both sites are expected to share similar quadrupolar coupling parameters (C_Q = −69.0 ± 0.2 MHz, η = 0.093 ± 0.003, δ_{iso} = 300 ± 100 ppm). The third chlorine site, 7c, can thus be assigned to the highest quadrupolar coupling constant (C_Q = −69.5 ± 0.2 MHz, η = 0.073 ± 0.003, δ_{iso} = 300 ± 150 ppm).[19] The chlorine site 7c has the shortest chlorine−chlorine contact length, and has a higher C_Q and lower η than the other two sites. Furthermore, the breadth of the discontinuities in the reported ^{35}Cl solid-state NMR spectrum[19] hints that sites 7a and 7b do have slightly different NMR parameters arising from the small differences in bond angles between both contacts.

For all compounds, simulations using exact theory as implemented in the QUEST program[40] were essential in obtaining accurate data. A comparison of the simulations obtained from second-order perturbation theory[60] and from an exact simulation is shown in Figure 6 for the low-frequency edge of the spectrum of compound **1**.

Each chlorine site in the compounds studied can thus be distinguished by ^{35}Cl solid-state NMR, with their different NMR parameters being attributed to their crystallographic environments. Despite the fact that these halogen bonds are weak, this technique is sensitive enough to observe changes in the EFG upon halogen bonding. There is a consistent increase

DOI: 10.1021/acs.jpcc.6b02806
J. Phys. Chem. C 2016, 120, 11121−11130

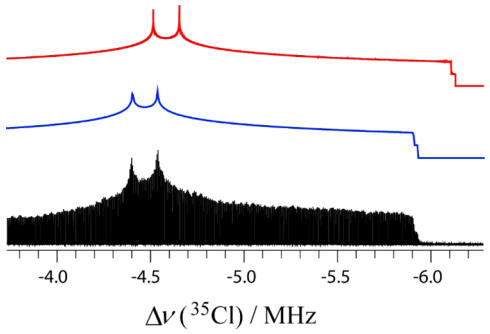

Figure 6. Detail of the ^{35}Cl SSNMR spectrum of compound **1** along with exact (blue) and second-order perturbation theory simulations (red). B_0 = 21.1 T.

in C_Q values for chlorine when compared to their nonhalogen bonded chemically equivalent counterparts. A concomitant decrease in η values is also generally noted. In compound **2**, an aberrant increase in η can be attributed to a close contact of the chlorine with a carbon atom on an adjacent molecule. The effect of the halogen bond on the EFG contrasts with the changes induced from a proton van der Waals contact, observed in compound **6**. In this case, the C_Q value decreased and η value increased due to the van der Waals contact. These results are in agreement with DFT calculations on a model system, shown in Figure 7. The results of the calculations show that C_Q is inversely proportional to the chlorine−nitrogen halogen bond length, and decreases as the bond deviates from linearity. Furthermore, η is insensitive to the bond length, but is significantly affected by the chlorine-nitrogen halogen bond angle, increasing as the angle deviates from linearity.

To conclude this section on our experimental results, we briefly discuss some additional attempts to probe the halogen bonds via SSNMR in these compounds. ^{35}Cl SSNMR has been shown to be a very sensitive tool to distinguish the nuclei based on their crystallographic environments, both in terms of sensitivity and experimental times. In contrast, as seen, for example, in Figures S10 and S11 of the SI, ^{13}C NMR was not able to clearly discriminate the carbon bonded to the chlorine with the halogen bond from its chemically equivalent nonhalogen bonded counterpart for compound **5**. The ^{13}C NMR spectra were not of sufficient resolution to allow the discrimination of carbons based on their crystallographic environment as was the case with ^{35}Cl. In the compounds that lacked protons (**1**−**4**), CP/MAS could not be used and thus experiment times were impractically lengthy due to long ^{13}C relaxation time constants. Furthermore, natural abundance Bloch decay ^{15}N NMR proved to be too insensitive to permit the acquisition of any signal, despite long experimental times. ^{15}N CP/MAS experiments for samples **5** and **6** were performed, but no signal was obtained. Thus, ^{35}Cl proved to be the nucleus of choice for measuring and distinguishing the effect of the halogen bond on other close contacts, both in terms of experimental time and sensitivity. However, this was not the case for compound **3**, which had a short T_2 relaxation time, making it very difficult to acquire any ^{35}Cl signal. This could perhaps be attributed to dynamics in this compound; however,

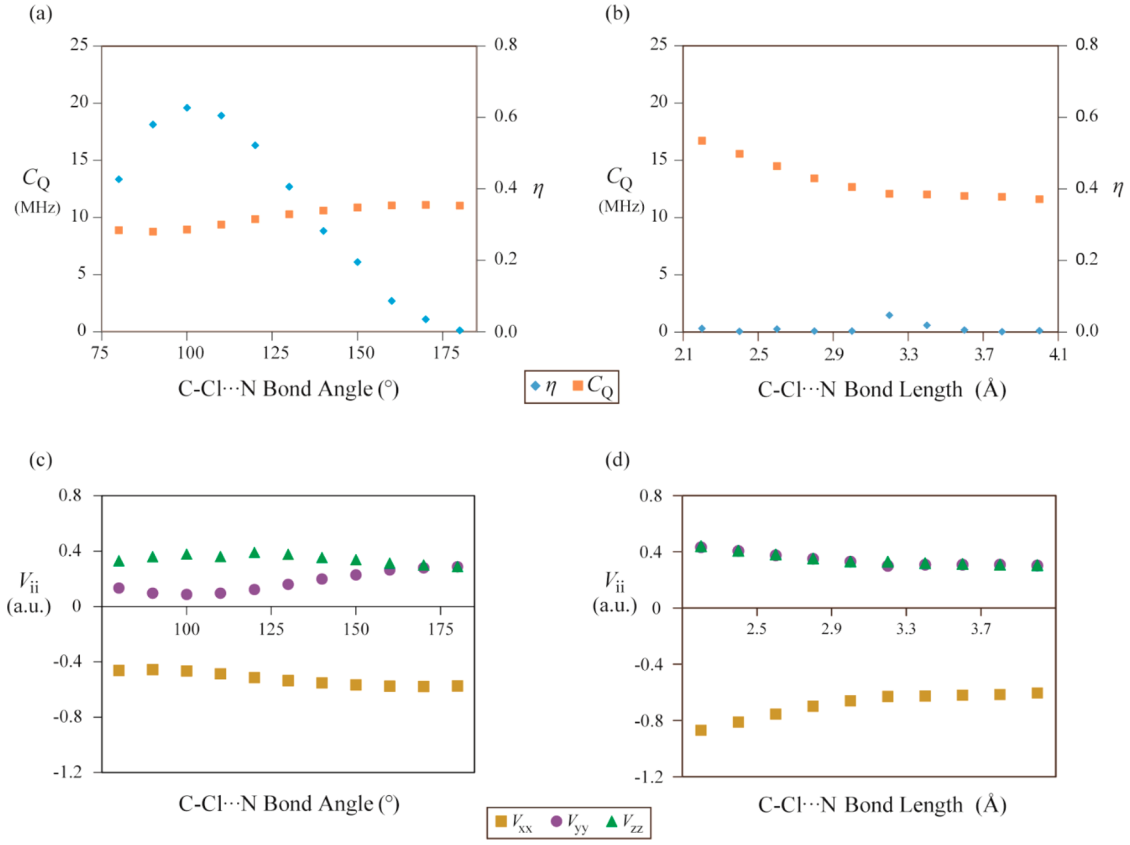

Figure 7. ^{35}Cl quadrupolar interaction parameters obtained from GGA-revPBE DFT calculations performed on a model of chloromethane halogen bonded with hydrogen cyanide (CH_3Cl···NCH). (a) The halogen bond angle is altered (fixed 3.00 Å halogen bond length). (b) The halogen bond length is altered (bond angle is fixed at 180°). The corresponding principal components of the EFG tensors are plotted in panels (c) and (d).

DOI: 10.1021/acs.jpcc.6b02806
J. Phys. Chem. C 2016, 120, 11121−11130

this issue was not explored any further. Efforts to obtain better spectra for **3** included increasing the number of transients, recrystallization, shortening the WURST pulses, and increasing the recycle delay. The acquisition of the full spectrum would have required an impractical amount of time and only the left and right sides were acquired. The resulting spectrum was still unsatisfactory, and attempts to extract the NMR parameters yielded a significant amount of uncertainty. Therefore, data for **3** were excluded from the analysis.

iii. NLMO Analysis. NLMO calculations were performed on cluster models built from the crystal structures by including, in addition to the molecule of interest, any additional molecules in close contact with chlorine (see Table 4). These calculations

Table 4. Contributions of the Bonding Orbital (BD) and Lone Pair Orbitals (LP) to V_{33} for Each Relevant Chlorine Site

compound/ site	total BD contribution to V_{33}	total LP contribution to V_{33}	V_{33} (a.u.)[a]	notes[b]
1a	−4.212 (28.38%)	7.920 (71.62%)	3.708	halogen bonded
1b	−4.197 (28.19%)	7.856 (71.81%)	3.659	nonhalogen-bonded counterpart
2a	−4.235 (28.44%)	7.896 (71.56%)	3.661	halogen bonded
2b	−4.211 (28.27%)	7.863 (71.73%)	3.652	nonhalogen-bonded counterpart
4a	−4.202 (28.30%)	7.791 (71.70%)	3.589	halogen bonded to N
4b	−4.190 (28.18%)	7.752 (71.82%)	3.562	halogen bonded to O
5a	−4.249 (28.46%)	7.885 (71.54%)	3.636	halogen bonded
5b	−4.263 (28.44%)	7.850 (71.56%)	3.587	nonhalogen-bonded counterpart
6a	−4.326 (28.77%)	7.812 (71.23%)	3.486	Cl···H contact
6b	−4.276 (28.52%)	7.839 (71.48%)	3.563	Cl···H contact counterpart
7a	−4.326 (28.90%)	7.688 (71.10%)	3.362	Cl···Cl contact
7b	−4.321 (28.96%)	7.702 (71.04%)	3.381	Cl···Cl contact
7c	−4.318 (28.93%)	7.720 (71.07%)	3.402	Cl···Cl contact

[a]Total contributions to V_{33} from the bonding and lone pair orbitals. [b]Sites are indicated in Figure 5, where the molecularly equivalent chlorine sites with no halogen bond are labeled "counterpart".

enable a visualization of the effect of the halogen bond by providing the contributions of each orbital to the EFG of the chlorine of interest. By comparing the contributions of each orbital to V_{33} for a halogen-bonded chlorine with those for a nonhalogen bonded chlorine, keeping in mind their chemical equivalence, one may attribute the changes in orbital contribution to the crystallographic environment, and hence the effect of halogen bonding on the EFG. It was observed that, upon halogen bonding, the chlorine-carbon bonding orbital's contribution to V_{33} increases in magnitude in the opposite direction to the lone pair's contribution to V_{33}. However, the increase in the lone pair contribution to V_{33} outweighs the increase in the bonding orbital's contribution. The outcome is an overall increase in the magnitude of V_{33}, resulting in an increase in the observed quadrupolar coupling constant upon halogen bonding.

In compound **1**, the comparison between sites 1a and 1b indicates a calculated increase in $|V_{33}|$ by 0.049 au upon halogen bonding, which results in the larger observed $|C_Q|$. This is manifested by an increase in the magnitude of the carbon-chlorine σ-bond contribution (see Figure 8), with a larger

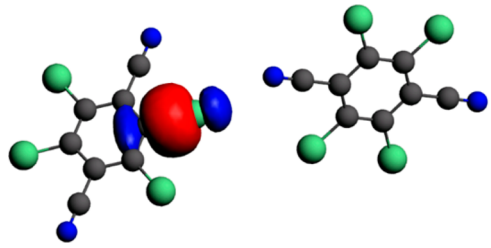

Figure 8. Electrostatic potential plot of the carbon-chlorine σ-bond NLMO, modeled to include the halogen bond between the chlorine and the nitrile group in compound **1**.

increase in the lone pair contribution to V_{33} upon halogen bonding. The comparison between sites 2a and 2b reveals the same trend, where V_{33} increases by 0.009 au, with the carbon-chlorine σ-bond contribution increasing in magnitude, and with a larger increase in the lone pair contribution. When comparing sites 4a to 4b, the differences between the chlorine with a halogen bond to nitrogen and the chlorine with a halogen bond to oxygen shows a decrease in the magnitude of the carbon-chlorine σ-bond contribution, but an increase in the lone pair contribution, with an overall increase in V_{33} by 0.027 au. This increase in V_{33} manifests itself in the larger $|C_Q|$ for the Cl···N interaction, which was observed experimentally. Comparison of sites 5a and 5b reveals an increase in V_{33} by 0.049 au upon halogen bonding, with an increase in the magnitude of the carbon-chlorine σ-bond contribution, and a larger increase in the lone pair contribution. By contrast, the opposite effect was observed in compound **6**, between sites 6a and 6b, where the carbon-chlorine σ-bond contribution increased in magnitude and the chlorine lone pair contribution decreases as a result of the hydrogen−carbon contact, thereby lowering V_{33} by 0.077 au. For **7**, it was observed that the chlorine 7c, with a shorter contact distance, had a carbon-chlorine σ-bond contribution of the same order as seen for 7a and 7b, but had a higher lone pair contribution to V_{33}. The total contributions amounted to an increase in V_{33} for chlorine 7c by 0.040 au and 0.021 au when compared to 7a and 7b, respectively. The results of these calculations are in agreement with the experimental results, where site 7c had the largest $|C_Q|$ value. This may be attributed to the shortest chlorine−chlorine contact distance, which reduces the carbon−chlorine σ-bond contribution to V_{33}.

CONCLUSIONS

A series of single-component crystalline halogen-bonded solids featuring chlorine halogen bond donors was characterized via a combination of X-ray diffraction, solid-state NMR and NQR spectroscopies, and computational chemistry. The effect of the halogen bond on the electric field gradient at chlorine was observed through the use of ^{35}Cl solid-state NMR with interpretation aided by molecular symmetry. Despite the breadth of the spectra, this approach was sensitive enough to allow for the resolution of multiple sites and for the quantification of small changes in the electric field gradient;

DOI: 10.1021/acs.jpcc.6b02806
J. Phys. Chem. C 2016, 120, 11121−11130

C_Q increases and η decreases upon halogen bonding (see Figure 9). Certainly one must be cognizant of the temperature

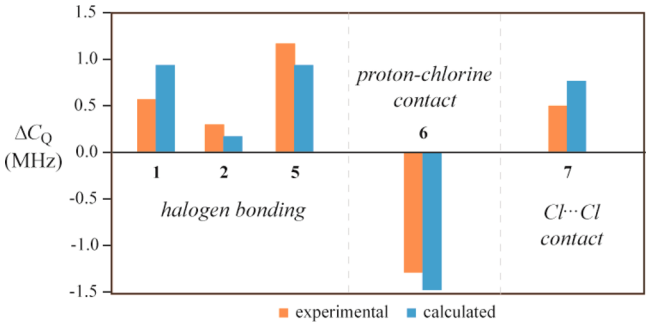

Figure 9. Experimental and GGA revPBE/TZP-calculated changes in $C_Q(^{35}Cl)$ upon halogen bonding (compounds **1**, **2**, and **5**), upon introduction of a proton−chlorine van der Waals contact (**6**), and upon shortening of a chlorine−chlorine contact (**7**).

dependence of these parameters, which could result in exceptions to the trends noted here. Results from NLMO calculations attributed these changes to an increase in the magnitude of the carbon-chlorine σ-bond contribution and a larger increase in the chlorine's lone pair contribution to the EFG upon halogen bonding, which overall causes an increase in the magnitude of the quadrupolar coupling constant. Furthermore, spectroscopic distinctions could be made between a chlorine-hydrogen contact and a chlorine−chlorine contact. This first direct ^{35}Cl solid-state NMR study of chlorine as a halogen bond donor expands the palette of NMR experiments available to characterize halogen bonds and demonstrates the physical insights available via this technique.

■ ASSOCIATED CONTENT

Supporting Information

The Supporting Information is available free of charge on the ACS Publications website at DOI: 10.1021/acs.jpcc.6b02806.

^{13}C solid-state NMR spectra, ^{35}Cl NQR spectra, deconvolutions of the ^{35}Cl solid-state NMR spectra, powder X-ray diffractograms, and additional computational analysis (PDF)

Crystallographic information files for **6** (CIF)

Crystallographic information files for **7** (CIF)

■ AUTHOR INFORMATION

Corresponding Author

*Tel: +1-613-562-5800 ext.2018; fax: +1-613-562-5170; e-mail: dbryce@uottawa.ca.

Notes

The authors declare no competing financial interest.

■ ACKNOWLEDGMENTS

D.L.B. is grateful to the Natural Sciences and Engineering Research Council (NSERC) of Canada for funding. We thank Dr. Ilia Korobkov for his X-ray crystallographic services, Dr. Victor Terskikh for assistance with NMR experiments, and Dr. Fréderic A. Perras for helpful discussions. Access to the 21.1 T NMR spectrometer was provided by the National Ultrahigh-Field NMR Facility for Solids (Ottawa, Canada), a national research facility funded by a consortium of Canadian Universities, supported by the National Research Council Canada and Bruker BioSpin, and managed by the University of Ottawa (http://nmr900.ca).

■ REFERENCES

(1) Desiraju, G. R.; Ho, P. S.; Kloo, L.; Legon, A. C.; Marquardt, R.; Metrangolo, P.; Politzer, P.; Resnati, G.; Rissanen, K. Definition of the Halogen Bond (IUPAC Recommendations 2013). *Pure Appl. Chem.* **2013**, *85*, 1711−1713.

(2) Politzer, P.; Murray, J. S. Halogen Bonding: An Interim Discussion. *ChemPhysChem* **2013**, *14*, 278−294.

(3) Clark, T.; Hennemann, M.; Murray, J. S.; Politzer, P. Halogen Bonding: The σ-Hole. *J. Mol. Model.* **2007**, *13*, 291−296.

(4) Huber, S. M.; Scanlon, J. D.; Jimenez-Izal, E.; Ugalde, J. M.; Infante, I. On the Directionality of Halogen Bonding. *Phys. Chem. Chem. Phys.* **2013**, *15*, 10350−10357.

(5) Bondi, A. van der Waals Volumes and Radii. *J. Phys. Chem.* **1964**, *68*, 441−451.

(6) Metrangolo, P.; Neukirch, H.; Pilati, T.; Resnati, G. Halogen Bonding Based Recognition Processes: A World Parallel to Hydrogen Bonding. *Acc. Chem. Res.* **2005**, *38*, 386−395.

(7) Metrangolo, P.; Meyer, F.; Pilati, T.; Resnati, G.; Terraneo, G. Halogen Bonding in Supramolecular Chemistry. *Angew. Chem., Int. Ed.* **2008**, *47*, 6114−6127.

(8) Cavallo, G.; Metrangolo, P.; Pilati, T.; Resnati, G.; Terraneo, G. *Halogen Bonding: A Long Overlooked Interaction*; Topics in Current Chemistry; Springer: Berlin, 2015; Vol. *358*, pp 1−18.

(9) Cavallo, G.; Metrangolo, P.; Milani, R.; Pilati, T.; Priimagi, A.; Resnati, G.; Terraneo, G. The Halogen Bond. *Chem. Rev.* **2016**, *116*, 2478−2601.

(10) Bryce, D. L.; Viger-Gravel, J. Solid-State NMR Study of Halogen-Bonded Adducts. *Top. Curr. Chem.* **2015**, *358*, 183−204.

(11) Weingarth, M.; Raouafi, N.; Jouvelet, B.; Duma, L.; Bodenhausen, G.; Boujlel, K.; Schöllhorn, B.; Tekely, P. Revealing Molecular Self-Assembly and Geometry of Non-Covalent Halogen Bonding by Solid-State NMR Spectroscopy. *Chem. Commun.* **2008**, 5981−5983.

(12) Viger-Gravel, J.; Leclerc, S.; Korobkov, I.; Bryce, D. L. Direct Investigation of Halogen Bonds by Solid-State Multinuclear Magnetic Resonance Spectroscopy and Molecular Orbital Analysis. *J. Am. Chem. Soc.* **2014**, *136*, 6929−6942.

(13) Xu, Y.; Viger-Gravel, J.; Korobkov, I.; Bryce, D. L. Mechanochemical Production of Halogen-Bonded Solids Featuring P═O···I−C Motifs and Characterization via X-ray Diffraction, Solid-State Multinuclear Magnetic Resonance, and Density Functional Theory. *J. Phys. Chem. C* **2015**, *119*, 27104−27117.

(14) Viger-Gravel, J.; Leclerc, S.; Korobkov, I.; Bryce, D. L. Correlation Between ^{13}C Chemical Shifts and the Halogen Bonding Environment in a Series of Solid para-Diiodotetrafluorobenzene Complexes. *CrystEngComm* **2013**, *15*, 3168−3177.

(15) Viger-Gravel, J.; Meyer, J. E.; Korobkov, I.; Bryce, D. L. Probing Halogen Bonds with Solid-State NMR Spectroscopy: Observation and Interpretation of $J(^{77}Se,^{31}P)$ Coupling in Halogen-Bonded P═Se···I Motifs. *CrystEngComm* **2014**, *16*, 7285−7297.

(16) Szell, P. M. J.; Bryce, D. L. Recent Advances in Chlorine, Bromine, and Iodine Solid-State NMR Spectroscopy. *Annu. Rep. NMR Spectrosc.* **2015**, *84*, 115−162.

(17) Chapman, R. P.; Widdifield, C. M.; Bryce, D. L. Solid-State NMR of Quadrupolar Halogen Nuclei. *Prog. Nucl. Magn. Reson. Spectrosc.* **2009**, *55*, 215−237.

(18) O'Dell, L. A.; Schurko, R. W. QCPMG Using Adiabatic Pulses for Faster Acquisition of Ultra-Wideline NMR Spectra. *Chem. Phys. Lett.* **2008**, *464*, 97−102.

(19) Perras, F. A.; Bryce, D. L. Direct Investigation of Covalently Bound Chlorine in Organic Compounds by Solid-State ^{35}Cl NMR Spectroscopy and Exact Spectral Line-Shape Simulations. *Angew. Chem., Int. Ed.* **2012**, *51*, 4227−4230.

(20) Widdifield, C. M.; Chapman, R. P.; Bryce, D. L. Chlorine, Bromine, and Iodine Solid-State NMR Spectroscopy. *Annu. Rep. NMR Spectrosc.* **2009**, *66*, 195−326.

(21) Lucken, E. A. C. *Nuclear Quadrupolar Coupling Constants*; Academic Press: London, 1969.
(22) Bersohn, R. Nuclear Electric Quadrupole Spectra in Solids. *J. Chem. Phys.* **1952**, *20*, 1505−1509.
(23) Widdifield, C. M.; Bryce, D. L. Solid-State ^{127}I NMR and GIPAW DFT Study of Metal Iodides and Their Hydrates: Structure, Symmetry, and Higher-Order Quadrupole-Induced Effects. *J. Phys. Chem. A* **2010**, *114*, 10810−10823.
(24) Dean, C.; Pollack, M.; Craven, B. M.; Jeffrey, G. A. A Nuclear Quadrupole Resonance and X-ray Study of the Crystal Structure of 1,2,4,5-Tetrachlorobenzene. *Acta Crystallogr.* **1958**, *11*, 710−718.
(25) Lucken, E. A. C. Structural Information from Nuclear Quadrupole Coupling Constants. *Z. Anal. Chem.* **1975**, *273*, 337−344.
(26) Das, A. K.; Basu, R. Nuclear Quadrupole Resonance Spectra of Charge Transfer Complexes. *Indian J. Chem.* **1983**, *22A*, 914−916.
(27) Semin, G. K.; Babushkina, T. A.; Khrlakyan, S. P.; Pervova, E. Y.; Shokina, V. V.; Knunyants, I. L. I^{127} NQR Spectra of Fluorinated α,ω-Diiodoalkanes and Complexes with Amines. *Theor. Exp. Chem.* **1971**, *4*, 179−181.
(28) Bowmaker, G. A.; Boyd, P. D. W. An SCF-MS-Xα Study of the Bonding and Nuclear Quadrupole Coupling in 1:1 Complexes of Amines with Diatomic Halogens and Interhalogens. *J. Chem. Soc., Faraday Trans. 2* **1987**, *83*, 2211−2223.
(29) Bowmaker, G. A.; Hacobian, S. Nuclear Quadrupole Resonance of Charge Transfer Complexes. I. The Trihalide Ions. *Aust. J. Chem.* **1968**, *21*, 551−564.
(30) Bowmaker, G. A.; Hacobian, S. Nuclear Quadrupole Resonance of Charge-Transfer Complexes. II. The Aminehalogen Complexes. *Aust. J. Chem.* **1969**, *22*, 2047−2059.
(31) Bowmaker, G. A. Nuclear Quadrupole Resonance of Charge Transfer Complexes. Part 3.—A ^{14}N and ^{35}Cl n.q.r. Study of the 1:1 Complex of 3,5-Dichloropyridine with Iodine Monochloride. *J. Chem. Soc., Faraday Trans. 2* **1976**, *72*, 1964−1969.
(32) Allen, F. H. The Cambridge Structural Database: A Quarter of a Million Crystal Structures and Rising. *Acta Crystallogr., Sect. B: Struct. Sci.* **2002**, *58*, 380−388.
(33) We use "chemically equivalent" to qualitatively refer to atoms that are clearly in the same chemical environment in a simple drawing of an isolated molecule; we do not mean to invoke the strict NMR definition of chemical equivalence.
(34) Britton, D. 2,4,5,6-Tetrachloro-1,3-dicyanobenzene, $Cl_4C_6(CN)_2$ and 2,3,5,6-Tetrachloro-1,4-dicyanobenzene, $Cl_4C_6(CN)_2$. *Cryst. Struct. Commun.* **1981**, *10*, 1501−1508.
(35) Britton, D. 3,4,5,6-Tetrachloro-1,2-dicyanobenzene, $Cl_4C_6(CN)_2$. *Cryst. Struct. Commun.* **1981**, *10*, 1509−1512.
(36) Zanotti, G.; Bardi, R.; Del Pra, A. Structure of 2,3-Dichloro-5,6-dicyano-p-benzoquinone (DDQ). *Acta Crystallogr., Sect. B: Struct. Crystallogr. Cryst. Chem.* **1980**, *36*, 168−171.
(37) Carter, V. B.; Britton, D. The Crystal Structures of 2,4,6-Trichlorobenzonitrile and 2,4,6-Tribromobenzonitrile. *Acta Crystallogr., Sect. B: Struct. Crystallogr. Cryst. Chem.* **1972**, *28*, 945−950.
(38) Pink, M.; Britton, D.; Noland, W. E.; Pinnow, M. J. 2,4,6-Trichloro-phenyl-iso-nitrile and 2,4,6-Tri-chloro-benzo-nitrile. *Acta Crystallogr., Sect. C: Cryst. Struct. Commun.* **2000**, *56*, 1271−1273.
(39) Massiot, D. M.; Farnan, I.; Gautier, N.; Trumeau, D.; Trokiner, J.; Coutures, J. P. ^{71}Ga and ^{69}Ga Nuclear Magnetic Resonance Study of beta-Ga_2O_3: Resolution of Four- and Six-fold Coordinated Ga Sites in Static Conditions. *Solid State Nucl. Magn. Reson.* **1995**, *4*, 241−248.
(40) Perras, F. A.; Widdifield, C. M.; Bryce, D. L. QUEST-QUadrupolar Exact SofTware: A Fast Graphical Program for the Exact Simulation of NMR and NQR Spectra for Quadrupolar Nuclei. *Solid State Nucl. Magn. Reson.* **2012**, *45*−*46*, 36−44.
(41) Clark, S. J.; Segall, M. D.; Pickard, C. J.; Hasnip, P. J.; Probert, M. I. J.; Refson, K.; Payne, M. C. First Principles Methods Using CASTEP. *Z. Kristallogr.* **2005**, *220*, 567−570.
(42) Adiga, S.; Aebi, D.; Bryce, D. L. EFGShield — A Program for Parsing and Summarizing the Results of Electric Field Gradient and Nuclear Magnetic Shielding Tensor Calculations. *Can. J. Chem.* **2007**, *85*, 496−505.
(43) Gee, M.; Wasylishen, R. E.; Laaksonen, A. A More Reliable Absolute Shielding Scale for Chlorine: Combined Experimental and Theoretical Approach. *J. Phys. Chem. A* **1999**, *103*, 10805−10812.
(44) Sundholm, D.; Olsen, J. Finite Element Multiconfiguration Hartree-Fock Determination of the Nuclear Quadrupole Moments of Chlorine, Potassium, and Calcium Isotopes. *J. Chem. Phys.* **1993**, *98*, 7152−7158.
(45) Kellö, V.; Sadlej, A. J. Determination of the Quadrupole Moment of the Halogen Nuclei (Cl,Br,I) From Molecular Data. *Mol. Phys.* **1996**, *89*, 127−137.
(46) Pyykkö, P. Year-2008 Nuclear Quadrupole Moments. *Mol. Phys.* **2008**, *106*, 1965−1974.
(47) te Velde, G.; Bickelhaupt, F. M.; Baerends, E. J.; Fonseca Guerra, C.; van Gisbergen, S. J. A.; Snijders, J. G.; Ziegler, T. Chemistry with ADF. *J. Comput. Chem.* **2001**, *22*, 931−967.
(48) Fonseca Guerra, C.; Snijders, J. G.; te Velde, G.; Baerends, E. J. Towards an Order-N DFT Method. *Theor. Chem. Acc.* **1998**, *99*, 391−403.
(49) *ADF2014, SCM, Theoretical Chemistry*; Vrije Universiteit: Amsterdam, The Netherlands, 2014 (http://www.scm.com).
(50) Zhang, Y.; Yang, W. Comment on "Generalized Gradient Approximation Made Simple. *Phys. Rev. Lett.* **1998**, *80*, 890.
(51) Van Lenthe, E.; Baerends, E. J. Optimized Slater-type Basis Sets for the Elements 1−118. *J. Comput. Chem.* **2003**, *24*, 1142−1156.
(52) Dennington, R.; Keith, T.; Millam, J. *GaussView*, version 4.1; Semichem Inc.: Shawnee Mission, KS, 2009.
(53) *APEX Software Suite* v.2012; Bruker AXS: Madison, WI, 2012.
(54) *SADABS*; Bruker AXS: Madison, WI, 2001.
(55) Sheldrick, G. M. *Cell_Now*; Bruker-AXS: Madison, WI, 2004.
(56) Sheldrick, G. M. Crystal Structure Refinement with SHELXL. *Acta Crystallogr., Sect. C: Struct. Chem.* **2015**, *71*, 3−8.
(57) Thallapally, P. K.; Nangia, A. A Cambridge Structural Database Analysis of the C−H···Cl Interaction: C−H···Cl- and C−H···Cl−M Often Behave as Hydrogen Bonds but C−H···Cl−C is Generally a van der Waals Interaction. *CrystEngComm* **2001**, *3*, 114−119.
(58) Metrangolo, P.; Resnati, G. Type II Halogen···Halogen Contacts are Halogen Bonds. *IUCrJ* **2014**, *1*, 5−7.
(59) Negita, H.; Shibata, K.; Kubo, T. Nuclear Quadrupole Resonances of 2,4,6-Trichlorobenzonitrile. *Bull. Chem. Soc. Jpn.* **1975**, *48* (2), 678−679.
(60) Eichele, K. *WSolids1*, ver. 1.21.3; Universität Tübingen: Tübingen, Germany, 2015.

DOI: 10.1021/acs.jpcc.6b02806
J. Phys. Chem. C 2016, 120, 11121−11130

Chapter 5 – $^{79/81}$Br Nuclear Quadrupole Resonance Spectroscopic Characterization of Halogen Bonds in Supramolecular Assemblies

Statement of Authenticity. The article presented in chapter 5 of this thesis was performed in collaboration with Paolo Vioglio Cerreia, at the time a doctoral student from the University of Turin in the group of Dr. Roberto Gobetto. Paolo is first author and had prepared samples **1** to **5**, perform the $^{79/81}$Br NQR experiments, and had an integral role in the manuscript. My role in this project was to carry out the DFT calculations, ^{13}C solid-state NMR and powder X-ray diffractions analysis, prepare parts of the manuscript including the figures, prepare compound **6**, find all missing $^{79/81}$Br NQR resonances, and contributed to the analysis and interpretation of the final results. Dr. David Bryce, Dr. Roberto Gobetto and Dr. Michele Chierotti are acknowledged for guidance, support, and contributions to the manuscript. Dr. Paul Morris is acknowledged for building the NQR probe that was essential for this experiment.

Permissions. I declare that I have obtained permission from all coauthors to include this article in my thesis. Chapter 5 was reproduced from *Chem. Sci.* **2018**, *9*, 4555-4561 with permission from the Royal Society of Chemistry. (DOI: 10.1039/C8SC01094C). The cover article (*Chemical Science*, volume 9, number 20, 28 May 2018) was reproduced by permission of The Royal Society of Chemistry.

Supporting Information. All supporting information for this article can be retrieved on the RSC website:

https://pubs.rsc.org/en/content/articlelanding/2018/sc/c8sc01094c#!divAbstract

Volume 9 | Number 20 | 28 May 2018 | Pages 4537–4720

Chemical Science

rsc.li/chemical-science

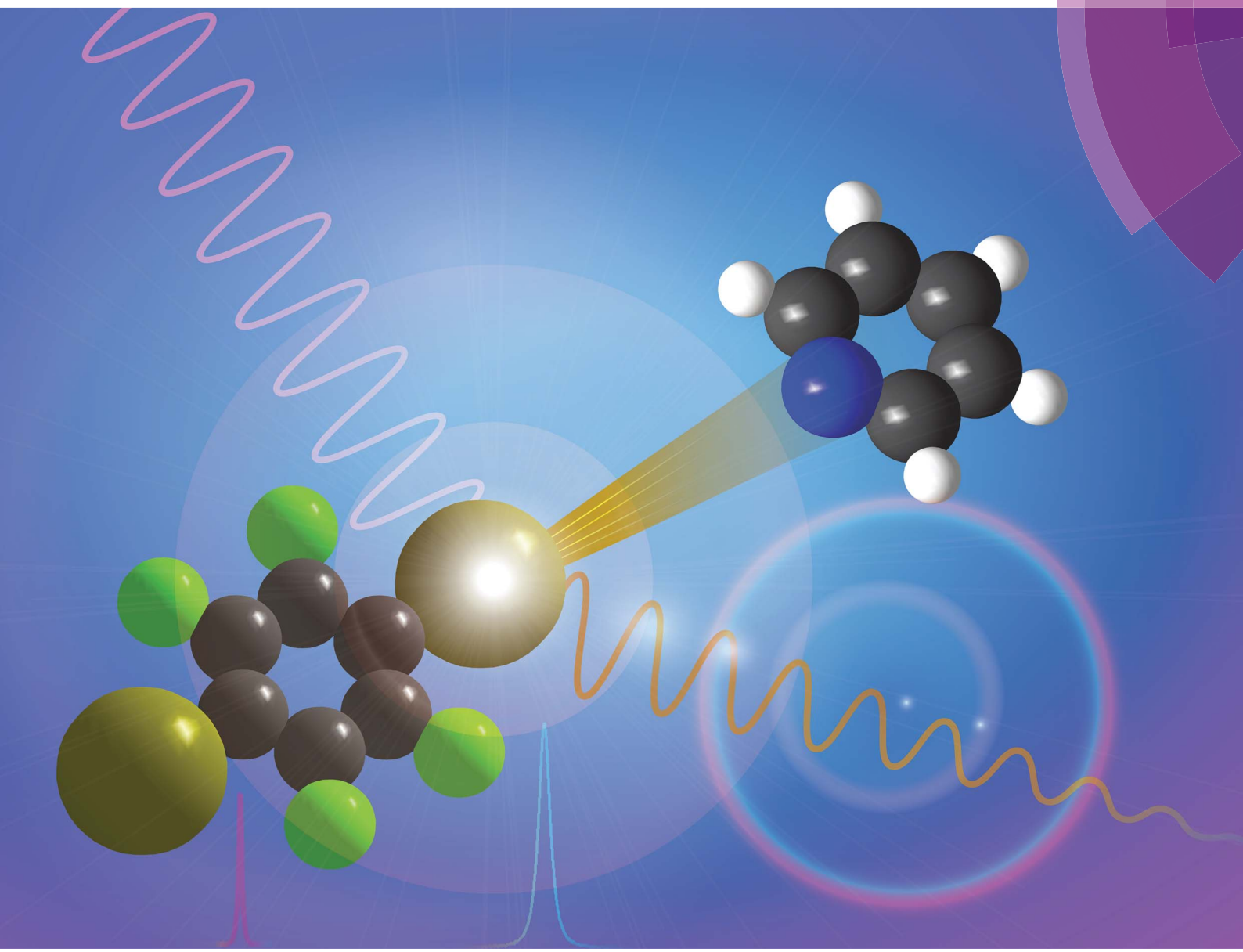

ISSN 2041-6539

ROYAL SOCIETY OF CHEMISTRY

EDGE ARTICLE

D. L. Bryce *et al.*

$^{79/81}$Br nuclear quadrupole resonance spectroscopic characterization of halogen bonds in supramolecular assemblies

Chemical Science

EDGE ARTICLE

View Article Online
View Journal | View Issue

Cite this: *Chem. Sci.*, 2018, **9**, 4555

$^{79/81}$Br nuclear quadrupole resonance spectroscopic characterization of halogen bonds in supramolecular assemblies†

P. Cerreia Vioglio, ‡[a] P. M. J. Szell, [b] M. R. Chierotti, [a] R. Gobetto [a] and D. L. Bryce *[b]

Despite the applicability of solid-state NMR to study the halogen bond, the direct NMR detection of $^{79/81}$Br covalently bonded to carbon remains impractical due to extremely large spectral widths, even at ultra-high magnetic fields. In contrast, nuclear quadrupole resonance (NQR) offers comparatively sharp resonances. Here, we demonstrate the abilities of $^{79/81}$Br NQR to characterize the electronic changes in the C–Br···N halogen bonding motifs found in supramolecular assemblies constructed from 1,4-dibromotetrafluorobenzene and nitrogen-containing heterocycles. An increase in the bromine quadrupolar coupling constant is observed, which correlates linearly with the halogen bond distance ($d_{Br\cdots N}$). Notably, $^{79/81}$Br NQR is able to distinguish between two symmetry-independent halogen bonds in the same crystal structure. This approach offers a rapid and reliable indication for the occurrence of a halogen bond, with experimental times limited only by the observation of $^{79/81}$Br NQR resonances.

Received 7th March 2018
Accepted 23rd April 2018

DOI: 10.1039/c8sc01094c

rsc.li/chemical-science

Introduction

The halogen bond (XB) consists of a non-covalent interaction between the area of lower electron density[1] associated with a covalently bonded halogen atom, named the σ-hole,[2,3] and a Lewis base. It is conveniently schematized as R–X···Y, where X is the halogen bond donor (strength: I > Br > Cl ≫ F),[4] R is a group covalently bonded to X, and Y represents the electron-rich nucleophilic region of the halogen bond acceptor.[5] With unique physicochemical properties such as directionality,[6,7] strength,[8,9] tunability,[10,11] hydrophobicity,[12] and selectivity,[13,14] the halogen bond has become an important tool in modern supramolecular chemistry.[15,16] Many promising applications are evident in medicinal chemistry,[17–19] catalysis,[20] and conductive materials,[21] to name a few, and full literature reviews covering key advances in the field are available.[22,23]

Solid-state nuclear magnetic resonance (SSNMR) is a powerful tool to assess the occurrence of the halogen bond,[24] to reliably determine phase purity,[25] and to quantitatively relate local structural changes to geometrical features of the interaction.[26,27]

A key advantage of using SSNMR to characterize the halogen bond is the ability to non-destructively analyze samples in their powdered form, offering information on the chemical shift, quadrupolar coupling, dipolar coupling, and *J*-coupling.[25,27–32] Notably, SSNMR experiments on ^{13}C, ^{15}N, ^{31}P, or ^{77}Se have been used at natural isotopic abundance to evaluate geometrical features of the halogen bond.[33–35] Direct observation of the halogen bond donor has been limited to the study of ^{35}Cl (nuclear electric quadrupole moment $Q(^{35}\mathrm{Cl}) = -81.65(80)$ mb)[36] covalently bonded to carbon,[31] due to the broad spectral widths associated with the heavier halogens. This broadening arises as a consequence of the greater quadrupole moments of $^{79/81}$Br ($Q(^{79}\mathrm{Br}) = 313(3)$ mb), ^{81}Br ($Q(^{81}\mathrm{Br}) = 262(3)$ mb), and especially ^{127}I ($Q(^{127}\mathrm{I}) = -696(12)$ mb),[36] resulting in impractically broad solid-state NMR spectra. As the great majority of halogen-bonded compounds exhibit a halogen covalently bonded to a carbon atom,[23] there have been various efforts towards the analysis of the ^{13}C resonances for studying the halogen bond donor. However, ^{13}C SSNMR spectroscopy of carbon covalently bonded to a quadrupolar halogen can be challenging due to the line shape distortion caused by residual dipolar coupling to the quadrupolar nucleus.[26,27]

As noted, $^{79/81}$Br and ^{127}I both remain inaccessible by SSNMR when they are covalently bonded to carbon. Conversely, nuclear quadrupole resonance (NQR) offers advantages over SSNMR to directly characterize the XB; it enables the direct detection of the XB donor site and does not require an external magnetic field. For an exposition of the relative advantages and disadvantages of SSNMR and NQR, readers are referred to a recent Concepts article.[37] The NQR frequencies for spin-3/2 nuclides,

[a]*Department of Chemistry and NIS Centre, University of Torino, Via Pietro Giuria 7, 10125 Torino, Italy*

[b]*Department of Chemistry and Biomolecular Sciences & Centre for Catalysis Research and Innovation, University of Ottawa, 10 Marie Curie Private, Ottawa, Ontario K1N 6N5, Canada. E-mail: dbryce@uottawa.ca; Fax: +1-613-562-5170; Tel: +1-613-562-5800 ext. 2018*

† Electronic supplementary information (ESI) available: ^{13}C SSNMR spectra, powder X-ray diffractograms. See DOI: 10.1039/c8sc01094c

‡ Present address: Aix-Marseille Université, CNRS, ICR (UMR 7273), 13397 Marseille cedex 20 (France).

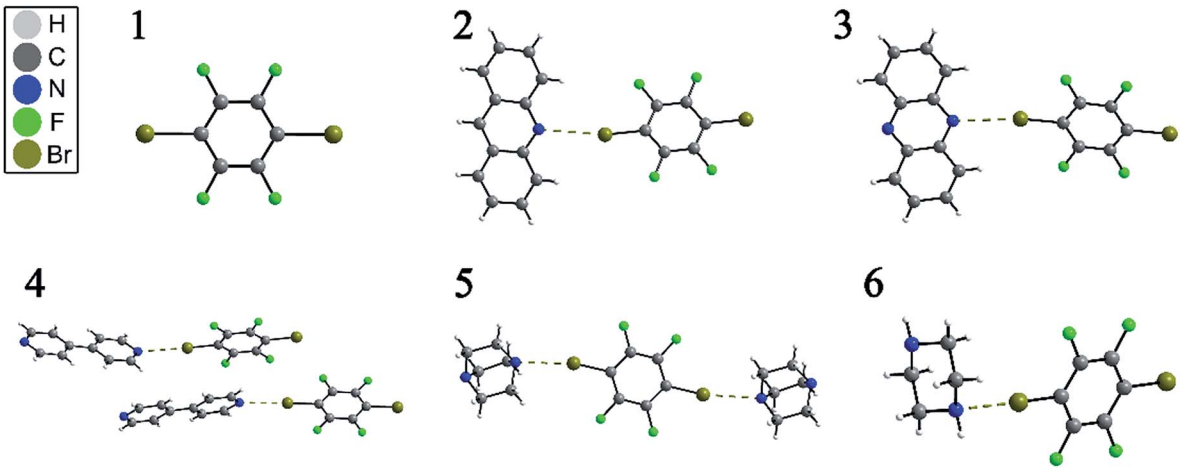

Fig. 1 Depiction of the X-ray crystal structures of *p*-dibromotetrafluorobenzene (**1**) and its cocrystals (**2–6**), showing the C–Br···N halogen bond by dashed brown lines.

such as ^{79}Br and ^{81}Br, are a product of the quadrupolar coupling constant (C_Q) and the asymmetry parameter (η), given by eqn (1):

$$\nu_Q = \frac{C_Q}{2}\sqrt{1+\frac{\eta^2}{3}} \quad (1)$$

$$C_Q = \frac{eV_{33}Q}{h} \quad (2)$$

$$\eta = \frac{V_{11}-V_{22}}{V_{33}} \quad (3)$$

In eqn (2) and (3), e refers to the fundamental charge; V_{11}, V_{22}, and V_{33} refer to components of the electric field gradient tensor ($|V_{33}| \geq |V_{22}| \geq |V_{11}|$); Q refers to the quadrupole moment of the nucleus; h refers to Planck's constant. In turn, the quadrupolar coupling parameters yield information on the electric field gradient (EFG) at the nucleus, providing information on electronic structure and bonding.[38]

NQR has long played a role in characterizing charge-transfer complexes, but sparse information exists on the "halogen bond" as defined above.[39–42] Consequently, the newest class of iconic halogen bond donors has not been thoroughly studied by NQR due in part to the fact that NMR has largely overtaken the field. Furthermore, clear and general relationships between the NQR frequencies and particular geometrical features have not yet been identified. Here, we report a systematic study of a series of prototypical C–Br···N XB motifs exhibiting different XB lengths and strengths (see Fig. 1) by ^{79}Br and ^{81}Br NQR spectroscopy. The geometrical features of the halogen bonds in each supramolecular assembly are summarized in Table 1. As the EFG at ^{79}Br and ^{81}Br are identical, the difference in the measured quadrupolar coupling constants for both isotopes is due to their different quadrupole moments (Q). Therefore, the ^{79}Br and ^{81}Br NQR frequencies should be related by a factor of ~1.19 [$Q(^{79}\text{Br})/Q(^{81}\text{Br})$], providing a built-in verification of the experimental results.

Results and discussion

The structures of pure *p*-dibromotetrafluorobenzene (*p*-DBrTFB) and a series of cocrystals featuring C–Br···N halogen bonds are shown in Fig. 1. The NQR experiments, consisting of one-dimensional spectra and nutation data, are presented in

Table 1 Geometrical parameters of the halogen bonds in compounds **1–6**, including the normalized distance parameter (R_{XB}), the C–Br···N halogen bond angle ($\theta_{C-Br\cdots N}$), and the Br···N halogen bond length ($d_{Br\cdots N}$)

Entry	Compound	CSD ref. 43	R_{XB}[a]	$\theta_{C-Br\cdots N}$ (°)	$d_{Br\cdots N}$ (Å)	Note
1	*p*-Dibromotetrafluorobenzene	ZZZAVJ ref. 44	—	—	—	
2	(Acridine)(**1**)	712 047 ref. 45	0.891[b]	172.13[b]	3.031[b]	
3	(Phenazine)(**1**)	712 045 ref. 45	0.878	172.59	2.985	
4	(4,4′-Bipyridine)(**1**)	199 297 ref. 46	0.846	177.21	2.878	Site 4A
			0.876	176.40	2.979	Site 4B
5	(1,4-Diazabicyclo[2.2.2]octane)(**1**)	649 676 ref. 47	0.851	167.69	2.894	Site 5A
			0.856	169.57	2.910	Site 5B
6	(Piperazine)(**1**)	649 675 ref. 47	0.847	177.72	2.881	

[a] The normalized distance parameter R_{XB} has been calculated as the ratio between the halogen bond length ($d_{Br\cdots N}$) and the sum of the van der Waals radii of Br and N. [b] The X-ray crystal structure shows disorder on the position of the nitrogen, resulting in two possible halogen bond geometries; the reported values herein are the averages over the two disordered halogen bond sites.

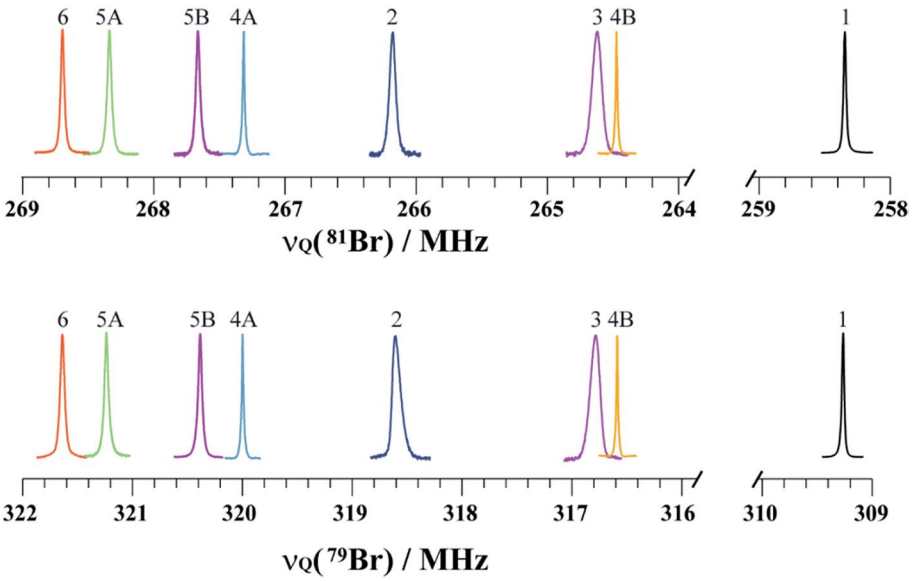

Fig. 2 Pure ^{81}Br and ^{79}Br NQR resonances of compounds **1–6** depicted on a unified scale to emphasise the shift in the NQR resonance frequencies. The two crystallographically inequivalent bromine sites in compounds **4** and **5** are denoted **4A** & **4B** and **5A** & **5B**, respectively. Regions between 264 and 259 MHz (^{81}Br) & 316 and 310 MHz (^{79}Br) did not have any resonances, and were removed for clarity.

Fig. 2 and 3, respectively. The data obtained from the ^{81}Br and ^{79}Br NQR experiments are summarized in Tables 2 and 3, respectively.

The search for the NQR resonances over the amplifier frequency range was the only time-determining step: once the resonance has been found, an excellent signal-to-noise ratio is achieved in about one minute on approximately 200 mg of sample. The signal frequency is characteristic of the local electronic environment at the bromine nucleus; hence, it provides direct information on the halogen bond. To the best of our knowledge, only a handful of data has been published in the literature regarding the characterization of the halogen bond by ^{81}Br NQR.[48] As shown in Fig. 2, the ^{79}Br and ^{81}Br NQR frequencies shift towards a higher frequency upon the formation of a halogen bond. As a general trend for the compounds studied herein, the shorter the halogen bond, the greater the shift (*vide infra*). This is consistent with previous ^{81}Br NQR results on Br···N adducts.[48]

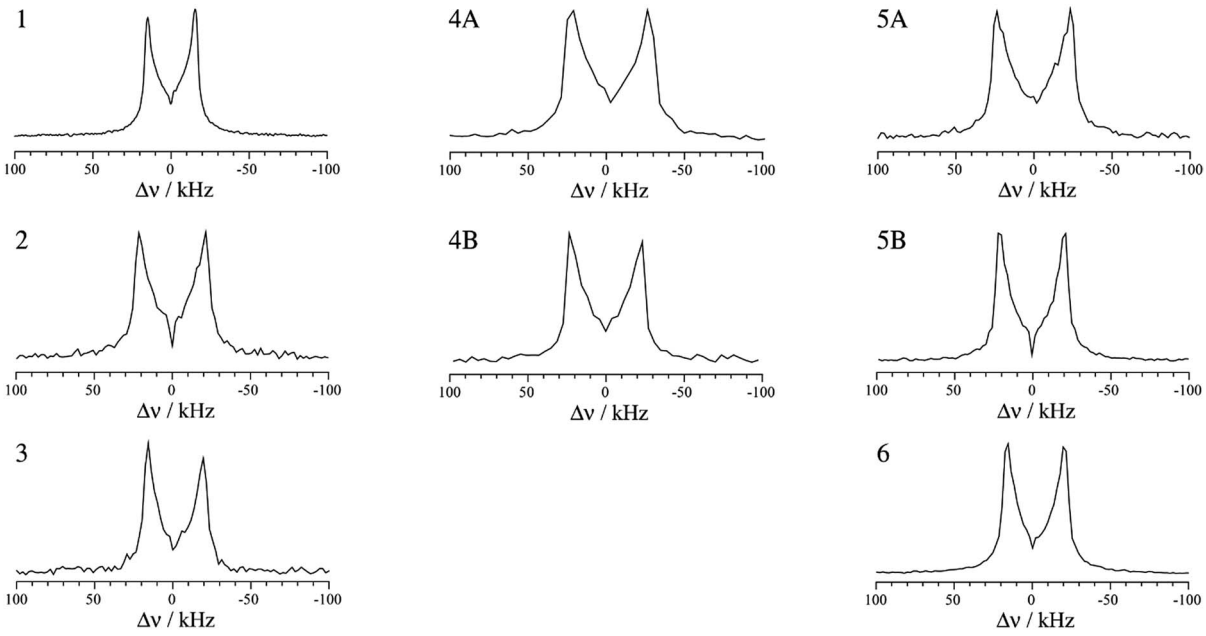

Fig. 3 ^{81}Br nutation-echo NQR spectra of compounds **1–6**. The most intense *F*1 slices are shown. As the positive part is merely the antisymmetric image of the negative half, the differences in intensity between the positive and the negative half are likely due to RF inhomogeneity.

Table 2 Experimental and DFT-calculated ^{81}Br NQR frequencies (ν_Q), and quadrupolar parameters (η, C_Q) of the halogen bonded compounds under investigation

Compounds	ν_Q exp. (MHz)	ν_Q calc.[a] (MHz)	η exp.[b]	η calc.	C_Q exp. (MHz)	C_Q calc. (MHz)	FWHM (kHz)
1	258.34 ± 0.02	264.8	0.13 ± 0.04	0.114	515.23 ± 1.79	528.4	23
2	266.22 ± 0.04	268.9	0.15 ± 0.07	0.117	530.45 ± 3.72	536.6	66
3	264.64 ± 0.04	266.9	0.12 ± 0.09	0.109	528.01 ± 3.81	532.8	84
4A	267.32 ± 0.01	270.4	0.10 ± 0.08	0.117	533.75 ± 2.85	539.5	17
4B	264.47 ± 0.01	269.5	0.14 ± 0.06	0.125	527.22 ± 2.95	537.7	15
5A	267.66 ± 0.04	268.7	0.15 ± 0.05	0.120	533.32 ± 2.67	536.2	30
5B	268.33 ± 0.04	268.8	0.14 ± 0.06	0.119	535.02 ± 3.00	536.3	40
6	268.69 ± 0.02	269.2	0.16 ± 0.06	0.116	535.10 ± 3.43	537.1	26

[a] The calculated ν_Q frequencies were obtained using eqn (1) and the corresponding calculated η and C_Q values. [b] Measured from the ^{81}Br nutation NQR spectra.

Notably, both ^{79}Br and ^{81}Br NQR provide clear differentiation between the two crystallographically inequivalent Br sites in compounds **4** and **5** (sites A and B), with the site assignments aided by DFT calculations. Importantly, in previous work on the C–Br···N motif, neither ^{15}N SSNMR of the halogen bond acceptor nor ^{13}C SSNMR of the halogen bond donor were able to discriminate two crystallographic sites.[26] Additionally, due to the large quadrupole moments of ^{79}Br and ^{81}Br, the NQR frequencies are very sensitive to subtle changes in the crystallographic environment. For instance, a 3.41 ± 0.03 MHz difference is observed between the ^{79}Br NQR frequencies of sites **4A** and **4B**, with a difference of 0.101 Å in $d_{Br\cdots N}$. In addition, comparing the two bromine sites in the X-ray crystal structure of **5** reveals a subtle difference of 0.016 Å in the $d_{Br\cdots N}$ between site **5A** and **5B**, while the value of $\theta_{C-Br\cdots N}$ differs by merely 1.88°. Despite these very small geometrical differences, a clear and unambiguous difference of 0.79 ± 0.05 MHz is measured between the two ^{79}Br NQR frequencies. In contrast, a ^{13}C SSNMR analysis of these halogen-bonded compounds did not resolve the two crystallographically independent ^{13}C sites due to residual dipolar coupling to both bromine isotopes (see ESI†).

For spin-3/2 nuclides such as $^{79/81}$Br, the pure one-dimensional NQR spectrum yields a single frequency which is related to the product of C_Q and η (see eqn (1)). In order to extract the individual EFG tensor components, several experimental methods have been proposed, such as Zeeman-perturbed NQR,[49] nutation NQR,[50,51] and level-crossing double resonance.[52] Among these techniques, nutation NQR does not require a complex experimental setup, allowing for the determination of the quadrupolar asymmetry parameter in a straightforward manner. Implemented as a two-dimensional experiment, nutation NQR involves recording series of spectra where the pulse lengths are increased between each one-dimensional spectrum. This experiment allows for the observation of the orientation dependence of the quadrupolar interaction relative to the radiofrequency field. The result allows the measurement of η, which can then be used to determine the value of C_Q.[50]

The highest intensity one-dimensional slices from the two-dimensional experimental ^{81}Br nutation NQR spectra are shown in Fig. 3. Although a stronger RF field may improve the spectral line shapes, our home-built probe is limited to lower power levels. However, using the equation and method proposed for a spin-3/2 nucleus by Harbison,[50,51] the experimental NQR line shapes have provided η values in agreement with the DFT calculated results (Tables 2 and 3). Confirmation bias was accounted for by measuring the maximum and minimum separation of the spectral singularities, thereby providing error limits on η.

After measuring η by ^{81}Br nutation NQR, the values of C_Q for both isotopes were calculated using eqn (1), as both

Table 3 Experimental and DFT-calculated ^{79}Br NQR frequencies (ν_Q), and quadrupolar parameters (η, C_Q) of the halogen bonded compounds under investigation

Compounds	ν_Q exp. (MHz)	ν_Q calc.[a] (MHz)	η exp.[b]	η calc.	C_Q exp. (MHz)	C_Q calc. (MHz)	FWHM (kHz)
1	309.32 ± 0.02	316.9	0.13 ± 0.04	0.114	616.92 ± 2.14	632.4	22
2	318.61 ± 0.05	321.9	0.15 ± 0.07	0.117	634.84 ± 4.45	642.3	95
3	316.81 ± 0.04	319.5	0.12 ± 0.09	0.109	632.25 ± 4.55	637.7	98
4A	320.00 ± 0.02	323.6	0.10 ± 0.08	0.117	638.94 ± 3.41	645.8	17
4B	316.59 ± 0.02	322.6	0.14 ± 0.06	0.125	631.12 ± 3.54	643.5	16
5A	320.45 ± 0.03	321.7	0.15 ± 0.05	0.120	638.52 ± 3.19	641.8	43
5B	321.24 ± 0.04	321.7	0.14 ± 0.06	0.119	640.39 ± 3.59	641.9	45
6	321.65 ± 0.02	322.2	0.16 ± 0.06	0.116	640.57 ± 4.10	642.9	29

[a] The calculated ν_Q frequencies were obtained using eqn (1) and the corresponding calculated values of η and C_Q. [b] Measured from the ^{81}Br nutation NQR spectra.

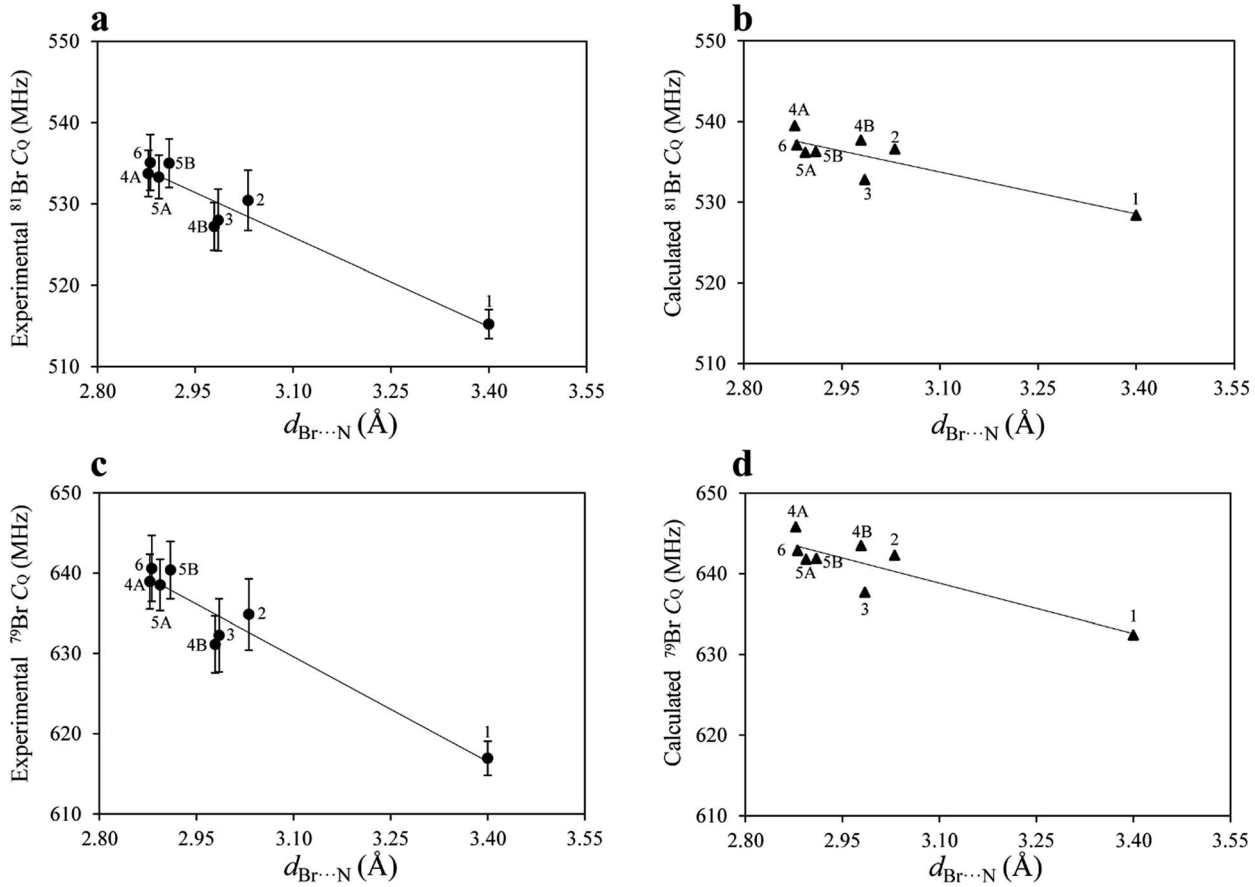

Fig. 4 Plot of the experimental ^{81}Br C_Q (a), calculated ^{81}Br C_Q (b), experimental ^{79}Br C_Q (c), and calculated ^{79}Br C_Q (d) as a function of the Br⋯N halogen bond length. The lines of best fit and Pearson's correlation coefficients are: (a) $C_Q = [-36.63 \pm 4.41]d_{Br\cdots N} + [639.45 \pm 13.22]$, and $R^2 = 0.920$; (b) $C_Q = [-17.32 \pm 4.03]d_{Br\cdots N} + [587.44 \pm 12.09]$, and $R^2 = 0.754$; (c) $C_Q = [-43.62 \pm 5.14]d_{Br\cdots N} + [764.81 \pm 15.42]$, and $R^2 = 0.923$; (d) $C_Q = [-20.87 \pm 4.84]d_{Br\cdots N} + [703.54 \pm 14.52]$, and $R^2 = 0.756$.

isotopes share the same η value. The C_Q values obtained for ^{79}Br and ^{81}Br are related by a ratio of 1.19, further confirming the experimental results. The DFT results are in good agreement with the experimental results, both in terms of η and C_Q. Although the experimental and calculated C_Q data are close, the DFT results are systematically larger. While dispersion corrections were used in the calculations, the calculated C_Q values were not as strongly correlated to the halogen bond geometry as were the experimental data (Fig. 4). For instance, the experimental $C_Q(^{79}\text{Br})$ values show an average increase of about 18 MHz upon halogen bond formation, whereas the calculated results suggest an average increase of only 10 MHz.

Upon plotting both the experimental and calculated C_Q data as a function of the corresponding Br⋯N halogen bond distances, shown in Fig. 4, good linear correlations are observed. The origin of this effect can be mainly attributed to the interaction between the lone pair electrons from the nitrogen and the bromine atoms, which has historically been referred to as charge transfer. The increase in C_Q observed for ^{79}Br and ^{81}Br upon halogen bonding is in agreement with the results for chlorine, obtained from previous ^{35}Cl SSNMR experiments.[31] In the case of the bromine halogen bond, C_Q increases by 15 to 18 MHz, whereas in the case of chlorine halogen bonds, C_Q increases by 0.3 to 1.2 MHz.

The ^{79}Br and ^{81}Br NQR observables are remarkably sensitive to the halogen bonding environment, to such an extent that they provide better evidence for the occurrence of a halogen bond compared to the ^{13}C and ^{15}N SSNMR chemical shift of the carbon covalently bonded to iodine, or the nitrogen on the halogen bond acceptor. To the best of our knowledge, this is the first time that such a large effect has been observed for bromine atoms involved in halogen bonding.

Conclusions

We have presented the first modern $^{79/81}$Br NQR study of halogen bonds, performed on a series of cocrystals based on 1,4-dibromotetrafluorobenzene and the C–Br⋯N motif. Through a combination of pure NQR and nutation NQR, we have measured both the quadrupolar coupling constant (C_Q) and the asymmetry parameter (η). We demonstrate that this approach is sensitive to small changes in the halogen bond geometry, with the C_Q in good correlation with the XB length. The sensitivity of the C_Q values to the halogen bond geometry proved to be superior to ^{13}C and ^{15}N chemical shifts obtained by

solid-state NMR, even allowing for the discrimination of several crystallographically inequivalent halogen bonds.

Although the time-determining factor of this technique was the search for the NQR resonances, the reported correlation can be used in future work to narrow the frequency range to be scanned. As NQR is performed in the absence of an applied magnetic field and does not require sophisticated equipment, it can be readily implemented as a tool to characterize the bromine halogen bond, in excellent complementarity with solid-state NMR and diffraction methods.

Experimental

The starting materials were purchased from Sigma Aldrich and used without further purification. Solvents were purchased from Fisher Scientific and used as received. The synthesis of the cocrystal of 1,4-dibromotetrafluorobenzene (**1**, *p*-DBrTFB) with acridine (acd) to give **2** ((*p*-DBrTFB)(acd)), or phenazine (phz) to give **3** ((*p*-DBrTFB)(phz)), was performed as reported by Jones and collaborators.[45] The synthesis of the cocrystal of **1** with 4,4′-bipyridine (bipy) to give **4** ((*p*-DBrTFB)(bipy)) was performed as reported by De Santis *et al.*[46] The synthesis of the cocrystal of **1** with either 1,4-diazabicyclo[2.2.2]octane (dabco) to give **5** ((*p*-DBrTFB)(dabco)) or piperazine (pip) to give **6** ((*p*-DBrTFB)(pip)), was performed as reported by Cinčić *et al.*[47] Powder X-ray diffraction and ^{13}C CPMAS SSNMR were carried out to ensure phase purity (see the ESI†).

Pulsed $^{79/81}$Br NQR experiments were performed in the absence of an applied magnetic field using a Bruker Avance III 400 NMR spectrometer. A home-built probe was used, which consisted of a tuning capacitor, a matching capacitor, and a solenoid. All samples were ground and packed in 4 mm o.d. glass tubes prior to being placed inside the probe's RF coil for NQR analysis. Each spectrum was acquired using a Hahn–Echo pulse sequence ($\pi/2$–τ–π–τ–acquire), with a 3 μs $\pi/2$ pulse and 6 μs π pulse. A total of 256 or 1024 transients were acquired depending on the signal intensity, with a recycle delay of 0.5 s. In order to search for the NQR frequencies, the applied RF was incremented in steps of 150 kHz. The experimental spectra were fit using QUEST.[53] Nutation NQR spectra were recorded as per ref. 50. DC correction was applied to each nutation spectrum.

Density functional theory (DFT) calculations were performed using the Amsterdam Density Functional (ADF) software[54] with the metaGGA TPSS[55] functional and the TZ2P basis set implemented in ADF. Dispersion forces were accounted for using Grimme3 BJDAMP.[56] Scalar and spin–orbit relativistic effects were accounted for using ZORA[57] as implemented in the ADF software.

Conflicts of interest

There are no conflicts to declare.

Acknowledgements

Dr Glenn Facey and Dr Eric Ye are thanked for technical support. P. C. V. thanks the Istituto Nazionale della Previdenza Sociale (INPS) for a scholarship. P. M. J. S. and D. L. B. thank the Natural Sciences and Engineering Research Council of Canada for scholarship and research funding, respectively.

Notes and references

1 P. Politzer and J. S. Murray, *Crystals*, 2017, **7**, 212.
2 P. Politzer and J. S. Murray, *ChemPhysChem*, 2013, **14**, 278–294.
3 P. Politzer, J. S. Murray and T. Clark, in *Halogen Bonding I: Impact on Materials Chemistry and Life Sciences*, ed. P. Metrangolo and G. Resnati, Springer-Verlag Berlin, Berlin, 2015, vol. 358, pp. 19–42.
4 T. Clark, M. Hennemann, J. S. Murray and P. Politzer, *J. Mol. Model.*, 2007, **13**, 291–296.
5 G. R. Desiraju, P. S. Ho, L. Kloo, A. C. Legon, R. Marquardt, P. Metrangolo, P. Politzer, G. Resnati and K. Rissanen, *Pure Appl. Chem.*, 2013, **85**, 1711–1713.
6 A. Mukherjee, S. Tothadi and G. R. Desiraju, *Acc. Chem. Res.*, 2014, **47**, 2514–2524.
7 T. J. Mooibroek and P. Gamez, *CrystEngComm*, 2013, **15**, 4565–4570.
8 P. Metrangolo, F. Meyer, T. Pilati, G. Resnati and G. Terraneo, *Angew. Chem., Int. Ed.*, 2008, **47**, 6114–6127.
9 K. Raatikainen and K. Rissanen, *CrystEngComm*, 2011, **13**, 6972–6977.
10 K. E. Riley, J. S. Murray, J. Fanfrlik, J. Řezáč, R. J. Solá, M. C. Concha, F. M. Ramos and P. Politzer, *J. Mol. Model.*, 2011, **17**, 3309–3318.
11 C. B. Aakeröy, M. Baldrighi, J. Desper, P. Metrangolo and G. Resnati, *Chem.–Eur. J.*, 2013, **19**, 16240–16247.
12 A. Priimagi, G. Cavallo, P. Metrangolo and G. Resnati, *Acc. Chem. Res.*, 2013, **46**, 2686–2695.
13 P. Metrangolo, H. Neukirch, T. Pilati and G. Resnati, *Acc. Chem. Res.*, 2005, **38**, 386–395.
14 G. Cavallo, P. Metrangolo, T. Pilati, G. Resnati, M. Sansotera and G. Terraneo, *Chem. Soc. Rev.*, 2010, **39**, 3772–3783.
15 C. B. Aakeröy and C. L. Spartz, in *Halogen Bonding I: Impact on Materials Chemistry and Life Sciences*, ed. P. Metrangolo and G. Resnati, Springer-Verlag Berlin, Berlin, 2015, vol. 358, pp. 155–182.
16 G. Berger, J. Soubhye and F. Meyer, *Polym. Chem.*, 2015, **6**, 3559–3580.
17 R. Wilcken, M. O. Zimmermann, A. Lange, A. C. Joerger and F. M. Boeckler, *J. Med. Chem.*, 2013, **56**, 1363–1388.
18 M. Baldrighi, G. Cavallo, M. R. Chierotti, R. Gobetto, P. Metrangolo, T. Pilati, G. Resnati and G. Terraneo, *Mol. Pharmaceutics*, 2013, **10**, 1760–1772.
19 M. Baldrighi, D. Bartesaghi, G. Cavallo, M. R. Chierotti, R. Gobetto, P. Metrangolo, T. Pilati, G. Resnati and G. Terraneo, *CrystEngComm*, 2014, **16**, 5897–5904.
20 D. Bulfield and S. M. Huber, *Chem.–Eur. J.*, 2016, **22**, 14434–14450.
21 H. M. Yamamoto, Y. Kosaka, R. Maeda, J. Yamaura, A. Nakao, T. Nakamura and R. Kato, *ACS Nano*, 2008, **2**, 143–155.

22 L. C. Gilday, S. W. Robinson, T. A. Barendt, M. J. Langton, B. R. Mullaney and P. D. Beer, *Chem. Rev.*, 2015, **115**, 7118–7195.
23 G. Cavallo, P. Metrangolo, R. Milani, T. Pilati, A. Priimagi, G. Resnati and G. Terraneo, *Chem. Rev.*, 2016, **116**, 2478–2601.
24 D. L. Bryce and J. Viger-Gravel, in *Halogen Bonding I: Impact on Materials Chemistry and Life Sciences*, ed. P. Metrangolo and G. Resnati, Springer-Verlag Berlin, Berlin, 2015, vol. 358, pp. 183–203.
25 C. M. Widdifield, G. Cavallo, G. A. Facey, T. Pilati, J. Lin, P. Metrangolo, G. Resnati and D. L. Bryce, *Chem.–Eur. J.*, 2013, **19**, 11949–11962.
26 P. Cerreia Vioglio, L. Catalano, V. Vasylyeva, C. Nervi, M. R. Chierotti, G. Resnati, R. Gobetto and P. Metrangolo, *Chem.–Eur. J.*, 2016, **22**, 16819–16828.
27 J. Viger-Gravel, S. Leclerc, I. Korobkov and D. L. Bryce, *CrystEngComm*, 2013, **15**, 3168–3177.
28 J. Viger-Gravel, S. Leclerc, I. Korobkov and D. L. Bryce, *J. Am. Chem. Soc.*, 2014, **136**, 6929–6942.
29 M. Weingarth, N. Raouafi, B. Jouvelet, L. Duma, G. Bodenhausen, K. Boujlel, B. Schöllhorn and P. Tekely, *Chem. Commun.*, 2008, 5981–5983.
30 Y. Xu, J. Viger-Gravel, I. Korobkov and D. L. Bryce, *J. Phys. Chem. C*, 2015, **119**, 27104–27117.
31 P. M. J. Szell and D. L. Bryce, *J. Phys. Chem. C*, 2016, **120**, 11121–11130.
32 R. J. Attrell, C. M. Widdifield, I. Korobkov and D. L. Bryce, *Cryst. Growth Des.*, 2012, **12**, 1641–1653.
33 P. Cerreia Vioglio, M. R. Chierotti and R. Gobetto, *CrystEngComm*, 2016, **18**, 9173–9184.
34 J. Viger-Gravel, I. Korobkov and D. L. Bryce, *Cryst. Growth Des.*, 2011, **11**, 4984–4995.
35 J. Viger-Gravel, J. E. Meyer, I. Korobkov and D. L. Bryce, *CrystEngComm*, 2014, **16**, 7285–7297.
36 P. Pyykkö, *Mol. Phys.*, 2008, **106**, 1965–1974.
37 P. M. J. Szell and D. L. Bryce, *Concepts Magn. Reson., Part A*, 2016, **45A**, e21412.
38 G. S. Harbison, in *Characterization of Materials*, John Wiley & Sons, Inc., 2012, pp. 1214–1232.
39 G. K. Semin, T. A. Babushkina, S. P. Khrlakyan, E. Y. Pervova, V. V. Shokina and I. L. Knunyants, *Theor. Exp. Chem.*, 1971, **4**, 179–181.
40 G. Bowmaker and S. Hacobian, *Aust. J. Chem.*, 1968, **21**, 551–564.
41 G. Bowmaker and S. Hacobian, *Aust. J. Chem.*, 1969, **22**, 2047–2059.
42 G. A. Bowmaker, *J. Chem. Soc., Faraday Trans. 2*, 1976, **72**, 1964–1969.
43 C. R. Groom, I. J. Bruno, M. P. Lightfoot and S. C. Ward, *Acta Crystallogr., Sect. B: Struct. Sci., Cryst. Eng. Mater.*, 2016, **72**, 171–179.
44 G. S. Pawley, G. A. Mackenzie and O. W. Dietrich, *Acta Crystallogr., Sect. A: Cryst. Phys., Diffr., Theor. Gen. Crystallogr.*, 1977, **A33**, 142–145.
45 D. Cinčić, T. Friščić and W. Jones, *Chem. Mater.*, 2008, **20**, 6623–6626.
46 A. De Santis, A. Forni, R. Liantonio, P. Metrangolo, T. Pilati and G. Resnati, *Chem.–Eur. J.*, 2003, **9**, 3974–3983.
47 D. Cinčić, T. Friščić and W. Jones, *Chem.–Eur. J.*, 2008, **14**, 747–753.
48 Y. M. Udachin, N. N. Artamonova, A. F. Volkov, A. S. Lebedeva and E. N. Gur'yanova, *J. Appl. Spectrosc.*, 1978, **29**, 812–816.
49 R. Ramachandran and E. Oldfield, *J. Chem. Phys.*, 1984, **80**, 674–677.
50 G. S. Harbison, A. Slokenbergs and T. M. Barbara, *J. Chem. Phys.*, 1989, **90**, 5292–5298.
51 G. S. Harbison and A. Slokenbergs, *Z. Naturforsch. A*, 1990, **45**, 575–580.
52 R. Blinc and J. Seliger, *Z. Naturforsch. A*, 1992, **47**, 333–341.
53 F. A. Perras, C. M. Widdifield and D. L. Bryce, *Solid State Nucl. Magn. Reson.*, 2012, **45–46**, 36–44.
54 G. te Velde, F. M. Bickelhaupt, E. J. Baerends, C. Fonseca Guerra, S. J. A. Van Gisbergen, J. G. Snijders and T. Ziegler, *J. Comput. Chem.*, 2001, **22**, 931–967.
55 J. Tao, J. P. Perdew, V. N. Staroverov and G. E. Scuseria, *Phys. Rev. Lett.*, 2003, **91**, 146401.
56 S. Grimme, S. Ehrlich and L. Goerigk, *J. Comput. Chem.*, 2011, **32**, 1456–1465.
57 E. van Lenthe, A. Ehlers and E. J. Baerends, *J. Chem. Phys.*, 1999, **110**, 8943–8953.

Chapter 6 – Investigating the Halogen Bond Donor by ^{127}I Nuclear Quadrupole Resonance Spectroscopy: Insights from the Electric Field Gradient

Statement of Authenticity. Chapter 6 of this thesis was performed with the assistance of Lorraine Grebert, an international student from the Université de Poitier (France). Her role in this project was to prepare the compounds, verify the sample quality by powder X-ray diffraction, and find the lower ^{127}I NQR transition for the samples in the study. My role in this project was to conceive and design the experiment, choose the samples, assist Lorraine in preparing and analyzing the samples, find the upper ^{127}I NQR transitions, perform all DFT calculations, grow crystals of **1e** and collect all the single crystal X-ray data, interpret all the results, and prepare the final manuscript. Dr. David Bryce is acknowledged for guidance, support, and in preparing the manuscript. Dr. Jeffrey Ovens is acknowledged for solving the crystal structure of compound **1e**, while Dr. Bulat Gabidullin is acknowledged for solving the crystal structure of **1b**. Dr. Paul Morris is acknowledged for building the NQR probe that was essential for this experiment. Dr. Glenn Facey is acknowledged for helping me set up the ^{127}I NQR experiments using the new Avance III HD console for the 500 MHz NMR instrument.

Permissions. I declare that I have obtained permission from all coauthors to include this article in my thesis. This manuscript consists of a preprint to be published.

Supporting Information. As this article has not yet been published, all supporting information is available in Appendix II.

Chapter 6 – Investigating the Halogen Bond Donor by ^{127}I Nuclear Quadrupole Resonance Spectroscopy: Insights from the Electric Field Gradient

Halogen bonding is a non-covalent interaction occurring between the area of lower electron density associated with a covalently bonded halogen (halogen bond donor),[1,2] named the σ-hole,[3,4,5] and a nucleophilic center, such as a Lewis base (halogen bond acceptor).[6] Over the last decades, halogen bonding has emerged as a versatile non-covalent interaction for use in crystal engineering,[7,8] pharmaceuticals,[9,10,11] material sciences,[12,13] and anion receptors,[14,15,16,17] to name a few, with several reviews available on the subject.[18,19,20] This interest can be attributed in part to its favorable properties such as its tuneability[21,22] and linearity.[23] Despite its widespread usage as a supramolecular tool, the nature behind the halogen bond has yet to gain widespread acceptance.[24,25,26,27]

Solid-state NMR (SSNMR) has been shown to be a powerful tool to characterize halogen bonded adducts,[28,29] offering information on the chemical shifts,[30,31] *J*-couplings,[32,33] dipolar coupling,[34] and quadrupolar coupling (QC).[35,36,37,38] As a crystal engineering tool, the ^{13}C chemical shifts were shown to be sensitive to the occurrence of a halogen bond,[30,31] while the I···N halogen bond length has been measured using ^{15}N-^{127}I dipolar coupling.[34] Recently, we have applied ^{13}C and ^{19}F solid-state NMR[39] to investigate the quality of samples prepared by alternative preparation methods, such as mechanochemistry[40] and cosublimation.[41]

SSNMR of quadrupolar nuclei (spin $I > ½$) can offer insights into the quadrupolar interaction, which is the coupling between the quadrupole moment of a nucleus and the electric field gradient (EFG). The EFG consists of the derivative of the electric field at a nucleus, which

can be expressed as a 2nd rank traceless tensor with 3 components, $|V_{33}| \geq |V_{22}| \geq |V_{11}|$. The quadrupolar coupling is conveniently expressed in terms of its magnitude, the quadrupolar coupling constant (C_Q, eq. 1), along with its shape, the asymmetry parameter (η, eq. 2).

$$C_Q = eV_{33}Q/h \qquad \text{eq. 1}$$

$$\eta = (V_{11} - V_{22})/V_{33} \qquad \text{eq. 2}$$

Here, e is the fundamental charge constant, Q is the quadrupole moment, and h is the Planck constant. As a result, the quadrupolar coupling yields information on the electronic structure, which can be used to refine crystal structures[42] and learn more about chemical bonding. An article detailing the interpretation of the quadrupolar coupling is available elsewhere.[43]

Despite the availability of higher magnetic fields, the covalently bonded quadrupolar halogens, including $^{35/37}$Cl (spin I = 3/2), $^{79/81}$Br (spin I = 3/2), and ^{127}I (spin I = 5/2), remain challenging or unamenable to SSNMR. Fortunately, nuclear quadrupole resonance (NQR) spectroscopy is well-suited for nuclei subject to large quadrupole coupling, which is the case for quadrupolar halogens, and can be performed using the same radiofrequency equipment included with a SSNMR spectrometer but in the absence of a magnetic field.[44] Rather than broad line shapes as in NMR, however, pure NQR yields relatively sharp resonances which relate to the quadrupolar interaction. While spin-3/2 nuclei have a single transition (1/2 → 3/2), spin-5/2 nuclei exhibit two possible single-quantum transitions (1/2 → 3/2 & 3/2 → 5/2). As a result, finding both NQR transitions yields both the C_Q and η, with the help of a conversion table[45] and spectral simulation software, such as QUEST.[46]

Historically, NQR has had an important role as an investigational tool for non-covalent interactions, which have carried the name “charge transfer complex” in the literature. Moreover,

the quadrupolar halogens are receptive nuclei to study by NQR, and have received a significant amount of exposure,[47] rendering it a convenient tool to investigate interactions involving the halogens. While the term "halogen bonding" has been coined relatively recently in the literature,[48,49] there are sparse experimental NQR studies available fitting its definition while being supported by X-ray crystallography. By combining SSNMR and NQR spectroscopy, we have characterized the C-Cl···N halogen bond by probing the ^{35}Cl nucleus,[50] and the C-Br···N halogen bond by $^{79/81}$Br NQR.[51] However, with C_Q values ranging from 1600 to 2100 MHz,[47,50,52,53] NQR experiments performed on the ^{127}I nucleus of a halogen bond donor are challenging, as the resonances can range nearly one hundred of MHz for ν_1, and over one hundred MHz for ν_2.

With iodine being the strongest and most popular halogen bond donor, here we turn our attention to the ^{127}I nucleus (spin $I = 5/2$) and approach this problem using a combination of NQR spectroscopy and X-ray crystallography. We apply ^{127}I NQR spectroscopy to a series of cocrystals exhibiting the C-I···N halogen bond featuring 1,4-diiodobenzene (**1**) as the halogen bond donor and nitrogen-containing heterocycles as the halogen bond acceptor (shown in Figure 2.6.1.), identifying two new cocrystals by ^{127}I NQR, with the structure of **1e** solved by X-ray crystallography. The halogen bond donor **1** was chosen as a result of the availability of crystal structures exhibiting the C-I···N motif and due to the ^{127}I NQR frequencies being attainable using our equipment, with its fluorinated analogue exceeding our current experimental capabilities. We interpret the trends in the EFG across all quadrupolar halogens through a natural localized molecular orbital (NLMO) analysis, providing a decomposition of the EFG in terms of the

contributions from molecular orbitals, creating a global summary from the ^{35}Cl, $^{79/81}Br$, and ^{127}I experimental results.

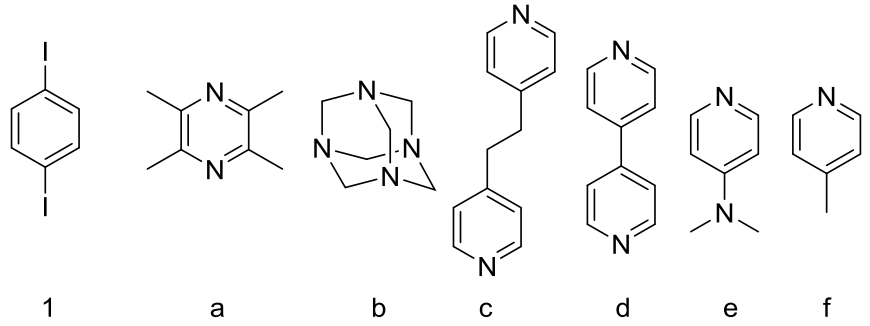

Figure 2.6.1. Molecular structure diagrams of the pure starting materials studied herein: 1,4-diiodobenzene (**1**), 2,3,5,6-tetramethylpyrazine (**a**), hexamethylenetetramine (**b**), 1,2-bis(4-pyridyl)ethane (**c**), 4,4'-bipyridyl (**d**), 4-dimethylaminopyridine (**e**), 4-methylpyridine (**f**).

Experimental.

1,4-diiodobenzene (98%) was purchased from Alfa Aesar. 2,3,5,6-tetramethylpyrazine (98%), hexamethylenetetramine, 1,2-bis(4-pyridyl)ethane (99%) 4,4'-bipyridyl (98%), 4-dimethylaminopyridine (99%) and 4-picoline (99%) were purchased from Sigma Aldrich. Solvents were purchased from Fisher Scientific. All solvents and reagents were used without further purification. Compound **1** was recrystallized from chloroform prior to the NQR analysis.[54] Compound **1a** was reproduced by cosublimation following literature procedure.[41] Compound **1b** was reproduced by solvent evaporation following the reported procedure.[55] Cocrystals **1c**,[30] **1d**,[55] **1e**, and **1f** were prepared by mechanochemical ball milling using a Retsch MM 400 ball mill. Both **1** and the respective Lewis base were added as powders successively to a 10 mL stainless steel milling jar in a 1:1 stoichiometric ratio for **1c** & **1d,** and 1:2 stoichiometric ratio for **1e** & **1f**. The ball millings were performed with a milling frequency of 30 Hz for a period of 45 minutes at room temperature using two stainless steel grinding balls. Single crystals of compound **1e** were grown

by cosublimation[41] using a home-built two-zoned tube furnace, heating **1** and **e** individually *in vacuo* from 25°C to 60°C at a rate of 40°C/hour, then from 60° to 100° at a rate of 20°C/hour, forming cocrystals at the center of the sublimation tube. The phase purity of each compound was verified by powder X-ray diffraction on a Rigaku Ultima IV instrument with a 2θ ranging from 5º to 65º at a rate of 1º per minute using CuKα radiation. Full experimental details, powder X-rays and ^{13}C solid-state NMR spectra can be found in the Appendix II.

^{13}C Solid-State NMR. The ^{13}C cross-polarization magic-angle spinning (CP/MAS) solid-state NMR experiments were performed on a Bruker Avance III NMR spectrometer operating at 9.4 T ($\nu_L(^{13}C)$ = 100.6 MHz) using a Bruker 4 mm HXY MAS probe. The $^{1}H \rightarrow {}^{13}C$ CP/MAS experiments were performed with a 3.5 μs proton π/2 pulse, a consistent 8 kHz MAS frequency, a 2000 μs contact time, and a 71 kHz ^{1}H decoupling frequency. The ^{13}C chemical shifts were referenced to glycine at 176.6 ppm (^{13}C=O) relative to tetramethylsilane (TMS). Further information, such as the recycle delays and the number of transients can be found in the Appendix II.

^{127}I Nuclear Quadrupole Resonance. The lower transitions (1/2 → 3/2) were acquired using the proton preamplifier of an Avance III 400 MHz NMR spectrometer using a Hahn echo (π/2 – τ – π – aq) pulse sequence with a τ delay of 28 μs and a π/2 pulse length of 2 μs, acquiring 1024 transients with a recycle delay of 0.5 seconds. The upper transitions (3/2 → 5/2) were acquired using the proton preamplifier of an Avance III HD 500 MHz NMR spectrometer using a Hahn echo (π/2 – τ – π – aq) pulse sequence with a τ delay of 20 μs and a π/2 pulse length of 8 μs. The full resonance was acquired using variable-offset cumulative spectral acquisition method (VOCS) using offset increments of 50 kHz acquiring 256 transients with a recycle delay of 0.5 seconds.[56] The

subspectra were coadded in the frequency domain to yield the full spectrum. In all cases, a homebuilt probe with a wide tuning range was used, consisting of a solenoid (RF) coil.

Single Crystal X-Ray Diffraction. Crystals of **1b** and **1e** were mounted on thin glass fibers using Parabar oil. Prior to data collection, the crystal of **1b** was cooled to 200 ± 2 K, whereas data for crystal **1e** were collected at room temperature. The data were collected on a Bruker Kappa ApexII single crystal diffractometer equipped with a sealed-tube Mo source (wavelength 0.71073 Å) with a Triumph monochromator and an ApexII CCD detector. The raw data collection and processing were performed with the Bruker Apex3 software package.[57] **1e** crystallized as a non-merohedral twin which was identified using CELL_NOW.[58] Semi-empirical absorption corrections based on equivalent reflections were applied using SADABS[59] for **1b** and TWINABS[60] for **1e** (taking into account twinning effects).[61] Systematic absences in the diffraction dataset and unit cell parameters were consistent with an orthorhombic *Cmcm* (#63) space group for **1b** and a triclinic $P\bar{1}$ (#2) space group for **1e**. The structures were solved by direct methods and refined with full-matrix least-squares procedures based on F^2, using ShelXL[62] WinGX,[63] and ShelXLe.[64] All non-hydrogen atoms were refined anisotropically. Final refinements for **1b** were performed taking into account twinning via HKLF5 data. Displacement ellipsoid plots for both structures were produced using ORTEP[65] (see the Appendix II), and uncertainties were estimated using PLATON for Windows.[66]

Computational chemistry. All DFT calculations were performed using the Amsterdam Density Functional software (ADF, 2018)[67,68,69] Models of the compounds studied here were generated using GaussView[70] using atomic positions taken from their respective crystal structures. The models used in the NLMO calculations consisted of chlorobenzene, chloropentafluorobenzene, bromobenzene, bromopentafluorobenzene, iodobenzene, and iodoperfluorobenzene interacting with pyridine at a $\theta_{\text{C-X}\cdots\text{N}}$ angle of 180º and varying the X···N distance. All models were optimized

prior to the calculations using a B3LYP functional and TZ2P basis set while constraining the halogen bond geometry, accounting for relativistic effects using ZORA[71] and dispersion corrections using Grimme3 BJDAMP.[72] The models used in the NLMO calculations were each optimized at an R_{XB} of 0.80 for consistency. The EFG and NLMO calculations were performed using the GGA revPBE functional with the TZ2P basis set, accounting for relativistic effects using ZORA.[71]

Results and Discussion

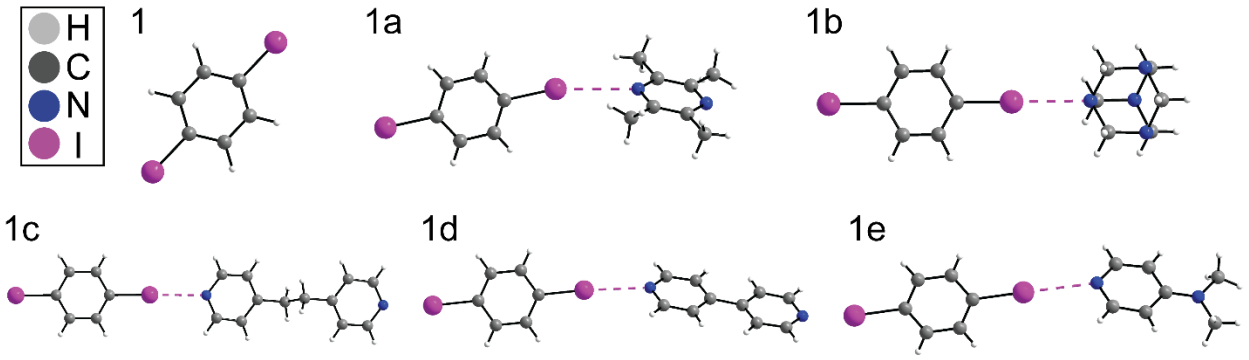

Figure 2.6.2. Depiction of the X-ray crystal structures of the compounds studied herein. The dashed magenta lines denote the I···N halogen bond.

The crystal structures under investigation here, presented in Figure 2.6.2, feature the molecule of **1** interacting with the nitrogen atom of the acceptor molecule *via* a I···N halogen bond. Each structure features a single iodine atom in the asymmetric unit exhibiting a halogen bond, with the geometric parameters of the halogen bond summarized in Table 2.6.1. Several structures have been taken from the CSD database, including **1**,[54] **1a**,[41] **1c**,[30] and **1d**.[55] While **1b** has been previously reported,[55] we report structure **1b** in the *Cmcm* space group, with the resulting structure being in much better agreement with the experimental powder X-ray diffractogram (see Figure

S6.2.5 of the Appendix II). Additionally, we report structure **1e** as a new structure, with the occurrence of a halogen bond being initially identified following the mechanochemical preparation using ^{127}I NQR spectroscopy. The resulting structure **1e** exhibits one I···N halogen bond in a 1:2 equivalence (**1**:**e**), with an absence of any significant secondary interaction such as hydrogen bonds. While structure **1e** was accessible by mechanochemistry, attempts at growing crystals suitable for single-crystal X-ray diffraction by slow evaporation did not yield a suitable cocrystal. As a result, crystals of **1e** were grown by cosublimation[41] over a period of ~4 hours, with the resulting structure being representative of the sample obtained from the mechanochemical ball milling, verified by powder X-ray diffraction. Selected X-ray crystallographic parameters of structures **1b** and **1e** can be found in the Appendix II.

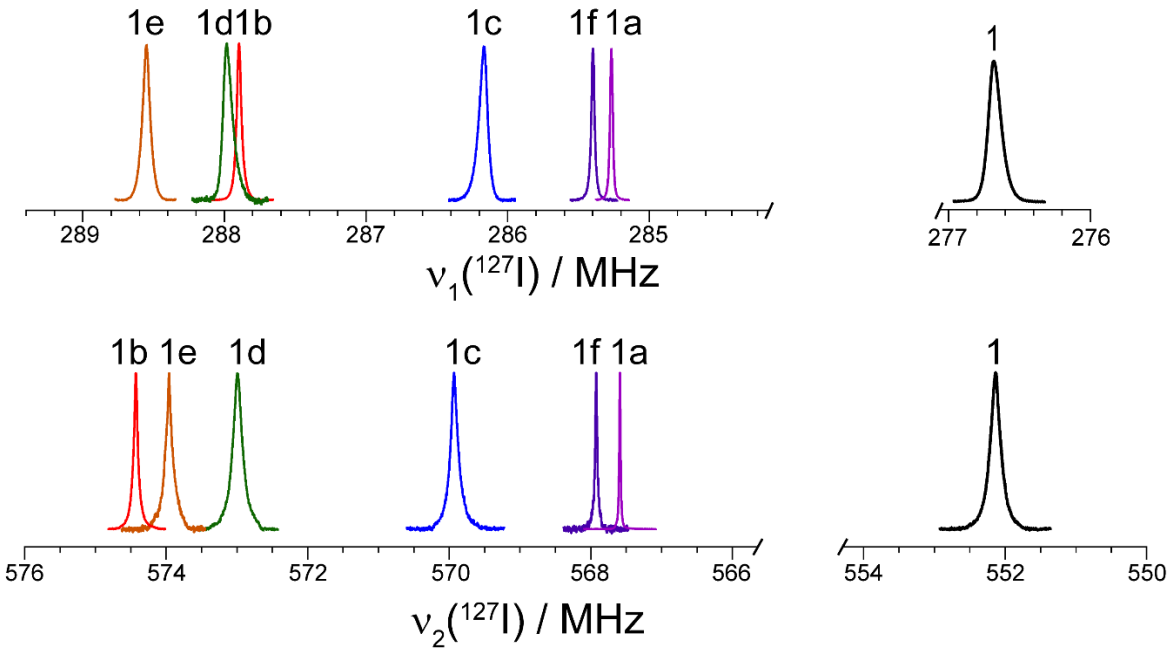

Figure 2.6.3. ^{127}I NQR spectra of **1** and the halogen bonded cocrystals studied herein, including two NQR transitions, ν_1 (1/2 → 3/2) and ν_2 (3/2 → 5/2). The regions between 277 - 284 MHz for ν_1 and 554 - 566 MHz for ν_2 were removed for clarity.

Both ^{127}I NQR transitions, shown in Figure 2.6.3, were acquired using consoles otherwise dedicated to SSNMR. In order to observe ν_1 in the region of 276 – 289 MHz, the proton channel of a 400 MHz SSNMR spectrometer was used, while the proton channel of a 500 MHz SSNMR spectrometer was used to observe ν_2 in the 550 – 576 MHz range. In both cases, given the high receptivity of the ^{127}I nucleus, a significant amount of signal was obtained for both the pure starting material and the cocrystals after only a few seconds. As the linewidths of the 3/2 → 5/2 transition exceeded the bandwidth of the probe at this high frequency, the full breadth of the resonance was acquired at steps of 50 kHz and coadded in frequency domain in order to reproduce the full signal.[56]

Using the frequencies of both ν_1 and ν_2, both the C_Q and η were determined and summarized in Table 2.6.1.

Table 2.6.1. Experimental NQR frequencies and quadrupolar coupling parameters (C_Q, η) obtained at room temperature (298 ± 2 K). The DFT-calculated quadrupolar coupling parameters are italicized.

sample	$d_{I\cdots N}$ / Å [a]	$\theta_{C\text{-}I\cdots N}$ / ° [a]	ν_1 / MHz	ν_2 / MHz	$\lvert C_Q \rvert$ / MHz	η
1	N/A	N/A	276.68 ± 0.03	552.1 ± 0.3	1841.0 ± 0.9 *-1894.2*	0.042 ± 0.004 *0.06*
1a	3.298(5)	167.25(17)	285.27 ± 0.01	567.6 ± 0.1	1893.6 ± 0.3 *-1922.6*	0.063 ± 0.001 *0.07*
1b	2.981(2)	173.26(9)	287.89 ± 0.01	574.4 ± 0.2	1915.4 ± 0.6 *-1917.2*	0.043 ± 0.003 *0.05*
1c	2.9674(18)	177.41(6)	286.17 ± 0.03	569.9 ± 0.3	1901.1 ± 0.9 *-1952.1*	0.057 ± 0.003 *0.05*
1d	3.032(3)	176.05(11)	287.98 ± 0.02	573.0 ± 0.4	1911.6 ± 1.2 *-1938.5*	0.063 ± 0.004 *0.07*
1e	3.031(4)	179.17(10)	288.55 ± 0.02	574.0 ± 0.3	1914.9 ± 0.9 *-1961.2*	0.065 ± 0.003 0.07
1f	N/A	N/A	285.40 ± 0.01	567.9 ± 0.1	1894.5 ± 0.3	0.063 ± 0.001

[a] Errors estimated with Platon for Windows.

Clear changes in the ^{127}I NQR frequencies are observed upon halogen bonding, with an increase of between 8.5 MHz and 11.9 MHz between the pure starting material and cocrystals for ν_1, and between 15.5 MHz and 22.3 MHz for ν_2. These large changes in the NQR frequencies have provided a reliable indicator for the occurrence of halogen bonding, which has allowed the successful cocrystallization of compound **1e** to be recognized. The smallest increase in the C_Q was of 52.6 ± 0.9 MHz for **1a** and the largest increase was of 73.9 ± 1.3 MHz for **1e**, with each of these increases attributed to the electronic changes occurring at the iodine atom upon the formation of the I···N halogen bond. In contrast to the changes observed in the C_Q, increases in η were

merely on the order of 0.02, with this minor change in η being attributed to the linearity of the halogen bond nearly maintaining the axial symmetry at the iodine atom, with the largest component of the EFG tensor remaining oriented along the C-I···N bond axis.

The observed increase in the ^{127}I C_Q was between 52.6 – 73.9 MHz upon halogen bonding, which follows the same trend encountered in our previous investigations of the ^{35}Cl and $^{79/81}$Br nuclei. The increase in the C_Q was between 0.3 – 1.2 MHz for ^{35}Cl,[50] whereas the increase in the C_Q for the ^{81}Br nucleus was of 12.0 – 19.9 MHz and for the ^{79}Br nucleus was of 14.2 – 23.7 MHz.[51] These changes represent increases of 0.4% to 1.6% for ^{35}Cl, 2.3% to 3.8% for $^{79/81}$Br, and 2.9% to 4.0% for ^{127}I. Each nucleus has a unique Sternheimer antishielding factor[73,74] and quadrupole moment (Q[^{127}I] = -617 mb; Q[^{79}Br] = 308.7(2) mb); Q[^{81}Br] = 257.9(2) mb; Q[^{35}Cl] = -81.12 mb),[75] with the latter taken into account using Eq. 1 and solving for V_{33}.

These increases in the C_Q is in agreement with previously reported ^{129}I Mössbauer results obtained in iodine···nitrogen complexes,[76,77,78,79] further supporting the trends. However, in contrast to our results, an earlier report investigating complexes formed between diiodoalkanes and amines by ^{127}I NQR has found a decrease in the NQR frequency by 6.8 MHz, with a proposed C-I···N motif resembling a halogen bond.[80] However, without support from X-ray results, it is difficult to attribute the motif solely by NQR shifts. We propose that the resulting structure from their investigation may not fit the formal definition of a halogen bond.

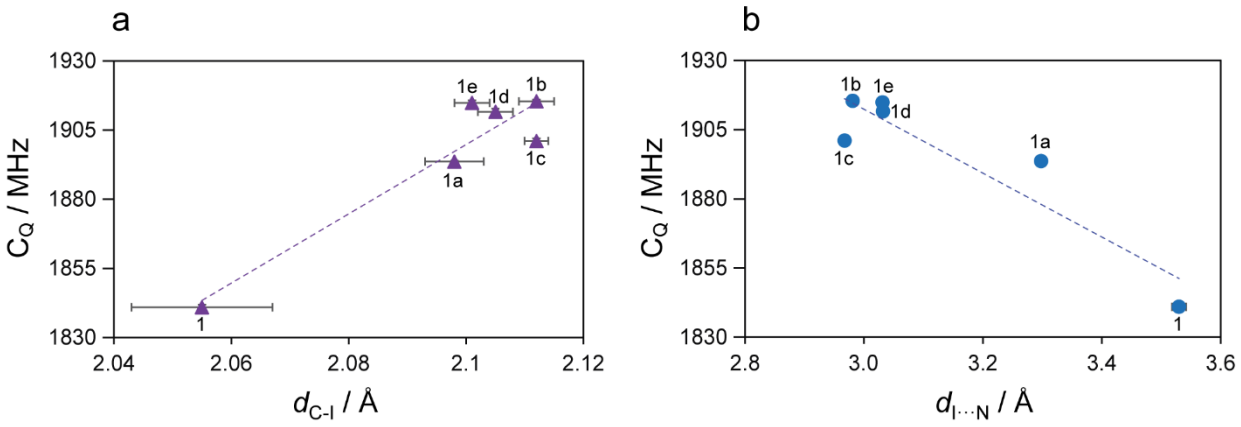

Figure 2.6.4. Experimental C_Q values (MHz) derived from ^{127}I NQR experiments as a function of (*a*) the C-I bond length (in Å) and (*b*) the I···N halogen bond length (in Å). The lines of best fit are: (*a*) $y = 1252.8x - 731.09$; $R^2 = 0.89$ and (*b*) $y = -115.5x + 2258.9$; $R^2 = 0.85$. The black bars denote the experimental errors derived from the X-ray and NQR data.

Shown in Figure 2.6.4, the changes in the C_Q correlate well with both the lengthening of the C-I covalent bond and with the I···N halogen bond length. It has been shown that the C-I bond stretches upon halogen bonding, with the resulting changes in the vibrational frequencies being a good identifier of halogen bonded complexes.[81] Further, the C-I bond lengthening associated with the halogen bond has been correlated with the ^{13}C chemical shift of the carbon covalently bonded to iodine, with changes on the order of several ppm observed in the ^{13}C SSNMR spectrum.[30,33] Consequently, the ^{127}I C_Q correlates with both the C-I covalent bond length and the halogen bond distance.

In order to further investigate the origin of the changes in the ^{127}I C_Q observed experimentally, in addition to our previous investigations on the ^{35}Cl and $^{79/81}$Br nuclei, we have performed a series of DFT calculations on a model of a haloperfluorobenzene (halo = chloro, bromo, iodo) interacting with a pyridine molecule, varying the X···N distance with an C-X···N angle fixed at 180°. The calculation results, shown in Figure 2.6.5, provides a decomposition of the largest component of the EFG tensor (V_{33}) in terms of the contributions of several molecular

orbitals, including contributions from: the lone pair orbitals on the halogen, the C-X bonding orbital, and the core orbitals of the halogen. The V_{33} effectively translates to the C_Q using eq. 1, accounting for the different quadrupole moments. This series of calculations was repeated on a model of non-fluorinated halobenzene interacting with pyridine (see Figure S6.2.3 of the Appendix II) in order to investigate the impact of fluorination on the changes in V_{33}. All calculated values can be found in the Tables S6.2.5 to S6.2.10 of the Appendix II.

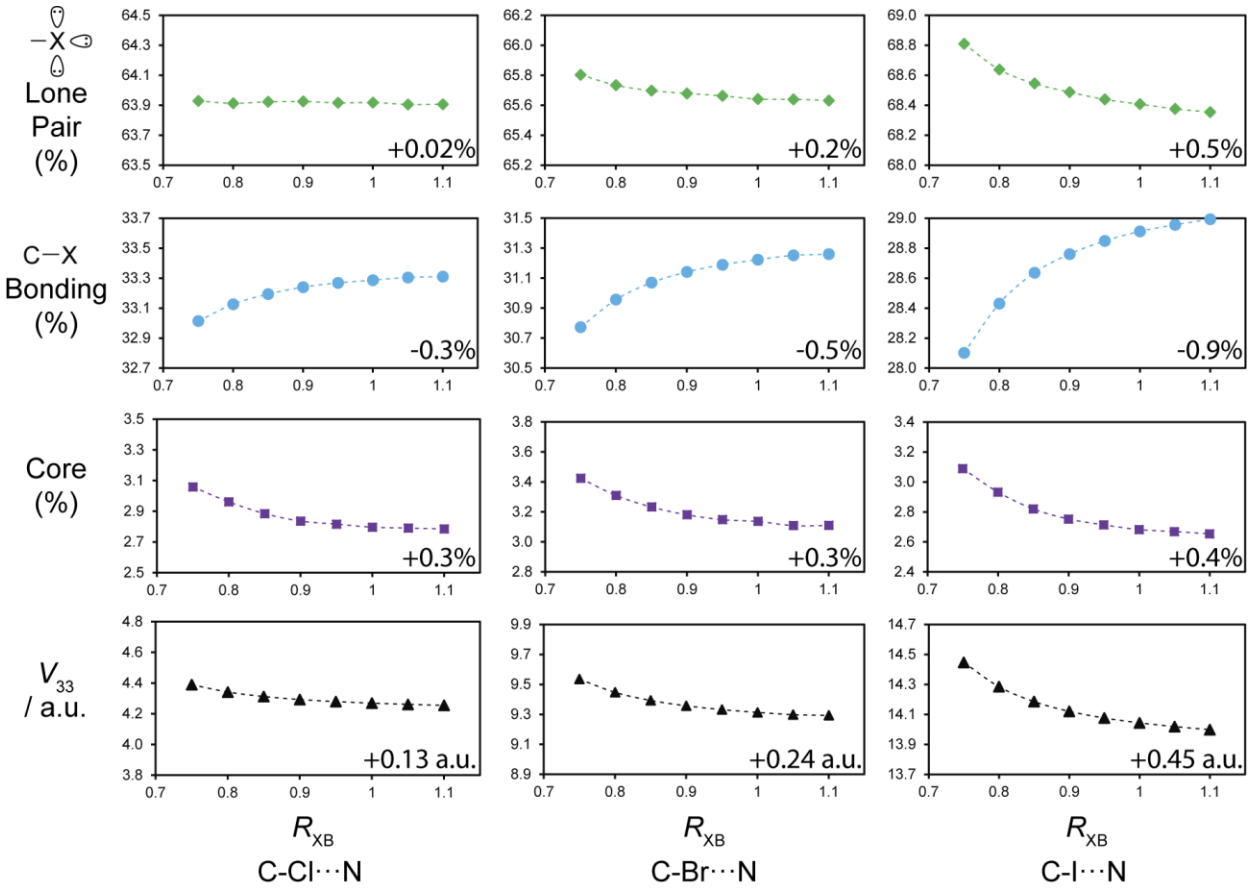

Figure 2.6.5. DFT-calculated natural localized molecular orbital (NLMO) contributions to V_{33} (black triangles) as a function of the normalized distance parameter, R_{XB}, including the absolute contributions from the lone pair orbitals (green diamonds), C-X bonding orbital (blue circles), and core orbitals (purple squares) for chlorine, bromine, and iodine in the C-X···N halogen bonding motif consisted of haloperfluorobenzene interacting with pyridine. The total percentage changes are shown on the corner of each graph.

The natural localized molecular orbital (NLMO) contributions to V_{33}, shown in Figure 2.6.5, are presented in percentage contributions to ease the interpretation, accounting for all contributions above 5% of V_{33}. The addition of the contributions from the lone pair, bonding, and core orbital yields the absolute value of V_{33}, and when in percentage, gives 100% of V_{33}. While the lone pair and core orbitals have a consistent positive contribution to V_{33}, the C-X bonding orbital has a negative contribution to V_{33}. As a result, a lowering in the contribution from the bonding orbital causes an overall increase in V_{33}. In order to account for differences in the van der Waals radii of the chlorine, bromine, and iodine atoms, the halogen bond length is expressed in the form of a normalized distance parameter (R_{XB}), the ratio of the halogen bond length and the sum of the van der Waals radii, rather than the halogen bond length.[82]

Across all halogens, an increase in V_{33} is observed, which is attributed to an increase in the lone pair & core orbital contributions, and a decrease in the C-X bonding orbital contributions, with these changes become more pronounced as the X···N distance is reduced (lower R_{XB}). Furthermore, the magnitude of change in the NLMO contributions increases in the order Cl < Br < I, which is manifested experimentally with the increases in the C_Q following the order Cl < Br < I. The changes in the C-X bonding orbital contribution is the most significant for all halogens, ranging from -0.3% for chlorine to -0.9% for iodine. The second largest changes occur in the lone pair orbital contributions, with an increase of 0.02% observed for chlorine and 0.5% for iodine

upon the reduction in R_{XB}. In comparison, the changes in the core orbitals does not vary significantly between the halogens, with an increase of 0.3% to 0.4% across all halogens.

The NLMO analysis carried out on the non-fluorinated halobenzene···pyridine model, shown in Figure S6.2.3 of the Appendix II, reveals the same trends in the contributions from the C-X bonding orbital and core orbital to V_{33}. However, rather than observing a consistent increase in the lone pair contributions for all halogens, a decrease of 0.1% and 0.03% is observed for chlorine and bromine, respectively, with an increase of 0.2% observed for iodine. This contrast between the fluorinated and non-fluorinated halobenzene may be attributed to the unfavorable formation of weak C-Cl···N and C-Br···N halogen bonds, causing changes in the molecular orbitals that differ from the strong halogen bond occurring with the perfluorinated donors.

Comparing these results to our previous NLMO investigations of the chlorine halogen bond donor, the trends in the absolute values for each contribution are in agreement, while the magnitude of change differs, especially in V_{33}.[50] For instance, there is a calculated increase in V_{33} of 0.009 a.u. comparing the halogen bonded site 2a to site 2b, whereas we have calculated a difference of 0.081 a.u. when comparing the results of the chloroperfluorobenzene at a geometry of R_{XB} 0.75 and 0.80. As a result, the smaller changes in V_{33} resulted in less pronounced changes in the percentile contributions and is attributed to the weaker halogen bond observed in those chloronitrile compounds.

Overall, this work combines data from our previous ^{35}Cl & $^{79/81}$Br studies on halogen bonding,[50,51] supporting the role of electronic rearrangements occurring on the halogen bond donor upon the formation of a halogen bond. The resulting changes in the EFG across all halides appears to be in agreement with previous discussions on the role of polarization in σ-hole interactions[2,83,84,85] and additional computational work.[86]

Conclusions

A series of halogen bonded cocrystals featuring 1,4-diiodobenzene as the halogen bond donor was investigated by ^{127}I nuclear quadrupole resonance spectroscopy, revealing an increase in the C_Q on the order of 52.6 to 73.9 MHz upon the formation of a halogen bond. In comparison to the experimental values from our previous work, we observe the largest changes in V_{33} in the order: I > Br > Cl. The trends observed here contrast a previous ^{127}I NQR analysis of C-I···N complexes, with the differences attributed to the iodine contact in those compounds not falling within the definition of a halogen bond. The changes in the C_Q observed here were interpreted with the use of DFT calculations, decomposing the contributions of V_{33} in terms of natural localized molecular orbitals. The results suggest that upon halogen bonding, there is an increase in the lone pair and core orbital contributions to V_{33}, while there is a decrease in the C-X bonding orbital contributions (X = Cl, Br, I), consistent with our previous investigation on the chlorine donor. Finally, the computational work suggests that the strength of the halogen bond donor may have an impact on the electronic reconfiguration occurring upon the formation of a halogen bond, with fluorinated donors incurring larger changes in V_{33}.

Conflicts of Interest

There are no conflicts to declare.

Acknowledgements

PMJS and DLB thank the Natural Sciences and Engineering Research Council of Canada for a scholarship and for research funding, respectively. We also thank Dr. Bulat Gabidullin and Dr. Jeffrey Ovens for their X-ray services.

Supporting Information Available

CIFs, powder X-ray diffractograms, and further experimental details are available in the Appendix II. For full diffraction datasets, refer to CCDC numbers 1898757 and 1898758.

References.

[1] Guo, N.; Maurice, R.; Teze, D.; Graton, J.; Champion, J.; Montavon, G.; Galland, N. *Nat. Chem.* **2018**, *10*, 428-434.

[2] Politzer, P.; Murray, J.S.; Clark, T. *Phys. Chem. Chem. Phys.* **2010**, *12*, 7748-7757.

[3] Clark, T.; Hennemann, M.; Murray, J.S.; Politzer, P. *J. Mol. Model.* **2007**, *13*, 291-296.

[4] Politzer, P.; Murray, J.S. *Crystals* **2017**, *7*, 212.

[5] Politzer, P.; Murray, J.S.; Clark, T.; Resnati, G. *Phys. Chem. Chem. Phys.* **2017**, *19*, 32166-32178.

[6] Desiraju, G.R.; Shing Ho, P.; Kloo, L.; Legon, A.C.; Marquardt, R.; Metrangolo, P.; Politzer, P.; Resnati, G.; Rissanen, K. *Pure Appl. Chem.* **2013**, *85*, 1711-1713.

[7] Mukherjee, A.; Tothadi, S.; Desiraju, G.R. *Acc. Chem. Res.* **2014**, *47*, 2514-2524.

[8] Aakeröy, C.B.; Wijethunga, T.K.; Desper, J. *J. Mol. Struc.* **2014**, *1072*, 20-27.

[9] Ford, M.C.; Shing Ho, P. *J. Med. Chem.* **2016**, *59*, 1655-1670.

[10] Baldrighi, M.; Bartesaghi, D.; Cavallo, G.; Chierotti, M.R.; Gobetto, R.; Metrangolo, P.; Pilati, T.; Resnati, G.; Terraneo, G. *CrystEngComm* **2014**, *16*, 5897-5904.

[11] Baldrighi, M.; Cavallo, G.; Chierotti, M.R.; Gobetto, R.; Metrangolo, P.; Pilati, T.; Resnati, G.; Terraneo, G. *Mol. Pharmaceutics* **2013**, *10*, 1760-1772.

[12] Salunke, J.K.; Durandin, N.A.; Ruoko, T.-P.; Candeias, N.R.; Vivo, P.; Vuorimaa-Laukkanen, E.; Laaksonen, T.; Priimagi, A. *Sci. Rep.* **2018**, *8*, 14431-

[13] Priimagi, A.; Cavallo, G.; Metrangolo, P.; Resnati, G. *Acc. Chem. Res.* **2013**, *11*, 2686-2695.

[14] Lim, J.Y.C.; Marques, I.; Félix, V.; Beer, P.D. *J. Am. Chem. Soc.* **2017**, *139*, 12228-12239.

[15] Barendt, T.A.; Robinson, S.W.; Beer, P.D. *Chem. Sci.* **2016**, *7*, 5171-5180.

[16] Barendt, T.A.; Docker, A.; Marques, I.; Félix, V.; Beer, P.D. *Angew. Chem. Int. Ed.* **2016**, *55*, 11069-11076.

[17] Riel, A.M.S.; Decato, D.A.; Sun, J.; Massena, C.J.; Jessop, M.J.; Berryman, O.B. *Chem. Sci.* **2018**, *9*, 5828-5836.

[18] Cavallo, G.; Metrangolo, P.; Milani, R.; Pilati, T.; Priimagi, A.; Resnati G.; Terraneo, G. *Chem. Rev.* **2016**, *116*, 2478-2601.

[19] Gilday, L.C.; Robinson, S.W.; Barendt, T.A.; Langton, M.J.; Mullaney, B.R.; Beer, P.D. *Chem. Rev.* **2015**, *115*, 7118-7195.

[20] Berger, G.; Soubhye, J.; Meyer, F. *Polym. Chem.* **2015**, *6*, 3559-3580.

[21] Riley, K.E.; Murray, J.S.; Fanfrlík, J.; Řezáč, J.; Solá, R.J.; Concha, M.C.; Ramos, F.M.; Politzer, P. *J. Mol. Model.* **2011**, *17*, 3309-3318.

[22] Riley, K.E.; Murray, J.S.; Fanfrlík, J.; Řezáč, J.; Solá, R.J.; Concha, M.C.; Ramos, F.M.; Politzer, P. *J. Mol. Model.* **2013**, *19*, 4651-4659.

[23] Huber, S.M.; Scanlon, J.D.; Jimenez-Izal, E.; Ugalde, J.M.; Infante, I. *Phys. Chem. Chem. Phys.* **2013**, *15*, 10350-10357.

[24] Thirman, J.; Engelage, E.; Huber, S.M.; Head-Gordon, M. *Phys. Chem. Chem. Phys.* **2018**, *20*, 905-915.

[25] Clark, T.; Politzer, P.; Murray, J.S. *WIREs Comput. Mol. Sci.* **2015**, *5*, 169-177.

[26] Politzer, P.; Murray, J.S.; Clark, T. *J. Mol. Model.* **2015**, *21*, 52.

[27] Legon, A.C. *Phys. Chem. Chem. Phys.* **2010**, *12*, 7736-7747.

[28] Cerreia Vioglio, P.; Chierotti, M.R.; Gobetto, R. *CrystEngComm,* **2016**, *18*, 9173-9184.

[29] Szell, P.M.J.; Bryce, D.L. *Modern Magn. Reson.* **2016**, pp. 1-18.

[30] Cerreia Vioglio, P.; Catalano, L.; Vasylyeva, V.; Nervi, C.; Chierotti, M.R.; Resnati, G.; Gobetto, R.; Metrangolo, P. *Chem. Eur. J.* **2016**, *22*, 16819-16828.

[31] Viger-Gravel, J.; Leclerc, S.; Korobkov, I.; Bryce, D.L. *CrystEngComm*. **2013**, *15*, 3168-3177.

[32] Xu, Y.; Viger-Gravel, J.; Korobkov, I.; Bryce, D.L. *J. Phys. Chem. C* **2015**, *119*, 27104-27117.

[33] Viger-Gravel, J.; Meyer, J.E.; Korobkov, I.; Bryce, D.L. *CrystEngComm*. **2014**, *16*, 7285-7297.

[34] Weingarth, M.; Raouafi, N.; Jouvelet, B.; Duma, L.; Bodenhausen, G.; Boujlel, K.; Schöllhorn, B.; Tekely, P. *Chem. Commun.* **2008**, 5981-5983.

[35] Viger-Gravel, J.; Leclerc, S.; Korobkov, I.; Bryce, D.L. *J. Am. Chem. Soc.* **2014**, *136*, 6929-6942.

[36] Widdifield, C.M.; Cavallo, G.; Facey, G.A.; Pilati, T.; Lin, J.; Metrangolo, P.; Resnati, G.; Bryce, D.L. *Chem. Eur. J.* **2013**, *19*, 11949-11962.

[37] Attrell, R.J.; Widdifield, C.M.; Korobkov, I.; Bryce, D.L. *Cryst. Growth Des.* **2012**, *12*, 1641-1653.

[38] Szell, P.M.J.; Cavallo, G.; Terraneo, G.; Metrangolo, P.; Gabidullin, B.; Bryce, D.L. *Chem. Eur. J.* **2018**, *24*, 11364-11376.

[39] Szell, P.M.J.; Gabriel, S.A.; Gill, R.D.D.; Wan, S.Y.H.; Gabidullin, B.; Bryce, D.L. *Acta Cryst.* **2017**, *C73*, 157-167.

[40] Szell, P.M.J.; Dragon, J.; Zablotny, S.; Harrigan, S.R.; Gabidullin, B.; Bryce, D.L. *New J. Chem.* **2018**, *42*, 10493-10501.

[41] Szell, P.M.J.; Gabriel, S.A.; Caron-Poulin, E.; Jeannin, O.; Fourmigué, M.; Bryce, D.L. *Cryst. Growth Des.* **2018**, *18*, 6227-6238.

[42] Perras, F.A.; Bryce, D.L. *J. Phys. Chem. C,* **2012**, *116*, 19472-19482.

[43] Autschbach, J.; Zheng, S.; Schurko, R.W. *Concepts Magn. Reson.* **2010**, *36A*, 84-126.

[44] Szell, P.M.J.; Bryce, D.L. *Concepts Magn. Reson.* **2016**, *45A*, e21412.

[45] Livington, R.; Zeldes, H. Table of Eigenvalues for Pure Quadrupole Spectra, Spin 5/2. *Oak Ridge, Tenn. : Oak Ridge National Laboratory*. **1955**.

[46] Perras, F.A.; Widdifield, C.M.; Bryce, D.L. *Solid State Nucl. Magn. Reson.* **2012**, *45-46*, 36-44.

[47] Lucken, E.A.C. *Nuclear Quadrupolar Coupling Constants;* Academic Press: London, 1969.

[48] Legon, A.C. *Angew. Chem. Int. Ed.* **1999**, *38*, 2686-2714.

[49] Metrangolo, P.; Resnati, R. *Chem. Eur. J.* **2001**, *7*, 2511-2519.

[50] Szell, P.M.J.; Bryce, D.L. *J. Phys. Chem. C* **2016**, *120*, 11121-11130.

[51] Cerreia Vioglio, P.; Szell, P.M.J.; Chierotti, M.R.; Gobetto, R.; Bryce, D.L. *Chem. Sci.* **2018**, *9*, 4555-4561.

[52] Szell, P.M.J.; Bryce, D.L. *Annu. Rep. NMR Spectrosc.* **2015**, *84*, 115-162.

[53] Widdifield, C.M.; Chapman, R.P.; Bryce, D.K.; *Annu. Rep. NMR Spectrosc*. **2009**, *66*, 195-326.

[54] Hinchliffe, A.; Munn, R.W.; Pritchard, R.G.; Spicer, C.J. *J. Mol. Struc.* **1985**, *130*, 93-96.

[55] Walsh, R.B.; Padgett, C.W.; Metrangolo, P.; Resnati, G.; Hanks, T.W.; Pennington, W.T. *Cryst. Growth Des.* **2001**, *1*, 165-175.

[56] Massiot, D.M.; Farnan, I.; Gautier, N.; Trumeau, D.; Trokiner, J.; Coutures, J.P. *Solid State Nucl. Magn. Reson.* **1995**, *4*, 241-248.

[57] APEX 2, Bruker AXS Inc., Madison, Wisconsin, USA, 2012.

[58] Sheldrick, G. M. (2008). CELL_NOW. Version 2008/4. Georg-August-Universität Göttingen, Göttingen, Germany

[59] Krause, L., Herbst-Irmer, R., Sheldrick, G. M. & Stalke, D. (2015). J. Appl. Crystallogr. 48.

[60] Sheldrick, G. M. (2012). TWINABS. Version 2012/1. Georg-August-Universität Göttingen, Göttingen, Germany.

[61] G.M. Sheldrick, SADABS, Program for empirical absorption correction of area detector data, University of Göttingen, Germany, 1996.

[62] G.M. Sheldrick, *Acta Cryst.*, 2015, C**71**, 3-8.

[63] L.J. Farrugia, *J. Appl. Crystallogr.*, 1999, **32**, 837-838.

[64] C. B. Hübschle, G. M. Sheldrick and B. Dittrich, ShelXle: a Qt graphical user interface for SHELXL, J. Appl. Cryst., 44, (2011) 1281-1284. [doi:10.1107/S0021889811043202]

[65] L.J. Farrugia, *J. Appl. Cryst.*, **2012**, 45, 849-854.

[66] A.L. Spek, *Acta Cryst.*, 2009, **D65**, 148-155.

[67] te Velde, G.; Bickelhaupt, F. M.; Baerends, E. J.; Fonseca Guerra, C.; van Gisbergen, S. J. A.; Snijders, J. G.; Ziegler, T. Chemistry with ADF. *J. Comput. Chem.* **2001**, *22*, 931-967.

[68] Fonseca Guerra, C.; J. G. Snijders; te Velde, G.; Baerends, E.J. Towards an Order-N DFT Method. *Theor. Chem. Acc.* **1998**, *99*, 391-403.

[69] ADF2018, SCM, Theoretical Chemistry, Vrije Universiteit, Amsterdam, The Netherlands, http://www.scm.com

[70] GaussView, Version 4.1, Dennington, R., Keith, T., Millam, J. *Semichem Inc., Shawnee Mission, KS,* **2009**.

[71] Van Lenthe, E.; Ehlers, A.; Baerends, E.J. *J. Chem. Phys.* **1999**, *110*, 8943-8953.

[72] Grimme, S.; Ehrlich, S.; Goerigk, L. *J. Comput. Chem.* **2011**, *32*, 1456-1465.

[73] Sternheimer, R. *Phys. Rev.* **1950**, *80*, 102-103.

[74] Sternheimer, R. *Phys. Rev.* **1951**, *84*, 244-253.

[75] Pyykkö, P. *Mol. Phys.* **2018**, *116*, 1328-1338.

[76] Wynter, C.I.; Hill, J.; Bledsoe, W.; Shenoy, G.K.; Ruby, S.L. *J. Chem. Phys.* **1969**, *50*, 3872.

[77] Bukshpan, S.; Goldstein, C.; Sonnino, T.; May, L.; Pasternak, M. *J. Chem. Phys.* **1975**, *62*, 2606-2609.

[78] Sakai, H.; Maeda, Y.; Ichiba, S.; Negita, H. *J. Chem. Phys.* **1980**, *72*, 6192-6198.

[79] Sakai, H.; Matsuyama, T>; Maeda, Y.; Yamaoka, H. *J. Chem. Phys.* **1981**, *75*, 5155-5159.

[80] G.K. Semin, T.A. Babushkina, S.P. Khralakyan, E.Ya. Pervova, V.V. Shokina, I.L. Knunyants, *Theor. Exp. Chem.* 1968, 4, 275-277.

[81] W. Wang, Y. Zhang, B. Ji, A. Tian, *J. Chem. Phys.* **2011**, *134*, 224303

[82] Bondi, A. *J. Phys. Chem.* **1964**, *68*, 441-451.

[83] Politzer, O.; Murray, J.S. *ChemPhysChem.* **2013**, *14*, 278-294.

[84] Politzer, P.; Murray, J.S.; Clark, T. *Phys. Chem. Chem. Phys.* **2013**, *15*, 11178-11189.

[85] Politzer, P.; Riley, K.E.; Bulat, F.A.; Murray, J.S. *Comput. Theor. Chem.* **2012**, *998*, 2-8.

[86] Duarte, D.J.R.; Sosa, G.L.; Peruchena, N.M.; Alkorta, I. *Phys. Chem. Chem. Phys.* **2016**, *18*, 7300-7309.

Summary of Part 2 – Investigating the Halogen Bond Donor

In this part of the thesis, we have fully characterized all quadrupolar halogen bond donors (chlorine, bromine, iodine) through a combination of solid-state NMR and NQR spectroscopy, affording the first direct insights on the change in the quadrupolar coupling upon the introduction of a halogen bond. In contrast to previous solid-state NMR investigations, we have directly probed the atom acting as the halogen bond donor rather than observing the adjacent carbon atom. As a result, significant changes in the quadrupolar coupling upon halogen bonding have been measured, which has provided information on the electronic rearrangement occurring at the halogen bond donor.

The chlorine halogen bond donor was investigated through a combination of ^{35}Cl solid-state NMR and NQR, taking advantage of crystallographic symmetry in order to discern the effect of the halogen bond. Our selection of compounds, which was found by searching the Cambridge Structural Database (CSD),[1] allowed us to complete the project without the need of relying on cocrystallizations. As the compounds were commercially available, the required sample sizes of ~500 mg were easily obtained, allowing for the acquisition of the ^{35}Cl spectrum at 21.1 T. The ^{35}Cl spectra resulted in an excellent signal-to-noise ratio despite spanning ~10 MHz, allowing for the extraction of the quadrupolar coupling parameters using spectral simulation. Shown in Figure 2.2 is the ^{35}Cl solid-state NMR spectrum of tetrachloroterephthalonitrile fitted with a two-site simulation.

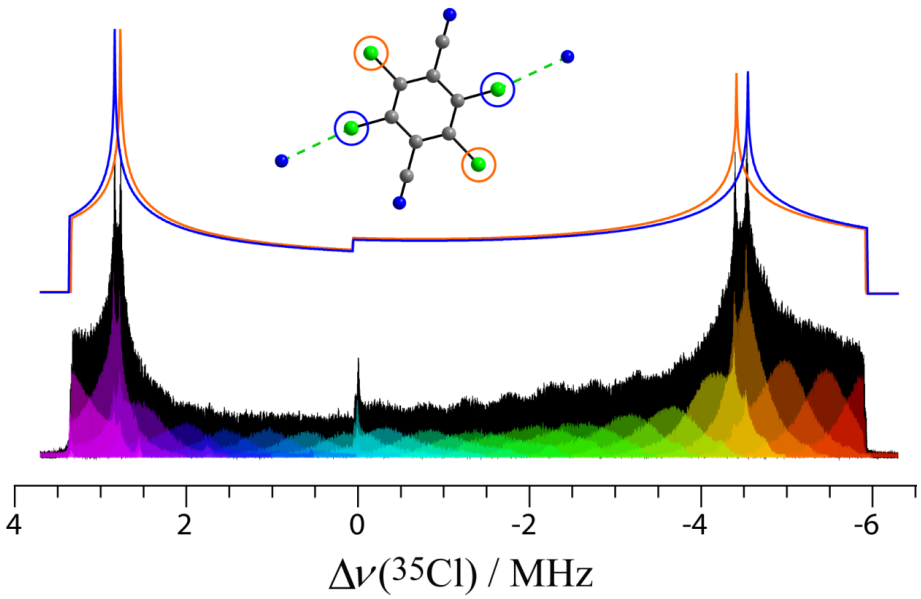

Figure 2.2. ^{35}Cl solid-state NMR spectrum of tetrachloroterephthalonitrile obtained at 21.1 T (black), showing each of the subspectra in color. The simulated spectrum is shown above, with the two colors corresponding to crystallographically unique sites on the crystal structure above.

In contrast to ^{35}Cl, which was amenable by solid-state NMR, the $^{79/81}$Br and ^{127}I nuclei were investigated primarily by NQR spectroscopy. Furthermore, the $^{79/81}$Br and ^{127}I projects were performed by investigating a series of cocrystals rather than single-component compounds, allowing for the comparison between the starting materials and a series of halogen bonded cocrystals. The $^{79/81}$Br NQR experiments provided a convenient indicator for the occurrence of halogen bonding, all in the absence of an expensive external magnetic field, with the C_Q correlating nicely to the length of the halogen bond.

This NQR crystallographic approach was later key to identifying cocrystals in Chapter 6 using ^{127}I NQR. The analysis was performed by individually ball milling a dozen nitrogen-containing heterocycles with 1,4-diiodobenzene, and subsequently combining all the samples into three mixtures. Given the high sensitivity of the experiment, the ^{127}I NQR experiment was

performed on these mixtures. This approach yielded one signal from the dozen of trials, which was later identified to be (1,4-diiodobenzene)(4-picoline) through the analysis of each individual sample at the resonant frequency. The result was a rapid identification of the successful cocrystal, which was later analyzed by X-ray crystallography.

A consistent increase in the quadrupolar coupling constants (C_Q) was observed upon the formation of a halogen bond featuring each quadrupolar halogen bond donor (chlorine, bromine, and iodine). The DFT calculations performed in Chapter 6 attribute these increases in the C_Q to a reduction in the carbon-iodine σ-bond contribution to V_{33}, with an increase in the lone-pair and core orbital contributions. These insights provide the first model on the electronic changes occurring at the halogen bond donor atom and may have implications on their reactivities, allowing for halogen bond-mediated synthesis.

References.

[1] Groom, C.R.; Bruno, I.J.; Lightfoot, M.P.; Ward, S.C. *Acta Cryst.* **2016**, *B72*, 171-179.

Part 3 – Characterizing the Halogen Bond Acceptor & Surrounding Environment

This part of the thesis is concerned on characterizing the halogen bond acceptor and its surrounding environment. The objective is to first develop solid-state NMR tools for characterizing halogen bonded adducts, second, to study how modifying the acceptor moiety affects the NMR response, and third, to investigate how the halogen bond affects the surrounding environment in terms of dynamics.

Solid-state NMR spectroscopy has a proven track record of characterizing the halogen bond acceptor, with the NMR response being sensitive to the geometry of the halogen bond.[1,2,3] Previous work on investigating the halogen bond acceptor by solid-state NMR has observed chemical shift changes observing the ^{13}C,[4] ^{15}N,[4,5] ^{19}F,[6] and ^{77}Se[7] isotopes. These chemical shift changes appeared to be diagnostic for the occurrence of the halogen bond, and in the case of ^{15}N at natural abundance,[2,5] even correlating with the halogen bond distance. An investigation using ^{15}N-enriched halogen bonded samples showed that one could extract the halogen bond distance using the ^{15}N-^{127}I dipolar coupling,[8] which serves to compliment the X-ray data, and even allowing for the refinement of the crystal structure. Another nucleus that has been useful to investigate the halogen bond acceptor is ^{31}P,[7,9] which is a receptive nucleus in part due to its high natural abundance. Due to its high receptivity, ^{31}P SSNMR was applied to follow mechanochemical reactions in real time[10] and characterize the changes in phosphorus-based halogen bond acceptors, such as triphenylphosphine selenide[7] and triphenylphosphine oxide.[9] Using these acceptors, it was shown that the $J(^{77}Se, ^{31}P)$ and $J(^{17}O, ^{31}P)$ couplings were sensitive to the halogen bond, with the magnitude of J generally reducing upon halogen bonding.[7,9] A

recent report from our group details the investigation of the first C-I···P halogen bonding motif using ^{31}P solid-state NMR.[11] While the ^{19}F nucleus is a very receptive nucleus, and fluorinated halogen bond donors are popular, ^{19}F solid-state NMR has been under-exploited, with only few studies.[6]

Investigations on quadrupolar halogen bond acceptors, notably ^{14}N,[4,6] ^{17}O,[9] $^{35/37}$Cl,[12,13] $^{79/81}$Br,[13,14] and ^{127}I,[6,13] have allowed for the characterization of both changes in the chemical shift and the quadrupolar coupling. Recent work performed on the C-I···X$^-$ motif (X = Cl, Br), observing the $^{35/37}$Cl and $^{79/81}$Br nuclei by NMR, in combination with quantum chemical calculations, have revealed how the EFG is oriented relative to the halogen bond, and how modifications to the halogen bonding geometry can affect the EFG.[12] Additionally, a series of haloanolinium halide (i.e. iodoanilinium chloride) has been characterized by solid-state NMR, but did not reveal inter-halogen trends in the quadrupolar coupling due to changes in the crystal structure.[13]

As solid-state NMR is well-suited for exploring molecular dynamics by observing changes in the relaxation times, there have been several investigations on the dynamics of halogen bonded adducts. The molecular rotations of a halogen bonded DABCO molecule have been investigated using ^{1}H solid-state NMR relaxometry, with the rotor on an axle configuration allowing the DABCO molecule to spin freely.[1516] Additionally, the rotor on an axle configuration has been exploited in analogous systems, using the halogen bond as a bonding interaction connecting the rotor to its axle.[17]

Clearly, much of the solid-state NMR work has focused on characterizing the halogen bond acceptor, in part due to the challenges associated with covalently bonded halogens which

has been discussed in the previous part of the thesis. In contrast, the halogen bond acceptor contains nuclei that are much more amenable by solid-state NMR, but in some cases requires isotopic labeling. These ambitions have been rewarding to understand the nature of the halogen bond, revealing changes in chemical shifts, and quadrupolar coupling. However, there are additional opportunities that have yet to be exploited, such as using ^{13}C and ^{19}F chemical shifts to refine crystal structures, analyzing the EFG of each halide halogen bond acceptor (Cl^-, Br^-, I^-) in a series of isomorphous compounds, and investigating how the halogen bond can directly influence the local molecular dynamics.

Chapter 7 of this thesis details a thorough investigation of halogen bonded cocrystals featuring the C-I···N motif, using 1,4-diiodotetrafluorobenzene and 1,3,5-trifluoro-2,4,6-triiodobenzene as the halogen bond donor. These donors are chosen due to their strength, their commercial availability, in addition to the availability of previously reported crystal structures in the CSD. Due to the presence of fluorine atoms, characterizing the perfluorinated halogen bond donor by $^{1}H \rightarrow ^{13}C$ solid-state NMR is challenging, offering little signal as a result of the distance between the ^{1}H and ^{13}C nuclei of the donor, in addition to the broadening effects arising from the ^{19}F dipolar coupling and *J*-coupling. Consequently, $^{19}F \rightarrow ^{13}C$ CP/MAS is investigated in efforts of obtaining higher resolution spectra and comparing it to the conventional $^{1}H \rightarrow ^{13}C$ CP/MAS. Furthermore, we apply ^{19}F solid-state NMR to characterize the halogen bond donor, with the chemical shifts being a clear indicator for cocrystallization. The high receptivity of the ^{19}F nucleus resulted in an excellent signal-to-noise ratio within 16 scans on merely 20 mg of sample, with the spectrum clearly showing the presence of side-phases, impurities, and remaining starting material. This approach offers several advantages, which is later exploited in Chapter 12 of this thesis in order to quickly analyze a large volume of samples prepared by cosublimation. The

^{13}C and ^{19}F solid-state NMR results from this chapter are complemented with DFT calculations, with a better agreement between calculated and experimental chemical shifts upon optimizing the geometry of the crystal structure. This approach of using a combination of NMR and DFT calculations to improve crystal structures is part of the rising field of *NMR Crystallography*.

In chapter 8, which was performed during my internship at the *Politecnico di Milano* (Italy) under the supervision of Dr. Pierangelo Metrangolo, we investigate supramolecular halogen bonded complexes based on 2-iodoethynylpyridine and 3-iodoethynylpyridine. These compounds are then converted to their HCl, HBr, and HI salts, with the X-ray crystal structure revealing the formation of characteristic charged dimers. Notably, many of these dimers share very close unit cell parameters, and are in some cases, isomorphous. Consequently, this has provided the opportunity of comparing the NMR response in a series of halogen bonding motifs: C-I···N, C-I···Cl^-, C-I···Br^-, and C-I···I^-. Furthermore, the crystal structures reveal the formation of N-H···X^- hydrogen bonds, allowing us to make a similar comparison for the hydrogen bond. In addition to X-ray crystallography, we apply ^{1}H, ^{13}C, ^{35}Cl, and $^{79/81}Br$ NMR spectroscopy in order to fully characterize these frameworks. The ^{1}H solid-state NMR allows for the observation of changes in the chemical shift of the proton participating in the hydrogen bond, while the ^{13}C solid-state NMR allows the characterization of the carbons of the iodoacetylene halogen bond donor as a function of the acceptor. In addition, the ^{35}Cl & $^{79/81}Br$ NMR allows for the direct investigation of the EFG across halides. The interpretation of these NMR responses is aided with a natural localized molecular orbital (NLMO) breakdown of the contributions to the chemical shifts and EFG.

Chapter 9 is focused on the changes in the environment surrounding the halogen bond moiety. This project was furthered from Chapter 7, which featured the halogen bond acceptor

2,3,5,6-tetramethylpyrazine. From the crystal structure, it was noticed that the iodine atom of the halogen bond donor was within or very close to the van der Waals radius of the proton of the methyl group. Much like a rock stuck in an electric kitchen mixer, it was expected that the methyl groups would slow down and require more energy to rotate as a consequence of having the iodine atom in the way. Using deuterium NMR relaxometry to extract the Arrhenius activation energy, however, the opposite was observed, and a significant decrease in the rotational energy barrier resulted from having the iodine atom in proximity to the methyl groups, with the halogen bond donor thus acting as a "dynamics catalyst". A series of cocrystals was devised in order to investigate this phenomenon further, which featured halogen bond donors, hydrogen bond donors, and the halide salts of 2,3,5,6-tetramethylpyrazine. In this case, the halide salts provide a control experiment for the presence of halogens near to the methyl group. This consists of the first study of halogen bonding acting as a dynamics catalyst, which could be used to improve pharmaceuticals, supramolecular catalysts, and molecular machines. Further, as this is the first study of its kind featuring the halogen bond, we coin the term *dynamics catalyst*.

References.

[1] Szell, P.M.J.; Bryce, D.L. *Modern Magn. Reson.* **2016**, pp. 1-18, New York, Springer.

[2] Cerreia Vioglio, P.; Chierotti, M.R.; Gobetto, R. *CrystEngComm.* **2016**, *18*, 9173-9184.

[3] Bryce, D.L.; Viger-Gravel, J. *Top. Curr. Chem.* **2015**, *358*, 183-204.

[4] Viger-Gravel, J.; Korobkov, I.; Bryce, D.L. *Cryst. Growth Des.* **2011**, *11*, 4984-4995.

[5] Cerreia Vioglio, P.; Catalano, L.; Vasylyeva, V.; Nervi, C.; Chierotti, M.R.; Resnati, G.; Gobetto, R.; Metrangolo, P. *Chem. Eur. J.* **2016**, *22*, 16819-16828.

[6] Widdifield, C.M.; Cavallo, G.; Facey, G.A.; Pilati, T.; Lin, J.; Metrangolo, P.; Resnati, G.; Bryce, D.L. *Chem. Eur. J.* **2013**, *19*, 11949-11962.

[7] Viger-Gravel, J.; Meyer, J.; Korobkov, I.; Bryce, D.L. *CrystEngComm.* **2014**, *16*, 7285-7297.

[8] Weingarth, M.; Raouafi, N.; Jouvelet, B.; Duma, L.; Bodenhausen, G.; Boujlel, K.; Schöllhorn, B.; Tekely, P. *Chem. Commun.* **2008**, 5981-5983.

[9] Xu, Y.; Viger-Gravel, J.; Korobkov, I.; Bryce, D.L. *J. Phys. Chem. C* **2015**, *119*, 27104-27117.

[10] Xu, Y.; Champion, L.; Gabidullin, B.; Bryce, D.L. *Chem. Commun.* **2017**, *53*, 9930-9933.

[11] Xu, Y.; Huang, J.; Gabidullin, B.; Bryce, D.L. *Chem. Commun.* **2018**, *54*, 11041-11043.

[12] Viger-Gravel, J.; Leclerc, S.; Korobkov, I.; Bryce, D.L. *J. Am. Chem. Soc.* **2014**, *136*, 6929-6942.

[13] Attrell, R.J.; Widdifield, C.M.; Korobkov, I.; Bryce, D.L. *Cryst. Growth Des.* **2012**, *12*, 1641-1653.

[14] Viger-Gravel, J.; Leclerc, S.; Korobkov, I.; Bryce, D.L. *J. Am. Chem. Soc.* **2014**, *136*, 6929-6942.

[15] Catalano, L.; Pérez-Estrada, S.; Terraneo, G.; Pilati, T.; Resnati, G.; Metrangolo, P.; Garcia-Garibay, M.A. *J. Am. Chem. Soc.* **2015**, *137*, 15386-15389.

[16] Catalano, L.; Pérez-Estrada, S.; Wang, H.-H.; Ayitou, A.J.-L.; Khan, S.A; Terraneo, G.; Metrangolo, P.; Brown, S.; Garcia-Garibay, M.A. *J. Am. Chem. Soc.* **2017**, *139*, 843-848.

[17] Lemouchi, C.; Vogelsberg, C.S.; Zorina, L.; Simonov, S.; Batail, P.; Brown, S.; Garcia-Garibay, M.A. *J. Am. Chem. Soc.* **2011**, *133*, 6371-6379.

Chapter 7 – ^{13}C and ^{19}F Solid-State NMR and X-ray Crystallographic Study of Halogen-Bonded Frameworks Featuring Nitrogen-Containing Heterocycles

Statement of Authenticity. I certify that I have prepared the following article featuring my own work, with guidance from my supervisor Dr. David Bryce. This article features work from undergraduate researchers: Shaina Gabriel, Russell Gill, and Shirley Wan. Their tasks were primarily to prepare compounds, and assist me in acquiring the solid-state NMR spectra. In addition to those tasks, Shaina Gabriel has performed a large portion of the computational work, and assisted me in the data interpretation. Dr. Bulat Gabidullin is acknowledged for acquiring and solving the crystal structures presented in the article. Dr. David Bryce is acknowledged for his support and contributions to the manuscript.

Permissions. I declare that I have obtained permission from all coauthors to include this article in my thesis. Chapter 7 has been reproduced from *Acta Cryst.* **2017**, *C73*, 157-167, with permission from the International Union of Crystallography.

(http://doi.org/10.1107/S2053229616015023)

Supporting Information. All supporting information for this article can be retrieved on the IUCr website: http://scripts.iucr.org/cgi-bin/paper?S2053229616015023

STRUCTURAL CHEMISTRY

ISSN: 2053-2296
journals.iucr.org/c

^{13}C and ^{19}F solid-state NMR and X-ray crystallographic study of halogen-bonded frameworks featuring nitrogen-containing heterocycles

Patrick M. J. Szell, Shaina A. Gabriel, Russell D. D. Gill, Shirley Y. H. Wan, Bulat Gabidullin and David L. Bryce

Acta Cryst. (2017). C**73**, 157–167

Acta Cryst C STRUCTURAL CHEMISTRY

ISSN 2053-2296

^{13}C and ^{19}F solid-state NMR and X-ray crystallographic study of halogen-bonded frameworks featuring nitrogen-containing heterocycles

Patrick M. J. Szell, Shaina A. Gabriel, Russell D. D. Gill, Shirley Y. H. Wan, Bulat Gabidullin and David L. Bryce*

Department of Chemistry and Biomolecular Sciences, University of Ottawa, 10 Marie-Curie Pvt., Ottawa, Ontario, K1N 6N5, Canada. *Correspondence e-mail: dbryce@uottawa.ca

Received 1 September 2016
Accepted 22 September 2016

Edited by G. P. A. Yap, University of Delaware, USA

Keywords: NMR crystallography; SSNMR; halogen-bonded frameworks; crystal structure; nitrogen-containing heterocycles; crystal engineering; DFT calculations.

CCDC references: 1505895; 1505894; 1505893

Supporting information: this article has supporting information at journals.iucr.org/c

Halogen bonding is a noncovalent interaction between the electrophilic region of a halogen (σ-hole) and an electron donor. We report a crystallographic and structural analysis of halogen-bonded compounds by applying a combined X-ray diffraction (XRD) and solid-state nuclear magnetic resonance (SSNMR) approach. Single-crystal XRD was first used to characterize the halogen-bonded cocrystals formed between two fluorinated halogen-bond donors (1,4-diiodotetrafluorobenzene and 1,3,5-trifluoro-2,4,6-triiodobenzene) and several nitrogen-containing heterocycles (acridine, 1,10-phenanthroline, 2,3,5,6-tetramethylpyrazine, and hexamethylenetetramine). New structures are reported for the following three cocrystals, all in the $P2_1/c$ space group: acridine–1,3,5-trifluoro-2,4,6-triiodobenzene (1/1), $C_6F_3I_3{\cdot}C_{13}H_9N$, 1,10-phenanthroline–1,3,5-trifluoro-2,4,6-triiodobenzene (1/1), $C_6F_3I_3{\cdot}C_{12}H_8N_2$, and 2,3,5,6-tetramethylpyrazine–1,3,5-trifluoro-2,4,6-triiodobenzene (1/1), $C_6F_3I_3{\cdot}C_8H_{12}N_2$. ^{13}C and ^{19}F solid-state magic-angle spinning (MAS) NMR is shown to be a convenient method to characterize the structural features of the halogen-bond donor and acceptor, with chemical shifts attributable to cocrystal formation observed in the spectra of both nuclides. Cross polarization (CP) from ^{19}F to ^{13}C results in improved spectral sensitivity in characterizing the perfluorinated halogen-bond donor when compared to conventional ^{1}H CP. Gauge-including projector-augmented wave density functional theory (GIPAW DFT) calculations of magnetic shielding constants, along with optimization of the XRD structures, provide a final set of structures in best agreement with the experimental ^{13}C and ^{19}F chemical shifts. Data for carbons bonded to iodine remain outliers due to well-known relativistic effects.

1. Introduction

Halogen bonding has attracted much interest in the last decade, which can in part be attributed to its great promise as a tuneable noncovalent interaction in crystal engineering (Cavallo *et al.*, 2016; Metrangolo *et al.*, 2005; Berger *et al.*, 2015). A halogen bond occurs when the region of positive electrostatic potential associated with a covalently bonded halogen (the halogen-bond donor), named the σ-hole (Clark *et al.*, 2007), interacts with a Lewis base (the halogen-bond acceptor) (Politzer & Murray, 2013; Desiraju *et al.*, 2013). The relative magnitude of the σ-hole increases with the polarizability of the electrons on the halogen (Lommerse *et al.*, 1996), with iodine having the largest σ-hole, followed by bromine and chlorine. Typical halogen-bond acceptors comprise electron-rich nucleophiles, such as nitrogen (Wang *et al.*, 2014), oxygen (Allen *et al.*, 1997), sulfur (Le Gal *et al.*, 2016), selenium (Viger-Gravel, Meyer *et al.*, 2014), and halide anions (Abate *et al.*, 2009). The resulting halogen bond is linear (Ramasubbu *et*

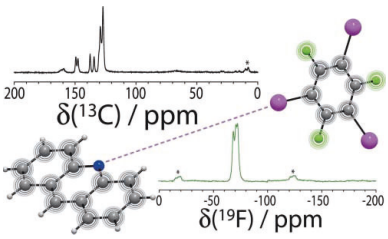

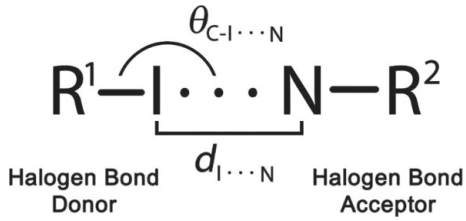

Figure 1
The halogen-bonding moiety under investigation, where iodine is the halogen-bond donor, nitrogen is the halogen-bond acceptor, and R^1 and R^2 are substituents. The distance, $d_{I\cdots N}$, and angle, $\theta_{C-I\cdots N}$, which characterize the halogen bond, are shown.

al., 1986), with a bond angle ($\theta_{C-X\cdots Y}$) typically between 150 and 180° (Desiraju *et al.*, 2013) and a bond length ($d_{X\cdots Y}$) of less than the sum of the van der Waals radii (Bondi, 1964) (d_{vdW}) of the electron donor and acceptor (Y and X). The normalized distance parameter (R_{XB}), given in equation (1), is the ratio of the halogen-bond length to the sum of the van der Waals radii, and provides a qualitative tool allowing one to recognize the presence of a halogen bond based on the interaction distance.

$$R_{XB} = \frac{d_{X\cdots Y}}{\sum d_{vdW}} \quad (1)$$

Halogen bonds are especially useful to crystal engineers, as the lattice geometry of a halogen-bonded framework can be rationally designed by altering the halogen-bond donor or the halogen-bond acceptor to yield the desired motif. The strength of the halogen bond can be tuned by adding electron-donating groups to the halogen-bond acceptor, and electron-withdrawing groups, such as fluorine, to the halogen-bond donor (Aakeröy *et al.*, 2016). For this reason, perfluorinated halogen-bond donors have been used extensively as they typically result in strong halogen bonds (Cavallo *et al.*, 2016). As for the halogen-bond acceptor, nitrogen is a versatile electron donor, which can be ascribed to the many functional groups in which nitrogen is found. The iodine–nitrogen halogen bond between perfluorinated halogen-bond donors and nitrogen-containing heterocycles, as illustrated in Fig. 1, is especially interesting due to its potential as a crystal-engineering tool.

Solid-state NMR (SSNMR) has proven to be a powerful investigational tool for crystal engineers, owing to its ability to offer information concerning the chemical and electronic environments of the nuclides of interest in a given material (Xu *et al.*, 2016; Szell & Bryce, 2016*a*; Bryce & Viger-Gravel, 2015). SSNMR is a nondestructive tool which can be applied even when diffraction techniques are unsuitable, such as in the case of an amorphous solid, and may also offer information on molecular dynamics. Dominated primarily by four interactions (magnetic shielding, dipolar coupling, *J*-coupling, and quadrupolar coupling), NMR crystallography is a rapidly burgeoning field that generally uses these NMR interactions to yield key attributes or full structural information on the compounds of interest. For instance, one can determine distances between atoms by measuring the homonuclear or the heteronuclear dipolar coupling (Harris *et al.*, 2009). In terms of halogen bonding, the halogen-bond donor (Szell & Bryce, 2016*b*) and the halogen-bond acceptor (Xu *et al.*, 2015, 2016; Widdifield *et al.*, 2013) have been probed by SSNMR, along with the measurement of *J*-couplings in the halogen-bond acceptor (Viger-Gravel, Meyer *et al.*, 2014; Xu *et al.*, 2015). NMR crystallography is an advantageous tool in the field of halogen bonding, offering information on the halogen bond's chemical and electronic environment which are otherwise unavailable by X-ray diffraction.

Despite this progress, the halogen bond remains somewhat underexplored by SSNMR, and nitrogen-containing heterocycles exhibiting a nitrogen–iodine halogen bond in particular have had limited coverage, with only a handful of studies reported to date (Widdifield *et al.*, 2013; Viger-Gravel *et al.*, 2011; Lemouchi *et al.*, 2011; Bouchmella *et al.*, 2008; Weingarth *et al.*, 2008). In this study, a series of nitrogen–iodine halogen-bonded cocrystals were prepared and investigated by X-ray diffraction, as well as ^{13}C and ^{19}F SSNMR, in order to establish a viable technique for crystal engineers and NMR crystallographers. Eight cocrystals were prepared by combining one of the two halogen-bond donors (**1** or **2**) with each of the acceptors (**A**, **B**, **C**, and **D**) shown in Fig. 2 [systematic names: 1,4-diiodotetrafluorobenzene (*p*-DITFB, **1**), 1,3,5-trifluoro-2,4,6-triiodobenzene (*sym*-TFTIB, **2**), acridine (ACD, **A**), 1,10-phenanthroline (PHN, **B**), 2,3,5,6-tetramethylpyrazine (TMP, **C**), and hexamethylenetetramine (HMT, **D**)]. The halogen-bond acceptors consist of nitrogen-containing heterocycles and were selected as a result of their concentrated charges localized on the nitrogen. In order to study both the halogen-bond donor and halogen-bond acceptor in these cocrystals, a new strategy is proposed. Due to the fact that the perfluorinated halogen-bond donors exhibit strong intramolecular ^{19}F–^{13}C dipolar coupling, and weak intermolecular ^{13}C–^{1}H dipolar coupling, ^{13}C SSNMR using $^{19}F\rightarrow{}^{13}C$ cross polarization (CP) should enable more efficient cross polarization and therefore an increase in the sensitivity of the ^{13}C SSNMR spectrum of the halogen-bond donor. Furthermore,

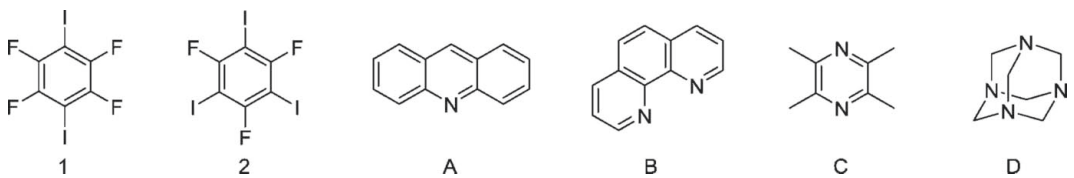

Figure 2
The pure component compounds used in this work. Donors: 1,4-diiodotetrafluorobenzene (*p*-DITFB, **1**) and 1,3,5-trifluoro-2,4,6-triiodobenzene (*sym*-TFTIB, **2**). Acceptors: acridine (ACD, **A**), 1,10-phenanthroline (PHN, **B**), 2,3,5,6-tetramethylpyrazine (TMP, **C**), and hexamethylenetetramine (HMT, **D**). Crystal structures are reported for **A2** (*i.e.* **A** + **2**), **B2** (*i.e.* **B** + **2**), and **C2** (*i.e.* **C** + **2**).

Table 1
Halogen-bond geometrical parameters, including the halogen-bond length ($d_{I\cdots N}$), halogen-bond angle ($\theta_{C-I\cdots N}$), and reduced distance parameter (R_{XB}).

	Compound	$d_{I\cdots N}$ (Å)	$\theta_{C-I\cdots N}$ (°)	R_{XB}
A1	(ACD)(*p*-DITFB)	2.971	176.55	0.842
A2	(ACD)(*sym*-TFTIB)	3.022	173.60	0.856
B1	(PHN)(*p*-DITFB)	3.010	159.03	0.853
		3.274	149.76	0.927
B2	(PHN)(*sym*-TFTIB)	3.020	175.68	0.856
		3.148	164.18	0.892
C1	(TMP)(*p*-DITFB)	3.067	177.15	0.869
C2	(TMP)(*sym*-TFTIB)	2.991	178.09	0.847
		2.993	179.81	0.848
D1	(HMT)(*p*-DITFB)	2.845	169.05	0.806
D2	(HMT)(*sym*-DITFB)	2.864	171.72	0.811
		2.879	170.53	0.816

the observation of ^{13}C signals of the nonfluorinated halogen-bond acceptor in the $^{19}F\rightarrow{}^{13}C$ spectrum would be a useful tool to indicate cocrystallization has occurred (*vide infra*). Lastly, fast magic angle spinning (MAS) ^{19}F SSNMR has been employed in order to probe the fluorine environments of the halogen-bond donors directly. Gauge-including projector augmented-wave (GIPAW) density functional theory (DFT) calculations were also performed to allow a DFT/NMR crystallographic structure refinement of the diffraction-based structures.

2. Experimental

2.1. Sample preparation

1,10-Phenanthroline was purchased from EMD Chemicals Inc. Acridine, hexamethylenetetramine, 2,3,5,6-tetramethylpyrazine, and 1,4-diiodotetrafluorobenzene were purchased from Sigma–Aldrich. 1,3,5-Trifluoro-2,4,6-triiodobenzene was purchased from Alfa Aesar. All compounds were used without further purification. Cocrystals **A1** (Cinčić *et al.*, 2008), **B1** (Syssa-Magalé *et al.*, 2005), **C1** (Syssa-Magalé *et al.*, 2005), **D1** (Walsh *et al.*, 2001), and **D2** (Syssa-Magalé *et al.*, 2014) were prepared according to published procedures. Samples of **A2** and **C2** were obtained from the slow evaporation of an equimolar solution of the donor and acceptor in acetonitrile at room temperature. In the case of **C2**, crystals suitable for SSNMR formed immediately. Crystals

Table 2
Single-crystal X-ray diffraction experimental details.

	A2	**B2**	**C2**
	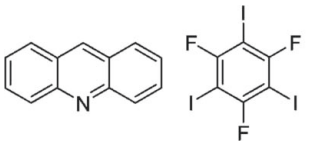	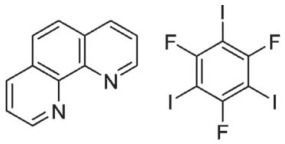	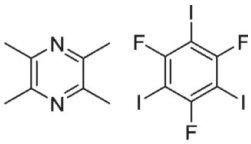
Crystal data			
Chemical formula	$C_6F_3I_3{\cdot}C_{13}H_9N$	$C_6F_3I_3{\cdot}C_{12}H_8N_2$	$C_6F_3I_3{\cdot}C_8H_{12}N_2$
M_r	688.97	689.96	645.96
Crystal system, space group	Monoclinic, $P2_1/c$	Monoclinic, $P2_1/c$	Monoclinic, $P2_1/c$
Temperature (K)	200	200	200
a, b, c (Å)	10.5079 (4), 12.5632 (5), 15.1563 (6)	8.6445 (3), 14.0472 (6), 15.8147 (6)	7.9818 (3), 26.7046 (9), 9.2220 (3)
β (°)	102.490 (2)	97.662 (2)	115.398 (2)
V (Å^3)	1953.47 (13)	1903.25 (13)	1775.69 (11)
Z	4	4	4
Radiation type	Mo $K\alpha$	Mo $K\alpha$	Mo $K\alpha$
μ (mm^{-1})	4.83	4.96	5.31
Crystal size (mm)	0.42 × 0.24 × 0.23	0.51 × 0.37 × 0.37	0.52 × 0.26 × 0.11
Data collection			
Diffractometer	Bruker APEXII CCD	Bruker APEXII CCD	Bruker APEXII CCD
Absorption correction	Multi-scan (*SADABS*; Bruker 2003)	Multi-scan (*SADABS*; Bruker, 2003)	Multi-scan (*SADABS*; Bruker, 2003)
T_{min}, T_{max}	0.500, 0.746	0.468, 0.746	0.443, 0.746
No. of measured, independent and observed [$I > 2\sigma(I)$] reflections	43868, 4835, 4541	28519, 4752, 4397	29591, 4238, 3892
R_{int}	0.022	0.024	0.042
(sin $\theta/\lambda)_{max}$ (Å^{-1})	0.667	0.668	0.658
Refinement			
$R[F^2 > 2\sigma(F^2)]$, $wR(F^2)$, S	0.022, 0.054, 1.05	0.025, 0.059, 1.15	0.029, 0.067, 1.19
No. of reflections	4835	4752	4238
No. of parameters	235	235	203
H-atom treatment	H-atom parameters constrained	H-atom parameters constrained	H-atom parameters constrained
$\Delta\rho_{max}$, $\Delta\rho_{min}$ (e Å^{-3})	1.10, −1.47	1.23, −0.60	0.59, −1.64

Computer programs: *APEX2* (Bruker, 2012), *SAINT* (Bruker, 2009), *XPREP* (Bruker, 2009), *SHELXT* (Sheldrick, 2015*a*), *SHELXL2014* (Sheldrick, 2015*b*), *WinGX* (Farrugia, 2012), *Mercury* (Macrae *et al.*, 2008) and *CIFTAB* (Sheldrick, 1997).

of **B** were obtained by slow evaporation from technical-grade acetone. Crystals of **B2** were obtained by slow evaporation of an equimolar solution of *sym*-TFTIB and 1,10-phenanthroline from chloroform at room temperature. Crystals were ground into fine powders for powder XRD and SSNMR experiments. The crystal structure for each powdered sample was verified by powder X-ray diffraction on a Rigaku Ultima IV instrument with 2θ ranging from 5 to 75° in increments of 0.02° using Cu $K\alpha$ radiation to ensure phase purity. Full information on the scanning range, scanning rates, and diffractograms may be found in the *Supporting information*.

2.2. ^{13}C solid-state NMR

The ^{1}H→^{13}C CP/MAS SSNMR experiments were performed at 9.4 T on a Bruker Avance III spectrometer, using a Bruker 4 mm HXY MAS probe with a spinning frequency of 10 (for **A**, **B**, **C**, and **D**) and 12 kHz (for **A1**, **A2**, **B1**, **B2**, **C1**, **C2**, **D1**, and **D2**). ^{1}H→^{13}C CP/MAS was used with a 5000 µs contact time, a proton $\pi/2$ pulse of 4.60 µs, and a ^{1}H decoupling frequency of 54.3 kHz. Chemical shifts were referenced to glycine at 176.4 ppm (^{13}C═O) relative to tetramethylsilane (TMS). The ^{19}F→^{13}C CP/MAS SSNMR experiments were performed at 11.7 T on a Bruker Avance spectrometer, using a Bruker 4 mm HXY MAS probe with various spinning speeds. ^{19}F→^{13}C CP/MAS was used with a 9000 µs contact time, a fluorine $\pi/2$ pulse of 4.00 µs, and a ^{19}F decoupling frequency of 62.5 kHz. The spectra were referenced to powdered polytetrafluoroethylene at 111.3 ppm (Liu & Schmidt-Rohr, 2001) relative to TMS. Full information on recycle delays, number of scans, and spinning speeds may be found in the *Supporting information*. Various spinning speeds were used to alleviate the overlap of the isotropic peaks with the spinning sidebands.

2.3. ^{19}F solid-state NMR

All ^{19}F NMR experiments were performed at 11.7 T on a Bruker Avance spectrometer, using a Bruker 2.5 mm HX MAS probe with a spinning frequency of 25 kHz. A Bloch decay was used with a $\pi/2$ pulse length of 1.75 µs and a recycle delay of 60 s. The spectra were referenced to powdered polytetrafluoroethylene at −122.2 ppm relative to $CFCl_3$ (Scheler, 1998). Full experimental conditions may be found in the *Supporting information*.

2.4. Computational details

All GIPAW DFT calculations were performed using the *Cambridge Serial Total Energy Package* (*CASTEP*) (Clark *et al.*, 2005) as part of *Materials Studio* (Accelrys, 2016). The Perdew–Burke–Ernzerhof (PBE) generalized gradient approximation (GGA) functional was used in all cases. Further information on energy cut-offs and *k*-points is given in the *Supporting information*. Several series of calculations were run in order to achieve convergence of the computed results, inasmuch as our computational resources would allow. X-ray structures were used as the input, both with full geometry optimization while maintaining the unit-cell dimensions and without geometry optimization. An additional set of calculations was performed on models generated by removing the halogen-bond acceptor from the original X-ray structures. The output files were parsed using *EFGShield* (Adiga *et al.*, 2007). The conversion of the calculated ^{19}F magnetic shielding values to chemical shifts was first explored using equation (2) reported by Sadoc *et al.* (2011); however, this relation was found not to be ideal for the presently studied compounds (*vide infra*).

$$\delta_{iso} = -0.80\sigma_{iso} + 89 \quad (2)$$

2.5. X-ray crystallography

Data collection results for compounds **A2**, **B2**, and **C2** represent the best data sets obtained in several trials for each sample. The crystals were mounted on thin glass fibers using paraffin oil. Prior to data collection, the crystals were cooled to 200±2 K. Selected X-ray crystallographic data are given in Table 2. The H atoms in **A2**, **B2**, and **C2** were treated as riding atoms in geometrically idealised positions, with C—H = 0.95 (aromatic) and 0.98 Å (methyl), and with U_{iso}(H) = 1.2U_{eq}(C) for the aromatic H atoms and 1.5U_{eq}(C) for the methyl H atoms.

3. Results and discussion

3.1. X-ray crystallography

The X-ray structures for compounds **A** (Braga *et al.*, 2010; CCDC 763820), **A1** (Cinčić *et al.*, 2008; CCDC 712048), **B** (Nelyubina *et al.*, 2014; CCDC 998980), **B1** (Syssa-Magalé *et al.*, 2005; CCDC 259705), **C** (Braam *et al.*, 1981), **C1** (Syssa-Magalé *et al.*, 2005; CCDC 259702), **D** (Becka & Cruickshank, 1963), **D1** (Walsh *et al.*, 2001; CCDC 161327), **D2** (Syssa-Magalé *et al.*, 2014; CCDC 1018109), **1** (Oh *et al.*, 2012; CCDC 819337), and **2** (Lucassen *et al.*, 2007; CCDC 293751) have been reported previously and found using the Cambridge Structural Database (CSD; Groom *et al.*, 2016). The single-crystal X-ray diffraction structures for **A2**, **B2**, and **C2** were determined presently in order to complete this information for the series of cocrystals under investigation. All the halogen-bonded cocrystals under investigation are illustrated in Fig. 3. In all cases, these compounds feature a C—I···N halogen bond between the donor and the acceptor. See Table 1 for a full description of the halogen-bonding geometry, including the halogen-bond distances ($d_{I\cdots N}$), the halogen-bond angles ($\theta_{C-I\cdots N}$), and the normalized distance parameters (R_{XB}). Selected X-ray crystallographic data are given in Table 2. The halogen bonds are moderately strong, with R_{XB} values as low as 81% for the **D** series.

The X-ray structure of **A2**, a cocrystal of ACD with *sym*-TFTIB, features a nearly linear C—I···N halogen bond (173.6°) and a halogen-bond length of 3.022 Å (R_{XB} = 0.856), as shown in Fig. 4. Moreover, the local mirror planes of the halogen-bond donor and the acceptor are nearly perpendicular to each other, which contrasts with the structure of **A1** (Cinčić *et al.*, 2008), where they are nearly parallel to each

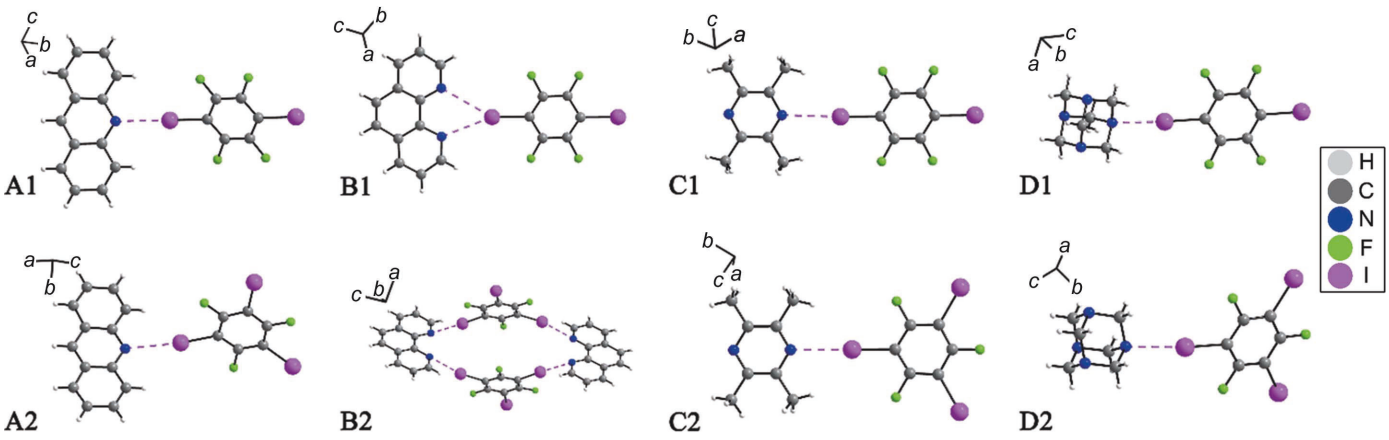

Figure 3
Depiction of the halogen-bonded donor–acceptor fragments from the X-ray crystal structures of **A1**, **A2**, **B1**, **B2**, **C1**, **C2**, **D1**, and **D2**, with the iodine–nitrogen halogen bonds denoted by dashed magenta lines. The halogen-bond lengths ($d_{I\cdots N}$) and the halogen-bond angles ($\theta_{C-I\cdots N}$) are listed in Table 1.

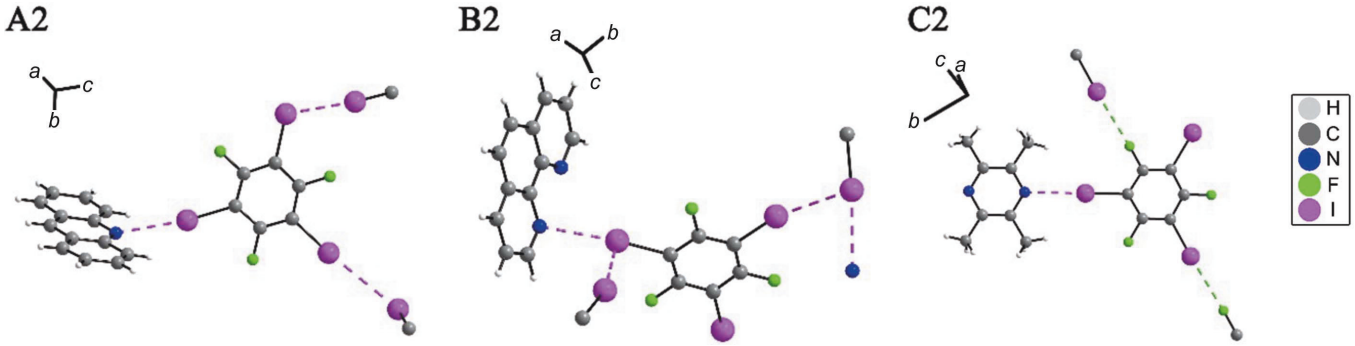

Figure 4
A detailed view of the halogen-bonded fragments from the X-ray crystal structures of **A2**, **B2**, and **C2**, with the iodine–nitrogen and the iodine–iodine halogen bonds denoted by dashed magenta lines. The iodine–fluorine close contact is denoted with a dashed green line.

other. The X-ray structure of **A2** reveals that the halogen-bond donor, *sym*-TFTIB, participates in one C—I···N halogen bond and one C—I···I halogen bond ($d_{I\cdots I}$ = 3.728 Å, R_{XB} = 0.942, $\theta_{C-I\cdots I}$ = 175.56°, and $\theta_{I\cdots I-C}$ = 106.62°). This is distinct from the X-ray structure of **A1**, which features two C—I···N halogen bonds to the donor (*p*-DITFB) and lacks any C—I···I halogen bond.

The X-ray structure of **B2**, a cocrystal of PHN and *sym*-TFTIB, is significantly distorted from the linear chain observed in compound **B1**, as portrayed in Fig. 3. In **B2**, the horizontal mirror plane of the 1,10-phenanthroline molecule is almost perpendicular to the horizontal mirror plane of *sym*-TFTIB. As a result, both 1,10-phenanthroline N atoms exhibit crystallographically distinct halogen bonds, one with a C—I···N length of 3.020 Å (R_{XB} = 0.856) and the other with a bond length of 3.148 Å (R_{XB} = 0.892). Their halogen-bond angles are 175.68 and 164.18°, respectively. The cocrystals form an intercalated complex, with two *sym*-TFTIB halogen-bond donors surrounded by two 1,10-phenanthroline halogen-bond acceptors. Each unit is then connected to the next by a C—I···I halogen bond ($d_{I\cdots I}$ = 3.751 Å, R_{XB} = 0.947, $\theta_{C-I\cdots I}$ = 162.95°, and $\theta_{I\cdots I-C}$ = 98.99°).

The X-ray structure of **C2** features two linear C—I···N halogen bonds, with angles of 178.09 and 179.81°, and halogen-bond lengths of 2.991 (R_{XB} = 0.847) and 2.993 Å (R_{XB} = 0.848), respectively. As a result of the 1,3,5-substitution pattern of the halogen-bond donor (*sym*-TFTIB) and the rigid acceptor (TMP), a zigzag chain framework is produced due to the occurrence of the halogen bond (see Fig. 5). Pairs of adjacent

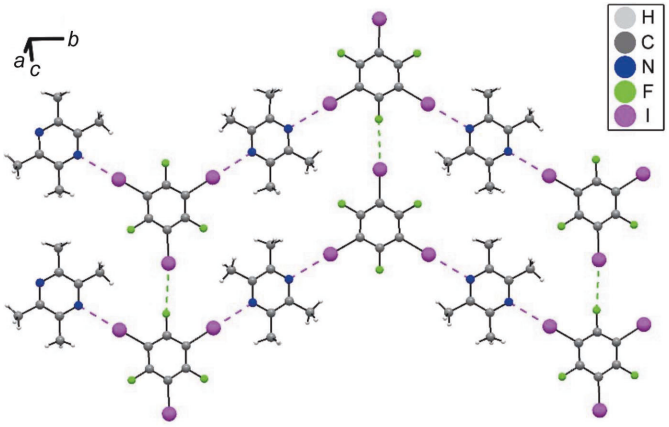

Figure 5
The crystal packing of **C2**, (TMP)(*sym*-TFTIB), displaying the zigzag chains formed by C—I···N halogen bonding, denoted by dashed magenta lines, and the inter-chain link established by C—I···F close contacts, denoted by dashed green lines.

chains are linked together by C—I···F close contacts ($d_{I\cdots F}$ = 3.133 Å).

3.2. ^{13}C solid-state NMR

Carbon-13 CP/MAS SSNMR spectroscopy was carried out on all samples to characterize both the halogen-bond donor and the halogen-bond acceptor in terms of their ^{13}C chemical shifts. ^{1}H→^{13}C CP proved to be an effective method in characterizing the halogen-bond acceptor as a result of the protons covalently bonded to the acceptor moieties (see Fig. 6). The chemical shifts of the carbons covalently bonded to nitrogen on the halogen-bond acceptor are listed in Table 3, and were assigned based on literature data for compound series **A** and **B** [Spectral Database for Organic Compounds (SDBS), 2016]. In the cases of **A2**, **B1**, and **B2**, splittings are observed for the carbons bonded to nitrogen due to their crystallographic inequivalency. Across all of the spectra, a ^{13}C chemical shift change for the carbons covalently bonded to nitrogen on the halogen-bond acceptor is observed when the starting material is compared to the halogen-bonded cocrystals. However, the magnitudes of these changes vary across all samples and do not correlate in a general manner with the halogen-bond distance or angle. These ^{13}C chemical shift changes are most pronounced for compound series **A**, **B**, and **D**, whereas only small ^{13}C chemical shift changes are observed for series **C**. The lack of a general correlation may be partly

Table 3
^{13}C chemical shifts of the carbons covalently bonded to nitrogen on the halogen-bond acceptors, obtained from ^{1}H→^{13}C cross polarization experiments.

	XB acceptor	δ_{iso}(^{13}C)/ppm[a] XB acceptor	δ_{iso}(^{13}C)/ppm[a] cocrystal with **1**	δ_{iso}(^{13}C)/ppm[a] cocrystal with **2**
A	ACD	148.7±1.6	148.7±0.2	149.6±0.3
				147.7±0.2
B	PHN	150.7±0.3	150.0±0.2	151.4±0.2
		145.0±0.2	148.4±0.2	149.4±0.2
			144.0±0.3	145.3±0.5
C	TMP	149.7±0.1	149.4±0.2	149.7±0.3
		149.0±0.1		
D	HMT	73.4±0.1	74.7±0.2	74.9±0.2
		73.2±0.1	71.8±0.2	71.8±0.2

Note: (*a*) the peak positions reported may not correspond exactly to the true chemical shifts as a result of peak overlap, and possibly due to residual ^{14}N dipolar coupling; however, the effect of the latter is expected to be negligible under the experimental conditions used.

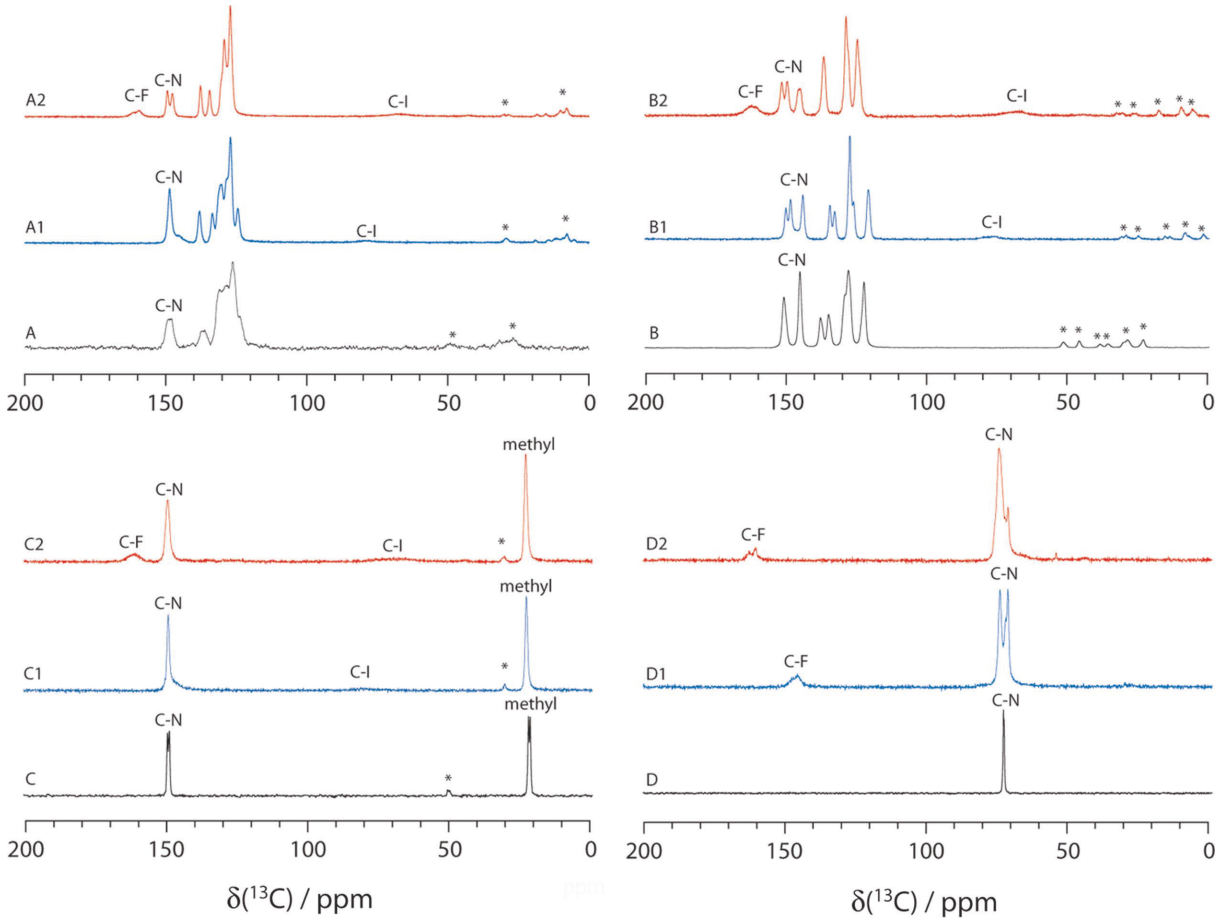

Figure 6
^{1}H→^{13}C CP/MAS solid-state NMR spectra with MAS speeds of 10 (black) and 12 kHz (blue and red), corresponding to **A** (acridine), **A1** (ACD)(*p*-DITFB), **A2** (ACD)(*sym*-TFTIB), **B** (1,10-phenanthroline), **B1** (PHN)(*p*-DITFB), **B2** (PHN)(*sym*-TFTIB), **C** (2,3,5,6-tetramethylpyrazine), **C1** (TMP)(*p*-DITFB), **C2** (TMP)(*sym*-TFTIB), **D** (hexamethylenetetramine), **D1** (HMT)(*p*-DITFB), and **D2** (HMT)(*sym*-TFTIB). Asterisks (*) denote spinning sidebands. The labels 'C—F' and 'C—I' denote the carbons covalently bonded to fluorine and iodine of the halogen-bond donors, respectively. The label 'C—N' denotes the carbons covalently bonded to nitrogen of the halogen-bond acceptors.

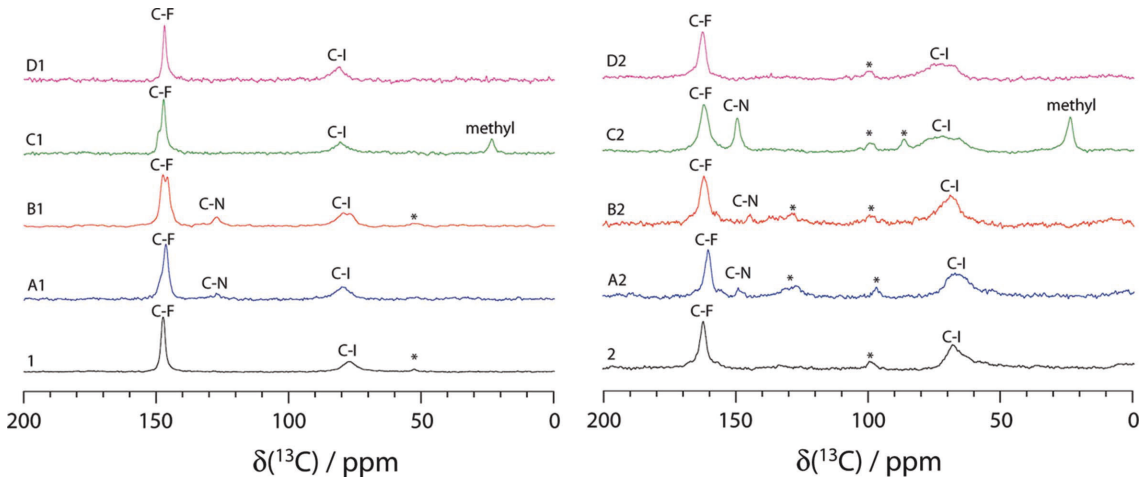

Figure 7
$^{19}F\rightarrow{}^{13}C$ CP/MAS solid-state NMR spectra corresponding to **1** (*p*-DITFB), **2** (*sym*-TFTIB), **A1** (ACD)(*p*-DITFB), **A2** (ACD)(*sym*-TFTIB), **B1** (PHN)(*p*-DITFB), **B2** (PHN)(*sym*-TFTIB), **C1** (TMP)(*p*-DITFB), **C2** (TMP)(*sym*-TFTIB), **D1** (HMT)(*p*-DITFB), and **D2** (HMT)(*sym*-TFTIB). Asterisks (*) denote spinning sidebands. The resonances denoted by 'C—N' and 'methyl' observed in the spectra of **A1**, **A2**, **C1**, and **C2** are a result of cross polarization from the XB donor to the XB acceptor. The labels 'C—F' and 'C—I' denote the carbons covalently bonded to fluorine and iodine of the halogen-bond donor, respectively. The label 'C—N' denotes the carbons covalently bonded to the nitrogen of the halogen-bond acceptor.

Table 4
^{13}C chemical shifts of the halogen-bond donor obtained from $^{19}F\rightarrow{}^{13}C$ cross polarization, and the calculated dipolar coupling second moments between the ^{19}F of the halogen-bond donor and the ^{13}C of the halogen-bond acceptor.

Compound	Experimental $\delta_{iso}(^{13}C)$/ppm	Asignments	Average calculated dipolar coupling second moment $(s^{-2})^b$
1	147.6±0.4	C—F	
	76.8±1.4	C—I	
2	162.6±0.9	C—F	
	67.6±2.4	C—I	
A1	146.5±0.4	C—F	1.41×10^5
	79.2±2.3	C—I	
A2	160.8±0.8	C—F	1.55×10^5
	66.1±4.7	C—I	
B1	147.7±0.5	C—F	2.02×10^5
	145.9±0.4	C—F	
	79.1±1.9	C—I	
	76.7±1.8	C—I	
B2	162.3±1.3	C—F	1.94×10^5
	68.5±3.3	C—I	
C1	147.4±0.4	C—F	2.15×10^5
	80.3±2.4	C—I	
C2	162.3±0.8	C—F	1.91×10^5
	71.5±11.0[a]	C—I	
D1	147.1±0.4	C—F	2.20×10^5
	80.8±2.7	C—I	
D2	162.8±0.9	C—F	1.03×10^5
	71.8±7.9[a]	C—I	

Notes: (*a*) the large uncertainty in the chemical shift reflects the fact that there are multiple unresolved carbon–iodine sites. (*b*) The second moment was calculated using equation (3), using the fluorine–carbon distances between the halogen-bond donor and the halogen-bond acceptor, with a cut-off distance of 10 Å.

due to the multiple crystallographic changes endured by the halogen-bond acceptor, in addition to the formation of the halogen bond. Moreover, the line shape changes of the ^{13}C resonances of the halogen-bond acceptor can be a further indicator of a change in the crystallographic environment. For instance, a significant broadening of the ^{13}C resonance of the carbon covalently bonded to nitrogen in the halogen-bond acceptor is observed for compound series **D**, with a resonance width at half-height of 55±2 Hz for **D**, 157±12 Hz for one of the resonances of **D1** (δ_{iso} = 74.7±0.2 ppm), and 252±15 Hz for one of the resonances of **D2** (δ_{iso} = 74.9±0.4 ppm). $^1H\rightarrow{}^{13}C$ CP/MAS may not be the most efficient approach to characterize the perfluorinated halogen-bond donor, as low signal intensity and broad resonances were obtained. Instead, $^{19}F\rightarrow{}^{13}C$ CP may be the more practical solution to obtain chemical shift information, *vide infra*.

While providing reliable ^{13}C chemical shifts for the halogen-bond acceptor, $^1H\rightarrow{}^{13}C$ CP provides only limited sensitivity for the carbons on the halogen-bond donor. Only weak broad resonances are observed for the halogen-bond donor as a result of the heteronuclear couplings to fluorine and inefficient CP from ^1H. Furthermore, many of the resonances of the halogen-bond acceptor overlap with those of the halogen-bond donor assigned to the carbons covalently bonded to fluorine and the carbons covalently bonded to iodine. In order to obtain adequate spectra of the carbons of the halogen-bond donor, $^{19}F\rightarrow{}^{13}C$ CP with fluorine decoupling was employed (see Fig. 7). Evidently, $^{19}F\rightarrow{}^{13}C$ CP/MAS fared better in producing resonances for the carbons on the perfluorinated halogen-bond donor as a result of efficient CP and fluorine decoupling. This increase in spectral quality allowed a more accurate measurement of the ^{13}C chemical shifts for both the carbon covalently bonded to fluorine and the carbon covalently bonded to iodine of the halogen-bond donor, as given in Table 4. In the cases of sample series **C** and **D**, insufficient resolution was achieved as a result of overlapping ^{13}C resonances for the carbon covalently bonded to iodine of the halogen-bond donor, leading to a higher uncertainty in their ^{13}C chemical shifts. It should be noted that this can be remedied using higher magnetic fields, as shown by Viger-Gravel *et al.* (2013).

The spatial proximity of the ^{19}F nuclei on the halogen-bond donor to the carbons on the halogen-bond acceptor allowed for $^{19}F\rightarrow{}^{13}C$ CP to the halogen-bond acceptor. In the cases of

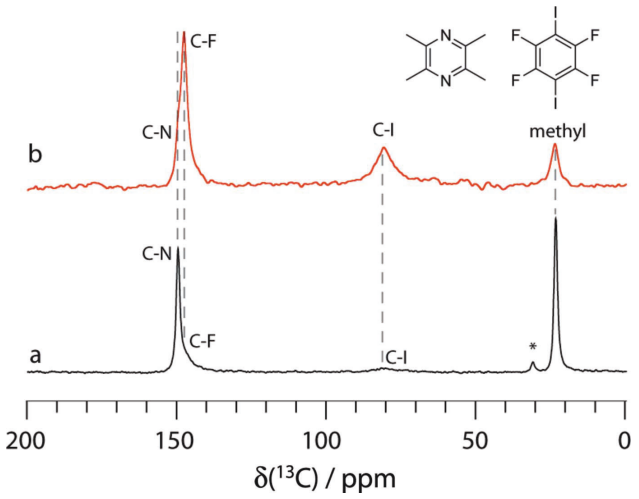

Figure 8
Comparison of the ^{13}C CP/MAS spectra of **C1** using (*a*) ^{1}H cross polarization and (*b*) ^{19}F cross polarization. Dashed lines are added as a guide. The asterisk (*) denotes the spinning sideband. The labels 'C—F' and 'C—I' denote the carbon covalently bonded to the fluorine and iodine of the halogen-bond donor, respectively. The label 'C—N' denotes the carbon covalently bonded to the nitrogen of the halogen-bond acceptor.

samples **C1**, **D1**, and **D2**, the ^{13}C resonances from the halogen-bond donor overlapped with the resonances of the halogen-bond acceptor. One can quantify the dipolar coupling from the ^{19}F nuclei of the halogen-bond donor to the ^{13}C nuclei of the halogen-bond acceptor by calculating the Van Vleck dipolar coupling second moment (Van Vleck, 1948) given in equation (3):

$$M_2^{I-S} = \frac{4}{15}\left(\frac{\mu_o}{4\pi}\right)\cdot\left(\frac{\hbar}{2\pi}\right)\gamma_I^2\gamma_S^2 I(I+1)\cdot N_I^{-1}\sum_s r_{IS}^{-6} \qquad (3)$$

Here, μ_o is the vacuum permeability, $\hbar$ is the reduced Planck constant, γ_I and γ_S are the gyromagnetic ratios of ^{19}F and ^{13}C, respectively, I is the spin quantum number of the observed spin (1/2), N_I is the number of spins observed, and r_{IS} are the internuclear distances. The ^{19}F–^{13}C second moment was calculated for each carbon of the halogen-bond acceptor, and the average values are presented in Table 4. A higher second moment, to a first approximation, translates into a more efficient CP process, which may lead to a more intense ^{13}C resonance of the halogen-bond acceptor. The observation of peaks associated with the acceptor is therefore a simple indicator that cocrystallization has occurred.

The ^{19}F→^{13}C CP experiments allowed a more precise measurement of the ^{13}C chemical shifts of the halogen-bond donors, particularly in the cases of signal overlap with the ^{13}C resonances of the halogen-bond acceptors. For instance, in the case of **C1**, overlap of the carbon–fluorine resonance of the halogen-bond donor and the aromatic carbons of the halogen-bond acceptor impeded the accurate measurement of the ^{13}C chemical shift of the halogen-bond donor, as illustrated in Fig. 8. However, as a result of the improved signal of the resonances of the halogen-bond donor from ^{19}F→^{13}C CP, these chemical shifts could easily be determined. This was also observed in the cases of carbon covalently bonded to iodine, as in compounds **D1** and **D2**, which did not provide adequate signal intensity using ^{1}H→^{13}C CP.

3.3. ^{19}F solid-state NMR

Due to its high receptivity, natural abundance, and wide chemical shift range, ^{19}F SSNMR has previously been used in characterizing halogen-bonded compounds (Widdifield *et al.*, 2013; Gao *et al.*, 2012; Pérez-Torralba *et al.*, 2014). ^{19}F MAS SSNMR spectra of all compounds were acquired (Fig. 9) and the ^{19}F chemical shifts of the perfluorinated halogen-bond donors are listed in Table 5. Changes in the ^{19}F chemical shift upon formation of a halogen-bonded cocrystal are demonstrated to be good independent indicators of cocrystallization. As a result of the large ^{19}F chemical shift range, small changes in the chemical environment, such as the formation of a halogen bond, may result in significant chemical shift changes. A notable decrease in the chemical shift has been observed for all samples, with the largest change of −10.9±0.4 ppm noted for compound **D2**. Furthermore, the resolution in combination

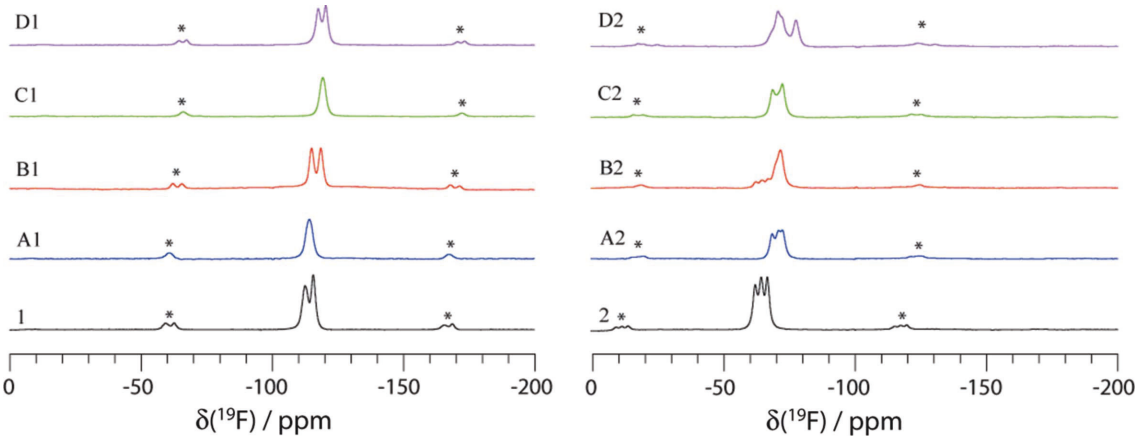

Figure 9
^{19}F solid-state NMR spectra with a MAS rate of 25 kHz, corresponding to **1** (*p*-DITFB), **2** (*sym*-TFTIB), **A1** (ACD)(*p*-DITFB), **A2** (ACD)(*sym*-TFTIB), **B1** (PHN)(*p*-DITFB), **B2** (PHN)(*sym*-TFTIB), **C1** (TMP)(*p*-DITFB), **C2** (TMP)(*sym*-TFTIB), **D1** (HMT)(*p*-DITFB), and **D2** (HMT)(*sym*-TFTIB). Asterisks (*) denote the spinning sidebands.

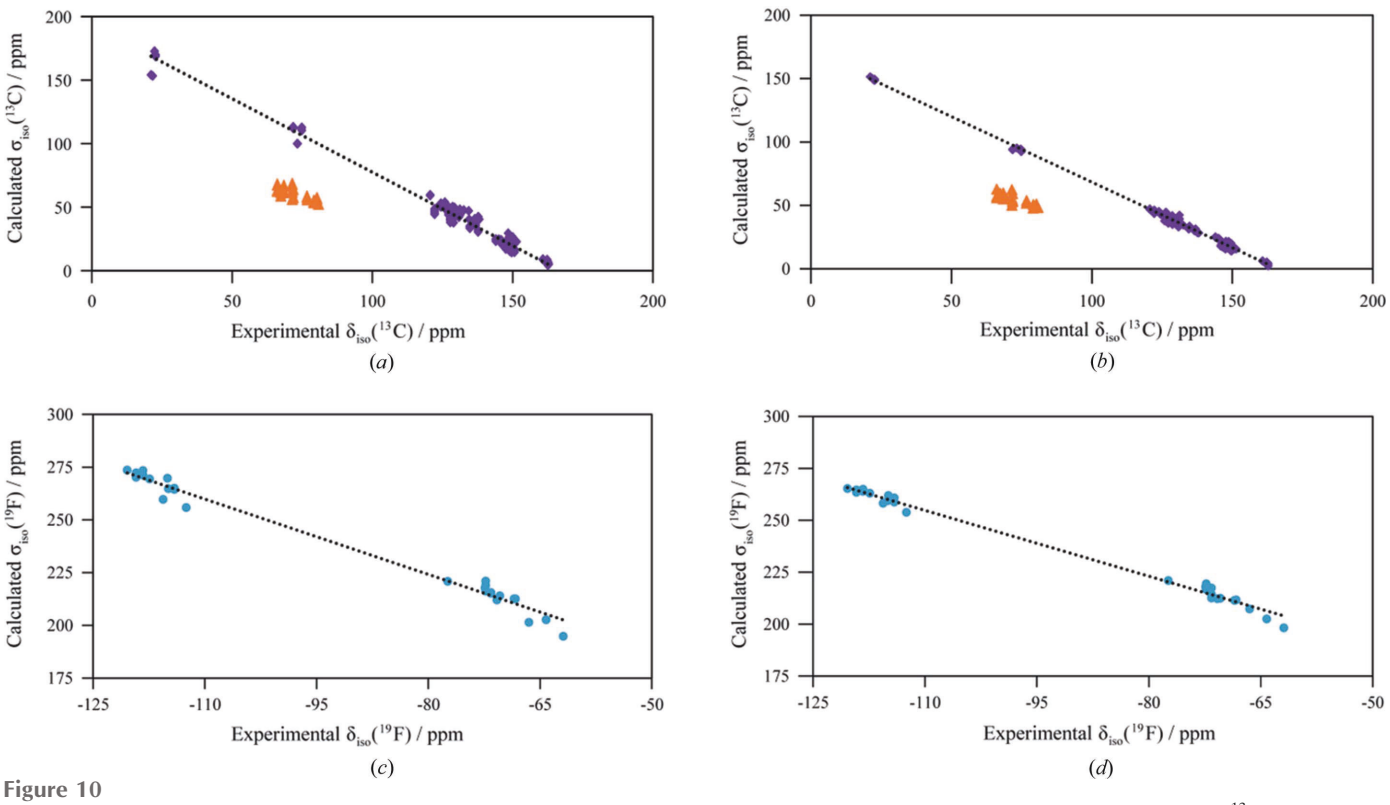

Figure 10
Plots of GIPAW DFT computed isotropic magnetic shielding constants *versus* experimental isotropic chemical shifts, showing data for ^{13}C, using (*a*) the experimental X-ray structures and (*b*) the optimized structures [data for carbons bonded to iodine (orange triangles) are not included in the fits], and data for ^{19}F, (*c*) using the experimental X-ray structures and (*d*) the optimized structures. The lines of best fit and Pearson's correlation coefficients are as follows: (*a*) $\sigma_{iso} = -1.1557\delta_{iso} + 193.09$ ppm, and $R^2 = 0.9868$; (*b*) $\sigma_{iso} = -1.0347\delta_{iso} + 171.88$ ppm, and $R^2 = 0.9964$; (*c*) $\sigma_{iso} = -1.1906\delta_{iso} + 128.93$ ppm, and $R^2 = 0.9847$; (*d*) $\sigma_{iso} = -1.0552\delta_{iso} + 138.67$ ppm, and $R^2 = 0.9919$.

Table 5
Experimental $\delta_{iso}(^{19}F)$ chemical shifts of the halogen-bond donor.

	XB Acceptor	$\delta_{iso}(^{19}F)$/ppm cocrystal with **1**	$\delta_{iso}(^{19}F)$/ppm cocrystal with **2**
	None (pure **1** or **2**)	−112.5±0.4	−61.9±0.2
		−115.6±0.3	−64.2±0.3
			−66.5±0.3
A	ACD	−114.1±0.7	−68.2±0.3
			−70.8±0.3
			−72.3±0.4
B	PHN	−114.9±0.3	−71.6±0.3
		−118.3±0.4	
C	TMP	−119.2±0.5	−68.5±0.3
			−72.3±0.4
D	HMT	−117.4±0.3	−70.4±0.4
		−120.4±0.3	−72.4±0.4
			−77.4±0.3

with the sensitivity of the chemical shifts allowed multiple crystallographic ^{19}F sites to be distinguished. In these cases, it is challenging to assign the chemical shift changes upon cocrystallization to specific crystallographic sites correctly, as one cannot easily determine which pairs of fluorine resonances should be compared.

GIPAW DFT calculations have become a standard feature of many recent NMR crystallography studies (Baias, Dumez *et al.*, 2013; Baias, Widdifield *et al.*, 2013; Salager *et al.*, 2010; Harris *et al.*, 2010; Widdifield *et al.*, 2016; Romao *et al.*, 2015; Widdifield & Bryce, 2009; Perras *et al.*, 2013; Perras & Bryce, 2012). We have carried out a series of such calculations of the ^{13}C and ^{19}F chemical shifts for the compounds studied herein, both with and without geometry optimization of the diffraction-based structures. All computed data are tabulated in the *Supporting information*. The computed ^{19}F isotropic chemical shifts generated from equation (2) are generally within several ppm of the experimental values; however, this equation follows from computations on metal fluorides (Sadoc *et al.*, 2011) and thus a recalibration was sought for the presently considered organic fluorides. This was achieved *via* the plot shown in Fig. 10, which depicts the calculated isotropic ^{19}F magnetic shielding constants *versus* the experimental chemical shifts. DFT geometry optimization of the single-crystal X-ray structure typically results in improved agreement with the experimental values, as quantified by the lines of best fit and correlation coefficients. Optimization results both in a slope closer to −1 (−1.0552 compared with −1.1906) and an R^2 value closer to unity (0.9919 *versus* 0.9847). Such a good agreement speaks to the high quality of the diffraction-based structures, but also shows that improved agreement with the NMR data is achievable through structure optimization.

A second series of calculations was subsequently performed based on the same X-ray structures, but with the removal of the halogen-bond acceptors. This approach allows one to model the impact of the C—I···N halogen bond on the ^{19}F

chemical shifts while also accounting for other crystallographic effects, such as the cases where the halogen-bond donor interacts with itself. In six of eight cases, the calculations predict a decrease in the ^{19}F chemical shifts upon the formation of a halogen-bonded cocrystal, which is in agreement with the experimental results (Table 5). For instance, one fluorine site in sample **C1** has a calculated change of −2.8 ppm and an experimental change of −3.6±0.5 ppm upon halogen bonding.

Many contemporary studies show that DFT refinement of a single-crystal X-ray structure results in a final structure which leads to DFT-computed chemical shifts that are in excellent agreement with experiment, in particular for ^{1}H (Baias, Dumez *et al.*, 2013; Baias, Widdifield *et al.*, 2013; Salager *et al.*, 2010). Such an NMR crystallographic approach provides convincing evidence that the resulting structures are in optimal agreement with both the X-ray and NMR data. Nevertheless, even in these cases, there may still be unacceptably large discrepancies between the experimental and computed ^{13}C chemical shifts. For halogen-bonded cocrystals featuring iodoperfluorobenzenes, we have previously shown that there often remains a large discrepancy between computed and experimental shifts, even when high-quality single-crystal structures are available (Viger-Gravel *et al.*, 2013; Viger-Gravel, Leclerc *et al.*, 2014). The reasons for this likely include the relativistic heavy-atom effect of the iodine on the ^{13}C chemical shifts, the difficulty in properly treating the noncovalent halogen-bonding interaction, as well as the usual possible limitations inherent to the functional used or the size of the system. The same types of results are seen for the current compounds (see *Supporting information*), *i.e.* computed ^{13}C isotropic chemical shifts are in reasonable agreement with experiment for several carbons, but for those bonded to iodine in particular, there remain significant discrepancies of several tens of ppm. While, given the context of our previous work in this area, this is not particularly surprising, it does serve as a *caveat* to NMR crystallographers that the quality of computed NMR parameters depends not only on the quality of the structural model, but also on the limitations of the computational method employed.

Shown in Fig. 10 are plots of the computed ^{13}C magnetic shielding constants *versus* the experimental chemical shifts. Several interesting findings are worth mentioning. First, the data clearly fall into two groups, *i.e.* those where carbon is bonded to iodine, and those where it is not. The latter data were fit and, as for the ^{19}F results, excellent correlations are observed, with improvements noted both in the slope (−1.0347 *versus* −1.1557), as well as the correlation coefficient (0.9964 *versus* 0.9868), upon DFT optimization of the X-ray structures. It should be noted that such a good agreement between experiment and computation is achieved only when the data are fit, as shown in Fig. 10. If one employs the experimental absolute shielding constant for ^{13}C in TMS, *i.e.* 184.1 ppm (Jameson & Jameson, 1987), the GIPAW DFT computed shifts deviate from the experimental ones much more significantly. Second, it is clear that the data for carbons bonded to iodine do not follow the same trend. These chemical shifts are clustered experimentally around 70 ppm, but the computed shifts are tens of ppm larger for the reasons described above. In summary, the carbon data lead to the same conclusion as do the fluorine data, that improved structures, as judged by the NMR data, are achievable through DFT structure optimization.

4. Conclusions

A series of halogen-bonded cocrystals was prepared featuring C—I···N halogen bonds between perfluorinated halogen-bond donors and nitrogen-containing heterocycles. Novel frameworks (**A2**, **B2**, and **C2**) have been characterized by single-crystal and powder X-ray diffraction. A further NMR crystallographic approach has provided both qualitative and quantitative information on these structures. ^{13}C solid-state NMR is a useful tool for probing the formation of a halogen bond by providing insights into the chemical environments of the cocrystals. There is a consistent chemical shift change for the halogen-bond acceptor upon the occurrence of a halogen bond and, in terms of the halogen-bond donor, the chemical shifts of the carbons covalently bonded to iodine increase. Moreover, ^{13}C solid-state NMR using ^{19}F→^{13}C CP proved to be an effective tool in obtaining better quality spectra of the halogen-bond donors in order to measure their isotropic chemical shifts with a higher accuracy when compared to ^{1}H→^{13}C CP. Additionally, ^{19}F→^{13}C cross polarization from the halogen-bond donor to the ^{13}C nuclei of the halogen-bond acceptor provides a convenient direct indication of cocrystallization. ^{19}F solid-state NMR has proven to be a powerful tool to characterize the perfluorinated halogen-bond donors as a result of short acquisition times, clearly identifiable chemical shift changes, and sensitivity, with the ^{19}F chemical shift decreasing upon halogen bonding. Finally, an XRD/DFT/NMR approach has been shown to provide final structures in best agreement with all experimental data.

Acknowledgements

DLB thanks the Natural Sciences and Engineering Research Council of Canada for research funding.

References

Aakeröy, C. B., Wijethunga, T. K., Desper, J. & Đaković, M. (2016). *Cryst. Growth Des.* **16**, 2662–2670.
Abate, A., Biella, S., Cavallo, G., Meyer, F., Neukirch, H., Metrangolo, P., Pilati, T., Resnati, G. & Terraneo, G. (2009). *J. Fluorine Chem.* **130**, 1171–1177.
Accelrys (2016). *Materials Studio*. Accelrys Software Inc., San Diego, California, USA.
Adiga, S., Aebi, D. & Bryce, D. L. (2007). *Can. J. Chem.* **85**, 496–505.
Allen, F. H., Lommerse, J. P. M., Hoy, V. J., Howard, J. A. K. & Desiraju, G. R. (1997). *Acta Cryst.* B**53**, 1006–1016.
Baias, M., Dumez, J.-N., Svensson, P. H., Schantz, S., Day, G. M. & Emsley, L. (2013). *J. Am. Chem. Soc.* **135**, 17501–17507.
Baias, M., Widdifield, C. M., Dumez, J.-N., Thompson, H. P. G., Cooper, T. G., Salager, E., Bassil, S., Stein, R. S., Lesage, A., Day, G. D. & Emsley, L. (2013). *Phys. Chem. Chem. Phys.* **15**, 8069–8080.
Becka, L. N. & Cruickshank, D. W. J. (1963). *Proc. Math. Phys. Eng. Sci.* **273**, 435–454.

Berger, G., Soubhye, J. & Meyer, F. (2015). *Polym. Chem.* **6**, 3559–3580.
Bondi, A. (1964). *J. Phys. Chem.* **68**, 441–451.
Bouchmella, K., Dutremez, S. G., Alonso, B., Mauri, F. & Gervais, C. (2008). *Cryst. Growth Des.* **8**, 3941–3950.
Braam, A. W. M., Eshuis, A. & Vos, A. (1981). *Acta Cryst.* B**37**, 730–732.
Braga, D., Grepioni, F., Maini, L., Mazzeo, P. P. & Rubini, K. (2010). *Thermochim. Acta*, **507–508**, 1–8.
Bruker (2003). *SADABS*. Bruker AXS Inc., Madison, Wisconsin, USA.
Bruker (2009). *SAINT* and *XPREP*. Bruker AXS Inc., Madison, Wisconsin, USA.
Bruker (2012). *APEX2*. Bruker AXS Inc., Madison, Wisconsin, USA.
Bryce, D. L. & Viger-Gravel, J. (2015). *Top. Curr. Chem.* **358**, 183–204.
Cavallo, G., Metrangolo, P., Milani, R., Pilati, T., Priimagi, A., Resnati, G. & Terraneo, G. (2016). *Chem. Rev.* **116**, 2478–2601.
Cinčić, D., Friščić, T. & Jones, W. (2008). *Chem. Mater.* **20**, 6623–6626.
Clark, T., Hennemann, M., Murray, J. S. & Politzer, P. (2007). *J. Mol. Model.* **13**, 291–296.
Clark, S. J., Segall, M. D., Pickard, C. J., Hasnip, P. J., Probert, M. I. J., Refson, K. & Payne, M. C. (2005). *Z. Kristallogr.* **220**, 567–570.
Desiraju, G. R., Shing Ho, P., Kloo, L., Legon, A. C., Marquardt, R., Metrangolo, P., Politzer, P., Resnati, G. & Rissanen, K. (2013). *Pure Appl. Chem.* **85**, 1711–1713.
Farrugia, L. J. (2012). *J. Appl. Cryst.* **45**, 849–854.
Gao, H. Y., Shen, Q. J., Zhao, X. R., Yan, X. Q., Pang, X. & Jin, W. J. (2012). *J. Mater. Chem.* **22**, 5336–5343.
Groom, C. R., Bruno, I. J., Lightfoot, M. P. & Ward, S. C. (2016). *Acta Cryst.* B**72**, 171–179.
Harris, R. K., Hodgkinson, P., Zorin, V., Dumez, J.-N., Elena-Herrmann, B., Emsley, L., Salager, E. & Stein, R. S. (2010). *Magn. Reson. Chem.* **48**, S103–S112.
Harris, R. K., Wasylishen, R. E. & Duer, M. J. (2009). Editors. *NMR Crystallography*. Chichester: Wiley.
Jameson, A. K. & Jameson, C. J. (1987). *Chem. Phys. Lett.* **134**, 461–466.
Le Gal, Y., Lorcy, D., Jeannin, O., Barrière, F., Dorcet, V., Lieffrig, J. & Fourmigué, M. (2016). *CrystEngComm*, **18**, 5474–5481.
Lemouchi, C., Vogelsberg, C. S., Zorina, L., Simonov, S., Batail, P., Brown, S. & Garcia-Garibay, M. A. (2011). *J. Am. Chem. Soc.* **133**, 6371–6379.
Liu, S.-F. & Schmidt-Rohr, K. (2001). *Macromolecules*, **34**, 8416–8418.
Lommerse, J. P. M., Stone, A. J., Taylor, R. & Allen, F. H. (1996). *J. Am. Chem. Soc.* **118**, 3108–3116.
Lucassen, A. C. B., Karton, A., Leitus, G., Shimon, L. J. W., Martin, J. M. L. & van der Boom, M. E. (2007). *Cryst. Growth Des.* **7**, 386–392.
Macrae, C. F., Bruno, I. J., Chisholm, J. A., Edgington, P. R., McCabe, P., Pidcock, E., Rodriguez-Monge, L., Taylor, R., van de Streek, J. & Wood, P. A. (2008). *J. Appl. Cryst.* **41**, 466–470.
Metrangolo, P., Neukirch, H., Pilati, T. & Resnati, G. (2005). *Acc. Chem. Res.* **38**, 386–395.
Nelyubina, Y. V., Korlyukov, A. A. & Lyssenko, K. A. (2014). *Mendeleev Commun.* **24**, 286–289.
Oh, S. Y., Nickels, C. W., Garcia, F., Jones, W. & Friščić, T. (2012). *CrystEngComm*, **14**, 6110–6114.
Pérez-Torralba, M., García, M. A., López, C., Torralba, M. C., Torres, M. R., Claramunt, R. M. & Elguero, J. (2014). *Cryst. Growth Des.* **14**, 3499–3509.
Perras, F. A. & Bryce, D. L. (2012). *J. Phys. Chem. C*, **116**, 19472–19482.
Perras, F. A., Korobkov, I. & Bryce, D. L. (2013). *CrystEngComm*, **15**, 8727–8738.
Politzer, P. & Murray, J. S. (2013). *ChemPhysChem*, **14**, 278–294.
Ramasubbu, N., Parthasarathy, R. & Murray-Rust, P. (1986). *J. Am. Chem. Soc.* **108**, 4308–4314.
Romao, C. P., Perras, F. A., Werner-Zwanziger, U., Lussier, J. A., Miller, K. J., Calahoo, C. M., Zwanziger, J. W., Bieringer, M., Marinkovic, B. A., Bryce, D. L. & White, M. A. (2015). *Chem. Mater.* **27**, 2633–2646.
Sadoc, A., Body, M., Legein, C., Biswal, M., Fayon, F., Rocquefelte, X. & Boucher, F. (2011). *Phys. Chem. Chem. Phys.* **13**, 18539–18550.
Salager, E., Day, G. M., Stein, R. S., Pickard, C. J., Elena, B. & Emsley, L. (2010). *J. Am. Chem. Soc.* **132**, 2564–2566.
Scheler, U. (1998). *Solid State Nucl. Magn. Reson.* **12**, 9–13.
Sheldrick, G. M. (1997). *CIFTAB*. University of Göttingen, Germany.
Sheldrick, G. M. (2015*a*). *Acta Cryst.* A**71**, 3–8.
Sheldrick, G. M. (2015*b*). *Acta Cryst.* C**71**, 3–8.
Spectral Database for Organic Compounds (SDBS) (2016). ^{13}C spectra; No. 1360 (**A**, acridine), No. 3559 (**B**, 1,10-phenanthroline), http://riodb01.ibase.aist.go.jp/sdbs/.
Syssa-Magalé, J.-L., Boubekeur, K., Leroy, J., Chamoreau, L.-M., Fave, C. & Schöllhorn, B. (2014). *CrystEngComm*, **16**, 10380–10384.
Syssa-Magalé, J.-L., Boubekeur, K., Palvadeau, P., Meerschaut, A. & Schöllhorn, B. (2005). *CrystEngComm*, **7**, 302–308.
Szell, P. M. J. & Bryce, D. L. (2016*a*). *Solid-State NMR Studies of Halogen Bonding*, in *Modern Magnetic Resonance*. In the press.
Szell, P. M. J. & Bryce, D. L. (2016*b*). *J. Phys. Chem. C*, **120**, 11121–11130.
Van Vleck, J. H. (1948). *Phys. Rev.* **74**, 1168–1183.
Viger-Gravel, J., Korobkov, I. & Bryce, D. L. (2011). *Cryst. Growth. Des.* **11**, 4984–4995.
Viger-Gravel, J., Leclerc, S., Korobkov, I. & Bryce, D. L. (2013). *CrystEngComm*, **15**, 3168–3177.
Viger-Gravel, J., Leclerc, S., Korobkov, I. & Bryce, D. L. (2014). *J. Am. Chem. Soc.* **136**, 6929–6942.
Viger-Gravel, J., Meyer, J. E., Korobkov, I. & Bryce, D. L. (2014). *CrystEngComm*, **16**, 7285–7297.
Walsh, R. B., Padgett, C. W., Metrangolo, P., Resnati, G., Hanks, T. W. & Pennington, W. T. (2001). *Cryst. Growth Des.* **1**, 165–175.
Wang, H., Hu, R. X., Pang, X., Gao, H. Y. & Jin, W. J. (2014). *CrystEngComm*, **16**, 7942–7948.
Weingarth, M., Raouafi, N., Jouvelet, B., Duma, L., Bodenhausen, G., Boujlel, K., Schöllhorn, B. & Tekely, P. (2008). *Chem. Commun.* pp. 5981–5983.
Widdifield, C. M. & Bryce, D. L. (2009). *Phys. Chem. Chem. Phys.* **11**, 7120–7122.
Widdifield, C. M., Cavallo, G., Facey, G. A., Pilati, T., Lin, J., Metrangolo, P., Resnati, G. & Bryce, D. L. (2013). *Chem. Eur. J.* **19**, 11949–11962.
Widdifield, C. M., Robson, H. & Hodgkinson, P. (2016). *Chem. Commun.* **52**, 6685–6688.
Xu, Y., Southern, S. A., Szell, P. M. J. & Bryce, D. L. (2016). *CrystEngComm*, **18**, 5236–5252.
Xu, Y., Viger-Gravel, J., Korobkov, I. & Bryce, D. L. (2015). *J. Phys. Chem. C*, **119**, 27104–27117.

Chapter 8 – Comparing the Halogen Bond to the Hydrogen Bond by Solid-State NMR Spectroscopy: Anion Coordinated Dimers from 2- and 3-Iodoethynylpyridine Salts

Statement of Authenticity. I certify that I have prepared the following article featuring my own work, with guidance from my supervisor Dr. David Bryce. Part of this work was performed at the Politecnico di Milano (Italy) under the supervision of Dr. Pierangelo Metrangolo. Dr. Victor Terskikh is acknowledged for assistance during my time at the 900 MHz NMR facility. Dr. Bulat Gabidullin is acknowledged for acquiring and solving the crystal structures presented in the article. Dr. Gabriella Cavallo, Dr. Giancarlo Terraneo, Dr. Pierangelo Metrangolo and Dr. David Bryce are acknowledged for support and contributions to the manuscript.

Permissions. I declare that I have obtained permission from all coauthors to include this article in my thesis. Chapter 8 has been reproduced from *Chem. Eur. J.* **2018**, *24*, 11364-11376, with permission from John Wiley & Sons, Inc. (DOI: 10.1002/chem.201801279)

Supporting Information. All supporting information for this article can be retrieved on the Wiley website:

https://onlinelibrary.wiley.com/doi/abs/10.1002/chem.201801279

Crystal Engineering

Comparing the Halogen Bond to the Hydrogen Bond by Solid-State NMR Spectroscopy: Anion Coordinated Dimers from 2- and 3-Iodoethynylpyridine Salts

Patrick M. J. Szell,[a] Gabriella Cavallo,[b] Giancarlo Terraneo,[b] Pierangelo Metrangolo,[b] Bulat Gabidullin,[a] and David L. Bryce*[a]

Abstract: Halogen bonding is an increasingly important tool in crystal engineering, and measuring its influence on the local chemical and electronic environment is necessary to fully understand this interaction. Here, we present a systematic crystallographic and solid-state NMR study of self-complementary halogen-bonded frameworks built from the halide salts (HCl, HBr, HI, HI_3) of 2-iodoethynylpyridine and 3-iodoethynylpyridine. A series of single crystal X-ray structures reveals the formation of discrete charged dimers in the solid state, directed by simultaneous $X^-\cdots H-N^+$ hydrogen bonds and $C-I\cdots X^-$ halogen bonds (X = Cl, Br, I). Each compound was studied using multinuclear solid-state magnetic resonance spectroscopy, observing ^1H to investigate the hydrogen bonds and ^{13}C, ^{35}Cl, and $^{79/81}Br$ to investigate the halogen bonds. A natural localized molecular orbital analysis was employed to help interpret the experimental results. ^1H SSNMR spectroscopy reveals a decrease in the chemical shift of the proton participating in the hydrogen bond as the halogen increases in size, whereas the ^{13}C SSNMR reveals an increased ^{13}C chemical shift of the C–I carbon for $C-I\cdots X^-$ relative to $C-I\cdots N$ halogen bonds. Additionally, ^{35}Cl and $^{79/81}Br$ SSNMR, along with computational results, have allowed us to compare the $C-I\cdots X^-$ halogen bond involving each halide in terms of NMR observables. Due to the isostructural nature of these compounds, they are ideal cases for experimentally assessing the impact of different halogen bond acceptors on the solid-state NMR response.

Introduction

Supramolecular chemistry has been established as an essential branch of chemistry, with the concept of charge transfer complexes recognized by the Nobel Prize in chemistry in 1969, and the first observations on crown ether complexes leading to the Nobel Prize in chemistry in 1987.[1,2] Alongside supramolecular chemistry, the field of crystal engineering was born, with the intention of designing the structures of solids with specific properties and for particular applications.[3] One of the most important tools in these fields has arguably been the hydrogen bond,[4] which has been extensively explored both in synthetic chemistry as well as in biological systems. Recent developments in the field of non-covalent interactions, including the theoretical aspects of σ-hole and π-hole interactions,[5–7] have offered the crystal engineer many additional tools in their pursuits of novel materials. From these interactions, the tetrel bond,[8] pnictogen bond,[9] chalcogen bond,[10] and halogen bond,[11] named from their electrophilic site,[12] have gained considerable attention.[13] The halogen bond is the most explored of these interactions, owing to its strength and versatility, with authoritative reviews on the subject available.[14,15]

The halogen bond is a non-covalent interaction between the region of positive electrostatic potential along the extension of a covalently bonded halogen, typically called the σ-hole,[16] and a Lewis base. The covalently bonded halogen, named the halogen bond donor (X), interacts with an electron donor, that is, the halogen bond acceptor (Y).[17] The halogen bond has been explored as a versatile interaction alternative to the hydrogen bond,[18] offering a highly linear bond ($\theta_{R-X\cdots Y}$ = 150–180°, where R denotes a covalently bonded substituent).[19–21] The presence of the halogen bond can be further recognized using the normalized distance parameter (R_{XB}), given in Equation (1), which is the quotient of the halogen bond length ($d_{X\cdots Y}$) and the sum of the van der Waals radii of both atoms participating in the halogen bond (d_{vdW}).[22] Thus, $R_{XB} < 1$ indicates the presence of a short contact, with smaller numbers suggesting a stronger halogen bond. If $R_{XB} > 1$, there is no contact to speak of. Halogen bonds are typically charac-

[a] P. M. J. Szell, Dr. B. Gabidullin, Prof. D. L. Bryce
Department of Chemistry and Biomolecular Sciences
University of Ottawa, 10 Marie Curie Private, Ottawa
Ontario, K1N 6N5 (Canada)
E-mail: dbryce@uottawa.ca

[b] Prof. G. Cavallo, Prof. G. Terraneo, Prof. P. Metrangolo
Laboratory of Supramolecular and Bionanomaterials
Department of Chemistry
Materials and Chemical Engineering "Giulio Natta"
Politecnico di Milano
Via L. Mancinelli 7, 20131 Milano (Italy)

Supporting information and the ORCID identification number(s) for the author(s) of this article can be found under:
https://doi.org/10.1002/chem.201801279.

terized by R_{XB} values of approximately 0.65 (very strong) to 0.95 (weak).

$$R_{XB} = \frac{d_{X\cdots Y}}{\sum d_{vdW}} \quad (1)$$

The halogen bond is highly tuneable, with the size of the σ-hole increasing with the size of the halogen.[16] The inclusion of electron withdrawing groups on the halogen bond donor moiety, such as fluorine[23,24] or the placement of halogens on ethynyl carbons,[25,26] further increases the magnitude of the σ-hole. For these reasons, the halogen bond is a valuable tool for the crystal engineer,[27,28] and a proper understanding will allow this interaction to be fully exploited.

Solid-state NMR (SSNMR) spectroscopy is a powerful tool to characterize the halogen bond,[29,30] offering insights into both the halogen bond acceptor and the halogen bond donor. The information offered by SSNMR is obtained through various parameters including chemical shifts,[31–33] the quadrupolar coupling tensor,[34–38] dipolar coupling,[39] and *J*-coupling;[38,40] these data are then used to provide structural, electronic, crystallographic, and/or dynamical information.[41] SSNMR experiments on the quadrupolar halides, $^{35/37}$Cl (spin $I=3/2$), $^{79/81}$Br (spin $I=3/2$), and ^{127}I (spin $I=5/2$), have provided direct information on the electric field gradient at the halogen bond acceptor,[34–36] which relates to the local and long-range molecular and crystal structures. The chlorine halogen bond donor has recently been directly probed by ultra-wideline ^{35}Cl SSNMR spectroscopy.[37]

Quadrupolar coupling results from the interaction between the electric field gradient (EFG) at a spin $>{}^1/_2$ nucleus and its electric quadrupole moment (*Q*). This quadrupolar interaction (QI) can be described by a traceless second-rank tensor with three components: $|V_{33}| \geq |V_{22}| \geq |V_{11}|$. The magnitude of the interaction is given by the quadrupolar coupling constant [C_Q, Eq. (2)], and the axial symmetry of the QI tensor is described by the asymmetry parameter [η, Eq. (3)].

$$C_Q = \frac{eV_{33}Q}{h} \quad (2)$$

$$\eta = (V_{11} - V_{22})/V_{33} \quad (3)$$

Despite the growing interest in iodoacetylenes,[42–47] there have been limited SSNMR studies of halogen-bonded compounds built with this functional group.[48–51] Furthermore, there have been no systematic investigations to date comparing the effects of various halogen bond acceptors in isostructural compounds on the SSNMR observables, and no information is available directly comparing the halogen bond to the hydrogen bond in terms of NMR responses. Here, we present the crystal structures for a series of self-complementary frameworks and charged dimers based on the halide salts of 2-iodoethynylpyridine (2-IEP) and 3-iodoethynylpyridine (3-IEP), shown in Figure 1, and investigate them by multinuclear solid-state magnetic resonance. In these examples, the halogen bond donor is the iodine on the acetylene group, whereas the halogen bond acceptor is either the nitrogen on the heterocycle for the neutral compounds, or the halide anions of the salts. The ^{13}C SSNMR spectra of these compounds allows us to compare the effect of the halogen bond to nitrogen, chloride, bromide, and iodide in terms of the chemical shift of the carbon covalently bonded to iodine, and the acetylene carbon. The hydrogen bonds in these frameworks are characterized by ^{1}H SSNMR, enabling the identification of trends in terms of the hydrogen bonding to chloride, bromide, and iodide. The observation of the halides using ^{35}Cl and $^{79/81}$Br NMR is supported by natural localized molecular orbital (NLMO) DFT calculations, an extension of the natural bond orbital analysis.[52] This approach uses molecular orbitals familiar to chemists to explain the origins of the observed NMR parameters. The results are expressed as a sum of Lewis contributions, which parallel the Lewis dot structure, and non-Lewis contributions.[53]

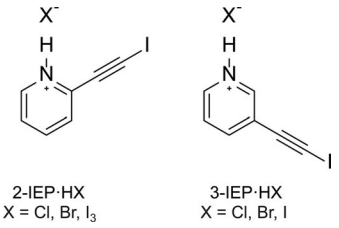

Figure 1. Compounds under investigation: 2-iodoethynylpyridine (2-IEP) and its HCl salt (2-IEP·HCl), HBr salt (2-IEP·HBr), HI_3 salt (2-IEP·HI_3); 3- IEP·HI)·iodoethynylpyridine (3-IEP) and its HCl salt (3-IEP·HCl), HBr salt (3-IEP·HBr), and HI salt (3-IEP·HI).

Results and Discussion

X-ray crystallography

Depictions of the X-ray crystal structures of the compounds under investigation are presented in Figure 2, and selected experimental crystallographic parameters are shown in Table S3. The triangular motif of the 2-IEP structure has been recently reported.[54,55] Each compound features a halogen bond, and in the cases of the halide salts, both halogen bonding and hydrogen bonding arise. A summary of the geometrical features for each compound, including the distances and angles of the halogen and hydrogen bonds, is given in Table 1.

Compounds 2-IEP·HCl and 2-IEP·HBr are isostructural and isomorphous, with each respective halide ion acting as both the halogen bond acceptor and hydrogen bond acceptor, resulting in charged dimers (Figure 2). The C–I···Cl$^-$ halogen bond ($R_{XB}=0.81$) is characterized by a slightly smaller reduced distance parameter than the C–I···Br$^-$ halogen bond ($R_{XB}=0.83$). This trend is also followed for the hydrogen bond lengths, with the analogous reduced distance parameters of the hydrogen bond (R_{HB}) being 0.75 for 2-IEP·HCl and 0.77 for 2-IEP·HBr. The halogen bond angle ($\theta_{C-I\cdots X^-}$) is very slightly more linear for 2-IEP·HCl versus 2-IEP·HBr, that is, 176.60(8)° compared to 175.75(10)°. The same holds for the hydrogen bond, with an angle ($\theta_{N-H^+\cdots X^-}$) of 159(2)° for 2-IEP·HCl and 155(3)° for 2-IEP·HBr. This counterintuitive decrease in angle with the size of the halide ion may be rationalized by considering the larger

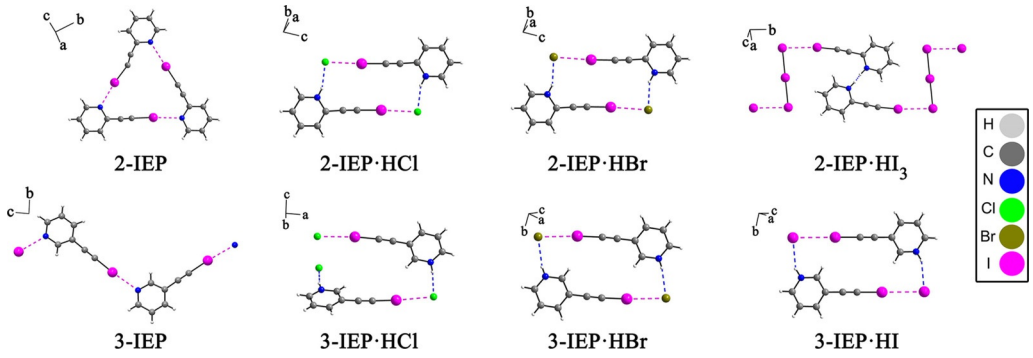

Figure 2. Depictions of the halogen bonded X-ray crystal structures of 2-iodoethynylpyridine (2-IEP), 3-iodoethynylpyridine (3-IEP), and their associated halide salts (HCl, HBr, HI, HI_3). The dashed magenta line denotes the halogen bond, whereas the dashed blue lines denote the hydrogen bonds. The geometrical details of these halogen bonds and hydrogen bonds are listed in Table 1.

Table 1. Summary of the halogen bond and hydrogen bond geometries of 2-IEP, 3-IEP, and their hydrohalide salts. The X represents the acceptor moiety: N, Cl^-, Br^-, or I^-. Errors are given in parentheses.

Compound	$d_{I\cdots X}$ [Å]	$d_{H\cdots X}$ [Å]	R_{XB}[b]	R_{HB}[b]	$\theta_{C-I\cdots X}$ [°]	$\theta_{N-H\cdots X^-}$ [°]	$\theta_{I\cdots X^-\cdots H}$ [°][c]
2-IEP	2.83(3)[a]		0.80		173.1(16)		
	2.84(2)[a]		0.80		177(2)		
	2.90(3)[a]		0.82		176.0(14)		
2-IEP·HCl	3.0217(8)	2.20(2)	0.81	0.75	176.60(8)	159(2)	94.1
2-IEP·HBr	3.1646(4)	2.36(3)	0.83	0.77	175.75(10)	155(3)	90.5
2-IEP·HI_3	3.448(4)		0.87		173.3(9)		
3-IEP	2.794(10)		0.79		176.0(3)		
3-IEP·HCl	3.1367(5)	2.16(2)	0.84	0.73	175.49(5)	171(2)	95.7
3-IEP·HBr	3.3001(4)	2.47(4)	0.86	0.81	169.31(9)	157(4)	87.7
3-IEP·HI	3.4713(7)	2.74(5)	0.88	0.86	170.3(2)	144(5)	89.3

[a] Three crystallographically distinct halogen bonds appear in the crystal structure of the 2-IEP trimer. [b] The normalized distance parameters of the halogen and hydrogen bonds. [c] The angle between the hydrogen and halogen bonds.

radius of the bromide ion, which elongates both the halogen bond and hydrogen bond, and strains the dimers.

In both 2-IEP·HCl and 2-IEP·HBr, the mixed halogen-bonded and hydrogen-bonded charged dimers are further assembled into supramolecular ribbons which develop along the (1,1,0) direction as shown in Figure 3. This arrangement is promoted by the hydrogen bonding interaction occurring between the belt of negative potential (labelled δ− in Figure 3) on the iodine atom and the aromatic hydrogen on the adjacent pyridinium ring (see Figure 3 for 2-IEP·HBr). It is known that when iodine is bound to a sp-hybridized carbon atom, iodine shows a remarkable anisotropic distribution of its electron density, developing an electron deficient area (σ-hole) along the elongation of the C–I bond and a belt of negative potential orthogonal to this bond. Additionally, the formation of the pyridinium moiety increases the Lewis acid character of the aromatic hydrogen atoms, making them good electron density acceptor sites (I1···H3 distance 3.11 Å in 2-IEP·HCl and 3.13 Å in 2-IEP·HBr). As a result, the C–I···X^- halogen bond synthon experiences a hydrogen bond coordinating the belt of negative potential surrounding the iodine halogen bond donor, and a hydrogen bond coordinating the Cl^-/Br^- acceptor. The resulting interactions create a ribbon-like motif as seen in Figure 3. As halide anions are spherical entities and are known to participate in many non-covalent interactions simultaneously, the charged ribbons interact via hydrogen bonding between the halide anions (Cl^- or Br^-) and the hydrogen atom, in the *ortho*-position relative to the N–H^+ moiety. These contacts result in the ribbons forming two-dimensional wave-like systems (Figure S8).

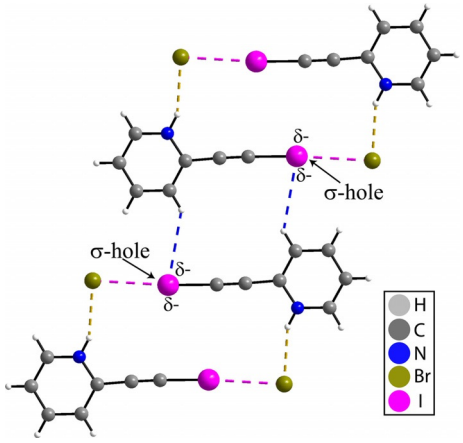

Figure 3. A supramolecular ribbon architecture is supported by C–I···Br^- halogen bonding (dashed magenta lines), N–H···Br^- hydrogen bonding (dashed brown lines) and C–H···I hydrogen bonding (dashed blue lines) interactions in 2-IEP·HBr. The σ-hole and the negative ESP on I are labelled.

2-IEP·HI was not obtained when repeating the synthesis with HI gas; instead, 2-IEP·HI_3 was obtained, perhaps due to the decomposition of HI gas into I_2. The structure of 2-IEP·HI_3 consists of an open framework, as shown in Figure 2, featuring a N–H^+···N hydrogen bond [$d_{N–H···N}$ = 1.805 Å, $\theta_{N–H···N}$ = 175.29°], and a halogen bond between the iodoacetylene group and the I_3^- anion [$d_{I···I}$ = 3.448(4) Å, $\theta_{C–I···I}$ = 173.3(9)°]. Due to a 0.5:0.5 partial occupancy of the hydrogen, we observe a superposition of N–H^+···N and N···$^+$H–N hydrogen bonds in the structural model. Overall, the structure shares a strong resemblance to the Greek keys motif as a result of the halogen bond to the first and third iodines of the I_3^- anion.

In contrast to the discrete triangular motif of 2-IEP, the crystal structure of 3-IEP displays an open zig-zag pattern with individual molecules linked together by C–I···N halogen bonds. The halogen bond distances are slightly shorter than those observed in 2-IEP ($d_{I···N}$ = 2.794(10) Å; $\theta_{C–I···N}$ = 176.0(3)°). The zig-zag networks interact via weak C–H···H–C contacts ($d_{H···H}$ = 2.31 Å), resulting in two-dimensional sheets. These sheets are stacked, forming the crystal of 3-IEP.

The structure of 3-IEP·HCl displays an open chain joined by C–I···Cl^- halogen bonds and N–H···Cl^- hydrogen bonds. The structure of 3-IEP·HCl is distinct from the 3-IEP·HBr and 3-IEP·HI structures, which consist of discrete charged dimers instead of an open framework. These charged dimers bear some resemblance to previously reported structures based on 3-bromopyridine.[56–59] Further, the ribbon motif reported for the 2-IEP·HCl and 2-IEP·HBr structures is also present in the 3-IEP·HBr and 3-IEP·HI structures. In these cases, the halides in the charged dimers are coordinated by the atoms in the *ortho*- and *meta*-positions relative to the N–H^+ moiety.

Throughout the 3-IEP·HX series presented here, the halogen bond distances and R_{XB} values increase as follows: 3-IEP·HCl (R_{XB} = 0.84), 3-IEP·HBr (R_{XB} = 0.86), 3-IEP·HI (R_{XB} = 0.88). The halogen bond angles ($\theta_{C–I···X^-}$) are most linear for 3-IEP·HCl, at 175.49(5)°, compared to 3-IEP·HBr at 169.31(9)°, and 3-IEP·HI at 170.3(2)°. Contrarily to the halogen bond, the hydrogen bond R_{HB} values differ considerably across the three structures, with values of 0.73, 0.81, and 0.86 for 3-IEP·HCl, 3-IEP·HBr, and 3-IEP·HI, respectively. The N–H^+···X^- hydrogen bond angles also vary, with the most linear hydrogen bond being that of 3-IEP·HCl at 171(2)°, followed by 3-IEP·HBr at 157(4)°, and 3-IEP·HI at 144(5)°.

The C–I···N halogen bonds of the neutral species consistently have the smallest R_{XB} values when compared to the charged samples, ranging between 0.79 and 0.82. Additionally, the C–I···N halogen bonds are the most linear, with $\theta_{C–I···N}$ angles between 173.1(16)° and 177(2)°. With regards to the halogen bonds involving the halides, the C–I···Cl^- halogen bond consistently had the smallest R_{XB} values when compared to the C–I···Br^- and C–I···I^- halogen bond, with the measured R_{XB} values increasing with the size of the halogen. These R_{XB} values are comparable to those for other structures featuring the C≡C–I···X^- motif.[26,50] For the N–H^+···X^- hydrogen bonds, the value of R_{HB} increased with the size of the halides, with 3-IEP·HCl having the smallest R_{HB} at 0.73, and 3-IEP·HI having the largest R_{HB} at 0.86. Notably, whereas the halogen bond angles range from 169.31(9)° to 177(2)°, a difference of 8(2)°, the hydrogen bond angle varies significantly, from 144(5)° to 171(2)°, a difference of 27(5)° across the series.

The charged dimers of 2-IEP and 3-IEP share many structural features, including the C–I···X^-···H–N^+ geometry surrounding the halide. Despite 3-IEP·HCl consisting of an open framework, the hydrogen and halogen bonds to the chloride anion share several geometrical features with the 2-IEP·HCl discrete dimer, such as $\theta_{I···X^-···H}$ values of 95.7° and 94.1°, respectively. Consequently, the halogen bonds and hydrogen bonds involving chloride, bromide, and iodide ions can be compared in terms of NMR observables. Although the neutral species (2-IEP, 3-IEP) do not share the same structural motifs as their halide salts, the C–I···N halogen bonds can be compared to the C–I···X^- halogen bonds in terms of ^{13}C chemical shifts of the carbon covalently bonded to iodine (C–I), and the acetylene carbon (C≡C–I).

^{1}H solid-state NMR spectroscopy

With the availability of high magic-angle spinning speeds, ^{1}H solid-state NMR has become a routine tool to characterize hydrogen bonded systems.[60,61] The ^{1}H MAS NMR spectra of 2-IEP·HI_3, 2-IEP·HBr, 2-IEP·HCl, 3-IEP·HI, 3-IEP·HBr, and 3-IEP·HCl are presented in Figure 4. The ^{1}H chemical shifts of the NH

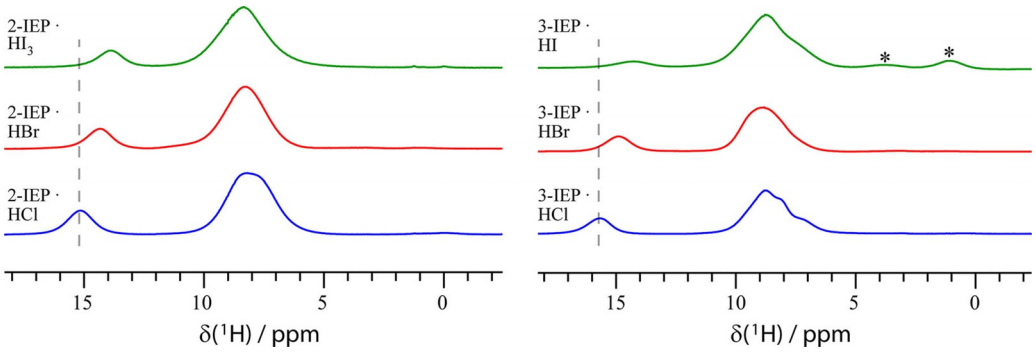

Figure 4. ^{1}H solid-state NMR spectra acquired at 21.1 T of the halide salts of 2-IEP and 3-IEP. The spectra of the HCl and HBr salts were acquired with a spinning frequency of 31.25 kHz, whereas those of the HI and HI_3 salts were acquired with a spinning frequency of 20 kHz. The dashed line serves as a guide to show the chemical shift of the hydrogen-bonded proton changes. The asterisks denote an impurity.

Table 2. Experimental and calculated ^{1}H chemical shifts of the N–H proton participating in the hydrogen bond in the halide salts of 2-IEP and 3-IEP.

Compound	Exptl $\delta(^1H)$ *N–H* [ppm]	Calcd $\delta(^1H)$ *N–H* [ppm]
2-IEP·HCl	15.14 ± 0.23	13.99
2-IEP·HBr	14.35 ± 0.24	12.79
2-IEP·HI_3	13.88 ± 0.21	13.39
3-IEP·HCl	15.68 ± 0.22	15.99
3-IEP·HBr	14.89 ± 0.18	14.80
3-IEP·HI	14.28 ± 0.30	13.70

protons are reported in Table 2. The following discussion focuses on the N–H proton, as it is directly participating in the N–H···X^- hydrogen bond. Within each series, a notable decrease in the ^{1}H chemical shift is observed as the size of the halide increases. For instance, the ^{1}H chemical shift for the 3-IEP·HX series decreases by 1.4 ± 0.4 ppm when comparing the chloride salt to the iodide salt. When comparing the 3-IEP·HCl salt to the HBr salt, a decrease of 0.8 ± 0.3 ppm is observed, approximately half of the shift observed for the iodide salt. This trend is also observed in the 2-IEP series, with a decrease of 0.8 ± 0.3 ppm when comparing the HCl salt to the HBr salt. It is to be noted that in the case of 2-IEP·HI_3, the ^{1}H chemical shift is also lower than for 2-IEP·HCl, despite the presence of a N–H···N hydrogen bond instead of a N–H···X^- hydrogen bond. The decreases in the ^{1}H chemical shifts upon the introduction of larger halides can be, in part, attributed to the heavy atom-light atom (HALA) effect, arising from increasing relativistic effects with the size of the halogen.[62–64]

To further look into the origin of this deshielding effect upon the introduction of larger halides, DFT calculations using ZORA corrections were performed on a model of each compound built from experimental Cartesian coordinates, both before and after geometry optimization. The complete results can be found in Table S4 (unoptimized geometry) and Table S5 (geometry optimized), listing the molecular orbital contributions to the isotropic shielding constant (σ_{iso}) of the $^+$N–H···X^- hydrogen bonded proton for each compound. The results were tabulated according to their molecular orbital contributions to σ_{iso}: core orbital contributions, halide ion lone pair contributions, N–H bonding orbital contributions, and bonding orbital contributions arising from all other atoms. The calculated $\sigma_{iso}(^1H)$ shielding values from the optimized geometries have been converted into chemical shifts ($\delta_{iso}(^1H)$) using Equation (4), in which σ_{ref} is 26.293 ppm,[65] and summarized alongside the experimental ^{1}H chemical shifts in Table 2.

$$\delta_{iso} = \frac{\sigma_{ref} - \sigma_{iso}}{1 - \sigma_{ref}} \quad (4)$$

Consequently, a higher shielding value (σ_{iso}) results in a lower chemical shift (δ_{iso}).

The calculated proton chemical shifts obtained from geometry-optimized structures are in good agreement with the experimental results, and better than the calculations performed on structures which were not geometry-optimized. In part, this is due to the correction of the N–H bond length, as proton positions obtained from X-ray crystallography have an associated uncertainty.[66,67] Moreover, the DFT results accurately reproduce the experimental trend that a decrease in the value of the proton chemical shift is seen as the size of the halide ion is increased. However, the calculated results for 2-IEP·HI_3 do not follow the above-mentioned trend, which we speculate is due to the presence of a $^+$N–H···N hydrogen bond in this structure instead of the $^+$N–H···X^- hydrogen bonds observed in the crystal structures of the other salts in the 2-IEP and 3-IEP series.

NLMO analysis of the proton magnetic shielding constants shows that the dominant orbital contribution to the $^+$N–^{1}H···X^- chemical shift changes is different in the 2-IEP series compared to the 3-IEP series. In the 2-IEP series, the halide ion lone pair contributions to σ_{iso} are largest in magnitude in the case of the chloride compound and smallest in the case of the iodide compound, corresponding to a decrease of the proton chemical shift as the size of the halide ion is increased. However, in the case of the 3-IEP series, the sum of bonding orbital contributions to σ_{iso} were found to be the most important for reproducing the experimentally observed trend, that is, to a decrease of the proton chemical shift as the size of the halide ion is increased. The more than 40 additional NLMO contributions to the ^{1}H magnetic shielding constants are not discussed further here due to their small magnitudes and lack of clear correlations to the total σ_{iso} values.

^{13}C Solid-state NMR spectroscopy

^{13}C SSNMR spectroscopy has been shown to be a versatile tool in characterizing both the halogen bond acceptor and the halogen bond donor, with the ^{13}C–I chemical shift being diagnostic for the occurrence of the halogen bond.[32,68] However, it is challenging to differentiate the effect of altering the identity of the halogen bond acceptor on the donor ^{13}C chemical shift, due to the fact that structural changes, such as the proximity of adjacent atoms and changes to the unit cell, can also have an effect on the ^{13}C chemical shifts. Therefore, isomorphous compounds sharing similar unit cell parameters, such as the compounds presented here, provide a means to attribute chemical shift changes to the identity of the bond acceptor, that is, Cl^-, Br^-, or I^-. Moreover, despite the fact that the neutral fragments are not isostructural and do not share similar unit cell parameters, the ^{13}C–I chemical shift can be used to compare the halogen bond involving nitrogen to the halogen bond involving a halide.

Presented in Figure 5 are the ^{13}C SSNMR spectra of 2-IEP, 3-IEP, and their halide salts, with a magnified view of the carbon resonance corresponding to the C–I carbon in the insets. As a result of residual dipolar coupling between ^{13}C and ^{127}I, the ^{13}C resonance for a C–I functional group is generally broadened and difficult to observe.[31,69,70] This is further aggravated by the quadrupolar nature of ^{127}I (spin $I = 5/2$) and the substantial C_Q values (> 1800 MHz) associated with covalently bonded iodine.[71] Although the resonances assigned to the C–I carbons on Figure 5 are broad and have a low signal intensity relative to the other resonances, they were clearly observed, and the

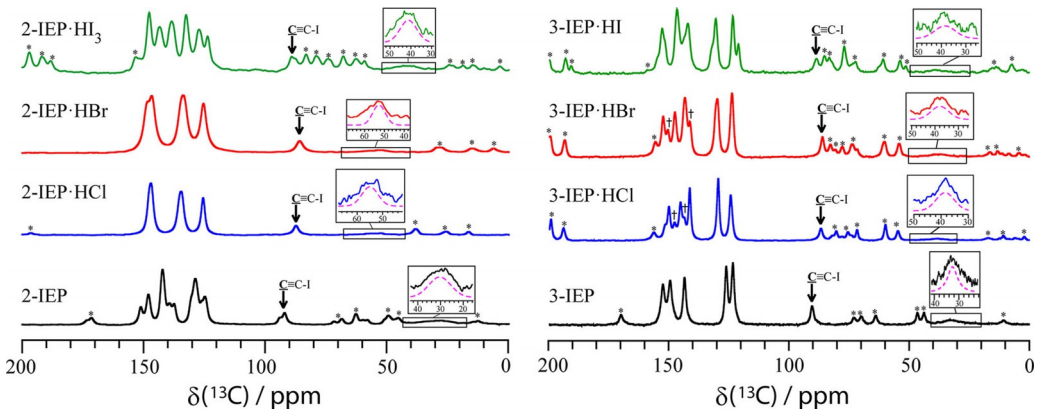

Figure 5. ^{13}C CP/MAS solid-state NMR spectra of 2-IEP, 3-IEP, and their hydrohalide salts. Variable spinning frequencies were used to prevent the overlap of spinning sidebands with the isotropic peaks. The magnified view of the C–I carbon resonance is shown in the inset. The asterisks denote spinning sidebands, while the daggers (†) denote the presence of a second phase.

^{13}C chemical shifts were determined using spectral simulations with WSolids software.[72] Due to the overlap of spinning sidebands with the isotropic chemical shifts, variable spinning speeds were used to separate the spinning sidebands from the isotropic peaks. The experimental and DFT calculated ^{13}C chemical shifts of the acetylene carbon (C≡C–I) and the carbon covalently bonded to iodine (C–I) of each compound are summarized in Table 3. In the aromatic region (≈140 to 160 ppm) of the spectra of 3-IEP·HCl and 3-IEP·HBr, the presence of resonances, denoted by †, are attributed to be the presence of a second phase in the sample. This second phase is also seen in the corresponding ^{35}Cl and $^{79/81}$Br SSNMR spectra (vide infra).

A significant ^{13}C–I chemical shift increase was observed between 2-IEP and each of the halide salts. Most notably, ^{13}C chemical shift increases for the C–I carbon of 27.1 ± 3.2 ppm when comparing 2-IEP to 2-IEP·HCl, 24.7 ± 2.6 ppm comparing 2-IEP to 2-IEP·HBr, and 13.4 ± 3.2 ppm comparing 2-IEP and 2-IEP·HI_3, were observed. For 3-IEP, a modest ^{13}C chemical shift increase was observed for the C–I carbon when comparing the neutral compound to that of the charged frameworks, with increases of 5.9 ± 1.4 ppm, 5.4 ± 1.9 ppm, and 5.9 ± 2.4 ppm seen for 3-IEP·HCl, 3-IEP·HBr, and 3-IEP·HI, respectively. In both the 2-IEP and 3-IEP series, the C–I···N halogen bond yielded the lowest chemical shift, and the C–I···Cl^- halogen bond yielded the highest chemical shift. Thus, especially in the case of the 2-IEP series, the counter ion has an important influence on the C–I chemical shift, with a 13.7 ± 3.3 ppm difference between 2-IEP·HCl and 2-IEP·HI_3.

Table 3. Experimental and DFT calculated ^{13}C chemical shifts of the acetylene carbon (**C**≡C–I) and the carbon covalently bonded to iodine (**C**–I) for 2-IEP, 3-IEP, and their hydrohalide salts.

	Exptl $\delta(^{13}C)$ **C**≡C–I [ppm]	Calcd $\delta(^{13}C)$ **C**≡C–I [ppm][a]	Exptl $\delta(^{13}C)$ **C**–I [ppm]	Calcd $\delta(^{13}C)$ **C**–I [ppm]
2-IEP	91.9 ± 0.2 93.6 ± 0.4	96.4	27.9 ± 2.2	39.9
2-IEP·HCl	87.2 ± 0.1	89.5	55.0 ± 2.3	93.4
2-IEP·HBr	85.8 ± 0.2	87.7	52.6 ± 1.3	91.2
2-IEP·HI_3	89.0 ± 0.2	74.6	41.3 ± 2.3	68.7
3-IEP	90.5 ± 0.2	93.4	32.6 ± 1.1	40.2
3-IEP·HCl	86.8 ± 0.2	89.8	38.5 ± 0.9	71.5
3-IEP·HBr	87.0 ± 0.2	87.9	38.0 ± 1.5	73.2
3-IEP·HI	88.9 ± 0.4	84.3	38.5 ± 2.1	65.7

Although the acetylene carbon (**C**≡C–I) does not directly participate in the halogen bond, its NMR response can provide valuable insights on the effect of the halogen bond on nearby substituents. Instead of an increase, as was noted above for the C–I ^{13}C chemical shift, a notable decrease in the ^{13}C chemical shift was observed for the acetylene carbon between the neutral fragments and the charged fragments. In this case, the neutral compounds exhibiting C–I···N halogen bonds have the highest ^{13}C chemical shifts at 91.9 ± 0.2 ppm and 90.5 ± 0.2 ppm for 2-IEP and 3-IEP, respectively. Upon introduction of the C–I···Cl^- halogen bond, the chemical shifts decreased to 87.2 ± 0.1 and 86.8 ± 0.2 ppm for 2-IEP and 3-IEP, respectively. In general, the chemical shift of the acetylene carbon in the charged dimers increases with the size of the halogen. The only exception is 2-IEP·HBr, which has the lowest chemical shift of 85.8 ± 0.2 ppm. For instance, between 3-IEP·HCl and 3-IEP·HI, a 2.1 ± 0.4 ppm difference in the ^{13}C chemical shift is observed, with the HCl salt having the lowest chemical shift. This trend follows for the halogen bond to Cl^- and I_3^-, as an increase of 1.8 ± 0.2 ppm is observed between 2-IEP·HCl and 2-IEP·HI_3.

The experimental ^{13}C chemical shifts are in good agreement with the ZORA DFT calculated chemical shifts for the acetylene carbons (**C**≡C–I), and in moderate agreement for the carbons covalently bonded to iodine (**C**–I). Given the broad chemical shift range associated with the ^{13}C isotope (≈250 ppm), the calculated acetylene chemical shifts are generally within 2% of the experimental values, while those for the C–I carbon are within 15% of the experimental values. The poorer agreement for the latter functional group has been previously discussed in the literature and can be attributed to iodine's relativistic effects,[73] in spite of attempting to correct for this using ZORA.[68,74] Despite this lower accuracy for the C–I carbon, the calculated ^{13}C chemical shifts do reflect the changes observed

experimentally, such as the significant increase in the ^{13}C chemical shift of the C–I carbon on going from the neutral C–I···N structures (2-IEP, 3-IEP) to the charged C–I···Cl^- structures (2-IEP·HCl, 3-IEP·HCl).

The NLMO analysis of the ^{13}C isotropic shielding constants suggests that the origins of the chemical shift changes may be similar in the case of the 2-IEP compounds and the 3-IEP compounds (see Tables S6 to S9 in the Supporting Information), in contrast to the case of the ^{1}H chemical shifts. Firstly, for the C–I carbon, there are four principal contributions to the ^{13}C isotropic shielding constant (σ_{iso}): carbon core orbitals, the bonding orbitals involving the acetylene carbon (the C≡C bond), the bonding orbital involving iodine, and the antibonding C–I orbital. Recall that an increased value of σ_{iso} results in a lower chemical shift. Following from the results in Table S7, in both series, the C–I bonding orbital contribution, which is negative in sign, increases in magnitude on going from the C–I···N motif to the C–I···X^- motif, causing σ_{iso} to decrease, and, consequently, δ_{iso} to increase. For instance, the contribution to σ_{iso} from the C–I bonding orbital is −54.6 ppm in 2-IEP, and increases in magnitude to −75.2 ppm in 2-IEP·HCl. Additionally, the contributions from the bonding orbitals involving the acetylene carbon (C≡C) also increase in magnitude upon the formation of the C–I···X^- motif, which further increases with the size of the halide ($I^- > Br^- > Cl^-$). For instance, the acetylene contribution to σ_{iso} is −20.2 ppm in 2-IEP, −43.4 ppm in 2-IEP·HCl, and −47.2 ppm in 2-IEP·HBr. Moreover, the C–I anti-bonding orbital contribution to σ_{iso} is generally larger in the C–I···N motif than the C–I···X^- motif, further leading to a lower δ_{iso} for the former. Following with the previous example, the C–I anti-bonding orbital contribution to σ_{iso} decreases from 20.5 ppm in 2-IEP to 16.9 ppm in 2-IEP·HCl. In total, the C–I and C≡C orbital contributions lead to a decrease in the σ_{iso} value, from 144.2 ppm in 2-IEP to 90.7 ppm in 2-IEP·HCl, and consequently the δ_{iso} value increases from 39.9 ppm in the C–I···N motif to 93.4 ppm in the C–I···Cl^- motif. These changes are generally greatest when Cl^- is the halogen bond acceptor, leading to the highest observed ^{13}C–I chemical shift in this motif.

This effect is further manifested in the case of the acetylene carbons (C≡C–I), where the contributions of the C–I bonding orbitals cause σ_{iso} to decrease upon the formation of the C–I···X^- motif, being most important in the case of the Cl^- anion and least important for the I^- anion. Following with the results from Table S9, the bonding orbital contributions involving the C–I carbon, which are negative in sign, increases in magnitude on going from the C–I···N motif to the C–I···X^- motif. For instance, this contribution is −37.3 ppm in 2-IEP and increases to −41.9 ppm in 2-IEP·HCl. Consequently, the calculated ^{13}C≡C–I chemical shifts decrease from 96.4 ppm in 2-IEP, to 89.5 ppm in 2-IEP·HCl. It is to be noted that the contributions to σ_{iso} of the acetylene carbon from the bonding orbitals involving the pyridine ring varies between each compound, being lowest for 3-IEP·HCl and highest for 3-IEP·HI.

^{35}Cl and $^{79/81}Br$ solid-state NMR spectroscopy

In order to further characterize the halogen bonding environments in the charged dimers, ^{35}Cl and $^{79/81}Br$ solid-state NMR spectroscopy was performed on the HCl salts and HBr salts, respectively. Due to difficulties in isolating large quantities of pure 2-IEP·HI_3 and 3-IEP·HI (and their thermal instabilities), along with the expected breadths of the NMR spectra, ^{127}I solid-state NMR was not attempted. The experimental ^{35}Cl and ^{81}Br spectra at 21.1 T were fit with QUEST[86] and are shown in Figure 6. The ^{35}Cl MAS spectra and the ^{79}Br spectra are shown

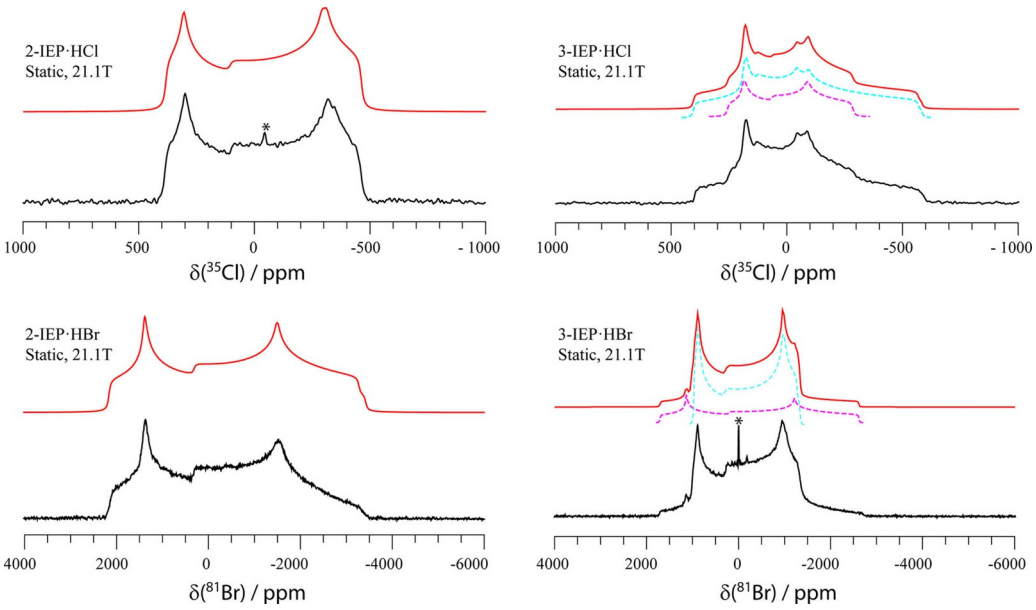

Figure 6. ^{35}Cl and ^{81}Br solid-state NMR at 21.1 T of 2-IEP·HCl, 3-IEP·HCl, and 2-IEP·HBr, 3-IEP·HBr, respectively. The experimental spectra are shown in black, and the red traces denote the simulated spectra. Deconvoluted simulated spectra are shown in dashed magenta and dashed cyan for 3-IEP·HCl and 3-IEP·HBr. Asterisks denote minor impurities. Difference spectra may be found in the Supporting Information.

in Figures S17 and S18. Additionally, DFT calculations (see the Experimental Section for details) were performed on cluster models of each compound to support the empirical results with a theoretical model, providing a breakdown of the molecular orbital contributions to the EFG at each halide. Although ^{127}I SSNMR spectroscopy was not feasible in these cases, NLMO calculations were performed in order to compare the EFG at each halide ion. Although the 2-IEP·HI structure was not obtained experimentally, a theoretical model of the 2-IEP·HI dimer was built based on the coordinates for 2-IEP·HBr in order to have a complete NLMO investigation of all the stable quadrupolar halides. In addition, a dimeric model of the 3-IEP·HCl was built based on the coordinates for 3-IEP·HBr to maintain consistency between all the calculations. It is to be noted that other contacts to the halides, such as the H···Cl contact discussed in the X-ray section, are not taken into account in our calculations in effort to isolate the effect the hydrogen and halogen bonding effects on the EFG. This lack of periodicity in the calculations is manifested in a lower agreement between experimental and calculated results, but did not impede the analysis.

Reasonable ^{35}Cl signal intensity was obtained for both samples, both in MAS and static experiments. The resulting ^{35}Cl chemical shift and quadrupolar coupling parameters of 2-IEP·HCl and 3-IEP·HCl, summarized in Table 4, reveal the similarities between both chloride ion environments. There are small differences of 14 ± 8 ppm and of 0.47 ± 0.09 MHz in the ^{35}Cl chemical shift and C_Q values, respectively. Such small differences are reasonable, considering the two salts share the same C–I···Cl$^-$···H–N$^+$ moiety. However, real differences in the halogen bonding and hydrogen bonding geometry between 2-IEP·HCl and 3-IEP·HCl are manifested in the η values and the chemical shift anisotropy parameters (Ω, κ), along with the Euler angles (α, β, γ). In the case of 3-IEP·HCl, a minor impurity was present which is attributed to the formation of a different polymorph, given the similarity of the NMR parameters [C_Q = 4.85 MHz, $\eta=0.40$, $\delta_{iso}=70$ ppm, $\Omega=35$ ppm, $\kappa=0$, $\alpha=30^\circ$, $\beta=10^\circ$, $\gamma=30^\circ$]. According to the signal intensity, the concentration of this second polymorph is of approximately 10%, and did not impede analysis. The trace impurity in 2-IEP·HCl, denoted by an asterisk, is NaCl(s), given its chemical shift and narrow line width.

Much like the ^{35}Cl NMR spectra, both the static ^{81}Br (Figure 5) and ^{79}Br (Figure S18) solid-state NMR spectra of 2-IEP·HBr and 3-IEP·HBr had reasonable signal intensities considering their large spectral widths. As bromine has two NMR active isotopes with unique quadrupole moments ($Q(^{81}Br)=262(3)$ mb, $Q(^{79}Br)=313(3)$ mb),[75] two different values of C_Q are expected [see Eq. (2)]. However, the EFG at both nuclides should be the same, with the resulting C_Q arising solely due to the difference in quadrupole moments. Therefore, the C_Q obtained from ^{79}Br NMR should be in agreement with the ^{81}Br NMR results after scaling by a factor of ≈1.19 [$Q(^{79}Br)/Q(^{81}Br)$], allowing us to verify the goodness of the spectral fitting. The trace impurity in 3-IEP·HB is NaBr(s), due to its chemical shift.

Comparing the NMR parameters between the bromide salts, 2-IEP·HBr has higher C_Q and δ_{iso} values versus 3-IEP·HBr. This bears resemblance to the comparison between 2-IEP·HCl and 3-IEP·HCl, in which case the former also had a higher value of C_Q and δ_{iso}. In contrast, the η values are not comparable between the chloride and bromide samples, perhaps due to the different contributions to $|V_{22}|$ and $|V_{11}|$. In addition, much like the 3-IEP·HCl sample, a minor impurity was measured in 3-IEP·HBr, which is also attributed to the occurrence of a different polymorph due to the similarities of the NMR parameters [$C_Q[^{81}Br]=38.9$ MHz, $C_Q[^{79}Br]=47.0$ MHz, $\eta=0.34$, $\delta_{iso}=200$ ppm]. According to the signal intensity, the concentration of this second polymorph is approximately 15%, and did not impede analysis.

Although the C_Q values for each of the halide ions are not immediately comparable, the $|V_{33}|$ eigenvalues can be extracted using Equation (2). As a result of the different electronic configurations of the halides, most importantly the inner-shell electrons, the Sternheimer antishielding factor may also be considered using Equation (4), as it has been shown to have a considerable impact on the observed EFG at a nucleus.[76,77]

$$eq_{obs} = (1-\gamma_\infty)eq_{lattice} \quad (5)$$

In Equation (5), the observed EFG (eq_{obs}) is related to the lattice EFG ($eq_{lattice}$) by an antishielding factor (1-γ_∞). The antishielding factor has a value of 43.0, 81.0, and 163.0 for $^{35/37}$Cl, $^{79/81}$Br, and ^{127}I, respectively.[78] The comparison of the EFG across the halides will allow for the electronic charge distributions at the halide participating in a hydrogen and halogen bond in the C–I···X$^-$···H–N$^+$ motif to be compared. An NLMO analysis was performed in order to quantify the contributions

Table 4. Experimental ^{35}Cl and ^{79,81}Br solid-state NMR parameters for the hydrochloride salts and hydrobromide salts of 2-IEP and 3-IEP.

	$\lvert C_Q \rvert$ [MHz]	$\lvert V_{33} \rvert$ [a.u.]	η	δ_{iso} [ppm][a]	Ω [ppm]	κ	α [°]	β [°]	γ [°]
2-IEP·HCl	6.65 ± 0.08	0.347 ± 0.004	0.15 ± 0.03	86 ± 6	40 ± 10	-0.2 ± 0.2	90 ± 40	90 ± 30	30 ± 20
3-IEP·HCl	6.18 ± 0.05	0.322 ± 0.003	0.61 ± 0.04	72 ± 5	70 ± 10	-0.6 ± 0.1	90 ± 10	80 ± 20	25 ± 10
2-IEP·HBr	(^{79}Br) 52.4 ± 0.04 (^{81}Br) 43.5 ± 0.04	0.730 ± 0.002	0.34 ± 0.03	250 ± 15	200 ± 60	0.5 ± 0.5	90 ± 50	55 ± 30	130 ± 20
3-IEP·HBr	(^{79}Br) 37.5 ± 0.05 (^{81}Br) 31.2 ± 0.04	0.520 ± 0.002	0.14 ± 0.03	215 ± 20	200 ± 50	0 ± 0.5	25 ± 5	80 ± 5	10 ± 10

[a] ^{35}Cl chemical shifts are referenced to −41.11 ppm relative to NaCl(s), whereas ^{79}Br and ^{81}Br chemical shifts are referenced to 1.29 ppm and 1.57 ppm relative to NaBr(s), respectively.

to the $|V_{33}|$, $|V_{22}|$, and $|V_{11}|$ eigenvalues, summarized in Tables S11, S13, and S15, respectively. This analysis serves as a complement to previous computational studies,[79–81] and analysis on NLMO contributions to the EFG,[34] with a focus on the differences between halide halogen bond acceptors. In this motif, the most important contributions to the EFG at the halides are: the core orbital contributions, lone pair orbital contributions, iodine bonding orbital contributions, and bonding orbital contributions involving the hydrogen bond. In order to compare the EFG across each halide, a consistent dimeric model was used for each compound, including theoretical dimeric models of 2-IEP·HI and 3-IEP·HCl.

Illustrated in Figure 7, the computational results for each geometry optimized discrete dimer reveal that the $|V_{33}|$ eigenvector is oriented perpendicularly to the axis of the dimer, the $|V_{22}|$ eigenvector is oriented towards the halogen bond donor,

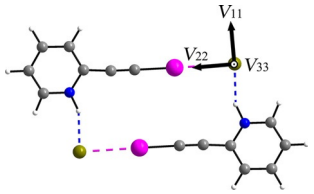

Figure 7. The bromine quadrupolar coupling tensor orientation of 2-IEP·HBr following a geometry optimization, showing $|V_{33}|$ oriented perpendicular to the plane of the dimer (towards the reader), $|V_{22}|$ aligned with the halogen bond, and $|V_{11}|$ oriented along the hydrogen bond.

and the $|V_{11}|$ eigenvector is aligned with the hydrogen bond. This orientation holds for each dimer, including the theoretical model of 2-IEP·HI. However, in the case of the dimeric model of 3-IEP·HCl, while $|V_{33}|$ remains oriented perpendicular to the dimer, the $|V_{22}|$ and $|V_{11}|$ eigenvectors deviate slightly from the halogen bond and hydrogen bond, respectively. As the eigenvectors have a consistent orientation towards the halogen bond or the hydrogen bond, a breakdown of the contributions to the EFG tensor for each halide offers insights into the molecular orbitals participating in these interactions. As for the calculations performed using experimental X-ray coordinates, $|V_{33}|$ is instead aligned with the halogen bond, $|V_{22}|$ is oriented perpendicular to the dimer, and $|V_{11}|$ remains aligned with the halogen bond. As the $|V_{33}|$ and $|V_{22}|$ eigenvectors have similar magnitudes, small changes in the local geometry, such as the correction of the N–H bond length, can contribute to the reorientation of the EFG tensor.

Following with the results using optimized geometries, the most important contribution to the $|V_{33}|$ eigenvector of the halide are the lone pair orbitals, followed by the core orbitals. The lone pair orbitals originating from the halogen bond donor did not have an important contribution (<6%), perhaps due to the eigenvector's orientation being perpendicular to the dimer. Furthermore, the calculations suggest that the halide's lone pair orbitals have the greatest relative contribution in $Br^- > I^- > Cl^-$. For instance, in the 3-IEP series, the relative contribution of the lone pair orbitals to $|V_{33}|$ for 3-IEP·HBr, 3-IEP·HCl, and 3-IEP·HI is of 92.4, 89.4, and 81.8%.

As for the $|V_{22}|$ eigenvector, which is oriented along the halogen bond, a significant negative contribution arises from the lone pair orbitals of the iodine from the halogen bond donor. Taking the 2-IEP series for example, the relative contribution from the halogen bond donor is most important in 2-IEP·HCl (12.5%), followed by 2-IEP·HBr (10.3%), and finally 2-IEP·HI (7.7%). These results suggest that in these compounds, the halogen bond has the highest relative contribution in the order of $Cl^- > Br^- > I^-$. This may support the reduction in the EFG tensor component oriented towards the halogen bond, with the relative contribution being largest for the chloride salts, and smallest in the iodide salts. Furthermore, while iodine's lone pair orbitals had a negative contribution to the $|V_{22}|$ eigenvector, they had a positive contribution to the $|V_{11}|$ and $|V_{33}|$ eigenvectors.

For the $|V_{11}|$ eigenvector, which is aligned with the hydrogen bond, the most important contributions are from the halide's lone pair orbital, followed by the core and bonding orbitals involving the nitrogen from the hydrogen bond. In these cases, however, the contributions from the hydrogen bond fluctuated considerably between samples. Clearly, however, the hydrogen bond had a negative contribution to $|V_{11}|$, with the magnitude generally increasing with the size of the halogen. For instance, for the 3-IEP series, the contribution for the HCl, HBr, and HI salts is 5.4, 16.0, and 29.5%, respectively. These results suggest a relative contribution from the hydrogen bond to the EFG component in the order of $I^- > Br^- > Cl^-$ in these compounds, in stark contrast of the trend observed for the halogen bond.

Shown in Figure 8 is a summary of the calculated and experimental $|V_{33}|$ eigenvalues for each halide in the 2-IEP and 3-IEP dimers. The overall EFG is largest in the iodide salts, followed by the bromide salts, and finally the chloride salts. Accounting for the Sternheimer antishielding factor for the HCl and HBr salts, shown in Figure S20, the relative $|V_{33}|$ for the 2-IEP series increases in the order of $Br^- > Cl^-$, both experimentally and computationally.

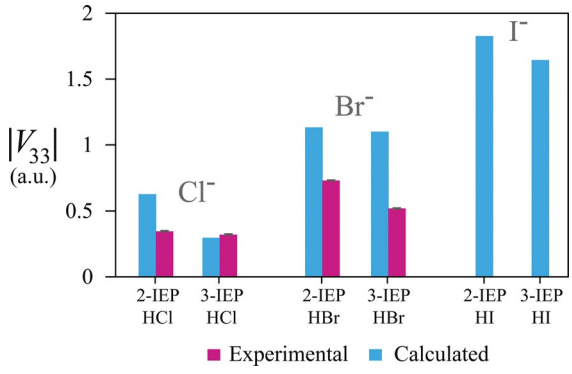

Figure 8. Experimental (magenta) and calculated (blue) $|V_{33}|$ of 2-IEP·HX and 3-IEP·HX (X = Cl^-, Br^-, I^-). The charged dimeric model was used in all calculations for consistency.

Conclusions

The crystal structures for a series of halide salts built from 2-iodoethynylpyridine (2-IEP) and 3-iodoethynylpyridine (3-IEP) are reported, featuring the cooperation of hydrogen and halogen bonds. In these compounds, the halogen bond maintains linearity, with an 8.85(9)° deviation in $\theta_{C-I\cdots X^-}$ across the series, whereas the hydrogen bond angle varies by 27(5)°. This is well in line with the higher directionality of halogen bond compared to the hydrogen bond. Each compound was investigated by multinuclear solid-state NMR: ^{1}H to investigate the nature of the hydrogen bond, ^{13}C to investigate the nature of the halogen bond, along with ^{35}Cl and $^{79/81}$Br to investigate the halogen bond acceptor. The ^{1}H SSNMR results show a shielding of the hydrogen bond donor as the size of the halogen increases, whereas the ^{13}C SSNMR shows a large chemical shift increase of the C–I carbon upon going from the C–I···N motif to the C–I···X$^-$ motifs. A direct investigation of the halide halogen bond acceptor by SSNMR, in addition to NLMO calculations, reveals an increase in the electric field gradients with the size of the halogen, summarized in Figure 8. Computational results from dimeric models suggest that, in this motif, the EFG eigenvector $|V_{22}|$ is oriented towards the halogen bond donor, whereas the smallest component of the EFG tensor, $|V_{11}|$, is oriented towards the hydrogen bond. In these compounds, the relative contribution to $|V_{22}|$ from the halogen bond increases in the order of $Cl^- > Br^- > I^-$, in contrast to the relative contributions to $|V_{11}|$ from the hydrogen bond, in the order of $I^- > Br^- > Cl^-$.

We speculate that the agreement between the experimental and computational data reported in this work could be further improved in the future by simultaneously invoking periodic boundary conditions along with higher-level relativistic effects while maintaining dispersion corrections.

Overall, this work demonstrates from crystal engineering and multinuclear solid-state magnetic resonance perspectives the relative influences and roles of halogen and hydrogen bonds. In the case of the former, the interplay of the two interactions resulted in a range of supramolecular architectures ranging from triangles to dimers to open chains and supramolecular wavy ribbons. From the solid-state NMR perspective, interaction tensor magnitudes and orientations have been demonstrated to be exquisitely sensitive to the two types of interactions and the role of different halogen bond donor moieties in determining the NMR response has been elucidated.

Experimental Section

2-Ethynylpyridine (98%), 3-ethynylpyridine (98%), phosphorus pentoxide (98%), anhydrous calcium chloride (96+%), aqueous HBr (42%), and aqueous HI (57%) were purchased from Sigma Aldrich and used without further purification. Aqueous HCl (38%) and all solvents were purchased from Fisher Scientific. 2-Iodoethynylpyridine[54] and 3-iodoethynylpyridine were synthesized using a literature procedure.[82] [3-iodoethynylpyridine: ^{1}H NMR ([D$_4$]MeOH, TMS, 300 MHz) 8.56, 8.47, 7.85, 7.40 ppm; ^{13}C NMR ([D$_4$]MeOH, TMS, 300 MHz) 153.2, 149.3, 141.2, 124.9, 122.7, 90.4, 17.6 ppm. HREI-MS: *m/z* elemental analysis calcd (%) for C_7H_4IN $[M]^+$: 228.938, found: 228.939]

The hydrohalide salts of 2-IEP and 3-IEP were produced by dissolving the appropriate compound in anhydrous ether and bubbling the hydrohalic acid gas through the solution. The HCl gas was generated by dropping hydrochloric acid on anhydrous $CaCl_2$. The HBr and HI gasses were generated by dropping hydrobromic acid or hydroiodic acid solution onto powdered phosphorus pentoxide. All gaseous acids were bubbled into the ether solution using a flow of argon, and the product precipitated immediately. Lower yields were obtained for the HBr and HI samples, perhaps due to the unstable nature of the acid in the gas phase. The product was filtered and dried. The neutral compounds were recrystallized from acetonitrile. All halide salts were recrystallized from methanol. Phase purity was verified by powder X-ray diffraction on a Rigaku Ultima IV instrument with a 2θ ranging from 5° to 65° at a rate of 1° per minute using CuKα radiation. All yields, melting points, and powder X-ray diffractograms may be found in the Supporting Information.

^{1}H solid-state NMR spectroscopy

All ^{1}H SSNMR experiments were performed in a magnetic field of 21.1 T using a Bruker 2.5 mm HX probe and a Bruker Avance II spectrometer. A rotor synchronized Hahn echo ($\pi/2$—τ—π—acq) was used in all cases, with a $\pi/2$ pulse of 2.5 μs. A MAS rate of 31.25 kHz was used for the chloride and bromide samples, whereas in the cases of the iodide samples, a spinning speed of 20 kHz was used. A recycle delay of 360 s was used in all cases, and 8 transients were acquired.

^{13}C solid-state NMR spectroscopy

All ^{13}C CP/MAS SSNMR experiments were performed in a magnetic field of 9.4 T ($\nu_L(^{13}C) = 100.6$ MHz) using a Bruker 4 mm HXY probe and a Bruker Avance III NMR spectrometer. $^{1}H \rightarrow {}^{13}C$ CP was used with a 4.6 μs proton $\pi/2$ pulse, a 2000 μs contact time, and a 54.3 kHz ^{1}H decoupling frequency. ^{13}C chemical shifts were referenced to glycine at 176.6 ppm (^{13}C=O) relative to tetramethylsilane (TMS). Variable spinning speeds were used to separate the spinning sidebands from the isotropic peaks, whereas in the cases of the iodide salts, slower spinning speeds were used to prevent sample decomposition. Further information, such as spinning speeds and the number of scans may be found in Table S2.

^{35}Cl solid-state NMR spectroscopy

Static ^{35}Cl SSNMR spectroscopy was performed in a magnetic field of 21.1 T on a Bruker Avance II NMR spectrometer, using a home-built probe with a 4 mm coil. A quadrupolar echo sequence was used ($\pi/2$—τ—$\pi/2$—acq) was used with a 3 μs $\pi/2$ pulse and a 66 μs echo delay. A total of 2048 transients were collected for 2-IEP·HCl, and 3072 transients were collected for 3-IEP·HCl. MAS experiments were performed using a Bruker 2.5 mm probe, spinning at 31.25 kHz, and using a rotor synchronized quadrupolar echo. A total of 20480 transients were collected for 2-IEP·HCl and 18432 transients were collected for 3-IEP·HCl. In all cases, a recycle delay of 3 s was used. All ^{35}Cl NMR spectra are referenced to NaCl(s) at −41.11 ppm.[83] The static ^{35}Cl spectra were fit using QUEST,[86] whereas the ^{35}Cl MAS spectra were fit with WSolids.[72] The Euler angles follow the passive ZYZ convention,[84] specified within QUEST[86] and WSOLIDS.[72]

$^{79/81}$Br solid-state NMR spectroscopy

Static ^{79}Br and ^{81}Br SSNMR was performed at 21.1 T on a Bruker Avance II NMR spectrometer, using a homebuilt probe with a 5 mm coil. The ^{81}Br acquisition was performed using a quadrupolar echo sequence ($\pi/2-\tau-\pi/2-$acq) with a 0.5 μs $\pi/2$ pulse and a 28.5 μs echo delay with continuous wave proton decoupling, and using a variable-offset cumulative spectral (VOCS)[85] acquisition method with offset changes of +/−500 kHz and 24576 transients. All ^{81}Br spectra were processed, and then coadded in the frequency domain to yield the full spectrum. All $^{79/81}$Br spectra were fit using QUEST.[86] The ^{79}Br acquisitions were performed using WURST-QCPMG,[87] with 10 μs pulse lengths, 2 MHz pulse bandwidth sweep from low to high frequency, acquiring 64 echoes with a 10 kHz spikelet separation (8 μs pulse ringdown, 70 μs echo time), and continuous wave proton decoupling. For both compounds, variable-offset cumulative spectral (VOCS)[85] acquisition method was used with offset changes of +/−500 kHz with a total of 2048 transients per spectrum. A total of five subspectra were acquired for each sample, processed, and then coadded in the frequency domain to yield the full spectrum. In all cases, a recycle delay of 0.5 s was used. The ^{79}Br and ^{81}Br spectra were referenced to KBr(s) at 54.31 ppm and 54.51 ppm, respectively.[83] The Euler angles follow the passive ZYZ convention,[84] specified within QUEST[86] and WSOLIDS.[72]

Computational details

All DFT and NLMO calculations were performed using the Amsterdam Density Functional software (ADF, 2016)[89–91] using the revised GGA exchange-correlation functional (revPBE) of Zhang and Yang.[92] Models for each compound were generated using GaussView, with atomic positions taken from the crystal structure. The models of 2-IEP·HCl, 2-IEP·HBr, 3-IEP·HBr, and 3-IEP·HI consisted of charged dimers. A theoretical model of the 2-IEP·HI dimer was built using the atomic coordinates from the 2-IEP·HBr dimer. In the case of 2-IEP, 3-IEP, 3-IEP·HCl, and 2-IEP·HI_3, the models included the halogen bond moiety and all interacting molecules. The geometry optimizations were performed using ADF, accounting for relativistic effects (ZORA) and dispersion forces using Grimme3 BJDAMP.[93] All compounds were optimized using the TZP basis set, with the exception of 2-IEP·HBr and the theoretical model of 2-IEP·HI, which were optimized using the TZ2P basis set. The geometry optimization of 2-IEP was performed using only two molecules from the trimer, whereas the geometry optimization of 3-IEP·HCl was performed using the atomic coordinates from 3-IEP·HBr due to convergence difficulties. All NMR calculations were performed using experimental Cartesian coordinates and subsequently on geometry optimized structures. The magnetic shielding tensor and EFG tensor calculations were performed using the TZ2P basis set. Scalar and spin-orbit relativistic effects were accounted for using the zeroth-order regular approximation (ZORA).[94] ^{1}H and ^{13}C calculated shielding constants were converted to chemical shifts using σ_{ref} values of 26.293 ppm[95] and 184.1 ppm,[96] respectively. EFG-Shield was used to extract the EFG tensor orientations.[84]

X-ray crystallography

Crystals of 2-IEP·HCl, 2-IEP·HBr, 2-IEP·HI_3, 3-IEP, 3-IEP·HCl, 3-IEP·HBr, and 3-IEP·HI were mounted on thin glass fibres using paraffin oil. Prior to data collection, the crystals were cooled to 200(2) K. The data were collected on Bruker AXS single-crystal diffractometer equipped with a sealed Mo tube (wavelength 0.71073 Å) and APEX II CCD detector. The raw data collection and reduction were done with the Bruker APEX II software package.[97] Semi-empirical absorption corrections based on equivalent reflections were applied with TWINABS[98] to 2-IEP·HI_3 (twinned data) and SADABS[99] for other datasets. Systematic absences in the diffraction dataset and unit cell parameters were consistent with triclinic $P\bar{1}$ (#2) space group for 3-IEP·HBr, 3-IEP·HI, 2-IEP·HBr, 2-IEP·HCl, monoclinic $P2/c$ (#13) for 3-IEP·HCl, monoclinic $P2_1/c$ (#14) for 2-IEP·HI_3, and orthorhombic *Pbcn* (#60) for 3-IEP. The structures were solved by direct methods and refined with full-matrix least-squares procedures based on F2, using SHELXL[100] and WinGX.[101] All non-H atoms were refined anisotropically. The hydrogen atoms bonded to the nitrogen (H(1) in 3-IEP·HCl, H(1) in 3-IEP·HBr, H(1) in 3-IEP·HI, H(1A) in 2-IEP·HBr, H(1A) in 2-IEP·HCl) were located in the difference Fourier map, while the remaining hydrogen atoms were placed at idealized positions. An exception was 2-IEP·HI_3 where the H(1) atom had to be refined as riding on a corresponding N(1) atom, because of the hydrogen atom's low 50% occupancy. DFIX restraint was applied to N–H bond distances in 3-IEP·HCl, 3-IEP·HI, 2-IEP·HBr, 2-IEP·HCl. The isotropic displacement parameters U_{iso} of the hydrogen atoms were constrained at 1.2 Ueq of the "parent" N atoms in 3-IEP·HCl, 3-IEP·HI, 2-IEP·HI_3; they were refined freely in 3-IEP·HBr, 2-IEP·HBr, 2-IEP·HCl. Displacement ellipsoid plots were produced using ORTEP,[102] and uncertainties were estimated using PLATON.[103] CCDC 11827955–1827961, contain the supplementary crystallographic data for this paper. These data are provided free of charge by The Cambridge Crystallographic Data Centre.

Acknowledgements

P.M.J.S. and D.L.B. thank the Natural Sciences and Engineering Research Council of Canada for research funding. Access to the 21.1 T NMR spectrometer was provided by the National Ultra-high-Field NMR Facility for Solids (Ottawa, Canada), a national research facility funded by a consortium of Canadian Universities, supported by the National Research Council Canada and Bruker BioSpin, and managed by the University of Ottawa (http://nmr900.ca).

Conflict of interest

The authors declare no conflict of interest.

Keywords: crystal engineering · crystallography · halogen bonding · hydrogen bonding · solid-state NMR

[1] The Nobel Prize in Chemistry **1969**. https://www.nobelprize.org/nobel_prizes/chemistry/laureates/1969/ (accessed July 20th, **2017**).
[2] The Nobel Prize in Chemistry **1987**. https://www.nobelprize.org/nobel_prizes/chemistry/laureates/1987/ (accessed 20 July, **2017**).
[3] G. R. Desiraju, *Crystal Engineering: The Design of Organic Solids*, Elsevier, **1989**.
[4] E. Arunan, G. R. Desiraju, R. A. Klein, J. Sadlej, S. Scheiner, I. Alkorta, D. C. Clary, R. H. Crabtree, J. J. Dannenberg, P. Hobza, H. G. Kjaergaard, A. C. Legon, B. Mennucci, D. J. Nesbitt, *Pure. Appl. Chem.* **2011**, *83*, 1619–1636.
[5] M. H. Kolár, P. Hobza, *Chem. Rev.* **2016**, *116*, 5155–5187.
[6] P. Politzer, J. S. Murray, T. Clark, *Top. Curr. Chem.* **2015**, *358*, 19–42.
[7] H. Wang, W. Wang, W. J. Jin, *Chem. Rev.* **2016**, *116*, 5072–5104.
[8] A. Bauzá, T. J. Mooibroek, A. Frontera, *Angew. Chem. Int. Ed.* **2013**, *52*, 12317–12321; *Angew. Chem.* **2013**, *125*, 12543–12547.

[9] S. Zahn, R. Frank, E. Hey-Hawkins, B. Kirchner, *Chem. Eur. J.* **2011**, *17*, 6034 – 6038.
[10] W. Wang, B. Ji, Y. Zhang, *J. Phys. Chem. A* **2009**, *113*, 8132 – 8135.
[11] F. F. Awwadi, R. D. Willett, K. A. Peterson, B. Twamley, *Chem. Eur. J.* **2006**, *12*, 8952 – 8960.
[12] G. Cavallo, P. Metrangolo, T. Pilati, G. Resnati, G. Terraneo, *Cryst. Growth Des.* **2014**, *14*, 2697 – 2702.
[13] A. C. Legon, *Phys. Chem. Chem. Phys.* **2017**, *19*, 14884 – 14896.
[14] G. Cavallo, P. Metrangolo, R. Milani, T. Pilati, A. Priimagi, G. Resnati, G. Terraneo, *Chem. Rev.* **2016**, *116*, 2478 – 2601.
[15] L. C. Gilday, S. W. Robinson, T. A. Barendt, M. J. Langton, B. R. Mullaney, P. D. Beer, *Chem. Rev.* **2015**, *115*, 7118 – 7195.
[16] T. Clark, M. Hennemann, J. S. Murray, P. Politzer, *J. Mol. Model.* **2007**, *13*, 291 – 296.
[17] G. R. Desiraju, P. Shing Ho, L. Kloo, A. C. Legon, R. Marquardt, P. Metrangolo, P. Politzer, G. Resnati, K. Rissanen, *Pure Appl. Chem.* **2013**, *85*, 1711 – 1713.
[18] P. Metrangolo, H. Neukirch, T. Pilati, G. Resnati, *Acc. Chem. Res.* **2005**, *38*, 386 – 395.
[19] M. Saccone, G. Cavallo, P. Metrangolo, A. Pace, I. Pibiri, T. Pilati, G. Resnati, G. Terraneo, *CrystEngComm* **2013**, *15*, 3102 – 3105.
[20] S. M. Huber, J. D. Scanlon, E. Jimenez-Izal, J. M. Ugalde, I. Infante, *Phys. Chem. Chem. Phys.* **2013**, *15*, 10350 – 10357.
[21] P. Politzer, J. S. Murray, T. Clark, *Phys. Chem. Chem. Phys.* **2010**, *12*, 7748 – 7757.
[22] A. Bondi, *J. Phys. Chem.* **1964**, *68*, 441 – 451.
[23] K. E. Riley, J. S. Murray, J. Fanfrlík, J. Řezáč, R. J. Solá, M. C. Concha, F. M. Ramos, P. Politzer, *J. Mol. Model.* **2011**, *17*, 3309 – 3318.
[24] K. E. Riley, J. S. Murray, J. Fanfrlík, J. Řezáč, R. J. Solá, M. C. Concha, F. M. Ramos, P. Politzer, *J. Mol. Model.* **2013**, *19*, 4651 – 4659.
[25] L. González, N. Gimeno, R. M. Tejedor, V. Polo, M. Blanca Ros, S. Uriel, J. L. Serrano, *Chem. Mater.* **2013**, *25*, 4503 – 4510.
[26] J. Lieffrig, O. Jeannin, M. Fourmigué, *J. Am. Chem. Soc.* **2013**, *135*, 6200 – 6210.
[27] C. B. Aakeröy, T. K. Wijethunga, J. Desper, *J. Mol. Struct.* **2014**, *1072*, 20 – 27.
[28] T. A. Logothetis, F. Meyer, P. Metrangolo, T. Pilati, G. Resnati, *New J. Chem.* **2004**, *28*, 760 – 763.
[29] P. C. Vioglio, M. R. Chierotti, R. Gobetto, *CrystEngComm* **2016**, *18*, 9173 – 9184.
[30] P. M. J. Szell, D. L. Bryce, *Modern Magnetic Resonce* **2016**, pp. 1 – 18, New York, Springer.
[31] J. Viger-Gravel, S. Leclerc, I. Korobkov, D. L. Bryce, *CrystEngComm* **2013**, *15*, 3168 – 3177.
[32] P. C. Vioglio, L. Catalano, V. Vasylyeva, C. Nervi, M. R. Chierotti, G. Resnati, R. Gobetto, P. Metrangolo, *Chem. Eur. J.* **2016**, *22*, 16819 – 16828.
[33] K. Bouchmella, S. G. Dutremez, B. Alonso, F. Mauri, C. Gervais, *Cryst. Growth Des.* **2008**, *8*, 3941 – 3950.
[34] J. Viger-Gravel, S. Leclerc, I. Korobkov, D. L. Bryce, *J. Am. Chem. Soc.* **2014**, *136*, 6929 – 6942.
[35] R. J. Attrell, C. M. Widdifield, I. Korobkov, D. L. Bryce, *Cryst. Growth Des.* **2012**, *12*, 1641 – 1653.
[36] C. M. Widdifield, G. Cavallo, G. A. Facey, T. Pilati, J. Lin, P. Metrangolo, G. Resnati, D. L. Bryce, *Chem. Eur. J.* **2013**, *19*, 11949 – 11962.
[37] P. M. J. Szell, D. L. Bryce, *J. Phys. Chem. C* **2016**, *120*, 11121 – 11130.
[38] Y. Xu, J. Viger-Gravel, I. Korobkov, D. L. Bryce, *J. Phys. Chem. C* **2015**, *119*, 27104 – 27117.
[39] M. Weingarth, N. Raouafi, B. Jouvelet, L. Duma, G. Bodenhausen, K. Boujlel, B. Schöllhorn, P. Tekely, *Chem. Commun.* **2008**, 5981 – 5983.
[40] J. Viger-Gravel, J. E. Meyer, I. Korobkov, D. L. Bryce, *CrystEngComm* **2014**, *16*, 7285 – 7297.
[41] C. Lemouchi, C. S. Vogelsberg, L. Zorina, S. Simonov, P. Batail, S. Brown, M. A. Garcia-Garibay, *J. Am. Chem. Soc.* **2011**, *133*, 6371 – 6379.
[42] D. E. Barry, C. S. Hawes, S. Blasco, T. Gunnlaugsson, *Cryst. Growth Des.* **2016**, *16*, 5194 – 5205.
[43] O. Dumele, D. Wu, N. Trapp, N. Goroff, F. Diederich, *Org. Lett.* **2014**, *16*, 4722 – 4725.
[44] W. N. Moss, N. S. Goroff, *J. Org. Chem.* **2005**, *70*, 802 – 808.
[45] M. Fourmigué, *Acta Crystallogr. Sect. B* **2017**, *73*, 138 – 139.
[46] N. S. Goroff, S. M. Curtis, J. A. Webb, F. W. Fowler, J. W. Lauher, *Org. Lett.* **2005**, *7*, 1891 – 1893.
[47] P. D. Rege, O. L. Malkina, N. S. Goroff, *J. Am. Chem. Soc.* **2002**, *124*, 370 – 371.
[48] See reference [25].
[49] M. Baldrighi, G. Cavallo, M. R. Chierotti, R. Gobetto, P. Metrangolo, T. Pilati, G. Resnati, G. Terraneo, *Mol. Pharm.* **2013**, *10*, 1760 – 1772.
[50] P. M. J. Szell, B. Gabidullin, D. L. Bryce, *Acta Crystallogr. Sect. B* **2017**, *73*, 153 – 162.
[51] P. M. J. Szell, J. Dragon, S. Zablotny, S. R. Harrigan, B. Gabidullin, D. L. Bryce, *New J. Chem.* **2018**, *42*, 10493 – 10501.
[52] A. E. Reed, F. Weinhold, *J. Chem. Phys.* **1985**, *83*, 1736 – 1740.
[53] E. D. Glendening, C. R. Landis, F. Weinhold, *WIREs Comput. Mol. Sci.* **2012**, *2*, 1 – 42.
[54] P. M. J. Szell, A. Siiskonen, L. Catalano, G. Cavallo, G. Terraneo, A. Priimagi, D. L. Bryce, P. Metrangolo, *New J. Chem.* **2018**, *42*, 10467 – 10471.
[55] C.-F. Ng, H.-F. Chow, T. C. W. Mak, *Angew. Chem. Int. Ed.* **2018**, *57*, 4986 – 4990; *Angew. Chem.* **2018**, *130*, 5080 – 5084.
[56] F. F. Awwadi, R. D. Willett, K. A. Peterson, B. Twamley, *J. Phys. Chem. A* **2007**, *111*, 2319 – 2328.
[57] A. Wang, R. Wang, I. Kalf, A. Dreier, C. W. Lehmann, U. Englert, *Cryst. Growth Des.* **2017**, *17*, 2357 – 2364.
[58] F. F. Awwadi, R. D. Willet, B. Twamley, *J. Mol. Struct.* **2009**, *918*, 116 – 122.
[59] M. Freytag, P. G. Jones, *Z. Naturforsch. B* **2001**, *56*, 889 – 896.
[60] S. P. Brown, H. W. Spiess, *Chem. Rev.* **2001**, *101*, 4125 – 4155.
[61] A. E. Aliev, K. D. M. Harris, *Struct. Bonding*, Springer-Verlag, Berlin **2004**, *108*.
[62] M. Kaupp, O. L. Malkina, V. G. Malkin, P. Pyykkö, *Chem. Eur. J.* **1998**, *4*, 118 – 126.
[63] P. Pyykkö, A. Görling, N. Rösch, *Mol. Phys.* **1987**, *61*, 195 – 205.
[64] P. Hrobárik, V. Hrobáriková, F. Meier, M. Repiský, S. Komorovský, M. Kaupp, *J. Phys. Chem. A* **2011**, *115*, 5654 – 5659.
[65] P. Garbacz, K. Jackowski, W. Makulski, R. E. Wasylishen, *J. Phys. Chem. A* **2012**, *116*, 11896 – 11904.
[66] A. K. Cheetham, A. P. Wilkinson, *Angew. Chem. Int. Ed. Engl.* **1992**, *31*, 1557 – 1570; *Angew. Chem.* **1992**, *104*, 1594 – 1608.
[67] P. Hodgkinson, C. M. Widdifield, *C&EN Global Enterp.* **2016**, *94*, 30 – 31.
[68] See reference [31].
[69] V. V. Terskikh, S. J. Lang, P. G. Gordon, G. D. Enright, J. A. Ripmeester, *Magn. Reson. Chem.* **2009**, *47*, 398 – 406.
[70] M. Kaupp, O. L. Malkina, V. G. Malkin, *Chem. Phys. Lett.* **1997**, *265*, 55 – 59.
[71] E. A. C. Lucken, *Nuclear Quadrupole Coupling Constants*, London, Academic Press Inc. **1969**.
[72] K. W. Eichele, Solids1 ver. 1.21.3, **2015**, Universität Tübingen.
[73] See reference [62].
[74] P. M. J. Szell, S. A. Gabriel, R. D. D. Gill, S. Y. H. Wan, B. Gabidullin, D. L. Bryce, *Acta Crystallogr. Sect. C* **2017**, *73*, 157 – 167.
[75] P. Pyykkö, *Mol. Phys.* **2001**, *99*, 1617 – 1629.
[76] R. Sternheimer, *Phys. Rev.* **1950**, *80*, 102 – 103.
[77] R. Sternheimer, *Phys. Rev.* **1951**, *84*, 244 – 253.
[78] D. L. Bryce, C. M. Widdifield, R. P. Chapman, R. J. Attrell, *eMagRes.* **2011**, 321 – 348.
[79] L. P. Wolters, F. M. Bickelhaupt, *ChemistryOpen* **2012**, *1*, 96 – 105.
[80] J. Řezáč, A. de la Lande, *Phys. Chem. Chem. Phys.* **2017**, *19*, 791 – 803.
[81] L. A. Santos, E. F. F. da Cunha, T. C. Ramalho, *J. Phys. Chem. A* **2017**, *121*, 2442 – 2451.
[82] K. Rajender Reddy, M. Vankateshwar, C. Uma Maheswari, P. Santhosh Kumar, *Tetrahedron Lett.* **2010**, *51*, 2170 – 2173.
[83] R. P. Chapman, C. M. Widdifield, D. L. Bryce, *Prog. Nucl. Magn. Reson. Spectrosc.* **2009**, *55*, 215 – 237.
[84] S. Adiga, D. Aebi, D. L. Bryce, *Can. J. Chem.* **2007**, *85*, 496 – 505.
[85] D. Massiot, I. Farnan, N. Gautier, D. Trumeau, A. Trokiner, J. P. Coutures, *Solid State Nucl. Magn. Reson.* **1995**, *4*, 241 – 248.
[86] F. A. Perras, C. M. Widdifield, D. L. Bryce, *Solid State Nucl. Magn. Reson.* **2012**, *45 – 46*, 36 – 44.
[87] L. A. O'Dell, R. W. Schurko, *Chem. Phys. Lett.* **2008**, *464*, 97 – 102.
[88] See reference [84].
[89] G. Te Velde, F. M. Bickelhaupt, E. J. Baerends, C. Fonseca Guerra, S. J. A. van Gisbergen, J. G. Snijders, T. Ziegler, *J. Comput. Chem.* **2001**, *22*, 931 – 967.

[90] C. Fonseca Guerra, J. G. Snijders, G. te Velde, E. J. Baerends, *Theor. Chem. Acc.* **1998**, *99*, 391 – 403.
[91] ADF2016, SCM, Theoretical Chemistry, Vrije Universiteit, Amsterdam, The Netherlands, http://www.scm.com.
[92] Y. Zhang, W. Yang, *Phys. Rev. Lett.* **1998**, *80*, 890.
[93] S. Grimme, S. Ehrlich, L. Goerigk, *J. Comput. Chem.* **2011**, *32*, 1456 – 1465.
[94] E. Van Lenthe, E. J. Baerends, *J. Comput. Chem.* **2003**, *24*, 1142 – 1156.
[95] See reference [65].
[96] A. K. Jameson, C. J. Jameson, *Chem. Phys. Lett.* **1987**, *134*, 461 – 466.
[97] Bruker (2012). APEX2. Bruker AXS Inc.; Madison, Wisconsin, USA.
[98] Bruker (2012). TWINABS. Bruker AXS Inc.; Madison, Wisconsin, USA.
[99] Bruker (2003). SADABS. Bruker AXS Inc.; Madison, Wisconsin, USA.
[100] G. M. Sheldrick, *Acta Crystallogr. Sect. C* **2015**, *71*, 3 – 8.
[101] L. J. Farrugia, *J. Appl. Crystallogr.* **1999**, *32*, 837 – 838.
[102] L. J. Farrugia, *J. Appl. Crystallogr.* **2012**, *45*, 849 – 854.
[103] A. L. Spek, *Acta Crystallogr. Sect. D* **2009**, *65*, 148 – 155.

Manuscript received: March 13, 2018
Revised manuscript received: May 1, 2018
Accepted manuscript online: May 31, 2018
Version of record online: July 5, 2018

Chapter 9 – Halogen Bonding as a Supramolecular Dynamics Catalyst

Statement of Authenticity. I certify that I have prepared the following article featuring my own work, with guidance from my supervisor Dr. David Bryce. This article features work from Scott Zablotny, tasked with preparing compounds, analyzing the compounds by powder X-ray diffraction, and performing the variable temperature deuterium experiments. Dr. David Bryce is acknowledged for support and contributions to the manuscript. Dr. Glenn Facey and Dr. Eric Ye are acknowledged for helpful discussions and assistance with the variable temperature deuterium experiments.

Permissions. I declare that I have obtained permission from all coauthors to include this article in my thesis. Chapter 9 has been reproduced with permission from the editors and was originally published at *Nature Communications,* **2019**. Full reference: *Nat. Commun.* **2019**, *10*, 916. (DOI: 10.1038/s41467-019-08878-8)

Supporting Information. The supporting information is presented in Appendix III.

nature COMMUNICATIONS

ARTICLE

https://doi.org/10.1038/s41467-019-08878-8 OPEN

Halogen bonding as a supramolecular dynamics catalyst

Patrick M.J. Szell [1], Scott Zablotny[1] & David L. Bryce [1]

Dynamic processes have many implications in functional molecules, including catalysts, enzymes, host-guest complexes, and molecular machines. Here, we demonstrate via deuterium NMR relaxation experiments how halogen bonding directly impacts the dynamics in solid 2,3,5,6-tetramethylpyrazine cocrystals, catalyzing the methyl group rotation. On average, we observe a reduction of 56% in the rotational activation energy of the methyl groups in the halogen bonded cocrystals, contrasting the reduction of 36% in the hydrogen bonded cocrystals, with respect to pure 2,3,5,6-tetramethylpyrazine. Density functional theory calculations attribute this superior catalytic ability of the halogen bond to the simultaneous destabilization of the staggered conformation and stabilization of the gauche conformation, overall reducing the rotational energy barrier. Furthermore, the calculations suggest that the catalytic ability of the halogen bond may be tuneable, with stronger halogen bond donors acting as superior dynamics catalysts. Thus, halogen bonding may play a role in both assembly and promoting dynamical processes.

[1] Department of Chemistry and Biomolecular Sciences & Centre for Catalysis Research and Innovation, University of Ottawa, Ottawa, ON K1N 6N5, Canada. Correspondence and requests for materials should be addressed to D.L.B. (email: dbryce@uottawa.ca)

The world of molecules and solids is far from static. Indeed, molecules exhibit well-known degrees of freedom, from simple rotations to more complex movements, which have been applied in the design of effective rotating catalysts[1], molecular gyroscopes[2], and to understand how guests, such as CO_2, behave once adsorbed in a host[3,4]. Dynamics also play pivotal roles in much larger systems, such as biological macromolecules[5], with faulty dynamical processes within enzymes being associated with disease[6]. Fortunately, these complex movements can be exploited, with molecular machines[7] recently having risen in prominence, yielding the 2016 Nobel Prize in Chemistry[8], with several configurations relying on rotations[9–11], such as molecular motors[12,13] and propellers[14]. However, the impact of introducing interacting moieties on such dynamical processes remains unclear, and the rapid rotations of methyl groups offer an opportunity to gain insights into how molecular rotations can be affected by changes in the local chemical environment.

There have been sparse reports on how van der Waals interactions, such as those associated with inter- or intramolecular contacts, can affect the energy barrier of a methyl group's rotation[15–18]. Counterintuitively, both increases and decreases in the rotational energy barrier have been observed upon the introduction of van der Waals contacts, rather than the perhaps expected consistent increase due to steric hindrance. Examples of decreases in the rotational energy barrier have been rationalized as resulting from the destabilization of the staggered conformation of the rotator, overall reducing the barrier[15]. This effect from van der Waals contacts on a methyl group has been observed in a select few instances in polymers[19] and proteins[20]. In the case of proteins, increases and decreases in the methyl rotational energy barrier have both been observed, and the presence of ligands has been shown to play a critical role in their internal dynamics[21]. While these effects are structurally localized, they potentially could be exploited in the design of ligands and molecular machines through the incorporation of functional groups associated with a potent dynamical catalytic ability.

Halogen bonding (RX···Y; X = I, Br, Cl, F; Y = electron donor) is a non-covalent interaction akin to the hydrogen bond[22] which is currently experiencing a surge of interest in supramolecular chemistry[23,24], and related fields due to its directionality[25] and tuneability (I > Br > Cl ≫ F)[26,27], allowing for the rational design of catalysts[28,29], and supramolecular frameworks[30,31]. Halogen bonding is defined as the attraction between the region of elevated electrostatic potential[32] on the halogen bond donor, associated with the electron-poor σ-hole[33], and an electron-rich halogen bond acceptor, such as a Lewis base or nucleophile[34]. Recently, halogen bonding has been introduced in the field of supramolecular rotators, in configurations such as the molecular rotor on axle[35,36] and a molecular top[37]. While halogen bonding served the role of an attractive interaction to maintain a particular geometry that best favors the rotation, the direct influence of halogen bonding contacts on the molecular dynamics was not the focus of these works.

Here, we show the first instance of halogen bonding having a direct influence on local dynamical processes, with the halogen bond donor acting as a dynamics catalyst superior to the hydrogen bond. In this context, dynamics catalysis refers to the reduction of the energy barrier associated with a dynamic process, such as rotation. To this end, we employ deuterium solid-state NMR spectroscopy and spin-lattice relaxation time constant (T_1) measurements on a series of cocrystals and salts featuring the halogen bond acceptor 2,3,5,6-tetramethylpyrazine (TMP), observing changes in the methyl group activation energy upon the introduction of a halogen bond or hydrogen bond, and comparing the results to those obtained for pure TMP and its halide salts (HCl, HBr). The TMP acceptor provides an ideal scaffold to study the effect of changes in the chemical environment on rotation, as the methyl groups are consistently located immediately adjacent to the non-covalent interaction being introduced.

Results

Structural elements. Samples **1**–**3**, shown in Fig. 1, consist of cocrystals featuring a I···N halogen bond [**1** (1,4-diiodotetrafluorobenzene)(TMP)[38]; **2** (1,3,5-trifluoro-2,4,6-triiodobenzene)(TMP)[39]; **3** (iodine)(TMP)][40], while samples **4** and **5** feature a O–H···N hydrogen bond [**4** (1,4-cyclohexanedicarboxylic acid)

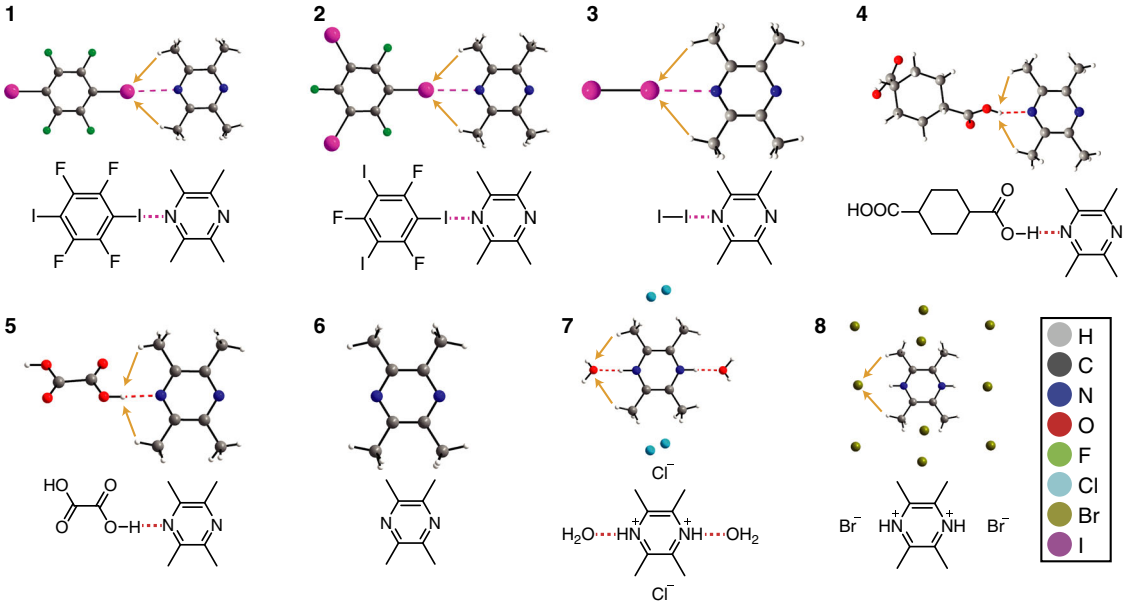

Fig. 1 Depictions of the X-ray crystal structures and molecular structures involving TMP (**1**–**8**) surveyed in this work. The dashed magenta lines denote the halogen bonds while the dashed red lines denote hydrogen bonds. The orange arrows denote close contacts between the protons on the methyl group and nearby atoms

Table 1 Methyl group rotational activation energy for each compound derived from the T_1 relaxation experiments

Compound	I···N/H···N bond length (Å)	Activation energy (kJ mol^{-1})	Note
1	3.0665(18)	2.84 ± 0.14	Halogen bonded
2	2.993(3)	3.24 ± 0.13	Halogen bonded
3	3.075(5)	3.62 ± 0.13	Halogen bonded
4	1.919	4.17 ± 0.09	Hydrogen bonded
5	1.809	5.02 ± 0.06	Hydrogen bonded
6	n/a	7.31 ± 0.17	Pure TMP
7	n/a	6.81 ± 0.16	HCl salt
8	n/a	13.64 ± 0.45	HBr salt

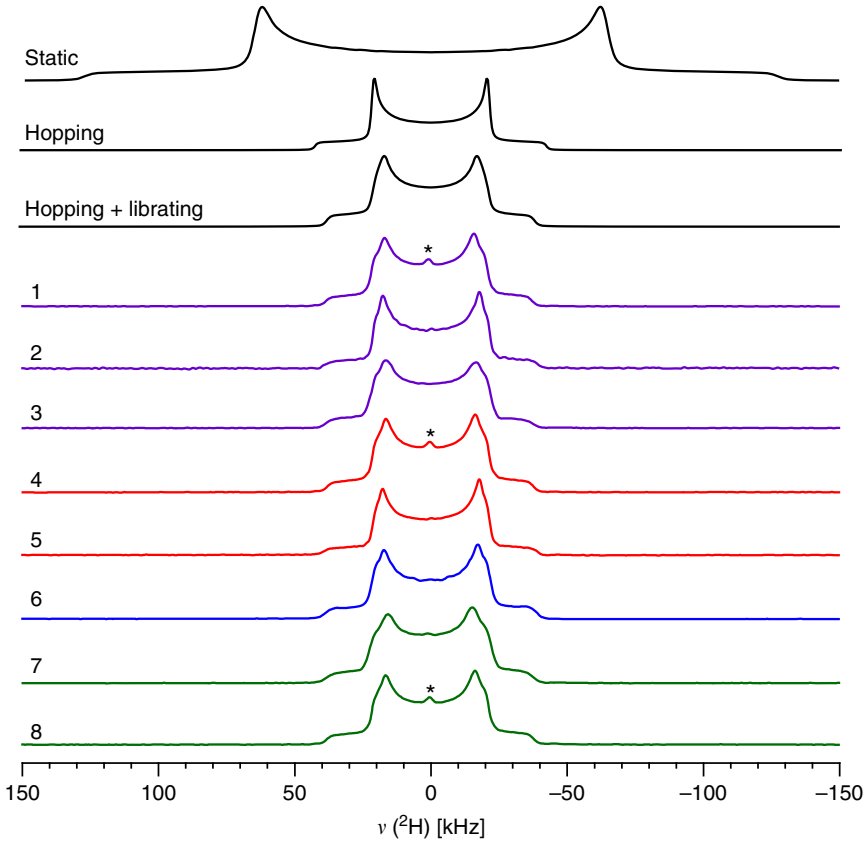

Fig. 2 Experimental static deuterium (^{2}H) solid-state NMR spectra of compounds **1**–**8** at room temperature. In black are the simulated spectra, in purple are the halogen bonded species, in red are the hydrogen bonded species, in blue is pure TMP, and the halide salts are in green. The asterisks denotes a trace quantity (<1%) of D_2O

(TMP)[41]; **5** (oxalic acid)(TMP)[41]]. Sample **6** consists of pure TMP (**6**, TMP)[42] and serves as a reference point for the activation energy, while the halide salts [**7** (2,3,5,6-tetramethylpyrazinium hydrochloride hydrate)[43], **8** (2,3,5,6-tetramethylpyrazinium hydrobromide)[43]] serve as controls for the presence of non-halogen-bonded halogens near the methyl groups. Unfortunately, the sample quality of the hydroiodide salt[43] was not satisfactory despite multiple preparatory attempts, and was therefore excluded from our analysis. The crystal structures mentioned here have been described elsewhere, with the halogen bond and hydrogen bond geometries summarized in Table 1. In brief, the halogen bond geometries are comparable across samples **1**, **2**, and **3**, with **2** having the shortest halogen bond and **3** having the longest halogen bond, placing an iodine atom in proximity to the rotating methyl groups of the acceptor. The hydrogen bonding geometries are also similar in samples **4** and **5**, although **4** has a hydrogen bond ~0.1 Å longer than that of sample **5**, with an O–H group in proximity to the methyl groups. Compound **7** is a hydrate, with the water molecule interacting with the N–H$^+$ moiety via a N–H···O hydrogen bond. The Cl^- anions in compound **7** occupy the spaces near the center between both methyl groups. In contrast, compound **8** is not a hydrate, with the Br^- anions distributed around the unit cell. Additional Cl^- and Br^- anions are shown in Fig. 1 for compounds **7** and **8**, respectively, to show the environment surrounding the methyl groups of interest. Across each sample, contacts to the methyl groups vary, with no clear trend in terms of distance or number of contacts. As a result, this series of compounds presents an ideal case enabling the assessment of the impact of a halogen bonding or hydrogen bonding moiety on the methyl group rotations.

Experimental activation energies. Solid-state NMR spectroscopy of deuterium, a quadrupolar nucleus (^{2}H, spin $I = 1$), has long been used for characterizing molecular dynamics. Under static

sample conditions, the ^{2}H solid-state NMR spectral line shape for a methyl group is diagnostic of its motion, with rapid motions typically causing an averaging effect and narrowing the spectra. Further, the quadrupolar coupling and lower magnetogyric ratio of ^{2}H renders it ideal for studies on dynamics, in contrast to ^{1}H (spin $I = ½$) that have NMR spectra typically dominated by dipolar coupling in the solid state. With a natural abundance of 0.0115%, isotopic enrichment is used to perform ^{2}H NMR experiments. This provides an opportunity to selectively label the methyl groups of interest here. Satisfactory enrichment of TMP was obtained through deuterium-proton exchange in a hot alkaline solution over one week, yielding a consistent deuterium enrichment factor across all samples.

The ^{2}H solid-state NMR spectra acquired at room temperature for each sample using a quadrupolar echo pulse sequence[44] are shown in Fig. 2, with the linewidths given in Supplementary Table 2. These experiments were carried out on stationary powdered samples. The resulting spectra are superimposable, suggesting unsurprisingly that the global nature of the methyl group dynamics is unchanged across the various samples. In order to extract a full and detailed description of the dynamics, the ^{2}H line shapes were simulated using EXPRESS[45] software. The spectra were fit to a threefold hopping model along with additional librational motions of the CH_3 groups. This libration, also qualitatively reproduced by DFT calculations (see Supplementary Figure 5), is rationalized by the rotation of the adjacent methyl group, causing an increase in the distance between both methyl groups in the gauche position as a result of steric effects. While the rapid rotation is responsible for narrowing the line shape, the libration is manifested as a broadening of the main spectral discontinuities (see the simulations in Fig. 2 and Supplementary Figures 3 and 4). Accordingly, the narrow line shape (35 ± 3 kHz horn separation) is consistent with rapidly rotating methyl groups, while there is an absence of other major dynamic processes such as a ring-flip of TMP along the halogen or hydrogen bond axis. In order to extract the thermodynamic parameters governing the methyl group rotation, the ^{2}H spin-lattice (T_1) relaxation time constants have been measured by solid-state NMR spectroscopy over a wide temperature range of ~140 °C at 20 °C intervals. These measurements were achieved by combining the quadrupolar echo[44] pulse sequence with the inversion recovery experiment. The T_1 relaxation time constants were measured using the integral of the entire line shape, and were determined to be nearly isotropic by measuring the T_1 values for separate parts of the spectrum. Furthermore, throughout the temperature range, apart from sample **8**, the ^{2}H line shape remained unchanged down to ~150 K, supporting an Arrhenius-dominated motion in the experimental temperature range[46]. A previous study on the T_1 relaxation time constants of pure TMP reveals that quantum tunneling is insignificant above temperatures of 80 K[47]. Consequently, in the high temperature regime, the Arrhenius activation energy can be conveniently extracted using Eq. 1:[48]

$$T_1 \propto \frac{1}{\tau_c} = A \exp\left(\frac{-E_a}{RT}\right) \quad (1)$$

In Eq. 1, τ_c corresponds to the correlation time, A is the pre-exponential factor, E_a is the Arrhenius activation energy, R is the gas constant, and T is the temperature. The activation energy can be extracted by plotting the natural logarithm of the T_1 relaxation time constant as a function of the inverse temperature ($1/T$), with the slope equal to $-E_a/R$. These data are plotted in Fig. 3 and tabulated in Supplementary Tables 3–10, with the fitting parameters given in Supplementary Table 1. Upon cooling sample

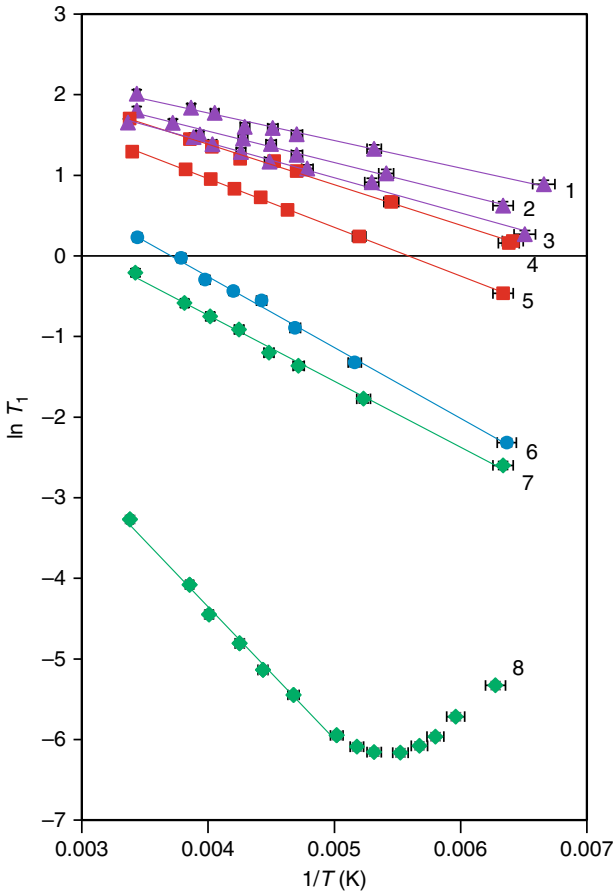

Fig. 3 Experimental ln T_1 relaxation times plotted as a function of the inverse temperature ($1/T$). The error bars represent an upper limit on instability in the temperature and the uncertainty of the T_1 relaxation time measurements

8 to 180 K, a line shape distortion was observed, which is associated with approaching the T_1 minimum. Consequently, supplementary data point sampling was performed for sample **8** at these lower temperatures, and the activation energy was extracted using data at higher temperatures. The activation energies are summarized in Table 1.

The activation energies associated with the methyl group rotation are lower for the cocrystals featuring a halogen bond (**1**–**3**) and a hydrogen bond (**4** and **5**) when compared to pure TMP (**6**). Moreover, the activation energies for the halogen bonded complexes were found to be significantly lower than those of the hydrogen bonded complexes, with **1** having an activation energy of nearly half that of **5**, for example. Halide salt **7**, which has a water molecule in proximity of the methyl groups, has a slightly lower activation energy when compared to the pure acceptor, while **8** has the highest activation energy, at 186% more than that of pure TMP.

Computational chemistry. To support the experimental results, a series of DFT calculations was carried out using the Amsterdam Density Functional (ADF)[49–51] software package on the cocrystals featuring perfluorinated halogen bond donors, in order to provide a theoretical basis for the observed reductions in the activation energy. The models of **1** and **2** consisted of TMP interacting with one nearby halogen bond donor, identical to the crystal structure depictions shown in Fig. 1. A series of linear transit calculations have been performed, altering the H–C–C–C dihedral angle from −180° to 90°, in steps of 2.5°, for the methyl

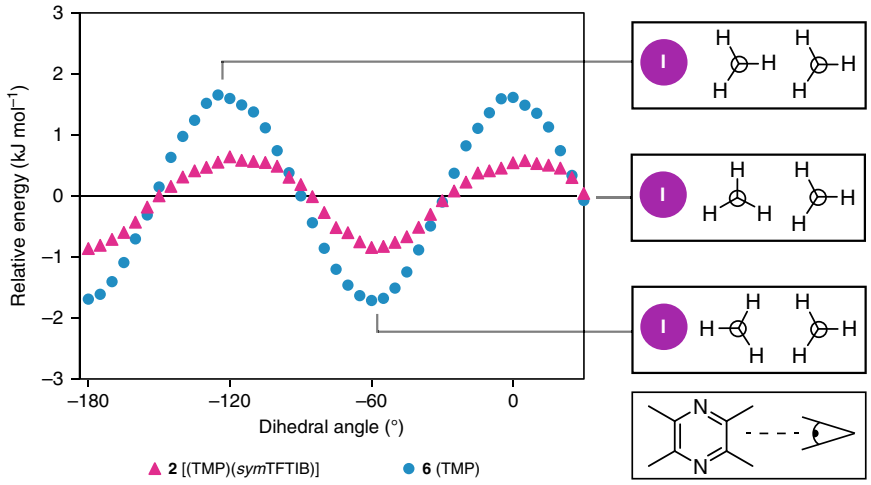

Fig. 4 DFT-calculated relative energy as a function of the methyl group dihedral angle (H-C-C-C). The blue circles denote pure TMP (**6**) and the magenta triangles denote cocrystal **2**. A diagram showing the methyl group geometry at the energy maximum, zero-crossing, and minimum is shown on the right. A depiction showing the perspective in the diagram is shown on the bottom right

group closest to the halogen bond donor. The energy was calculated at every point of the methyl group rotation after a geometry optimization cycle, while maintaining a constrained dihedral angle. The calculated activation energies were approximated by subtracting the energy minimum from the energy maximum. For both models, the energy minimum of a single methyl group rotation consisted of the staggered conformation (methyl groups 180° out of phase), while the energy maximum consisted of the gauche conformation (methyl groups in-phase). As a result of only rotating a single methyl group, the energy associated with that rotation could be estimated.

The results of the DFT calculations are shown in Fig. 4, comparing the relative energy of compounds **2** and **6**, upon the rotation of the methyl group. The results comparing structure **1** to structure **6** are shown in Supplementary Figure 6. The pseudo-sinusoidal nature of the energy upon the rotation of the methyl group is consistent with a C_3 rotation, with three energy minima in a full 360° rotation due to the presence of three hydrogen atoms on the methyl group. Upon the introduction of a halogen bond, there is a clear increase in the energy minimum and a decrease in the energy maximum, with an overall energy barrier reduction of 58% for **1** and 56% for **2** when compared to pure TMP, in agreement with the experimental values. The orientation of the adjacent methyl group not interacting with iodine did not significantly impact the overall catalytic effect, with the results of the calculations shown in Supplementary Figure 7.

A series of calculations was then carried out comparing the effect of the halogen bond length ($d_{I\cdots N}$) on the methyl group activation energy, shown in Fig. 5. This was performed by calculating the energy difference between the in-phase and out-of-phase conformations on a model of TMP interacting with either iodomethane or iodotrifluoromethane, varying the distance between both fragments from an R_{XB} value of 1.10 to 0.75, at 0.05 increments. For clarity, here we use R_{XB} to refer to the quotient of the halogen bond length ($d_{I\cdots N}$) and the sum of their van der Waals radii ($R_{XB} = d_{I\cdots N}/\Sigma d_{vdw}$).

As shown in Fig. 5, the I···N distance plays a clear role in reducing the rotational activation energy barrier, with the catalytic abilities of the halogen bond being most pronounced between R_{XB} of 0.85 and 0.95. The difference in the energy curves between iodomethane and iodotrifluoromethane presented in Fig. 5 is quite substantial, suggesting that the catalytic effect associated with the halogen bond isn't merely due to the presence of an iodine atom, but the choice of the donor moiety may also

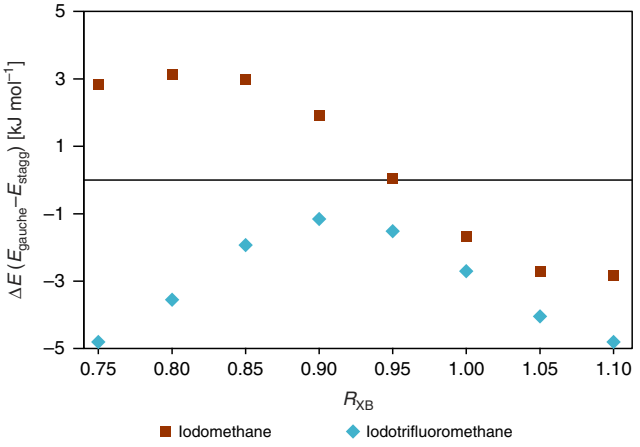

Fig. 5 Calculated energy difference between the staggered and gauche conformations of TMP as a function of the I···N halogen bond length (expressed as R_{XB}), interacting with either iodomethane (red squares) or iodotrifluoromethane (blue diamonds)

play a role. In the case of the non-fluorinated iodomethane, the energy barrier crosses the zero energy point at $R_{XB} = 0.95$, suggesting that the gauche conformation becomes energetically favorable rather than the staggered conformation at short I···N distance. In contrast, when interacting with iodotrifluoromethane, the staggered conformation remains energetically favorable as the halogen bond distance is decreased, reaching an energy minimum at an R_{XB} of 0.90. We refer to this effect as catalytic because the halogen bond is not consumed or destroyed during the process of methyl rotation.

Discussion

The experimental activation energies, summarized in Table 1 and Fig. 6, are lowest for the halogen bonded cocrystals (**1**–**3**), followed by the hydrogen bonded cocrystals (**4**, **5**), the pure TMP (**6**) and the halide salts (**7**, **8**). Furthermore, the activation energies of **1**–**3** are amongst the lowest in the literature for a methyl group rotation, comparable to 2,6-dimethylnaphthalene and 1,3,5-trichloro-2,4,6-trimethylbenzene, having activation energy of 1.6[18] and 2.4 kJ mol^{-1} [52], respectively. In the case of the latter, the low energy barrier has been attributed to the chlorine

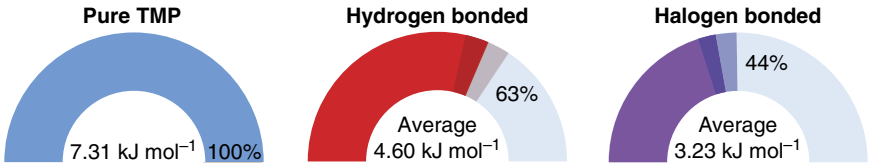

Fig. 6 Summary of the reduction in the experimentally measured activation energy associated with the rotation of the methyl groups. The average activation energies are given for the halogen bonded and hydrogen bonded cocrystals

substitution, in contrast to the 8.0 kJ mol^{-1} barrier observed in hexamethylbenzene[53]. As a point of reference, the rotational activation energy of a methyl group in organic molecules typically spans from 6.3 to 24 kJ mol^{-1} [47,54]. The reduction in the methyl group activation energy observed in the cocrystals studied here is attributed to the presence of the halogen bond donor and hydrogen bond donor in proximity to the methyl groups, as no clear trends can be discerned relating the number of contacts to the methyl groups (see Supplementary Figures 1 & 2) or to the crystal packing. Furthermore, the mere presence of halogen atoms in proximity to the methyl groups was not sufficient to catalyze the methyl group rotation, with compound **8** instead exhibiting a significant increase in the activation energy. The slight decrease in the activation energy observed in compound **7** can be rationalized by the presence of a water molecule participating in a O···N contact near the methyl groups, despite the presence of chloride anions. As a result, the catalytic effect observed in compounds **1**–**3** appears to be unique to covalently bonded halogens.

The DFT results on isolated models of **1**, **2**, and **6** (Fig. 4 and Supplementary Figure 6) suggest that this catalytic effect associated with the halogen bond is a result of the destabilization of the staggered conformation and the stabilization of the gauche conformation. Consequently, the difference between the energy maximum and minimum is reduced in the halogen bonded cocrystals, causing a net reduction in the activation energy. This is in contrast to the previous theoretical investigations on the catalytic effect of van der Waals contacts involving hydrogen on methyl groups, revealing primarily an increase in the energy minimum[15]. A potential mechanism for the destabilization of the staggered conformation may be due to the repulsion between the protons of the methyl group, which carry a positive electrostatic potential (+74.5 kJ mol^{-1}; see Supplementary Figure 9), and the positive σ-hole of the halogen bond donor. As the electrostatic potential between the protons of the methyl group is slightly negative (−5.7 kJ mol^{-1}), this may cause an attractive interaction to the σ-hole of the halogen bond, leading to a stabilizing effect. In this respect, a larger σ-hole would lead towards a stronger hydrogen···iodine interaction, further reducing the rotational energy barrier. (Another less plausible mechanism for the reduction of the energy barrier could be related to the skeletal flexing of TMP upon halogen bonding. However, an inspection of the crystal structures shows that the structural changes induced upon halogen bonding are tiny (e.g., C–C–CH_3 angle in TMP changes by 1° and distance between the two methyl carbons changes by ~0.01 Å). It is not clear how these changes would result in a lower activation energy in the halogen bonded systems.)

The DFT results suggest that the distance between the iodine and the methyl rotors plays an important role in determining the catalytic ability of the halogen bond, being most significant for R_{XB} values between 0.85 and 0.95. With an average R_{XB} value for the C–I···N fragment of 0.85 according to the Cambridge Structural Database[55], these halogen bonds seem to be in the ideal range to act as a dynamical catalyst. When comparing the catalytic ability of iodomethane and iodotrifluoromethane as a function of the I···N distance by DFT calculations, a striking difference between both curves is observed, suggesting that the addition of electron withdrawing groups may alter the catalytic abilities of the halogen atom, and may allow for a tuneable dynamics catalyst. This is supported experimentally, with the catalytic ability of the halogen bond donor following the calculated molecular electrostatic potential of the σ-hole (see Supplementary Figure 8). The calculated potential of the σ-hole, highest in **1** at 168 kJ mol^{-1}, followed by **2** at 162 kJ mol^{-1}, and **3** at 155 kJ mol^{-1}, satisfyingly follows the order of reduction in the methyl group rotational energy barrier.

In conclusion, we have shown how halogen bonding plays a direct role as a supramolecular dynamics catalyst through the use of ^{2}H solid-state NMR relaxation experiments. In the cases shown here, the catalytic impact of the halogen bond surpasses that of the hydrogen bond. Computational support suggests that this is achieved by destabilizing the staggered conformation and stabilizing the gauche conformation, resulting in an overall reduction of the activation energy barrier. Further, this catalytic effect may be tuneable by changing the electron withdrawing substitutions adjacent to the halogen bond donor. Consequently, the halogen bond may not only be a versatile interaction useful in crystal engineering, but may bring a unique ability of promoting dynamics within functional molecules, such as enzymes, catalysts, and molecular machines.

Methods

Sample preparation. 2,3,5,6-tetramethylpyrazine (98%), 1,4-diiodotetrafluorobenzene (99%), iodine (99%), oxalic acid (99%), and hydrobromic acid (48%) were purchased from Sigma Aldrich. 1,3,5-trifluoro-2,4,6-triiodobenzene was purchased from Alfa Aesar. 1,4-cyclohexanedicarboxylic acid (99%) was purchased from Acros Organics. Deuterium oxide (> 99% deuterium) was purchased from Cambridge Isotope Laboratories. Hydrochloric acid (~38%) and all solvents were purchased from Fisher Scientific.

2,3,5,6-tetramethylpyrazine was deuterated following a modified literature procedure[56]. To a 50 mL glass pressure tube, 35 mL of a 0.6 M NaOH solution in D_2O was added, followed by the addition of 2.05 g of 2,3,5,6-tetramethylpyrazine. The glass vessel was placed in the oven at 90 °C, at which point the 2,3,5,6-tetramethylpyrazine dissolved completely, and left for 7 days. The glass pressure tube was removed from the oven and allowed to return to room temperature, allowing for the deuterated 2,3,5,6-tetramethylpyrazine to crystallize. The solution was filtered and rinsed with water. The product was sublimed (yield = 57%), affording 2,3,5,6-tetramethylpyrazine with a deuterium enrichment factor of ~60.1%. Compounds **1**[38], **2**[39], **7**[43], and **8**[43] were reproduced using their literature procedure using the deuterated product. Compound **3**[40] was prepared by cosublimation[57] by combining I_2 and the deuterated 2,3,5,6-tetramethylpyrazine in a round bottom sublimation apparatus. Compounds **4**[41] and **5**[41] were prepared mechanochemically using a Retsch MM400 ball mill, by placing both the deuterated 2,3,5,6-tetramethylpyrazine and hydrogen bond donor at equimolar quantities in a 10 mL stainless steel ball mill jar. The products were ground for 30 min at a frequency of 25 Hz, using two stainless steel milling balls. The crystal structure for each powdered sample was verified by powder X-ray diffraction on a Rigaku Ultima IV instrument unless otherwise stated, with 2θ ranging from 5 to 65° in increments of 0.02° using Cu Kα radiation. The powder X-ray diffractograms are shown in Supplementary Figures 10 to 17.

^{2}H solid-state NMR. All ^{2}H solid-state NMR experiments were performed at 4.7T ($\nu_L(^2H)$ = 30.7 MHz) using a Bruker Avance III console and a single-channel wideline probe fitted with a 5 mm coil. Static ^{2}H spectra were acquired using a quadrupolar echo[44] ($\pi/2$–τ–$\pi/2$–τ) pulse sequence, using a 4.7 µs $\pi/2$ pulse length, and a 20 µs τ delay. The T_1 relaxation experiments were performed using a quadrupolar echo coupled with an inversion recovery sequence at variable temperatures. The temperature was controlled by flowing dry nitrogen gas through

a heat exchanger submerged in liquid nitrogen, and subsequently heated inside the probe to the desired temperature. The temperature was regulated using a Bruker variable temperature controller with the thermocouple placed near the sample, while the sample temperature was measured by placing a copper/constantan thermocouple directly on the RF coil, while using an ice water bath as a reference.

Computational. The DFT calculations were performed using the Amsterdam Density Functional software (ADF 2017)[49–51]. Models were built from the experimental atomic coordinates taken from the crystal structures, featuring one halogen bond donor interacting with 2,3,5,6-tetramethylpyrazine. Each model was initially optimized using the TZ2P basis set, accounting for dispersion forces using Grimme3 BJDAMP[58] and relativistic effects using ZORA[59]. Linear transit calculations were performed using the TZ2P basis set by rotating the methyl group at steps of 2.5° relative to the H–C–C–C dihedral angle, performing a geometry optimization routine at each step, and calculating the energy. Single point energy calculations were performed using pre-optimized models of the staggered and gauche conformers with variable distances and halogen bond donor fragments. The QZ4P basis set was used for all iodine atoms in the linear transit and single point energy calculations. The molecular electrostatic surface potential surfaces were generated using Gaussian 09[60] with the B3LYP functional and the 3-21G basis set, and visualized using GaussView[61] at 0.002 e a.u.$^{-1}$. The resulting molecular electrostatic potential values for the σ-hole were found to be in agreement with previous reports[62].

Data availability

The authors declare that all data supporting the findings of this study are available within the paper and its supplementary information files.

Received: 17 October 2018 Accepted: 4 February 2019
Published online: 22 February 2019

References

1. Biswas, P. K., Saha, S., Paululat, T. & Schmittel, M. Rotating catalysts are superior: suppressing product inhibition by anchimeric assistance in four-component catalytic machinery. *J. Am. Chem. Soc.* **140**, 9038–9041 (2018).
2. Godinez, C. E., Zepeda, G. & Garcia-Garibay, M. A. Molecular compasses and gyroscopes. II. Synthesis and characterization of molecular rotors with axially substituted bis[2-(9-triptycyl)ethynyl]arenes. *J. Am. Chem. Soc.* **124**, 4701–4707 (2002).
3. Wang, W. D., Lucier, B. E. G., Terskikh, V. V., Wang, W. & Huang, Y. Wobbling and hopping: studying dynamics of CO_2 adsorbed in metal-organic frameworks via ^{17}O solid-state NMR. *J. Phys. Chem. Lett.* **5**, 3360–3365 (2014).
4. Zhang, Y., Lucier, B. E. G. & Huang, Y. Deducing CO_2 motion, adsorption locations and binding strengths in a flexible metal-organic framework without open metal sites. *Phys. Chem. Chem. Phys.* **18**, 8327–8341 (2016).
5. Davey, J. A., Damry, A. M., Goto, N. K. & Chica, R. A. Rational design of proteins that exchange on functional timescales. *Nat. Chem. Biol.* **13**, 1280–1285 (2017).
6. Schuetz, A. K. & Kay, L. E. A dynamic molecular basis for malfunction in disease mutants of p97/VCP. *eLife* **5**, e20143 (2016).
7. Erbas-Cakmak, S., Leigh, D. A., McTernan, C. T. & Nussbaumer, A. L. Artificial molecular machines. *Chem. Rev.* **115**, 10081–10206 (2015).
8. The Nobel Prize in Chemistry 2016. https://www.nobelprize.org/nobel_prizes/chemistry/laureates/2016/ (2016).
9. Kelly, T. R., De Silva, H. & Silva, R. A. Unidirectional rotary motion in a molecular system. *Nature* **401**, 150–152 (1999).
10. Karlen, S. D. et al. Symmetry and dynamics of molecular rotors in amphidynamic molecular crystals. *Proc. Natl. Acad. Sci. USA.* **107**, 14973–14977 (2010).
11. Jiang, X., Rodríguez-Molina, B., Nazarian, N. & Garcia-Garibay, M. A. Rotation of a bulky triptycene in the solid state: toward engineered nanoscale artificial molecular machines. *J. Am. Chem. Soc.* **136**, 8871–8874 (2014).
12. Wu, Y. et al. A multistage rotational speed changing molecular rotor regulated by pH and metal cations. *Nat. Commun.* **9**, 1953 (2018).
13. Koumura, N., Zijlstra, R. W. J., van Delden, R. A., Harada, N. & Feringa, B. L. Light-driven monodirectional molecular rotor. *Nature* **401**, 152–155 (1999).
14. Simpson, C. D. et al. Nanosized molecular propellers by cyclodehydrogenation of polyphenylene dendrimers. *J. Am. Chem. Soc.* **126**, 3139–3147 (2004).
15. Baudry, J. van der Waals interactions and decrease of the rotational barrier of methyl-sized rotators: a theoretical study. *J. Am. Chem. Soc.* **128**, 11088–11093 (2006).
16. Hembree, W. I. & Baudry, J. Three-dimensional mapping of microenvironmental control of methyl rotational barriers. *J. Phys. Chem. B* **115**, 8575–8580 (2011).
17. Khazaei, S. & Sebastiani, D. Methyl rotor quantum states and the effect of chemical environment in organic crystals: γ-picoline and toluene. *J. Chem. Phys.* **145**, 234506 (2016).
18. Wang, X. et al. Intramolecular and intermolecular contributions to the barriers for rotation of methyl groups in crystalline solids: electronic structure calculations and solid-state NMR relaxation measurements. *J. Org. Chem.* **76**, 5170–5176 (2011).
19. Alvarez, F., Alegría, A., Colmenero, J., Nicholson, T. M. & Davies, G. R. Origin of the distribution of potential barriers for methyl group dynamics in glassy polymers: a molecular dynamics simulation in polyisoprene. *Macromolecules* **33**, 8077–8084 (2000).
20. Baudry, J. & Smith, J. C. Can proteins and crystals self-catalyze methyl rotations? *J. Phys. Chem. B* **109**, 20572–20578 (2005).
21. Krishnan, M. & Smith, J. C. Response of small-scale, methyl rotors to protein-ligand association: a simulation analysis of calmodulin-peptide binding. *J. Am. Chem. Soc.* **131**, 10083–10091 (2009).
22. Metrangolo, P., Neukirch, H., Pilati, T. & Resnati, G. Halogen bonding based recognition processes: a world parallel to hydrogen bonding. *Acc. Chem. Res.* **38**, 386–395 (2005).
23. Gilday, L. C. et al. Halogen bonding in supramolecular chemistry. *Chem. Rev.* **115**, 7118–7195 (2015).
24. Cavallo, G. et al. The halogen bond. *Chem. Rev.* **116**, 2478–2601 (2016).
25. Huber, S. M., Scanlon, J. D., Jimenez-Izal, E., Ugalde, J. M. & Infante, I. On the directionality of halogen bonding. *Phys. Chem. Chem. Phys.* **15**, 10350–10357 (2013).
26. Riley, K. E. et al. Halogen bond tunability I: the effects of aromatic fluorine substitution on the strengths of halogen-bonding interactions involving chlorine, bromine, and iodine. *J. Mol. Model.* **17**, 3309–3318 (2011).
27. Riley, K. E. et al. Halogen bonding tunability II: the varying roles of electrostatic and dispersion contributions to attraction in halogen bonds. *J. Mol. Model.* **19**, 4651–4659 (2013).
28. Chan, Y.-C. & Yeung, Y.-Y. Halogen bond catalyzed bromocarbocyclization. *Angew. Chem. Int. Ed.* **57**, 3483–3487 (2018).
29. Carreras, L., Serrano-Torné, M., van Leeuwen, P. W. N. M. & Vidal-Ferran, A. XBphos-Rh: a halogen-bond assembled supramolecular catalyst. *Chem. Sci.* **9**, 3644–3648 (2018).
30. Lieffrig, J., Jeannin, O. & Fourmigué, M. Expanded halogen-bonded anion organic networks with star-shaped iodoethynyl-substituted molecules: from corrugated 2D hexagonal lattices to pyrite-type 2-fold interpenetrated cubic lattices. *J. Am. Chem. Soc.* **135**, 6200–6210 (2013).
31. Kumar, V. et al. Halogen bonded Borromean networks by design: topology invariance and metric tuning in a library of multi-component systems. *Chem. Sci.* **8**, 1801–1810 (2017).
32. Politzer, P. & Murray, J. S. σ-hole interactions: perspectives and misconceptions. *Crystals* **7**, 212 (2017).
33. Clark, T., Hennemann, M., Murray, J. S. & Politzer, P. Halogen bonding: the σ-hole. *J. Mol. Model.* **13**, 291–296 (2007).
34. Desiraju, G. R. et al. Definition of the halogen bond (IUPAC recommendations 2013). *Pure Appl. Chem.* **85**, 1711–1713 (2013).
35. Catalano, L. et al. Dynamic characterization of crystalline supramolecular rotors assembled through halogen bonding. *J. Am. Chem. Soc.* **137**, 15386–15389 (2015).
36. Catalano, L. et al. Rotational dynamics of diazabicyclo[2.2.2]octane in isomorphous halogen-bonded co-crystals: entropic and enthalpic effects. *J. Am. Chem. Soc.* **139**, 843–848 (2017).
37. Lemouchi, C. et al. Ultra-fast rotors for molecular machines and functional materials via halogen bonding: crystals of 1,4-bis(iodoethynyl)bicyclo[2.2.2] octane with distinct gigahertz rotation at two sites. *J. Am. Chem. Soc.* **133**, 6371–6379 (2011).
38. Syssa-Magalé, J.-L., Boubekeur, K., Palvadeau, P., Meerschaut, A. & Schöllhorn, B. The tailoring of crystal structures via the self-assembly of organic coordination compounds by N···I non-covalent halogen bonds: co-crystal of sterically hindered N-heterocycles and 1,4-diiodo-tetrafluorobenzene. *CrystEngComm* **7**, 302–308 (2005).
39. Szell, P. M. J. et al. ^{13}C and ^{19}F solid-state NMR and X-ray crystallographic study of halogen-bonded frameworks featuring nitrogen-containing heterocycles. *Acta Cryst.* **C73**, 157–167 (2017).
40. Bailey, R. D., Buchanan, M. L. & Pennington, W. T. Molecular complexes of 1,4-diazines with iodine. *Acta Cryst.* **C48**, 2259–2262 (1992).
41. Weyna, D. R., Shattock, T., Vishweshwar, P. & Zaworotko, M. J. Synthesis and structural characterization of cocrystals and pharmaceutical cocrystals: mechanochemistry vs slow evaporation from solution. *Cryst. Growth Des.* **9**, 1106–1123 (2009).
42. Braam, A. W. M., Eshuis, A. & Vos, A. Tetramethylpyrazine at 300 and 100 K. *Acta Cryst.* **B37**, 730–732 (1981).

43. Lu, J. & Kochi, J. K. Charge-modulated associates of anionic donors with cationic π-acceptors: crystal structures of ternary synthons leading to molecular wires. *Cryst. Growth Des.* **9**, 291–296 (2009).
44. Davis, J. H., Jeffrey, K. R., Bloom, M., Valic, M. I. & Higgs, T. P. Quadrupolar echo deuteron magnetic resonance spectroscopy in ordered hydrocarbon chains. *Chem. Phys. Lett.* **42**, 390–394 (1976).
45. Vold, R. L. & Hoatson, G. L. Effects of jump dynamics on solid state nuclear magnetic resonance line shapes and spin relaxation times. *J. Magn. Reson.* **198**, 57–72 (2009).
46. Kowalewski, J. & Liljefors, T. On the relationship between the potential barrier and the activation energy for the internal rotation of a methyl group. *Chem. Phys. Lett.* **64**, 170–174 (1979).
47. Takeda, S. & Chihara, H. Methyl rotation in 1,2,4,5-tetramethylbenzene and tetramethylpyrazine in the solid state. Tunneling spectra by proton NMR. *J. Magn. Reson.* **54**, 285–299 (1983).
48. Spěváček, J. & Schneider, B. Determination of the activation energies of relaxation processes from integrated intensities of the NMR bands of high resolution spectra. *Czech. J. Phys.* **B24**, 593–604 (1974).
49. Te Velde, G. et al. Chemistry with ADF. *J. Comp. Chem.* **22**, 931–967 (2001).
50. Fonseca Guerra, C., Snijders, J. G., te Velde, G. & Baerends, E. J. Towards an order-N DFT method. *Theo. Chem. Acc.* **99**, 391–403 (1998).
51. Baerends, E. J. et al. ADF2017, SCM, Theoretical Chemistry, Vrije Universiteit, Amsterdam, The Netherlands. http://www.scm.com (2014).
52. Takeda, S., Fujiwara, T. & Chihara, H. Methyl rotation in 1,3,5-trichloro-2,4,6-trimethylbenzene as studied by nuclear magnetic resonance: a comparison with methyl rotation in hexamethylbenzene. *J. Phys. Soc. Jpn.* **58**, 1793–1800 (1989).
53. Allen, P. S. & Cowking, A. Nuclear magnetic resonance study of molecular motions in hexamethylbenzene. *J. Chem. Phys.* **47**, 4286–4289 (1967).
54. Beckmann, P. A. Nonexponential ^{1}H spin-lattice relaxation and methyl group rotation in molecular solids. *Solid State Nucl. Magn. Reson.* **71**, 91–95 (2015).
55. Groom, C. R., Bruno, I. J., Lightfoot, M. P. & Ward, S. C. The Cambridge Structural Database. *Acta Cryst.* **B72**, 171–179 (2016).
56. Vincent, J. S. Paramagnetic resonance of the triplet state of tetramethylpyrazine. *J. Chem. Phys.* **47**, 1830–1833 (1967).
57. Szell, P. M. J. et al. Cosublimation: a rapid route toward otherwise inaccessible halogen-bonded architectures. *Cryst. Growth Des.* **18**, 6227–6238 (2018).
58. Grimme, S., Ehrlich, S. & Goerigk, L. Effect of the damping function in dispersion corrected density functional theory. *J. Comput. Chem.* **32**, 1456–1465 (2011).
59. van Lenthe, E., Ahlers, A. & Baerends, E.-J. Geometry optimizations in the zero order regular approximation for relativistic effects. *J. Chem. Phys.* **110**, 8943–8953 (1999).
60. Frisch, M. J. et al. *Gaussian 09, Revision A.02* (Gaussian, Inc., Wallingford CT, 2016).
61. Dennington, R., Keith, T. & Millam, J. *GaussView, Version 4.1* (Semichem, Inc., Shawnee Mission, 2007).
62. Aakeröy, C. B., Wijethunga, T. K., Desper, J. & Đaković, M. Electrostatic potential differences and halogen-bond selectivity. *Cryst. Growth Des.* **16**, 2662–2670 (2016).

Acknowledgements

P.M.J.S. and D.L.B. thank the Natural Sciences and Engineering Research Council of Canada for a scholarship and for research funding, respectively. The authors wish to thank Dr. Glenn A. Facey and Dr. Eric Ye for helpful discussions and assistance with the variable temperature experiments. The authors also thank Compute Canada for access to computing resources.

Author contributions

P.M.J.S. conceived and designed experiments, performed quantum chemical calculations, analyzed data, and prepared the manuscript. S.Z. prepared the samples, performed the variable temperature experiments, analyzed data, and revised the manuscript. D.L.B. conceived and designed experiments, supervised the work, provided guidance, and prepared the manuscript.

Additional information

Supplementary Information accompanies this paper at https://doi.org/10.1038/s41467-019-08878-8.

Competing interests: The authors declare no competing interests.

Reprints and permission information is available online at http://npg.nature.com/reprintsandpermissions/

Journal Peer Review Information: *Nature Communications* thanks Pierre Kennepohl and other anonymous reviewer(s) for their contribution to the peer review of this work.

Publisher's note: Springer Nature remains neutral with regard to jurisdictional claims in published maps and institutional affiliations.

Summary of Part 3 – Characterizing the Halogen Bond Acceptor & Surrounding Environment

In this part of the thesis, we have characterized the halogen bond acceptor and the surrounding environment using solid-state NMR spectroscopy. With these various approaches, we have shown that NMR spectroscopy is a versatile tool to characterize cocrystals and its impurities, to characterize changes in the EFG of a halide atom, and to characterize the changes in the local molecular dynamics surrounding the halogen bond.

In Chapter 7, we have applied a combination of ^{19}F and ^{13}C solid-state NMR spectroscopy in order to characterize halogen bonded cocrystals. We have shown that the ^{19}F chemical shift changes upon cocrystallization is a rapid and reliable indicator for the occurrence of a halogen bond, while offering an excellent signal-to-noise ratio in only a few minutes. Further, the technique was sensitive enough to identify side phases and excess starting materials, which proved to be an asset for the development of cosublimation in Chapter 12. In addition, we have surveyed the use of $^{19}F \rightarrow {}^{13}C$ cross-polarization and compared it to the routine $^{1}H \rightarrow {}^{13}C$ cross polarization. The former was shown to be superior for characterizing the halogen bond donor, yielding a better signal with higher resolution. However, the latter was most effective at characterizing the halogen bond acceptor, with the ^{13}C chemical shifts changing upon cocrystallization. The experimental ^{19}F and ^{13}C chemical shifts were compared to the calculated chemical shifts, with a better agreement between experimental and computational results when using optimized crystal structures. As a result, solid-state NMR was shown to be a useful method for improving the crystal structures of halogen bonded compounds.

In Chapter 8, we have exploited the C-I···N halogen bond in order to prepare self-assembling molecules, yielding the first halogen bonded supramolecular triangle.[1] This trimer was discussed in more detail in a separate article not featured in this thesis, which featured additional work from groups in Milan and Finland.[1] Coincidentally, a separate group in Hong Kong published the same trimer at the same time.[2] The molecules in this study were further manipulated to yield their HCl, HBr, and HI salt, creating unique halogen bonded charged dimers. As a result, we have compared the C-I···N halogen bond to the C-I···X^- halogen bonds (X = Cl, Br, I) *via* a thorough multinuclear magnetic resonance study, focusing on the following nuclei: ^{1}H, ^{13}C, ^{35}Cl, and $^{79/81}Br$. Based on these experiments, we have concluded that the halogen bond's relative contribution to the EFG in the C-I···X^- motif increases in the order of Cl > Br > I, which strongly contrasts that of the hydrogen bond.

Finally, in Chapter 9, we have demonstrated *via* deuterium NMR relaxation experiments how halogen bonding directly impacts the dynamics in solid 2,3,5,6-tetramethylpyrazine cocrystals, with the first report of the halogen bond catalyzing the molecular dynamics. On average, the rotational activation energy of the methyl groups was reduced by 56% in halogen bonded cocrystals, overshadowing the reduction of 36% observed in hydrogen bonded cocrystals, with respect to pure 2,3,5,6-tetramethylpyrazine. In contrast, an increase in the rotational energy barrier was observed in the halide salts of 2,3,5,6-tetramethylpyrazine, supporting the role of halogen bonding in reducing the energy barrier. Our DFT calculations suggest that this catalytic ability of the halogen bond may be tuneable, with stronger halogen bond donors acting as superior dynamics catalysts. Thus, halogen bonding may not only play a role in the assembly of supramolecular complexes but could also have implications in promoting dynamical processes. This could have a potential role in supramolecular catalysts, molecular

machines, and in the next generation of pharmaceutical through the correction of defective enzyme dynamics.

References.

[1] Szell, P.M.J.; Siiskonen, A.; Catalano, L.; Cavallo, G.; Terraneo, G.; Priimagi, A.; Bryce, D.L.; Metrangolo, P. *New J. Chem.* **2018**, *42*, 10467-10471.

[2] Ng, C.-F.; Chow, H.-F.; Mak, T.C.W. *Angew. Chem. Int. Ed.* **2018**, *57*, 4986-4990.

Part 4 - Crystal Engineering, Mechanochemistry & Cosublimation

The rational design of materials to exhibit desirable properties encompasses the field of *crystal engineering*.[1] Rather than using a brute force approach, crystal engineering may be beneficial in shortening research and development times, perhaps even reducing costs. Non-covalent interactions are a useful tool for the crystal engineer, in part because they require less energy to form than covalent bonds. Furthermore, the self-organizing and self-correcting properties of non-covalent interactions are additional benefits, whereas broken covalent bonds in a framework can remain a defect. Historically, the hydrogen bond has played an important role in crystal engineering and has been used to design supramolecular architectures.[2]

As a result of its tuneability and linearity, favoring interactions angles ($\theta_{R\text{-}X\cdots Y}$) between 150 – 180°,[3] the halogen bond has been featured in crystal engineering,[4,5,6] and the parallel between hydrogen bonding and halogen bonding has been drawn.[7] Following several initial reports in the late 1990's, interest in halogen bonding has grown to hundreds of articles being published every year.[8] Many of the early studies aimed to establish the halogen bond as a tool for crystal engineering by investigating its role as a bonding interaction.[9,10,11] The rise of fluorinated halogen bond donors has clearly impacted the field,[12,13] with the popular halogen bond donor *1,4-diiodotetrafluorobenzene* now being frequently featured in crystal engineering articles.[14,15,16,17,18]

While fluorination is a convenient method of activating the halogen bond donor,[12] the addition of fluorine atoms does have secondary consequences on the physico-chemical properties of the materials. For instance, fluorination of 1,4-diiodobenzene to 1,4-diiodotetrafluorobenzene

renders the halogen bond donor significantly more hydrophobic, making fluorination potentially less attractive for use in aqueous applications, such as in pharmaceuticals and the life sciences. However, an alternate strong halogen bond donor does exist, which is the iodoacetylene functional group (also called iodoethynyl in the literature).[19,20] In this moiety, the iodine is located on an SP-hybridized carbon, with the triple bond acting as an electron withdrawing group. Consequently, the iodine atom on an iodoacetylene group demonstrates a characteristically strong polarization of the σ–hole,[21,22,23] with a comparison to other halogen bond donors shown in Figure 4.1. This halogen bonding moiety is therefore convenient, as it can be easily included in small molecules yielding an effective halogen bond donor, rather than resorting solely on fluorination.

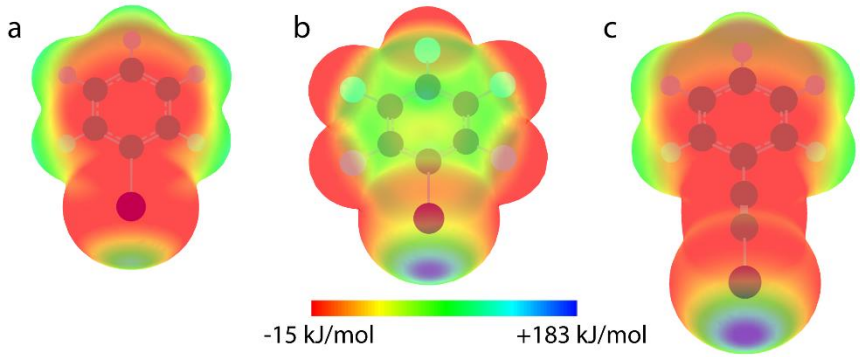

Figure 4.1. Calculated electrostatic potential surface of iodobenzene (**a**, 101.3 kJ/mol), iodoperfluorobenzene (**b**, 171.3 kJ/mol), and iodoethynylbenzene (**c**, 183.8 kJ/mol). The calculations were performed using the B3LYP functional and 3-21g basis set.

A drawback to the iodoacetylene group is its lower bench stability. Exposure to sunshine, humidity, and heat may eventually lead to the degradation of the sample quality. The iodoacetylene group has been proposed for use in antimicrobials,[24] herbicide,[25] and has been featured in pharmaceutical preservative[26] and in antifungal products.[27] The germicidal properties

may be a result from the release of iodine, analogous to the application of povidone-iodine.[28] While the lower stability for some compounds featuring the iodoacetelyne group is known, the molecules featured in the studies presented here were observationally stable at ambient conditions, and showed no signs of deterioration.

The potential of iodoacetylenes in crystal engineering has been previously exploited in the literature,[29,30,31,32] dating as far back to a report on the structure of iodocyanoacetylene 1962.[33] Early reports of diiodobutadiyne and diiodohexatriyne have been cocrystallized with bispyridyl derivatives, showing the potential of the C≡C-I···N halogen bonds for crystal engineering.[34] Monomers bearing the iodoacetylene group have been polymerized to yield iodinated polymers, which could then be cocrystallized, resulting in the formation of halogen bonded copolymers.[35,36] Recently, the halogen bond involving (iodoethynyl)benzene has been investigated in solution, revealing a high affinity for the quinuclidine halogen bond acceptor.[37] The group of Dr. Aakeröy has made several comparisons between the ethynyl hydrogen bond and the iodoacetylene halogen bond,[38,39] and has also exploited the iodoethynyl group to yield unique architectures, such as a diamondoid structure[40] and supramolecular rectangles.[41] Dr. Marc Fourmigué's group has also published several article featuring the iodoacetylene group,[42] such as the halogen bonded cocrystals of 1,3,5-tri(iodoethynyl)-2,4,6-trifluorobenzene with a series of halide salts,[43] which served as a starting point to Chapter 10.

One crystal engineering approach is the addition of iodoacetylenes on either a benzene[44,45] or pyridine ring,[46] which can then be cocrystallized with a halogen bond acceptor, affording unique supramolecular complexes. By then varying the halogen bond acceptor, rapid screening of supramolecular architectures can be performed, rather than synthesizing new molecules. For instance, the combination of 1,4-di(iodoethynyl)benzene, a pillar[5]arene, and

1,4-bis(1-imidazolyl)butane yielded a polypseudorotaxane,[47] avoiding the need for the lengthy synthesis typically associated with conventional rotaxanes. Several alternative arrangements bearing the iodoacetylene group have been reported,[48] such as the 3-iodopropiolamides,[49] cavitands,[50,51,52] and even in organometallics.[53]

The iodoethynyl group has been featured in functional materials, such as in supramolecular rotors. In this case, the halogen bond acts as an axle,[54] permitting the rotation of either the donor[55] or acceptor[56] molecule. Other applications include organic conductors, where the iodoacetylene is used as a tool to engineer the material to exhibit electrical conductance[57,58,59] or insulation.[60] Recently, a porous organic structure featuring the iodoacetylene group has been reported using a Tröger's base as the backbone.[61]

In Chapter 8 of Part 3 of this thesis, we have exploited the iodoacetylene group as a crystal engineering tool in 2-iodoethynylpyridine and 3-iodoethynylpyridine. While this study has focused on the solid-state NMR responses to changes in the halogen bond acceptor, it is worth reviewing the crystal structures that were obtained. Notably, 2-iodoethynylpyridine exhibits self-complimentary I···N halogen bonds, forming the first supramolecular triangle.[62] In contrast, 3-iodoethynylpyridine, with its *meta* configuration, organizes in a zig-zag pattern rather than a supramolecular trimer. The inclusion of halide acids, such as hydrogen chloride, enabled a relatively easy form of crystal engineering, with the resulting product organizing in charged supramolecular dimers. Select structures are shown in Figure 4.2.

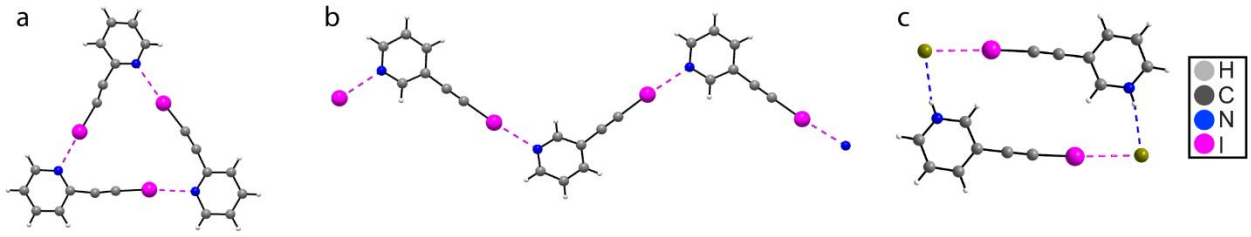

Figure 4.2. Depiction of the crystal structures of (a) 2-iodoethynylpyridine,[62] (b) 3-iodoethynylpyridine, and (c) 3-iodoethynylpyridine hydrobromide. The dashed magenta line denotes the halogen bond, whereas the dashed blue line denotes the hydrogen bond.

In Chapter 10 of this thesis, we investigate a previously reported halogen bond donor 1,3,5-tri(iodoethynyl)-2,4,6-trifluorobenzene[43] (henceforth abbreviated as *sym*TIETB) by cocrystallizing it with a series of halide salts. This project aimed to characterize this new halogen bond donor by multinuclear magnetic resonance spectroscopy, in addition to discovering new crystal structures which furthers its role in crystal engineering. A series of halide salts were chosen with increasing size in order to survey the impact of the cation size on the framework motif. Moreover, we analyze the ^{13}C & ^{19}F NMR spectra in solution, revealing a complex combination of ^{13}C – ^{19}F *J*-couplings.

While crystal engineering certainly has its advantages, a potential pitfall is reproducibility and scalability of the product. Investigating cocrystals using a robust synthetic method can help avoid this problem, increasing the odds of uncovering reproducible compounds. To this end, mechanochemistry is a favorable synthetic method for preparing supramolecular architectures, and has been previously used to prepare halogen bonded cocrystals.[63,64] In particular, Dr. Tomislav Friščić and Dr. Dominik Cinčić have been pioneers in the field, having published numerous articles on the subject.[65,66,67,68] Recent work by Dr. Cinčić includes halogen bonded pharmaceutical cocrystals,[69] as well as cocrystals based on *N*-bromophthalimide[70] and

conventional perfluorinated donors.[71] Among the benefits of mechanochemistry, it requires lower volumes of conventional organic solvents, in addition to shorter preparation times.[72,73] It has even been possible to follow these mechanochemical reactions *in situ* using powder X-ray diffraction.[74]

In Chapter 11 of this thesis, we survey the mechanochemical preparation of 3-iodoethynylbenzoic acid with a series of nitrogen-containing heterocycles, with the intention of easily preparing concurrent halogen bonded & hydrogen bonded frameworks featuring this new donor molecule. We show that the products obtained by mechanochemical ball milling are comparable to the products obtained from solvent-evaporation methods using ^{13}C solid-state NMR spectroscopy, with the overall process of milling being able to reduce preparation times and solvent requirements. As a result, bulk quantities of the final cocrystallized product can be quickly prepared without the need of large solvent quantities.

In certain circumstances, obtaining a product in its powdered form from ball milling can limit the analysis of the crystal structure. While the structure can be obtained by powder X-ray methods using techniques such as the Reitveld refinement,[75] it can be challenging to get the structure from complex products having many degrees of freedom, such as cocrystals. As a result, the products obtained from mechanochemical ball milling must be further manipulated in order to obtain single crystals of quality for single crystal X-ray diffraction, such as the case in Chapter 11.

In Chapter 12 of this thesis, we establish cosublimation to prepare halogen bonded cocrystals, avoiding the need of mechanochemistry and solvent-evaporation methods. This technique relies on the solid-gas phase transitions of molecules, which is favored by strong

vacuums and high temperatures (approximate range of 100 – 200°C). While conventional sublimation is typically performed to purify products, here we use a two-zoned tube furnace in order to sublime a halogen bond donor and acceptor together, forming the final cocrystal. We have since designed and constructed our own two-zoned tube furnace intended to perform cosublimation experiments, with a picture of the furnace and a reusable glass tube shown in Figure 4.3. Both the furnace and glass tube were designed by myself.

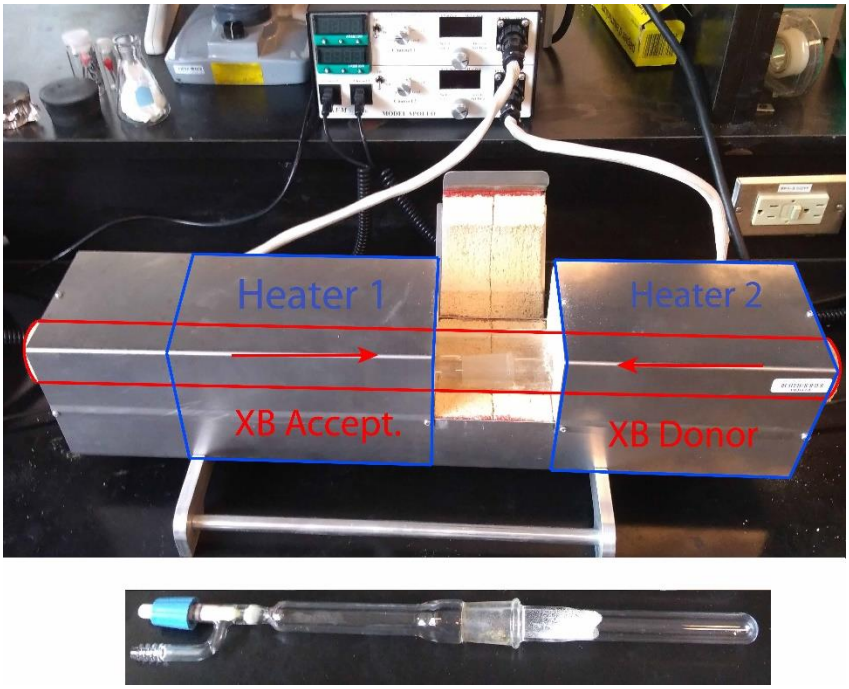

Figure 4.3. Home-built two-zoned tube furnace designed to perform cosublimation experiments. The labels denote the two heating elements (Heater 1 & Heater 2), along with the relative position of the building blocks to be sublimed (labelled XB Accept. & XB Donor). The arrows denote the relative movement of the donor/acceptor molecules. Below is a custom-designed and reusable cosublimation tube following an experiment.

On one end of the glass tube, we have the halogen bond donor, while the other end of the glass tube contains the halogen bond acceptor. Upon their sublimation, the compounds migrate towards the center of the tube where they meet and deposit, forming the halogen bonded

cocrystal. The temperature of both compounds can be carefully controlled in order to favor their sublimation, and temperature ramps were employed to further force the compounds to slowly migrate down the tube. The result of this process allows us to achieve cocrystals suitable for single crystal X-ray diffraction within one day, with the technique named "overnight cosublimation". An analogous technique using a common laboratory sublimation apparatus, which has been named "expedited cosublimation" in the article for clarity, allowed for the preparation microcrystalline products within 15 minutes, greatly accelerating the rate of discovery – and all in the complete absence of any organic solvents. Furthermore, sublimation was surveyed as an effective method of purifying cocrystallized products from a range of techniques, rather than dissolving the product in solvent and simply restarting the process.

The purpose of Chapter 12 is to establish cosublimation as the ultimate tool for growing halogen bonded cocrystals. These experiments were performed during my internship at the Université de Rennes 1 (Rennes, France), under the supervision of Dr. Marc Fourmigué. There, they had a custom-made tube furnace and the facilities required to make great advancements using cosublimation.

References.

[1] Tiekink, E.R.T.; Vittal, J.; Zaworotko, M. *Organic Crystal Engineering: Frontiers in Crystal Engineering*. John Wiley & Sons Ltd, West Sussex, **2010**.

[2] Aakeröy, C.B.; Seddon, K.R. *Chem. Rev.* **1993**, *22*, 397-407.

[3] Huber, S.M.; Scanlon, J.D.; Jimenez-Izal, E.; Ugalde, J.m.; Infante, I. *Phys. Chem. Chem. Phys.* **2013**, *15*, 10350-10357.

[4] Cavallo, G.; Metrangolo, P.; Milani, R.; Pilati, T.; Priimagi, A.; Resnati, G.; Terraneo, G. *Chem. Rev.* **2016**, *116*, 2478-2601.

[5] Mukherjee, A.; Teyssandier, J.; Hennrich, G.; De Feyter, S.; Mali, K.S. *Chem. Sci.* **2017**, *8*, 3759-3769.

[6] Mukherjee, A.; Tothadi, S.; Desiraju, G.R. *Acc. Chem. Res.* **2014**, *47*, 2514-2524.

[7] Metrangolo, P.; Neukirch, H.; Pilati, T.; Resnati, G. *Acc. Chem. Res.* **2005**, *38*, 386-395.

[8] Web of Science Version 5.31. [database online]. Philadelphia, PA: Clarivate Analytics; 2018. www.webofknowledge.com. Accessed December 17th 2018.

[9] Metrangolo, P.; Resnati, G. *Chem. Eur. J.* **2001**, *7*, 2511-2519.

[10] Ranganathan, A.; Pediredid, V.R. *Tetrahedron Lett.* **1998**, *39*, 1803-1806.

[11] Thalladi, V.R.; Goud, B.S.; Hoy, V.J.; Allen, F.H.; Howard, J.A.K.; Desiraju, G.R. *Chem. Commun.* **1996**, 401-402.

[12] Riley, K.E.; Murray, J.S.; Fanfrlík, J.; Řezáč, J.; Solá, R.J.; Concha, M.N.; Ramos, F.M.; Politzer, P. *J. Mol. Model.* **2011**, *17*, 3309-3318.

[13] Ding, X.-H.; ou, C.-J.; Wang, S.; Xie, L.-H.; Lin, J.-Y.; Wang, J.-P.; Huang, W. *CrystEngComm*. **2017**, *19*, 5504-5521.

[14] Capucci, D.; Balestri, D.; Mazzeo, P.P.; Pelagatti, P.; Rubini, K.; Bacchi, A. *Cryst. Growth Des.* **2017**, *17*, 4958-4964.

[15] Pfrunder, M.C.; Micallef, A.S.; Rintoul, L.; Arnold, D.P.; Davy, K.J.P.; McMurtrie, J. *Cryst. Growth Des.* **2014**, *14*, 6041-6047.

[16] Ji, B.; Wang, W.; Deng, D.; Zhang, Y. *Cryst. Growth Des.* **2011**, *11*, 3622-3628.

[17] Ramakrishnan, R.; Mallia, A.R.; Niyas, M.A.; Sethy, R.; Hariharan, M. *Cryst. Growth Des.* **2016**, *16*, 6327-6336.

[18] Christopher Pigge, F.; Kapadia, P.P.; Swenson, D.C. *CrystEngComm*. **2013**, *15*, 4386-4391.

[19] Perkins, C.; Libri, S.; Adams, H.; Brammer, L. *CrystEngComm.* **2012**, *14*, 3033-3038.

[20] Gao, K.; Goroff, N.S. *J. Am. Chem. Soc.* **2000**, *122*, 9320-9321.

[21] Aakeröy, C.B.; Wijethunga, T.K.; Desper, J.; Đaković, M. *Cryst. Growth Des.* **2015**, *15*, 3853-3861.

[22] Aakeröy, C.B.; Baldrighi, M.; Desper, J.; Metrangolo, P.; Resnati, G. *Chem. Eur. J.* **2013**, *19*, 16240-16247.

[23] Nguyen, S.T.; Ellington, T.L.; Allen, K.E.; Gorden, J.D.; Rheingold, A.K.; Tschumper, G.S.; Hammer, N.I.; Watkins, D.L. *Cryst. Growth Des.* **2018**, *18*, 3244-3254.

[24] Burckhardt, U.; Zimmermann, M. Iodoethynyl pyridine compounds. US 3778441 A, March 5, 1971.

[25] Hou, Z.-K.; Ren, Y.-G.; Huang, M.-Z.; Song, J.; Chen, L.-G. *Acta Cryst.* **2004**, *E60*, o1336-o1337.

[26] Baldrighi, M.; Cavallo, G.; Chierotti, M.R.; Gobetto, R.; Metrangolo, P.; Pilati, T.; Resnati, G.; Terraneo, G. *Mol. Pharmaceutics* **2013**, *10*, 1760-1772.

[27] Baldrighi, M.; Bartesaghi, D.; Cavallo, G.; Chierotti, M.R.; Gobetto, R.; Metrangolo, P.; Pilati, T.; Resnati, G.; Terraneo, G. *CrystEngComm*. **2014**, *16*, 5897-5904.

[28] Reimer, K.; Wichelhaus, T.A.; Schäfer, V.; Rudolph, P.; Kramer, A.; Wutzler, P.; Ganzer, D.; Fleischer, W. *Dermatology*. **2002**, *204*, 114-120.

[29] Ghassemzadeh, M.; Harms, K.; Dehnicke, K. *Chem. Ber.* **1996**, *129*, 115-120.

[30] Batsonov, A.S.; Howard, J.A.K. *Acta Cryst.* **2000**, *C56*, 252-253.

[31] Barrès, A.-L.; El-Ghayoury, A.; Zorina, L.V.; Canadell, E.; Auban-Senzier, P.; Batail, P. *Chem. Commun.* **2008**, 2194-2196.

[32] Bouchmella, K.; Boury, B.; Dutremez, S.G.; van der Lee, A. *Chem. Eur. J.* **2007**, *13*, 6130-6138.

[33] Borgen, B.; Hassel, O.; Römming, C. *Acta Chem. Scand.* **1962**, *16*, 2469-2470.

[34] Goroff, N.S.; Curtis, S.M.; Webb, J.A.; Fowler, F.W.; Lauher, J.W. *Org. Lett.* **2005**, *7*, 1891-1893.

[35] Luo, L.; Wilhelm, C.; Sun, A.; Grey, C.P.; Lauher, J.W.; Goroff, N.S. *J. Am. Chem. Soc.* **2008**, *130*, 7702-7709.

[36] Sun, A.; Lauher, J.W.; Goroff, N.S. *Science.* **2006**, *312*, 1030-1034.

[37] Dumele, O.; Wu, D.; Trapp, N.; Goroff, N.; Diederich, F. *Org. Lett.* **2014**, *16*, 4722-4725.

[38] Gamekkanda, J.C.; Sinha, S.A.; Desper, J.; Đaković, M.; Aakeröy, C.B. *New J. Chem.* **2018**, *42*, 10539-10547.

[39] Aakeröy, C.B. Welideniya, D.; Desper, J. *CrystEngComm*. **2017**, *19*, 11-13.

[40] Gunawardana, C.A.; Đaković, M.; Aakeröy, C.B. *Chem. Commun.* **2018**, *54*, 607-610.

[41] Wijethunga, T.K.; Đaković, M.; Desper, J.; Aakeröy, C.B. *Acta Cryst.* **2017**, *B73*, 163-167.

[42] Lieffrig, J.; Yamamoto, H.M.; Kusamoto, T.; Cui, H.; Jeannin, O.; Fourmigué, M.; Kato, R. *Cryst. Growth Des.* **2011**, *11*, 4267-4271.

[43] Lieffrig, J.; Jeannin, O.; Fourmigué, M. *J. Am. Chem. Soc.* **2013**, *135*, 6200-6210.

[44] González, L.; Gimeno, N.; Tejedor, R.M.; Polo, V.; Blanca Ros, M.; Uriel, S.; Serrano, J.L. *Chem. Mater.* **2013**, *25*, 4503-4510.

[45] González, L.; Tejedor, R.M.; Royo, E.; Gaspar, b.; Munárriz, J.; Chanthapally, A.; Serrano, J.L.; Vittal, J.J.; Uriel, S. *Cryst. Growth Des.* **2017**, *17*, 6212-6223.

[46] Barry, D.E.; Hawes, C.S.; Blasco, S.; Gunnlaugsson, T. *Cryst. Growth Des.* **2016**, *16*, 5194-5205.

[47] Eichstaedt, K.; Wicher, B.; Gdaniec, M.; Połoński, T. *CrystEngComm.* **2016**, *18*, 5807-5810.

[48] Maugeri, L.; Lébl, T.; Cordes, D.B.; Slawin, A.M.Z.; Philp, D. *J. Org. Chem.* **2017**, *82*, 1986-1995.

[49] Kratzer, P.; Ramming, B.; Römisch, S.; Maas, G. *CrystEngComm.* **2015**, *17*, 4486-4494.

[50] Turunen, L.; Pan, F.; Beyeh, N.K.; Cetina, M.; Trant, J.F.; Ras, R.H.A.; Rissanen, K. *CrystEngComm.* **2017**, *19*, 5223-5229.

[51] Turunen, L.; Bayeh, N.K.; Pan, F.; Valkonen, A.; Rissanen, K. *Chem. Commun.* **2014**, *50*, 15920-15923.

[52] Turunen, L.; Pan, F.; Beyeh, N.K.; Trant, J.F.; Ras, R.H.A.; Rissanen, K. *Cryst. Growth Des.* **2018**, *18*, 513-520.

[53] Schottenberger, H.; Wurst, K.; Buchmeiser, M.R. *J. Organomet. Chem.* **1999**, *584*, 301-309.

[54] Simonov, S.; Zorina, L.; Wzietek, P.; Rodríguez-Fortea, A.; Canadell, E.; Mézière, C.; Bastien, G.; Lemouchi, C.; Garcia-Garibay, M.A.; Batail, P. *Nano Lett.* **2018**, *18*, 3780-3784.

[55] Lemouchi, C.; Vogelsberg, C.S.; Zorina, L.; Simonov, S.; Batail, P.; Brown, S.; Garcia-Garibay, M.A. *J. Am. Chem. Soc.* **2011**, *133*, 6371-6379.

[56] Catalano, L.; Perez-Estrada, S.; Wang, H.-H.; Ayitou, A.J.-L.; Khan, S.I.; Terraneo, G.; Metrangolo, P.; Brown, S.; Garcia-Garibay, M.A. *J. Am. Chem. Soc.* **2017**, *139*, 843-848.

[57] Yamamoto, H.M.; Maeda, R.; Yamaura, J.-I.; Kato, R. *J. Mater. Chem.* **2001**, *11*, 1034-1041.

[58] Torubaev, Y.V.; Lyssenko, K.A.; Barzilovich, P.Y.; Saratov, G.A.; Shaikh, M.M.; Singh, A.; Mathur, P. *CrystEngComm*. **2017**, *19*, 5114-5121.

[59] Yamamoto, H.M.; Yamaura, J.-I.; Kato, R. *J. Am. Chem. Soc.* **1998**, *120*, 5905-5913.

[60] Yamamoto, H.M.; Kosaka, Y.; Maeda, R.; Yamaura, Y.-I.; Nakao, A.; Nakamura, T.; Kato, R. *ACS Nano.* **2008**, *2*, 143-155.

[61] González, L.; Graus, S.; Tejedor, R.M.; López, P.; Elguero, J.; Serrano, J.L.; Uriel, S. *CrystEngComm.* **2018**, *20*, 3167-3170.

[62] Szell, P.M.J.; Siiskonen, A.; Catalano, L.; Cavallo, G.; Terraneo, G.; Priimagi, A.; Bryce, D.L.; Metrangolo, P. *New J. Chem.* **2018**, *42*, 10467-10471.

[63] Mittapalli, S.; Perumalla, D.S.; Nangia, A. *IUCrJ.* **2017**, *4*, 243-250.

[64] Xu, Y.; Viger-Gravel, J.; Korobkov, I.; Bryce, D.L. *J. Phys. Chem. C* **2015**, *119*, 27104-27117.

[65] Cinčić, D.; Friščić, T.; Jones, W. *Chem. Eur. J.* **2008**, *14,* 747-753.

[66] Cinčić, D.; Friščić, T.; Jones, W. *J. Am. Chem. Soc.* **2008**, *130*, 7524-7525.

[67] Bedeković, N.; Stilinović, V.; Friščić, T.; Cinčić, D. *New J. Chem.* **2018**, *42*, 10584-10591.

[68] Lisac, K.; Nemec, V.; Topić, F.; Arhangelskis, M.; Hindle, P.; Tran, R.; Huskić, I.; Morris, A.J.; Friščić, T.; Cinčić, D. *Cryst. Growth Des.* **2018**, *18*, 2387-2396.

[69] Choquesillo-Lazarte, D.; Nemec, V.; Cinčić, D. *CrystEngComm.* **2017**, *19*, 5293-5299.

[70] Eraković, M.; Nemec, V.; Lež, T.; Porupski, I.; Stilinović, V.; Cinčić, D. *Cryst. Growth Des.* **2018**, *18*, 1182-1190.

[71] Carletta, A.; Zbačnik, M.; Van Gysel, M.; Vitković, M.; Tumanov, N.; Stilinović, V.; Wouters, J.; Cinčić, D. *Cryst. Growth Des.* **2018**, *18*, 6833-6842.

[72] Tan, D.; Friščić, T. *Eur. J. Org. Chem.* **2018**, *1*, 18-33.

[73] Do, J.-L.; Friščić, T. *ACS Cent. Sci.* **2017**, *3*, 13-19.

[74] Katsenis, A.D.; Puškarić, A.; Štrukil, V.; Mottillo, C.; Julien. P.A.; Užarević, K.; Pham, M.-H.; Do, T.-O.; Kimber, S.A.J.; Lazić, P.; Magdysyuk, O.; Dinnebier, R.E.; Halasz, I.; Friščić, T. *Nat. Comm.* **2015**, *6*, 6662.

[75] Reitveld, H.M. *J. Appl. Cryst.* **1969**, *2*, 65-71.

Chapter 10 – 1,3,5-Tri(iodoethynyl)-2,4,6-trifluorobenzene: Halogen-Bonded Frameworks and NMR Spectroscopic Analysis

Statement of Authenticity. I certify that I have prepared the following article featuring my own work. Dr. David Bryce is acknowledged for guidance, support, and contributions to the manuscript. Dr. Bulat Gabidullin is acknowledged for acquiring and solving the crystal structures presented in the article.

Permissions. I declare that I have obtained permission from all coauthors to include this article in my thesis. Chapter 10 has been reproduced from *Acta Cryst.* **2017**, *B73*, 153-162, with permission from the International Union of Crystallography.

(DOI: doi.org/10.1107/S2052520617000944)

Supporting Information. All supporting information for this article can be retrieved on the IUCr website: https://scripts.iucr.org/cgi-bin/paper?xm5005

electronic reprint

STRUCTURAL SCIENCE
CRYSTAL ENGINEERING
MATERIALS

ISSN: 2052-5206
journals.iucr.org/b

1,3,5-Tri(iodoethynyl)-2,4,6-trifluorobenzene: halogen-bonded frameworks and NMR spectroscopic analysis

Patrick M. J. Szell, Bulat Gabidullin and David L. Bryce

Acta Cryst. (2017). B**73**, 153–162

Acta Cryst B
STRUCTURAL SCIENCE
CRYSTAL ENGINEERING
MATERIALS
ISSN 2052-5206

1,3,5-Tri(iodoethynyl)-2,4,6-trifluorobenzene: halogen-bonded frameworks and NMR spectroscopic analysis

Patrick M. J. Szell, Bulat Gabidullin and David L. Bryce*

Department of Chemistry and Biomolecular Sciences and Centre for Catalysis Research and Innovation, University of Ottawa, 10 Marie Curie Private, Ottawa, Ontario K1N 6N5, Canada. *Correspondence e-mail: dbryce@uottawa.ca

Received 30 November 2016
Accepted 18 January 2017

Edited by M. Erdelyi, University of Gothenburg, Sweden

Keywords: NMR spectroscopy; halogen bond; crystal engineering; iodine; X-ray diffraction; isotope shift.

CCDC references: 1528339; 1528340; 1528341; 1528342; 1528343; 1528344; 1528345; 1528346

Supporting information: this article has supporting information at journals.iucr.org/b

Halogen bonding is the non-covalent interaction between the region of positive electrostatic potential associated with a covalently bonded halogen atom, named the σ-hole, and a Lewis base. Single-crystal X-ray diffraction structures are reported for a series of seven halogen-bonded cocrystals featuring 1,3,5-tris(iodoethynyl)-2,4,6-trifluorobenzene (1) as the halogen-bond donor, and bromide ions (as ammonium or phosphonium salts) as the halogen-bond acceptors: (1)·$MePh_3PBr$, (1)·$EtPh_3PBr$, (1)·acetonyl-Ph_3PBr, (1)·Ph_4PBr, (1)·[bis(4-fluorophenyl)methyl]triphenylphosphonium bromide, and two new polymorphs of (1)·Et_3BuNBr. The cocrystals all feature moderately strong iodine–bromide halogen bonds. The crystal structure of pure [bis(4-fluorophenyl)methyl]triphenylphosphonium bromide is also reported. The results of a crystal engineering strategy of varying the size of the counter-cation are explored, and the features of the resulting framework materials are discussed. Given the potential utility of (1) in future crystal engineering applications, detailed NMR analyses (in solution and in the solid state) of this halogen-bond donor are also presented. In solution, complex ^{13}C and ^{19}F multiplets are explained by considering the delicate interplay between various J couplings and subtle isotope shifts. In the solid state, the formation of (1)·Et_3BuNBr is shown through significant ^{13}C chemical shift changes relative to pure solid 1,3,5-tris(iodoethynyl)-2,4,6-trifluorobenzene.

1. Introduction

Halogen bonding consists of a non-covalent interaction between the region of positive electrostatic potential associated with a covalently bonded halogen (the halogen-bond donor), dubbed the σ-hole (Politzer *et al.*, 2008, 2014; Wang *et al.*, 2016; Kolář & Hobza, 2016) and a Lewis base (the halogen-bond acceptor; Desiraju *et al.*, 2013). There has been substantial recent interest in understanding the halogen bond, as it offers a linear and tuneable interaction to crystal engineers (Aakeröy *et al.*, 2014; Berger *et al.*, 2015). Two recently published authoritative reviews offer a broad perspective on the field (Cavallo *et al.*, 2016; Gilday *et al.*, 2015). As a result of the σ-hole, the halogen-bond angle ($\theta_{R-X\cdots Y}$) ranges from ~ 150 to 180° (Awwadi *et al.*, 2006). The normalized distance parameter (R_{XB}) is a qualitative tool for assessing the halogen bond, which consists of the quotient of the halogen-bond length ($d_{X\cdots Y}$) and the sum of the relevant van der Waals radii (d_{vdW}; Bondi, 1964), given in equation (1).

$$R_{XB} = \frac{d_{X\cdots Y}}{\sum d_{vdW}} \quad (1)$$

The halogen bond is in some respects analogous to the hydrogen bond (Metrangolo *et al.*, 2005), with a few additional features (Cavallo *et al.*, 2015). The predictability of the

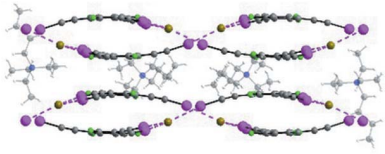

halogen-bonding motif is a result of σ-hole interaction directionality, and therefore has a large potential as a tool for crystal engineering (Perera *et al.*, 2016). The tuneability of the halogen bond arises as a result of the magnitude of the σ-hole, which typically increases with the size of the halogen and with the electron-withdrawing capacity of the substituents on the halogen. Consequently, perfluorinated aromatic halogen-bond donors, such as 1,4-diiodotetrafluorobenzene, are common in the field of halogen bonding (Riley *et al.*, 2011). The iodoacetylene functional group has also garnered interest as a versatile halogen-bond donor (González *et al.*, 2013; Baldrighi *et al.*, 2013), with the first structure reported in the Cambridge Structural Database (CSD; Groom *et al.*, 2016) in 1960 by Gagnaux & Susz (1960). Iodoalkynes have since received considerable attention both in solution (Dumele *et al.*, 2014) and in the solid state (Goroff *et al.*, 2005; Sun *et al.*, 2006; Turunen *et al.*, 2014; Wilhelm *et al.*, 2008; Bouchmella *et al.*, 2007; Perkins *et al.*, 2012). Furthermore, iodoacetylenes have been shown to rank among the strongest halogen-bond donors in the presence of electron-withdrawing groups, such as nitro and fluorine substituents (Aakeröy *et al.*, 2015).

The halogen-bond acceptor consists of a nucleophilic or electron-donating entity (Desiraju *et al.*, 2013), and can be considered to be equally as tuneable as the halogen-bond donor (Aakeröy *et al.*, 2014). With the addition of electron-donating groups, the halogen-bond acceptor moiety can be tuned to be a stronger nucleophile. The elements acting as the nucleophilic sites of the halogen-bond acceptors may include nitrogen (Szell *et al.*, 2017), oxygen (Allen *et al.*, 1997), sulfur (Le Gal *et al.*, 2016), halides (Abate *et al.*, 2009) and more. Halide anions, such as those found in phosphonium and ammonium salts, have been demonstrated to be strong and flexible halogen-bond acceptors (Metrangolo *et al.*, 2008). This flexibility arises from the ability to select and vary both the type of counter-cation and the size of the halide.

Solid-state NMR has been shown to be a versatile technique to probe the chemical and electronic environment of the halogen bond, with three recent literature reviews available (Szell & Bryce, 2016*a*; Bryce & Viger-Gravel, 2015; Vioglio, Catalano *et al.*, 2016). From the information available, notable trends in the chemical shifts of the halogen-bond donor and halogen-bond acceptor have been observed (Viger-Gravel *et al.*, 2013; Szell & Bryce, 2016*b*; Vioglio, Chierotti & Gobetto, 2016). Consequently, changes in chemical shifts provide a diagnostic tool to probe cocrystallization phenomena.

The halogen-bond donor 1,3,5-tris(iodoethynyl)-2,4,6-trifluorobenzene [*sym*-TIETFB, (1)] has been demonstrated by Fourmigué and coworkers to be strong and versatile (Lieffrig *et al.*, 2013). Further to their study, here we present a series of halogen-bonded cocrystal frameworks formed between phosphonium and ammonium bromide salts and (1). The sizes of the phosphonium counter-cation vary from small to bulky. The general halogen-bonding scheme under investigation is shown in Fig. 1. The components used in the cocrystallizations are shown in Fig. 2. Bromide salts were chosen due to the known occurrence of halogen-bonded structures consisting of 1,3,5-trifluoro-2,4,6-triiodobenzene interacting with bromide anions (Triguero *et al.*, 2008; Cavallo *et al.*, 2010), thus providing some direction for the choice of new counter-cations. Although cocrystallization between (1) and Ph_4PBr has been previously attempted, no structure was reported (Lieffrig *et al.*, 2013). This series will aid in providing further data on the relationships between the size of the counter-cation and the resulting halogen-bonded framework. In addition, complete analyses of the ^{13}C and ^{19}F NMR spectra of (1) in solution are given, and cocrystallization-induced chemical shifts are reported through the use of ^{13}C solid-state NMR. The crystal structure of [bis(4-fluorophenyl)methyl]-triphenylphosphonium bromide, one of the salts used in this study, is also reported.

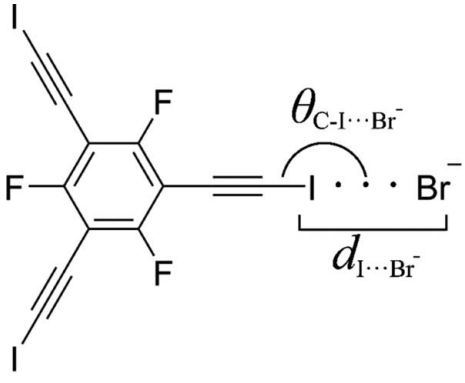

Figure 1
The iodine–bromide halogen-bonding moiety under investigation, where I is the halogen-bond donor and Br^- is the halogen-bond acceptor.

2. Experimental

2.1. Sample preparation

1,3,5-Trifluoro-2,4,6-triiodobenzene, *trans*-dichlorobis-(triphenylphosphine)palladium(II), copper(I) iodide, *N*-iodosuccinimide, triethylamine, acetonyltriphenylphosphonium bromide, (1-butyl)triethylammonium bromide, acetyl bromide, and 4,4′-difluorobenzhydrol were purchased from Alfa Aesar. Reagent-grade tetrahydrofuran and acetone were purchased from Fisher Scientific. Ethynyltrimethylsilane, silver nitrate, methyltriphenylphosphonium bromide, ethyltriphenylphosphonium bromide, tetraphenylphosphonium

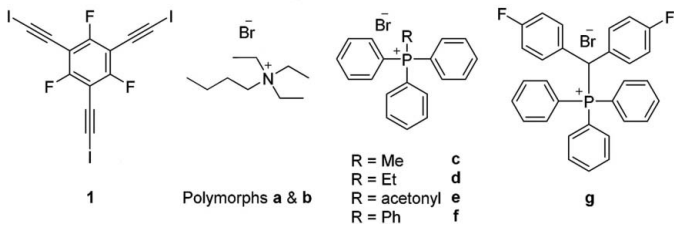

Figure 2
Molecular diagrams of the halogen-bond donor (1), and the halogen-bond acceptors (*a*)–(*g*) used in this study.

bromide and triphenylphosphine were purchased from Sigma Aldrich. All reagents were used without further purification.

Compound (1) was prepared according to literature methods (Lieffrig *et al.*, 2013). Compound (*g*) ([bis(4-fluorophenyl)methyl]triphenylphosphonium bromide) was synthesized following literature procedures using 1,1′-(bromomethylene)bis[4-fluorobenzene] and triphenylphosphine (Ammer *et al.*, 2013), with a yield of 35% (m.p. 505 K). [^{1}H NMR, MeOH-d_4 (saturated), 300 MHz, ref. TMS (0.1%) p.p.m.: 7.87 (m), 7.42 (m), 7.71 (m), 7.68 (m), 7.38 (m), 7.06 (t). ^{13}C NMR, MeOH-d_4 (saturated), 300 MHz, ref. MeOH-d_4 to 49.00 p.p.m.: 164.2 (doublet, J = 249.0 Hz), 136.5 (doublet, J = 2.9 Hz), 136.1 (doublet, J = 9.1 Hz), 133.8 (quartet, J = 6.8 Hz), 131.4 (doublet, J = 12.4 Hz), 130.5 (triplet, J = 3.6 Hz), 119.0 (doublet, J = 82.8 Hz), 117.3 (doublet, J = 22.1 Hz), 47.3 (doublet, J = 44.7 Hz).] 1,1′-(Bromomethylene)bis[4-fluorobenzene] was prepared from 4,4′-difluorobenzhydrol using acetyl bromide, following a literature procedure (Brown *et al.*, 2010).

Cocrystals were prepared by adding a solution of (1) to a solution of the following ammonium and phosphonium bromide salts: Et_3BuNBr (*a*, *b*), $MePh_3PBr$ (*c*), $EtPh_3PBr$ (*d*), acetonyl-Ph_3PBr (*e*), Ph_4PBr (*f*), [bis(4-fluorophenyl)methyl]triphenylphosphonium bromide [(bis(4-FPM)PPh_3), (*g*)]. All solutions were prepared with a minimum amount of solvent. Sample (1*a*) was prepared in chloroform, and samples (1*b*) to (1*g*) were crystallized from acetonitrile. The solution was allowed to slowly evaporate, yielding: [(*sym*-TIETFB)(Et_3BuNBr)] (1*a*), [(*sym*-TIETFB)$_2$(Et_3BuNBr)$_2$] (1*b*), [(*sym*-TIETFB)($MePh_3PBr$)·MeCN] (1*c*), [(*sym*-TIETFB)($EtPh_3PBr$)] (1*d*), [(*sym*-TIETFB)(acetonyl-Ph_3PBr)·MeCN] (1*e*), [(*sym*-TIETFB)(Ph_4PBr)·MeCN] (1*f*), [(*sym*-TIETFB)(bis(4-FPM)PPh_3)·2MeCN] (1*g*). Experimental masses, yields, and melting points may be found in the supporting information.

2.2. X-ray crystallography

The crystals of (1*a*), (1*b*), (1*c*), (1*d*), (1*e*), (1*f*), (1*g*) and (*g*) were mounted on thin glass fibers using paraffin oil. Prior to data collection, the crystals were cooled to 200 (2) K. The data were collected on a Bruker AXS single-crystal diffractometer equipped with a sealed Mo tube (wavelength 0.71073 Å) and APEXII CCD detector. The raw data collection and reduction were done with the Bruker *APEX*II software package (Bruker, 2012). Semi-empirical absorption corrections based on equivalent reflections were applied (Bruker, 2003). Systematic absences in the diffraction dataset and unit-cell parameters were consistent with orthorhombic *Pbca* (#61) for (1*a*), monoclinic *C*2/*c* (#15) for (1*b*), (1*c*), (1*e*) and (1*f*), monoclinic $P2_1/n$ (#14) for (1*g*) and (*g*), and cubic $Pa\bar{3}$ (#205) for (1*d*). The structures were solved by direct methods and refined with full-matrix least-squares procedures based on F^2, using *SHELXL* (Sheldrick, 2015) and *WinGX* (Farrugia, 1999). All non-H atoms were refined anisotropically. The positions of H atoms were calculated based on the geometry of the related non-H atoms. Displacement ellipsoid plots were produced using *ORTEP* (Farrugia, 2012) (see the supporting information), and uncertainties were estimated using *PLATON* for Windows (Spek, 2009).

In (1*a*) the 1,3,5-tris(iodoethynyl)-2,4,6-trifluorobenzene molecule crystallizes with one bromide anion and one butyltriethylammonium cation. The latter is disordered over two positions with 0.536 (10):0.464 (10) occupancies. Restraints were applied to bond distances, angles and anisotropic displacement parameters (ADPs) of the disordered molecule.

The asymmetric unit of (1*b*) has two 1,3,5-tris(iodoethynyl)-2,4,6-trifluorobenzene molecules, two bromide anions and two butyltriethylammonium cations. The C33—C34 group is disordered over two positions with 0.83 (3):0.17 (3) occupancies. The N2···C40 butyltriethylammonium cation is disordered over two positions with 0.57 (3):0.43 (3) occupancies. Restraints and constraints were used for refinement of bond distances, angles and ADPs of the disordered groups.

The data for (1*c*) was twinned and the refinement was done using the HKLF5 file, giving a 0.73:0.27 ratio of components. The asymmetric unit contains molecules of 1,3,5-tris(iodoethynyl)-2,4,6-trifluorobenzene, acetonitrile, a half of the methyltriphenylphosphonium cation, and a half of the bromide anion. The cation of methyltriphenylphosphonium lies on a twofold rotation axis and is disordered over two positions. Constraints were applied to the atom distances in the methyltriphenylphosphonium residue, and restraints were used for ADPs of all atoms.

In (1*d*) the 1,3,5-tris(iodoethynyl)-2,4,6-trifluorobenzene molecules and the bromide anion lie on a threefold axis. The ethyltriphenylphosphonium cation is 33% occupied and is located near a threefold rotoinversion axis. This corresponds to a model of two molecules disordered over six positions. Due to heavy disorder, the displacement parameters for atoms of ethyltriphenylphosphonium were refined as equal to each other and isotropic, and rigid-body constraints were applied to the phenyl rings.

The structure of (1*e*) has one acetonyltriphenylphosphonium cation, one bromide anion, two molecules of 1,3,5-tris(iodoethynyl)-2,4,6-trifluorobenzene, and two acetonitrile molecules in the asymmetric unit. The acetonyltriphenylphosphonium lies on a twofold rotation axis. It is disordered over two positions with 0.5:0.5 occupancies. Restraints were applied to the ADPs of disordered acetonyl and phenyl groups.

The asymmetric unit of (1*f*) contains one 1,3,5-tris(iodoethynyl)-2,4,6-trifluorobenzene molecule, one acetonitrile, half of a tetraphenylphosphonium cation, and half of a bromide anion. The tetraphenylphosphosnium and bromide moieties lie on twofold rotation axes. No restraints or constraints were applied.

The asymmetric unit of (1*g*) contains one bis(4-FPM)PPh_3 cation, one bromide anion, one acetonitrile molecule, and one 1,3,5-tris(iodoethynyl)-2,4,6-trifluorobenzene molecule. The acetonitrile molecule is disordered over two positions with equal (50%) occupancies. Restraints were applied to bond distances and ADPs of the acetonitrile.

In (*g*) the cation crystallizes with one bromide anion. No restraints were applied.

Table 1
Selected single-crystal X-ray crystallographic data for compounds (1*a*), (1*b*), (1*c*), (1*d*), (1*e*), (1*f*), (1*g*) and (*g*).

Experiments were carried out at 200 K with Mo $K\alpha$ radiation using a Bruker APEXII CCD. H-atom parameters were constrained.

	(1*a*)	(1*b*)	(1*c*)	(1*d*)
Crystal data				
Chemical formula	$C_{12}F_3I_3{\cdot}C_{10}H_{24}N{\cdot}Br$	$C_{12}F_3I_3{\cdot}C_{10}H_{24}N{\cdot}Br$	$C_{19}H_{18}P{\cdot}2C_{12}F_3I_3{\cdot}2C_2H_3N{\cdot}Br$	$C_{20}H_{20}P{\cdot}2C_{12}F_3I_3{\cdot}Br$
M_r	820.03	820.03	1602.96	3069.76
Crystal system, space group	Orthorhombic, *Pbca*	Monoclinic, *C*2/*c*	Monoclinic, *C*2/*c*	Cubic, $Pa\bar{3}$
a, *b*, *c* (Å)	15.7522 (5), 22.3326 (7), 15.5213 (5)	31.434 (4), 14.8275 (19), 26.724 (4)	10.6026 (12), 16.3599 (19), 30.679 (4)	22.3941 (15), 22.3941 (15), 22.3941 (15)
β (°)	90	116.034 (7)	97.626 (5)	90
V (Å^3)	5460.2 (3)	11192 (3)	5274.5 (11)	11231 (2)
Z	8	16	4	4
D_x (Mg m^{-3})	1.995	1.947	2.019	1.816
μ (mm^{-1})	4.93	4.81	4.38	4.10
Crystal size (mm)	0.15 × 0.12 × 0.09	0.11 × 0.06 × 0.01	0.22 × 0.11 × 0.01	0.24 × 0.18 × 0.12
Data collection				
Absorption correction	Multi-scan *SADABS* (Bruker, 2003)	Multi-scan *SADABS* (Bruker, 2003)	Multi-scan *TWINABS* (Bruker, 2003)	Multi-scan *SADABS* (Bruker, 2003)
T_{min}, T_{max}	0.556, 0.746	0.578, 0.746	0.335, 0.745	0.556, 0.746
No. of measured, independent and observed [$I > 2\sigma(I)$] reflections	77 024, 6773, 5501	65 445, 10 111, 5235	5572, 5572, 4060	96 410, 4615, 3422
R_{int}	0.042	0.082	†	0.045
(sin $\theta/\lambda)_{max}$ (Å^{-1})	0.667	0.600	0.629	0.667
Refinement				
$R[F^2 > 2\sigma(F^2)]$, $wR(F^2)$, S	0.083, 0.183, 1.22	0.049, 0.138, 1.02	0.141, 0.384, 1.06	0.062, 0.191, 1.05
No. of reflections	6773	10 111	5572	4615
No. of parameters	379	595	294	146
No. of restaints	524	228	441	12
$\Delta\rho_{max}$, $\Delta\rho_{min}$ (e Å^{-3})	1.56, −1.62	0.76, −0.72	2.99, −1.62	2.20, −1.08

	(1*e*)	(1*f*)	(1*g*)	(*g*)
Crystal data				
Chemical formula	$C_{21}H_{20}OP{\cdot}2C_{12}F_3I_3{\cdot}2C_2H_3N{\cdot}Br$	$C_{24}H_{20}P{\cdot}2C_{12}F_3I_3{\cdot}2C_2H_3N{\cdot}Br$	$C_{45}H_{27}BrF_5I_3NP$	$C_{31}H_{24}BrF_2P$
M_r	1645.00	1665.03	1168.25	545.38
Crystal system, space group	Monoclinic, *C*2/*c*	Monoclinic, *C*2/*c*	Monoclinic, $P2_1/n$	Monoclinic, $P2_1/n$
a, *b*, *c* (Å)	10.5098 (5), 16.2789 (7), 30.9417 (15)	10.5544 (3), 16.4031 (4), 30.8221 (8)	10.7807 (5), 28.8937 (12), 14.8900 (6)	10.7103 (4), 18.08967 (6), 13.6486 (5)
β (°)	95.6557 (19)	96.1095 (12)	93.368 (2)	96.2767 (17)
V (Å^3)	5268.0 (4)	5305.8 (2)	4630.1 (3)	2629.53 (16)
Z	4	4	4	4
D_x (Mg m^{-3})	2.074	2.084	1.676	1.378
μ (mm^{-1})	4.39	4.35	2.97	1.66
Crystal size (mm)	0.15 × 0.11 × 0.10	0.26 × 0.24 × 0.22	0.18 × 0.16 × 0.15	0.31 × 0.20 × 0.12
Data collection				
Absorption correction	Multi-scan *SADABS* (Bruker, 2003)	Multi-scan *SADABS* (Bruker, 2003)	Multi-scan *SADABS* (Bruker, 2003)	Multi-scan *SADABS* (Bruker, 2003)
T_{min}, T_{max}	0.601, 0.746	0.633, 0.746	0.624, 0.746	0.540, 0.746
No. of measured, independent and observed [$I > 2\sigma(I)$] reflections	35 395, 6513, 6031	24 116, 6501, 5916	55 736, 11 400, 9926	23 062, 6468, 5130
R_{int}	0.039	0.022	0.029	0.038
(sin θ/λ_{max}) (Å^{-1})	0.672	0.668	0.668	0.667
Refinement				
$R[F^2 > 2\sigma(F^2)]$, $wR(F^2)$, S	0.066, 0.155, 1.12	0.025, 0.065, 1.01	0.044, 0.102, 1.19	0.032, 0.091, 1.05
No. of reflections	6513	6501	11 400	6468
No. of parameters	333	309	534	316
No. of restraints	135	0	24	0
$\Delta\rho_{max}$, $\Delta\rho_{min}$ (e Å^{-3})	1.35, −1.78	0.90, −1.03	1.23, −0.88	0.74, −0.23

† Compound (1*c*) was refined over twinned data, and most of the reflections are composite.

Table 2
Halogen-bond geometrical parameters, including the number of halogen bonds to the bromide ion (coordination number), the halogen-bond length ($d_{I\cdots Br}$), the halogen-bond angle ($\theta_{C-I\cdots Br}$), the reduced distance parameter (R_{XB}), and the sum of halogen-bond angles ($\Sigma_{I\cdots X\cdots I}$).

Compound	Coordination No.	Iodine label	I···Br$^-$ distance (Å)	C—I···Br$^-$ angle (°)	R_{XB}	$\Sigma\theta_{I\cdots X\cdots I}$ (sum of angles)
(1*a*)	3	I1	3.2121 (18)	168.2 (4)	0.84	302.06 (14)
		I2	3.1636 (18)	174.6 (5)	0.83	
		I3	3.2569 (19)	177.0 (5)	0.85	
(1*b*)	3 (Br7)	I2	3.2854 (17)	169.5 (4)	0.86	358.03 (14)
		I5	3.2241 (15)	170.3 (3)	0.84	
		I6	3.2735 (15)	178.0 (4)	0.86	
	3 (Br8)	I1	3.2410 (15)	174.2 (4)	0.85	358.03 (12)
		I3	3.1651 (16)	170.9 (4)	0.83	
		I4	3.2443 (18)	172.3 (3)	0.85	
(1*c*)	4	I1	3.298 (2)	176.6 (7)	0.86	365.26 (28)
		I3	3.275 (3)	174.9 (7)	0.86	
(1*d*)	6	I1	3.2908 (9)	172.9 (3)	0.86	1078.68 (24)
		I2	3.2417 (8)	171.7 (3)	0.85	
(1*e*)	4	I1	3.2989 (12)	172.6 (3)	0.87	364.09 (11)
		I2	3.3254 (9)	176.5 (3)	0.87	
(1*f*)	4	I1	3.3400 (6)	176.68 (9)	0.87	364.47 (4)
		I3	3.2610 (5)	172.54 (9)	0.85	
(1*g*)	3	I1	3.2849 (8)	165.79 (15)	0.86	355.98 (6)
		I2	3.2939 (7)	171.40 (14)	0.86	
		I3	3.1893 (7)	178.14 (15)	0.84	

2.3. Solution NMR spectroscopy

^{13}C solution NMR experiments were performed at 11.7 T using a Bruker Avance spectrometer and a Bruker HXY probe. A Bloch decay using a $\pi/6$ pulse of 8.10 µs was used with and without ^{19}F decoupling. The recycle delay was 10 s. 512 transients were acquired for the decoupled spectrum and 5120 transients for the spectrum without decoupling. ^{13}C experiments were repeated at 7.1 T on a Bruker Avance spectrometer, using a $\pi/6$ pulse of 5.25 µs and a recycle delay of 30 s (1632 transients). ^{19}F experiments were performed at 7.1 T on a Bruker Avance spectrometer with a $\pi/6$ pulse of 6.5 µs and a recycle delay of 1 s (128 transients). Except where noted, samples were prepared as saturated solutions of (1) in methanol-d_4. ^{13}C chemical shifts were referenced to the methanol resonance at 49.00 p.p.m., and the ^{19}F chemical shifts were internally referenced to the ^{1}H signal of TMS (0.1% TMS in MeOH-d_4) using a Ξ value of 0.940866982 (Maurer & Kalbitzer, 1996).

2.4. Solid-state NMR spectroscopy

^{13}C solid-state NMR experiments were carried out at 9.4 T on a Bruker Avance III spectrometer, using a Bruker 4 mm HXY MAS probe. A rotor-synchronized Hahn-echo ($\pi/2 - \pi$) pulse sequence was used for compound (1), with a $\pi/2$ pulse of 5.30 µs, acquiring 5408 transients with a recycle delay of 60 s and a MAS frequency of 10 kHz. Cross polarization from protons under MAS was used for compound (1*b*), with a 4.60 µs proton $\pi/2$ pulse, 2.5 ms contact time, 20 s recycle delay and a MAS frequency of 8 kHz. Chemical shifts were referenced using solid glycine at 176.4 p.p.m. relative to TMS.

3. Results and discussion

3.1. X-ray crystallography: description of the framework materials

The X-ray structures for compounds (1*a*) [$C_{12}F_3I_3$, $C_{10}H_{24}N$, Br], (1*b*) [$C_{12}F_3I_3$, $C_{10}H_{24}N$, Br], (1*c*) [$C_{19}H_{18}P$, 2($C_{12}F_3I_3$), 2(C_2H_3N), Br], (1*d*) [$C_{20}H_{20}P$, 2($C_{12}F_3I_3$), Br], (1*e*) [$C_{21}H_{20}OP$, 2($C_{12}F_3I_3$), 2(C_2H_3N), Br], (1*f*) [$C_{24}H_{20}P$, 2($C_{12}F_3I_3$), 2(C_2H_3N), Br], (1*g*) [$C_{31}H_{24}F_2P$, $C_{12}F_3I_3$, C_2H_3N, Br] and (*g*) [$C_{31}H_{24}BrF_2P$] were solved, and selected experimental single-crystal X-ray data are reported in Table 1. Compounds (1*a*) and (1*b*) are polymorphs and they are also distinct from the previously reported polymorph (Lieffrig *et al.*, 2013). All structures feature iodine···bromide halogen bonds. Parameters describing the halogen-bond geometry and environment for each structure are

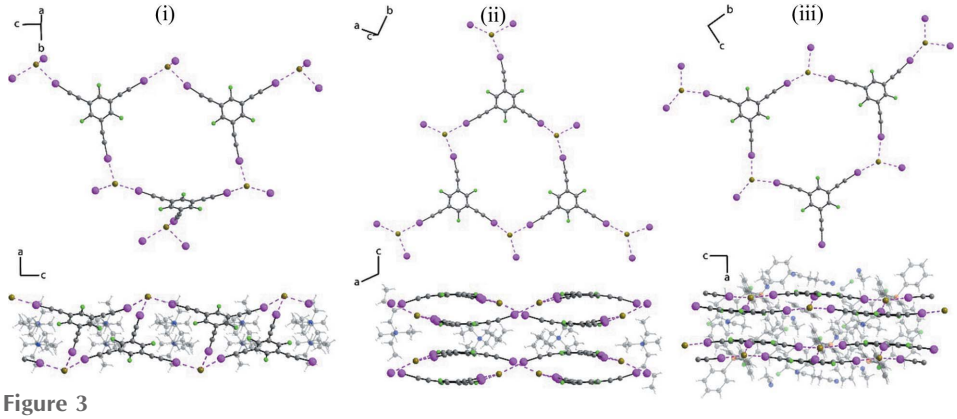

Figure 3
Depiction of the halogen-bonding motifs from the X-ray structures of compounds (1*a*) (i), (1*b*) (ii) and (1*g*) (iii), with three halogen bonds to each bromide anion. The upper diagram shows the resulting frameworks with the counter-cation removed, and the lower diagram is a side view showing the halogen-bonded motifs and the arrangements of the counter-cations. The iodine···bromide halogen bonds are represented by dashed magenta lines, and the counter-cations have been rendered transparent in the second row for illustrative purposes.

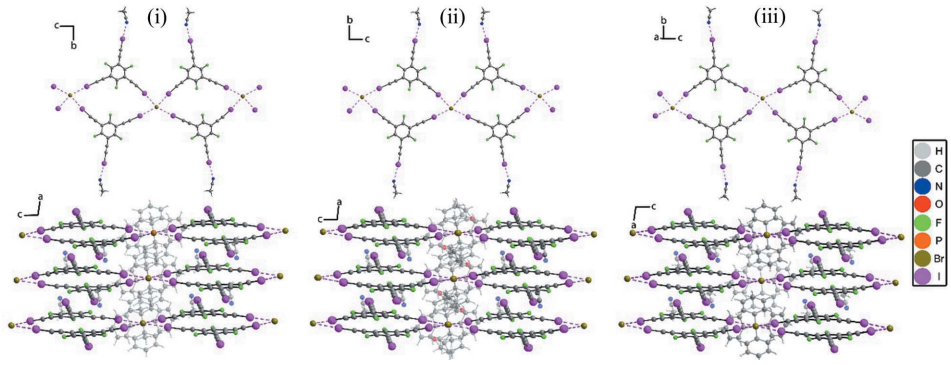

Figure 4
Depiction of the halogen-bonding motifs from the X-ray structures of (1*c*) (i), (1*e*) (ii) and (1*f*) (iii), with four halogen bonds to each bromide anion. The upper row shows the frameworks with the counter-cations removed, and the lower row is a side view showing the halogen bonds and the arrangements of the counter-cations. The iodine···bromide halogen bonds are represented by dashed magenta lines, and the counter-cations have been rendered transparent for illustrative purposes.

reported in Table 2. For all cocrystals of (1), halogen bonds with moderate R_{XB} values are observed. They vary over a small range, from 0.83 in (1*a*) and (1*b*), to 0.87 in (1*e*) and (1*f*). The number of iodoacetylene molecules coordinating to the bromide anion varies from structure to structure, with the lowest coordination number being 3 for compounds (1*a*), (1*b*) and (1*g*), and the highest coordination number being 6 for compound (1*d*). Due to this high coordination number, the highest sum of angles is for the nearly octahedral compound (1*d*) at 1078.68 (24)°. The lowest sum of angles is for compound (1*a*), at 302.06 (14)°. In addition to iodine···bromide halogen bonds, the structures of (1*c*), (1*e*) and (1*f*) reveal a distinct iodine interacting with the acetonitrile solvent molecule present in the unit cell. Depictions of the halogen-bonding motifs and nature of the frameworks formed for all compounds are presented in Figs. 3, 4 and 5.

As mentioned previously, the bromide anions in compounds (1*a*), (1*b*) and (1*g*) are coordinated by three iodines. The I···Br$^-$···I angles differ significantly between structures, but each framework results in a honeycomb pattern, as shown in Fig. 3. Each honeycomb has a unique geometry, and these are skewed in different ways. The ligand in compound (1*a*) has a halogen bond which is perpendicular to the honeycomb network, resulting in a slight zigzag pattern between the honeycombs. Each honeycomb is interweaved, with the Et_3BuN^+ counter-cation occupying the residual spaces. The counter-cation of compound (1*a*) is disordered, having an overlap of two possible positions. In comparison to (1*a*), the honeycomb network in compound (1*b*) is undulated when viewed from the side, as a result of the ligand flexing to accommodate the halogen bond. Two honeycombs are interweaved, forming sheets that stack together, with the spaces between the sheets occupied by the Et_3BuN^+ counter-cation. Structures (1*a*) and (1*b*) are distinct from the previously reported cocrystals of (1) and Et_3BuNBr (Lieffrig *et al.*, 2013), which had six halogen bonds to the bromide anion. In contrast to the honeycombs in (1*a*) and (1*b*), the honeycomb network in compound (1*g*) is relatively flat, with only a slight undulation. The networks are not interweaved, forming sheets composed of a single layer of (1), with the spaces filled by the counter-cation and acetonitrile. Although there are two acetonitrile molecules in the asymmetric unit, they are not coordinated by iodines. The lack of interweaving could be attributed to the size of the counter-cation, which may help to support individual honeycomb networks.

The structures of compounds (1*c*), (1*e*) and (1*f*) each have four iodines coordinating to the bromide anion. The resulting halogen-bonded frameworks form chains, with each chain link comprised of two molecules of (1) each coordinating two bromide anions, as shown in the top row of Fig. 4. The resulting framework topology is constant across the three structures, with the formation of pockets between the chains, which are occupied by their respective counter-cations. Each compound has a unique halogen-bonding geometry, as noted in Table 2. Consequently, the angle between the chain links differs between the structures. Each tetrahedral phosphonium counter-cation is composed of three phenyl groups and one different substituent: methyl (1*c*), acetonyl (1*e*) or phenyl (1*f*). Both the methyl group of the counter-cation of (1*c*) and the acetonyl group of (1*e*) are disordered with the phenyl groups, with two likely positions. This disorder can be attributed to the lack of interactions promoting a specific orientation of the counter-cation. Contrarily, there is no disorder in the X-ray structure of (1*f*). In all three structures, acetonitrile is present in the crystal and is coordinated to iodine. The halogen bonds between (1) and acetonitrile are very similar in geometry across all structures with (1*c*) [$d_{I\cdots N}$ = 3.000 (3) Å, R_{XB} = 0.85,

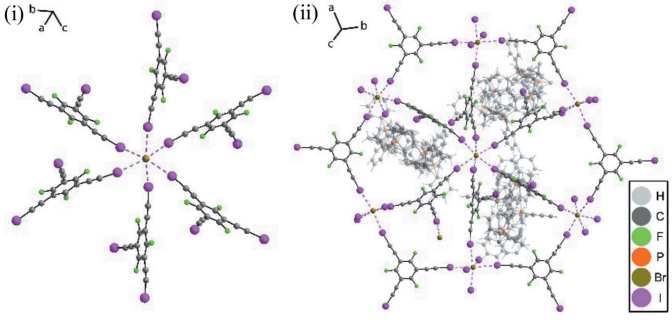

Figure 5
Depiction of the halogen-bonding motif from the X-ray crystal structure of compound (1*d*), showing (i) iodine coordination to the bromide anion and (ii) the honeycomb network formed as a result of halogen bonding. The counter-cations in (i) have been removed, and were rendered transparent in (ii) for illustrative purposes. The counter-cations that were overlapping the framework in (ii) were omitted for clarity. The iodine···bromine halogen bonds are denoted by a dashed magenta line.

Table 3
The ^{13}C NMR chemical shifts (δ), J coupling constants and isotope shifts [$\Delta^{19}F(^{13/12}C)$] of (1) in methanol-d_4.

Assignment	δ (^{13}C) (p.p.m.)	J coupling constant (Hz)	$^{n}\Delta^{19}F(^{13/12}C)$ (p.p.m.)
(i)	165.5 ± 0.1	260.3 ± 0.5 Hz 7.4 ± 0.5 Hz (*meta*-F)	−0.09 ± 0.01 p.p.m.†
(ii)	100.9 ± 0.1	20.8 ± 0.4 (*ortho*-F) 4.4 ± 0.4 (*para*-F) 5.5 ± 0.5 (virtual)	−0.05 ± 0.02 p.p.m.‡
(iii)	77.9 ± 0.1	1.1 ± 0.2 Hz to *ortho*-F 5.5 ± 0.5 Hz (virtual)	−0.01 ± 0.01 p.p.m.§
(iv)	26.5 ± 0.1	3.3 ± 0.3 Hz (all)	–

† One bond isotope shift. ‡ Two bond isotope shift. § Three bond isotope shift.

$\theta_{C-I\cdots N}$ = 172.2 (10)°, $\theta_{I\cdots N-C}$ = 128 (3)°] having the shortest halogen bond, followed by (1*e*) [$d_{I\cdots N}$ = 3.028 (14) Å, R_{XB} = 0.86, $\theta_{C-I\cdots N}$ = 171.2 (4)°, $\theta_{I\cdots N-C}$ = 130.9 (13)°] and (1*f*) [$d_{I\cdots N}$ = 3.043 (3) Å, R_{XB} = 0.86, $\theta_{C-I\cdots N}$ = 172.08 (12)°, $\theta_{I\cdots N-C}$ = 131.7 (3)°].

Compound (1*d*) has six iodines halogen-bonded to the bromide anion, with a resulting cubic symmetry ($Pa\bar{3}$). The geometry surrounding the bromide anion is near-octahedral. Every iodine of the halogen-bond donor is participating in a C—I···Br$^-$ halogen bond. The resulting halogen-bonded framework is a large honeycomb network with a slight undulation, supported by interlaced halogen bonds. The I atoms are coordinated to a central bromide anion, with the void spaces filled with counter-cations, as illustrated in Fig. 5. The counter-cations are heavily disordered over six positions. Although the geometry of the halogen bonds surrounding the bromide anion is unique in this structure, the overall motif of the honeycomb shares many similarities with the previously reported octahedrally coordinated cocrystal formed with Et_3BuNBr ($Ia\bar{3}$ space group; Lieffrig *et al.*, 2013).

Compound (*g*) is the halogen-bond acceptor of compound (1*g*). The X-ray structure of (*g*) consists of a bromide anion which participates in a hydrogen bond with the C—H group ($d_{H\cdots Br}$ = 2.76 Å, $\theta_{C-H\cdots Br}$ = 174°, R_{HB} = 0.94), and has two proton contacts to the nearby phenyl groups ($d_{H\cdots Br}$ = 2.90 Å, $\theta_{C-H\cdots Br}$ = 154°, R_{HB} = 0.95, $d_{H\cdots Br}$ = 3.04 Å, $\theta_{C-H\cdots Br}$ = 175°, R_{HB} = 0.99). These proton contacts surround the halide, following the same arrangement of the previously reported structures (Ammer *et al.*, 2013).

To summarize, the consistencies within the sets of frameworks composed of three-coordinate, four-coordinate and six-coordinate bromide anions have been discussed. The three-coordinate frameworks form hexagonal honeycombs, with the counter-cations occupying the void spaces. In the case of the largest counter-cation, structure (1*g*), the void space is occupied by a single molecule of (*g*). This flat honeycomb structure occupied by a large counter-cation was also the case in the structure reported with bis(triphenylphosphoranylidene)ammonium chloride (Lieffrig *et al.*, 2013). Despite the similarities between the counter-cations based on RPh_3PBr (1*c*) (*R* = methy), (1*d*) (*R* = ethyl), (1*e*) (*R* = acetonyl) and (1*f*) (*R* = phenyl), the choice of counter-cation did not always yield the same bromide coordination. Although structures (1*c*), (1*e*) and (1*f*) strongly resembled each other, structure (1*d*) was significantly different from the other structures, demonstrating that the choice of the counter-cation may not always predictably lead to the desired framework.

3.2. NMR spectroscopy

In the second part of this paper, we shift focus towards properly understanding the NMR spectroscopic properties of halogen-bond donor (1) in solution and in the solid state. This information should prove valuable in subsequent studies of halogen-bonded complexes of (1), both in solution and in the solid state.

The ^{13}C chemical shifts for (1) have been previously reported in a solution of chloroform-*d* (Lieffrig *et al.*, 2013), but required further attention to fully interpret the spectrum. ^{19}F–^{13}C J couplings are known to have a considerable effect on ^{13}C NMR spectra (Weigert & Roberts, 1970), and are especially important for perfluorinated halogen-bond donors. Illustrated in Fig. 6 and summarized in Table 3, the ^{13}C NMR spectrum of (1) in deuterated methanol gives rise to four unique resonances, with each resonance corresponding to a set of three chemically equivalent carbon nuclei due to the C_{3h} molecular symmetry. Due to the strong ^{19}F–^{13}C J couplings, experiments with ^{19}F decoupling were also used to help measure the exact ^{13}C chemical shifts. The resonances can be assigned to the C atoms covalently bonded to fluorine: (i) [$\delta(^{13}C)$ = 165.5 ± 0.1 p.p.m.] the C atoms at the *ipso* position; (ii) [$\delta(^{13}C)$ = 100.9 ± 0.1 p.p.m.] the C atoms at the acetylene position; (iii) [$\delta(^{13}C)$ = 77.9 ± 0.1 p.p.m.] and the C atoms

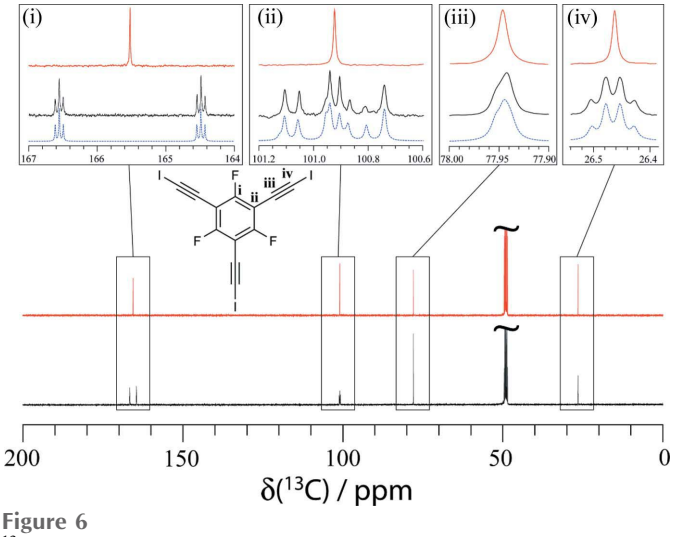

Figure 6
^{13}C solution NMR spectra of *sym*-TIETFB (1) dissolved in methanol-d_4 with ^{19}F decoupling (red), without ^{19}F decoupling (black), and simulation (blue dashed). Projections of the resonances are shown in the top boxes which correspond to, from left to right, the C atoms covalently bonded to fluorine (i), the C atoms on the *ipso* position (ii), the acetylene C atoms (iii), and the carbon covalently bonded to iodine (iv). The spectra were acquired on a 500 MHz NMR spectrometer and are internally referenced to methanol-d_4 at 49.00 p.p.m.

Table 4
Carbon–fluorine J coupling constant for carbon (i) and the ^{13}C chemical shift of carbon (iv) in different deuterated solvents.

All spectra were acquired using saturated solutions.

Solvent	$J(^{13}C, ^{19}F)$ of carbon (i) (Hz)†	$\delta(^{13}C)$ of carbon (iv) (p.p.m.)
Chloroform-d	263.8 ± 0.8	19.8 ± 0.1
Benzene-d_6	262.2 ± 0.9	20.9 ± 0.1
Acetonitrile-d_3	260.3 ± 0.9	25.2 ± 0.1
Acetone-d_6	260.2 ± 0.9	25.8 ± 0.1
Methanol-d_4	260.3 ± 0.9	26.5 ± 0.1
Dimethyl sulfoxide-d_6	258.8 ± 0.9	32.4 ± 0.1

† Coupled to the covalently bonded to fluorine.

covalently bonded to iodine; (iv) [$\delta(^{13}C)$ = 26.5 ± 0.1 p.p.m.]. The chemical shift of the carbon at the *ipso* position (ii) had apparently not been previously reported (Lieffrig *et al.*, 2013), perhaps due to difficulties in observing the resonance as a result of long relaxation times and its large breadth. The observed resonance for the carbon covalently bonded to fluorine is a doublet of triplets (AXY_2 spin system) due to the coupling to the covalently bonded fluorine [$J(^{13}C, ^{19}F)$ = 260.3 ± 0.9 Hz] and the fluorines in the *meta* position relative to the observed ^{13}C [$J(^{13}C, ^{19}F)$ = 7.4 ± 0.5 Hz]. These $J(^{13}C, ^{19}F)$ coupling constants also affect the ^{19}F spectrum (*see below*). Following the notation of Gombler (1982), a one-bond isotope shift of $^{1}\Delta^{19}F(^{13/12}C)$ = −0.09 ± 0.01 p.p.m. was observed in the ^{19}F spectrum as a result of the presence of the ^{13}C isotope for the carbon covalently bonded to fluorine. This isotope shift is in agreement with the literature in terms of magnitude and sign (Jameson, 1977). For example, $\Delta^{19}F(^{13/12}C)$ isotope shifts were observed on the ^{19}F spectrum of (3*S*,4*R*)-4-(4-fluorophenyl)-3-hydroxymethyl-1-methylpiperidine, with the $^{1}\Delta^{19}F(^{13/12}C)$ = −0.0863 p.p.m., $^{2}\Delta^{19}F(^{13/12}C)$ = −0.0253 p.p.m., $^{3}\Delta^{19}F(^{13/12}C)$ = −0.0057 p.p.m., and $^{4}\Delta^{19}F(^{13/12}C)$ = −0.0031 p.p.m. (Navrátilová, 2001).

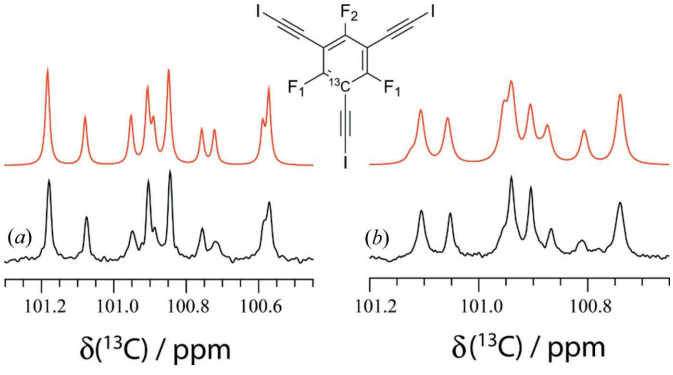

Figure 7
Experimental (black) and simulated (red) ^{13}C NMR spectra of the C atoms in the *ipso* position at Larmor frequencies of (*a*) 75 MHz and (*b*) 125 MHz. The multiplet pattern results from a combination of effects, including J coupling and isotope shifts.

The ^{13}C multiplet observed for carbon (ii) (AX_2Y) can be attributed to a combination of the coupling to the neighboring fluorines in the *ortho* position [$J(^{13}C, ^{19}F)$ = 20.8 ± 0.4 Hz], the coupling to the fluorine in the *para* position [$J(^{13}C, ^{19}F)$ = 4.4 ± 0.4 Hz], and the virtual coupling between fluorines [$J(^{19}F, ^{19}F)$ = 5.5 ± 0.5 Hz]. Additionally, a two-bond isotope shift of the order of $^{2}\Delta^{19}F(^{13/12}C)$ = −0.05 ± 0.02 p.p.m. has been observed for the fluorines in the *ortho* position. The small chemical shift difference between the fluorines in the *ortho* position and the *para* position introduces further second-order effects to the multiplet of carbon ii, which are a function of the quotient of the frequency difference ($\Delta\nu$, Hz) and the J coupling constant. Consequently, two different ^{13}C NMR spectra were fit iteratively using *DAISY* (Bruker, 2007) at field strengths of 300 MHz and 500 MHz to ensure accurate fits, with the resulting fittings shown in Fig. 7. In order to further visualize the effect of the ^{19}F isotope shift on the multiplet of carbon ii, a series of simulations varying the value of the isotope shift [$^{2}\Delta^{19}F(^{13/12}C)$] may be found in Fig. S1 of the supporting information.

The acetylene carbon (iii) gave rise to an asymmetric singlet as a result of weak ^{13}C–^{19}F J coupling, of the order of 1.1 ± 0.2 Hz. The line shape is a result of the further virtual ^{19}F–^{19}F coupling described for the *ipso* carbon, still of the order of $J(^{19}F, ^{19}F)$ = 5.5 ± 0.5 Hz. The carbon covalently bonded to iodine (iv) gave rise to an apparent quartet with a ^{13}C–^{19}F J coupling constant of 3.3 ± 0.3 Hz.

In addition, chemical shifts and J coupling constants were observed to be sensitive to the solvent being used for the experiment. The effect of the solvent on the chemical shift was

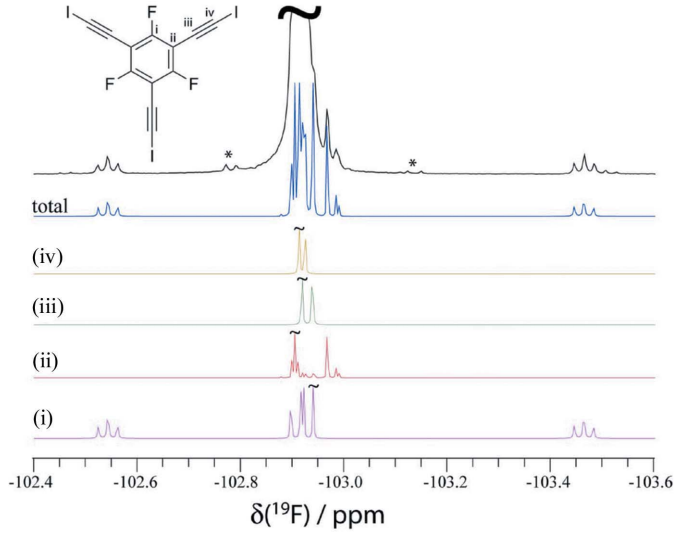

Figure 8
Magnified view of the experimental (black) ^{19}F NMR spectrum of (1) in deuterated methanol. The simulations were performed using the parameters from Table 3. The numbered simulations are ^{19}F subspectra, whereby a ^{13}C spin was assumed present at each of the four carbon positions in turn. Subtle isotope effects play an important role in the final appearance of the spectra. The total simulation does not include the strong peak from ^{19}F resonances in molecules with all ^{12}C isotopes. Asterisks denote minor impurities.

most prominent for the carbon covalently bonded to iodine. For instance, the ^{13}C chemical shift for carbon (iv) in saturated solutions varied from 19.8 ± 0.1 p.p.m. in chloroform-d to 32.4 ± 0.1 p.p.m. in dimethyl sulfoxide-d_6. A similar solvent effect has been previously observed for other iodoalkynes (Webb *et al.*, 2004). Solvent effects on the ^{19}F–^{13}C J coupling constants have not been previously reported for (1), and this effect was most easily observed for the carbon covalently bonded to fluorine. For instance, the $J(^{13}C, ^{19}F)$ constant for the C—F carbon in chloroform-d was 263.8 ± 0.8 Hz and 258.8 ± 0.9 Hz in dimethyl sulfoxide-d_6. Other $J(^{13}C, ^{19}F)$ coupling constants were not significantly affected. The ^{13}C chemical shifts for carbon (iv) and the ^{13}C–^{19}F J coupling values for carbon (i) in a series of solvents are reported in Table 4.

The experimental ^{19}F solution NMR spectrum appears to consist of a single dominant resonance at −102.92 ± 0.01 p.p.m. in MeOH-d_4 (see the supporting information). However, the magnified view, illustrated in Fig. 8, shows the effects of the ^{13}C J couplings and isotope shifts on the ^{19}F NMR spectrum. The ^{19}F NMR spectrum was simulated using the same coupling and isotope shift parameters determined from the ^{13}C NMR spectrum (Table 3), and is in good agreement with the experimental ^{19}F NMR spectrum. Due to its low natural abundance, the intensities of peaks associated with the presence of ^{13}C are very low compared with the dominant resonance. Despite their low intensity, these results clearly corroborate the interpretation of the ^{13}C NMR spectra. The doublet of triplets, resulting from the one bond isotope shift and the ^{19}F–^{13}C J coupling to carbon (i), is also associated with a central multiplet near −102.9 p.p.m. A multiplet is also observed due to the two bond isotope shift and the ^{19}F–^{13}C J coupling to carbon (ii), manifested as two sharp peaks at −102.97 ± 0.01 and −102.99 ± 0.01 p.p.m. The right shoulder of the dominant resonance, at −102.94 ± 0.01 p.p.m., is attributed to the three-bond isotope shift caused by carbon (iii). The effects of carbon (iv) are negligible, as they are overwhelmed by the dominant ^{19}F resonance arising from the isotopologue with no ^{13}C spins.

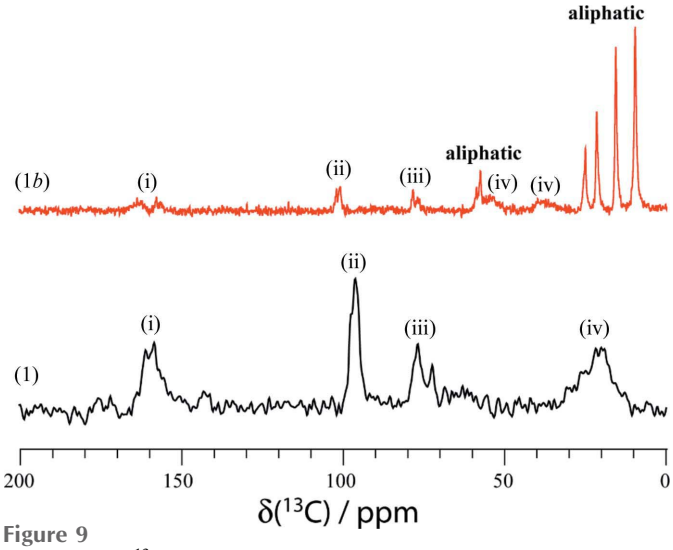

Figure 9
Experimental ^{13}C solid-state NMR spectra of compounds (1*b*) (red) and (1) (black), using a CP/MAS Hahn-echo pulse sequence at MAS frequencies of 8 kHz and 10 kHz, respectively. ^{1}H decoupling was used for the acquisition of the spectrum of (1*b*), and no decoupling was used for the acquisition of the spectrum of (1). The labels denote the carbon covalently bonded to fluorine (i), the carbon on the *ipso* position (ii), the acetylene carbon (iii), the carbon covalently bonded to iodine (iv), and the aliphatic C atoms of the counter-cation of (1*b*) (aliphatic).

The effects of carbon–fluorine J couplings were also observed in the solid-state NMR spectrum of (1). The ^{13}C Hahn-echo solid-state magic angle-spinning NMR spectrum of (1), illustrated in Fig. 9, yielded broad resonances. The breadth of these resonances can be attributed to the ^{13}C–^{19}F couplings discussed in the solution-state NMR spectra, and the carbon–iodine resonance is further broadened as a result of the ^{13}C–^{127}I residual dipolar coupling. In addition to broad lines, the spectrum also suffers from a moderate signal-to-noise ratio. This is due to the absence of hydrogen atoms in (1), which are typically used in ^{1}H → ^{13}C cross-polarization experiments to notably enhance the signal-to-noise ratio of the ^{13}C NMR spectrum and also reduce the experimental time. Similar arguments apply to the cocrystals of (1), although some weak cross-polarization can be obtained from the protons on the counter-cations. For these reasons, and because only small amounts of pure materials were obtained in this study (see the supporting information), it was not practical to obtain high-quality spectra for all cocrystals. Nevertheless, for compound (1*b*), a clear and substantial shift in the resonance of the carbon directly bonded to iodine is observed as a result of halogen-bond formation. These large shifts, of the order of +18 and +35 p.p.m. (two different peaks presumably due to crystallographically non-equivalent sites in the cocrystal), are in agreement with established trends in ^{13}C shifts of aromatic *ipso*-C atoms upon halogen bonding (Vioglio, Chierotti & Gobetto, 2016; Viger-Gravel *et al.*, 2013; Webb *et al.*, 2004; Moss & Goroff, 2005).

4. Conclusions

Single-crystal X-ray diffraction structures have been reported for a series of seven halogen-bonded cocrystals featuring 1,3,5-tris(iodoethynyl)-2,4,6-trifluorobenzene as the halogen-bond donor, and bromide ions (as ammonium or phosphonium salts) as the halogen-bond acceptors. The resulting frameworks form honeycomb structures of variable geometry and with a variable number of halogen bonds to the bromide ion. While the counter-cations generally occupy the void spaces in the present work, the construction of halogen-bonded frameworks with potential gas storage applications is an appealing prospect which may be facilitated in the future by ligands enabling directional and multidentate interactions such as (1).

An analysis of the ^{13}C and ^{19}F NMR spectra of (1) in solution revealed a subtle interplay between various spin–spin coupling interactions and small isotope shifts. The understanding afforded by this analysis should provide a sound footing for interpreting the spectra of related halogen-bond donors and their halogen-bonded complexes. Solid-state ^{13}C NMR analysis of (1) and its cocrystal with Et_3BuNBr revealed

substantial halogen-bond-induced shifts of the carbon directly bonded to iodine, in accordance with the trends known for aromatic carbon chemical shifts of halogen-bond donors.

Acknowledgements

DLB thanks the Natural Sciences and Engineering Research Council for a Discovery Grant and a Discovery Accelerator Supplement.

Funding information

Funding for this research was provided by: Natural Sciences and Engineering Research Council of Canada.

References

Aakeröy, C. B., Wijethunga, T. K. & Desper, J. (2014). *J. Mol. Struct.* **1072**, 20–27.

Aakeröy, C. B., Wijethunga, T. K., Desper, J. & Đaković, M. (2015). *Cryst. Growth Des.* **15**, 3853–3861.

Abate, A., Biella, S., Cavallo, G., Meyer, F., Neukirch, H., Metrangolo, P., Pilati, T., Resnati, G. & Terraneo, G. (2009). *J. Fluor. Chem.* **130**, 1171–1177.

Allen, F. H., Lommerse, J. P. M., Hoy, V. J., Howard, J. A. K. & Desiraju, G. R. (1997). *Acta Cryst.* B**53**, 1006–1016.

Ammer, J., Nolte, C., Karaghiosoff, K., Thallmair, S., Mayer, P., de Vivie-Riedle, R. & Mayr, H. (2013). *Chem. Eur. J.* **19**, 14612–14630.

Awwadi, F. F., Willett, R. D., Peterson, K. A. & Twamley, B. (2006). *Chem. Eur. J.* **12**, 8952–8960.

Baldrighi, M., Cavallo, G., Chierotti, M. R., Gobetto, R., Metrangolo, P., Pilati, T., Resnati, G. & Terraneo, G. (2013). *Mol. Pharm.* **10**, 1760–1772.

Berger, G., Soubhye, J. & Meyer, F. (2015). *Polym. Chem.* **6**, 3559–3580.

Bondi, A. (1964). *J. Phys. Chem.* **68**, 441–451.

Bouchmella, K., Boury, B., Dutremez, S. G. & van der Lee, A. (2007). *Chem. Eur. J.* **13**, 6130–6138.

Brown, A. R., Kuo, W.-K. & Jacobsen, E. N. (2010). *J. Am. Chem. Soc.* **132**, 9286–9288.

Bruker (2003). *SADABS*. Bruker AXS Inc., Madison, Wisconsin, USA.

Bruker (2007). *DAISY*, Version 2.0.0. Bruker Biospin GmbH, Rheinstetten, Germany.

Bruker (2012). *APEX*II. Bruker AXS Inc., Madison, Wisconsin, USA.

Bryce, D. L. & Viger-Gravel, J. (2015). *Top. Curr. Chem.* **358**, 183–203.

Cavallo, G., Biella, S., Lü, J., Metrangolo, P., Pilati, T., Resnati, G. & Terraneo, G. (2010). *J. Fluor. Chem.* **131**, 1165–1172.

Cavallo, G., Metrangolo, P., Milani, R., Pilati, T., Priimagi, A., Resnati, G. & Terraneo, G. (2016). *Chem. Rev.* **116**, 2478–2601.

Cavallo, G., Metrangolo, P., Pilati, T., Resnati, G. & Terraneo, G. (2015). *Top. Curr. Chem.* **358**, 1–17.

Desiraju, G. R., Ho, P. S., Kloo, L., Legon, A. C., Marquardt, R., Metrangolo, P., Politzer, P., Resnati, G. & Rissanen, K. (2013). *Pure Appl. Chem.* **85**, 1711–1713.

Dumele, O., Wu, D., Trapp, N., Goroff, N. & Diederich, F. (2014). *Org. Lett.* **16**, 4722–4725.

Farrugia, L. J. (1999). *J. Appl. Cryst.* **32**, 837–838.

Farrugia, L. J. (2012). *J. Appl. Cryst.* **45**, 849–854.

Gagnaux, P. & Susz, B. P. (1960). *Helv. Chim. Acta*, **43**, 948–956.

Gilday, L. C., Robinson, S. W., Barendt, T. A., Langton, M. J., Mullaney, B. R. & Beer, P. D. (2015). *Chem. Rev.* **115**, 7118–7195.

Gombler, W. (1982). *J. Am. Chem. Soc.* **104**, 6616–6620.

González, L., Gimeno, N., Tejedor, R. M., Polo, V., Ros, M. B., Uriel, S. & Serrano, J. L. (2013). *Chem. Mater.* **25**, 4503–4510.

Goroff, N. S., Curtis, S. M., Webb, J. A., Fowler, F. W. & Lauher, J. W. (2005). *Org. Lett.* **7**, 1891–1893.

Groom, C. R., Bruno, I. J., Lightfoot, M. P. & Ward, S. C. (2016). *Acta Cryst.* B**72**, 171–179.

Jameson, C. J. (1977). *J. Chem. Phys.* **66**, 4983–4988.

Kolář, M. H. & Hobza, P. (2016). *Chem. Rev.* **116**, 5155–5187.

Le Gal, Y., Lorcy, D., Jeannin, O., Barrière, F., Dorcet, V., Lieffrig, J. & Fourmigué, M. (2016). *CrystEngComm*, **18**, 5474–5481.

Lieffrig, J., Jeannin, O. & Fourmigué, M. (2013). *J. Am. Chem. Soc.* **135**, 6200–6210.

Maurer, T. & Kalbitzer, H. R. (1996). *J. Magn. Reson. B.* **113**, 177–178.

Metrangolo, P., Meyer, F., Pilati, T., Resnati, G. & Terraneo, G. (2008). *Chem. Commun.* pp. 1635–1637.

Metrangolo, P., Neukirch, H., Pilati, T. & Resnati, G. (2005). *Acc. Chem. Res.* **38**, 386–395.

Moss, W. N. & Goroff, N. S. (2005). *J. Org. Chem.* **70**, 802–808.

Navrátilová, H. (2001). *Magn. Reson. Chem.* **39**, 727–730.

Perera, M. D., Desper, J., Sinha, A. S. & Aakeröy, C. B. (2016). *CrystEngComm.* **18**, 8631–8636.

Perkins, C., Libri, S., Adams, H. & Brammer, L. (2012). *CrystEngComm*, **14**, 3033–3038.

Politzer, P., Murray, J. S. & Clark, T. (2014). *Top. Curr. Chem.* **358**, 19–42.

Politzer, P., Murray, J. S. & Concha, M. C. (2008). *J. Mol. Model.* **14**, 659–665.

Riley, K. E., Murray, J. S., Fanfrlík, J., Řezáč, J., Solá, R. J., Concha, M. C., Ramos, F. M. & Politzer, P. (2011). *J. Mol. Model.* **17**, 3309–3318.

Sheldrick, G. M. (2015). *Acta Cryst.* C**71**, 3–8.

Spek, A. L. (2009). *Acta Cryst.* D**65**, 148–155.

Sun, A., Lauher, J. W. & Goroff, N. S. (2006). *Science*, **312**, 1030–1034.

Szell, P. M. J. & Bryce, D. L. (2016*a*). *J. Phys. Chem. C*, **120**, 11121–11130.

Szell, P. M. J. & Bryce, D. L. (2016*b*). *Modern Magnetic Resonance*, pp. 1–18. New York: Springer.

Szell, P. M. J., Gabriel, S. A., Gill, R. D. D., Wan, S. Y. H., Gabidullin, B. & Bryce, D. L. (2017). *Acta Cryst.* C**73**, 157–167.

Triguero, S., Llusar, R., Polo, V. & Fourmigué, M. (2008). *Cryst. Growth Des.* **8**, 2241–2247.

Turunen, L., Beyeh, N. K., Pan, F., Valkonen, A. & Rissanen, K. (2014). *Chem. Commun.* **50**, 15920–15923.

Viger-Gravel, J., Leclerc, S., Korobkov, I. & Bryce, D. L. (2013). *CrystEngComm*, **15**, 3168–3177.

Vioglio, P. C., Catalano, L., Vasylyeva, V., Nervi, C., Chierotti, M. R., Resnati, G., Gobetto, R. & Metrangolo, P. (2016). *Chem. Eur. J.* **22**, 16819.

Vioglio, P. C., Chierotti, M. R. & Gobetto, R. (2016). *CrystEngComm*, **18**, 9173–9184.

Wang, H., Wang, W. & Jin, W. J. (2016). *Chem. Rev.* **116**, 5072–5104.

Webb, J. A., Klijn, J. E., Hill, P. A., Bennett, J. L. & Goroff, N. S. (2004). *J. Org. Chem.* **69**, 660–664.

Weigert, F. J. & Roberts, J. D. (1970). *J. Am. Chem. Soc.* **93**, 2361–2369.

Wilhelm, C., Boyd, S. A., Chawda, S., Fowler, F. W., Goroff, N. S., Halada, G. P., Grey, C. P., Lauher, J. W., Luo, L., Martin, C. D., Parise, J. B., Tarabrella, C. & Webb, J. A. (2008). *J. Am. Chem. Soc.* **130**, 4415–4420.

Chapter 11 – Mechanochemistry and Cocrystallization of 3-iodoethynylbenzoic Acid with Nitrogen-Containing Heterocycles: Concurrent Halogen and Hydrogen Bonding

Statement of Authenticity. I certify that I have prepared the following article featuring my own work, with guidance from my supervisor Dr. David Bryce. This article features work from Julien Dragon, an international student from France, in addition to Scott Zablotny and Stephen Harrigan which were undergraduate students. Their tasks were primarily in preparing the compounds, developing the methodology, and characterizing the products by solution NMR and powder X-ray diffraction. Dr. Bulat Gabidullin is acknowledged for solving the crystal structures presented in the article. Dr. David Bryce is acknowledged for support and contributions to the manuscript.

Permissions. I declare that I have obtained permission from all coauthors to include this article in my thesis. Chapter 11 was reproduced from *New J. Chem.*, **2018**, *42*, 10493-10501 with permission from the Centre National de la Recherche Scientifique (CNRS) and the Royal Society of Chemistry. (DOI: 10.1039/C8NJ00437D). The cover article (*New Journal of Chemistry*, volume 42, number 13, 7 July 2018) was reproduced by permission of The Royal Society of Chemistry.

Supporting Information. All supporting information for this article can be retrieved on the RSC website:

https://pubs.rsc.org/en/content/articlelanding/2018/nj/c8nj00437d#!divAbstract

Volume 42 | Number 13 | 7 July 2018 | Pages 10435–11214

NJC

New Journal of Chemistry

A journal for new directions in chemistry

rsc.li/njc

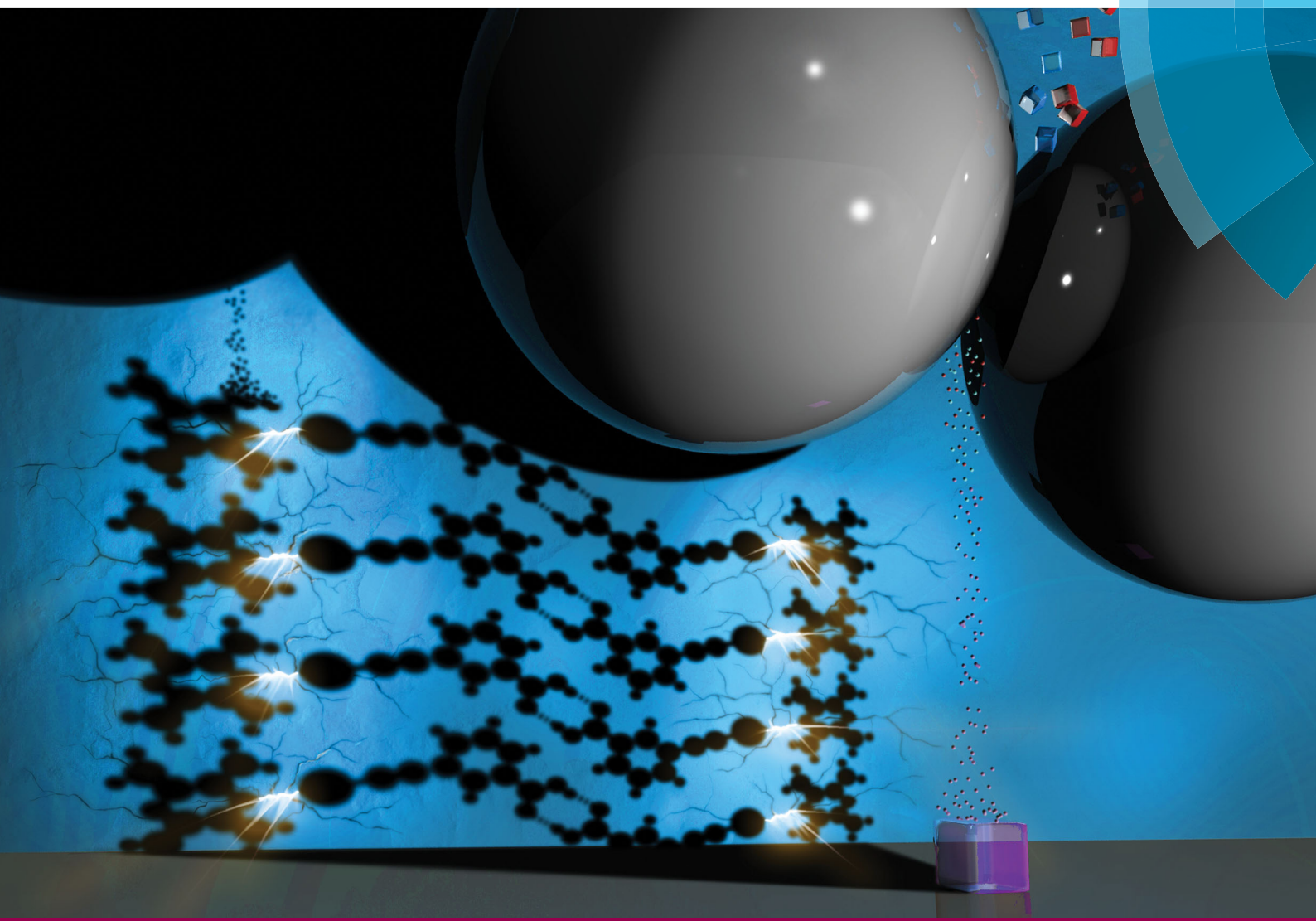

Featuring the themed issue: The halogen bond: a new avenue in recognition and self-assembly

ISSN 1144-0546

ROYAL SOCIETY OF CHEMISTRY

PAPER

David L. Bryce *et al.*

Mechanochemistry and cocrystallization of 3-iodoethynylbenzoic acid with nitrogen-containing heterocycles: concurrent halogen and hydrogen bonding

cnrs

NJC

PAPER

View Article Online
View Journal

Cite this: DOI: 10.1039/c8nj00437d

Mechanochemistry and cocrystallization of 3-iodoethynylbenzoic acid with nitrogen-containing heterocycles: concurrent halogen and hydrogen bonding†

Patrick M. J. Szell, Julien Dragon, Scott Zablotny, Stephen R. Harrigan, Bulat Gabidullin and David L. Bryce *

Halogen bonding has been shown to be a versatile interaction for crystal engineering purposes, with characteristics that parallel those of hydrogen bonding. Here, we explore the potential of a new halogen bond donor, 3-iodoethynylbenzoic acid (**1**), which is functionalized with both halogen bond donor and hydrogen bond donor groups. We explore its crystal engineering potential by cocrystallizing it with a series of nitrogen-containing heterocycles, namely 2,3,5,6-tetramethylpyrazine, 1,4-diazabicyclo[2.2.2]octane, piperazine, and hexamethylenetetramine. In total, we report six new single-crystal X-ray diffraction structures, including those of **1** and five of its halogen-bonded cocrystals. The halogen-bonded cocrystals are further investigated using ^{13}C magic-angle spinning solid-state NMR spectroscopy and the observed changes in chemical shifts are attributed to particular structural or crystallographic features. The ^{13}C chemical shift of the ethynyl carbon bonded to the aromatic ring consistently decreased by several ppm upon halogen bond formation while that of the ethynyl carbon bonded to iodine increased. Furthermore, we show that these cocrystals are also readily prepared by mechanochemical ball milling, allowing for the rapid screening of cocrystal formation based on this halogen bond donor.

Received 24th January 2018,
Accepted 9th March 2018

DOI: 10.1039/c8nj00437d

rsc.li/njc

Introduction

Many have drawn the parallel between halogen bonds and hydrogen bonds,[1–3] partly due to their potential in crystal engineering applications.[4] The halogen bond is a non-covalent interaction involving the electrophilic region of a covalently bonded halogen (denoted X), often called the σ-hole,[5,6] and an electron-rich species or Lewis base (denoted Y).[7] The field of halogen bonding has experienced a surge of interest in the last decade,[8–10] finding roles in anion receptors,[11,12] medicinal chemistry,[13] and optical materials,[14] to name a few of the many applications of this interaction.[15,16] Due to the σ-hole forming along the extension of the covalent bond,[17] the halogen bond favors a linear interaction,[18] with halogen bond angles ($\theta_{R-X\cdots Y}$) typically ranging between 150° and 180°, where R denotes a substituent. In addition, the halogen bond is said to be a highly tuneable interaction,[19,20] with the magnitude of the σ-hole increasing with the size of the halogen[5] and through the addition of electron withdrawing groups, such as fluorine.[19] The presence of the halogen bond, in addition to a qualitative interpretation of its strength, is reflected by the reduced distance parameter, R_{XB}, which is the ratio of the halogen bond distance ($d_{X\cdots Y}$) to the sum of the van der Waals radii (d_{vdW}), given in eqn (1).[21]

$$R_{XB} = \frac{d_{X\cdots Y}}{\sum d_{vdW}} \quad (1)$$

The iodoethynyl group has been especially attractive as a halogen bond donor due to the electron-withdrawing abilities of the acetylene group, rendering iodine a stronger halogen bond donor.[22,23] Recently, the iodoethynyl group has been experiencing an increase in interest as a halogen bond donor,[24–29] and has been featured in several arrangements on benzene rings,[30–36] and aliphatic carbons.[37–39] Although the crystal structures of iodobenzoic acids have been investigated,[40,41] to our knowledge, the iodoethynyl group has yet to be featured on a benzoic acid backbone, which would give the resulting molecule the capabilities of both halogen and hydrogen bonding.

With the intention of preparing halogen bonded cocrystals on a large scale while minimizing the associated environmental footprint arising from solvent usage, mechanochemistry has

Department of Chemistry and Biomolecular Sciences & Centre for Catalysis Research and Innovation, University of Ottawa, 10 Marie Curie Private, Ottawa, Ontario K1N 6N5, Canada. E-mail: dbryce@uottawa.ca; Fax: +1-613-562-5170; Tel: +1-613-562-5800 ext. 2018

† Electronic supplementary information (ESI) available: CIFs, powder X-ray diffractograms, further experimental details. CCDC 1817459 and 1817906–1817910. For ESI and crystallographic data in CIF or other electronic format see DOI: 10.1039/c8nj00437d

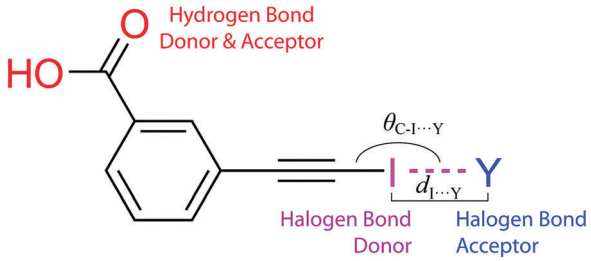

Fig. 1 Molecular structure of 3-iodoethynylbenzoic acid (**1**), showing the halogen bond donor (iodine, in magenta), the halogen bond acceptor (Y, in blue), and the carboxylic acid group acting as the hydrogen bond donor & acceptor (red).

been proposed as a powerful synthetic route to this end.[42–45] In particular, ball milling has been shown to be an elegant technique for preparing cocrystals by grinding the halogen bond donor and acceptor together, yielding the final product as a powder.[46,47] This milling process can be performed with a tiny fraction of the solvent needed for traditional crystallization methods (such as slow evaporation), and in many cases, can be performed entirely without the use of any solvents.[48,49] Furthermore, ball milling boasts the benefit of reproducible conditions, allowing for precise grinding frequencies and grinding times.[50] Here, we introduce a new halogen bond donor, 3-iodoethynylbenzoic acid (**1**), which features an iodoethynyl group as a halogen bond donor and a carboxylic acid group acting as a hydrogen bond donor & acceptor, shown in Fig. 1, and explore its potential in crystal engineering.

Through a series of cocrystallizations with nitrogen-containing heterocycles **a–d** (Fig. 2), we show that 3-iodoethynylbenzoic acid (**1**) can be used to create new cocrystals held together in part by both halogen bonds and hydrogen bonds. Additionally, we demonstrate that bulk quantities of these cocrystals can be prepared quickly using mechanochemistry, allowing for the rapid screening of products. Solid-state NMR is particularly well suited for this application, as ^{13}C chemical shift changes have been shown to be diagnostic for the occurrence of the halogen bond.[24,35,39,51–60]

Experimental

3-Ethynylbenzoic acid, silver nitrate, 2,3,5,6-tetramethylpyrazine, piperazine, hexamethylenetetramine, and 1,4-diazabicyclo[2.2.2]-octane were purchased from Sigma Aldrich. *N*-Iodosuccinimide was purchased from Alfa Aesar. Reagent grade acetone was purchased from Fisher Scientific. All compounds were used without further purification.

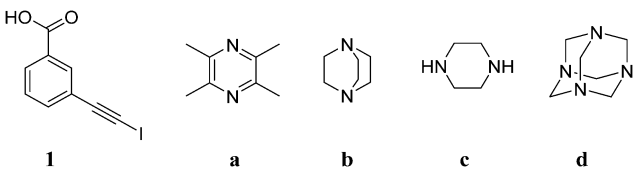

Fig. 2 Molecular structures of the compounds under investigation in this study: 3-iodoethynylbenzoic acid (**1**), 2,3,5,6-tetramethylpyrazine (**a**), 1,4-diazabicyclo[2.2.2]octane (**b**), piperazine (**c**), and hexamethylenetetramine (**d**).

N-Iodosuccinimide (0.77 g, 34.2 mmol) and silver nitrate (0.12 g, 6.84 mmol) were added successively to a solution of 3-ethynylbenzoic acid (0.50 g, 34.2 mmol) in 20 mL of reagent grade acetone. The reaction mixture was stirred at 0 °C for 8 h. The crude product was filtered and the solvent was removed under reduced pressure. The residue was dissolved in 10 mL of acidified water (pH ~ 2) and extracted with dichloromethane (3 × 25 mL). The organic layers were combined and successively washed with sodium thiosulfate (1 × 25 mL) and brine (1 × 25 mL). The organic phase was then dried over magnesium sulfate and evaporated under reduced pressure to yield the product with small traces of succinimide. The product was recrystallized from acetonitrile to yield pure crystals of **1**. 3-Iodoethynylbenzoic acid: ^{1}H NMR ($CDCl_3$, 300 MHz) 8.18 ppm (triplet, J = 1.5 Hz), 8.06 ppm (doublet of triplets, J_1 = 7.9 Hz, J_2 = 1.5 Hz), 7.66 ppm (doublet of triplets, J_1 = 7.9 Hz, J_2 = 1.5 Hz), 7.44 ppm (triplet, J = 7.9 Hz) ^{13}C NMR ($CDCl_3$, 300 MHz) 170.9 ppm, 137.4 ppm, 134.3 ppm, 130.5 ppm, 129.6 ppm, 128.7 ppm, 124.2 ppm, 93.0 ppm, 8.5 ppm. m.p. 182 °C. HREI-MS: m/z calcd for $C_9H_5IO_2$ $[M]^+$: 271.933, found: 271.932. Yield: 80%.

All cocrystals were first prepared by adding an equimolar solution of **1** to a solution of the following Lewis bases: 2,3,5,6-tetramethylpyrazine (TMP, **a**), 1,4-diazabicyclo[2.2.2]octane (DABCO, **b**), piperazine (PIP, **c**), and hexamethylenetetramine (UTP, **d**). Samples **1a**, **1b**, and **1d** were prepared using a minimum of acetonitrile, whereas samples **1c(i)** and **1c(ii)** were prepared using a minimum of methanol. In all cases, the final solutions were allowed to slowly evaporate, yielding: [(3-iodoethynylbenzoic acid)$_2$(2,3,5,6-tetramethylpyrazine)] **1a** (m.p. 154 °C), [(3-iodoethynylbenzoate)(1,4-diazabicyclo[2.2.2]octanium)] **1b** (m.p. 174 °C), [(3-iodoethynylbenzoate)(piperazinium)] **1c(i)** (m.p. 144 °C), [(3-iodoethynylbenzoate)$_2$(piperazinium)] **1c(ii)**, and [(3-iodoethynylbenzoic acid)(hexamethylenetetramine)] **1d** (m.p. 186 °C).

The mechanochemical preparation of each of the cocrystals was performed using a Retsch MM 400 ball mill. Both **1** and the respective Lewis base were added as powders successively to 10 mL stainless steel milling jars in an equimolar quantity. Ball milling was performed with a milling frequency of 25 Hz for a period of 30 minutes at room temperature, using two 5 mm stainless steel grinding balls. No liquids were added to the milling jars. The preparation of compound **1c(ii)** was not attempted by ball milling. The phase purity of each compound was verified by powder X-ray diffraction on a Rigaku Ultima IV instrument with 2θ ranging from 5° to 65° at a rate of 1° per minute (0.02° step size) using CuKα radiation. All masses used and powder X-ray diffractograms can be found in the ESI.†

^{13}C solid-state NMR

All ^{13}C cross-polarization magic-angle spinning (CP/MAS) solid-state NMR experiments were performed at 9.4 T ($\nu_L(^{13}C)$ = 100.6 MHz) using a Bruker 4 mm HXY probe and a Bruker Avance III NMR spectrometer. ^{1}H → ^{13}C CP was used with a 4.6 μs proton π/2 pulse, a 2000 μs contact time, and a 54.3 kHz ^{1}H decoupling frequency. ^{13}C chemical shifts were referenced to glycine at 176.6 ppm (^{13}C=O) relative to tetramethylsilane (TMS). Variable spinning speeds were used to separate the

spinning sidebands from the isotropic peaks. Further information, such as spinning speeds, recycle delays, and the number of transients can be found in the ESI.†

Single crystal X-ray diffraction

The crystals were mounted on thin glass fibers using paraffin oil. Prior to data collection, crystals were cooled to 200 ± 2 K. The data were collected on a Bruker AXS single crystal diffractometer equipped with a sealed Mo tube source (wavelength 0.71073 Å) and an APEX II CCD detector. The raw data collection and processing were performed with the Bruker APEX II software package.[61] Semi-empirical absorption corrections based on equivalent reflections were applied.[62] Systematic absences in the diffraction dataset and unit cell parameters were consistent with triclinic $P\bar{1}$ (#2) for **1a**, monoclinic $P2_1/n$ (#14) for **1**, monoclinic $P2_1/c$ (#14) for **1c(ii)** and **1d**, and monoclinic $C2/c$ (#15) for **1b** and **1c(i)**. The structures were solved by direct methods and refined with full-matrix least-squares procedures based on F^2, using SHELXL[63] and WinGX.[64] All non-hydrogen atoms were refined anisotropically. The hydrogen atoms bonded to the oxygen atoms were located in the difference Fourier map and refined freely while the remaining hydrogen atoms were placed in idealized positions. Displacement ellipsoid plots were produced using ORTEP[65] (see the ESI†), and uncertainties were estimated using PLATON for Windows.[66]

For **1**, **1b**, and **1c(i)**, no additional restraints or constraints were applied. For **1a**, the two adjacent molecules form a hydrogen-bonded dimer *via* carboxyl groups. The two H atoms of these groups are disordered over four positions. Each position was modelled with a fixed 50% occupancy and refined with restraints applied to O–H bond distances (DFIX in Shelx). No other additional restraints or constraints were applied. Compound **1d** was twinned and consisted of two domains. The refinement was done using the HKLF5 file. The second domain's contribution was 0.327(2). No additional restraints or constraints were applied. The lattice of **1c(ii)** is monoclinic with β close to 90°. The crystal was twinned by rotation about [100], which was resolved using TWIN/BASF in Shelx. The second domain's contribution was 0.220(1). No additional restraints or constraints were applied.

Crystal structure datasets have been uploaded to the Cambridge Crystallographic Data Centre (CCDC numbers 1817459 and 1817906–1817910).†

Results and discussion

(i) X-ray crystallography

The X-ray crystal structures for a series of cocrystals based on 3-iodoethynylbenzoic acid and several nitrogen-containing heterocycles are reported, with depictions of the crystal structures presented in Fig. 3. The crystal structures of **1** and its five cocrystals are shown to feature halogen bonds as well as hydrogen bonds. The geometrical parameters of the halogen bonds are presented in Table 1. Details of the X-ray crystal structures are given in Table 2.

The crystal structure of **1** features two molecules linked by O–H···O hydrogen bonds between the carboxylic acids, with the iodoacetylene group coordinating an adjacent acetylene group *via* a halogen bond, denoted C–I···C≡C. These interactions result in a corrugated sheet packing motif. Several instances have been reported in the Cambridge Structural Database (CSD)[67] of halogen

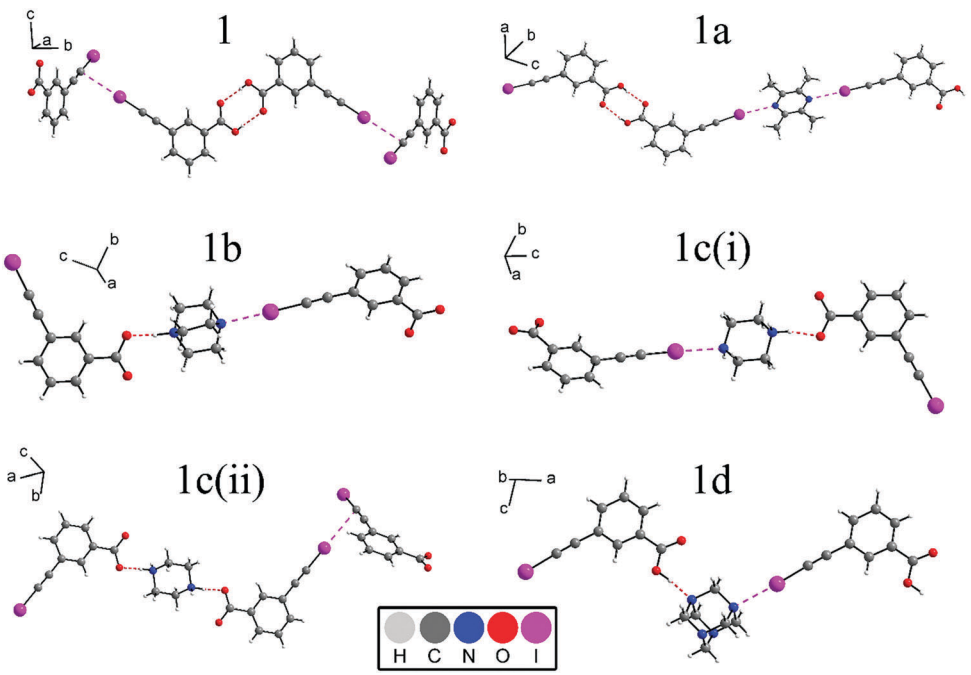

Fig. 3 Depiction of the X-ray crystal structures of 3-iodoethynylbenzoic acid (**1**) and five cocrystals. Disorder of the COOH proton in **1a** is not shown for clarity. Image prepared using Diamond version 4.4.1.

Table 1 Halogen bonding geometry of **1** and the cocrystals under investigation. The parameters include: the halogen bond moiety, the halogen bond length ($d_{I\cdots Y}$), the normalized distance parameter of the halogen bond (R_{XB}), and the halogen bond angle ($\theta_{C-I\cdots Y}$). The subscripted Y represents the acceptor moiety, *i.e.*, N or the acetylene group (C≡C). Experimental errors are given in parentheses

Compound	XB moiety	XB length ($d_{I\cdots Y}$)/Å	R_{XB}	XB angle $\theta_{C-I\cdots Y}$ (°)
1	C–I···C≡C	3.397(4)	0.92	179.20(13)
	C–I···C≡C	3.382(4)	0.92	159.76(13)
1a	C–I···N	3.021(3)	0.86	174.46(12)
	C–I···N	2.999(3)	0.85	176.26(11)
1b	C–I···N	2.741(6)	0.78	175.0(5)
1c(i)	C–I···N	2.800(2)	0.79	178.28(9)
1c(ii)	C–I···C≡C	3.435(3)	0.93	172.32(14)
	C–I···C≡C	3.431(3)	0.93	153.84(11)
1d	C–I···N	2.804(12)	0.79	175.8(5)

bonding to acetylene groups,[23,28,29,34,36,39,68,69] which is attributed to the high electron density surrounding the bond, acting as a nucleophilic site, analogous to π-bonding. As the halogen bond is coordinating the carbon–carbon bond and not an individual carbon atom, the geometrical parameters were determined by measuring $d_{I\cdots C}$ and $\theta_{C-I\cdots C}$ to both carbon atoms of the acetylene group. In this case, the halogen bond is oriented more towards the C–I carbon of the iodoacetylene group ($d_{X\cdots Y}$ = 3.397(4), $\theta_{C-I\cdots C\equiv C}$ = 179.20(13)°), with a marginally shorter bond to the other acetylene carbon ($d_{X\cdots Y}$ = 3.382(4) Å, $\theta_{C-I\cdots C\equiv C}$ = 159.76(13)°). The hydrogen bonding motif is typical of carboxylic acids, with the O–H side of the carboxylic acid acting as the hydrogen bond donor and the carbonyl group acting as the hydrogen bond acceptor.

Cocrystal **1a** consists of two molecules of **1** cocrystallized with 2,3,5,6-tetramethylpyrazine, a versatile halogen bond acceptor. The structure exhibits two unique C–I···N halogen bonds coordinating the nitrogens of 2,3,5,6-tetramethylpyrazine (R_{XB} = 0.86, $\theta_{C-I\cdots N}$ = 174.46(12)°; R_{XB} = 0.85, $\theta_{C-I\cdots N}$ = 176.26(11)°), with two molecules of **1** in the asymmetric unit. The approximate σ_h molecular plane of **a** is oriented nearly perpendicularly to the approximate σ_h molecular planes of the two molecules of **1**. Similar to the X-ray structure of **1**, the carboxylic acids are linked by C=O···H–O hydrogen bonds. Overall, the alternation between hydrogen bonds and halogen bonds forms **1**···**1**···**a**···**1**···**1**···**a** continuous chains. Each chain interacts with adjacent chains by weak C–H···O hydrogen bonding, forming a one-dimensional sheet of **1**···**1**···**a**···**1**···**1**···**a** chains. These sheets are then stacked one above the other to form the crystals of **1a**.

1b is formed between **1** and 1,4-diazabicyclo[2.2.2]octane, with the basic amine group from **b** deprotonating the carboxylic acid group of **1**. The structure exhibits alternating C–I···N halogen bonds and $^{-}$O···H–N^{+} hydrogen bonds, resulting in

Table 2 Selected single-crystal X-ray crystallographic data for compounds **1**, **1a**, **1b**, **1c(i)**, **1c(ii)**, and **1d**

Compound	**1**	**1a**	**1b**	**1c(i)**
Empirical formula	$C_9H_5IO_2$	$C_{26}H_{22}I_2N_2O_4$	$C_{15}H_{17}I_1N_2O_2$	$C_{13}H_{15}I_1N_2O_2$
FW (g mol^{-1})	272.03	680.25	384.20	358.17
Crystal color	Yellow	Colourless	Colourless	Colourless
Crystal size (mm)	0.280 × 0.067 × 0.010	0.236 × 0.186 × 0.138	0.345 × 0.132 × 0.044	0.394 × 0.173 × 0.166
Crystal system	Monoclinic	Triclinic	Monoclinic	Monoclinic
Crystal space group	$P2_1/n$	$P\bar{1}$	$C2/c$	$C2/c$
T (K)	200(2)	200(2)	200(2)	200(2)
a (Å)	4.7508(4)	7.7194(6)	17.5218(8)	15.2720(4)
b (Å)	28.730(2)	9.1772(10)	6.5563(3)	6.6017(2)
c (Å)	6.5630(5)	19.1992(15)	27.7452(12)	28.5827(9)
α (°)	90	83.6240(10)	90	90
β (°)	92.119(5)	88.7390(10)	107.586(3)	104.9710(10)
γ (°)	90	70.9770(10)	90	90
V (Å^3)	895.17(12)	1277.7(2)	3038.4(2)	2783.92(14)
Z	4	2	8	8
R_1(final)	0.0330	0.0302	0.0441	0.0274
wR_2(final)	0.0752	0.0584	0.1013	0.0546

Compound	**1c(ii)**	**1d**
Empirical formula	$C_{11}H_{10}I_1N_1O_2$	$C_{15}H_{17}I_1N_4O_2$
FW (g mol^{-1})	315.10	412.23
Crystal color	Colourless	Colourless
Crystal size (mm)	0.811 × 0.238 × 0.108	0.256 × 0.176 × 0.154
Crystal system	Monoclinic	Monoclinic
Crystal space group	$P2_1/c$	$P2_1/c$
T (K)	200(2)	200(2)
a (Å)	16.7005(8)	14.465(5)
b (Å)	8.0961(4)	16.493(5)
c (Å)	8.3096(4)	6.958(2)
α (°)	90	90
β (°)	90.243(3)	101.304(4)
γ (°)	90	90
V (Å^3)	1123.52(9)	1627.7(9)
Z	4	4
R_1(final)	0.0338	0.0845
wR_2(final)	0.0729	0.1783

1···**b**···**1**···**b** chains. Due to the iodoethynyl group being in the *meta* position relative to the carboxylic acid group in **1**, the resulting chain forms a zig-zag motif. The zig-zag chains interact with each other through hydrogen bonds between the protons on **b** and the oxygens on the carboxylic acid group of **1**, forming a one-dimensional sheet. These sheets are then stacked to form the crystal **1b**.

Structures **1c(i)** and **1c(ii)** were both obtained from the cocrystallization of **1** and piperazine, with **1c(i)** being in a 1 : 1 stoichiometry, and **1c(ii)** being in a 2 : 1 stoichiometry. Both structures are unique, with **1c(i)** being the result of a single proton transfer from **1** to piperazine, and **1c(ii)** being the result of two protons transferring from **1** to piperazine. Structure **1c(i)** has a C–I···N halogen bond between **1** and the unprotonated nitrogen of piperazine, while the protonated nitrogen participates in a $^{-}$O···H–N^{+} hydrogen bond. Much like in structure **1b**, zig-zag **1**···**c**···**1**···**c** chains are formed, with each zig-zag chain interacting with adjacent chains *via* C–H···O hydrogen bonds between the protons from **c** and the carboxylic acid from **1**. The zig-zag chains form a one-dimensional sheet, which are stacked *via* N–H···O hydrogen bonds to form the crystal **1c(i)**. In structure **1c(ii)**, however, the piperazine molecule is doubly protonated, with both nitrogen atoms participating in $^{-}$O···H–N^{+} hydrogen bonds, producing a **1**···**c**···**1** hydrogen-bonded fragment. The iodoacetylene groups on both sides of this fragment coordinate the acetylene groups (C–I···C≡C) of a neighboring molecule, creating a convoluted network. The hydrogen atoms present on the piperazine molecule participate in C–H···O hydrogen bonds to the oxygen atoms of the carboxylic acid group, linking the **1**···**c**···**1** fragments together. Notably, **1c(ii)** was only found in trace quantities from the solvent evaporation method, and was not observed from the mechanochemical preparation (*vide infra*). In fact, the single crystal X-ray analysis of the cocrystals grown from the slow evaporation of **1** and piperazine first yielded structure **1c(ii)**. However, upon analyzing the bulk sample by powder X-ray diffraction, it became apparent that a representative crystal structure was not initially obtained. Despite the low odds, it happened that a small crystal from the low-population structure was inadvertently analyzed first. A single crystal X-ray diffraction experiment on a second crystal yielded structure **1c(i)** which was in agreement with the powder X-ray data. This case highlights the importance of performing powder X-ray diffraction on powdered samples in order to ensure the structure of the bulk sample. Otherwise, this discrepancy in the crystal structure would have gone unnoticed.

Cocrystal **1d** is formed between **1** and hexamethylenetetramine, with the carboxylic acid group of **1** maintaining its proton. The structure exhibits a C–I···N halogen bond and a O–H···N hydrogen bond, forming a **1**···**d**···**1**···**d** chain. Due to the coordination pattern of the halogen and hydrogen bonds to **d**, and the *meta* substitution pattern of **1**, the chain forms a tight zig-zag, much like structures **1b** and **1c(i)** (Fig. 4). The zig-zag chains interact with one another through both C=O···H–C and C–I···H–C interactions, forming a self-contained cyclic structure with 11 vertices (4 non-covalent interactions, 7 covalent bonds), highlighted in light pink in Fig. 4. In contrast to the C–I···N halogen bond, which operates *via* the σ-hole on the iodine, the hydrogen bond is orthogonal to the C–I covalent bond, interacting with the nucleophilic contour region[9,70] of iodine. The zig-zag sheets are then stacked to form crystal **1d**.

The structures reported herein present a combination of O–H···O, O–H···N, or N–H^{+}···$^{-}$O hydrogen bonds, with simultaneous C–I···C≡C or C–I···N halogen bonds. These motifs were used as queries for a CSD database[67] search, in order to place these non-covalent interactions in the context of a greater library of structures. Despite the relatively limited results available on halogen bonded structures relative to the abundance of hydrogen bonded structures, the search results suggest, unsurprisingly, a higher degree of linearity in the C–I···N halogen bond compared to O–H···O, N–H^{+}···$^{-}$O, and O–H···N hydrogen bonds. The halogen bond's tendency towards linearity is clearly observed in the present work, with C–I···N bond angles ranging from 174.46(12)° in **1a** to 178.28(9)° in **1c(i)**. In contrast, the N–H^{+}···$^{-}$O hydrogen bonds observed in structures **1b**, **1c(i)**, and **1c(ii)**, have bond angles ranging from 168(3)° to 175(5)°, O–H···H hydrogen bond angles in structures **1a** and **1** ranging from 160(7)° to 177(8)°, and a O–H···N hydrogen bond angle of 169(1)° in compound **1d**. Furthermore, for compounds featuring

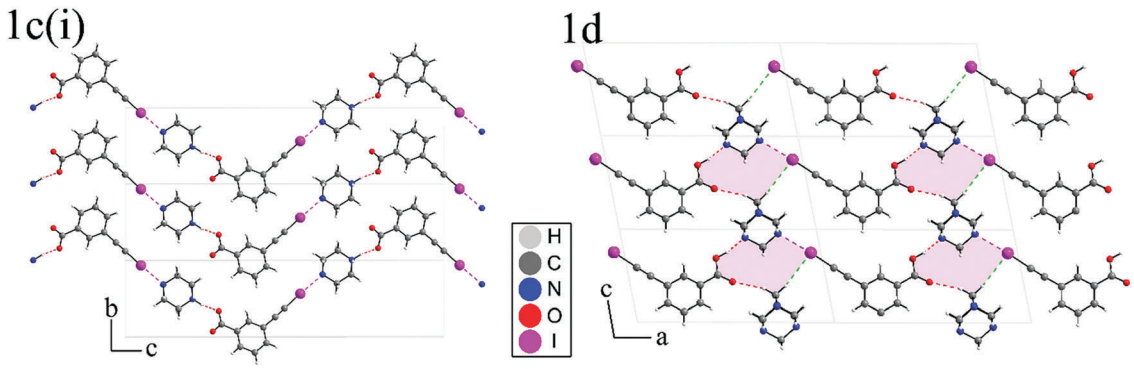

Fig. 4 Depiction of the crystal packing for **1c(i)** and **1d**. The dashed magenta lines denote the C–I···N halogen bonds, the dashed red lines denote the hydrogen bonds, and the dashed green lines denote the C–H···I contacts. The unit cell edges are shown in light grey. Image prepared using Diamond version 4.4.1.

a C–I···C≡C halogen bond, although two sets of angles can be derived depending on which carbon is selected, the most linear angles range from 172.32(14)° to 179.20(13)°, in compounds **1c(ii)** and **1**, respectively. It is evident that the combination of iodoethynyl and benzoic acid groups has led to new structures connected by concurrent halogen and hydrogen bonds.

The compounds **1a** and **1d** are deemed cocrystals due to the C–I···N halogen bond between the two molecular components in the crystal. However, the crystal structures of compounds **1b** and **1c(i)** suggest the formation of a salt. Structure **1c(ii)** is also best referred to as a salt rather than a cocrystal due to the transfer of both protons from the carboxylic acid group to piperazine, with the iodine interacting with the acetylene group from an adjacent molecule of **1** in the unit cell. However, as proton positions are derived from X-ray data, there remains uncertainty on whether these compounds are indeed salts or cocrystals.[71]

(ii) ^{13}C solid-state NMR spectroscopy

A series of ^{13}C solid-state CP/MAS NMR experiments, the results of which are illustrated in Fig. 5, were performed in order to characterize **1** and its cocrystals in terms of ^{13}C chemical shifts. Due to cross polarization from the protons located on the halogen bond donor, in contrast to perfluorinated donors,[60] ^{13}C signal was abundant, and the CP/MAS method provided a straightforward manner by which to characterize both the halogen bond donor and acceptor in the samples. The ^{13}C chemical shifts of the carboxylic acid (C̲OOH) carbon, acetylene carbon (C̲≡C–I), and carbon covalently bonded to iodine (C̲–I), are provided in Table 3. As a general trend, the COOH carbons show a relatively small chemical shift difference upon cocrystal formation, with the largest change observed being 3.1 ± 0.1 ppm when comparing samples **1** and **1d**. It is to be noted that the chemical shift trend of the COOH carbon did not reliably indicate whether deprotonation had occurred. For instance, between the ^{13}C chemical shifts of the deprotonated carboxylic acid groups in samples **1b** and **1c(i)**, the chemical shift in **1b** decreased by 2.0 ± 0.1 ppm, whereas the chemical shift in **1c(i)** increased by 1.2 ± 0.1 ppm, when compared to **1**. More advanced NMR experiments have recently been developed and applied to accurately determine the position of the protons in related salts and cocrystals,[71] and these are the subject of ongoing work in our laboratory.

As for the halogen bond donor, the chemical shifts of the C̲–I carbons are known to be useful in characterizing the local halogen bond environment.[52,58] Presently, the C̲–I ^{13}C chemical shifts were the most sensitive to the formation of the halogen bond, with an increase of 11.6 ± 1.3 ppm observed between compounds **1** and **1c(i)**. However, as a result of spectral overlap combined with the difficulty of observing carbons covalently bonded to iodine,[52] the C–I resonances could not be readily observed at 9.4 T in compounds **1a**, **1b**, and **1d**. As sample **1c(ii)** was only produced in trace quantities, we were not able to compare the C–I···N halogen bond to the C–I···C≡C halogen bond in terms of ^{13}C chemical shifts. In terms of the C̲≡C–I carbon, the ^{13}C chemical shift is highest for pure **1**, and consistently decreases upon cocrystallization, with these changes attributed to the formation of the C–I···N halogen bond. The largest decrease in

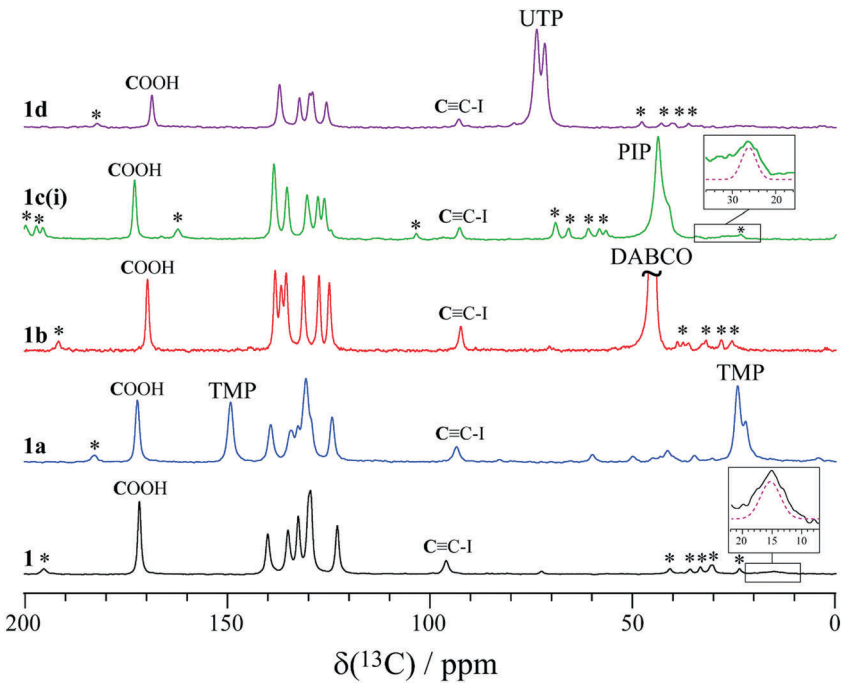

Fig. 5 ^{13}C CP/MAS solid-state NMR spectra acquired at variable spinning speeds to minimize sideband overlap, corresponding to **1** (10 kHz), **1a** (9 kHz), **1b** (10 kHz), **1c(i)** (7 kHz), and **1d** (9 kHz). The labels indicate the carboxylic acid carbon (C̲OOH), the acetylene carbon (C̲≡C–I), and the halogen bond acceptors. The resonances of the C–I carbons are shown in the insets. The inset for **1c(i)** was acquired at an MAS frequency of 8 kHz due to an overlapping spinning sideband.

Table 3 Experimental ^{13}C chemical shifts of the carboxylic acid carbon (C̲OOH), the acetylene carbon (C̲≡C–I), and the carbon covalently bonded to iodine (C̲–I)

Compound	$\delta(^{13}C)$ C̲OOH (ppm)	$\delta(^{13}C)$ C̲≡C–I (ppm)	$\delta(^{13}C)$ C̲–I (ppm)
1	171.7 ± 0.1	96.0 ± 0.1	14.9 ± 0.4
1a	172.3 ± 0.1	93.3 ± 0.1	[a]
1b	169.7 ± 0.1	92.4 ± 0.1	[a]
1c(i)	172.9 ± 0.1	92.8 ± 0.1	26.2 ± 1.2
1d	168.6 ± 0.1	92.8 ± 0.1	[a]

[a] Unresolved due to resonance overlap or poor signal.

the ^{13}C chemical shift for the C̲≡C–I carbon was observed for compound **1b** (3.6 ± 0.1 ppm).

As shown previously in related systems,[54,59] the ^{13}C chemical shift of the carbon covalently bonded to the nitrogen on the halogen bond acceptor can also be a good indicator for the occurrence of cocrystallization. Presently, compound **1a** showed an increase in the ^{13}C chemical shift upon cocrystallization, *i.e.*, of 2.2 ± 0.2 ppm and 0.9 ± 0.1 ppm for the methyl groups, and a minor (<0.5 ppm) change for the carbon covalently bonded to nitrogen in 2,3,5,6-tetramethylpyrazine. This is in agreement with our previous investigations on this acceptor,[60] with 1,4-diiodotetrafluorobenzene (*p*-DITFB) and 1,3,5-trifluoro-2,4,6-triiodobenzene (*sym*-TITFB) as halogen bond donors. In these cases, we have previously observed little change in the ^{13}C chemical shifts of the carbon covalently bonded to nitrogen and an increase of between 0.7 ± 0.1 and 1.5 ± 0.1 ppm for the methyl groups.

In contrast to the results for compound **1a**, a decrease in the ^{13}C chemical shifts for the carbons covalently bonded to the nitrogen in the halogen bond acceptor were observed for samples **1b**, **1c(i)**, and **1d**. For instance, upon cocrystallization, a decrease of 2.8 ± 0.1 ppm was observed for the carbons of 1,4-diazabicyclo[2.2.2]octane in compound **1b** and a decrease of 3.0 ± 0.2 ppm was observed for the carbons of piperazine in compound **1c(i)**. For compound **1d**, two resonances have been observed for the carbons covalently bonded to nitrogen, which can be attributed to the inequivalent carbon sites in the crystal structure. Consequently, decreases of 2.0 ± 0.1 ppm and of <0.1 ppm were observed for the different carbons of hexamethylenetetramine, when compared to the pure starting material. This is in partial agreement with our previous results,[60] where we have observed both an increase of up to 1.4 ± 0.1 ppm and a decrease of 1.8 ± 0.1 ppm upon cocrystallization with *p*-DITFB and *sym*-TITFB.

(iii) Mechanochemical sample preparation

With the intention of reducing the usage of solvents and decreasing preparation time, ball milling was investigated as a synthetic technique in the preparation of cocrystals **1a**, **1b**, **1c(i)**, and **1d**. Each compound was readily reproduced through

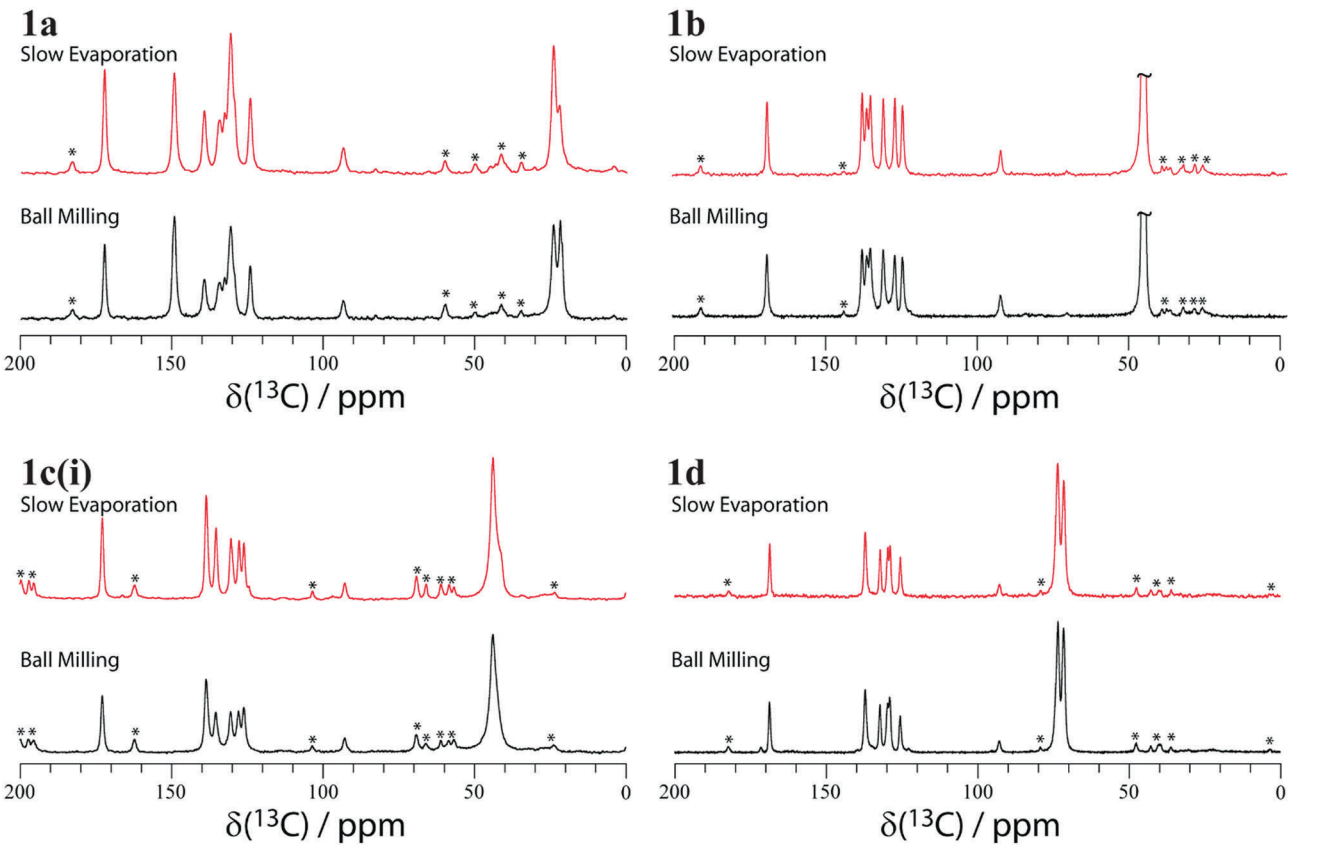

Fig. 6 ^{13}C solid-state CP/MAS NMR spectra of cocrystal products obtained from ball milling and from slow evaporation. The asterisks denote spinning sidebands.

ball milling, reducing the preparation time from days down to 30 minutes, without the need for any solvents. Each product was analyzed by powder X-ray diffraction (see the ESI†) in addition to ^{13}C solid-state NMR in order to compare the slow-evaporated product to the ball-milled product. Shown in Fig. 6 is a ^{13}C solid-state NMR comparison between the powdered products obtained from slow evaporation and ball milling. Clearly, the products compare very well. The only minor exception is in sample **1a**, where an excess of TMP is observed at 21.8 ± 0.1 ppm, which corresponds precisely to the chemical shift of the TMP starting material. This is also manifested in greater signal intensity at 149.6 ± 0.1 ppm, corresponding to the aromatic carbons of TMP. The uncocrystallized TMP results from using a slight excess of TMP during the sample preparation. This excess TMP could not be discriminated in the PXRD (see Fig. S2 of the ESI†), demonstrating one of the benefits of acquiring routine ^{13}C CP/MAS SSNMR spectra on such materials. In all other cases, the ball milling resulted in comparable products, sharing the same chemical shifts and line shapes.

Conclusions

We have investigated 3-iodoethynylbenzoic acid in the capacity of a dual hydrogen bond and halogen bond donor by cocrystallizing it with a series of nitrogen-containing heterocycles: 2,3,5,6-tetramethylpyrazine, 1,4-diazabicyclo[2.2.2]octane, piperazine, and hexamethylenetetramine. The combination of iodoethynyl and benzoic acid groups has led to new structures connected by concurrent halogen and hydrogen bonds. A total of six X-ray crystal structures have been reported, including the starting material and five cocrystals. These cocrystals were analyzed by ^{13}C solid-state NMR spectroscopy in order to attribute the changes in chemical shifts to the occurrences of the hydrogen bond and halogen bond. The ^{13}C chemical shift of the ethynyl carbon bonded to the aromatic ring consistently decreased by several ppm upon cocrystallization and halogen bond formation while that of the ethynyl carbon bonded to iodine increased. Finally, the production of these cocrystals *via* slow evaporation methods is readily duplicated by ball milling in the absence of solvents, allowing for rapid preparation and polymorph screening. A CSD search shows only 65 structures featuring ethynyl-I···N halogen bonds, suggesting that the potential applications of this halogen-bonded motif remain unexplored relative to those of more iconic halogen bond donors (*e.g.*, *p*-diioditetrafluorobenzene) and relative to purely hydrogen-bonded systems.

Conflicts of interest

There are no conflicts to declare.

Acknowledgements

PMJS and DLB thank the Natural Sciences and Engineering Research Council of Canada for a scholarship and for research funding, respectively. We are grateful to Estelle Caron-Poulin for technical assistance.

References

1 P. Metrangolo, H. Neukirch, T. Pilati and G. Resnati, *Acc. Chem. Res.*, 2005, **38**, 386–395.
2 C. C. Robertson, J. S. Wright, E. J. Carrington, R. N. Perutz, C. A. Hunter and L. Brammer, *Chem. Sci.*, 2017, **8**, 5392–5398.
3 T. Shirman, M. Boterashvili, M. Orbach, D. Freeman, L. J. W. Shimon, M. Lahav and M. E. van der Boom, *Cryst. Growth Des.*, 2015, **15**, 4756–4759.
4 A. Mukherjee, S. Tothadi and G. R. Desiraju, *Acc. Chem. Res.*, 2014, **47**, 2514–2524.
5 T. Clark, M. Hennemann, J. S. Murray and P. Politzer, *J. Mol. Model.*, 2007, **13**, 291–296.
6 P. Politzer and J. S. Murray, *Crystals*, 2017, **7**, 212–226.
7 G. R. Desiraju, P. S. Ho, L. Kloo, A. C. Legon, R. Marquardt, P. Metrangolo, P. Politzer, G. Resnati and K. Rissanen, *Pure Appl. Chem.*, 2013, **85**, 1711–1713.
8 L. C. Gilday, S. W. Robinson, T. A. Barendt, M. J. Langton, B. R. Mullaney and P. D. Beer, *Chem. Rev.*, 2015, **115**, 7118–7195.
9 G. Cavallo, P. Metrangolo, R. Milani, T. Pilati, A. Priimagi, G. Resnati and G. Terraneo, *Chem. Rev.*, 2016, **116**, 2478–2601.
10 A. Priimagi, G. Cavallo, P. Metrangolo and G. Resnati, *Acc. Chem. Res.*, 2013, **46**, 2686–2695.
11 M. J. Langton, S. W. Robinson, I. Marques, V. Félix and P. D. Beer, *Nat. Chem.*, 2014, **6**, 1039–1043.
12 A. Brown and P. D. Beer, *Chem. Commun.*, 2016, **52**, 8645–8658.
13 R. Wilcken, M. O. Zimmermann, A. Lange, A. C. Joerger and F. M. Boeckler, *J. Med. Chem.*, 2013, **56**, 1363–1388.
14 J.-C. Christopherson, F. Topić, C. J. Barrett and T. Friščić, *Cryst. Growth Des.*, 2018, **18**, 1245–1259.
15 F. Meyer and P. Dubois, *CrystEngComm*, 2013, **15**, 3058–3071.
16 P. Metrangolo and G. Resnati, *Halogen Bonding: Fundamentals and Applications*, Springer, Berlin, 2008.
17 P. Politzer, J. S. Murray, T. Clark and G. Resnati, *Phys. Chem. Chem. Phys.*, 2017, **19**, 32166–32178.
18 S. M. Huber, J. D. Scanlon, E. Jimenez-Izal, J. M. Ugalde and I. Infante, *Phys. Chem. Chem. Phys.*, 2013, **15**, 10350–10357.
19 K. E. Riley, J. S. Murray, J. Fanfrlík, J. Řezáč, R. J. Solá, M. C. Concha, F. M. Ramos and P. Politzer, *J. Mol. Model.*, 2011, **17**, 3309–3318.
20 K. E. Riley, J. S. Murray, J. Fanfrlík, J. Řezáč, R. J. Solá, M. C. Concha, F. M. Ramos and P. Politzer, *J. Mol. Model.*, 2013, **19**, 4651–4659.
21 A. Bondi, *J. Phys. Chem.*, 1964, **68**, 441–451.
22 C. B. Aakeröy, T. K. Wijethunga, J. Desper and M. Đaković, *Cryst. Growth Des.*, 2015, **15**, 3853–3861.
23 C. B. Aakeröy, D. Welideniya and J. Desper, *CrystEngComm*, 2017, **19**, 11–13.

24 L. Luo, C. Wilhelm, A. Sun, C. P. Grey, J. W. Lauher and N. S. Goroff, *J. Am. Chem. Soc.*, 2008, **130**, 7702–7709.
25 C. Perkins, S. Libri, H. Adams and L. Brammer, *CrystEngComm*, 2012, **14**, 3033–3038.
26 N. S. Goroff, S. M. Curtis, J. A. Webb, F. W. Fowler and J. W. Lauher, *Org. Lett.*, 2005, **7**, 1891–1893.
27 A. Sun, J. W. Lauher and N. S. Goroff, *Science*, 2006, **312**, 1030–1034.
28 C. Lemouchi, C. S. Vogelsberg, L. Zorina, S. Simonov, P. Batail, S. Brown and M. A. Garcia-Garibay, *J. Am. Chem. Soc.*, 2011, **133**, 6371–6379.
29 O. Dumele, D. Wu, N. Trapp, N. Goroff and F. Diederich, *Org. Lett.*, 2014, **16**, 4722–4725.
30 L. González, N. Gimeno, R. M. Tejedor, V. Polo, M. B. Ros, S. Uriel and J. L. Serrano, *Chem. Mater.*, 2013, **25**, 4503–4510.
31 J. C. Gamekkanda, A. S. Sinha, J. Desper, M. Đaković and C. B. Aakeröy, *Crystals*, 2017, **7**, 226–244.
32 H. M. Yamamoto, R. Maeda, J.-I. Yamaura and R. Kato, *J. Mater. Chem.*, 2001, **11**, 1034–1041.
33 O. Dumele, B. Schreib, U. Warzok, N. Trapp, C. A. Schalley and F. Diederich, *Angew. Chem., Int. Ed.*, 2017, **56**, 1152–1157.
34 J. Lieffrig, O. Jeannin and M. Fourmigué, *J. Am. Chem. Soc.*, 2013, **135**, 6200–6210.
35 P. M. J. Szell, B. Gabidullin and D. L. Bryce, *Acta Crystallogr., Sect. B: Struct. Sci., Cryst. Eng. Mater.*, 2017, **73**, 153–162.
36 A.-L. Barrès, A. El-Ghayoury, L. V. Zorina, E. Canadell, P. Auban-Senzier and P. Batail, *Chem. Commun.*, 2008, 2194–2196.
37 M. Baldrighi, G. Cavallo, M. R. Chierotti, R. Gobetto, P. Metrangolo, T. Pilati, G. Resnati and G. Terraneo, *Mol. Pharmaceutics*, 2013, **10**, 1760–1772.
38 K. Bouchmella, B. Boury, S. G. Dutremez and A. van der Lee, *Chem. – Eur. J.*, 2007, **13**, 6130–6138.
39 M. Baldrighi, D. Bartesaghi, G. Cavallo, M. R. Chierotti, R. Gobetto, P. Metrangolo, T. Pilati, G. Resnati and G. Terraneo, *CrystEngComm*, 2014, **16**, 5897–5904.
40 C. L. Nygren, C. C. Wilson and J. F. C. Turner, *J. Phys. Chem. A*, 2005, **109**, 2586–2593.
41 H. P. Klug, E. Mack Jr. and F. C. Blake, *J. Am. Chem. Soc.*, 1929, **51**, 2880–2888.
42 D. Cinčić, T. Friščić and W. Jones, *J. Am. Chem. Soc.*, 2008, **130**, 7524–7525.
43 Y. Xu, L. Champion, B. Gabidullin and D. L. Bryce, *Chem. Commun.*, 2017, **53**, 9930–9933.
44 J. Mavračić, D. Cinčić and B. Kaitner, *CrystEngComm*, 2016, **18**, 3343–3346.
45 Y. Xu, J. Viger-Gravel, I. Korobkov and D. L. Bryce, *J. Phys. Chem. C*, 2015, **119**, 27104–27117.
46 D. Cinčić, T. Friščić and W. Jones, *Chem. – Eur. J.*, 2008, **14**, 747–753.
47 V. Nemec and D. Cinčić, *CrystEngComm*, 2016, **18**, 7425–7429.
48 G. A. Bowmaker, *Chem. Commun.*, 2013, **49**, 334–348.
49 J.-L. Do and T. Friščić, *Synlett*, 2017, **28**, 2066–2092.
50 C. F. Burmeister and A. Kwade, *Chem. Soc. Rev.*, 2013, **42**, 7660–7667.
51 J. Viger-Gravel, I. Korobkov and D. L. Bryce, *Cryst. Growth Des.*, 2011, **11**, 4984–4995.
52 J. Viger-Gravel, S. Leclerc, I. Korobkov and D. L. Bryce, *CrystEngComm*, 2013, **15**, 3168–3177.
53 C. M. Widdifield, G. Cavallo, G. A. Facey, T. Pilati, J. Lin, P. Metrangolo, G. Resnati and D. L. Bryce, *Chem. – Eur. J.*, 2013, **19**, 11949–11962.
54 D. L. Bryce and J. Viger-Gravel, *Top. Curr. Chem.*, 2015, **358**, 183–204.
55 J. Viger-Gravel, S. Leclerc, I. Korobkov and D. L. Bryce, *J. Am. Chem. Soc.*, 2014, **136**, 6929–6942.
56 J. Viger-Gravel, J. E. Meyer, I. Korobkov and D. L. Bryce, *CrystEngComm*, 2014, **16**, 7285–7297.
57 P. Cerreia Vioglio, L. Catalano, V. Vasylyeva, C. Nervi, M. R. Chierotti, G. Resnati, R. Gobetto and P. Metrangolo, *Chem. – Eur. J.*, 2016, **22**, 16819–16828.
58 P. M. J. Szell and D. L. Bryce, in *Modern Magnetic Resonance*, ed. G. A. Webb, Springer, Berlin, 2016, pp. 1–18, DOI: 10.1007/978-3-319-28275-6_92-1.
59 P. Cerreia Vioglio, M. R. Chierotti and R. Gobetto, *CrystEngComm*, 2016, **18**, 9173–9184.
60 P. M. J. Szell, S. A. Gabriel, R. D. D. Gill, S. Y. H. Wan, B. Gabidullin and D. L. Bryce, *Acta Crystallogr., Sect. C: Struct. Chem.*, 2017, **73**, 157–167.
61 APEX 2, Bruker AXS Inc., Madison, Wisconsin, USA, 2012.
62 G. M. Sheldrick, *SADABS, Program for empirical absorption correction of area detector data*, University of Göttingen, Germany, 1996.
63 G. M. Sheldrick, *Acta Crystallogr., Sect. C: Struct. Chem.*, 2015, **71**, 3–8.
64 L. J. Farrugia, *J. Appl. Crystallogr.*, 1999, **32**, 837–838.
65 L. J. Farrugia, *J. Appl. Crystallogr.*, 2012, **45**, 849–854.
66 A. L. Spek, *Acta Crystallogr., Sect. D: Biol. Crystallogr.*, 2009, **65**, 148–155.
67 C. R. Groom, I. J. Bruno, M. P. Lightfoot and S. C. Ward, *Acta Crystallogr., Sect. B: Struct. Sci., Cryst. Eng. Mater.*, 2016, **72**, 171–179.
68 J. D. Dunitz, H. Gehrer and D. Britton, *Acta Crystallogr., Sect. B: Struct. Sci.*, 1972, **28**, 1989–1994.
69 D. Lehnherr, J. M. Alzola, E. B. Lobkovsky and W. R. Dichtel, *Chem. – Eur. J.*, 2015, **21**, 18122–18127.
70 P. Politzer, J. S. Murray and M. C. Concha, *J. Mol. Model.*, 2008, **14**, 659–665.
71 L. Rajput, M. Banik, J. R. Yarava, S. Joseph, M. K. Pandey, Y. Nishiyama and G. R. Desiraju, *IUCrJ*, 2017, **4**, 466–475.

Chapter 12 – Cosublimation: A Rapid Route Towards Otherwise Inaccessible Halogen-Bonded Architectures

Statement of Authenticity. I certify that I have prepared the following article featuring my own work, with guidance from my supervisor Dr. David Bryce. This work was performed during my time at the Université de Rennes 1, under the supervision of Dr. Marc Fourmigué. This article features work from Shaina Gabriel and Estelle Caron-Poulin, undergraduate researchers at the University of Ottawa. Shaina's roles included performing experiments validating the experimental procedures, growing crystals of **3d**, and preparing the ^{15}N-labelled sample of **3d**. Estelle's role included performing some powder X-ray diffraction analysis. Dr. Olivier Jeannin, Dr. Marc Fourmigué, and Dr. David Bryce are acknowledged for helpful discussions, support and contributions to the manuscript. Dr. Olivier Jeannin and Dr. Bulat Gabidullin are acknowledged for acquiring and solving the crystal structures presented in the article.

Supporting Information. All supporting information for this article can be retrieved on the ACS website:

https://pubs.acs.org/doi/10.1021/acs.cgd.8b01089

October 2018
Volume 18
Number 10
pubs.acs.org/crystal

CRYSTAL GROWTH & DESIGN

INTEGRATING THE FIELDS OF CRYSTAL ENGINEERING AND CRYSTAL GROWTH FOR THE SYNTHESIS AND APPLICATIONS OF NEW MATERIALS

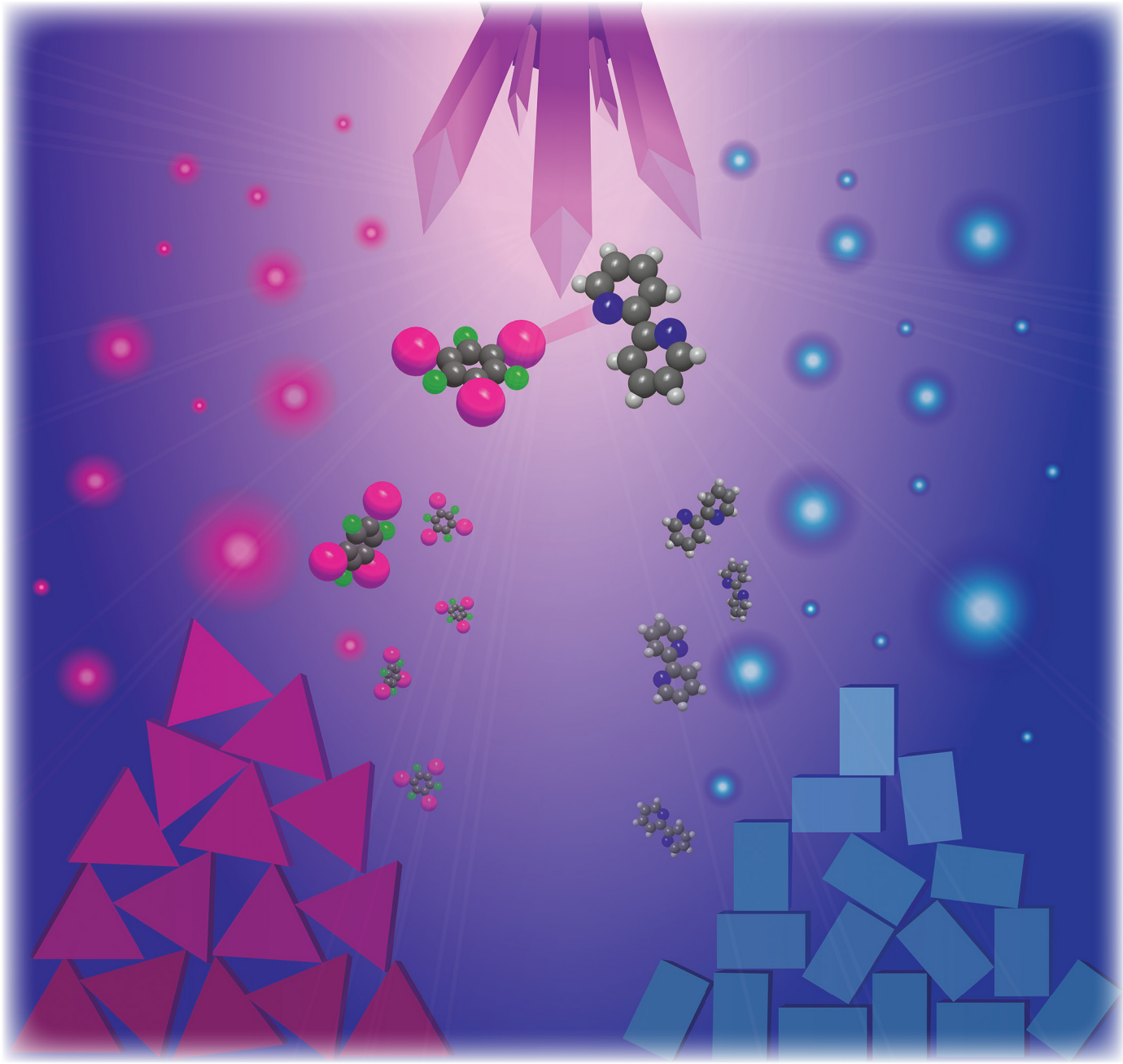

ACS Publications
Most Trusted. Most Cited. Most Read.

www.acs.org

CRYSTAL GROWTH & DESIGN

Article

Cite This: *Cryst. Growth Des.* 2018, 18, 6227−6238

pubs.acs.org/crystal

Cosublimation: A Rapid Route Toward Otherwise Inaccessible Halogen-Bonded Architectures

Patrick M.J. Szell,[‡] Shaina A. Gabriel,[‡] Estelle Caron-Poulin,[‡] Olivier Jeannin,[†] Marc Fourmigué,[†] and David L. Bryce*[,‡]

[‡]Department of Chemistry and Biomolecular Sciences & Centre for Catalysis Research and Innovation, University of Ottawa, 10 Marie Curie Private, Ottawa, Ontario K1N 6N5, Canada

[†]Institut des Sciences Chimiques de Rennes, Univ Rennes, CNRS, UMR 6226, Campus de Beaulieu, 35042 Rennes, France

Supporting Information

ABSTRACT: Several synthetic techniques are available for the preparation of halogen-bonded adducts, including traditional solvent-evaporation methods and mechanochemistry. With the intention of reducing solvent usage and experimental times, we establish cosublimation as a synthetic technique for preparing halogen-bonded cocrystals, focusing on the C−I···N motif involving nitrogen-containing heterocycles. We selected four common halogen-bond donors (I_2, 1,4-diiodobenzene, 1,4-diiodotetrafluorobenzene, 1,3,5-trifluoro-2,4,6-triiodobenzene) and four halogen-bond acceptors (2,3,5,6-tetramethylpyrazine, 1,4-diazabicyclo[2.2.2]octane, 2,2′-bipyridyl, 1-adamantanecarbonitrile), by virtue of their range in volatility, and explored all 16 combinations via the following methods: solvent evaporation, overnight cosublimation in a sealed glass tube using a two-zone furnace, and expedited cosublimation in a vacuum sublimation apparatus. We show that the raw crystals obtained from overnight cosublimation are of suitable quality for single-crystal X-ray diffraction, resulting in five new crystal structures, two of which are, currently, unobtainable through other methods. Of these new structures, the first halogen bond to the nitrile group of 1-adamantanecarbonitrile is reported, resulting in the formation of a supramolecular rotor in a spinning top configuration as evidenced by ^{13}C and ^{15}N solid-state NMR spectroscopy. Strikingly, the cosublimation approach overcomes an anticooperative halogen-bonding effect to produce fully saturated cocrystals of the tritopic halogen bond donor 1,3,5-trifluoro-2,4,6-triiodobenzene with 1,4-diazabicyclo[2.2.2]octane. Finally, we show that cosublimation can be used to rapidly prepare and purify bulk samples using a vacuum sublimation apparatus, enabling the scalable preparation of halogen-bonded cocrystals within 10 to 30 min using common laboratory equipment. The methods described here enable a broad exploration of the polymorphic landscape and may be extended to the facile preparation of other classes of cocrystals.

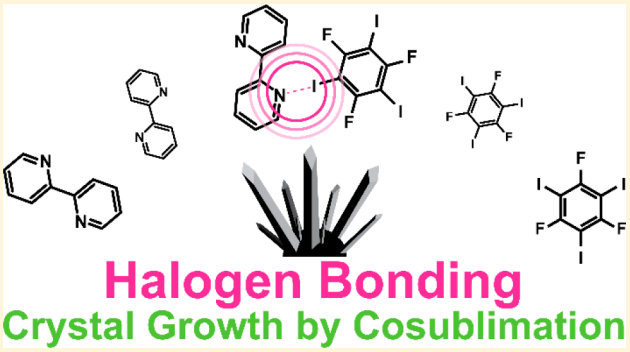

INTRODUCTION

Preparing high-quality crystalline samples suitable for analysis can be a difficult task, and yet, it is paramount to a multitude of chemical and biochemical studies. With the emergence of X-ray crystallography over the last century, several techniques have been proposed for growing crystals,[1] such as solvent evaporation and vapor diffusion, to name a few. Establishing a range of crystallization techniques is essential for the successful growth of crystals, perhaps even rendering new structures accessible. As a result of various difficulties and particularities encountered in crystal growth, such as twinning, it is often referred to as an *art*.[2]

Cocrystals, which are composed of two or more molecules often interacting via noncovalent interactions,[3,4] offer the advantages of increased manipulability and the tailoring of desirable physicochemical properties,[5,6] and they are tunable for various purposes by varying the functional groups on one or more components.[7,8] The preparation of cocrystals can be challenging,[9,10] in part due to the competition between the cocrystallization and the crystallization of the pure components. However, successfully preparing a cocrystal is often fruitful, and it has been a subject of investigation, for instance, in pharmaceuticals[11−13] and optical materials.[14,15] Moreover, cocrystallization allows for the study of noncovalent interactions, for instance, by investigating their X-ray crystal structures or spectroscopic properties. Indeed, a series of cocrystals can offer insights into noncovalent interactions, which has been particularly advantageous in the field of σ-hole-based interactions,[16,17] such as halogen bonding.

Halogen bonding (XB) is a noncovalent interaction between the electrophilic region associated with a covalently bonded halogen,[18,19] named the σ-hole on the halogen-bond

Received: July 18, 2018
Revised: August 23, 2018
Published: August 28, 2018

DOI: 10.1021/acs.cgd.8b01089
Cryst. Growth Des. 2018, 18, 6227−6238

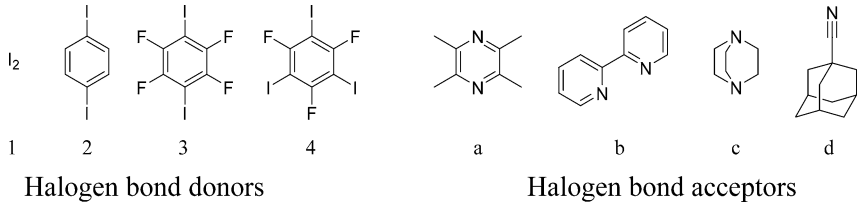

Figure 1. Pure components of the cocrystals used in this work. The XB donors include iodine (**1**), 1,4-diiodobenzene (**2**), 1,4-diiodotetrafluorobenzene (**3**), and 1,3,5-trifluoro-2,4,6-triiodobenzene (**4**). The XB acceptors include: 2,3,5,6-tetramethylpyrazine (**a**), 2,2′-bipyridyl (**b**), 1,4-diazabicyclo[2.2.2]octane (**c**), and 1-adamantanecarbonitrile (**d**).

donor,[20,21] and a nucleophile or Lewis base, the halogen-bond acceptor.[22] Recently, halogen bonding has experienced a surge of interest,[23−28] in part due to the directionality of the interaction favoring bond angles ($\theta_{R-X\cdots Y}$) nearing 180° [29] and its tunability,[30,31] altogether allowing for the rational design of frameworks[32,33] and molecules relevant to biochemical systems.[34,35] The presence of a halogen bond can be further rationalized based on the reduced distance parameter, R_{XB}, which is the quotient of the halogen-bond distance ($d_{X\cdots Y}$) and the sum of the van der Waals radii ($\sum d_{vdw}$),[36] given in eq 1:

$$R_{XB} = \frac{d_{X\cdots Y}}{\sum d_{vdw}} \quad (1)$$

Halogen bonding has since found prominence in several areas of chemistry, including medicinal chemistry,[37−39] anion recognition,[40,41] supramolecular rotors,[42,43] and catalysis,[44−46] to name a few.

Perhaps the most important tool for the investigation of the halogen bond has been single-crystal X-ray diffraction (SCXRD), which offers precise atomic coordinates, thereby allowing the halogen-bond geometry to be measured. In parallel, solid-state NMR (SSNMR) has been shown to be a powerful complementary crystallographic tool,[47−49] with many recent studies focused on characterizing the halogen bond by observing changes in chemical shifts,[50−52] *J*-couplings,[53,54] and quadrupolar coupling constants.[55−57] We recently advanced ^{19}F and ^{13}C SSNMR as probes for the occurrence of halogen bonding to perfluorinated halogen-bond donors;[58] in particular, the relevant chemical shifts are sensitive to the local chemical environment. Further, the high sensitivity and the large chemical shift range associated with the ^{19}F nucleus is ideal for discerning the starting material from the cocrystals, which is also advantageous in identifying new crystal phases.

Where large quantities of halogen-bonded materials are desired (>100 mg), crystallization methods requiring solvent evaporation or solvent diffusion can be tedious to perform, often requiring many days or perhaps weeks to achieve the desired product in sufficient quantity. Mechanochemistry has been shown to be a favorable route for the halogen-bond synthon,[54,59−62] offering a scalable and rapid method of preparing halogen-bonded cocrystals,[63,64] all without the need of large volumes of solvents. However, mechanochemistry by ball milling[65] has the inconvenience of yielding powdered products, requiring further manipulations to prepare a sample for SCXRD.

Sublimation and deposition, which correspond to the phase transitions from solid to gas, and gas to solid, respectively, are fast and scalable methods for crystal growth.[66] These processes carry several advantages such as simplicity of the experimental apparatus and the complete absence of solvents. Sublimation performed simultaneously on two compounds has been referred to alternately as codeposition or cosublimation in the literature,[67−69] with the technique varying in terms of experimental methodology across studies.[70−72] We proceed with the name cosublimation to emphasize that this process begins with building blocks in their solid state, which are then sublimed in vacuo using a vacuum pump, a heating source, and a surface for the deposition. In the field of halogen bonding, vapor deposition of the donor and acceptor moieties has been shown to form frameworks, but these limited investigations remain focused on surfaces.[73] For example, the preparation of halogen-bonded cocrystals by physical vapor deposition has been reported on a silicon substrate.[74] To our knowledge, only a select instance of cosublimation has been reported for the growth of crystals featuring halogen bonds.[75]

Despite this limited exposure, cosublimation does offer several advantages to the field of halogen-bonded cocrystals, including rapid screening capabilities, and the elimination of all solvent interactions. Here, we apply cosublimation to a series of halogen-bond donors and acceptors, in an effort to uncover structures otherwise inaccessible by solvent-evaporation methods. We investigate the potential of cosublimation for growing single crystals, for preparing bulk quantities of product with a vacuum sublimation apparatus, and the potential of purifying powdered cocrystals by sublimation. To grow single crystals suitable for SCXRD, the halogen-bond donor and acceptor were sealed in vacuo at opposite ends of a 25 cm glass tube. Heating the glass tube in a two-zone tube furnace allows for the separate temperature control of the donor and acceptor, favoring the growth of cocrystals by sublimation. To this end, four halogen-bond donors and four halogen-bond acceptors with a range of volatility were selected (Figure 1), focusing on the I···N motif. All 16 combinations were explored using two sublimation techniques: using a two-zone tube furnace under static vacuum and using a sublimation apparatus under dynamic vacuum, henceforth referred to as "overnight cosublimation" and "expedited cosublimation", respectively. The products from both techniques are compared to the products obtained by slow evaporation and fully analyzed by ^{13}C and ^{19}F SSNMR, melting point measurements, powder X-ray diffraction (PXRD), infrared (IR) spectroscopy, and elemental analysis.

EXPERIMENTAL SECTION

1,4-Diiodobenzene (*p*DIB), 2,2′-bipyridyl (BIPY), 1-adamantanemethanol, (diacetoxyiodo)benzene, 2,2,6,6-tetramethylpiperidine-1-oxyl (TEMPO), 1-adamantanecarbonitrile (ADCN), and 2,3,5,6-tetramethylpyrazine (TMP) were purchased from Alfa Aesar. Iodine (I_2) was purchased from Acros Organics. 1,4-Diiodotetrafluorobenzene (*p*DITFB), 1,4-diazabicyclo[2.2.2]octane (DABCO), and ^{15}N-ammonium acetate (98% ^{15}N atoms) were purchased from Sigma-Aldrich. 1,3,5-Trifluoro-2,4,6-triiodobenzene (*sym*TFTIB) was purchased from Fluorochem. All compounds were used without further purification.

DOI: 10.1021/acs.cgd.8b01089
Cryst. Growth Des. 2018, 18, 6227−6238

All solvents were purchased from a commercial supplier and used without further purification. The ^{15}N-labeled 1-adamantanecarbonitrile was prepared from 1-adamantanemethanol and ^{15}N-ammonium acetate using a reported method.[76] Melting points were measured on an Electrothermal 1A6304 melting point apparatus. The infrared spectroscopy was performed on a PerkinElmer Spectrum Two ATR FT-IR spectrometer, scanning from 4000 to 450 cm^{-1}. The phase purity for each powdered sample was verified by PXRD on a Rigaku Ultima IV instrument with 2θ ranging from 5 to 55° in increments of 0.02° at a rate of 1°/min using Cu Kα radiation. No data processing or baseline corrections were employed. All melting points, infrared spectra, powder X-ray diffractograms, elemental analysis, and ^{13}C/^{19}F solid-state NMR spectra can be found in the Supporting Information.

Slow Evaporation Procedure. The halogen-bond donor and the halogen-bond acceptor were separately dissolved in either acetonitrile, chloroform, or ethanol. The halogen-bond donor solution was added dropwise to the halogen-bond acceptor solution. The solution was left to slowly evaporate over the course of several days, affording the final product. See the Supporting Information for the precise experimental procedures for all 16 combinations.

Overnight Cosublimation Procedure. To opposite ends of a 25 cm thin-necked glass tube (see Figure 2a), the halogen-bond donor and the halogen-bond acceptor were carefully added. The glass tube was then sealed in vacuo, with a typical pressure of 1 × 10^{-1} mbar. In a home-built, two-zone tube furnace (Figure 2b), both segments of the tube containing the halogen-bond donor and acceptor were individually heated from room temperature to an initial temperature of ∼20 °C below the melting point and slowly raised to a temperature of 20 °C above the melting point, at a rate of 0.04 °C/min. The total sublimation times varied, starting from 20 h, yielding crystals near the center of the tube. The sublimation tube was slowly returned to room temperature over a period of 1 h, scored with a glass cutting tool, and opened. The crystals were removed and analyzed without further purification. The precise experimental conditions, including pressure, temperatures, and sublimation times for all 16 compounds are given in the Supporting Information.

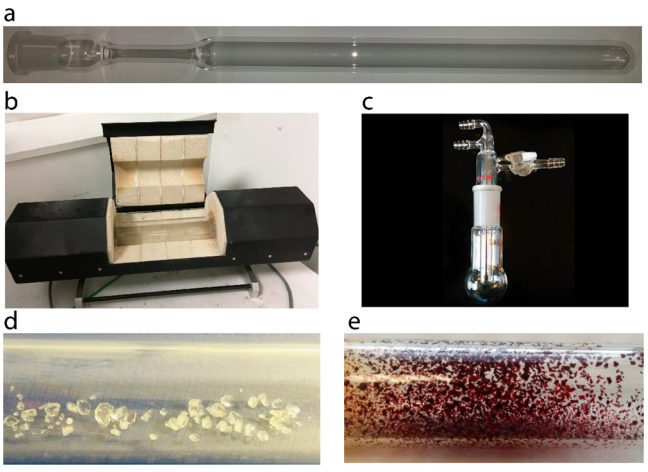

Figure 2. (a) Empty 25 cm thin-necked glass tube. The halogen-bond donor and acceptor are added to opposite extremities of the tube and sealed in vacuo. (b) Two-zone tube furnace used for the overnight cosublimation. (c) Sublimation apparatus used for the expedited cosublimation. Crystals of **3a-ii** (d), and **1a** (e), obtained by overnight cosublimation.

Expedited Cosublimation Procedure. The halogen-bond donor and the halogen-bond acceptor were added to a round-bottom sublimation apparatus (see Figure 2c). While the coldfinger was cooled with refrigerated water, the sublimation apparatus was submerged into an oil bath while under a vacuum of 1 × 10^{-1} mbar. The temperature of the oil bath was generally kept between 50 and 100 °C and varied according to the melting point of the compounds. The sublimation times varied between 10 and 30 min, affording the product on the coldfinger. See the Supporting Information for the precise experimental conditions for the preparation of all 16 combinations.

^{13}C Solid-State NMR. All ^{13}C cross-polarization magic-angle spinning (CP/MAS) solid-state NMR experiments were performed at 9.4 T (ν_L(^{13}C) = 100.6 MHz) using a Bruker 4 mm HXY probe and a Bruker Avance III NMR spectrometer. ^{1}H → ^{13}C CP was used with a 4.6 μs proton $\pi/2$ pulse, a 2000 μs contact time, and a 54.3 kHz ^{1}H decoupling frequency. ^{13}C chemical shifts were referenced to glycine at 176.6 ppm (^{13}C═O) relative to tetramethylsilane (TMS). A consistent spinning speed of 8 kHz was used for all samples, and 512 transients were acquired for all cocrystals. For the cocrystals, the recycle delay was 3 s for series **c** (DABCO) and **d** (ADCN), 5 s for series **a** (TMP), and 20 s for the series **b** (BIPY). Experimental details for the starting materials are given in Table S1 of the Supporting Information.

^{19}F Solid-State NMR. All ^{19}F NMR experiments were performed at 7.05 T (ν_L(^{19}F) = 282.5 MHz) on a Bruker Avance spectrometer, using a Bruker 2.5 mm HX MAS probe with a spinning frequency of 25 kHz. A Hahn echo ($\pi/2 - \tau - \pi - \tau$) was used with a $\pi/2$ pulse length of 2.30 μs, a τ delay of two rotor periods, a recycle delay of 20 s, and 16 transients were collected. The spectra were referenced to $BF_3{\cdot}OEt_2$ at −152.8 ppm relative to $CFCl_3$.[77]

Single-Crystal X-ray Diffraction. Single crystals of **2a**, **3a-ii**, **4b**, and **4c-iii** were mounted on a cryoloop, while a crystal of **3d** was mounted on a thin glass fiber using paraffin oil. The data were collected on a APEX II Bruker AXS diffractometer at room temperature for **2a**, **3a-ii**, **4b**, and **4c-iii** and at 200(2) K for **3d**, using graphite-monochromated Mo Kα radiation (λ = 0.710 73 Å). The raw data collection and reduction were done with the Bruker APEX II software package.[78] Structures were solved by direct methods (SIR-92)[79] and refined (SHELXL-2014/7)[80] by full-matrix least-squares methods, as implemented in the WinGX software package.[81] Absorption corrections were applied. Hydrogen atoms were introduced at calculated positions (riding model), included in structure factor calculations, and not refined. Crystallographic data were deposited with the Cambridge Crystallographic Data Centre as supplementary publication data: CCDC 1854043 for **2a**, CCDC 1854044 for **3a-ii**, CCDC 1854304 for **3d**, CCDC 1854045 for **4b**, and CCDC 1854052 for **4c-iii**. Additional crystallographic information is available in the Supporting Information. Figures were generated with Diamond version 4.5.1.[82] Displacement ellipsoid plots were produced using ORTEP,[81] and uncertainties were estimated using PLATON.[83]

RESULTS AND DISCUSSION

i. Cocrystal Growth by Overnight Cosublimation. Cocrystallizations by overnight cosublimation (see Figure 2a,b) fared exceptionally well, yielding crystals suitable for SCXRD in almost all cases. Examples of crystals obtained from sublimation are shown in Figure 2d,e. As these trials were attempted at the 300 mg scale to isolate sufficient quantities for analysis, sublimation times were between 20 and 72 h, although sublimation times were shorter when performed on a smaller scale. In contrast, crystal growth by slow evaporation typically required several days, with the total time varying according to the solvent and its evaporation rate. Of the 16 combinations attempted here, 12 combinations successfully cosublimed, from which five new crystal structures were identified: **2a**, **3a-ii**, **3d**, **4b**, and **4c-iii**. Notably, structures **3a-ii** and **4c-iii** were only observed by cosublimation, while structures **3a-i**,[84] **4c-i**,[85] and **4c-ii**[86] obtained from slow evaporation have been previously described. A summary of the XB geometries and selected crystallographic parameters of all the structures is given in Tables 1 and 2, respectively. As for the four failed combinations (**1d**, **2b**, **2d**, and **4d**), these

DOI: 10.1021/acs.cgd.8b01089
Cryst. Growth Des. 2018, 18, 6227−6238

Table 1. Summary of the Halogen-Bonded Cocrystals Obtained by Cosublimation Performed in a Glass Tube and in a Vacuum Sublimation Apparatus

acceptor/donor	I_2 (**1**)	*p*DIB (**2**)	*p*DITFB (**3**)	*sym*TFTIB (**4**)
TMP (**a**)	successful	new structure	new structure	successful
BIPY (**b**)	inconclusive	no cocrystals	successful	new structure
DABCO (**c**)	inconclusive	successful	successful	new structure
ADCN (**d**)	no cocrystals	no cocrystals	new structure	no cocrystals

cocrystals were also not accessible by slow evaporation, with the failure attributed to donor−acceptor incompatibility. For instance, the XB acceptor ADCN is the weakest among the acceptors studied here and only yielded cocrystals with *p*DITFB, forming structure **3d**. In cases **1b** and **1c**, both the PXRD and ^{13}C SSNMR support the occurrence of a mixed-phase product, perhaps due to the instability associated with cocrystals featuring I_2. A description of the new crystal structures is given below, highlighting their differences with previously reported structures.

Structure **2a** shares the same motif as structure **3a-i**,[84] featuring an alternating chain of **2**···**a**···**2**···**a**, shown in Figure 3. However, the molecular plane of **2** is nearly perpendicular to the molecular plane of **a**, which contrasts with the structure of **3a-i**, where the molecular planes of **3** and **a** are nearly parallel. Furthermore, the XB in structure **2a** (R_{XB} = 0.93, $d_{I\cdots N}$ = 3.298(5) Å, $\theta_{C-I\cdots N}$ = 167.25(17)°) is much longer and less linear than that in structure **3a-i** (R_{XB} = 0.87, $d_{I\cdots N}$ = 3.067(2) Å, $\theta_{C-I\cdots N}$ = 177.15(7)°). Notably, structure **2a** has the highest R_{XB} and therefore the longest XB in this study, seen in Table 2. The longer XB and lower linearity is attributed to the lack of fluorine atoms on **2**, which would otherwise strengthen the XB.[30] Interestingly, the transparent crystals of **2a** opacified over the course of a few days, indicating possible metastability. This metastability is further supported by the PXRD and ^{13}C SSNMR spectra (see Figures S5 and S6 of the Supporting Information), showing a lower agreement between the samples obtained from slow evaporation and cosublimation.

The structure **3a-ii**, shown in Figure 3, was only observed by overnight cosublimation, with the PXRD and ^{19}F SSNMR suggesting an absence of this crystalline phase in the product obtained by slow evaporation (see Figures S9 and S11 of the Supporting Information). The structure **3a-ii** is unique from **3a-i**,[84] having a 1:2 ratio between **3** and **a**, instead of a 1:1 ratio. Overall, the structure features a **3**···**a**···**3**···**a** XB chain, with an extra molecule of **a** not participating in XB. Rather, the molecules of **a** interact with each other via π-stacking, forming columns of **a** in alternating right angles. The two unique molecules of **a** can be discerned in the ^{13}C SSNMR spectra of **3a-ii** obtained from overnight cosublimation (see Figure S10 of the Supporting Information), with the chemical shift differences between both molecules attributed to the occurrence of the XB to only one **a**. In our previous study,[58] we reported an

Table 2. Summary of the I···N Halogen-Bonding Geometries Observed in This Study[a]

compound	XB length ($d_{I\cdots Y}$), Å	R_{XB}[b]	XB angle $\theta_{R-I\cdots N}$[c] (deg)	CSD No.	reference
1a	3.086(4)	0.87	177.5	VUKDOU	R. D. Bailey et al.[75]
1b	2.604(1)	0.74	179.4	CECZAL	S. Pohl[87]
1c	2.366(4)	0.67	178.4	HEKZEE	A. Peuronen et al.[88]
1d					no cocrystals
2a	3.298(5)	0.93	167.25(17)		this work
2b					no cocrystals
2c	2.928(5)	0.83	175.4(2)	VOMHOV	D. Cinčić et al.[89]
	2.959(5)	0.84	176.3(2)		
2d					no cocrystals
3a-i	3.067(2)	0.87	177.15(7)	JAQMAQ	J.-L. Syssa-Magalé et al.[84]
3a-ii	3.001(4)	0.85	177.51(15)		this work
3b-i	3.158(3)	0.89	169.61(11)	ISIJEZ01	J.-L. Syssa-Magalé et al.[84]
3b-ii	3.111(3)	0.88	169.37(9)	ISIJEZ	M. Bolte[90]
3c	2.739(5)	0.78	173.09(2)	ISIHUN01	Cinčić et al.[91] and Syssa-Magalé et al.[86]
	2.748(5)	0.78	174.2(2)	ISIHUN02	
3d	3.050(4)	0.86	173.88(9)		this work
4a	2.991(3)	0.85	178.09(12)	SAJCUE	P. M. J. Szell et al.[58]
	2.993(3)	0.85	179.81(11)		
4b	2.968(6)	0.84	170.0(2)		this work
	2.969(6)	0.84	171.8(2)		
4c-i	2.757(3)	0.78	173.89(11)	DATCIM	M. C. Pfrunder et al.[85]
4c-ii	2.874(4)	0.81	166.11(15)	RORWIG	J.-L. Syssa-Magalé et al.[86]
	2.866(4)	0.81	172.55(15)		
4c-iii	2.801(4)	0.79	176.56(16)		this work
	2.855(3)	0.81	168.80(13)		
	2.909(4)	0.82	167.73(13)		
4d					no cocrystals

[a]The parameters include: the halogen-bond length ($d_{I\cdots N}$), the normalized distance parameter of the halogen bond (R_{XB}), the halogen-bond angle ($\theta_{R-I\cdots N}$), the CSD reference code, and appropriate citation. Experimental errors are given in parentheses. [b]R_{XB} values were calculated from eq 1 using a $\sum d_{vdW}$ of 3.53 Å. [c]R denotes the substituent (I or C).

DOI: 10.1021/acs.cgd.8b01089
Cryst. Growth Des. 2018, 18, 6227−6238

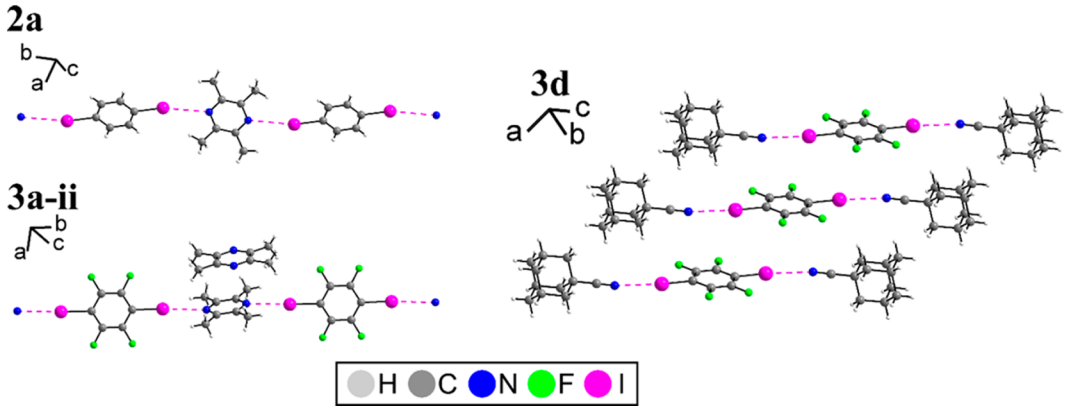

Figure 3. Detailed view of the halogen-bonded networks from the X-ray crystal structures of the cocrystals **2a** (upper left), **3a-ii** (lower left), and **3d** (right) obtained in this study. The dashed magenta line denotes an iodine−nitrogen halogen bond.

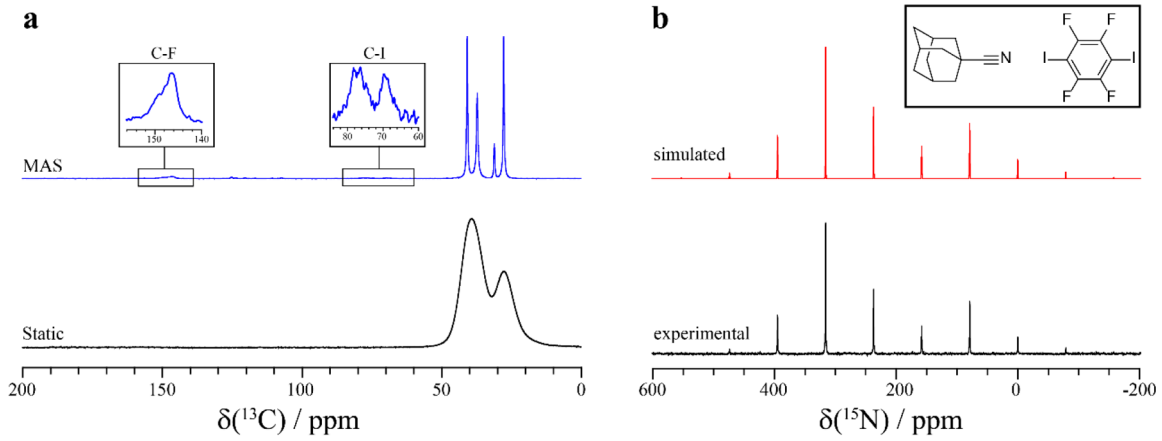

Figure 4. ^{13}C and ^{15}N (right) solid-state NMR spectra of compound **3d**. (a) Experimental ^{13}C cross-polarization SSNMR spectra acquired under static (bottom left, black) and MAS conditions (upper, blue). (insets) Magnified views of the C−F and C−I resonances. (b) Experimental ^{15}N SSNMR spectrum acquired at a 4 kHz MAS frequency (bottom, black) and the WSOLIDS[95] simulated spectrum (upper, red).

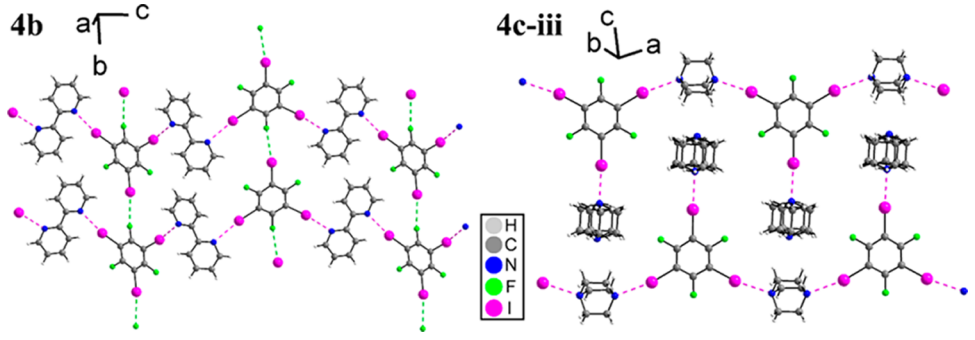

Figure 5. Crystal structures of **4b** (left) and **4c-iii** (right), obtained by cosublimation.

increase in the ^{13}C chemical shift of the methyl groups of **a** upon XB, whereas the carbons covalently bonded to the nitrogen decreased in chemical shift. Further, as the XB geometry in **3a-ii** (R_{XB} = 0.85, $d_{I\cdots N}$ = 3.001(4) Å, $\theta_{C-I\cdots N}$ = 177.51(15)°) is subtly shorter than the XB geometry observed in **3a-i** ($d_{I\cdots N}$ = 3.067(2) Å), a lower ^{13}C chemical shift corresponding to the carbons covalently bonded to nitrogen is observed in **3a-ii** (147.2 ± 0.2 ppm) than in **3a-i** (149.8 ± 0.3 ppm).

Structure **3d**, shown in Figure 3, features the first instance of XB to the nitrile group of ADCN in the Cambridge Structural Database (CSD).[92] The XB geometry (R_{XB} = 0.86, $d_{I\cdots N}$ = 3.050(4) Å, $\theta_{C-I\cdots N}$ = 173.88(9)°) is moderately short, consistent with the fact that nitrile groups are not the strongest nitrogen-containing XB acceptors.[93] As a result of the electron donating nature of the adamantyl group, ADCN is a relatively strong nitrile XB acceptor.[94] While the C≡N···I bond angles in the CSD range between 90 and 180°, here, the XB is coordinating the apex of the nitrile group, resulting in a C≡N···I bond angle of 167.43°.

As molecular adamantane is known for its molecular rotations in the solid state, ADCN has been previously investigated for its molecular rotation.[96−98] It can be seen in the crystal structure of **3d** acquired at 200(2) K that there is a

DOI: 10.1021/acs.cgd.8b01089
Cryst. Growth Des. 2018, 18, 6227−6238

lack of contacts to the adamantane portion of ADCN, suggesting that related molecular rotations may also be present in the cocrystals. This is further supported by the ^{13}C SSNMR spectrum acquired at room temperature under static conditions, which has a relatively narrow line width of 950 ± 25 Hz for the CH_2 carbons, despite the lack of magic angle spinning. This narrowing of the resonances can be attributed to the rotation of the adamantane ring, which results in averaging of carbon chemical shift anisotropy and some dipolar interactions. In comparison, molecular adamantane, which is known for its plasticity, has a line width of 270 ± 10 Hz under the same conditions, on the same order as this ADCN cocrystal. In contrast, the ^{15}N SSNMR performed on the ^{15}N-enriched ADCN cocrystal, shown in Figure 4b, reveals a sizable chemical shift anisotropy ($\delta_{iso}(^{15}N)$ = 237.0 ± 0.1 ppm; Ω = 425 ± 30 ppm; κ = 1.00 ± 0.2), attributed to the nitrogen remaining fixed in space as a result of XB. The distinctions between the dynamics displayed in the crystal structure and in the SSNMR spectra may be attributed to the temperature difference of nearly 100 K during their acquisitions. Overall, this configuration resembles a spinning top, akin to similar reports in the literature.[42] However, a full dynamical analysis of the ADCN rotations is beyond the scope of this study, and it has not been investigated further.

In structure **4b**, shown in Figure 5, BIPY and *sym*TFTIB are cocrystallized in a 1:1 stoichiometry, featuring two nearly equivalent C−I···N XBs (R_{XB} = 0.84, $d_{I\cdots N}$ = 2.968(6) Å, $\theta_{C-I\cdots N}$ = 170.0(2)°; R_{XB} = 0.84, $d_{I\cdots N}$ = 2.969(6), $\theta_{C-I\cdots N}$ = 171.8(2)°). Because of the nitrogen on the pyridyl rings being in the trans position, a zigzag architecture is formed, with the chains linked by a C−I···F halogen contact ($d_{I\cdots F}$ = 3.310(4) Å, $\theta_{C-I\cdots F}$ = 172.3(2)°). Structure **4b** is similar to previous reports featuring *sym*TFTIB and a series of other 4,4′-bipyridyl derivatives,[99,100] with the resulting donor molecule participating in two instead of the potential three C−I···N XBs. This preference was previously rationalized as an anticooperative effect of the XB in polytopic donors, with the C−I···N binding energy decreasing with each additional XB.[99] This was further observed in cocrystals featuring *N,N′*-diodo-dimethylhydantoin as the XB donor, with the introduction of a XB affecting the neighboring iodine's capability to form XBs.[101]

Several cocrystal structures featuring *sym*TFTIB and DABCO have been reported, with donor/acceptor stoichiometries varying from 1:1 (one C−I···N XB)[85] to 1:2 (two C−I···N XBs).[86] The structure of **4c-iii** reported herein and shown in Figure 5 has a 1:2 stoichiometry between the donor and acceptor molecules, and importantly it features a full saturation of the donor with all three iodines participating in C−I···N halogen bonds. Notably, this structure has only been observed in the sample obtained from slow overnight cosublimation. Three unique XBs are observed in the structure (R_{XB} = 0.79, $d_{I\cdots N}$ = 2.801(4) Å, $\theta_{C-I\cdots N}$ = 176.56(16)°; R_{XB} = 0.81, $d_{I\cdots N}$ = 2.855(3) Å, $\theta_{C-I\cdots N}$ = 168.80(13)°; R_{XB} = 0.82, $d_{I\cdots N}$ = 2.909(4) Å, $\theta_{C-I\cdots N}$ = 167.73(13)°), resulting in a zigzag C−I···N backbone complemented by DABCO molecules each participating in one C−I···N XB (see Figure 5). The large ∼0.1 Å distinction between the XB lengths can be rationalized by the anticooperativity of the shortest XB, which weakens the next two iodine donor sites. The second shortest XB further weakens the third iodine, resulting in a longer XB. In contrast, despite the different acquisition temperature, the $d_{I\cdots N}$ XB lengths are much shorter in structure **4c−i**, which exhibits a single C−I···N XB ($d_{I\cdots N}$ = 2.757(3) Å), presenting a difference of 0.15 Å in comparison to structure **4c-iii**. To our knowledge, only three reports are available in the literature featuring a fully saturated *sym*TFTIB XB donor with neutral XB acceptors, including cocrystals with 4-(*N,N*-dimethylamino)pyridine,[102] 1,3,4-oxadiazole derivatives,[103] and a *N*-salicylidene Schiff base.[104] Shown in Figure 6, ^{19}F SSNMR was able to rapidly identify a new phase, **4c-iii**.

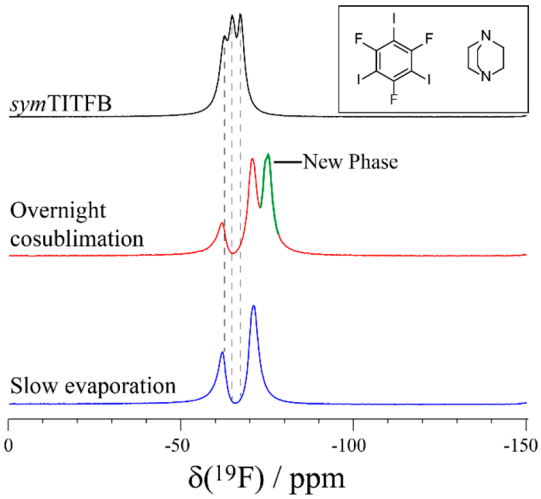

Figure 6. ^{19}F solid-state NMR (ν_{MAS} = 25 kHz) spectra of sample **4c** obtained from slow evaporation (blue), overnight cosublimation (red), and the pure starting material (black). The new phase, assigned to structure **4c-iii**, is shown in green. The dashed line serves as a guide.

With experimental NMR times of ∼5 min performed on ∼12 μL of sample and resulting in an excellent signal-to-noise ratio,[58] ^{19}F SSNMR of the bulk samples obtained from cosublimation served as a useful tool for quickly identifying new crystallographic phases. An example spectrum of combination **4c** obtained from cosublimation, shown in Figure 6, is compared to the sample obtained from slow evaporation and the starting material. A new phase can clearly be identified at −75.3 ± 0.6 ppm; this is assigned to structure **4c-iii**. This is easily distinguished from the product obtained from slow evaporation, structure **4c−i**, with ^{19}F chemical shifts of −62.1 ± 0.3 and −70.8 ± 0.3 ppm. The lower ^{19}F chemical shift observed in structure **4c-iii** is attributed to the presence of three concurrent XBs, with the three fluorine atoms sharing similar chemical environments. However, structure **4c−i** features only one C−I···N XB to DABCO, one C−I···I type II contact, and one I···F contact. Consequently, two fluorine atoms are situated adjacent to the C−I···N XB, while the third fluorine is participating in the I···F contact. Because of the nearly 2:1 signal intensity observed for the compound obtained via slow evaporation, the fluorine atom participating in the I···F contact was assigned to the lower chemical shift of −62.1 ± 0.3 ppm, while the fluorine atoms adjacent to the C−I···N XB were assigned to the resonance at −70.8 ± 0.3 ppm. In general, as a result of the advantages of ^{19}F SSNMR, it proved to be the most valuable analytical tool in characterizing the fluorinated samples. The general trend observed here is that the ^{19}F chemical shifts decrease upon C−I···N halogen bonding, with the resulting spectrum being a rapid and unambiguous indicator of cocrystallization, along with the identification of new crystallographic phases. In contrast, although the ^{13}C

DOI: 10.1021/acs.cgd.8b01089
Cryst. Growth Des. 2018, 18, 6227−6238

Table 3. Selected Single-Crystal X-ray Crystallographic Data for Compounds 2a, 3a-ii, 3d, 4b, 4c-iii

compound	**2a**	**3a-ii**	**3d**	**4b**	**4c-iii**
empirical formula	$C_{14}H_{16}I_2N_2$	$C_{22}H_{24}F_4I_2N_4$	$C_{28}H_{30}F_4I_2N_2$	$C_{16}H_8F_3I_3N_2$	$C_{18}H_{24}F_3I_3N_4$
FW (g/mol)	466.10	674.25	724.34	665.94	734.12
crystal color	colorless	colorless	colorless	colorless	colorless
crystal size (mm)	0.24 × 0.23 × 0.18	0.45 × 0.38 × 0.09	0.507 × 0.252 × 0.129	0.27 × 0.08 × 0.06	0.03 × 0.02 × 0.01
crystal system	triclinic	triclinic	monoclinic	orthorhombic	triclinic
crystal space group	$P\bar{1}$	$P\bar{1}$	$P2_1/n$	$Pna2_1$	$P\bar{1}$
T (K)	296(2)	296(2)	200(2)	296(2)	296(2)
a (Å)	6.1555(11)	7.3019(11)	6.8334(5)	7.7491(13)	6.5306(5)
b (Å)	6.2811(11)	9.6012(14)	10.4688(8)	9.4426(17)	10.5839(7)
c (Å)	10.4557(19)	10.0739(15)	19.0137(15)	25.814(5)	18.9338(13)
α (deg)	78.165(6)	69.341(4)	90	90	80.694(2)
β (deg)	88.432(6)	69.659(4)	96.662(4)	90	88.633(2)
γ (deg)	85.422(6)	82.976(5)	90	90	72.192(2)
V (Å^3)	394.37(12)	619.63(16)	1351.01(18)	1888.9(6)	1229.13(15)
Z	1	1	2	4	2
R_1 (final)	0.0431	0.0398	0.0325	0.0265	0.0361
wR_2 (final)	0.1143	0.0791	0.0808	0.0595	0.0672

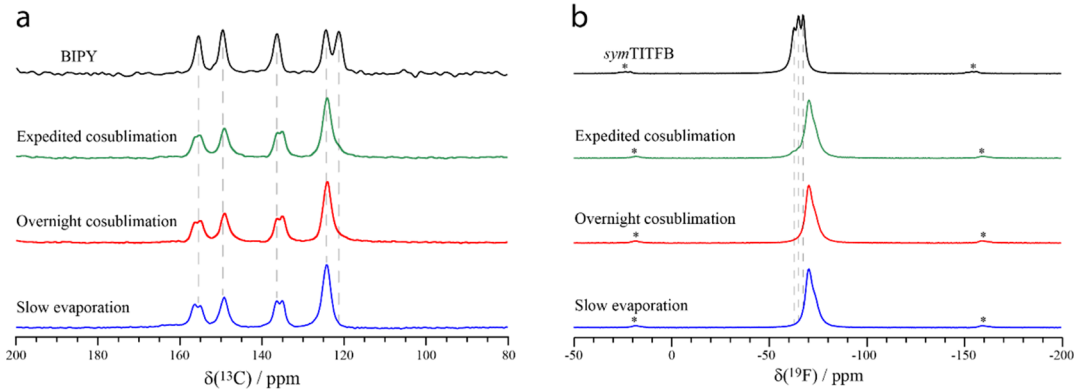

Figure 7. ^{13}C CP/MAS (a) and ^{19}F (b) MAS solid-state NMR spectra of compound **4b** obtained from slow evaporation (blue), overnight cosublimation (red), expedited cosublimation (green), and their corresponding starting materials (black). The dashed lines serve as a guide to discern the starting material from the cocrystals. The asterisks denote spinning sidebands.

chemical shifts of the carbon covalently bonded to nitrogen generally increased upon the formation of a halogen bond, experimental times were significantly longer, required more sample, and the chemical shift changes were small.

The crystals obtained by overnight cosublimation were of diffraction quality, with crystal sizes varying according to sublimation times (Table 3). In some cases, such as for compound **3a-ii**, individual single crystals of up to 85 mg were obtained, which can be useful when large single crystals are required, such as in single-crystal NMR. In these cases, however, rapid cooling of the crystals should be avoided, as the thermal shock resulted in cracking and popping of larger crystals. However, this was easily avoided by simply allowing the furnace to return to room temperature over a period of 30 min to 1 h before removing the sample. Furthermore, of the cocrystals studied here, only compound **1c** yielded a powder by overnight cosublimation, precluding its analysis by SCXRD. In general, the samples with **1** proved to be the most difficult to prepare by cosublimation, and they were the least consistent with the products obtained by slow evaporation.

In six of the seven successful cocrystals featuring a fluorinated halogen-bond donor, the products obtained from overnight cosublimation consisted of a single phase, which was investigated by performing both PXRD and SSNMR on the entirety of the products. This homogeneity was achieved by employing temperature ramps on the order of 0.04 °C per minute, along with prolonging cosublimation times upon visual inspection. The steady temperature ramps allowed for all starting material to be sublimed and to migrate toward the center of the tube, while avoiding melting. Initial temperatures were chosen to be ∼20 °C under the melting point of the compound and then were slowly increased to 20 °C above the melting point of the compound over the course of several hours. In some cases, the temperatures were adjusted to ensure that the XB donor and acceptor were migrating at equal rates. Delightedly, implementing temperature ramps reduced the need for "finding" precise temperatures, as eventually the compounds sublimed and migrated toward the center of the tube. In the cases of volatile starting materials, such as combinations **1a** and **1c**, heating was not necessary, and simply sealing the two starting materials in vacuo resulted in the formation of cocrystalline product within minutes. An additional advantage of using cosublimation was the possibility of visually following the cocrystallization in the clear glass tube. The cocrystals prepared here had a different morphology than the starting materials, allowing for the temperatures to be adjusted on the fly or for the cosublimation times to be extended if required. As a result of the soft and solventless nature of cosublimation, the experimental aspects discussed here may be valuable for the preparation of cocrystals based on

DOI: 10.1021/acs.cgd.8b01089
Cryst. Growth Des. 2018, 18, 6227−6238

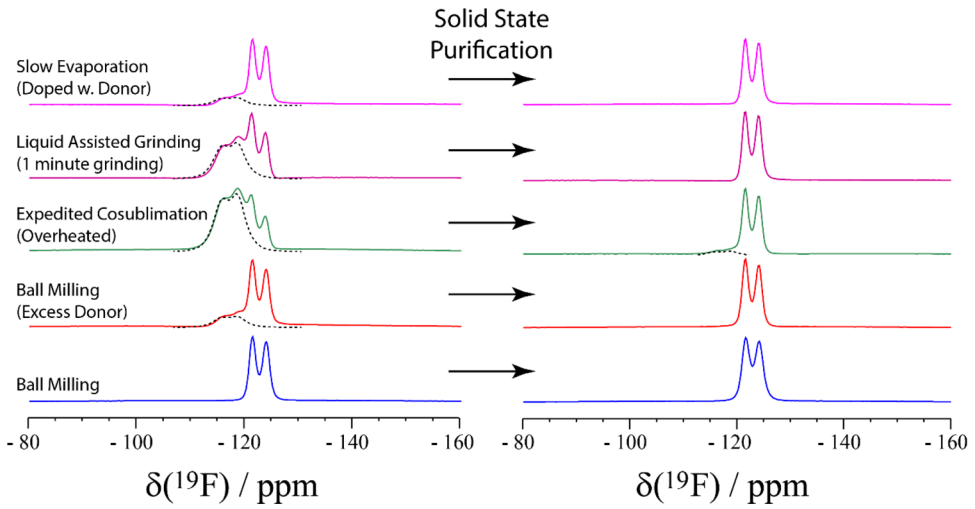

Figure 8. ^{19}F solid-state NMR spectra of compound **3c** prepared by several synthetic techniques. The spectra on the left were acquired before purification, whereas the spectra on the right were acquired on the same samples after purification. The dashed black line corresponds to the starting material.

noncovalent interactions other than halogen bonds, such as the emerging chalcogen, pnictogen, and tetrel bonds.[17]

ii. Expedited Cosublimation and Solid-State Purification. The preparation of each cocrystal was attempted by placing both the XB donor and acceptor in a vacuum sublimation apparatus, with this overall process referred to as expedited cosublimation in an effort to even further reduce preparation times. The product collected on the coldfinger was then compared to the products obtained by slow evaporation and sublimation performed in a glass tube. Expedited cosublimation successfully reproduced the halogen-bonded cocrystals obtained by slow evaporation, with sublimation times ranging between 10 and 30 min. As an example, the ^{13}C and ^{19}F SSNMR spectra of compound **4b** prepared by slow evaporation and both sublimation techniques (in a sealed glass tube and a sublimation apparatus) are shown in Figure 7. The line shapes are superimposable across all synthetic methods, indicating that the same product was obtained in each case. Further, apart from preparation **4c**, both the PXRD and SSNMR data support the presence of a single phase in the samples successfully prepared by expedited cosublimation. In the case of preparation **4c**, a small quantity of a second phase was observed in the ^{19}F SSNMR spectrum, assigned to structure **4c-iii**. While the sample obtained from the slow evaporation method took several days to prepare, and the sample from overnight cosublimation took ∼93 h, the sample obtained from the expedited cosublimation apparatus took merely 30 min, with comparable yields and no solvent usage. Consequently, the shortened preparation times offered by cosublimation can be particularly advantageous for screening a large array of cocrystals.

In contrast to cosublimation performed in a glass tube, single crystals suitable for SCXRD were not obtained when using a vacuum sublimation apparatus. This may be a result of the crystal growth being performed on the order of 30 min, resulting in the growth of microcrystalline sample. Furthermore, structure **3c-ii**, which was only obtained by overnight cosublimation, was not observed when repeating the procedure in a vacuum sublimation apparatus, perhaps as the technique favors structures with lower conformational energy. As the vacuum sublimation apparatus does not offer the ability to adjust the temperature of the XB donor and acceptor individually, it was more sensitive to vapor pressure mismatch, which was manifested in lower synthetic yields.

In some cases, trace quantities of starting materials were observed in the product obtained from the coldfinger on a sublimation apparatus. Separating the starting materials from the cocrystal is challenging, as dissolving the product would sacrifice the cocrystals. As sublimation is traditionally regarded as a purification technique, we attempted to purify the compound by subliming the starting materials, leaving the pure cocrystal. This is rationalized by the cocrystallized product having a lower vapor pressure than the starting materials,[105] with sublimation exploiting this difference. To this end, compound **3c** was prepared by a multitude of synthetic techniques, purposely adding excess donor in some cases, to show that sublimation can be relevant to a range of synthetic techniques. These cocrystal preparation methods include: ball milling, ball milling with 20% excess donor, expedited cosublimation with excess donor and excess heat, liquid-assisted grinding in a mortar and pestle with an insufficient grinding time of 1 min, and slow evaporation subsequently doped with 20% excess donor. Once prepared, each product was split into two parts, with only one part purified by sublimation under a vacuum of $\sim 1 \times 10^{-1}$ mbar and a temperature of 70 °C, for up to 15 min. Each product was analyzed by ^{19}F SSNMR before and after purification, shown in Figure 8, to observe the presence of *p*DITFB starting material. Additional ^{13}C SSNMR, IR spectroscopy, PXRD, and elemental analysis examinations were performed on each product, the results of which can be found in the Supporting Information.

The impure samples of **3c** clearly show an important presence of excess *p*DITFB in the ^{19}F SSNMR spectra, which is denoted by a dashed black line. In contrast, the samples purified by sublimation show a significant reduction in excess starting material, with none being detected in most cases. As for sample **3c** prepared by expedited cosublimation, the slight presence of excess *p*DITFB in the product is attributed to insufficient sublimation times, given the abundance of excess starting material in the impure product. In contrast to the ^{19}F SSNMR spectra observing the XB donor, the ^{13}C spectra

DOI: 10.1021/acs.cgd.8b01089
Cryst. Growth Des. 2018, 18, 6227−6238

observing the XB acceptor were less clear, given the smaller chemical shift changes of 0.4 ± 0.1 ppm between pure DABCO and the cocrystal. However, the ^{13}C SSNMR spectra support the formation of the cocrystals in each product, with the resulting broader line shape suggesting the presence of excess acceptor in the unpurified products. Upon purification by sublimation, an improvement in the ^{13}C line shapes is observed, resulting in superimposable spectra across all samples. Control experiments consisting of heating combination **3c** at atmospheric pressure suggest that the overall purification process is primarily due to sublimation rather than the thermal formation of cocrystals (see Figures S45 and S46 of the Supporting Information). Although heating did result in the formation of cocrystals, it did not remove excess starting materials from the powdered product.

CONCLUSIONS

Cosublimation has allowed for the rapid screening of cocrystals, yielding crystals suitable for single-crystal X-ray diffraction, in as little as 20 h. This method has yielded novel and previously inaccessible halogen-bonded architectures. Among the new structural motifs investigated here, a distinguishably weaker and less linear halogen bond is present in structure **2a**, in comparison to its perfluorinated analogue, **3a–i**. The cosublimation method enabled the preparation of the first cocrystal featuring a halogen bond to the nitrile group of 1-adamantanecarbonitrile, resulting in a novel solid-state molecular rotor. Third, the structure of the cocrystal formed between the tritopic halogen-bond donor *sym*TFTIB and DABCO, observed only in the sublimated product, reveals a donor fully saturated by halogen bonds, thereby overcoming an anticooperative halogen-bonding effect. When performed in a vacuum sublimation apparatus, cocrystal preparation times were reduced to under 30 min. This technique also provides the opportunity to purify powdered cocrystals. Overall, we have shown that sublimation is a promising technique in the areas of cocrystal engineering and halogen bonding, and sublimation has performed exceptionally well for the iconic perfluorinated halogen-bond donors. As a result of the forgiving nature of the technique to differences in volatility, it is anticipated that cosublimation may find broad usage across the field of crystal engineering and in the study of noncovalent interactions. The method enables broader explorations of the polymorphic energy landscape.

ASSOCIATED CONTENT

Supporting Information

The Supporting Information is available free of charge on the ACS Publications website at DOI: 10.1021/acs.cgd.8b01089.

Synthetic details, experimental procedures, NMR spectra, IR spectra, PXRD data, ORTEP plots, and elemental analyses (PDF)

Accession Codes

CCDC 1854043–1854045, 1854052, and 1854304 contain the supplementary crystallographic data for this paper. These data can be obtained free of charge via www.ccdc.cam.ac.uk/data_request/cif, or by emailing data_request@ccdc.cam.ac.uk, or by contacting The Cambridge Crystallographic Data Centre, 12 Union Road, Cambridge CB2 1EZ, UK; fax: +44 1223 336033.

AUTHOR INFORMATION

Corresponding Author

*Phone: +1-613-562-5800 ext. 2018. Fax: +1-613-562-5170 E-mail: dbryce@uottawa.ca.

ORCID

David L. Bryce: 0000-0001-9989-796X

Notes

The authors declare no competing financial interest.

ACKNOWLEDGMENTS

P.M.J.S. and D.L.B. thank the Natural Sciences and Engineering Research Council of Canada for a scholarship and for research funding, respectively. We are grateful to L.-A. Roy for technical assistance and to Dr. B. Gabidullin for X-ray services.

REFERENCES

(1) Nishinaga, T. Progress in art and science of crystal growth and its impacts on modern society. *Jpn. J. Appl. Phys.* **2015**, *54*, 050101.

(2) Gilman, J. J. *The Art and Science of Growing Crystals;* John Wiley & Sons Inc.: New York, 1963.

(3) Aitipamula, S.; Banerjee, R.; Bansal, A. K.; Biradha, K.; Cheney, M. L.; Choudhury, A. R.; Desiraju, G. R.; Dikundwar, A. G.; Dubey, R.; Duggirala, N.; Ghogale, P. P.; Ghosh, S.; Goswami, P. K.; Goud, N. R.; Jetti, R. R. K. R.; Karpinski, P.; Kaushik, P.; Kumar, D.; Kumar, V.; Moulton, B.; Mukherjee, A.; Mukherjee, G.; Myerson, A. S.; Puri, V.; Ramanan, A.; Rajamannar, T.; Reddy, C. M.; Rodriguez-Hornedo, N.; Rogers, R. D.; Row, T. N. G.; Sanphui, P.; Shan, N.; Shete, G.; Singh, A.; Sun, C. C.; Swift, J. A.; Thaimattam, R.; Thakur, T. S.; Kumar Thaper, R.; Thomas, S. P.; Tothadi, S.; Vangala, V. R.; Variankaval, N.; Vishweshwar, P.; Weyna, D. R.; Zaworotko, M. J. Polymorphs, Salts, and Cocrystals: What's in a Name? *Cryst. Growth Des.* **2012**, *12*, 2147–2152.

(4) Grothe, E.; Meekes, H.; Vlieg, E.; ter Horst, J. H.; de Gelder, R. Solvates, Salts, and Cocrystals: A Proposal for a Feasible Classification System. *Cryst. Growth Des.* **2016**, *16*, 3237–3243.

(5) Bolton, O.; Matzger, A. J. Improved Stability and Smart-Material Functionality Realized in an Energetic Cocrystal. *Angew. Chem., Int. Ed.* **2011**, *50*, 8960–8963.

(6) Rybtchinski, B. Adaptive Supramolecular Nanomaterials Based on Strong Noncovalent Interactions. *ACS Nano* **2011**, *5*, 6791–6818.

(7) Liu, K.; Kang, Y.; Wang, Z.; Zhang, X. Reversible and Adaptive Functional Supramolecular Materials: "Noncovalent Interaction" Matters. *Adv. Mater.* **2013**, *25*, 5530–5548.

(8) Rupasinghe, T. P.; Hutchins, K. M.; Bandaranayake, B. S.; Ghorai, S.; Karunatilake, C.; Bučar, D.-K.; Swenson, D. C.; Arnold, M. A.; MacGillivray, L. R.; Tivanski, A. V. Mechanical Properties of a Series of Macro- and Nanodimensional Organic Cocrystals Correlate with Atomic Polarizability. *J. Am. Chem. Soc.* **2015**, *137*, 12768–12771.

(9) Spitzer, D.; Risse, B.; Schnell, F.; Pichot, V.; Klaumünzer, M.; Schaefer, M. R. Continuous engineering of nano-cocrystals for medical and energetic applications. *Sci. Rep.* **2014**, *4*, 6575.

(10) Halasz, I.; Puškarić, A.; Kimber, S. A. J.; Beldon, P. J.; Belenguer, A. M.; Adams, F.; Honkimäki, V.; Dinnebier, R. E.; Patel, B.; Jones, W.; Štrukil, V.; Friščić, T. Real-Time In Situ Powder X-ray Diffraction Monitoring of Mechanochemical Synthesis of Pharmaceutical Cocrystals. *Angew. Chem., Int. Ed.* **2013**, *52*, 11538–11541.

(11) Qiao, N.; Li, M.; Schlindwein, W.; Malek, N.; Davies, A.; Trappitt, G. Pharmaceutical cocrystals: An Overview. *Int. J. Pharm.* **2011**, *419*, 1–11.

(12) Schultheiss, N.; Newman, A. Pharmaceutical Cocrystals and Their Physicochemical Properties. *Cryst. Growth Des.* **2009**, *9*, 2950–2967.

(13) Remenar, J. F.; Morissette, S. L.; Peterson, M. L.; Moulton, B.; MacPhee, J. M.; Guzmán, H. R.; Almarsson, Ö. Crystal Engineering of

Novel Cocrystals of a Triazole Drug with 1,4-Dicarboxylic Acids. *J. Am. Chem. Soc.* **2003**, *125*, 8456−8457.
(14) Sun, L.; Zhu, W.; Yang, F.; Li, B.; Ren, X.; Zhang, X.; Hu, W. Molecular cocrystals: design, charge-transfer and optoelectronic functionality. *Phys. Chem. Chem. Phys.* **2018**, *20*, 6009−6023.
(15) Christopherson, J.-C.; Topić, F.; Barrett, C. J.; Friščić, T. Halogen-Bonded Cocrystals as Optical Materials: Next-Generation Control over Light-Matter Interactions. *Cryst. Growth Des.* **2018**, *18*, 1245−1259.
(16) Politzer, P.; Murray, J. S.; Clark, T.; Resnati, G. The σ-hole revisited. *Phys. Chem. Chem. Phys.* **2017**, *19*, 32166−32178.
(17) Cavallo, G.; Metrangolo, P.; Pilati, T.; Resnati, G.; Terraneo, G. Naming Interactions from the Electrophilic Site. *Cryst. Growth Des.* **2014**, *14*, 2697−2702.
(18) Metrangolo, P.; Meyer, F.; Pilati, T.; Resnati, G.; Terraneo, G. Halogen Bonding in Supramolecular Chemistry. *Angew. Chem., Int. Ed.* **2008**, *47*, 6114−6127.
(19) Politzer, P.; Murray, J. S.; Clark, T. Halogen Bonding: an electrostatically-driven highly directional noncovalent interaction. *Phys. Chem. Chem. Phys.* **2010**, *12*, 7748−7757.
(20) Clark, T.; Hennemann, M.; Murray, J. S.; Politzer, P. Halogen bonding: the σ-hole. *J. Mol. Model.* **2007**, *13*, 291−296.
(21) Politzer, P.; Murray, J. S. σ-Hole Interactions: Perspectives and Misconceptions. *Crystals* **2017**, *7*, 212−226.
(22) Desiraju, G. R.; Ho, P. S.; Kloo, L.; Legon, A. C.; Marquardt, R.; Metrangolo, P.; Politzer, P.; Resnati, G.; Rissanen, K. Definition of the halogen bond (IUPAC Recommendations 2013). *Pure Appl. Chem.* **2013**, *85*, 1711−1713.
(23) Cavallo, G.; Metrangolo, P.; Milani, R.; Pilati, T.; Priimagi, A.; Resnati, G.; Terraneo, G. The Halogen Bond. *Chem. Rev.* **2016**, *116*, 2478−2601.
(24) Gilday, L. C.; Robinson, S. W.; Barendt, T. A.; Langton, M. J.; Mullaney, B. R.; Beer, P. D. Halogen Bonding in Supramolecular Chemistry. *Chem. Rev.* **2015**, *115*, 7118−7195.
(25) Li, B.; Zang, S.-Q.; Wang, L.-Y.; Mak, T. C. W. Halogen Bonding: A powerful, emerging tool for constructing high-dimensional metal-containing supramolecular networks. *Coord. Chem. Rev.* **2016**, *308*, 1−21.
(26) Berger, G.; Soubhye, J.; Meyer, F. Halogen bonding in polymer science: from crystal engineering to functional supramolecular polymers and materials. *Polym. Chem.* **2015**, *6*, 3559−3580.
(27) Lieffrig, J.; Jeannin, O.; Fourmigué, M. Expanded Halogen-Bonded Anion Organic Networks with Star-Shaped Iodoethynyl-Substituted Molecules: From Corrugated 2D Hexagonal Lattices to Pyrite-Type 2-Fold Interpenetrated Cubic Lattices. *J. Am. Chem. Soc.* **2013**, *135*, 6200−6210.
(28) Riel, A. M. S.; Decato, D. A.; Sun, J.; Massena, C. J.; Jessop, M. J.; Berryman, O. B. The intramolecular hydrogen bonded-halogen bond: a new strategy for preorganization and enhanced binding. *Chem. Sci.* **2018**, *9*, 5828−5836.
(29) Huber, S. M.; Scanlon, J. D.; Jimenez-Izal, E.; Ugalde, J. M.; Infante, I. On the directionality of halogen bonding. *Phys. Chem. Chem. Phys.* **2013**, *15*, 10350−10357.
(30) Riley, K. E.; Murray, J. S.; Fanfrlík, J.; Řezáč, J.; Solá, R. J.; Concha, M. C.; Ramos, F. M.; Politzer, P. Halogen bond tunability I: the effects of aromatic fluorine substitution on the strengths of halogen-bonding interactions involving chlorine, bromine, and iodine. *J. Mol. Model.* **2011**, *17*, 3309−3318.
(31) Riley, K. E.; Murray, J. S.; Fanfrlík, J.; Řezáč, J.; Solá, R. J.; Concha, M. C.; Ramos, F. M.; Politzer, P. Halogen bond tunability II: the varying roles of electrostatic and dispersion contributions to attraction in halogen bonds. *J. Mol. Model.* **2013**, *19*, 4651−4659.
(32) Priimagi, A.; Cavallo, G.; Metrangolo, P.; Resnati, G. The Halogen Bond in the Design of Functional Supramolecular Materials: Recent Advances. *Acc. Chem. Res.* **2013**, *46*, 2686−2695.
(33) Mukherjee, A.; Tothadi, S.; Desiraju, G. R. Halogen Bonds in Crystal Engineering: Like Hydrogen Bonds yet Different. *Acc. Chem. Res.* **2014**, *47*, 2514−2524.
(34) Auffinger, P.; Hays, F. A.; Westhof, E.; Ho, P. S. Halogen bonds in biological molecules. *Proc. Natl. Acad. Sci. U. S. A.* **2004**, *101*, 16789−16794.
(35) Scholfield, M. R.; Vander Zanden, C. M.; Carter, M.; Ho, P. S. Halogen bonding (X-bonding): A biological perspective. *Protein Sci.* **2013**, *22*, 139−152.
(36) Bondi, A. van der Waals Volumes and Radii. *J. Phys. Chem.* **1964**, *68*, 441−451.
(37) Ho, P. S. Halogen bonding in medicinal chemistry: from observation to prediction. *Future Med. Chem.* **2017**, *9*, 637−640.
(38) Wilcken, R.; Zimmermann, M. O.; Lange, A.; Joerger, A. C.; Boeckler, F. M. Principles and Applications of Halogen Bonding in Medicinal Chemistry and Chemical Biology. *J. Med. Chem.* **2013**, *56*, 1363−1388.
(39) Ford, M. C.; Ho, P. S. Computational Tools To Model Halogen Bonds in Medicinal Chemistry. *J. Med. Chem.* **2016**, *59*, 1655−1670.
(40) Ravi, A.; Oshchepkov, A. S.; German, K. E.; Kirakosyan, G. A.; Safonov, A. V.; Khrustalev, V. N.; Kataev, E. A. Finding a receptor design for selective recognition of perrhenate and pertechnetate: hydrogen *vs.* halogen bonding. *Chem. Commun.* **2018**, *54*, 4826−4829.
(41) Molina, P.; Zapata, F.; Caballero, A. Anion Recognition Strategies Based on Combined Noncovalent Interactions. *Chem. Rev.* **2017**, *117*, 9907−9972.
(42) Catalano, L.; Perez-Estrada, S.; Wang, H.-H.; Ayitou, A.J.-L.; Khan, S. I.; Terraneo, G.; Metrangolo, P.; Brown, S.; Garcia-Garibay, M. A. Rotational Dynamics of Diazabicyclo[2.2.2]octane in Isomorphous Halogen-Bonded Co-crystals: Entropic and Enthalpic Effects. *J. Am. Chem. Soc.* **2017**, *139*, 843−848.
(43) Lemouchi, C.; Vogelsberg, C. S.; Zorina, L.; Simonov, S.; Batail, P.; Brown, S.; Garcia-Garibay, M. A. Ultra-fast Rotors for Molecular Machines and Functional Materials via Halogen Bonding: Crystals of 1,4-Bis(iodoethynyl)bicycle[2.2.2]octane with Distinct Gigahertz Rotation at Two Sites. *J. Am. Chem. Soc.* **2011**, *133*, 6371−6379.
(44) Chan, Y.-C.; Yeung, Y.-Y. Halogen Bond Catalyzed Bromocarbocyclization. *Angew. Chem., Int. Ed.* **2018**, *57*, 3483−3487.
(45) Carreras, L.; Serrano-Torné, M.; van Leeuwen, P. W. N. M.; Vidal-Ferran, A. XBPhos-Rh: a halogen-bond assembled supramolecular catalyst. *Chem. Sci.* **2018**, *9*, 3644−3648.
(46) Gliese, J.-P.; Jungbauer, S. H.; Huber, S. M. A halogen-bonding-catalyzed Michael addition reaction. *Chem. Commun.* **2017**, *53*, 12052−12055.
(47) Vioglio, P. C.; Chierotti, M. R.; Gobetto, R. Solid-state nuclear magnetic resonance as a tool for investigating the halogen bond. *CrystEngComm* **2016**, *18*, 9173−9184.
(48) Szell, P. M. J.; Bryce, D. L. Solid-State NMR Studies of Halogen Bonding. In *Modern Magnetic Resonance;* Springer: New York, 2016; pp 1−18.
(49) Bryce, D. L.; Viger-Gravel, J. Solid-State NMR Study of Halogen-Bonded Adducts. *Top. Curr. Chem.* **2014**, *358*, 183−204.
(50) Szell, P. M. J.; Cavallo, G.; Terraneo, G.; Metrangolo, P.; Gabidullin, B.; Bryce, D. L. Comparing the Halogen Bond to the Hydrogen Bond by Solid-State NMR: Anion Coordinated Dimers from 2- & 3-Iodoethynylpyridine Salts. *Chem. - Eur. J.* **2018**, *24*, 11364.
(51) Viger-Gravel, J.; Leclerc, S.; Korobkov, I.; Bryce, D. L. Correlation between ^{13}C chemical shifts and the halogen bonding environment in a series of solid *para*-diiodotetrafluorobenzene complexes. *CrystEngComm* **2013**, *15*, 3168−3177.
(52) Cerreia Vioglio, P.; Catalano, L.; Vasylyeva, V.; Nervi, C.; Chierotti, M. R.; Resnati, G.; Gobetto, R.; Metrangolo, P. Natural Abundance ^{15}N and ^{13}C Solid-State NMR Chemical Shifts: High Sensitivity Probes of the Halogen Bond Geometry. *Chem. - Eur. J.* **2016**, *22*, 16819−16828.
(53) Viger-Gravel, J.; Meyer, J. E.; Korobkov, I.; Bryce, D. L. Probing halogen bonds with solid-state NMR spectroscopy: observation and interpretation of $J(^{77}Se, ^{31}P)$ coupling in halogen-bonded P = Se···I motifs. *CrystEngComm* **2014**, *16*, 7285−7297.

DOI: 10.1021/acs.cgd.8b01089
Cryst. Growth Des. 2018, 18, 6227−6238

(54) Xu, Y.; Viger-Gravel, J.; Korobkov, I.; Bryce, D. L. Mechanochemical Production of Halogen-Bonded Solids Featuring P = O···I-C Motifs and Characterization via X-ray Diffraction, Solid-State Multinuclear Magnetic Resonance, and Density Functional Theory. *J. Phys. Chem. C* **2015**, *119*, 27104−27117.
(55) Szell, P. M. J.; Bryce, D. L. ^{35}Cl Solid-State NMR and Computational Study of Chlorine Halogen Bond Donors in Single-Component Crystalline Chloronitriles. *J. Phys. Chem. C* **2016**, *120*, 11121−11130.
(56) Cerreia Vioglio, P.; Szell, P. M. J.; Chierotti, M. R.; Gobetto, R.; Bryce, D. L. $^{79/81}$Br nuclear quadrupole resonance spectroscopic characterization of halogen bonds in supramolecular assemblies. *Chem. Sci.* **2018**, *9*, 4555−4561.
(57) Viger-Gravel, J.; Leclerc, S.; Korobkov, I.; Bryce, D. L. Direct Investigation of Halogen Bonds by Solid-State Multinuclear Magnetic Resonance Spectroscopy and Molecular Orbital Analysis. *J. Am. Chem. Soc.* **2014**, *136*, 6929−6942.
(58) Szell, P. M. J.; Gabriel, S. A.; Gill, R. D. D.; Wan, S. Y. H.; Gabidullin, B.; Bryce, D. L. ^{13}C and ^{19}F solid-state NMR and X-ray crystallographic study of halogen-bonded frameworks featuring nitrogen-containing heterocycles. *Acta Crystallogr., Sect. C: Struct. Chem.* **2017**, *C73*, 157−167.
(59) Szell, P. M. J.; Dragon, J.; Zablotny, S.; Harrigan, S. R.; Gabidullin, B.; Bryce, D. L. Mechanochemistry and cocrystallization of 3-iodoethynylbenzoic acid with nitrogen-containing heterocycles: concurrent halogen and hydrogen bonding. *New J. Chem.* **2018**, *42*, 10493−10501.
(60) Cinčić, D.; Friščić, T.; Jones, W. A Stepwise Mechanism for the Mechanochemical Synthesis of Halogen-Bonded Cocrystal Architectures. *J. Am. Chem. Soc.* **2008**, *130*, 7524−7525.
(61) Choquesillo-Lazarte, D.; Nemec, V.; Cinčić, D. Halogen bonded cocrystals of active pharmaceutical ingredients: pyrazinamide, lidocaine and pentoxifylline in combination with haloperfluorinated compounds. *CrystEngComm* **2017**, *19*, 5293−5299.
(62) Mavračić, J.; Cinčić, D.; Kaitner, B. Halogen bonding of N-bromosuccinimide by grinding. *CrystEngComm* **2016**, *18*, 3343−3346.
(63) Eraković, M.; Nemec, V.; Lež, T.; Porupski, I.; Stilinović, V.; Cinčić, D. Halogen Bonding of *N*-Bromophthalimide by Grinding and Solution Crystallization. *Cryst. Growth Des.* **2018**, *18*, 1182−1190.
(64) Lisac, K.; Nemec, V.; Topić, F.; Arhangelskis, M.; Hindle, P.; Tran, R.; Huskić, I.; Morris, A. J.; Friščić, T.; Cinčić, D. Experimental and Theoretical Investigation of Structures, Stoichiometric Diversity, and Bench Stability of Cocrystals with a Volatile Halogen Bond Donor. *Cryst. Growth Des.* **2018**, *18*, 2387−2396.
(65) Katsenis, A. D.; Puškarić, A.; Štrukil, V.; Mottillo, C.; Julien, P. A.; Užarević, K.; Pham, M.-H.; Do, T.-O.; Kimber, S. A. J.; Lazić, P.; Magdysyuk, O.; Dinnebier, R. E.; Halasz, I.; Friščić, T. *In Situ* X-ray diffraction monitoring of a mechanochemical reaction reveals a unique topology metal-organic framework. *Nat. Commun.* **2015**, *6*, 6662.
(66) Mullin, J. W. *Crystallization;* Butterworth-Heinemann: Burlington, MA, 2001; pp 358−363.
(67) Kobyakov, P. S.; Moore, A.; Raguse, J. M.; Swanson, D. E.; Sampath, W. S. Deposition and characterization of $Cd_{1-x}Mg_xTe$ thin films grown by a novel cosublimation method. *J. Vac. Sci. Technol., A* **2014**, *32*, 021511.
(68) Robinson, S. W.; Haynes, D. A.; Rawson, J. M. Co-crystal formation with 1,2,3,5-dithiadiazolyl radicals. *CrystEngComm* **2013**, *15*, 10205−10211.
(69) Qian, H.-F.; Wang, Y.-G.; Geng, J.; Huang, W. A rare case of a dye co-crystal showing better dyeing performance. *CrystEngComm* **2015**, *17*, 2083−2086.
(70) Zhang, T.; Yu, Q.; Li, X.; Ma, X. Preparation of 2:1 urea-succinic acid cocrystals by sublimation. *J. Cryst. Growth* **2017**, *469*, 114−118.
(71) Eddleston, M. D.; Sivachelvam, S.; Jones, W. Screening for polymorphs of cocrystals: a case study. *CrystEngComm* **2013**, *15*, 175−181.
(72) Shan, N.; Zaworotko, M. J. The role of cocrystals in pharmaceutical science. *Drug Discovery Today* **2008**, *13*, 440−446.
(73) Boterashvili, M.; Lahav, M.; Shankar, S.; Facchetti, A.; van der Boom, M. E. On-Surface Solvent-Free Crystal-to-Co-crystal Conversion by Non-Covalent Interactions. *J. Am. Chem. Soc.* **2014**, *136*, 11926−11929.
(74) Shirman, T.; Freeman, D.; Posner, Y. D.; Feldman, I.; Facchetti, A.; van der Boom, M. E. Assembly of Crystalline Halogen-Bonded Materials by Physical Vapor Deposition. *J. Am. Chem. Soc.* **2008**, *130*, 8162−8163.
(75) Bailey, R. D.; Buchanan, M. L.; Pennington, W. T. Molecular Complexes of 1,4-Diazines with Iodine. *Acta Crystallogr., Sect. C: Cryst. Struct. Commun.* **1992**, *C48*, 2259−2262.
(76) Vatèle, J.-M. One-Pot Oxidative Conversion of Alcohols into Nitriles by Using a TEMPO/PhI(OAc)$_2$/NH$_4$OAc System. *Synlett* **2014**, *25*, 1275−1278.
(77) Scheler, U. High-speed MAS-NMR investigations on radiation-modified fluoropolymers. *Solid State Nucl. Magn. Reson.* **1998**, *12*, 9−13.
(78) *APEX2;* Bruker AXS Inc.: Madison, WI, 2012.
(79) Altomare, A.; Cascarano, G.; Giacovazzo, C.; Guagliardi, A.; Burla, M. C.; Polidori, G.; Camalli, M. *SIR*92 − a program for automatic solution of crystal structures by direct methods. *J. Appl. Crystallogr.* **1994**, *27*, 435.
(80) Sheldrick, G. M. *SHELXT*- Integrated space-group and crystal-structure determination. *Acta Crystallogr., Sect. A: Found. Adv.* **2015**, *A71*, 3−8.
(81) Farrugia, L. J. *WinGX* and *ORTEP for Windows*: an update. *J. Appl. Crystallogr.* **2012**, *45*, 849−854.
(82) Brandenburg, K. *Diamond*, version 4.5.1; Crystal Impact: Bonn, Germany, 2018.
(83) Spek, A. L. Structure validation in chemical crystallography. *Acta Crystallogr., Sect. D: Biol. Crystallogr.* **2009**, *D65*, 148−155.
(84) Syssa-Magalé, J.-L.; Boubekeur, K.; Palvadeau, P.; Meerschaut, A.; Schöllhorn, B. The tailoring of crystal structures *via* the self-assembly of organic coordination compounds by N···I non-covalent halogen bonds: co-crystals of sterically hindered N-heterocycles and 1,4-diiodotetrafluorobenzene. *CrystEngComm* **2005**, *7*, 302−308.
(85) Pfrunder, M. C.; Micallef, A. S.; Rintoul, L.; Arnold, D. P.; Davy, K. J. P.; McMurtrie, J. Exploitation of the Menshutkin Reaction for the Controlled Assembly of Halogen Bonded Architectures Incorporating 1,2-Diiodotetrafluorobenzene and 1,3,5-Triiodotrifluorobenzene. *Cryst. Growth Des.* **2012**, *12*, 714−724.
(86) Syssa-Magalé, J.-L.; Boubekeur, K.; Leroy, J.; Chamoreau, L.-M.; Fave, C.; Schöllhorn, B. Directed synthesis of a halogen-bonded open porphyrin network. *CrystEngComm* **2014**, *16*, 10380−10384.
(87) Pohl, S. Synthese und Kristallstruktur eines polymeren Addukts von 2.2′-Dipyridil mit Iod: $C_{10}H_8N_2I_6$. *Z. Naturforsch., B: J. Chem. Sci.* **1983**, *38b*, 1535−1538.
(88) Peuronen, A.; Valkonen, A.; Kortelainen, M.; Rissanen, K.; Lahtinen, M. Halogen Bonding-Based "Catch and Release": Reversible Solid-State Entrapment of Elemental Iodine with Monoalkylated DABCO Salts. *Cryst. Growth Des.* **2012**, *12*, 4157−4169.
(89) Cinčić, D.; Friščić, T.; Jones, W. Structural Equivalence of Br and I Halogen Bonds: A Route to Isostructural Materials with Controllable Properties. *Chem. Mater.* **2008**, *20*, 6623−6626.
(90) Bolte, M. *CSD Communication*, 2004, deposition No. 232562.
(91) Cinčić, D.; Friščić, T.; Jones, W. Isostructural Materials Achieved by Using Structurally Equivalent Donors and Acceptors in Halogen-Bonded Cocrystals. *Chem. - Eur. J.* **2008**, *14*, 747−753.
(92) Groom, C. R.; Bruno, I. J.; Lightfoot, M. P.; Ward, S. C. The Cambridge Structural Database. *Acta Crystallogr., Sect. B: Struct. Sci., Cryst. Eng. Mater.* **2016**, *B72*, 171−179.
(93) Laurence, C.; Graton, J.; Berthelot, M.; El Ghomari, M. J. The Diiodine Basicity Scale: Toward a General Halogen-Bond Basicity Scale. *Chem. - Eur. J.* **2011**, *17*, 10431−10444.

DOI: 10.1021/acs.cgd.8b01089
Cryst. Growth Des. 2018, 18, 6227−6238

(94) Le Questel, J.-Y.; Berthelot, M.; Laurence, C. Hydrogen-bond acceptor properties of nitriles: a combined crystallographic and ab initio theoretical investigation. *J. Phys. Org. Chem.* **2000**, *13*, 347−358.
(95) Eichele, K. *WSolids1,* version 1.21.3; Universität Tübingen, 2015.
(96) Amoureux, J. P.; Castelain, M.; Bee, M.; Arnaud, B.; Shouteenten, M. L. An N.M.R. study of molecular motions in the plastic phases of 1-cyanoadamantane. *Mol. Phys.* **1981**, *42*, 119−127.
(97) Amoureux, J. P.; Decressain, R.; Sahour, M.; Cochon, E. Molecular motions in glassy crystal cyanoadamantane: a proton spin-lattice relaxation study. *J. Phys. II* **1992**, *2*, 249−259.
(98) Sauvajol, J. L.; Lefebvre, J.; Amoureux, J. P.; Bée, M. Dynamical properties of 1-cyanoadamantane in the disordered phase. *J. Phys. C: Solid State Phys.* **1982**, *15*, 6523−6532.
(99) Lucassen, A. C. B.; Karton, A.; Leitus, G.; Shimon, L. J. W.; Martin, J. M. L.; van der Boom, M. E. Co-Crystallization of Sym-Triiodo-Trifluorobenzene with Bipyridyl Donors: Consistent Formation of Two Instead of Anticipated Three N···I Halogen Bonds. *Cryst. Growth Des.* **2007**, *7*, 386−392.
(100) Ding, X.-H.; Ou, C.-J.; Wang, S.; Xie, L.-H.; Lin, J.-Y.; Wang, J.-P.; Huang, W. Co-crystallization of 1,3,5-trifluoro-2,4,6-triiodobenzene (1,3,5-TFTIB) with a variety of Lewis bases through halogen-bonding interactions. *CrystEngComm* **2017**, *19*, 5504−5521.
(101) Nicolas, I.; Barrière, F.; Jeannin, O.; Fourmigué, M. Sequential Halogen Bonding with Ditopic Donors: σ-Hole Evolutions upon Halogen Bond Formation. *Cryst. Growth Des.* **2016**, *16*, 2963−2971.
(102) Roper, L. C.; Präsang, C.; Kozhevnikov, V. N.; Whitwood, A. C.; Karadakov, P. B.; Bruce, D. W. Experimental and Theoretical Study of Halogen-Bonded Complexes of DMAP with Di- and Triiodofluorobenzenes. A Complex with a Very Short N···I Halogen Bond. *Cryst. Growth Des.* **2010**, *10*, 3710−3720.
(103) Hidalgo, P. I.; Leal, S.; Jiménez, C. A.; Vöhringer-Martinez, E.; Herrera, B.; Pasán, J.; Ruiz-Pérez, C.; Bruce, D. W. Extending the halogen-bonded supramolecular synthon concept to 1,3,4-oxadiazole derivatives. *CrystEngComm* **2016**, *18*, 42−47.
(104) Carletta, A.; Zbačnik, M.; Vitković, M.; Tumanov, N.; Stilinović, V.; Wouters, J.; Cinčić, D. Halogen-bonded cocrystals of *N*-salicylidene Schiff bases and iodoperfluorinated benzenes: hydroxyl oxygen as halogen bond acceptor. *CrystEngComm*. In press. **2018** DOI: 10.1039/C8CE01145A.
(105) Aakeröy, C. B.; Wijethunga, T. K.; Benton, J.; Desper, J. Stabilizing volatile liquid chemicals using co-crystallization. *Chem. Commun.* **2015**, *51*, 2425−2428.

DOI: 10.1021/acs.cgd.8b01089
Cryst. Growth Des. 2018, 18, 6227−6238

Summary of Part 4 – Crystal Engineering, Mechanochemistry & Cosublimation

In Chapter 10, we have prepared a series of halogen bonded frameworks built from 1,3,5-tri(iodoethynyl)-2,4,6-trifluorobenzene (*sym*TIETFB), uncovering a series of six novel crystal structures exhibiting halogen bonds. In summary, we have observed some unique hexagonal frameworks, with the halide being coordinated with up to six halogen bonds. The size of the cation was shown to play a contributing factor to the framework, with larger cations favoring loose packing, including a honeycomb network. The halogen bond donor was investigated by solution and solid-state NMR, revealing complex *J*-couplings between the ^{19}F and ^{13}C isotopes. Since the release of this article in the special issue in halogen bonding in *Acta Crystallographica*, it has garnered a scientific commentary by Dr. Marc Fourmigué, highlighting the structures accessible using this halogen bond donor.[1]

One difficulty encountered during this work was the usage of solvent-evaporation as a synthetic method to prepare the cocrystals. This technique created a bottleneck in the production, typically requiring a week or more to prepare the final product. Upon the failure of the cocrystallization, there were many degrees of freedom to consider in diagnosing why it had failed, including the choice of solvent, evaporation rate, donor-acceptor mismatch, presence of impurities, and perhaps environmental impacts such as humidity and temperature variations. This has prompted our investigations of alternative preparation methods, such as mechanochemistry and cosublimation.

Not shown in the article of Chapter 10 is a new porous crystal structure, formed between *sym*TIETFB and propyltriphenylphosphonium bromide. This structure features characteristic

channels through the crystal, which would have allowed for the penetration of guest molecules within the crystal lattice. A depiction of the porous crystal structure is shown in Figure 4.4.

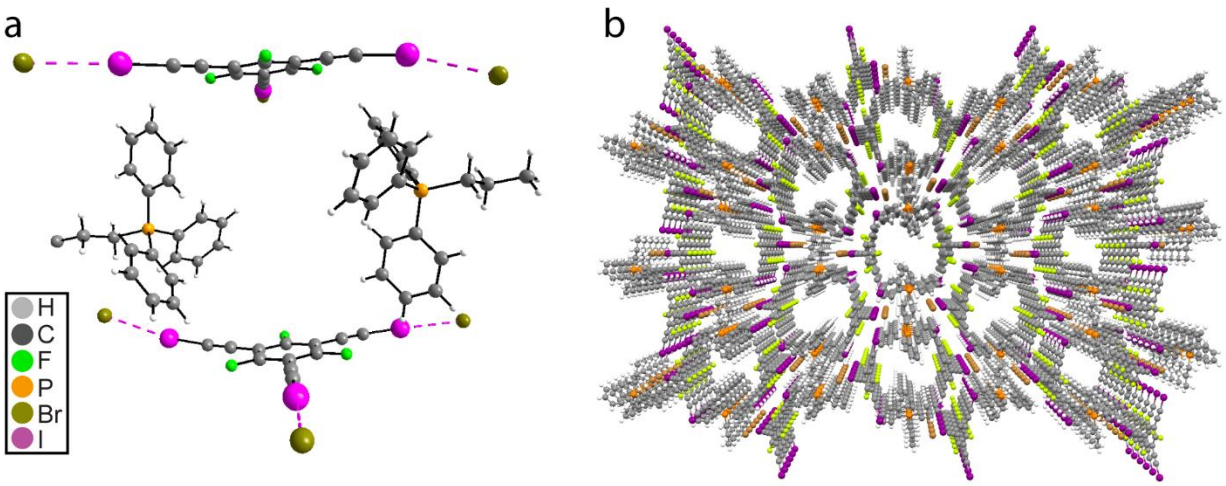

Figure 4.4. Depiction of the crystal structure formed between 1,3,5-tri(iodoethynyl)-2,4,6-trifluorobenzene and propyltriphenylphosphonium bromide. The halogen bonded motif surrounding the pores is shown in **a**, while the crystal packing is shown in **b**, with stereoscopic perspective to clearly show the pore geometry.

While the structure was a potentially exciting avenue of research, it was unfortunately irreproducible despite hundreds of attempts and therefore not included in the original work.

In chapter 11, we use a mechanochemical route towards obtaining a series of halogen bonded cocrystals formed between a new halogen bond donor, 3-iodoethynylbenzoic acid, and nitrogen-containing heterocycles. Featuring both a hydrogen bonding moiety (carboxylic acid) and a halogen bond donor (iodoacetylene), we have observed a combination of hydrogen & halogen bonding in the crystal frameworks. Of interest was structure **1a** which exhibited a hydrogen bonded dimer *via* the carboxylic acid bridging, with the iodoethynyl group then coordinating a 2,3,5,6-tetramethylpyrazine molecule. The final publication, which was featured

as a cover article for a special issue in halogen bonding, serves to support the role of mechanochemistry in preparing halogen bonded cocrystals. Using this approach, our preparation times have been reduced from three to seven days, down to a single hour of ball milling. The combination of ^{13}C solid-state NMR and powder X-ray diffraction supports the occurrence of successful cocrystallization, with the ^{13}C resonance of the C-I carbon being a reliable indicator for the occurrence of halogen bonding.

Using the mechanochemical approach, we have recently been able to achieve a series of unique halogen bonded frameworks featuring the halogen bond donors 3-iodoethynylpyridine and 3-iodoethynylbenzoic acid from Chapter 8 and Chapter 11, respectively, and a series of halide salts. These structures were prepared by Estelle Caron-Poulin and Vincent Morin during their Honours project. Shown in Figure 4.5 are depictions of selected crystal structures.

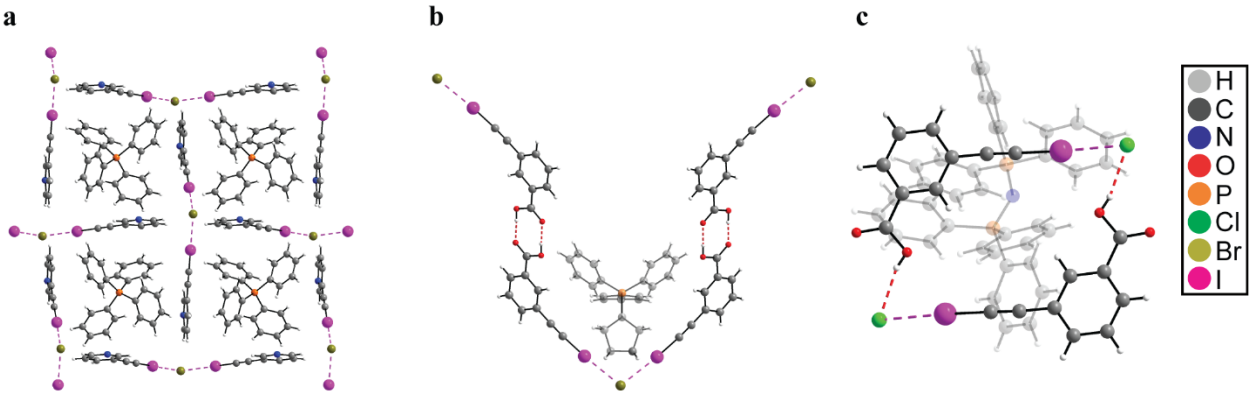

Figure 4.5. Depiction of crystal structures featuring the halogen bond donors 3-iodoethynylpyridine (**a**) and 3-iodoethynylbenzoic acid (**b**, **c**) with a series of halide salts.

The crystal structures shown in Figure 4.5 exhibit unique frameworks, such as a cation encapsulated by C-I···Br^- halogen bonding (Figure 4.5a), an alternating halogen bonding and hydrogen bonding corrugated network, and C-I···Cl^-···H-O dimerization. These compounds

have been prepared at an accelerated rate using mechanochemical routes, with the discovery further opening doors in the field of halogen bonded cocrystallization.

Finally, in chapter 12, we establish cosublimation as a method for the rapid and reliable preparation of halogen bonded cocrystals, which has been featured as a cover article of the journal *Crystal Growth and Design*. We show that this technique can prepare halogen bonded cocrystals in record times, taking a few hours to prepare crystals suitable for single crystal X-ray diffraction, and ~15 minutes to prepare bulk microcrystalline samples. Furthermore, we apply cosublimation to purify cocrystals obtained from several synthetic methods; thereby allowing the rapid removal of excess starting materials from the final product, rather than simply having to restart the process. Overall, this synthetic method was shown to be very convenient, and we have since built our own two-zoned tube furnace in our laboratory in effort of increasing our crystal engineering capabilities. Cosublimation has been applied to some of our recent studies, such as Chapter 6 and Chapter 9, allowing the projects to be completed within the time frame of my doctoral studies.

References.

[1] Fourmigué, M. *Acta Cryst.* **2017**, *B73*, 153-162.

Part 5 – Final Conclusions

5.1 - Recapitulations.

The halogen bond has been experiencing a rise in interest over the last decade, with its directionality and tuneability being key in creating new supramolecular architectures. Since the first reports in the late 1990's,[1,2] the number of crystal structures published every year in the CSD[3] featuring a halogen bond has grown significantly, shown in Figure 5.1. This growth is likely to be maintained for many years to come, especially as halogen bonding finds new applications. In parallel, other σ-hole based interactions, such as the chalcogen and pnictogen bonds, will likely experience an increase in interest in the coming years, with part of the halogen bonding community shifting their focus on these emerging interactions.[4]

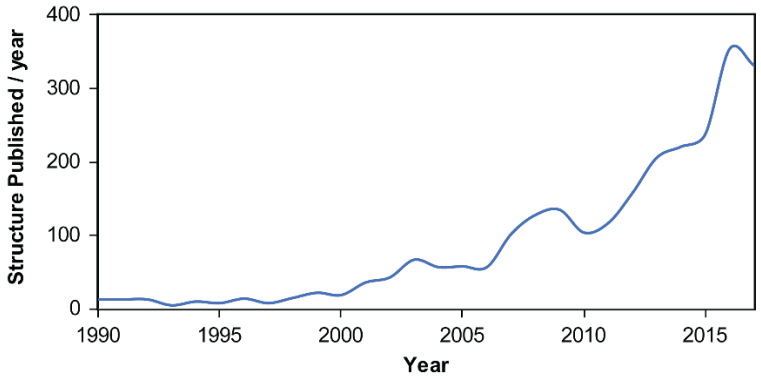

Figure 5.1. Number of crystal structures published per year in the CSD[3] featuring either the C-X···N or C-X···O halogen bonding motif (X = Br, I), between 1990 and 2017.

The halogen bond can be divided into its two components: the halogen bond donor with the halogen atom, and the electron-rich halogen bond acceptor. In this thesis, we have analyzed each individual component of the halogen bond, the surrounding environment, its application in crystal engineering, and several synthetic methods for preparing halogen bonded materials. In

Part 1 of this thesis, we have introduced the halogen bond and presented the fundamental theory necessary to understand the analytical approaches presented in this thesis. Additionally, we have compared solid-state NMR to NQR spectroscopy in Chapter 3, with a focus on the quadrupolar halogens to further illustrate the potential roles of both spectroscopic techniques used for characterizing the halogen bond donor.

Part 2 of the thesis has focused on characterizing the changes in the electric field gradient of the halogen bond donor upon the formation of C-X···N halogen bonds (X = Cl, Br, I). In Chapter 4, we have applied a combination of solid-state NMR and NQR spectroscopy observing the ^{35}Cl nucleus to investigate the C-Cl···N halogen bond in a series of chloronitrile compounds. While the chlorine halogen bond is certainly weak and thus challenging to cocrystallize, the interpretation of the changes in the EFG was aided by molecular symmetry. The observed increase in the C_Q upon halogen bonding was between 0.3 and 1.2 MHz. This study was the first direct investigation of the halogen bond donor using ^{35}Cl solid-state NMR spectroscopy.

Chapter 5 detailed the first modern $^{79/81}$Br NQR investigation of the C-Br···N halogen bond, in cocrystals built between 1,4-dibromotetrafluorobenzene and a series of nitrogen-containing heterocycles. As the two bromine isotopes are spin-3/2, nutation NQR was used to measure η, which was key in determining the C_Q from pure $^{79/81}$Br NQR frequencies. This project, performed in collaboration with a research group at the University of Turin (Italy), revealed an increase in the $^{79/81}$Br C_Q on the order of 12 – 20 MHz upon the occurrence of the halogen bond, with NQR being proposed as an effective tool to determine whether a synthetic trial has successfully cocrystallized.

The analysis of the halogen bond donor is completed in Chapter 6, applying ^{127}I NQR to investigate the iodine-based halogen bond, featuring 1,4-diiodobenzene in a series of cocrystals with nitrogen-containing heterocycles. As the ^{127}I nucleus has a spin of 5/2, the two NQR transitions are used to determine both the C_Q and η, affording the complete EFG tensor. The changes in the C_Q are between 52.6 – 73.9 MHz, and overall the changes in the V_{33} follow the order: I > Br > Cl. A series of DFT calculations individually performed a chlorine, bromine, and iodine-based halogen bond donor (haloperfluorobenzene) interacting with a pyridine molecule at varying distances attributes these changes in the C_Q to an increase in the core orbital & lone pair contributions to V_{33}, with a reduction in the contributions from the C-X bonding orbital upon the formation of a halogen bond.

In Part 3 of this thesis, we have investigated the halogen bond acceptor and the environment surrounding the halogen bond. In Chapter 7 of this thesis, we have investigated a series of cocrystals featuring the C-I···N motif with perfluorinated halogen bond donors (1,4-diiodotetrafluorobenzene, 1,3,5-trifluoro-2,4,6-triiodobenzene). Given the high receptivity of the ^{19}F nucleus, we have characterized these cocrystals using both ^{13}C and ^{19}F solid-state NMR. The ^{19}F NMR approach proved to be an under-exploited tool, with the analysis performed on ~20 mg of sample affording a spectrum in a few minutes. The ^{19}F chemical shifts were sensitive to the occurrence of a halogen bond and were used to discern the presence of excess reagents and side phases. This approach proved to be an asset to Chapter 12 of this thesis, allowing for the analysis of the cosublimed products. Furthermore, the ^{13}C solid-state NMR was performed using ^{1}H → ^{13}C cross-polarization to characterize the acceptor molecule, and ^{19}F → ^{13}C cross-polarization to characterize the donor molecule. As a result, a significant increase in signal intensity and resolution was obtained for the donor molecule, allowing for a precise chemical

shift measurement. The extracted ^{19}F and ^{13}C chemical shifts were shown to be advantageous to improve X-ray crystal structures, which was amongst the first NMR crystallographic approaches of refining halogen bonded crystal structures.

In Chapter 8, performed in collaboration with Dr. Metrangolo's research group at the *Politecnico di Milano* (Italy), we have presented a series of self-complimentary halogen bonded compounds based on the halide salts of 2-iodoethynylpyridine and 3-iodoethynylpyridine. In most cases, the halide salts formed a discrete charged dimer, whereas the crystal structure of 2-iodoethynylpridine, which has been published in our separate article,[5] consisted of the first report of a neutral halogen bonded triangle. The isomorphous nature of the compounds in this study was exploited, comparing the ^{13}C, ^{35}Cl and $^{79/81}Br$ solid-state NMR responses across several halogen bonding motifs (C-I···Cl^-; C-I···Br^-; C-I···I^-). The ^{13}C chemical shifts of the carbon covalently bonded to iodine was highest in the order: C-I···Cl^- > C-I···Br^- > C-I···I^- > C-I···N. Further, the ^{35}Cl and $^{79/81}Br$ spectra revealed that the contributions of the halogen bond to the EFG of the halide is larger than that of the hydrogen bond, increasing in relative contributions to V_{22} in the order of Cl^- > Br^- > I^-. In contrast, the contributions from the hydrogen bond to V_{11} increased in the order of I^- > Br^- > Cl^-, opposite to the trend observed for the halogen bond.

In Chapter 9, we have investigated the environment surrounding the halogen bond, using the rotating methyl groups of 2,3,5,6-tetramethylpyrazine (TMP) as a model. By cocrystallizing the deuterated TMP acceptor molecule with a series of halogen bond donors, we have successfully placed an iodine atom in proximity of the rotating methyl groups using C-I···N halogen bonding. Using deuterium NMR relaxation experiments, we have shown that the rotational energy barrier of the methyl groups is reduced by 56% in the halogen bonded cocrystals, surpassing the reduction of 36% observed in the hydrogen bonded cocrystals.

Computational results attribute this catalytic effect to the destabilization of the staggered conformation and a stabilization of the gauche conformation, overall causing the rotational energy barrier to decrease. This study is the first report of halogen bonding directly influencing nearby dynamics, and we have proposed the term *dynamics catalyst* to describe this role.

In Part 4 of this thesis, we have applied the halogen bond to engineer crystals and explore alternative synthetic methods of preparing these materials, including mechanochemistry and cosublimation. In Chapter 10, we surveyed a series of halogen bonded cocrystals featuring 1,3,5-tri(iodoethynyl)-2,4,6-trifluorobenzene (*sym*TIETFB) as the halogen bond donor and halide salts as the halogen bond acceptor. We have shown the possibility of obtaining variably complex supramolecular architectures, such as a honeycomb network, by modifying the size of the cation, with the prospect of eventually constructing porous materials capable of gas absorption.

In Chapter 11 of this thesis, we have prepared a series of halogen bonded cocrystals featuring nitrogen-containing heterocycles and a new halogen bond donor, 3-iodoethynylbenzoic acid, which features both halogen and hydrogen bonding capabilities. The crystal structures of the products studied in this project exhibit a complex concurrence of both halogen and hydrogen bonds, allowing access to new supramolecular motifs. These compounds were shown to be accessible by mechanochemical ball milling, allowing the products to be obtained without the need of large solvent volumes, and all within one hour.

In Chapter 12 of this thesis, performed in collaboration with Dr. Fourmigué's research group at the *Université de Rennes 1* (France), we have pioneered cosublimation as a synthetic method for preparing halogen bonded cocrystals. Performed entirely in the absence of any organic solvents, cosublimation has allowed for cocrystals to be rapidly prepared, yielding

crystals suitable for X-ray diffraction within a few hours and microcrystalline samples within 15 minutes. In order to fully investigate this technique, four halogen bond donors and four halogen bond acceptors were chosen with varying degrees of volatility, and these 16 combinations were prepared by overnight cosublimation using a two-zoned tube furnace, expedited cosublimation using a laboratory sublimation apparatus, and the conventional solvent-evaporation method. We have shown through multinuclear magnetic resonance that the products obtained from each synthetic technique were comparable, and in some cases, cosublimation has yielded new structures that were otherwise inaccessible through solvent-evaporation.

5.2 - Perspectives.

The future of halogen bonding will likely see new applications in emerging materials, such as in supramolecular actuators and gas absorbing materials. Arguably, the halogen bond may remain to be the most favorable of the emerging σ-hole interactions due to the linearity of the C-X$\cdots$Y motif and the relative magnitude of the σ-hole. Further, halogens are associated with a degree of biocompatibility, which contrasts the toxic chalcogen bond donors (selenium, tellurium), pnictogen bond donors (arsenic, antimony), and tetrel bond donors (lead), with the other elements being predominantly weaker. Consequently, I anticipate that the directionality of the halogen bond will play a larger role in upcoming pharmaceuticals, allowing for an increased affinity between the drug candidates and its target.

Part 2 of this thesis has provided the first systematic investigation of the electronic structures of the halogen bond donor upon the formation of a C-X$\cdots$N halogen bond (X = Cl, Br, I). This electronic reconfiguration, interpreted using molecular orbitals, may have implications

on the reactivity of the halogen atom, with halogen bonded intermediates serving a potential role in mediating the reactivity of solid-state synthesis. This approach could allow for the preparation of complex organic products while significantly reducing the need of organic solvents and catalysts based on precious metals (e.g. palladium-based catalysts). In addition, such process could expedite the discovery of drugs, relying on mechanochemistry to quickly prepare therapeutic candidates for screening rather than employing conventional solvent-based techniques. Consequently, the insights presented here may provide the foundation for a new branch of solid-state synthesis based on the halogen bond.

In Part 3 of this thesis, we have exploited solid-state NMR to investigate the halogen bond acceptor and the environment surrounding the halogen bond. With ^{19}F solid-state NMR having remarkable sensitivity and a large chemical shift range, this approach will likely play a continuing role in the characterization of perfluorinated halogen bond donors. The use of NMR crystallography to refine the X-ray crystal structures of halogen bonded compounds using ^{19}F and ^{13}C chemical shifts has been demonstrated, with the resulting structures being in better agreement with experimental results. While X-ray crystallography may be limited by the crystallinity of the sample, NMR crystallography is applicable to characterize even amorphous products, boasting a large benefit that will continue to gain traction in the future of the NMR community. Moreover, solid-state NMR has offered unique insights into the electronic structure of the halide halogen bond acceptor in a series of isomorphous frameworks, with a relative contribution to the electric field gradient from the halogen bond increasing in the order of $Cl^- > Br^- > I^-$. Overall, this has given the understanding of the electronic changes occurring on both sides of the halogen bonding interaction.

We have shown the first instance of the halogen bond having a direct impact on the local dynamics. Through this work, we have coined the term *dynamics catalyst*, which refers to the ability of the halogen bond to reduce the rotational energy barrier of a nearby methyl group. As dynamics have been shown to play a pivotal role in some catalysts,[6] diseased proteins,[7] and in molecular machines,[8,9,10,11] we propose that incorporating the halogen bond could be advantageous in correcting faulty dynamics in proteins or to enhance the function of these emerging classes of molecules. As a result, the use of halogenated pharmaceuticals could lead to a new class of medicinal products, with the ability to both target a therapeutic site in addition to catalyzing its dynamics.

Apart from impacts on dynamics and reactivity, the utility of the halogen bond in crystal engineering has had a clear role throughout this thesis. Among the products of the crystal engineering endeavors exploiting the halogen bond presented here is the first supramolecular triangle, a series of discrete charged dimers, and unique supramolecular architectures formed through concurrent halogen and hydrogen bonds. These examples illustrate the potential of halogen bonding for the construction of frameworks and will likely continue to see applications in the development of emerging materials. Further, we have shown the possibility of achieving fully organic porous structures, which could have potential interest for gas absorption. Such porous materials could be used to curb industrial emissions, including carbon dioxide. The metal-free nature of these materials may render them more cost effective while removing the need of mass-producing materials with toxic heavy metals. As we have shown mechanochemistry to be a convenient method of fabricating halogen bonded frameworks, the discovery of porous materials could potentially benefit from a mechanochemical production in efforts of reducing the cost associated with their preparation.

Lastly, we have pioneered cosublimation as a solvent-free method of preparing halogen bonded cocrystals at an accelerated rate, yielding crystals suitable for single crystal X-ray diffraction within a few hours. Cosublimation has provided a technique of preparing otherwise inaccessible halogen bonded frameworks, while completely eliminating the environmental footprint associated with conventional synthetic methods. Given the ability of varying the temperature and pressure for each component of the desired complex, this approach could be key in the discovery of materials featuring emerging interactions, such as the tetrel bond. Further, the solvent-free nature of the technique can be beneficial for compounds that may be unstable in solvents, which greatly increases the number of compounds accessible to this technique. This is also to the benefit of air-sensitive and moisture-sensitive chemicals, with the ability of preparing cosublimation experiment under inert atmosphere. Consequently, cosublimation is expected to flourish as the technique of choice for preparing cocrystals, with additional opportunities of preparing materials consisted of volatile building blocks featuring exotic elements, including those featuring transition metals.

References for Part 5.

[1] Legon, A.C. *Angew. Chem. Int. Ed.* **1999**, *38*, 2686-2714.

[2] Metrangolo, P.; Resnati, R. *Chem. Eur. J.* **2001**, *7*, 2511-2519.

[3] Groom, C.R.; Bruno, I.J.; Lightfoot, M.P. Ward, S.C. *Acta Cryst.* **2016**, *B72*, 171-179. Database accessed on December 25th, 2018.

[4] Cavallo, G.; Metrangolo, P.; Pilati, T.; Resnati, G.; Terraneo, G. *Cryst. Growth Des.* **2014**, *14*, 2697-2702.

[5] Szell, P.M.J.; Siiskonen, A.; Catalano, L.; Cavallo, G.; Terraneo, G.; Priimagi, A.; Bryce, D.L.; Metrangolo, P. *New J. Chem.* **2018**, *42*, 10467-10471.

[6] Biswas, P. K.; Saha, S.; Paululat, T.; Schmittel, M. *J. Am. Chem. Soc.* **2018**, *140*, 9038-9041.

[7] Schuetz, A.K.; Kay, L.E. *eLIFE*. **2016**, *5*, e20143.

[8] Erbas-Cakmak, S.; Leigh, D.A.; McTernan, C.T.; Nussbaumer, A.L. *Chem. Rev.* **2015**, *115*, 10081-10206.

[9] Kelly, T.R.; De Silva, H.; Silva, R.A. *Nature*. **1999**, *401*, 150-152.

[10] Karlen, S.D.; Reyes, H.; Taylor, R.E.; Khan, S.I. *Proc. Natl. Acad. Sci. U.S.A.* **2010**, *107*, 14973-14977.

[11] Jiang, X.; Rodríguez-Molina, B.; Nazarian, N.; Garcia-Garibay, M.A. *J. Am. Chem. Soc.* **2014**, *136*, 8871-8874.

Appendix I - List of Publications & Conference Attendance

List of publications.

1. **P.M.J. Szell**, L. Grébert, D.L. Bryce. Rapid Identification of Halogen Bonds in Cocrystalline Powders via ^{127}I Nuclear Quadrupole Resonance Spectroscopy. *Submitted article.*

2. **P.M.J. Szell**, S. Zablotny, D.L. Bryce. Halogen Bonding as a Supramolecular Dynamical Catalyst. *Nature Communications.* (2019) **10**, 916. **Editor's Highlight.** Press release by UOttawa and Fulcrum (March 2019).

3. **P.M.J. Szell**, S.A. Gabriel, E. Caron-Poulin, O. Jeannin, M. Fourmigué, D.L. Bryce. Cosublimation: A Rapid Route towards Otherwise Inaccessible Halogen Bonded Architectures. *Crystal Growth & Design*. (2018) **18**, 6227-6238. **Front cover article.**

4. C. Leroy, **P.M.J. Szell**, D.L. Bryce. On the Importance of Accurate Nuclear Quadrupole Moments in NMR Crystallography. *Magnetic Resonance in Chemistry.* (2019) **57**, 265-267.

5. P. Cerreia Vioglio, **P.M.J. Szell**, M.R. Chierotti, R. Gobetto, D.L. Bryce. Exploring the Potential of $^{79/81}$Br Nuclear Quadrupolar Resonance Spectroscopy to Characterize the Halogen Bond in C-Br···N Supramolecular Assemblies. *Chemical Science* (2018) **9**, 4555-4561. **Front cover article.**

6. **P.M.J. Szell**, G. Cavallo, G. Terraneo, P. Metrangolo, B. Gabidullin, D.L. Bryce. Comparing the Halogen Bond to the Hydrogen Bond by Solid-State NMR: Anion Coordinated Dimers from 2- & 3-Iodoethynylpyridine Salts. *Chemistry: A European Journal* (2018) **24**, 11364-11376.

7. **P.M.J. Szell**, B. Gabidullin, D.L. Bryce. 3-(1,2,2-triiodoethenyl)benzoic acid. *IUCrData,* (2018) **3**, x180258.

8. **P.M.J. Szell**, J. Dragon, S. Zablotny, S.R. Harrigan, B. Gabidullin, D.L. Bryce. Mechanochemistry and Cocrystallization of 3-Iodoethynylbenzoic Acid with Nitrogen-Containing Heterocycles: Concurrent Halogen and Hydrogen Bonding. *New Journal of Chemistry.* (2018) **42**, 10493-10501. **Cover Article. Reviewer recommended article.**

9. **P.M.J. Szell**, A. Siiskonen, L. Catalano, G. Cavallo, G. Terraneo, A. Priimagi, D.L. Bryce, P. Metrangolo. Halogen-Bond Driven Self-Assembly of Triangular Macrocycles. *New Journal of Chemistry.* (2018) **42**, 10467-10471.

10. M. Branca, V. Dichiarante, C. Esterhuysen, **P.M.J. Szell**. Highlights from the Faraday Discussion Halogen Bonding in Supramolecular and Solid State Chemistry, July 10-12th 2017, Ottawa, Canada. *Chemical Communications*. (2017) **53**, 11615-11621.

11. **P.M.J. Szell**, B. Gabidullin, D.L. Bryce. 1,3,5-Tri(iodoethynyl)-2,4,6-trifluorobenzene: Halogen-Bonded Frameworks and NMR Spectroscopy Analysis. *Acta Crystallographica* (2017) B**73**, 153-162. **Scientific commentary on this article:** *Acta. Cryst.* (2017) B**73**, 138-139.

12. **P.M.J. Szell**, S.A. Gabriel, R.D.D. Gill, S.Y.H. Wan, B. Gabidullin, D.L. Bryce. ^{13}C and ^{19}F Solid-State NMR and X-Ray Crystallographic Study of Halogen-Bonded Frameworks Featuring Nitrogen-Containing Heterocycles. *Acta Crystallographica* (2017) C**72**, 157-167. **List of most highly cited article in the journal.**

13. **P.M.J. Szell**, D.L. Bryce. Solid-State NMR Studies of Halogen Bonding. *Modern Magnetic Resonance* (2016), 1-18.

14. **P.M.J. Szell**, D.L. Bryce. Solid-State Nuclear Magnetic Resonance and Nuclear Quadrupole Resonance as Complementary Tools to Study Quadrupolar Nuclei. *Concepts in Magnetic Resonance.* (2016) **45A**, e21412.

15. Y. Xu, S.A. Southern, **P.M.J. Szell**, D.L. Bryce. The Role of Solid-State Nuclear Magnetic Resonance in Crystal Engineering. *CrystEngComm.* (2016) **18**, 5236-5252.

16. **P.M.J. Szell**, D.L. Bryce. ^{35}Cl Solid-State NMR and Computational Study of Chlorine Halogen Bond Donors in Single-Component Crystalline Chloronitriles. *Journal of Physical Chemistry C.* (2016) **120**, 11121-11130.

17. D.A. Safin, **P.M.J. Szell**, A. Keller, I. Korobkov, D.L. Bryce, M. Murugesu. Interaction of 2,4,6-tris(2-pyrimidyl)-1,3,5-triazine (TPymT) with CoX_2 (X = Cl, Br) in water: Trapping of new self-assembled water-chloride/bromide clusters in a $[Co(bpca)_2]^+$ host (bpca = bis(2-pyrimidylcarbonyl)amidate anion). *New Journal of Chemistry.* (2015) **39**, 7147-7152.

18. **P.M.J. Szell**, D.L. Bryce. Recent Advances in Chlorine, Bromine, and Iodine Solid-State NMR Spectroscopy. *Annual Reports on Nuclear Magnetic Resonance Spectroscopy.* (2015) **84**, 115-162.

List of conference presentations.

1. **P.M.J. Szell**, S.A. Gabriel, E. Caron-Poulin, O. Jeannin, M. Fourmigué, D.L. Bryce, *Cosublimation: A Rapid Route towards Halogen Bonded Cocrystals Yielding Otherwise Inaccessible Architectures.* Oral presentation. The 5th Crystal Engineering and Emerging Materials Workshop of Ontario and Quebec (CEMWOQ-5), Montreal, Quebec, July 2018. **"Outstanding Presentation" prize.**

2. **P.M.J. Szell**, S.A. Gabriel, E. Caron-Poulin, O. Jeannin, M. Fourmigué, D.L. Bryce, *Cosublimation: A Rapid Route towards Halogen Bonded Cocrystals Yielding Otherwise Inaccessible Architectures.* International Symposium on Halogen Bonding (ISXB-3), Greenville, North Carolina, United States of America, June 2018.

3. **P.M.J. Szell**, S.A. Gabriel, E. Caron-Poulin, O. Jeannin, M. Fourmigué, D.L. Bryce, *Preparing Cocrystals Featuring Non-Covalent Interactions by Cosublimation.* IUPAC Workshop, Greenville, North Carolina, United States of America, June 2018. **"Best Poster" prize.**

4. **P.M.J. Szell**, S.A. Gabriel, E. Caron-Poulin, O. Jeannin, M. Fourmigué, D.L. Bryce, *Cosublimation: A Rapid Route towards Halogen Bonded Cocrystals Yielding Otherwise Inaccessible Architectures.* Oral presentation. Ottawa-Carleton Chemistry Institute (OCCI) day, Ottawa, Ontario, May 2018.

5. **P.M.J. Szell**, D.L. Bryce, *NMR and X-ray Crystallography of Halogen Bonded Organic Frameworks.* MaSCE Meeting, November 2017, Rennes, France.

6. **P.M.J. Szell**, G. Cavallo, G. Terraneo, P. Metrangolo, D.L. Bryce, *Multinuclear Solid-State Magnetic Resonance of 2-/3-iodoethynylpyridine and their Hydrohalide Salts: A Direct Comparison between the Halogen Bond and the Hydrogen Bond,* poster presentation & flash presentation. Halogen Bonding in Supramolecular and Solid State Chemistry (Faraday Discussion), Ottawa, Ontario, July 2017. **Poster prize.**

7. **P.M.J. Szell**, D.L. Bryce, *Multinuclear Solid-State NMR of Halogen Bonded Frameworks*, poster presentation. 58th Experimental Nuclear Magnetic Resonance Conference (ENC), Pacific Grove, California, March 2017. **Travel stipend award. "NMR is Science" second place winner.**

8. **P.M.J. Szell**, L. Brunet, R.D.D. Gill, S.Y.H. Wan, D.L. Bryce, *^{1}H, ^{13}C, and ^{15}N Solid-State NMR Investigations of Halogen Bonded Frameworks Featuring Nitrogen-Containing Heterocycles*, poster presentation. 99th Canadian Chemistry Conference (CSC), Halifax, Nova Scotia, June 2016.

9. **P.M.J. Szell**, L. Brunet, R.D.D. Gill, S.Y.H. Wan, D.L. Bryce, *^{1}H, ^{13}C, and ^{15}N Solid-State NMR Investigations of Halogen Bonded Frameworks Featuring Nitrogen-Containing Heterocycles*, poster presentation. Ottawa-Carleton Chemistry Institute day (OCCI), Ottawa, Ontario, June 2016.

10. **P.M.J. Szell**, L. Brunet, R.D.D. Gill, S.Y.H. Wan, D.L. Bryce, *^{1}H, ^{13}C, and ^{15}N Solid-State NMR Investigations of Halogen Bonded Frameworks Featuring Nitrogen-Containing Heterocycles*, poster presentation. The 3rd Crystal Engineering and Emerging Materials Workshop of Ontario and Quebec (CEMWOQ-3), Windsor, Ontario, May 2016. **Poster prize.**

11. **P.M.J. Szell**, D.L. Bryce, *Investigating the Halogen Bond Donor by Covalent ^{35}Cl Solid-State NMR*, oral presentation. Montreal-Ottawa-Toronto NMR mini-symposium, Hamilton, Ontario, October 2015.

12. **P.M.J. Szell**, D.L. Bryce, *Investigating the Halogen Bond Donor by Covalent ^{35}Cl Solid-State NMR*, poster presentation. Ampere NMR School, Zakopane, Poland, June 2015.

13. **P.M.J. Szell**, I. Korobkov, D.L. Bryce, *Probing Halogen Bonded Frameworks Formed with 1,3,5-tri(iodoethynyl)-2,4,6-trifluorobenzene by Solid-State NMR*, poster presentation. Montreal-Ottawa-Toronto NMR mini-symposium, Montreal, Quebec, October 2014.

Appendix II – Supporting Information for Chapter 6: Investigating the Halogen Bond Donor by ^{127}I Nuclear Quadrupole Resonance Spectroscopy: Insights from the Electric Field Gradient

1.0 - Melting Points.

Table 6.2.1. Experimental melting points for each compound in this study.

compound	melting point / °C
1	130 – 132
1a	75 - 79
1b	124 – 125
1c	148 – 150
1d	142 – 144
1e	122 – 124
1f	124 – 126

Table 6.2.2. Experimental masses, method, and solvent usage the preparation of each cocrystal.

compound	mass donor	mass acceptor	synthetic method	solvent usage	recovered
1a	0.2265 g	0.0930 g	cosublimation	none	82%
1b	0.6103 g	0.2558 g	solvent evaporation	CH_2Cl_2	
1c	0.5104 g	0.2862 g	ball milling	50 µL CH_2Cl_2	94%
1d	0.3370 g	0.1614 g	ball milling	none	92%
1e	0.1777 g	0.1285 g	ball milling	50 µL CH_2Cl_2	
1f	0.3935 g	0.115 mL	ball milling	25 µL ACN	86%

2.0 - ^{13}C Solid-state NMR Acquisition Parameters.

Table 6.2.3. Experimental ^{13}C solid-state NMR acquisition parameters,

compound	number of scans	recycle delay / s	MAS frequency / kHz
1	3072	20	8
1a	512	5	8
1b	5632	10	8
1c	512	20	8
1d	2560	20	8
1e	512	20	8

3.0 - Single Crystal X-Ray crystallographic data.

Table 6.2.4. Selected single-crystal X-ray crystallographic data for compounds **1b** and **1e**.

compound	**1b**	**1e**
empirical formula	$C_{12}H_{16}I_2N_4$	$C_{10}H_{12}N_2I$
FW (g/mol)	470.09	287.12
crystal color	colourless	colourless
crystal size (mm)	0.34 x 0.27 x 0.20	0.20 x 0.27 x 0.40
crystal system	orthorhombic	triclinic
crystal space group	*Cmcm*	*P* -1
T (K)	200(2)	296(2)
a (Å)	9.5052(9)	7.6991(7)
b (Å)	7.5833(8)	7.9609(8)
c (Å)	20.499(2)	9.5740(9)
α (˚)	90	109.572(5)
β (˚)	90	94.948(5)
γ (˚)	90	99.546(5)
V (Å³)	1477.6(3)	538.86(9)
Z	4	2
R_1 (final)	0.0216	0.0283
wR_2 (final)	0.0541	0.0628

4.0 - ORTEP Plots.

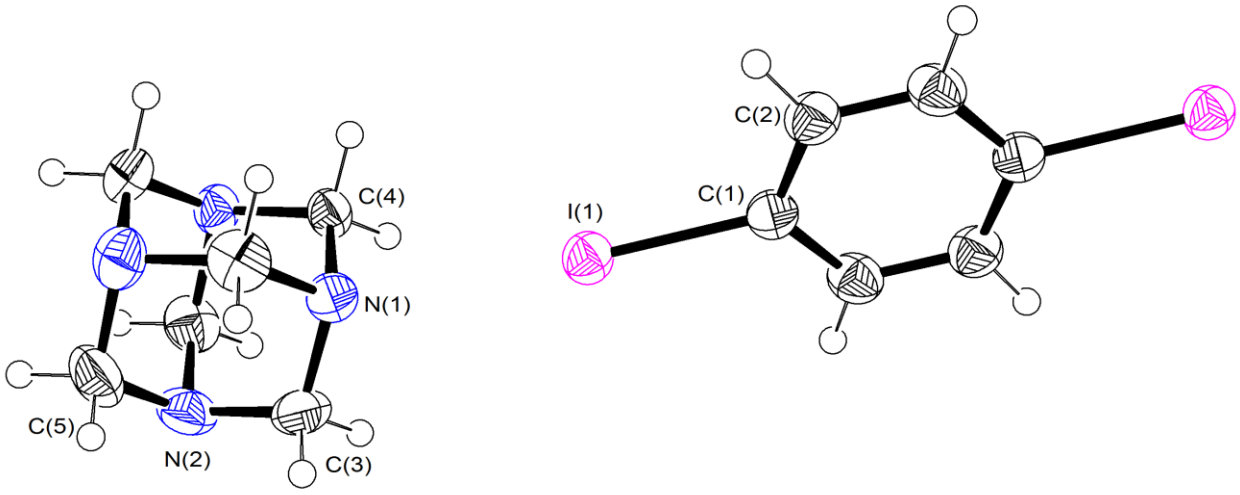

Figure 6.2.1. Thermal ellipsoid plot of structure **1b**. Only crystallographically unique atoms have been labelled.

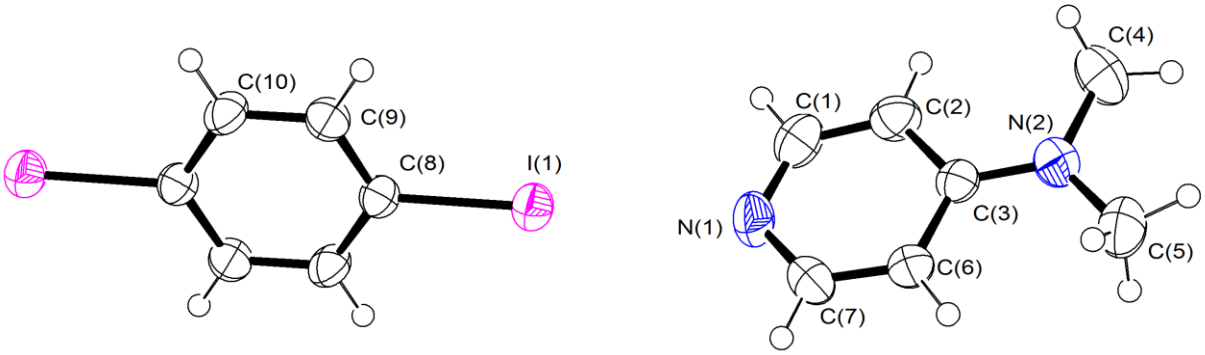

Figure 6.2.2. Thermal ellipsoid plot of structure **1e**. Only crystallographically unique atoms have been labelled.

5.0 – NLMO Calculations

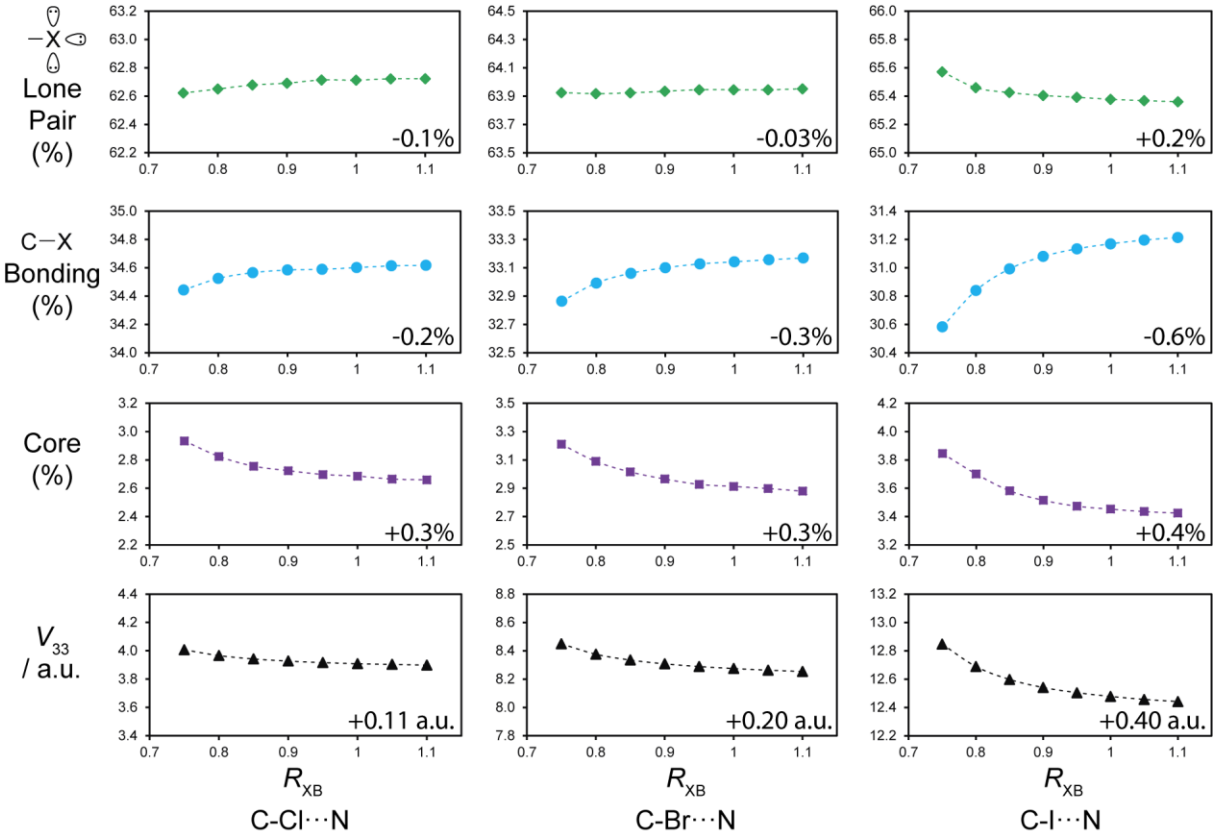

Figure 6.2.3. DFT-calculated natural localized molecular orbital (NLMO) contributions to V_{33} (black triangles) as a function of the normalized distance parameter, R_{XB}, including the absolute contributions from the lone pair orbitals (green diamonds), C-X bonding orbital (blue circles), and core orbitals (purple squares) for chlorine, bromine, and iodine in the C-X···N halogen bonding motif consisted of halobenzene interacting with pyridine. The total percentile changes are shown on the corner of each graph. This figure is similar to Figure 4 of the main text, but for non-fluorinated halogen-bond donors.

Table 6.2.5. NLMO contributions to V_{33} of the ^{35}Cl nucleus of a chloroperfluorobenzene···pyridine model as a function of the normalized distance parameter (R_{XB}).

R_{XB}	lone pair contributions		bonding orbital contributions		core orbital contributions		V_{33}
	(a.u.)	(%)	(a.u.)	(%)	(a.u.)	(%)	(a.u.)
0.75	8.312	63.99	-4.260	32.79	0.418	3.22	4.470
0.80	8.257	63.93	-4.264	33.01	0.395	3.06	4.389
0.85	8.223	63.91	-4.262	33.13	0.381	2.96	4.341
0.90	8.200	63.92	-4.258	33.19	0.370	2.88	4.312
0.95	8.183	63.92	-4.255	33.24	0.363	2.84	4.293
1.00	8.171	63.92	-4.253	33.27	0.360	2.82	4.279
1.05	8.161	63.92	-4.250	33.29	0.357	2.80	4.269
1.10	8.153	63.91	-4.249	33.30	0.356	2.79	4.261

Table 6.2.6. NLMO contributions to V_{33} of the ^{35}Cl nucleus of a chlorobenzene···pyridine model as a function of the normalized distance parameter (R_{XB}).

R_{XB}	lone pair contributions		bonding orbital contributions		core orbital contributions		V_{33}
	(a.u.)	(%)	(a.u.)	(%)	(a.u.)	(%)	(a.u.)
0.75	8.067	62.62	-4.437	34.44	0.378	2.93	4.007
0.80	8.028	62.65	-4.424	34.52	0.362	2.83	3.966
0.85	8.004	62.68	-4.414	34.57	0.352	2.76	3.943
0.90	7.985	62.69	-4.405	34.58	0.347	2.72	3.928
0.95	7.974	62.71	-4.398	34.59	0.343	2.70	3.917
1.00	7.962	62.71	-4.393	34.60	0.341	2.69	3.909
1.05	7.955	62.72	-4.390	34.61	0.338	2.66	3.904
1.10	7.947	62.72	-4.386	34.62	0.337	2.66	3.899

Table 6.2.7. NLMO contributions to V_{33} of the $^{79/81}$Br nucleus of a bromoperfluorobenzene···pyridine model as a function of the normalized distance parameter (R_{XB}).

R_{XB}	lone pair contributions		bonding orbital contributions		core orbital contributions		V_{33}
	(a.u.)	(%)	(a.u.)	(%)	(a.u.)	(%)	(a.u.)
0.75	16.316	65.80	-7.630	30.77	0.849	3.42	9.536
0.80	16.306	65.73	-7.679	30.96	0.821	3.31	9.447
0.85	16.299	65.70	-7.708	31.07	0.802	3.23	9.393
0.90	16.293	65.68	-7.725	31.14	0.789	3.18	9.357
0.95	16.289	65.66	-7.737	31.19	0.781	3.15	9.332
1.00	16.283	65.64	-7.745	31.22	0.778	3.14	9.314
1.05	16.278	65.64	-7.750	31.25	0.771	3.11	9.298
1.10	16.274	65.63	-7.751	31.26	0.771	3.11	9.294

Table 6.2.8. NLMO contributions to V_{33} of the $^{79/81}$Br nucleus of a bromobenzene···pyridine model as a function of the normalized distance parameter (R_{XB}).

R_{XB}	lone pair contributions		bonding orbital contributions		core orbital contributions		V_{33}
	(a.u.)	(%)	(a.u.)	(%)	(a.u.)	(%)	(a.u.)
0.75	15.767	63.92	-8.106	32.86	0.792	3.21	8.449
0.80	15.743	63.92	-8.126	32.99	0.761	3.09	8.376
0.85	15.729	63.92	-8.135	33.06	0.742	3.02	8.335
0.90	15.717	63.93	-8.137	33.10	0.729	2.97	8.308
0.95	15.705	63.95	-8.136	33.13	0.719	2.93	8.289
1.00	15.696	63.95	-8.135	33.14	0.715	2.91	8.275
1.05	15.687	63.95	-8.134	33.16	0.711	2.90	8.263
1.10	15.679	63.95	-8.132	33.17	0.706	2.88	8.254

Table 6.2.9. NLMO contributions to V_{33} of the ^{127}I nucleus of a iodoperfluorobenzene···pyridine model as a function of the normalized distance parameter (R_{XB}).

R_{XB}	lone pair contributions		bonding orbital contributions		core orbital contributions		V_{33}
	(a.u.)	(%)	(a.u.)	(%)	(a.u.)	(%)	(a.u.)
0.75	22.696	68.81	-9.269	28.10	1.019	3.09	14.447
0.80	22.730	68.64	-9.415	28.43	0.971	2.93	14.285
0.85	22.752	68.54	-9.505	28.64	0.936	2.82	14.186
0.90	22.768	68.49	-9.561	28.76	0.915	2.75	14.121
0.95	22.775	68.44	-9.600	28.85	0.903	2.71	14.076
1.00	22.778	68.41	-9.627	28.91	0.893	2.68	14.044
1.05	22.778	68.38	-9.646	28.96	0.889	2.67	14.019
1.10	22.772	68.35	-9.659	28.99	0.884	2.65	13.998

Table 6.2.10. NLMO contributions to V_{33} of the ^{127}I nucleus of a iodobenzene···pyridine model as a function of the normalized distance parameter (R_{XB}).

R_{XB}	lone pair contributions		bonding orbital contributions		core orbital contributions		V_{33}
	(a.u.)	(%)	(a.u.)	(%)	(a.u.)	(%)	(a.u.)
0.75	21.691	65.57	-10.117	30.58	1.272	3.85	12.847
0.80	21.686	65.46	-10.217	30.84	1.226	3.70	12.689
0.85	21.680	65.43	-10.270	30.99	1.187	3.58	12.597
0.90	21.675	65.40	-10.300	31.08	1.165	3.52	12.541
0.95	21.667	65.39	-10.316	31.13	1.151	3.47	12.504
1.00	21.659	65.38	-10.326	31.17	1.144	3.45	12.477
1.05	21.650	65.37	-10.332	31.20	1.138	3.44	12.457
1.10	21.639	65.36	-10.334	31.21	1.134	3.43	12.441

6.0 - Powder X-ray Diffraction.

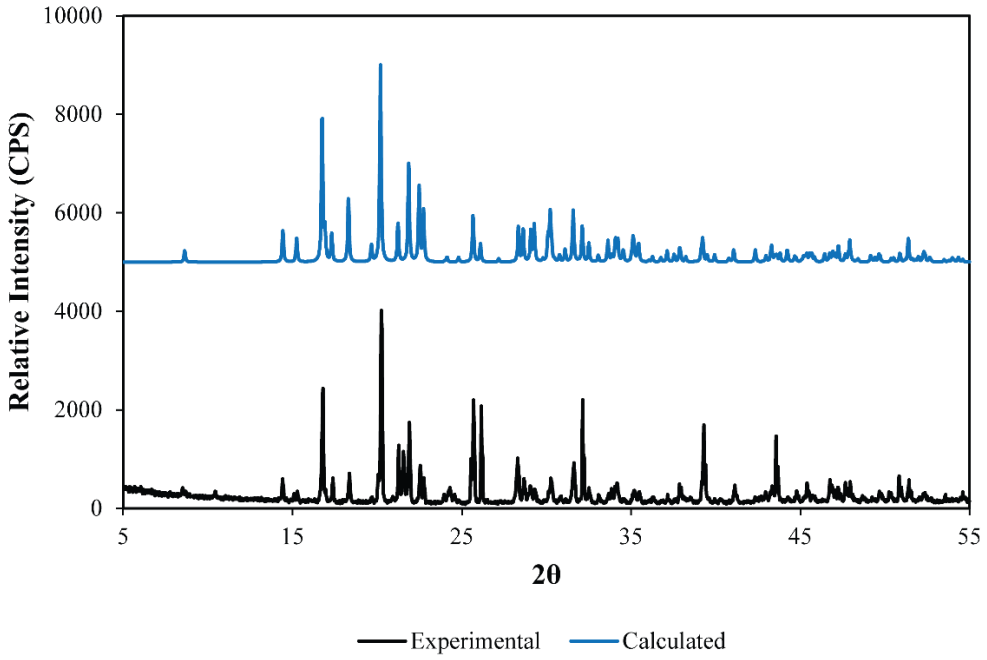

Figure 6.2.4. Experimental and calculated powder X-ray diffraction pattern for compound **1a** (1,4-diiodobenzene)(2,3,5,6-tetramethylpyrazine). The diffractogram was acquired at a speed of 5° per minute.

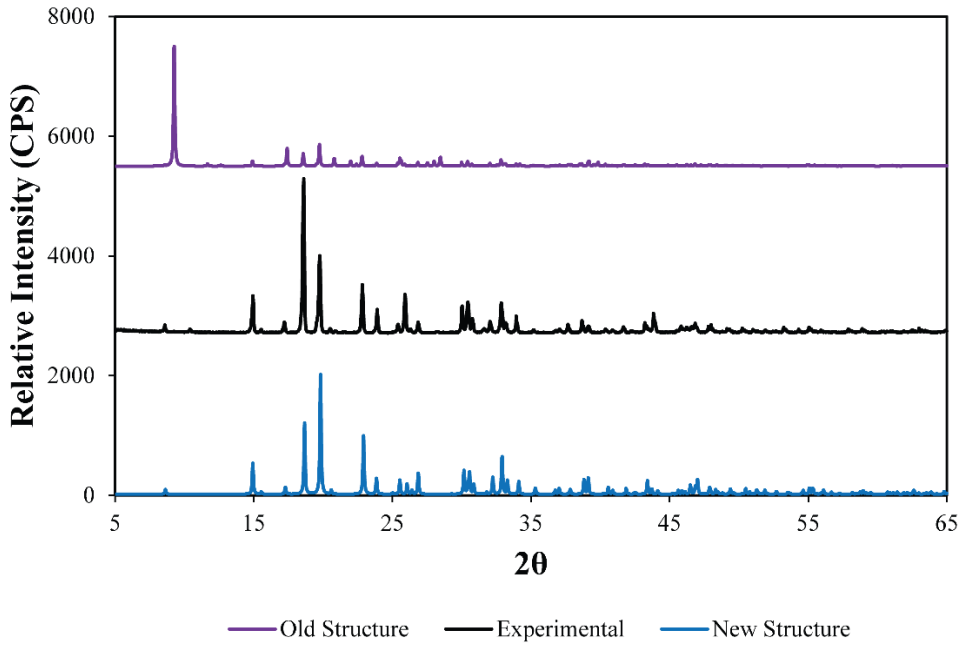

Figure 6.2.5. Experimental and calculated powder X-ray diffraction patterns for compound **1b** (1,4-diiodobenzene)(hexamethylenetetramine). The diffractogram in purple (top) was calculated using the previously reported structure, while the diffractogram in blue (bottom) was calculated using the structure reported herein.

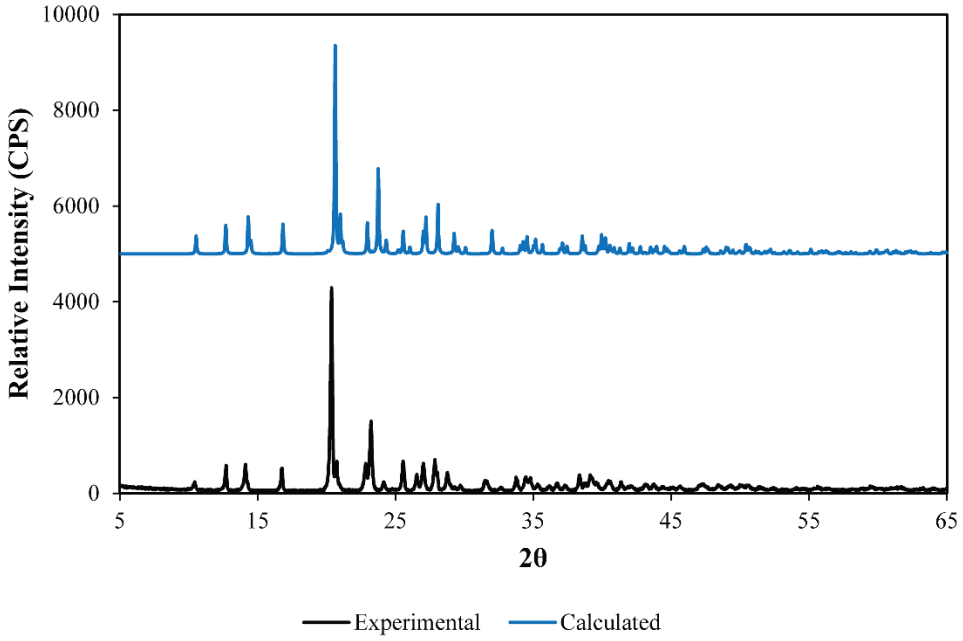

Figure 6.2.6. Experimental and calculated powder X-ray diffraction pattern for compound **1c** (1,4-diiodobenzene)(1,2-bis(4-pyridyl)ethane).

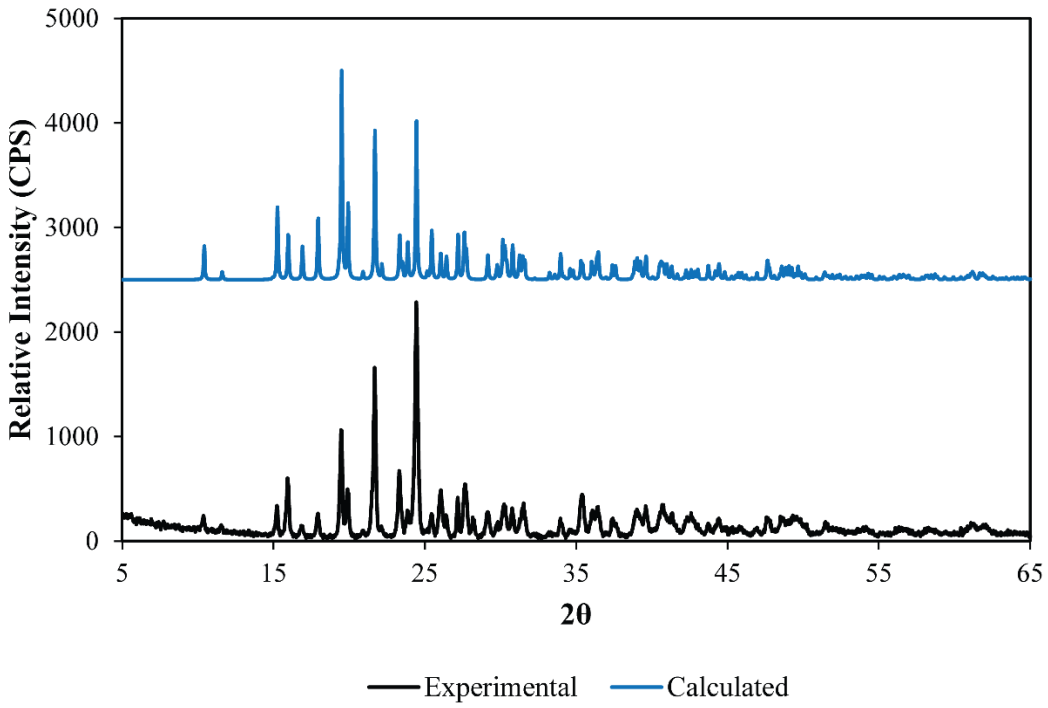

Figure 6.2.7. Experimental and calculated powder X-ray diffraction pattern for compound **1d** (1,4-diiodobenzene)(4,4'-bipyridyl).

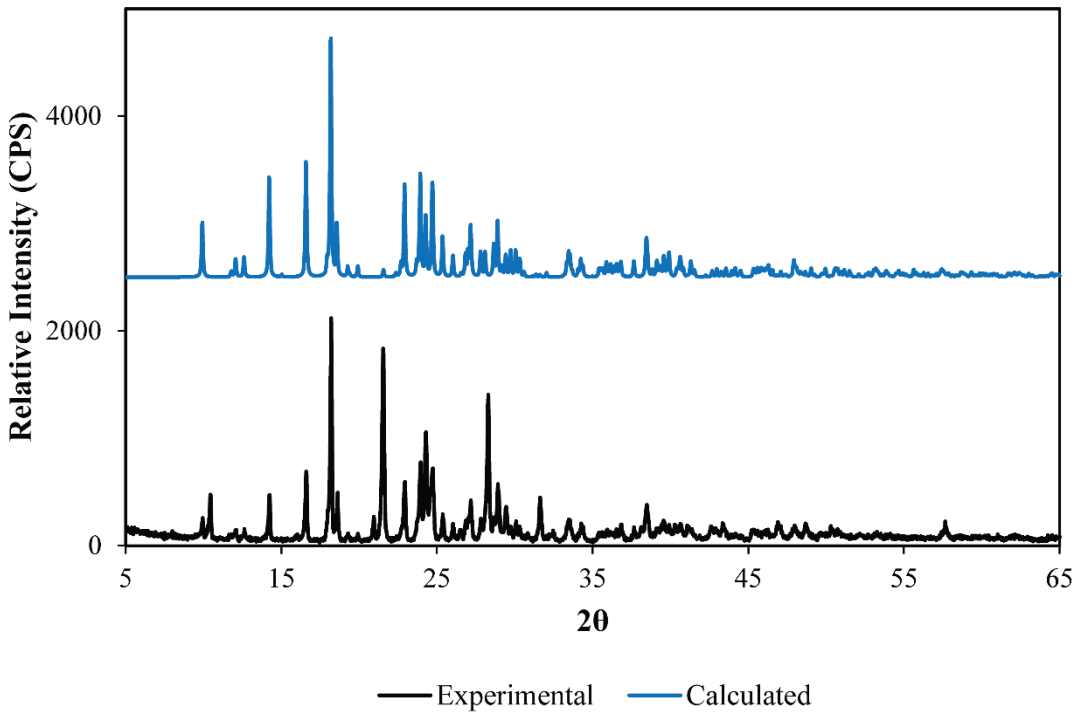

Figure 6.2.8. Experimental and calculated powder X-ray diffraction pattern for compound **1e** (1,4-diiodobenzene)(4-dimethylaminopyridine).

7.0 - ^{13}C Solid-State NMR.

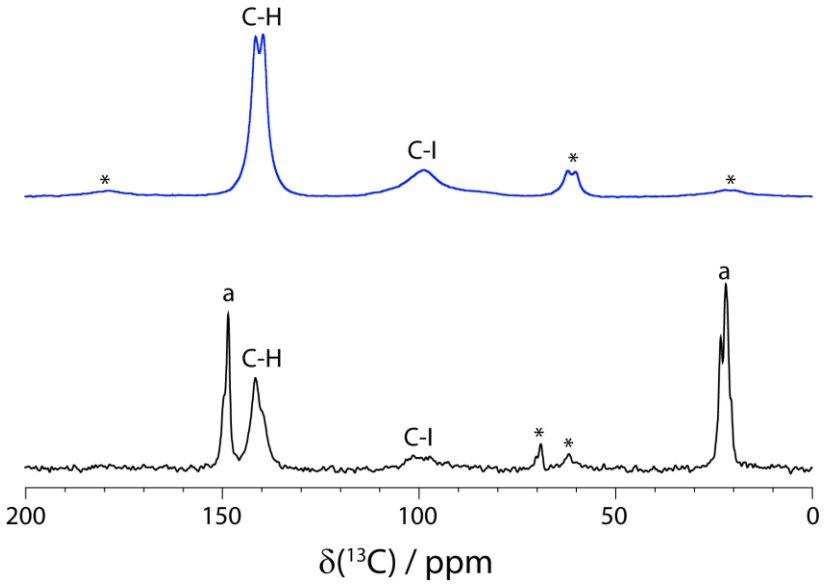

Figure 6.2.9. Experimental ^{13}C solid-state NMR spectra of compound **1a** (1,4-diiodobenzene)(2,3,5,6-tetramethylpyrazine) in black (lower), and 1,4-diiodobenzene in blue (upper). The labels denote the C-H and C-I carbons of 1,4-diiodobenzene, the carbons of the acceptor, and the asterisks denote spinning sidebands.

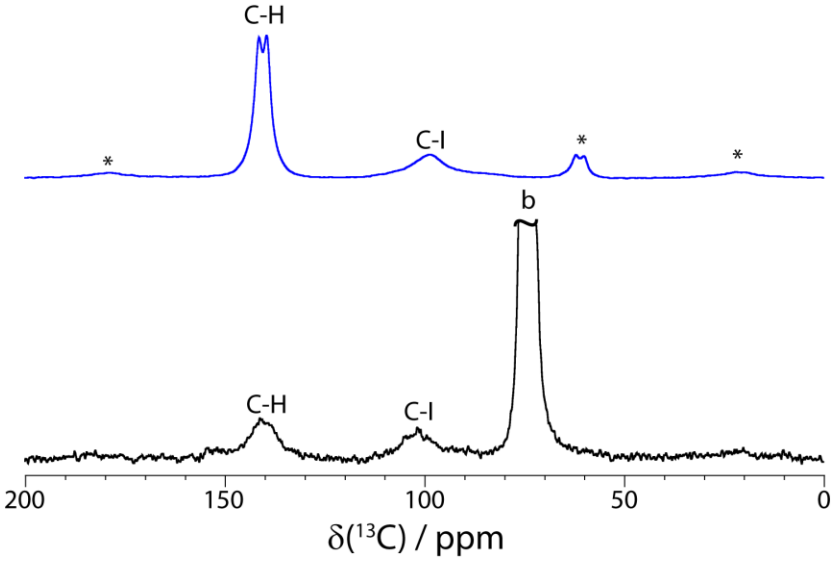

Figure 6.2.10. Experimental ^{13}C solid-state NMR spectra of compound **1b** (1,4-diiodobenzene)(1,4-diazabicyclo[2.2.2]octane) in black (lower), and 1,4-diiodobenzene in blue (upper). The labels denote the C-H and C-I carbons of 1,4-diiodobenzene, the carbons of the acceptor, and the asterisks denote spinning sidebands.

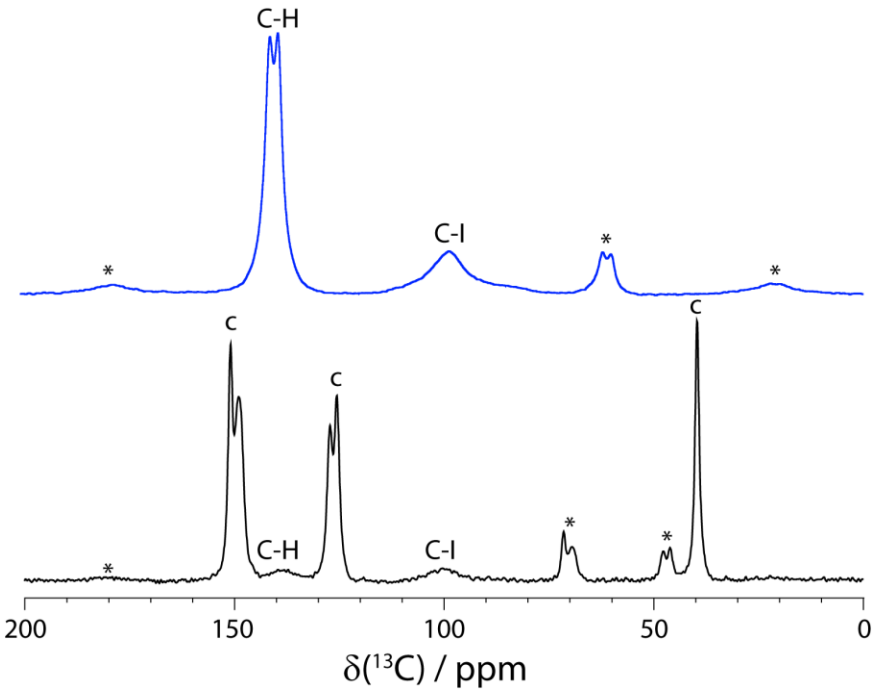

Figure 6.2.11. Experimental ^{13}C solid-state NMR spectra of compound **1c** (1,4-diiodobenzene)(4-(2-(pyridine-4-yl)ethyl)pyridine) in black (lower), and 1,4-diiodobenzene in blue (upper). The labels denote the C-H and C-I carbons of 1,4-diiodobenzene, the carbons of the acceptor, and the asterisks denote spinning sidebands.

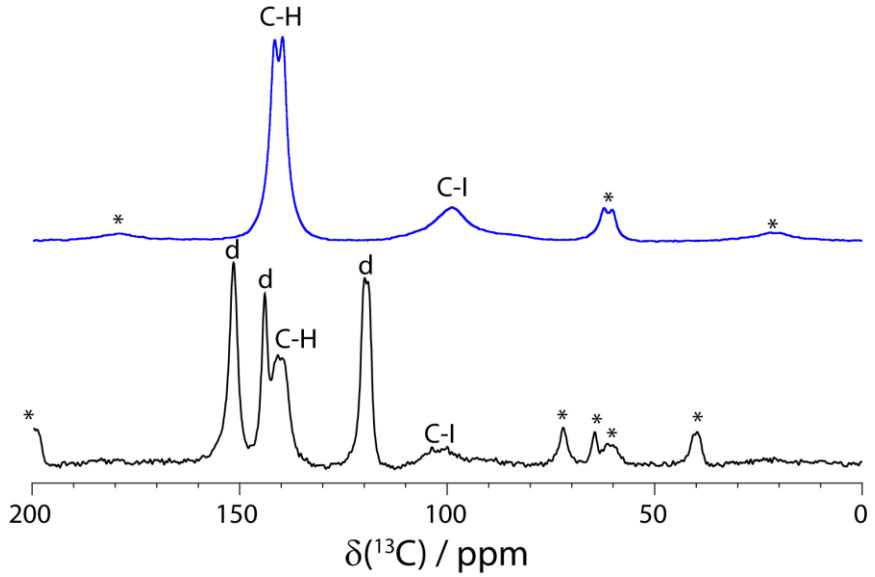

Figure 6.2.12. Experimental ^{13}C solid-state NMR spectra of compound **1d** (1,4-diiodobenzene)(4,4'-bipyridyl) in black (lower), and 1,4-diiodobenzene in blue (upper). The labels denote the C-H and C-I carbons of 1,4-diiodobenzene, the carbons of the acceptor, and the asterisks denote spinning sidebands.

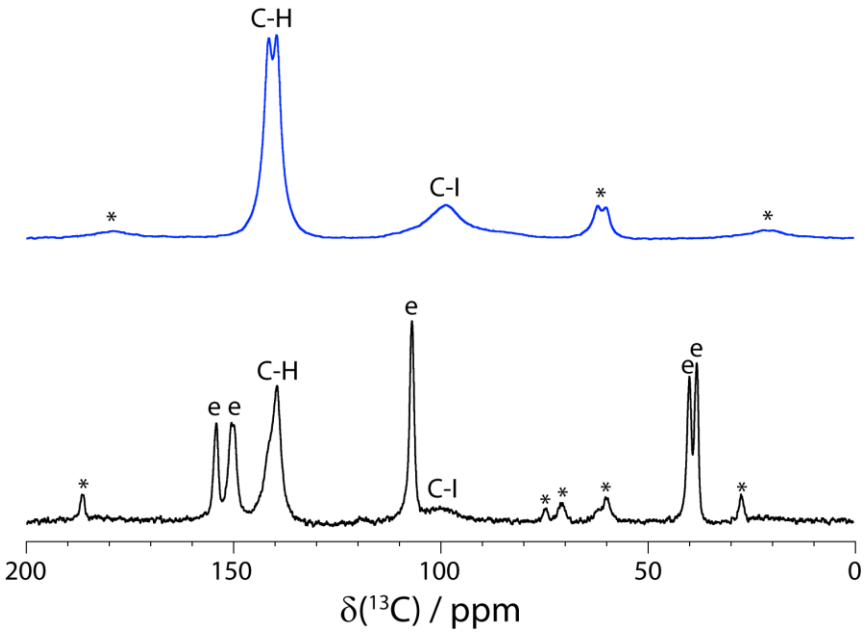

Figure 6.2.13. Experimental ^{13}C solid-state NMR spectra of compound **1e** (1,4-diiodobenzene)(4-dimethylaminopyridine) in black (lower), and 1,4-diiodobenzene in blue (upper). The labels denote the C-H and C-I carbons of 1,4-diiodobenzene, the carbons of the acceptor, and the asterisks denote spinning sidebands.

Appendix III – Supporting information for Chapter 9: Halogen Bonding as a Supramolecular Dynamics Catalyst

1.0 – Methyl Group Contact Analysis

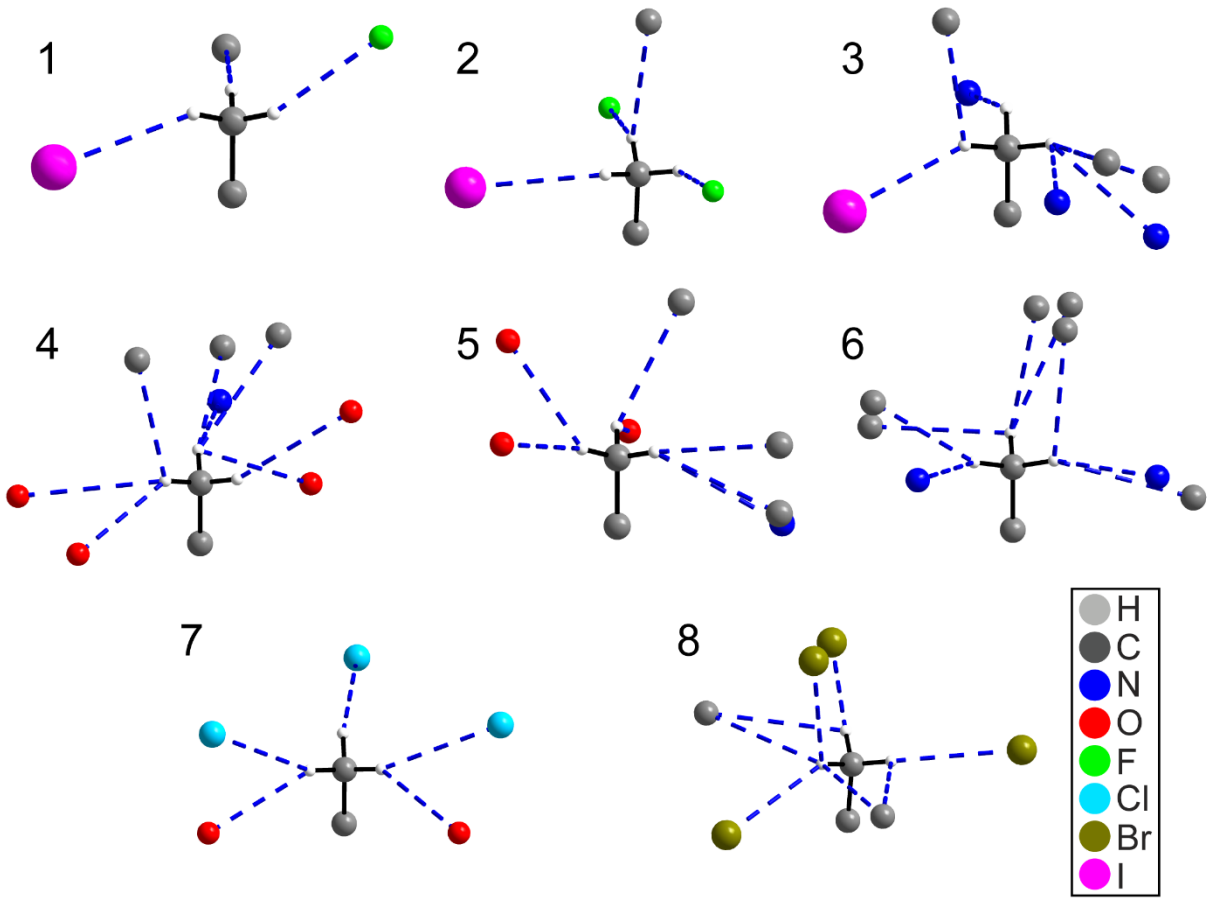

Supplementary Figure 6.3.1. Depiction showing the intermolecular contacts within 3.3 Å of the protons of a methyl group in their respective crystal structure. Hydrogen···hydrogen contacts are not shown for clarity. The same structures with the inclusion of hydrogen···hydrogen contacts can be seen in Supplementary Figure 6.3.1.

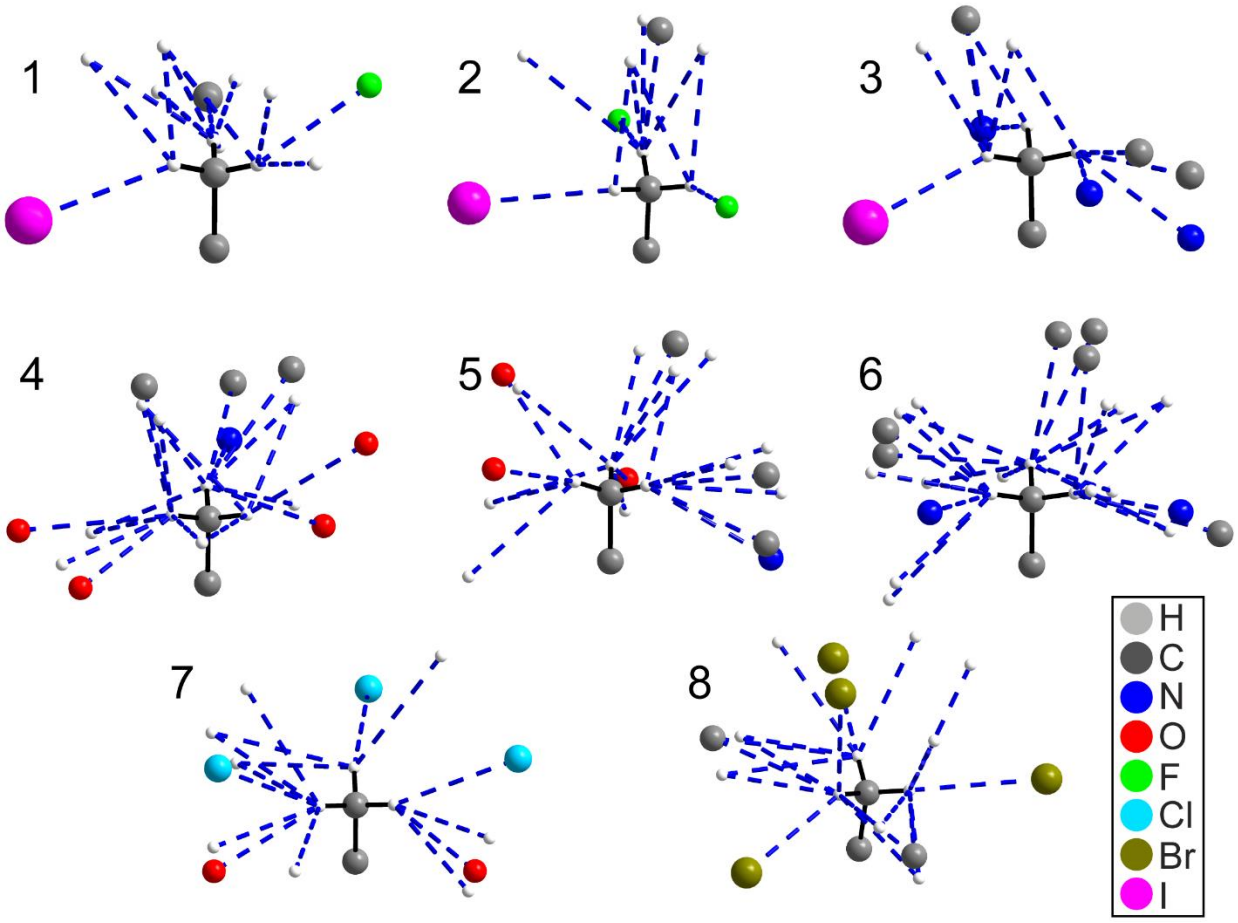

Supplementary Figure 6.3.2. Depiction showing the intermolecular contacts within 3.3 Å of the protons of a methyl group in their respective crystal structure. The above figure is identical to Supplementary Figure 6.3.1, but includes hydrogen···hydrogen contacts.

2.0 – Supporting EXPRESS Simulations

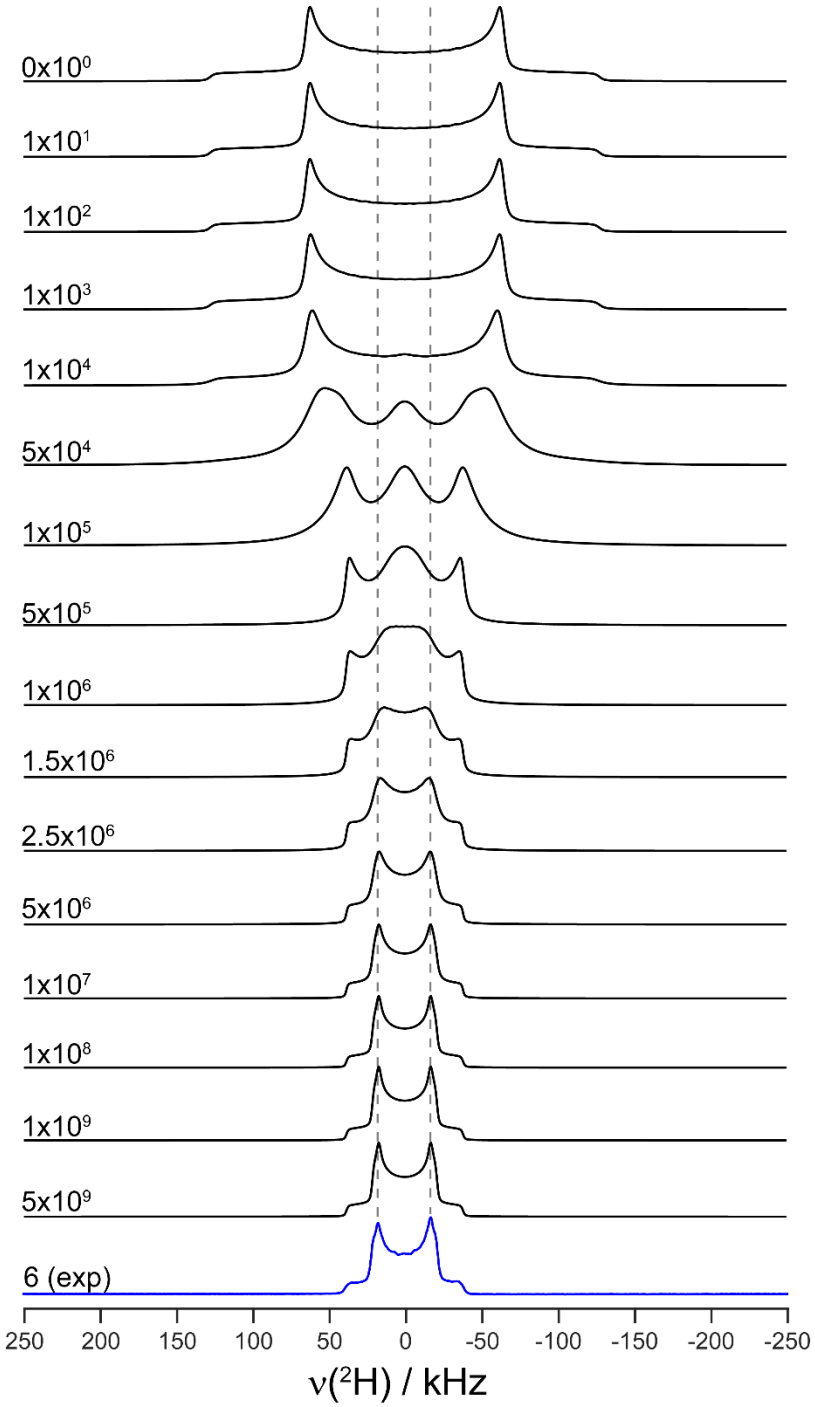

Supplementary Figure 6.3.3. Hydrogen-2 line shape simulations under static conditions for a methyl group exhibiting both rotation and libration, varying the rate constant (denoted on the left) for both movements from 0 to $5x10^9$. The simulations were performed using EXPRESS.[1] The experimental ^2H spectrum for sample **6** is shown in blue. The dashed line serves as a guide.

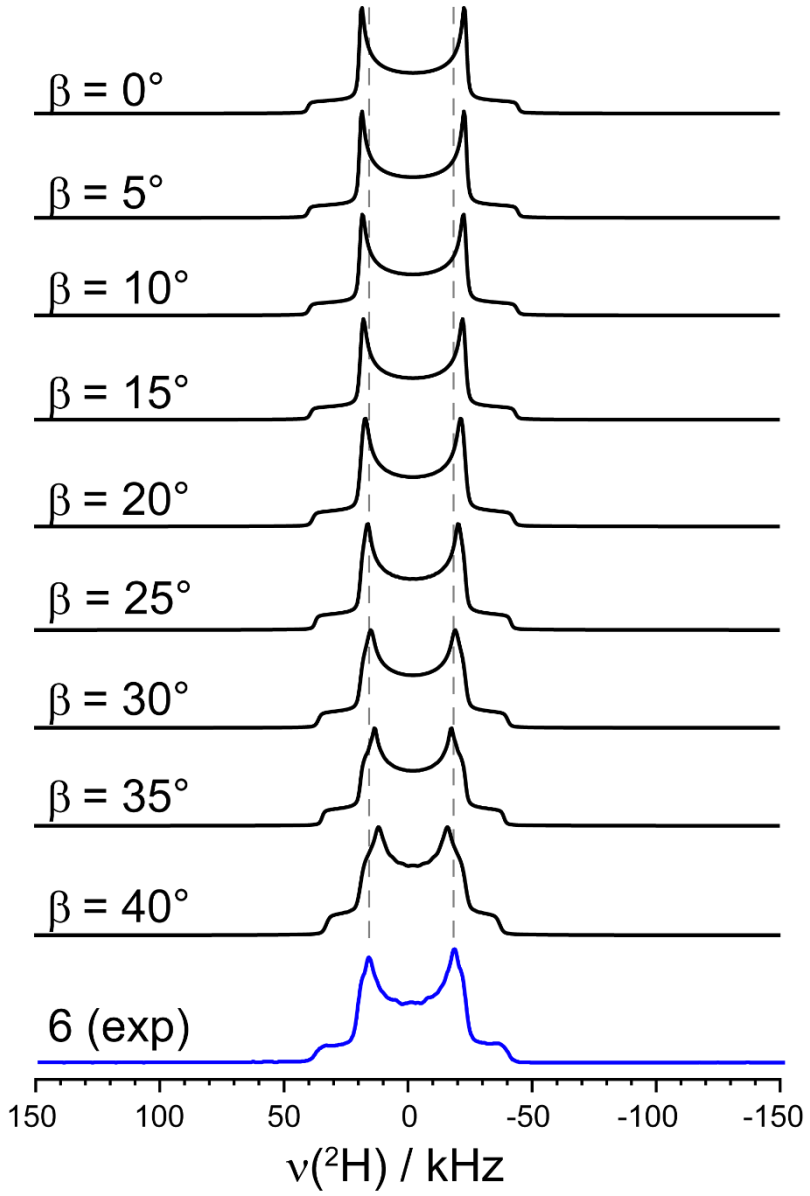

Supplementary Figure 6.3.4. Hydrogen-2 line shape simulations under static conditions for a methyl group exhibiting both rotation and libration, varying the methyl group libration angle from $\beta = 0°$ to $\beta = 40°$. The simulations were performed using EXPRESS.[1] The experimental ^2H spectrum for sample **6** is shown in blue. The dashed line serves as a guide.

Supplementary Methods: Express simulation parameters. Express simulations were performed using experimental conditions (ν_L, pulse length, delays), a 3-fold hopping model [(α_1, β_1, γ_1) = (0, 70.5, 0); (α_2, β_2, γ_2) = (0, 70.5, 120); (α_3, β_3, γ_3) = (0, 70.5, 240)] with simultaneous libration [(α_1, β_1, γ_1) = (0, 0, 0); (α_2, β_2, γ_2) = (0, 30, 0)] at a rate of $k = 5x10^9$, with C_Q =170 kHz and $\eta = 0$. The simulations in Supplementary Figure 6.3.3 were obtained by varying k, while the simulations of Supplementary Figure 6.3.4 were obtained by varying β_2 of the methyl group libration.

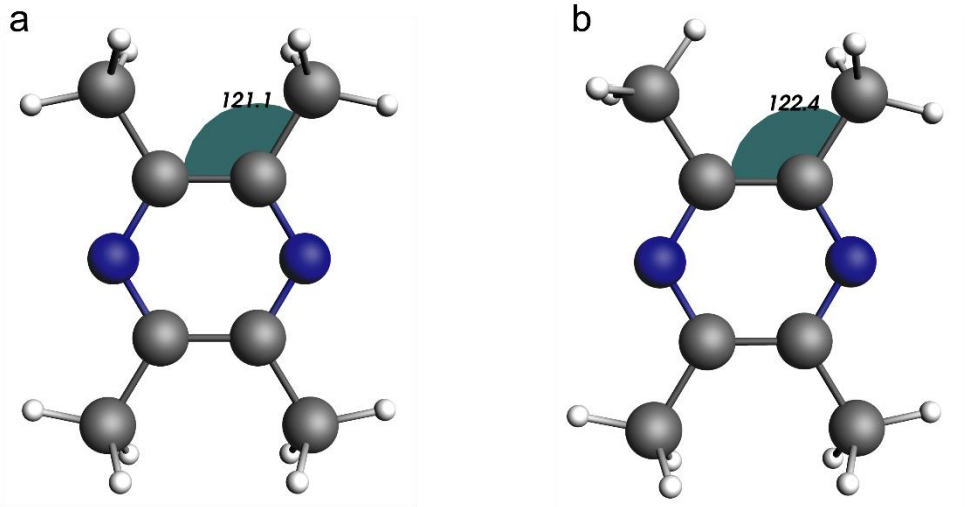

Supplementary Figure 6.3.5. ADF simulation[2] of sample **6** upon the rotation of a single methyl group, showing the libration of the adjacent methyl group as a result of the methyl rotation. The staggered conformation is shown in **a**, and the gauche conformation is shown in **b**.

3.0 - Variable Temperature T_1 Relaxation Time Constant Measurements.

Supplementary Table 6.3.1. Variable temperature T_1 relaxation time constant fitting parameters for compound **1** to **8**.

compound	activation energy (kJ mol^{-1})	ln(A)[a]	R^2 [b]	note
1	2.84 ± 0.13	3.14 ± 0.08	0.989	halogen bonded
2	3.24 ± 0.13	3.11 ± 0.07	0.991	halogen bonded
3	3.62 ± 0.13	3.15 ± 0.07	0.993	halogen bonded
4	4.17 ± 0.09	3.39 ± 0.05	0.997	hydrogen bonded
5	5.02 ± 0.06	3.37 ± 0.03	0.999	hydrogen bonded
6	7.31 ± 0.17	3.26 ± 0.09	0.997	pure TMP
7	6.81 ± 0.16	2.54 ± 0.09	0.997	HCl salt
8	13.64 ± 0.45 [c]	2.21 ± 0.23 [c]	0.995 [c]	HBr salt

[a] Arrhenius pre-exponential factor from eq. 1.
[b] Coefficient of determination.
[c] Fit using the T_1 relaxation time constants measured between 199 K and 295 K.

Supplementary Table 6.3.2. Observed separation (in kHz) between the horns of the Pake doublet for each spectrum at room temperature.

compound	Δν / kHz[a]	note
1	33 ± 1	halogen bonded
2	35 ± 1	halogen bonded
3	33 ± 1	halogen bonded
4	33 ± 1	hydrogen bonded
5	35 ± 1	hydrogen bonded
6	35 ± 1	pure TMP
7	32 ± 1	HCl salt
8	33 ± 1	HBr salt

Supplementary Table 6.3.3. T_1 relaxation time constant at various temperature increments for compound **1**.

Temperature (K) (± 2 K)	T_1 Relaxation time constant (s) (± 5%)
150.2	2.437
188.1	3.779
212.6	4.517
221.6	4.882
233.0	4.963
246.8	5.891
258.7	6.297
291.1	7.488

Supplementary Table 6.3.4. T_1 relaxation time constant at various temperature increments for compound **2**.

Temperature (K) (± 2 K)	T_1 Relaxation time constant (s) (± 5%)
157.8	1.869
184.8	2.785
212.6	3.510
222.2	4.004
233.8	4.292
254.1	4.502
268.8	5.204
291.1	6.079

Supplementary Table 6.3.5. T_1 relaxation time constant at various temperature increments for compound **3**.

Temperature (K) (± 2 K)	T_1 Relaxation time constant (s) (± 5%)
153.6	1.308
188.8	2.496
208.9	2.952
222.8	3.220
234.7	3.629
247.9	3.995
257.4	4.360
297.2	5.223

Supplementary Table 6.3.6. T_1 relaxation time constant at various temperature increments for compound **4**.

Temperature (K) (± 2 K)	T_1 Relaxation time constant (s) (± 5%)
155.9	1.203
156.7	1.173
183.5	1.954
212.6	2.865
221.1	3.242
235.0	3.334
248.2	3.865
259.3	4.265
296.0	5.505

Supplementary Table 6.3.7. T_1 relaxation time constant at various temperature increments for compound **5**.

Temperature (K) (± 2 K)	T_1 Relaxation time constant (s) (± 5%)
157.8	0.629
192.4	1.272
216.0	1.770
226.4	2.070
237.6	2.301
248.7	2.597
261.6	2.925
294.2	3.643

Supplementary Table 6.3.8. T_1 relaxation time constant at various temperature increments for compound **6**.

Temperature (K) (± 2 K)	T_1 Relaxation time constant (s) (± 5%)
157.1	0.099
193.7	0.267
213.2	0.410
226.1	0.575
238.1	0.646
251.4	0.744
264.0	0.976
290.6	1.261

Supplementary Table 6.3.9. T_1 relaxation time constant at various temperature increments for compound **7**.

Temperature (K) (± 2)	T_1 Relaxation time constant (s) (± 5%)
157.8	0.074
191.1	0.169
212.0	0.256
223.1	0.301
235.6	0.401
249.0	0.473
262.2	0.557
292.1	0.813

Supplementary Table 6.3.10. T_1 relaxation time constant at various temperature increments for compound **8**.

Temperature (K) (± 2)	T_1 Relaxation time constant (s) (± 5%)
159.3	0.0049
167.8	0.0033
172.4	0.0026
176.2	0.0023
181.1	0.0021
188.1	0.0021
193.1	0.0023
199.2	0.0026
213.8	0.0043
225.5	0.0059
235.3	0.0082
249.5	0.0117
259.5	0.0169
295.7	0.0381

3.0 – Computational Support

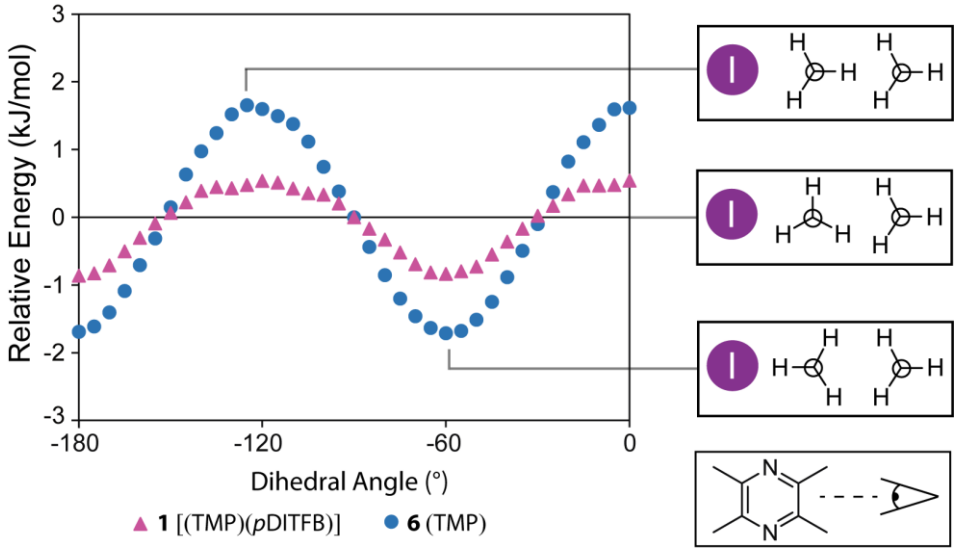

Supplementary Figure 6.3.6. DFT-calculated relative energy as a function of the methyl group dihedral angle (H-C-C-C). The blue circles denote pure TMP (**6**), whereas the magenta triangles denote the cocrystals featuring *p*DITFB (**1**). A diagram showing the orientation of both methyl groups at the energy maximum, zero-point, and minimum is shown on the right. A depiction showing the perspective in the diagram is shown on the bottom right. The rotational energy barrier of **6** is 3.34 kJ mol^{-1}, whereas the rotation energy barrier of **1** is of 1.39 kJ mol^{-1} for an overall energy reduction of 58%.

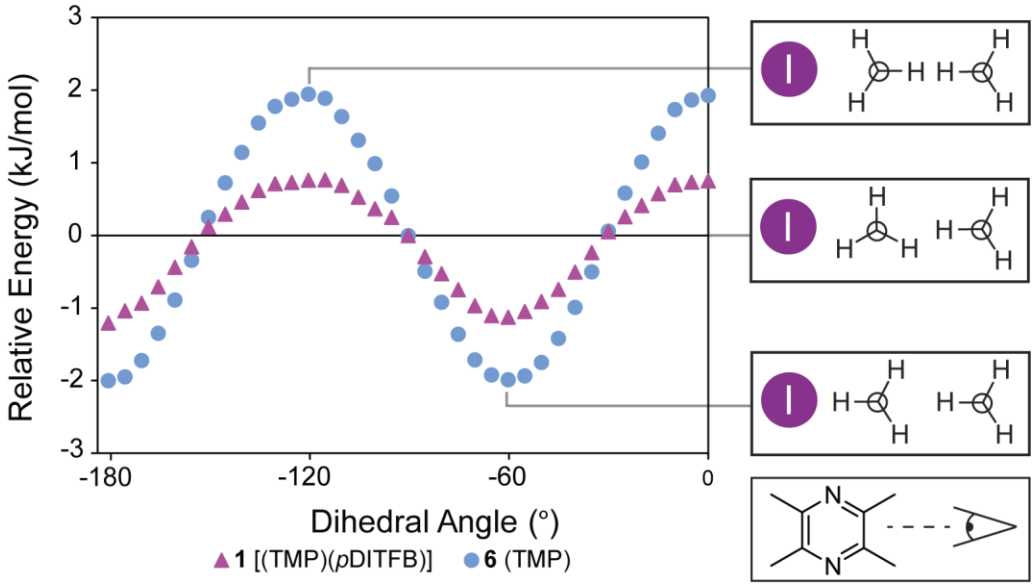

Supplementary Figure 6.3.7. DFT-calculated relative energy as a function of the methyl group dihedral angle (H-C-C-C). The blue circles denote pure TMP (**6**), whereas the magenta triangles denote the cocrystals featuring *p*DITFB (**1**). A diagram showing the orientation of both methyl groups at the energy maximum, zero-point, and minimum is shown on the right. A depiction showing the perspective in the diagram is shown on the bottom right. The calculations shown in Supplementary Figure 6.3.7 are the same as in Supplementary Figure 6.3.6 but with the second methyl group reoriented. The rotational energy barrier of **6** in this conformation is 3.95 kJ mol^{-1}, whereas the rotation energy barrier of **1** in this conformation is of 1.97 kJ mol^{-1} for an overall energy reduction factor of 50%.

3.1 – Calculated Molecular Electrostatic Potential Surface

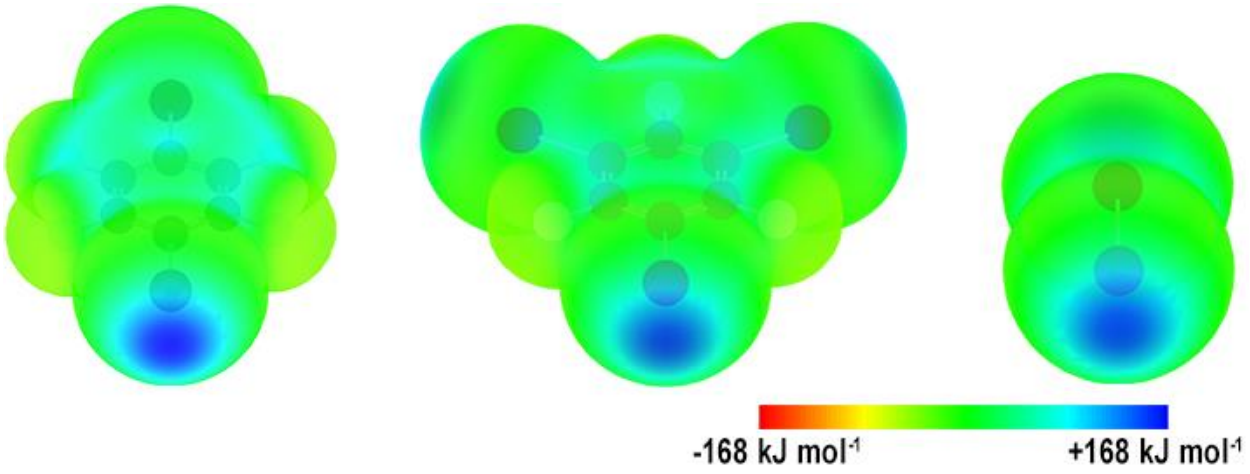

Supplementary Figure 6.3.8. Calculated molecular electrostatic potential surface generated at 0.002 e a.u.$^{-1}$ of 1,4-diiodotetrafluorobenzene (*p*DITFB, 168 kJ mol^{-1}), 1,3,5-trifluoro-2,4,6-triiodobenzene (*sym*TITFB, 162 kJ mol^{-1}), and iodine (I_2, 155 kJ mol^{-1}). The positive region in blue corresponds to the σ-hole.

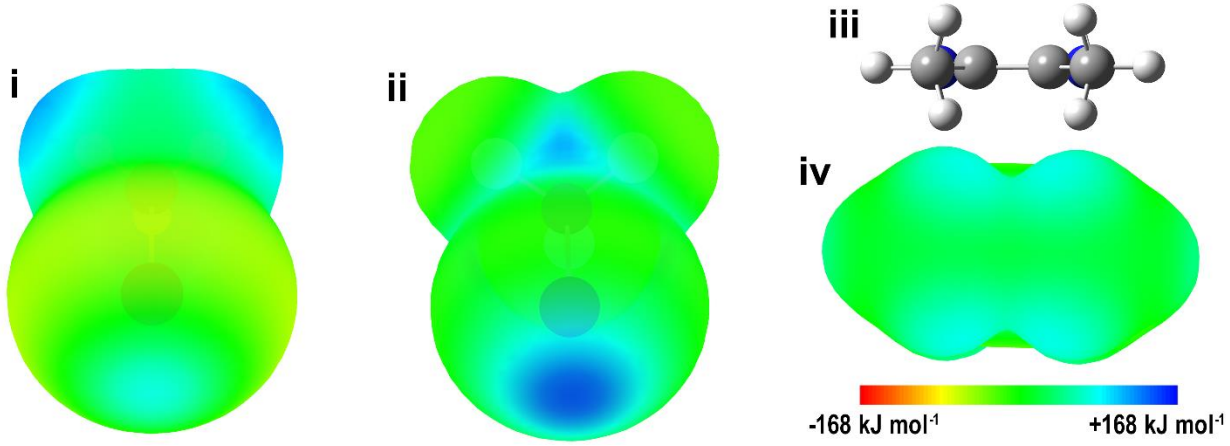

Supplementary Figure 6.3.9. Calculated molecular electrostatic potential surface generated at 0.002 e a.u.$^{-1}$ of (i) iodomethane (76.6 kJ mol^{-1}), (ii) trifluoroiodomethane (right, 149.7 kJ mol^{-1}), and (iv) 2,3,5,6-tetramethylpyrazine. The diagram in (iii) shows the orientation of the 2,3,5,6-tetramethylpyrazine molecule in iv. The positive region of the iodine atom in blue corresponds to the σ-hole.

4.0 - Powder X-ray Diffraction.

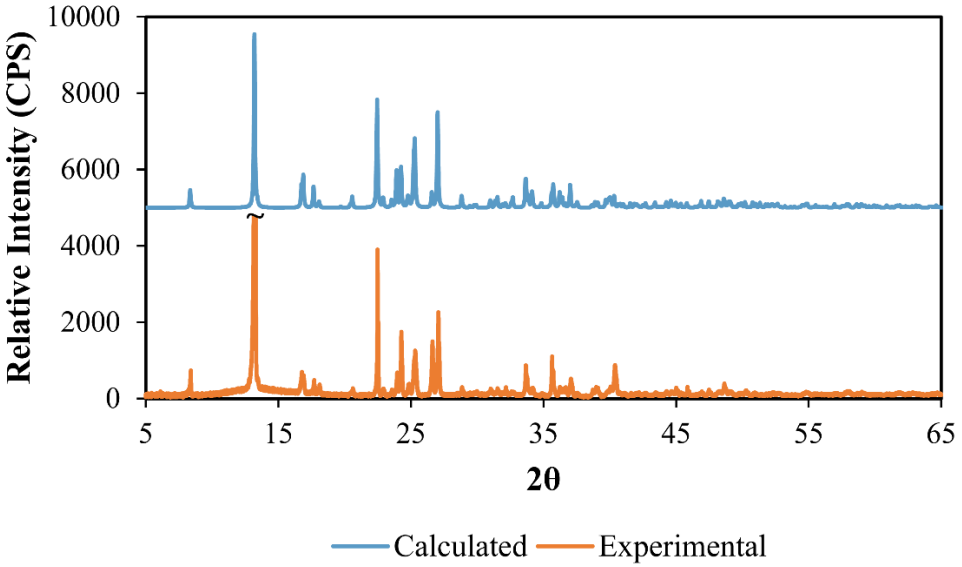

Supplementary Figure 6.3.10. Experimental and calculated powder X-ray diffractogram of compound **1** [(2,3,5,6-tetramethylpyrazine)(1,4-diiodotetrafluorobenzene)]. The powder X-ray was acquired on a PANalytical Empyrean using the same acquisition parameters. Baseline correction was implemented. The tilde over the diffraction at 13º indicates that it was cut for proper scaling.

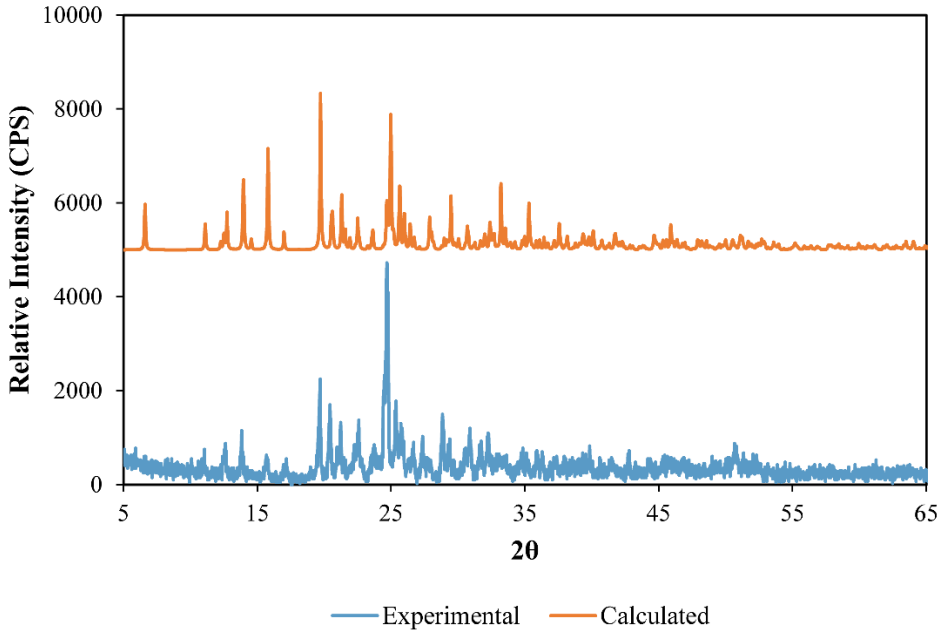

Supplementary Figure 6.3.11. Experimental and calculated powder X-ray diffractogram of compound **2** [(2,3,5,6-tetramethylpyrazine)(1,3,5-trifluoro-2,4,6-triiodobenzene)].

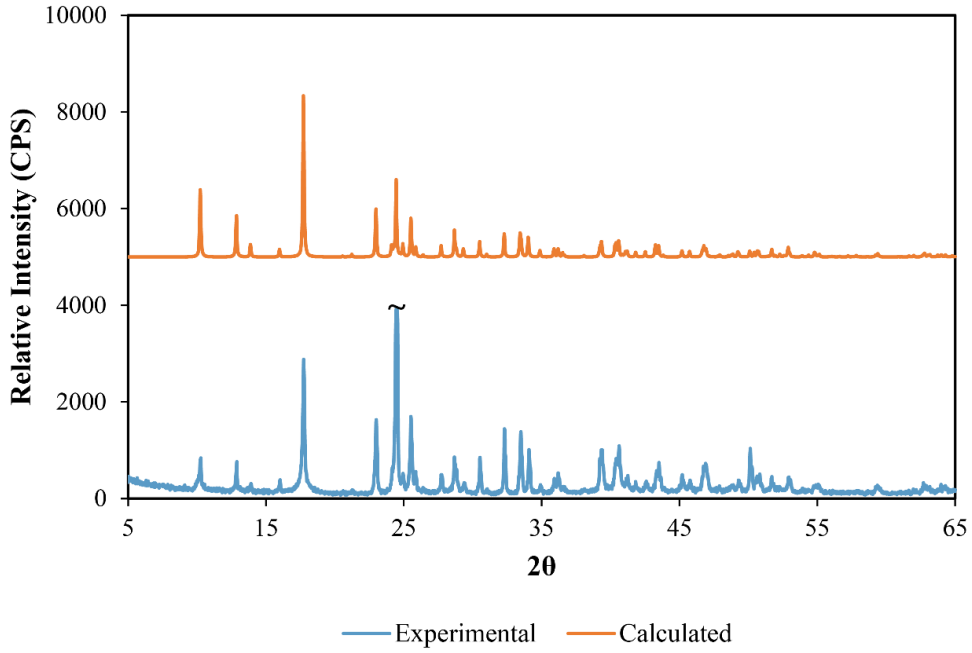

Supplementary Figure 6.3.12. Experimental and calculated powder X-ray diffractogram of compound **3** [(2,3,5,6-tetramethylpyrazine)(iodine)]. The tilde over the diffraction at 24º indicates that it was cut for proper scaling.

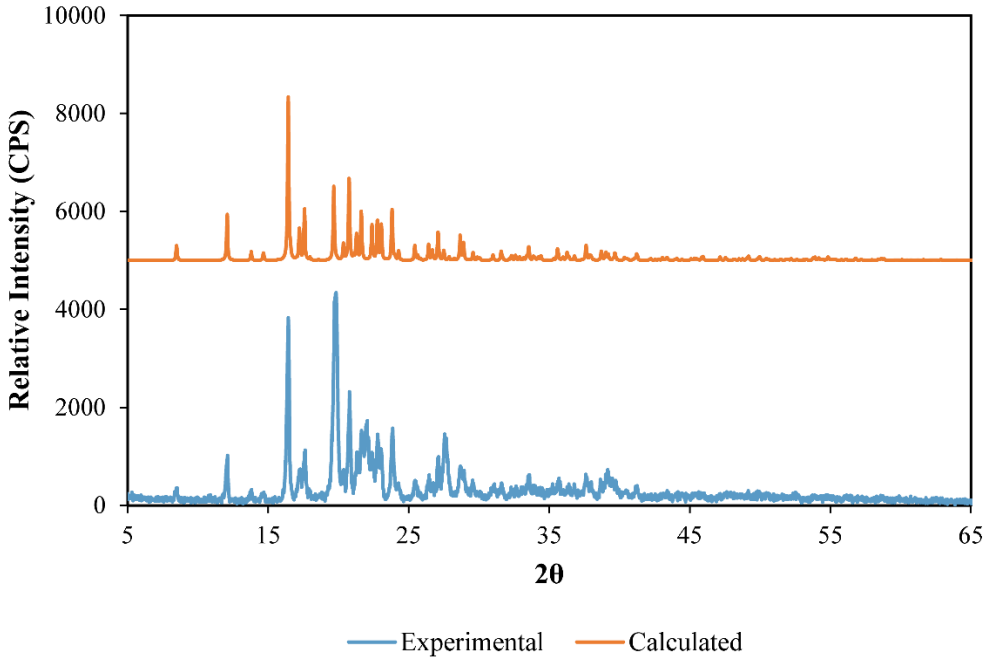

Supplementary Figure 6.3.13. Experimental and calculated powder X-ray diffractogram of compound **4** [(2,3,5,6-tetramethylpyrazine)(1,4-cyclohexanedicarboxylic acid)].

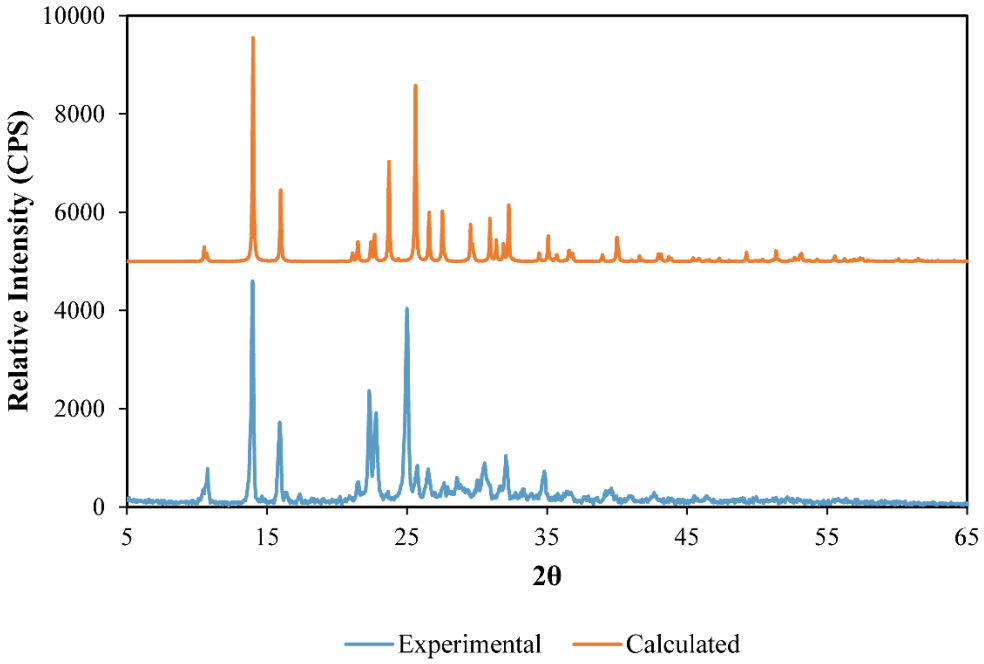

Supplementary Figure 6.3.14. Experimental and calculated powder X-ray diffractogram of compound **5** [(2,3,5,6-tetramethylpyrazine)(oxalic acid)].

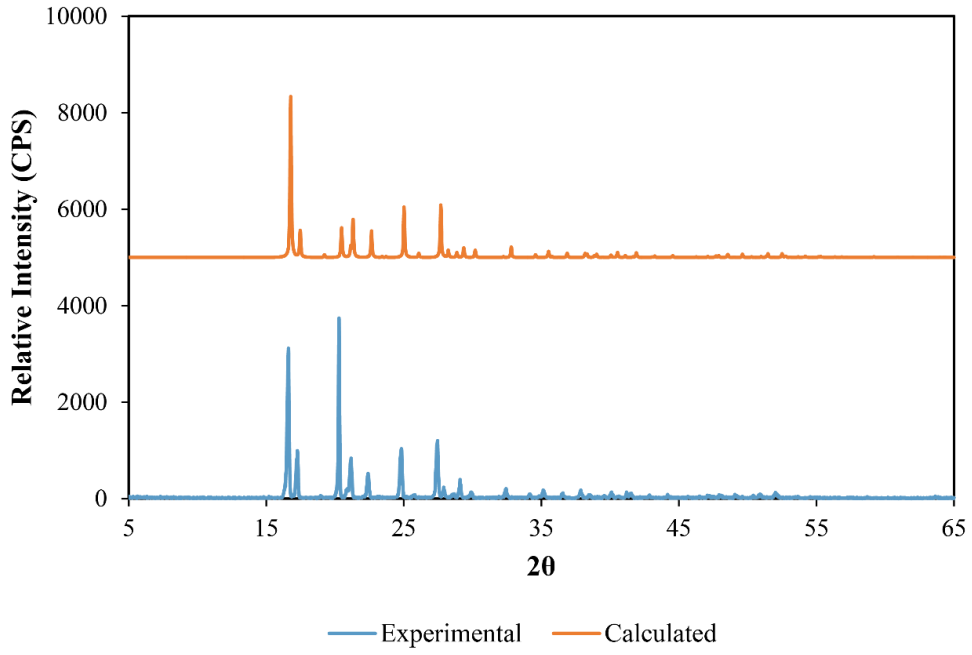

Supplementary Figure 6.3.15. Experimental and calculated powder X-ray diffractogram of compound **6** [2,3,5,6-tetramethylpyrazine].

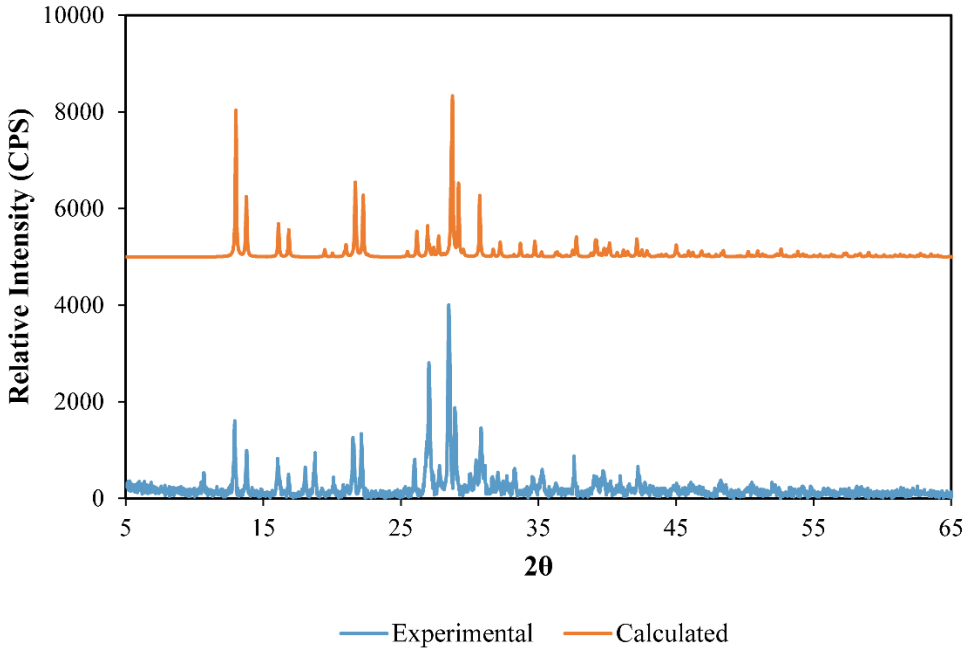

Supplementary Figure 6.3.16. Experimental and calculated powder X-ray diffractogram of compound **7** [2,3,5,6-tetramethylpyrazinium hydrochloride].

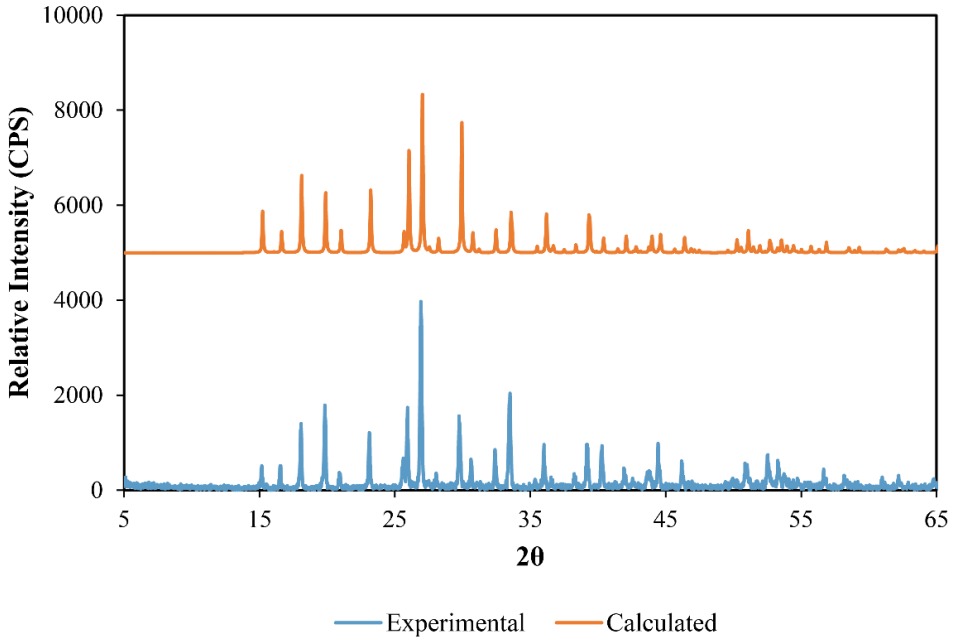

Supplementary Figure 6.3.17. Experimental and calculated powder X-ray diffractogram of compound **8** [2,3,5,6-tetramethylpyrazinium hydrobromide].

Supplementary References.

[1] Vold, R.L. & Hoatson, G.L. Effects of jump dynamics on solid state nuclear magnetic resonance line shapes and spin relaxation times. *J. Magn. Reson.* **198**, 57-72 (2009).

[2] ADF2017, SCM, Theoretical Chemistry, Vrije Universiteit, Amsterdam, The Netherlands.